THE PHYSICAL REVIEW

VOLUME 93 Second Series NUMBER 4

FEBRUARY 15, 1954

Published for the

AMERICAN PHYSICAL SOCIETY

by the

AMERICAN INSTITUTE OF PHYSICS

Incorporated

LANCASTER, PA., AND NEW YORK, N. Y.

A journal of

Published by the American Institute of
for the

AMERICAN PHYSICAL SO

Officers

President

H. A. Barnes
Cornell University
Ithaca, New York

Vice-President

R. T. Birge
University of California,
Berkeley, California

Secretary

K. K. Darrow
Bell Telephone Laboratories
Office:
Columbia University
New York 27, New York

Treasurer

G. B. Pegram
Columbia University
New York 27, New York

Local Secretary
for the Pacific Coast

J. Kaplan
University of California
Angeles
Los Angeles, California

Managing Editor

S. A. Goudsmit
Brookhaven National Labo
Upton, Long Island
New York

The Physical R
Entered as second-class mat
Acceptance for mailing at special rate

THE
PHYSICAL REVIEW

A journal of experimental and theoretical physics established by E. L. Nichols in 1893

SECOND SERIES, VOL. 93, NO. 4 FEBRUARY 15, 1954

The Thickness of the Helium Film

LOTHAR MEYER
Institute for the Study of Metals, University of Chicago, Chicago, Illinois
(Received November 11, 1953)

It is suggested that the change in thickness of the helium film at the λ point is not caused by any essential change in the thermodynamic relation between film thickness, pressure, and temperature. It can be a result of the onset of superfluidity below the λ point which causes a great change in the rate of approach to equilibrium and consequently of the average of the film thickness during the experimental fluctuation of pressure and temperature.

THE thickness of the helium film in contact with bulk liquid has usually been measured by using a vertically oriented specimen hanging in the vapor space and touching the liquid at its lower end.[1] It has been found that the thickness of the film is markedly different above and below the λ point, changing from a thickness of 10–15 layers above the λ point to values an order of magnitude higher at temperatures below the λ point, this change occurring within a temperature region of a few thousandths of a degree, as the λ point is crossed.

This abrupt change of thickness under saturation conditions means that at constant *thickness* the equilibrium pressure of the vapor in contact with the film must change sharply at the λ point. However, thermodynamics puts rather sharp limitations on this change.[2] The equilibrium pressure of this one-component system is a measure of the free energy, which cannot change in this manner; therefore, some other explanation must be sought.

It is the purpose of this note to point out a mechanism to resolve this apparent paradox.

The adsorption isotherm of helium and of other simple gases goes asymptotically to infinity—at least mathematically—as the equilibrium pressure P over the film approaches P_0, the vapor pressure of the bulk liquid. Theoretical considerations by Frenkel,[3] Halsey,[4] Hill,[5] and McMillan and Teller[6] have shown that at high saturations the isotherms should have the form

$$n^3=\frac{k}{\ln(P/P_0)}, \tag{1}$$

where n is the number of adsorbed layers and k is a constant. Bowers[7] has shown that Eq. (1) represents his data quite well for the adsorption of N_2, A, O_2, and He at high saturations (P/P_0~0.70 to 0.99). For a given adsorption system the constant k is a function of temperature, and for helium is found to lie between 15 and 25 in the neighborhood of the λ point.

In Table I is given for helium the number of adsorbed layers in films at four values of the saturation P/P_0 between 0.9900 and 1.0000, as calculated from Eq. (1), with a chosen value of $k=20$. Table I represents, therefore, an extrapolation of the direct measurements of Bowers, using Eq. (1) for the extrapolation.

Even under the most carefully controlled conditions P and T will fluctuate during an experiment, with the result that P/P_0 changes by at least 0.1 percent, and in many cases even by as much as 1 percent, i.e., over the whole range given in Table I.

In such a case the experimentally determined value of the film thickness will correspond to the average of P/P_0 *only* if the changes in thickness occur rapidly enough to follow the fluctuations in P/P_0 without appreciable delay. If, after a disturbance, the approach to equi-

[1] For experimental details and a review of the data, see R. Bowers, Phil. Mag. 44, 1309 (1953).
[2] Compare: Earl Long and Lothar Meyer, Advances in Phys. 2, 1, 1953; Phil. Mag. 44, 788 (1953).
[3] J. Frenkel, *Kinetic Theory of Liquids* (Oxford University Press, London, 1946), p. 332.
[4] G. D. Halsey, J. Chem. Phys. 16, 931 (1948).
[5] T. L. Hill, J. Chem. Phys. 14, 263, 441 (1946); 15, 767 (1947); 17, 580, 668 (1949); *Advances in Catalysis* (Academic Press, Inc., New York, 1952), Vol. IV, p. 225.
[6] W. G. McMillan and E. Teller, J. Chem. Phys. 19, 25 (1951).
[7] R. Bowers, Phil. Mag. 44, 467, 485 (1953).

TABLE I. Thickness of helium film in numbers of statistical layers as a function of the saturation according to Eq. (1).

P/P_0	n
0.9900	12.6
0.9990	27.2
0.9999	58.4
1.0000	∞

librium is slow compared to the period of the fluctuations, the observed film thickness can deviate considerably from the value which corresponds to the average P/P_0 during the experiment.

Equilibrium between a condensed phase and its vapor is usually established extremely fast by evaporation and condensation. In the case of helium, the kinetic flux vapor film is $\sim$1 g/cm^2/sec (reference 1), whereas less than 10^{-8} g/cm^2 are sufficient to change the thickness by one layer. However, Picus[8] has pointed out that for helium films this mechanism is inhibited because of the relatively high heat of vaporization. The heat capacity of the film and substrate system is so small that any change of film thickness by condensation or evaporation would lead to such strong local heating or cooling, respectively, that the process is stopped immediately. It can proceed only at a rate such that the heat of vaporization is dissipated (or provided). Above the λ point, this is a very slow process indeed.[9]

It may safely be assumed that above the λ point the approach to equilibrium between film and vapor is sufficiently slow to allow a considerable lag between the fluctuations in P/P_0 and the resulting changes in film thickness; e.g., if P/P_0 was initially low, and is increasing, the number of adsorbed layers will increase only with considerable delay. If, however, P/P_0 drops from a temporarily high value to a lower saturation, the film can rid itself of the excess fluid comparatively fast. Bulk liquid is formed which simply runs off the vertical walls, eventually forming drops. This drop formation has been observed by Burge and Jackson[10] and by Ham and Jackson[11] even below the λ point.

[8] G. S. Picus, thesis, University of Chicago, 1953 (unpublished).

[9] Bowers (reference 1) observed that even below the λ point the approach to equilibrium between film thickness and pressure, after a change of pressure, required minutes in his geometry, and was roughly proportional to the film flow rate; this is consistent with the argument, since below the λ point the heat transport which governs the rate of condensation or evaporation is determined by the superfluid motion of the film.

[10] E. J. Burge and L. C. Jackson, Proc. Roy. Soc. (London) **A205**, 270 (1951).

[11] A. C. Ham and L. C. Jackson, Phil. Mag. **44**, 214 (1953).

Since, according to these arguments, the film thickness can decrease more rapidly than it can increase, the average observed thickness will, therefore, be smaller than that which corresponds to the average of P/P_0 during the experiment, and may even be expected to be rather near to that corresponding to the lowest value of P/P_0 reached during the fluctuations. The observed values of 10–25 layers are consistent with this interpretation.

The situation is radically changed as soon as the temperature is lowered below the λ point. In this region the well-known superfluidity of the film provides a new and fast mechanism for changing the film thickness, which can now increase about as fast as it can decrease, because superfluid film can run up from the reservoir of bulk liquid. The approach to equilibrium by evaporation and condensation is enhanced to the same degree as heat transport in the film is provided by superfluid flow.[12]

The asymmetry in the speed with which the film thickness can follow fluctuations in P/P_0 is therefore removed below the λ point; consequently, the average thickness must move from the low values found above the λ point to values which more nearly correspond to the equilibrium case of $P/P_0=1$, somewhere between 50–∞ layers, according to Table I. (The average film thickness will then be determined by other factors, such as gravity, geometry, etc., not subject to the fluctuation arguments presented here.) In this way the observed film thickness can change by a considerable factor at the λ point, although the thermodynamic relationship between n and P/P_0 remains the same.

The comparatively great differences in the results of different investigators (compare reference 1) may result, at least in part, from the effects described above. The average observed film thickness should depend on the amplitude and period of the fluctuations in temperature and pressure during a given experiment. Since these fluctuations are not easily measured, and actually were never recorded, it seems impossible for the time being to try a quantitative analysis of the discrepancies between the results of different investigators.

Thanks are due E. A. Long and M. H. Cohen for criticism and advice.

[12] Even below the λ point the thickness of the film is smaller by a factor of about 2.5 when the specimen is not touching the bulk liquid (compare reference 1). This evidence is quite consistent with the picture that the flow of film from the reservoir of bulk liquid is necessary to shift the average observed thickness to the high values observed in the He II region.

The Heat Capacity of Gadolinium from 15 to 355°K*

M. Griffel, R. E. Skochdopole, and F. H. Spedding
Institute for Atomic Research, Iowa State College, Ames, Iowa

(Received August 17, 1953)

The heat capacity of gadolinium has been measured over the temperature range 15 to 355°K. An enhanced heat capacity associated with the ferromagnetic transition was observed, with maximum at 18.6°C. The thermodynamic functions were computed and are tabulated for various temperatures. The results are discussed in connection with theories of ferromagnetism.

INTRODUCTION

EXPERIMENTAL investigation of the enhanced heat capacity associated with ferromagnetic transitions is of interest in considering theories of ferromagnetism. Stoner[1] has on a number of occasions discussed the thermodynamics of ferromagnetism and in his collective electron theory[2] has developed expressions for the magnetic and electronic contributions to the heat capacity. His work has been extended by Wohlfarth.[3]

Statistical theories by Firgau,[4] Takagi,[5] and Weiss[6] based on the Ising model also lead to expressions for the heat capacity and predict the magnitude of its discontinuity at the Curie temperature.

Of the familiar ferromagnetics, Ni and Fe have been most thoroughly investigated while Co has received less attention.[7] In this series there is an increased difficulty of accurate work concomitant with the higher Curie temperatures of both Fe and Co and the phase transformations encountered in the case of Fe. Some work has also been done on ferromagnetic compounds such as MnAs,[8] MnP,[9] and a Heusler alloy.[10]

Gd was the fourth ferromagnetic element to be discovered;[11] it has a Curie temperature of only 18.6°C so that the transition falls in a temperature range that is especially suitable for accurate measurement of the heat capacity. We have made such measurements in the temperature interval of 15 to 355°K and have calculated the various thermodynamic functions.

EXPERIMENTAL

The Gd metal was made by reduction with Ca of the anhydrous fluoride. Procedures for the ion exchange separation of the Gd and for the reduction were previously developed in this laboratory.[12,13] Ten buttons were first made and then recast in a Ta crucible; during this process the excess Ca is distilled off. The Ta is easily stripped or machined off the casting. The final sample, after machining, was in the form of a right circular cylinder 6.58 cm high and 3.67 cm in diameter. It weighed 505.29 g. Spectrographic analysis showed it to contain approximately 0.1 percent Sm, less than 0.1 percent Y, less than 0.3 percent Ta, less than 0.04 percent Ca. Si, Fe, and Mg were present to less than 0.01 percent. Other rare earths were not detected.

The adiabatic calorimeter and experimental techniques were the same as those used in a previous investigation of Th.[14] The 130-ohm heater was of No. 38 constantan wire noninductively wound in a helical groove of a copper shell which fitted tightly into a hole machined along the axis of the Gd cylinder. The latter was suspended as such within the adiabatic shield of the calorimeter. The Pt resistance thermometer was, in turn, slipped into the heater shell. The thermometer has a nominal ice-point resistance of 25 ohms (which was checked just prior to its use) and was calibrated for us by the National Bureau of Standards. A weighed amount of Apiezon T grease was used to insure good thermal contact; this grease may be taken to a higher temperature than can Lubriseal before melting occurs. Leads from the thermometer and from the heater were wrapped around a small ring which fitted into a reentrant well directly beneath the thermometer; this ring was held to the Gd by small screws.

The heat capacity of the Gd was obtained by subtraction of the heat capacity of the heater-thermometer core and other small parts (such as the ring and the small blocks holding the thermocouples) from the heat capacity of the complete assembly. For this auxiliary determination the heater-thermometer core and other parts were fitted into a thin copper shell having the same inside dimensions as the well in the gadolinium

* Contribution No. 284 from the Institute for Atomic Research and Department of Chemistry, Iowa State College, Ames, Iowa. Work was performed in the Ames Laboratory of the U. S. Atomic Energy Commission.

[1] E. C. Stoner, Phil. Mag. **22**, 81 (1936); Trans. Roy. Soc. (London) **A235**, 165 (1936).

[2] E. C. Stoner, Proc. Roy. Soc. (London) **A169**, 339 (1939).

[3] E. P. Wohlfarth, Revs. Modern Phys. **25**, 211 (1953). This review includes references to relevant previous work.

[4] U. Firgau, Ann. Physik **40**, 295 (1941).

[5] Y. Takagi, Proc. Phys. Math. Soc. Japan **23**, 553 (1941).

[6] P. R. Weiss, Phys. Rev. **74**, 1493 (1948).

[7] K. K. Kelley, Bureau of Mines Bulletin 476 (U. S. Government Printing Office, Washington, D. C., 1949), presents a comprehensive bibliography. The most accurate work on nickel is that of C. Sykes and H. Wilkinson, Proc. Phys. Soc. (London) **50**, 834 (1938).

[8] L. F. Bates, Proc. Roy. Soc. (London) **A117**, 681 (1928).

[9] B. G. Whitmore, Phil. Mag. **7**, 125 (1929).

[10] W. Sucksmith and H. H. Potter, Proc. Roy. Soc. (London) **A112**, 157 (1926).

[11] Urbain, Weiss, and Trombe, Compt. rend. **200**, 2132 (1935).

[12] F. H. Spedding *et al.*, J. Am. Chem. Soc. **69**, 2812 (1947).

[13] F. H. Spedding and A. H. Daane, J. Am. Chem. Soc. **74**, 2783 (1952).

[14] M. Griffel and R. E. Skochdopole, J. Am. Chem. Soc. **75**, 5250 (1953).

TABLE I. Atomic heat capacity of gadolinium in cal deg^{-1} (g atom)$^{-1}$ (experimental points).[a] Atomic weight = 156.9. 0°C = 273.16°K.

Mean T °K	Approx. ΔT	C_p	Mean T °K	Approx. ΔT	C_p	Mean T °K	Approx. ΔT	C_p	Mean T °K	Approx. ΔT	C_p
Series I			177.67	4.29	8.258	295.67	2.23	9.216	280.54	2.11	11.858
58.57	4.52	5.268	181.94	4.25	8.324	297.93	2.31	8.878	282.68	2.18	12.119
62.97	4.29	5.542	186.18	4.21	8.394	300.26	2.37	8.637	284.61	1.68	12.384
67.16	4.10	5.792	190.36	4.17	8.466	302.64	2.42	8.457			
71.19	3.97	5.963	194.51	4.13	8.538	305.02	2.46	8.296	286.27	1.65	12.635
75.10	3.85	6.135	198.62	4.09	8.613	307.49	2.49	8.177	287.63	1.08	12.873
78.90	3.75	6.286							288.70	1.06	13.121
			202.69	4.05	8.693	309.97	2.51	8.103	289.74	1.04	13.410
82.59	3.65	6.431	206.72	4.01	8.781	312.49	2.54	8.001	290.66	0.82	13.681
86.21	3.57	6.559	210.87	4.58	8.856	315.03	2.56	7.944	291.47	0.80	13.850
89.75	3.51	6.664	215.42	4.52	8.953	317.59	2.59	7.827			
93.24	3.46	6.754	219.91	4.47	9.048				292.30	0.87	12.782
96.67	3.41	6.835	224.35	4.41	9.164	Series II			293.28	1.08	10.229
100.52	4.29	6.928				15.10	3.59	0.467	294.39	1.15	9.586
			228.74	4.35	9.265	18.00	2.22	0.754	295.85	1.78	9.211
104.78	4.22	7.025	233.08	4.30	9.380	19.96	1.69	0.989	297.95	2.46	8.881
108.97	4.16	7.111	237.36	4.23	9.512	21.51	1.41	1.189	300.43	2.53	8.627
113.10	4.10	7.194	241.57	4.18	9.640	23.45	2.47	1.453			
117.18	4.05	7.278	245.74	4.12	9.759	26.05	2.73	1.814	303.90	4.83	8.368
121.21	4.00	7.347	249.83	4.04	9.945				308.78	4.95	8.132
125.19	3.96	7.413				28.66	2.49	2.177	313.75	5.04	7.970
			253.87	3.97	10.108	31.30	2.79	2.537	318.80	5.12	7.834
128.69	3.92	7.475	257.84	3.90	10.299	34.28	3.16	2.944	323.90	5.18	7.731
132.59	3.88	7.539	266.31	3.73	10.748	37.31	2.91	3.326	329.05	5.22	7.666
136.46	3.85	7.601	273.60	3.56	11.251	40.19	2.85	3.654			
140.28	3.81	7.656	279.62	3.39	11.775	45.10	3.45	4.175	334.24	5.26	7.600
144.08	3.78	7.725	282.95	3.28	12.296				339.47	5.31	7.512
147.84	3.74	7.786				48.43	3.20	4.488	344.74	5.37	7.421
			285.41	1.66	12.516	51.54	3.02	4.752			
151.57	3.71	7.831	287.05	1.63	12.791	54.48	2.87	4.979	Series IV		
155.69	4.51	7.897	288.65	1.58	13.148	62.89	6.44	5.542	337.33	5.15	7.482
160.18	4.46	7.974	290.21	1.54	13.565	Series III			342.43	5.17	7.454
164.62	4.42	8.047	291.75	1.56	13.383	274.43	2.21	11.284	347.54	5.21	7.378
169.01	4.37	8.122	293.54	2.05	10.048	276.44	1.81	11.474	352.70	5.24	7.323
173.36	4.33	8.189				278.42	2.14	11.637	357.82	5.26	7.287

[a] Corrections for slope are included in Table II.

cylinder. Subtraction of the heat capacity of the weighed shell using the data of Giauque and Meads[15] (confirmed by our own redetermination) gave the net heat capacity of the remainder. The thermochemical calorie is taken as 4.1840 absolute j.

In this work there occurred a difficulty which we did not previously encounter in the case of Cu or Th. This difficulty was associated with the poor thermal conductivity of gadolinium. As a result, for our rates of heating (which ranged from 0.15 to 0.45 deg per min), the temperature at the surface of the Gd was not uniform. It therefore was necessary to make an extensive series of investigations of the temperature distribution on the surface during a heating and of the heat leakage modulus between the Gd and the adiabatic shield. This work showed that by optimum placement of the thermocouples the shield could be controlled to the mean surface temperature of the cylinder. Under these conditions the corrections were made negligible; in the most unfavorable circumstances actually encountered the corrections would have been small.

[15] W. F. Giauque and P. F. Meads, J. Am. Chem. Soc. **63**, 1897 (1941).

RESULTS

The results of our measurements are given in Table I and are shown in Fig. 1. The values of C_p in Table II were taken from large smoothed curves. Four series of measurements were made. Series I extended from 58 to 317°K, series II from 15 to 63°K, series III extended from 274 to 345°K and series IV from 337 to 358°K. The experimental points lie within 0.1 percent of the smoothed curve with most points much closer than this. Because of the decreasing sensitivity of the thermometer the accuracy is limited to 1 percent at 20°K; 0.3 percent at 30°K. Above 35°K, the accuracy is believed to be 0.1 percent.

In Table III are listed the entropy, the enthalpy, and the Gibbs function. The extrapolation below 15°K was by means of a Debye function with $\theta = 152$.

DISCUSSION

The quantitative interpretation of heat capacity data for ferromagnetics is still very rudimentary, and experiments of this type may, in time, serve as a guide for further modification of theory. Nevertheless, it seems worthwhile to examine our results in light of existing theoretical schemes. We are interested in comparing (a) the "magnetic" entropy with its theoretical value,

(b) the heat capacity associated with the energy of magnetization with its value predicted from magnetization data alone, and (c) the discontinuity of the heat capacity at the Curie point with theoretical predictions.

The measured heat capacity at constant pressure C_p, regarded as the sum of several contributing factors, may be written as

$$C_p = C_q + C_m + C_e + \delta C. \quad (1)$$

In this equation C_q, C_m, and C_e are, respectively, the lattice, the magnetic, and the electronic contributions; and δC, the dilatation term, is the difference between the heat capacities at constant pressure and constant volume. Such a decomposition, admittedly not rigorous, may form the basis for discussion since to a first approximation the several terms are independent. Both C_m and C_e are electronic in origin but are treated as distinct.

Our results represent qualitatively the same type of behavior evidenced by Fe and Ni. The rise from the low-temperature side starts much earlier than would be expected; the discontinuity has a pronounced knee on the high-temperature side. For an extended range the heat capacity remains appreciably higher than would be expected from a combination of lattice and electronic terms.

We have calculated C_q under the assumption that it may be represented by a single Debye curve. In obtaining a value of Θ_D from our measurements at the lowest temperatures we should take account of the electronic heat capacity. If $C_v \sim C_p = \gamma T + AT^3$, then a plot of C_p/T *vs* T^2 permits evaluation of γ. This method is of use only in the T^3 region and its application to our three lowest points leads to values of γ which are certainly too high. Until accurate measurements at lower temperatures are available, we are constrained to assume that the γ coefficient of Gd is the same as that of La, namely 16×10^{-4}.[16] After subtraction of the electronic contribution from each of the first three entries in Table II, we calculate Θ_D as 152, 150, and 148. We adopt the value 152, which is considerably above the value 132 which may be regarded as characteristic for La.[16] The values of C_q[17] entered in Table II were found by use of the tables of Beattie. The total lattice contribution to the entropy at 360°K is $S_{360}-S_0 = 13.115$ cal/M deg. With our previous assumption as to the coefficient γ and the linearity with T of the electronic heat capacity, we calculate that its contribution to the entropy at 360°K is 0.576 cal/M deg. Hence the sum of the lattice and electronic contributions to the entropy is 13.691 cal/deg g atom.

The dilatation correction is made uncertain by lack of data over the complete range of temperature. The isothermal compressibility κ has been determined by Bridgman;[18] at room temperature it is 25×10^{-7} cm²/kg. The coefficient of volume expansion β from −195°C to 300°C may be inferred from the work of Trombe and Foex[19] which indicates that from −150°C to the Curie temperature the linear expansion coefficient is zero. Hence, application of the usual expression $C_p - C_v$

TABLE II. Heat capacity of gadolinium in cal deg^{-1} (g atom)$^{-1}$. Atomic weight = 156.9. 0°C = 273.16°K.

T°K	C_p	C_q	T°K	C_p	C_q
15.0	0.456	0.435	190	8.458	5.775
20	0.995	0.936	195	8.547	5.784
25	1.664	1.542	200	8.641	5.793
30	2.363	2.151	205	8.738	5.801
35	3.035	2.704	210	8.842	5.808
40	3.632	3.180	215	8.944	5.815
45	4.160	3.579	220	9.051	5.822
50	4.627	3.911	225	9.170	5.828
55	5.012	4.186	230	9.299	5.833
60	5.361	4.414	235	9.440	5.839
65	5.670	4.604	240	9.592	5.844
70	5.922	4.763	245	9.757	5.848
75	6.134	4.902	250	9.953	5.853
80	6.337	5.010	255	10.168	5.857
85	6.520	5.108	260	10.408	5.861
90	6.670	5.191	265	10.673	5.865
95	6.796	5.263	270	10.979	5.868
100	6.914	5.326	275	11.349	5.871
105	7.026	5.381	280	11.802	5.875
110	7.134	5.429	285	12.446	5.878
115	7.235	5.471	290	13.468	5.880
120	7.329	5.509	295	9.402	5.883
125	7.417	5.543	300	8.667	5.886
130	7.499	5.573	305	8.316	5.888
135	7.577	5.601	310	8.086	5.891
140	7.655	5.624	315	7.926	5.893
145	7.734	5.647	320	7.805	5.895
150	7.813	5.667	325	7.715	5.897
155	7.893	5.685	330	7.650	5.899
160	7.973	5.701	335	7.586	5.901
165	8.054	5.716	340	7.499	5.902
170	8.135	5.730	345	7.415	5.904
175	8.215	5.743	350	7.350	5.906
180	8.293	5.754	355	7.309	5.907
185	8.374	5.765			

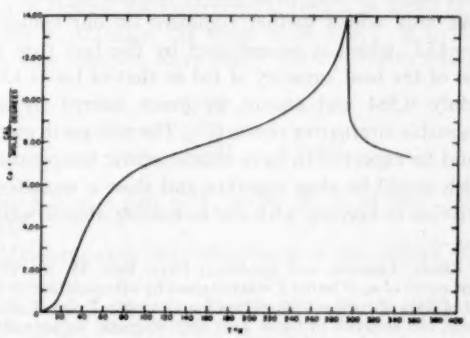

FIG. 1. Heat capacity of gadolinium at constant pressure.

[16] Parkinson, Simon, and Spedding, Proc. Roy. Soc. (London) **A207**, 137 (1951).

[17] J. A. Beattie, J. Math. and Phys. **6**, 1 (1926).

[18] P. W. Bridgman, Proc. Am. Acad. Arts Sci. **82**, 99 (1953).

[19] F. Trombe and M. Foex, Compt. rend. **235**, 42 (1952).

TABLE III. Thermodynamic functions of gadolinium.

T°K	$S-S_0^\circ$ Cal/g atom deg	$(H^\circ-H_0^\circ)/T$ Cal/g atom deg	$-(F^\circ-H_0^\circ)/T$ Cal/g atom deg
15	0.155	0.116	0.039
50	2.797	1.875	0.922
100	6.880	3.948	2.932
150	9.867	5.098	4.769
200	11.770	5.878	5.892
250	13.820	6.545	7.275
293	15.610	7.246	8.364
298.16	15.774	7.284	8.490
300	15.828	7.293	8.535
360	17.238	7.364	9.874

$=T\nu\beta^2/\kappa$ shows that over the range mentioned the correction is negligible. Over the interval of 16 to 100°C, the linear expansion coefficient is constant and approximately equal to 8.3×10^{-6} deg^{-1}. At 25°C, we may thus take $\beta=25\times10^{-6}$ deg^{-1} and $\kappa=25\times10^{-7}$ cm^2/kg and find that C_v is about 0.034 cal/M deg less than C_p. The correction for other temperatures above 25°C may be assumed to vary by the factor $T/298$.

We may now inquire as to the entropy associated with the magnetic heat capacity. In the case of Gd both the saturation moment and the paramagnetic susceptibility variation may be accounted for by the same carrier as in the "ideal" magnetically dilute Gd salts.[20] The spectroscopic state of the trivalent ion is $^8S_{7/2}$, representing a parallel alignment of the seven electrons in the $4f$ shell. Hence, the entropy associated with the complete ordering of the spins is $R\ln8$ or 4.132 cal/M deg. We may neglect the entropy associated with the dilatation, and from the calculations presented above the magnetic entropy at 360°K is 3.547 cal/deg g atom. This is 0.585 below the value $R\ln8$. It should be remarked that even above 360°K there probably remains an appreciable magnetic contribution so that, especially in view of the uncertainties associated with Θ_D and γ, the discrepancy is not disturbing.

In the formal Weiss treatment, which postulates the existence of an internal field of magnitude $N\rho\sigma$, the internal energy per g associated with the intrinsic magnetization is $U=-\frac{1}{2}N\rho\sigma^2$. Assuming a constant density, the corresponding heat capacity is $C_m=-\frac{1}{2}AN\rho/J\times(\partial\sigma^2/\partial T)$. In these equations, σ is the intrinsic magnetization per g at temperature T, ρ is the density, N is the Weiss molecular field coefficient (not necessarily independent of T), J is the Joule mechanical equivalent of heat, and A is the atomic weight. From measurements of the paramagnetic susceptibility above the Curie temperature, it is possible to estimate $N\rho$. With the additional knowledge of $\partial\sigma^2/\partial T$ at various temperatures, it is then possible to evaluate the corresponding heat capacities and compare them with our more directly obtained values.

Kriessman and McGuire[21] have reported that the molar paramagnetic susceptibility may be represented as $\chi_m=8.21/T-25.5$, T being in °C. The Curie constant per g is then 0.0524, and the effective magneton number $\mu_{eff}=(3\kappa C_m/\beta^2N)^{\frac{1}{2}}$ is 8.15, corresponding closely to a spin of 7/2. On the basis of the Weiss theory the g susceptibility is given by the expression $\chi=C/(T-\theta)=C/(T-N\rho C)$, so that $N\rho$ is 5.70×10^3. Values of $\partial\sigma^2/\partial T$ in the range from 8 to 14°C may be estimated from the work of Elliott, Legvold, and Spedding.[22] From their curve we estimate that $\partial\sigma^2/\partial T$ at 8, 10, and 14°C is, respectively, -230, -290, and -507, so that from the equation $C_m=-(AN\rho/2J)(\partial\sigma^2/\partial T)$ we would predict the magnetic heat capacities 4.9_1, 6.1_7, and 10.8 cal/M deg. These may be compared with 5.60, 5.85, and 6.46 on the basis of Eq. (1).

The next item to be considered is the discontinuity in the heat capacity. Since the initially abrupt drop on the high-temperature side glides into a more gradual decrease, it is customary to extrapolate back from that side and take the discontinuity as the difference between the maximum heat capacity and the extrapolated point. Such a procedure yields for the discontinuity a value of about 7 cal/M deg, which is very similar to that found in the case of Fe, and about 3.5 times that found for Ni. But whereas the Weiss theory[23] comes close to agreement with experiment for both Ni and Fe, there is no such agreement for Gd. The same must be said for the statistical theories of Firgau,[4] Takagi,[5] and Weiss[6] which are based on the Ising model and are essentially equivalent. For simple cubic, body-centered cubic, or face-centered cubic lattices, the discontinuity in the heat capacity is found to be

$$\Delta C=\frac{3R}{8}\frac{Z^2(Z-2)}{Z-1}\left(\ln\frac{Z}{Z-2}\right)^2 \text{ cal/M deg},$$

where Z is the number of nearest neighbors. We may assume that the value would not be essentially different for hexagonal closest packing. For $Z=12$, the discontinuity is 3.24 cal/M deg, assigning one spin per atom. There seems no way to fit this to the case of Gd.

We may add a further comment on our choice of $\Theta_D=152°$ which is necessitated by the fact that the ratio of the heat capacity of Gd to that of La at 15°K is only 0.584 and cannot be much altered by any reasonable alternative choice of γ. The rare-earth metals would be expected to have characteristic temperatures which would be close together and show a monatomic variation in keeping with the increasing atomic weight

[20] L. Pauling, Proc. Natl. Acad. Sci. U. S. **39**, 551 (1953).
[21] C. J. Kriessman and T. R. McGuire, Phys. Rev. **90**, 374 (1953).
[22] Elliott, Legvold, and Spedding, Phys. Rev. **91**, 28 (1953). Their curve of $\sigma_0\gamma^3$ *versus* T was obtained by extrapolation to zero field of lines of constant magnetization in an $H-T$ plot. Unfortunately, the behavior of Gd is such that magnetic isothermals do not have a lengthy straight-line portion close to zero field such as is characteristic of Ni. This factor introduces some uncertainty into the extrapolation.
[23] For development of the equations see R. Becker and W. Döring, *Ferromagnetismus* (Julius Springer, Berlin, 1939), p. 67.

and the generally decreasing atomic volume. We may speculate as to whether the tighter binding in the case of Gd is primarily to be associated with its ferromagnetism. A determination of the characteristic temperature of Lu will thus be of interest.

ACKNOWLEDGMENTS

We wish to express our thanks to Dr. Jack Powell for preparing the rare earth salts, to Mr. Karl Gschneidner for preparing the metal, and to Mr. Lloyd Hanson for help with the calculations.

PHYSICAL REVIEW VOLUME 93, NUMBER 4 FEBRUARY 15, 1954

The Isotope Effect in Superconductivity

JULES DE LAUNAY
Naval Research Laboratory, Washington, D. C.
(Received October 7, 1953)

The isotope effect in superconductors is usually summarized by giving the observed values of β in the equation $M^{\beta}T_c=$constant, where M is the isotopic mass and T_c the superconducting transition temperature. Fröhlich predicted the value $\beta=1/2$, but the measurements in some instances show deviations from this prediction. An explanation of the deviation of β from 1/2 is offered based on an analog of Wien's displacement law applicable to the vibration spectrum of real crystal lattices. The departure of β from the value 1/2 is attributed to the departure of the frequency spectrum from a simple power law. For many superconducting elements, β may be estimated from specific heat data, when such data are available to the desired degree of accuracy. A value of β is calculated for Sn which is in good agreement with some of the experiments. The large value 0.73 observed for Pb is shown to be reasonable. The values of β for the other superconducting elements are discussed. It is concluded that the observed deviations of β from 1/2 are not necessarily in conflict with the theories of Fröhlich and Bardeen.

INTRODUCTION

THE various isotopes of a superconducting element have different transition temperatures T_c. This is the isotope effect discovered simultaneously by Maxwell of the National Bureau of Standards[1] and by Reynolds, Serin, Wright, and Nesbitt of Rutgers University.[2] Shortly after the discovery, the Rutgers group showed that the data of the mercury isotopes could be correlated by the formula $M^{\frac{1}{2}}T_c=$constant, where M is the isotopic mass.[3,4] Since then, it has become customary to represent the data in the form[5]

$$M^{\beta}T_c=\text{constant}, \tag{1}$$

and to express the experimental results in terms of the power β. Actually, the range of M and T_c is so small that one observes more nearly the equivalent relation,

$$\beta=-\frac{MdT_c}{T_cdM}=-\frac{d\log T_c}{d\log M}, \tag{2}$$

arising from a plot of T_c *versus* M, or of $\log T_c$ *versus* $\log M$.

Measurements have been made of the isotope effect for Sn, Pb, Hg, and Tl.[4,6–11] A review of the data to the end of 1952 can be found in an article by Maxwell.[12] The results seem to indicate that β is close to $\frac{1}{2}$ for some metals, with, however, significant departures, particularly for Pb. The observed values of β are shown in Table I taken from Maxwell's review article.[12]

At the time that the data were being collected which led to the discovery of the isotope effect, Fröhlich[13] was developing a theory of superconductivity which attributed the cause of superconductivity to the interaction of the electrons with the phonon field. The theory was developed for the temperature 0°K and led to a threshold magnetic field H_0 proportional to $M^{-\frac{1}{2}}$. From this, one surmises that $T_c\propto M^{-\frac{1}{2}}$ from the fairly well established correlation $H_0\propto T_c$. Thus, one can take Fröhlich's theory as having predicted the isotope effect. Bardeen also proposed a similar theory at about the same time. A review of both theories has been given by Bardeen.[14] Neither theory has been developed to the extent required to include significant departures from the $\frac{1}{2}$ power law.

[1] E. Maxwell, Phys. Rev. **78**, 477 (1950); **79**, 173 (1950).
[2] Reynolds, Serin, Wright, and Nesbitt, Phys. Rev. **78**, 487 (1950).
[3] Serin, Reynolds, and Nesbitt, Phys. Rev. **78**, 813 (1950); **80**, 761 (1950).
[4] Serin, Reynolds, and Nesbitt, Phys. Rev. **84**, 691 (1951).
[5] Herzfeld, Maxwell, Scott, Phys. Rev. **79**, 911 (1950).
[6] E. Maxwell, Phys. Rev. **86**, 735 (1952).
[7] Lock, Pippard, and Shoenberg, Proc. Cambridge Phil. Soc. **47**, 811 (1951).
[8] Reynolds, Serin, and Lohman, Phys. Rev. **86**, 162 (1952).
[9] Allen, Dawton, Bär, Mendelssohn, and Olsen, Nature **166**, 1071 (1950).
[10] M. Olsen, Nature **168**, 245 (1951).
[11] E. Maxwell and O. S. Lutes, Jr., Phys. Rev. **86**, 649 (1952).
[12] E. Maxwell, Phys. Today **5**, No. 12, 14 (1952).
[13] H. Fröhlich, Phys. Rev. **79**, 845 (1950).
[14] J. Bardeen, Revs. Modern Phys. **23**, 261 (1951).

TABLE I. The observed values of p of Eq. (2).

Element	p	Source
Sn	0.505±0.019	Maxwell[a]
Sn	0.462±0.014	Lock, Pippard, and Shoenberg[b]
Sn	0.46±0.02	Serin, Reynolds, and Lohman[c]
Sn	0.50	Olsen, Bär, and Mendelssohn[d]
Pb	0.73±0.05	Olsen[e]
Hg	0.504	Reynolds, Serin, and Nesbitt[f]
Tl	0.50±0.05	Maxwell[g]

[a] See reference 6.
[b] See reference 7.
[c] See reference 8.
[d] See reference 9.
[e] See reference 10.
[f] See reference 4.
[g] See reference 11.

In this paper, we shall develop an idea already proposed[15] and show how it leads to departures of the power p from the value $\frac{1}{2}$. The discussion here is independent of the theories of Fröhlich and Bardeen, though it may be regarded as supplementing these theories. We are concerned here with the *disappearance* of superconductivity at T_c rather than with its *cause*.

THE CRITICAL TEMPERATURE

The properties of a superconductor change as the temperature rises from 0°K to T_c. In order that these properties be temperature dependent, the electrons must be sensitive to the phonon bath in which they reside. At what the observer calls a "critical temperature T_c," we may say that the electrons find themselves in a "critical phonon field." When the phonon field is less excited than the critical state, the metal is a superconductor; when the field is more excited than the critical state, the metal is a normal conductor. This much follows rather trivially from the experimental facts and elementary notions from the theory of metals.

Now suppose that a given superconductor is at the temperature T_c and imagine that the mass of the atoms is decreased slightly without changing the temperature. Then, from lattice dynamics, the phonon field is less excited than the critical state and the metal is a superconductor. Thus, it is of secondary importance to the electrons that the temperature did not change. To return the phonon field to the critical state, while maintaining the mass at its lower value, heat must be supplied. This increases the temperature to a new T_c, higher than the original value.

The question then is how shall we relate the critical phonon field to T_c. The wavelengths, or more accurately, the propagation vectors, of lattice waves are determined by the lattice geometry and boundary conditions[16] and not by the mass of the isotope. This results in the frequency ν and velocity c being proportional to $M^{-\frac{1}{2}}$ for a given propagation vector. We suspect, too, that it is the propagation vector of lattice waves (and perhaps only the longitudinal component of these waves) which is important in interactions between electrons and lattice waves. Consequently, we shall characterize the state of the phonon field by the energy density $E(\lambda)$ at some *wavelength* λ. We do not know what wavelengths are the most important, so we suppose that it is sufficient to identify the state by the wavelength λ_m at which $E(\lambda)$ is maximum. Beginning with a given temperature T_c, a change in M shifts the peak of $E(\lambda)$. This shift may be restored by a corresponding change in T_c, and thus a generalization of Wien's displacement law applicable to real lattices will be derived. From this we can evaluate p.

THE DISPLACEMENT LAW

It is customary in lattice dynamics to employ the expression[16]

$$E(\nu)d\nu = \text{const}\frac{h\nu g(\nu)d\nu}{e^{h\nu/kT}-1} \tag{3}$$

to derive the atomic heat. The energy of the modes with frequencies between ν and $\nu+d\nu$ is $E(\nu)d\nu$. The distribution of the modes is represented by $g(\nu)$. Transforming from the variable ν to the variable λ in Eq. (3), we obtain

$$E(\lambda)d\lambda = \text{const}\frac{g(c/\lambda)d\lambda}{\lambda^3(e^{hc/kT\lambda}-1)}. \tag{4}$$

Setting the derivative $dE/d\lambda$ equal to zero and using the abbreviations

$$x = h\nu/kT = hc/kT\lambda,$$

and

$$\Lambda = 3-\frac{\lambda\, dg}{g\, d\lambda} = 3+\frac{\nu\, dg}{g\, d\nu} = 3+\frac{d\log g(\nu)}{d\log\nu}, \tag{5}$$

we find the following displacement formula:

$$e^{-x} = 1-x/\Lambda. \tag{6}$$

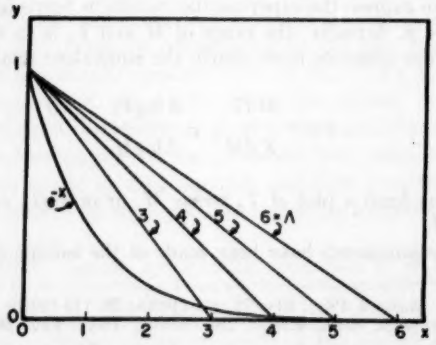

FIG. 1. The intersections of the parametric curves representing Eq. (6) yield the value of x. The straight lines are the plots of $y=1-(x/\Lambda)$ for the indicated value of Λ. It can be seen that for $\Lambda>3$, a good approximation is $x=\Lambda$.

[15] J. de Launay, Phys. Rev. 79, 398 (1950).
[16] See, for example, Charles Kittel, *Introduction to Solid State Physics* (John Wiley and Sons, Inc., New York, 1953).

The displacement law represented by Eq. (6) is more general than that required at the low temperatures at which superconductivity usually occurs. In our domain of interest $g(\nu)$ is an increasing function of ν so that Λ is greater than 3. If we write Eq. (6) in the parametric form

$$y=\epsilon^{-x}, \quad y=1-x/\Lambda$$

and plot the system of curves for $\Lambda \gtrsim 3$ shown in Fig. 1 we see that the solution of the transcendental equation is

$$x\sim\Lambda. \tag{7}$$

Formula (7) gives a value of x too large by the amount $\sim\Lambda\epsilon^{-\Lambda}$. In most cases this correction is negligible. Using Eq. (5), Eq. (7) can be written explicitly as

$$T=\frac{hc}{k\lambda_m}\Lambda^{-1}=\frac{hc}{k\lambda_m}\left(3+\frac{d\log g}{d\log\nu}\right)^{-1}. \tag{8}$$

THE ISOTOPE LAW

Let us formulate the isotope law for the special case in which $g(\nu)$ is an increasing function of ν. From Eqs. (2) and (8) (with $T=T_c$), we obtain for p:

$$p=-\frac{M}{T}\frac{dT}{dM}=-\frac{M}{T}\frac{d}{dM}\left[\left(\frac{hc}{k\lambda_m}\right)\left(3+\frac{d\log g}{d\log\nu}\right)^{-1}\right].$$

Since c varies as $M^{-\frac{1}{2}}$, we can differentiate c with respect to M, where it occurs explicitly, and obtain

$$p=\frac{1}{2}+M\frac{d}{dM}\log\left(3+\frac{d\log g}{d\log\nu}\right).$$

Now we also have $\nu\propto M^{-\frac{1}{2}}$. Thus, we can transform the last expression to the more convenient form

$$p=\frac{1}{2}-\frac{\nu}{2}\frac{d}{d\nu}\log\left(3+\frac{d\log g}{d\log\nu}\right). \tag{9}$$

An alternative form of the isotope law which we shall find useful is [see Eqs. (5) and (9)]:

$$p=\frac{1}{2}+\frac{M}{\Lambda}\frac{d\Lambda}{dM}. \tag{10}$$

LATTICE VIBRATIONS AND THE ISOTOPE LAW

Not very much is known about $g(\nu)$ for real monatomic lattices. The only adequate calculation of a lattice spectrum to which we can refer, at the present time, is that of Leighton for the face-centered cubic monatomic lattice.[17] Figure 2 shows $g(\nu)$ of each of the three branches (broken curves) and the sum (continuous curve), for a special choice of the elastic constants. The general character of the curve for $g(\nu)$ does not depend, however, on these constants. We do not expect,

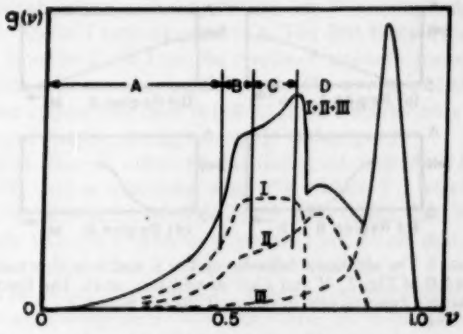

FIG. 2. A plot of $g(\nu)$ *vs* ν taken from Leighton (reference 17). The unit of ν here is its maximum value. The broken curves show the three branches I, II, III. The solid curve is the sum of these branches.

either, that the qualitative properties of the curve will change greatly from one crystal class to the next. So we shall assume that the qualitative aspects of $g(\nu)$ presented in Fig. 2 are typical of the metallic elements.

Figure 2 shows the spectrum divided roughly into four regions: A, B, C, D. In regions A, B, and C, $g(\nu)$ is an increasing function of ν, but in the remainder D, the function $g(\nu)$ decreases on occasion. So our comments must be limited to regions A, B, and C. Fortunately, the superconducting elements all have dominant wavelengths at T_c confined to these regions. It will help the discussion if we write $g(\nu)$ in the form

$$g(\nu)=\text{const}\nu^{N(\nu)}. \tag{11}$$

The value of $N(\nu)$ is 2 for a simple Debye spectrum. For a real lattice, $N(\nu)$ is a variable approaching the value 2 at low frequencies. From the lattice dynamics of face-centered cubic crystals the low-frequency end of $g(\nu)$ can be represented by the polynomial

$$g(\nu)=a_1\nu^2+a_2\nu^4+\cdots=\sum_1^n a_n\nu^{2n}, \tag{12}$$

in which all of the coefficients are positive. This has been pointed out by Leighton.[17] Comparing this with Eq. (11), we see that $N(\nu)$ begins with the value 2 near $\nu=0$, and increases steadily, approaching some value between 2 and $2n$. We have labelled this region by A. In the region B, N is decreasing, and decreases more rapidly with increasing ν than it did in region A. In region C, N does not seem to be changing very much, though it is difficult to be certain. Another of Leighton's curves (not shown in Fig. 2) shows the curve in region C concave downward instead of upward.

We shall next examine the qualitative behavior of Λ in regions A and B, and from this, estimate the behavior of p. If N is a constant, then it follows from Eq. (5) that

$$\Lambda=3+N. \tag{13}$$

In this case, Eq. (10) shows that $p=\frac{1}{2}$. In region A,

[17] R. B. Leighton, Revs. Modern Phys. **20**, 165 (1948).

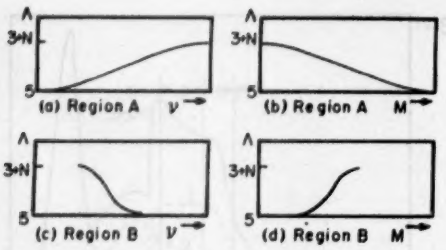

FIG. 3. The schematic behavior of Λ *vs* ν, and Λ *vs* M in regions A and B of Fig. 2. M and ν are in arbitrary units. The function Λ changes more rapidly in region B than in region A.

$N(\nu)$ changes from 2 to some value $N(>2)$. The schematic behavior of Λ as a function of ν is shown in Fig. 3(a). Figure 3(b) shows the schematic behavior of Λ as a function of $M(\nu \propto M^{-1})$. The corresponding behavior of Λ in region B is shown in Fig. 3(c), (d). The behavior of p can now be ascertained. In Fig. 3(b) we see that $d\Lambda/dM$ is negative, while in Fig. 3(d) it is positive. Consequently, from this and Eq. (10), we deduce that when the dominant wavelength falls in region A, then $p<\frac{1}{2}$; and in region B, then $p>\frac{1}{2}$. Furthermore, since $d\Lambda/dM$ can be larger in B than in A, we can expect larger deviations from $\frac{1}{2}$ in B than in A. A schematic representation of p in regions A and B is shown in Fig. 4.

So far, the discussion has been purely qualitative. This has been primarily because of the lack of any really quantitative information concerning the functions $g(\nu)$ for the various superconductors. However, in the region A, which we define as that region in which $g(\nu)$ is described by Eq. (12), we shall make a quantitative calculation of p in terms of quantities obtainable from atomic heat data. Most superconductors have their transition temperature T_c in the Debye T^3 region of atomic heat. The measured atomic heat however, does not fit a T^3 law, even after allowance has been made for the electron contribution. Regarding the Debye characteristic temperature Θ_D as a function of the temperature rather than a strict constant, one obtains from the data curves similar to the one shown in Fig. 5. Now we can calculate both p and Θ_D from the polynomial form of $g(\nu)$. The formulas so obtained enable us to compute p from the atomic heat data.

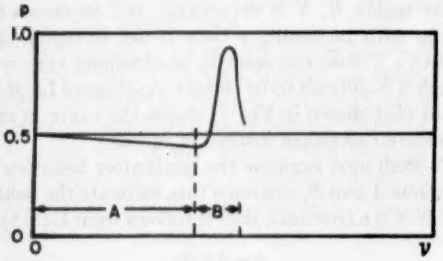

FIG. 4. The schematic behavior of p as a function of the frequency at which the peak of $E(\lambda)$ occurs.

First we compute p by substituting from Eq. (12) into Eq. (9), obtaining

$$p=\frac{1}{2}-\frac{1}{2}\frac{d}{d\nu}\log\Big[\sum_1^n(2n+3)b_n\nu^{2n}/\sum_1^n b_n\nu^{2n}\Big], \quad (14)$$

where b_n is the ratio a_n/a_1. If all coefficients b_n are positive, we see at once that $p<\frac{1}{2}$.

Next we compute the atomic heat by substituting for g in Eq. (3) from Eq. (12), integrating over the range $0\leqslant\nu\leqslant\infty$, and then differentiating with respect to T. The result is

$$C_V=K\sum_1^n b_nB_{n+1}(2\pi)^{2n+2}(k/h)^{2n+2}T^{2n+1}, \quad (15)$$

where K is a constant. The b_n are identical with those in Eq. (14). B_n is the nth Bernoulli number ($B_1=1/6$, $B_2=1/30$, $B_3=1/42$, etc.). From Eq. (15), we easily

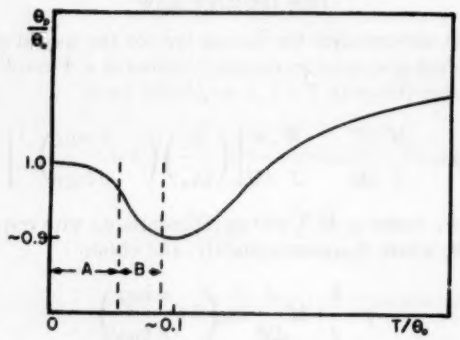

FIG. 5. A plot of Θ_D/Θ_0 *vs* T/Θ_0. The regions A and B correspond qualitatively to those of Fig. 2.

obtain for Θ_D, the relation:

$$\frac{1}{\Theta_D{}^3}=\frac{1}{\Theta_0{}^3}\Big[1+\sum_2^n b_n\frac{B_{n+1}}{B_2}(2\pi)^{2n-2}(kT/h)^{2n-2}\Big]. \quad (16)$$

In the derivation of Eq. (16), we disposed of such constants as K by defining Θ_0 as the value of Θ_D at $T=0°K$. In principle, one determines the coefficients b_n of Eq. (16) by fitting the formula to the results of experimental work presented in the form illustrated in Fig. 5. Then p is determined by the substitution of these values of b_n into Eq. (14).

In many cases, T_c occurs at such a low temperature relative to Θ_0 that only the T^2 term in Eq. (16) need be considered in the polynomial. For these cases, Eq. (16) reduces to

$$\Theta_D=\Theta_0\Big[1-b_2\frac{20\pi^2}{21}\Big(\frac{kT}{h}\Big)^2\Big].$$

Let the symbol θ denote the fraction $(\Theta_0-\Theta_D)/\Theta_0$. It is evident that if b_2 is positive, then θ is positive and

less than unity. We have for θ:

$$\theta = b_2 \frac{20\pi^2}{21}\left(\frac{kT}{h}\right)^2. \tag{17}$$

The corresponding formula for p is

$$p = \frac{1}{2} - \frac{0.4 b_2 \nu^2}{(1+b_2\nu^2)[1+(7/5)b_2\nu^2]}. \tag{18}$$

We now wish to express $b_2\nu^2$ occurring in Eq. (18) in terms of known quantities. Using Eq. (17), we first notice that

$$b_2\nu^2 = \frac{21}{20\pi^2}\left(\frac{h\nu}{kT}\right)^2\theta.$$

Experimental data on atomic heat indicate that, in the range of Eq. (17), $|\theta| < 0.1$ Also the correction to $\frac{1}{2}$ in Eq. (18) is small compared to $\frac{1}{2}$. This permits us to use the approximation $(h\nu/kT) \sim 5$, the value for a Debye spectrum. Consequently, a good approximation to the value of $b_2\nu^2$ is

$$b_2\nu^2 \sim 105\theta/4\pi^2.$$

When this is substituted into Eq. (18), we finally arrive at a simple formula for p in terms of the well-defined quantity θ:

$$p = \frac{1}{2} - \frac{1.06\theta}{(1+2.66\theta)(1+3.72\theta)}. \tag{19}$$

There is some reason to believe that the electrons interact principally with longitudinal waves. An isotropic crystal has a branch of purely longitudinal waves (III of Fig. 2) and two branches of purely transverse waves (I, II, of Fig. 2). A real crystal, however, is anisotropic and all three branches contain waves which are neither longitudinal nor transverse. If the average wave of branches I and II has as much as 10 percent of its amplitude parallel to the propagation vector, then these longitudinal components of the waves dominate those in branch III at low temperatures. If, in addition, the distribution of longitudinal components in branches I and II follows $g(\nu)$ in region A, then formula (19) will still be valid.

COMPARISON WITH EXPERIMENT

The data of Keesom and van Laer for Sn give[18]

$$\Theta_D = \Theta_0(1-0.0033T^2).$$

From this we obtain $\theta = 0.0455$ and $p = 0.463$. A 10 percent error in the coefficient of T^2 corresponds to only about 2 percent error in p. The first three data for Sn listed in Table I are the results of magnetic measurements whereas the fourth is not. The average of these three compatible data is 0.475. If we consider only the second datum, the agreement is rather good.

The $\Theta_D - T$ curve of Pb shows an inflection near 5.5°K and a minimum near 9°K. Thus T_c, which is 7.2°K, falls in region B of Fig. 5. This shows that Pb is likely to have a value of p greater than $\frac{1}{2}$ and that the rather large value 0.73 is entirely feasible.

The atomic heat data for mercury and thallium are not sufficiently well known to enable us to compute p. However, since $T_c/\Theta_0 \sim 0.04$ for Hg, T_c is near the inflection point near which the regions A and B join. Thus the value of p for Hg should be almost $\frac{1}{2}$, though it is difficult to ascertain whether the value is slightly greater or less than $\frac{1}{2}$. Thallium is definitely in region A and thus p should differ only slightly from $\frac{1}{2}$. Thus the values of p shown in Table I for these two elements are consistent with the theory.

DISCUSSION

It is possible to make an estimate of p for the remainder of the superconducting elements. Lead has the highest ratio T_c/Θ (~ 0.08). The next highest ratio is that of Hg, and probably La, being about 0.04. All other known superconducting elements have values of T_c/Θ considerably less than this, and in about half these elements, less than 0.01. On this basis, Pb is probably the only superconducting element with p significantly larger than $\frac{1}{2}$. Practically all of the elements should have $p = \frac{1}{2}$ or very slightly different from $\frac{1}{2}$. Of these elements, there exist accurate atomic heat data only for In.[19] According to these data, $\theta = 0.0113$ and, therefore, $p = 0.489$.

If the treatment of the isotope effect given in this paper is correct, then the observed deviations of p from $\frac{1}{2}$ are not in conflict with the value $\frac{1}{2}$ predicted by Fröhlich inasmuch as his value was based on the theory at 0°K.[20]

The author wishes to acknowledge here the $\Theta_D - T$ curves of various superconducting elements kindly provided by J. R. Clement, and the stimulating conversations on the subject of this paper held with both Clement and R. T. Webber.

[18] W. H. Keesom and P. H. van Laer, Physica **5**, 193 (1938).

[19] J. R. Clement and E. H. Quinnell, Phys. Rev. **92**, 258 (1953).

[20] It is true that the measurements on Sn by Lock *et al.* (reference 7) suggest a 0.462 power for the relation $M^pH_0 = \text{constant}$. However, one cannot overlook the fact that this value is an extrapolation to 0°K. Further, if one takes the value of 0.462 for the effect on T_c and 1/2 for that on H_0, the value of ΔH_0 would then be 9.5 instead of 8.9 gauss. This value is not in disagreement with the data, if the data of their "virgin material" are also included.

Dislocations in Plastically Deformed Germanium

G. L. Pearson, W. T. Read, Jr., and F. J. Morin
Bell Telephone Laboratories, Murray Hill, New Jersey
(Received November 3, 1953)

Both *n*- and *p*-type germanium rods were deformed plastically by bending. Etch pits were observed on the two active slip planes. Hall effect, conductivity, and lifetime were measured on both control and deformed samples. The results are consistent with the idea that edge dislocations in germanium are associated with acceptor-type energy levels in the middle or upper half of the gap.

BOTH *n*- and *p*-type germanium rods were deformed by bending into a radius of about 5 cm while heated to around 650°C. The samples were cleaned in KCN[1] and heated by passing a current through them in air—a method that introduces negligible "thermium."

In uniform plastic bending, the minimum-energy distribution of dislocations is determined by the curvature and the orientation of the crystal axes. The long dimension of the samples was [$\bar{1}$10] and the axis of bending [110]. Figure 1 is a micrograph showing etch pits on the (111) face. Vogel[2] and Gallagher[3] have shown that pits appear where dislocations meet the surface and are most easily seen on {111} faces. As observed by Gallagher, the pits lie in rows along the traces of the two active slip planes ($\bar{1}$11) and (1$\bar{1}$1). The measured density of pits, about 3×10^6 cm^{-2}, is about a third of the minimum calculated from the curvature—a discrepancy that may be due to the difficulty of resolving closely spaced dislocations.

Measurements of conductivity, Hall effect, and lifetime were made on (1) a control, (2) a heated, and (3) a heated and deformed sample. In 15-ohm·cm *p*-type material deformation had a negligible effect on mobility and carrier density. Figures 2 and 3 show Hall mobility and conductivity for 15-ohm·cm *n*-type germanium containing arsenic impurity. The heating alone introduced about 3×10^{13} acceptor centers per cm^3. The results suggest that deformation introduces acceptor-type energy levels[4,5] lying in the middle or upper half of the gap. These levels are probably associated with the dangling bonds on edge dislocations; the unpaired dangling electron accepts another electron to form a pair. As extra electrons from the conduction band join the dislocation, the dislocation becomes a negatively charged line surrounded by a cylindrical region of positive space charge; thus the electrostatic potential is distorted in the vicinity of a dislocation.

The Hall angle was measured with both the current and magnetic field at right angles to the dislocations (Hall voltage parallel to the dislocations). Hall mobility was calculated by assuming that the electrons on the dislocation do not conduct. The mobility in the deformed sample of Fig. 2 in the range 15°–300°K is that which would result if the dislocations added (to the thermal

Fig. 1. Etch pits on (111) face of germanium crystal bent about [110] axis.

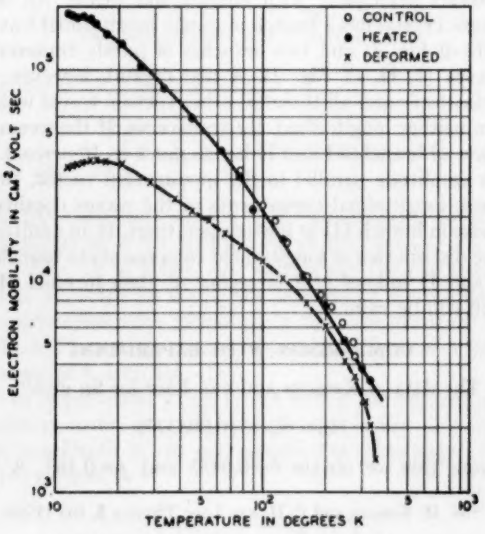

Fig. 2. Electron mobility *versus* temperature of (1) control, (2) heated, and (3) deformed germanium single crystal.

[1] R. A. Logan, Phys. Rev. **91**, 757 (1953).
[2] Vogel, Pfann, Corey, and Thomas, Phys. Rev. **90**, 489 (1953).
[3] C. J. Gallagher, Phys. Rev. **92**, 846 (1953).
[4] C. J. Gallagher, Phys. Rev. **88**, 721 (1952).
[5] W. C. Ellis and E. S. Greiner, Phys. Rev. **92**, 1061 (1953).

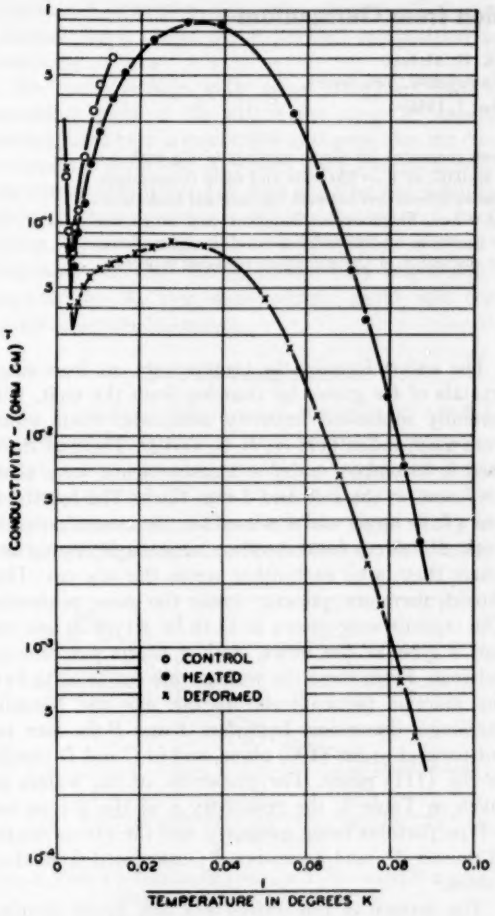

FIG. 3. Conductivity *versus* $1/T$.

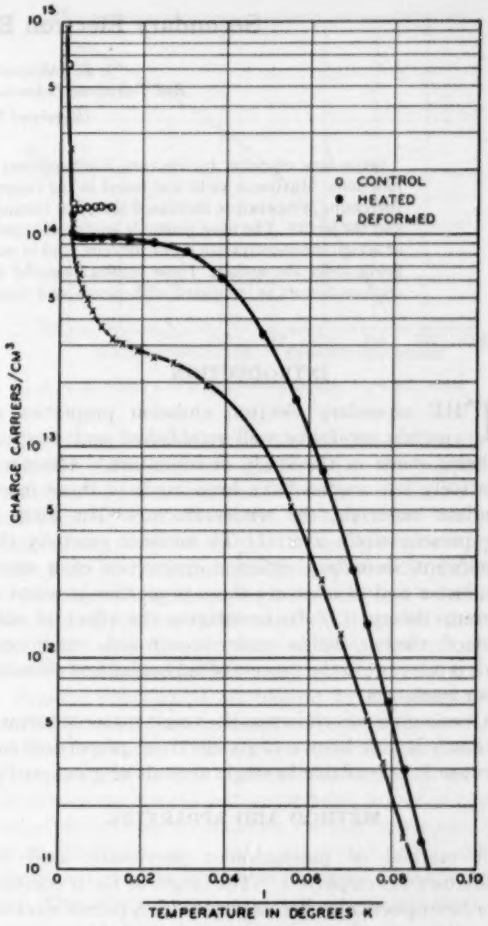

FIG. 4. Electron density *versus* $1/T$.

scattering of the control) scattering with a constant mean free path of 9.5×10^{-5} cm.

In the high-temperature range of Fig. 2 the difference between the two curves may be due to the fact that the space charge around a dislocation distorts the streamlines; this could give an apparent reduction in mobility even when the effect of the dislocations on mean free time is negligible. Such distortion of the streamlines affects both Hall angle and conductivity in the same way and therefore introduces no error into the calculation of carrier concentration, Fig. 4, which is found from the ratio of conductivity to Hall angle.

Because the dislocations are charged, even a density of dislocations of the order of 10^7 cm^{-2} can have a relatively large effect on mobility, especially at low temperature. It is planned to publish a detailed analysis of scattering from a charged dislocation in a later paper. It will also be shown in a later paper that the occupation of dislocation-acceptor centers is governed by Fermi statistics only when the fraction of centers occupied is negligibly small—of the order of 10^{-6} in the present case. As the temperature is lowered below room temperature, the fraction steadily increases and reaches a maximum of about 0.1 near the absolute zero of temperature. The data of Fig. 4 is consistent with a single energy level about 0.2 ev below the conduction band.

The number of dislocations required to explain the conductivity and Hall effect data is 2 to 3 times the minimum value, 10^7 cm^{-2}, calculated from the curvature.

As reported by Gallagher,[4] deformation drastically reduces minority carrier lifetime in both *n*- and *p*-type germanium; typical values were 300μsec in the control, 50μsec in the heated, and less than 1μsec in the heated and deformed sample.

We wish to thank W. Shockley for his helpful discussions, E. E. Thomas for preparing the micrograph, and W. W. Feldman and J. P. Maita for assistance with the experimental measurements.

Secondary Electron Emission from Germanium

J. B. JOHNSON* AND K. G. MCKAY
Bell Telephone Laboratories, Murray Hill, New Jersey
(Received November 2, 1953)

Secondary emission by electron bombardment has been measured for single crystals of Ge with p-n junctions. Maximum yield was found in the range $\delta=1.15\pm0.03$, at $V_p\approx500$ volts and room temperature. Increasing temperature decreased the yield because of a small interaction between the internal secondaries and the lattice. The most probable energy of emission was 1–2 ev. There was no change in yield with donor or acceptor concentration up to $10^{19}/cm^3$, and in particular there was no detectable effect of the space-charge fields under the surface. These results form the basis for discussion of the secondary emission process in semiconductors as compared with metals and insulators.

INTRODUCTION

THE secondary electron emission properties of metals are fairly well established and progress is being made in the study of insulators.[1,2] However, relatively few studies have been made of those intermediate materials, the semiconductors. The aims of the present study are: (1) To measure carefully the significant secondary emission properties of a semiconductor and to interpret those properties in terms of current theory. (2) To investigate the effect of subsurface electric fields under controlled conditions. This is relevant to the process of field-enhanced emission from insulators.

Germanium was chosen as the target material because so much is now known of its electrical properties[3] and because it is available in single crystals of great purity.

METHOD AND APPARATUS

A method of measurement previously used for insulators was employed.[4,5] The target of Ge is centered in a hemispherical collector electrode. A pulsed electron beam of energy V_p strikes the target and the secondary current flows to the collector. Current in the target circuit is amplified and displayed on an oscilloscope, showing the primary current when the collector is negative, and the excess of secondary over primary when it is positive.

TABLE I. Composition of Ge wafers.

Wafer	*A*	*B*	*C,D*
ρ_n (ohm cm)	0.06	5.5	0.0046
Additive	Sb	As	Ga+Sb
N_n (cm^{-3})	6×10^{16}	6×10^{14}	3.4×10^{18}
ρ_p (ohm cm)	0.08	0.8	0.008
Additive	Sb+Ga	As+Ga	Ga
N_p (cm^{-3})	8×10^{16}	7×10^{15}	1.4×10^{19}

The wafers forming the targets were cut from single crystals of Ge grown by drawing from the melt, with carefully controlled impurity additions.[6] Four wafers were used, called here *A*, *B*, *C*, and *D*. The first three, used in secondary emission measurements, were about 5×7 mm on the side and 2 mm thick. The fourth, *D*, was a little larger and was used for the contact potential work. *D* was cut from the same large single crystal as *C* where they faced each other across the saw cut. They should, therefore, present closely the same properties. The crystals were grown so as to be p type at one end and n type at the other, with a sharp p-n junction between. From these the wafers were cut so as to have the junction perpendicular to the side and bisecting the longer dimension. In wafers *A* and *B* the face was cut parallel to the (100) plane, and in *C* and *D* parallel to the (111) plane. The properties of the wafers are given in Table I, the resistivity ρ of the p-type and n-type portions being measured and the excess density of donors N_n and acceptors N_p calculated from these values.[7]

The surface of the wafers was first finely abraded, then etched with a mixture of HNO_3, HF, and Br and finally washed carefully with distilled water leaving the surface unpolluted.

The targets were mounted in experimental tubes with great cleanliness. These were pumped on a system with mercury vapor pumps, with extensive outgassing. The usual procedure was baking of the tubes for hours at 400–500°C, heating the wafers to a dull red temperature, and sealing off at a pressure near 10^{-8} mm Hg. Some wafers were resurfaced and repumped several times.

EXPERIMENTAL RESULTS

A. δ-V_p Curves

The yield δ as a function of the primary energy V_p is plotted in Fig. 1 for the case of wafer *C*. Curve *a* refers to room temperature. The maximum yield is about 1.2, at about 500 volts. The other wafers gave values very close to this, the range for different wafers with repeated treatments being $\delta_{max}=1.12-1.18$. This

* Now with Edison Laboratory, Thomas A. Edison, Inc., West Orange, New Jersey.

[1] K. G. McKay, "Secondary electron emission," *Recent Advances in Electronics* (Academic Press, Inc., New York, 1948), Vol. 1, p. 65.

[2] A. J. Decker and A. van der Ziel, Phys. Rev. **86**, 755 (1952).

[3] E. M. Conwell, Proc. Inst. Radio Engrs. **40**, 1327 (1952).

[4] J. B. Johnson, Phys. Rev. **73**, 1058 (1948).

[5] J. B. Johnson and K. G. McKay, Phys. Rev. **91**, 582 (1953).

[6] They were grown by G. K. Teal and M. Sparks.

[7] Pearson, Struthers, and Theuerer, Phys. Rev. **77**, 809 (1950).

is within 5 percent of the value given by Koller and Burgess[8] for a target of unspecified composition and treatment.

We can conclude with some assurance that the secondary yield of Ge within the range of impurity content used here is essentially unchanged by the donor or acceptor additives. A foreign atom concentration to the extent of 0.01 percent does not alter the secondary emission process, which is still characteristic of the Ge lattice. These foreign atoms evidently do not act as "emission centers." Being ionized they might not be expected to, so that such centers could still occur under other circumstances.

B. δ *vs* Temperature

No appreciable temperature variation of yield has been found in the case of clean metals.[9] Insulators are found to have a marked reduction of yield with increasing temperature.[5,10] Curve *b* of Fig. 1 shows an appreciable reduction of yield in Ge in the range of V_p near and above the maximum. The variation over a range of

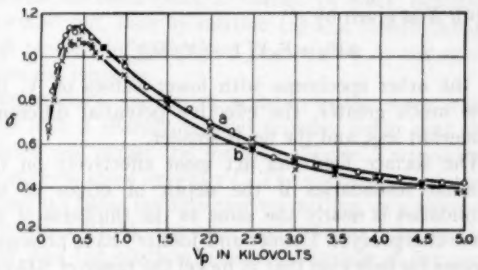

FIG. 1. Yield δ *vs* bombarding voltage V_p for wafer *C*. Curve (*a*) room temperature, (*b*) $T=525$°C.

temperatures is shown in Fig. 2 measured near the second crossover where $\delta=1.00$ and with a thermocouple on the target. As with insulators, the reduction in yield is not merely proportional to the yield itself but also depends on V_p, being smallest for low V_p. This indicates that the effect is not due to increase of work function with temperature but is concerned with the body properties.

It could be argued that the decrease in yield at higher temperatures is caused by the increased interaction between the internal secondaries and the augmented density of free electrons in the conduction band. This argument can be eliminated as follows: At room temperature, there is no appreciable difference between the yield of target *B* and target *C* although *B* contains

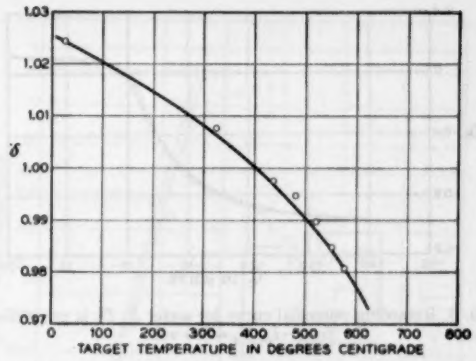

FIG. 2. Yield δ *vs* target temperature. $V_p=800$ volts.

6×10^{14} free electrons/cm³ on the *n* side and *C* contains, 3.4×10^{18} electrons/cm³. At 600°C, the respective free-electron concentrations have risen to 7×10^{16}/cm³ and 3.5×10^{18}/cm³. However, in both cases the high-temperature yield has dropped below the room temperature yield by the same amount in spite of the disparity in the proportional increases in free-electron concentration. From this we must conclude that the effect on the yield of a free-electron concentration of up to 3×10^{18}/cm³ is negligible.

Another conceivable mechanism for the temperature coefficient of δ is that the range of the primaries increases with temperature. This appears entirely unreasonable. Thus we conclude that in Ge collisions of electrons with the lattice are a small but appreciable source of energy loss of the internal secondaries, the loss to free electrons being negligible and that connected with raising electrons across the forbidden gap of 0.7 ev predominating. This distinguishes the semiconductor from the metal where the predominant loss is to nearly free electrons with negligible temperature effect, and from the insulator where, at energies that are low but still sufficient for escape the loss in lattice collisions must predominate and the temperature effect is therefore relatively large.

C. Energy Distribution

By applying retarding or aiding potentials to the collector, the distribution-in-energy of the secondary electrons was estimated. Figure 3 shows the current in the target circuit as a function of potential on the collector, obtained with wafer *B*. The corresponding distribution in energy obtained by differentiation is given in Fig. 4. The contact potential of the collector, a film of colloidal graphite, should not be far from that of the Ge target[11] so that the curve needs little shift because of contact potential. This would make the most probable energy of the secondaries about 1 ev. However, the flat target violates the condition for the

[8] L. R. Koller and J. S. Burgess, Phys. Rev. **70**, 571 (1948).
Note added in proof:—A paper by H. Gobrecht and F. Speer [Z. Physik **135**, 602 (1953)] reports values of δ for targets of polycrystalline and evaporated germanium generally somewhat higher than ours and showing a slight rise at greater impurity content than we used here.
[9] D. E. Wooldridge, Phys. Rev. **58**, 316 (1940).
[10] J. B. Johnson, Phys. Rev. **92**, 843 (1953).
[11] The work function of evaporated films of Ge is about 4.8 volts according to Apker, Taft, and Dickey, Phys. Rev. **74**, 1462 (1948).

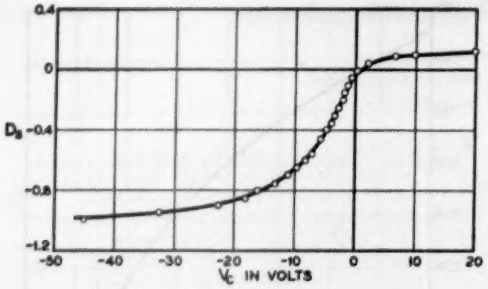

FIG. 3. Retarding potential curve for wafer *B*. D_s is proportional to $i_s - i_p$. $V_p = 500$ volts.

true spherical symmetry required, and also, there is the condition of "negative energy" electrons on the right that usually appear in this type of measurement. These may be due to tertiary electrons released from the collector by reflected primaries, or to patch potentials on the surface of the target that require the collector to be positive in order to overcome their retarding effect on secondaries from certain areas. In any case, the result is such that this kind of distribution curve should not be taken too literally because the maximum may be shifted by these extraneous effects.

D. Yield *vs* Sub-Surface Electric Field

One of the mechanisms invoked in the process of secondary electron emission from insulators is field-enhancement. This means that an electric field existing within the target near the bombarded surface may increase or decrease the yield of secondary electrons. Since sub-surface fields are known to exist in Ge, with calculable strength and distribution, the opportunity is presented of quantitatively observing the effects of such fields.

The energy levels available to mobile electrons and positive holes in Ge do not remain at a constant distance from the Fermi level as the surface is approached. This is attributed to the presence of surface states where holes or electrons are trapped, leaving a space-charge layer under the surface to balance the surface charge, the layer being largely devoid of the mobile carriers. Thus, in this layer there is an electric field that can be calculated on plausible assumptions, and the field in *p*-type Ge is opposite in direction from that in *n*-type Ge. No difference greater than 0.1 volt in external contact potential has been found[12] between *p*-type and *n*-type Ge treated the same way, and therefore, the fields must exist inside rather than outside the surfaces. It was this fact of having opposite fields on the two sides of a sharp *p-n* junction with the surfaces subjected to exactly the same treatment that made this experiment on secondary yield attractive.

Target *C* was particularly well adapted for this comparison, since in it the high carrier concentration makes the thickness of the space-charge layers comparable with the range of the electrons involved. Calculations[13] show that in this specimen the bottom of the conduction band is lowered in energy by 0.30 volt on the *n*-type side, and the top of the valence band is raised by 0.35 volt on the *p*-type side, relative to the Fermi level. We do not know the exact distribution of this total shift of 0.65 volt, but a serviceable assumption is that it is divided equally between the two space-charge layers at the *n* and the *p* surfaces, $\Delta V = 0.32$ volt each. By the procedure used for calculations on the Schottky depletion layer, we can compute the thickness of this layer, assuming that the impurity concentration remains the same from the interior to the surface,

$$l_0 = (K\Delta V/2\pi eN)^{\frac{1}{2}}. \quad (1)$$

N is the density of donors or acceptors, K the dielectric constant which is here 16, e the electronic charge. We obtain for the *n*-type side $l_{0n} = 130$A and for the *p*-type side, $l_{0p} = 65$A. The corresponding fields at the surface are $E_0 = 2\Delta V/l_0 = 0.49 \times 10^6$ and 0.98×10^6 v/cm. The potential drop with respect to the surface at the depth X is given by

$$\Delta V_X = E_0 X[1 - (X/2l_0)]. \quad (2)$$

In the other specimens with lower values of N, the l_0 is much greater, the effective potential difference somewhat less, and the fields smaller.

The surface field can act most effectively on the internal secondaries if the depth of origin of the secondaries is nearly the same as the thickness of the space-charge layer. Diemer and Jonker[14] have presented reasons for believing that in nickel the range of 500-volt primary electrons is 50A. On the basis of the ratio of densities, this should be about 85A for Ge, both materials having $V_{p\max}$ at about 500 volts. Similarly, Bruining[15] deduces that the mean depth of origin of

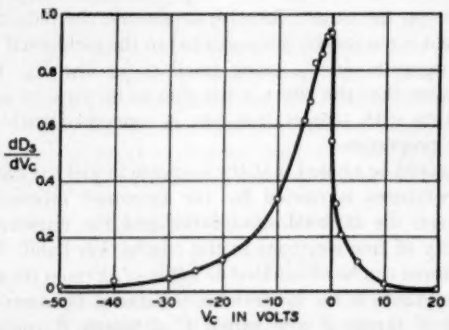

FIG. 4. Approximate energy distribution of secondary electrons obtained by differentiation of the curve in Fig. 3.

[12] W. H. Brattain and J. Bardeen, Bell System Tech. J. **32**, 1 (1953).

[13] W. Shockley, *Electrons and Holes in Semiconductors* (D. van Nostrand and Company, Inc., New York, 1950), Chap. 10.

[14] M. Diemer and J. L. H. Jonker, Philips Research Repts. **5**, 161 (1950).

[15] H. Bruining, *Die Sekundär-Elektronen-Emission fester Körper* (J. Springer, Berlin, 1942), p. 71.

secondaries from 500-volt primaries in nickel is 30A, or 50A in Ge if the density relation holds. These values are of the same order of magnitude as the calculated thickness of the space-charge layer for wafer C, so that in this specimen the effect of the internal field should be nearly a maximum.

The internal fields are in such directions as to urge electrons toward the surface in the p-type material and toward the interior in the n type. The potential change between the surface and the point of origin of a carrier may be considered for that carrier to be equivalent to a nearly comparable change in the work function at the surfaces. This should have an effect on the secondary yield, which can roughly be computed by a relation derived by Wooldridge[16] for metals of high work function, and which agrees well with data by Treloar[17] on molybdenum and tungsten. It is

$$\Delta \log_e \delta_{max} \doteq 0.1 \Delta\varphi, \tag{3}$$

where $\Delta\varphi$ is the change in work function. By relation (2) the potential drop ΔV_X at 50A is for the n-type side 0.20 volt and for the p-type side 0.30 volt. If we identify the sum of these with a change in work function, $\Delta\varphi = 0.50$ volt, then by relation (3) δ_{max} should change by 5 percent in going from one surface to the other across the junction.

Accordingly, numerous point-by-point scans were made with a sharply focused primary beam over the surfaces and across the junction. Figure 5 reproduces one of these scans on wafer C. The value of δ is plotted against the beam position control reading, at a value of V_p where $\delta \doteq 1.00$. The scan covers about $\frac{1}{4}$ in. on the wafer, and the junction is near the middle of the scan from left to right. Small variations in δ were found along the surface, but in the many runs made on this and the other wafers there was never any step as large as 1 percent that could be identified with the junction.

Explanations for this absence of field effect can be postulated as follows:

(a) In spite of evidence at lower impurity concentration there may be in this heavily doped specimen C an external difference of contact potential that reduces the internal potential drops.

(b) In the heat and vacuum treatment of the wafers,

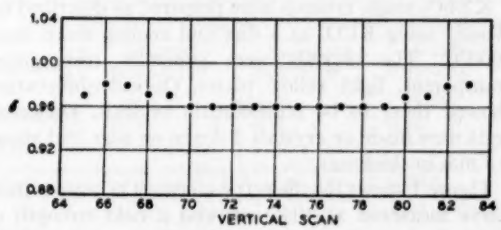

FIG. 5. Yield δ vs spot position on wafer C. $V_p = 1000$ volts. The n-p junction cuts across the middle of the scan.

[16] D. E. Wooldridge, Phys. Rev. **56**, 562 (1939).
[17] L. R. G. Treloar, Proc. Phys. Soc. (London) **49**, 392 (1937).

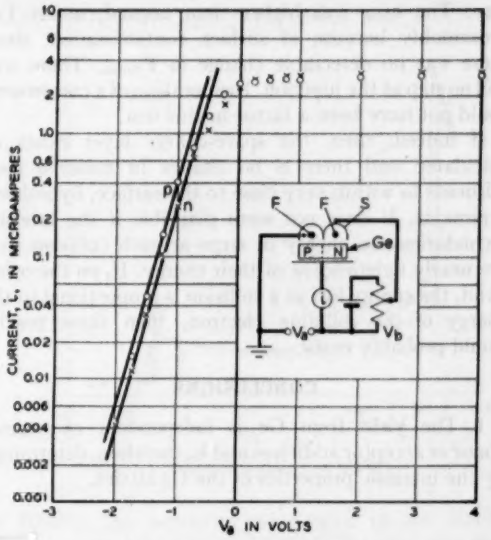

FIG. 6. Measurement of contact potential difference between n- and p-type sections of wafer D.

the second additive may have evaporated preferentially from the surface, leaving both surfaces either n or p type to a depth as great as the maximum escape range of the secondaries.

(c) There is a subsurface field, but the collision processes of the secondaries are such that momentum in the direction of the surface gained by the electrons from the field does not build up but is dissipated at each inelastic collision.

Hypothesis (a) was checked on wafer D, with measurement of contact potential difference (cpd) between the two sides of the junction. Contact potential measurements were made with the use of a tungsten filament as electron emitter and the Ge as counter electrode. The usual semilog plots of current vs voltage established the difference in contact potential between different areas of the Ge. The measurements were made with a circuit in which the filament heating current was zero in the alternate ac half-cycles where the current readings were observed. This was done after various vacuum treatments, from long bake at up to 600°C to short bake at 300°C. In no case was the cpd more than about 0.2 volt. Figure 6 gives the result for the case of the mildest vacuum treatment where there could have been no appreciable evaporation of any constituent. The difference between the two retarding-potential curves is within 0.1 volt. Confirming other result, then, there is no appreciable difference in cpd between the n- and p-type sides of this specimen.

Hypothesis (b) was checked with wafer C. After a fresh etch it was mounted in the tube which was then processed by long pumping and by outgassing the electron gun but without heating the wafer above room temperature. The wafer was then scanned in the usual

way. The δ_{max} was higher than normal, about 1.6, presumably because of surface contamination, since there was no detectable change in $V_{p\max}$. There was still no step at the junction. Evaporation of a constituent could not have been a factor in this test.

If indeed, then, the space-charge layer exists as calculated and there is no change in material constituents to within very close to the surface, hypothesis *c* remains. It does not seem plausible if the internal secondaries lose energy in steps at each collision that are nearly independent of their energy. If, on the other hand, the energy lost at a collision is proportional to the energy of the colliding electron, then these results would probably ensue.

CONCLUSIONS

1. The yield from Ge is independent of normal donor or acceptor additives and is, therefore, determined by the intrinsic properties of the Ge lattice.

2. The yield from Ge has a small but appreciable temperature coefficient. This is taken as evidence for a small interaction between the internal secondaries and the lattice.

3. The interaction is negligible between internal secondaries and free electrons or positive holes up to concentrations of about $10^{19}/cm^3$.

4. No evidence has been found that strong subsurface fields affect the yield from Ge. It is believed that this is a result of the detailed mechanism of energy loss of the internal secondaries and that it does not rule out the possibility of field effects in other materials such as insulators.

ACKNOWLEDGMENTS

We wish to acknowledge stimulating discussions with Conyers Herring and W. H. Brattain. The specimens were prepared by H. C. Meier.

PHYSICAL REVIEW VOLUME 93, NUMBER 4 FEBRUARY 15, 1954

Phase Transitions in Ferroelectric $KNbO_3$†

G. SHIRANE, H. DANNER, A. PAVLOVIC,* AND R. PEPINSKY
X-Ray and Crystal Structure Laboratory, Pennsylvania State University, State College, Pennsylvania
(Received October 30, 1953)

It is shown that ferroelectric $KNbO_3$ undergoes another phase transition at −10°C in addition to two phase transitions previously reported at 225° and 435°C. At this lowest phase transition $KNbO_3$, on cooling, changes its orthorhombic structure to a rhombohedral one, and this change is accompanied by a sharp change of the dielectric constant. The specific heat anomalies at three transitions were measured, and the results are compared with the case of $BaTiO_3$.

DIELECTRIC measurements of $KNbO_3$ by Matthias and Remeika[1] revealed a ferroelectric Curie point at 435°C and a further transition at 225°C. An x-ray and optical study by Wood[2] revealed a cubic perovskite structure above the Curie point at 435°C, which transforms on cooling first to a tetragonal structure and then to an orthorhombic structure at the aforementioned two transition points. These transitions are related to the phase transitions in $BaTiO_3$ at 120°C and 0°C.[3] A further transition occurs in $BaTiO_3$ at −80°C, in which the structure changes from orthorhombic to rhombohedral. The above investigators found no significant change in the dielectric constant of $KNbO_3$ between room temperature and −190°C,[1] and no optical change was observed between 25° and −50°C.[2]

A preliminary dielectric study[4] carried out in our laboratory on $KNbO_3$ single crystals, prepared without flux, did show a sharp peak in the dielectric constant at −50°C on cooling and −35°C on heating, indicating the existence of a phase transition at this point. A further study has now been carried out on the dielectric, structural, and thermal properties of this lowest phase.

$KNbO_3$ single crystals were prepared as described by Wood,[2] using KCO_3 as a flux and cooling down from 1000°C. The crystals were generally rectangular, transparent, light yellow plates. Optical observation showed them to be multidomain crystals. Dielectric tests were made on crystals 2–3 mm on edge and about 0.3 mm in thickness.

Figure 1 shows the dielectric constant *vs* temperature curve measured at 10 kc/sec and a field strength of about 5 v/cm. The heating and cooling rate was about 1°C/min. In agreement with previous data, this curve shows a very sharp change in dielectric constant at

† Research supported by Contract No. N6onr-26919 with the U. S. Office of Naval Research, and Contract No. AF33(039)-12645 with the Aeronautical Research Laboratory, Wright Air Development Center.
* Owens-Illinois Research Fellow.
[1] B. T. Matthias and J. P. Remeika, Phys. Rev. **82**, 727 (1951).
[2] E. A. Wood, Acta Cryst. **4**, 353 (1951).
[3] See, for instance, A. Von Hippel, Revs. Modern Phys. **22**, 221 (1950).
[4] Pepinsky, Thakur, and McCarty, Phys. Rev. **86**, 650 (1952).

220° and 420°C on heating. In addition to these, there is an abrupt change in the dielectric constant at −10°C on heating. On cooling, these three transitions occur at 410°, 200°, and −55°C. A very large temperature hysteresis of about 45°C at the lowest phase change appears in the several crystals examined.

Powder photographs of $KNbO_3$ were taken with CuK_α radiation in a Norelco powder camera of 11.4-cm diameter. Orthorhombic cell dimensions $a=5.721$A, $b=3.973$A, $c=5.695$A were obtained at room temperature, in good agreement with the previous data.[2,5] The lowest-temperature phase was examined in our low-temperature camera, 10-cm diameter, using CuK_α radiation. Diffraction patterns at −140°C showed pseudo-cubic lines of perovskite type, but small although definite line splittings were observed in a few high angle lines such as (422), (332), and (420). The line splittings could be explained by assuming a rhombohedral lattice and considering both line spacings and intensities. Special attention was paid to the (400) reflections, which show no multiplet except that due to the α_1,α_2 doublet; and this excluded the possibilities of tetragonal or orthorhombic lattices. The lattice parameters calculated from (422) and (332) line groups are $a=4.016\pm0.002$A and $\alpha=89°50'\pm1'$.

Since $\alpha<90°$, this rhombohedral lattice is derived from an ideal cubic lattice by an elongation along [111]. This corresponds to the same lattice as that of the lowest phase in $BaTiO_3$. Polarizing microscope observations also showed the three phase transitions at temperatures of the dielectric anomalies; and extinction positions are in accordance with the x-ray determined symmetry of each phase. If we reduce the three transition temperatures by dividing by the Curie temperature, they are 1, 0.69, 0.49 and 1, 0.71, 0.38 for $BaTiO_3$ and $KNbO_3$, respectively. $KNbO_3$ is the only one perovskite-type ferroelectric which has been found to show three transitions similar to those of $BaTiO_3$.

To further compare the transitions in these two crystals, a study was made of the specific heat anomaly at the three transitions in $KNbO_3$. Ceramic $KNbO_3$ was prepared by firing a mixture of K_2CO_3 and Nb_2O_5 at 1050°C. An adiabatic calorimeter of the Nernst type,[6] holding about 50 g of $KNbO_3$ powder, was used for the lower-temperature measurements. Another adiabatic calorimeter of Nagasaki-Takagi[7] type, containing about 15 g of $KNbO_3$ powder, was used at high temperatures. The measurements were carried out by heating the specimens continuously at a rate of 0.5 to 1°C/min. Sharp peaks in the specific heats appeared at the three transition temperatures.

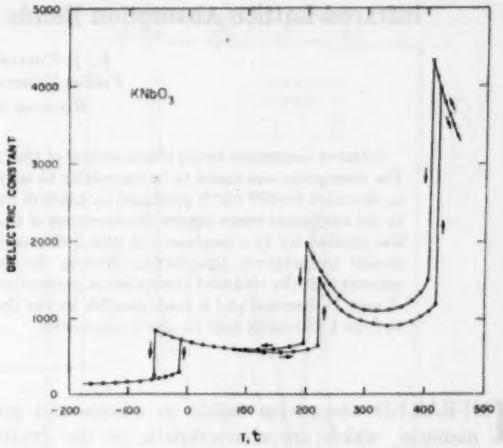

FIG. 1. Dielectric constant of $KNbO_3$.

The values of the transition energies integrated from the curves are shown in Table I, together with data on $BaTiO_3$. The larger transition energies in $KNbO_3$ could be explained in terms of the larger lattice distortions in $KNbO_3$ as compared with the corresponding transitions in $BaTiO_3$. It may be interesting to point out that the relative ratio of the three entropy changes are nearly the same in these two crystals; and, moreover, the entropy changes at the Curie points of these two crystals are approximately proportional to their $[(c/a)-1]$ values in the tetragonal phase.

To permit a more detailed comparison of these two crystals, and especially to apply Devonshire's theory[8] of $BaTiO_3$ to $KNbO_3$, we must know the values of the Curie constant and the spontaneous polarization at the Curie point. Unfortunately, reliable values of these quantities in $KNbO_3$ are difficult to obtain, because of the relatively high conductivity near the Curie point at 430°C.

The authors express their gratitude to Mr. R. E. Newnham for preparation of the single crystals.

TABLE I. Transition energy ΔE (cal/mole) and entropy change ΔS (cal/mole degree) at the three transitions in $BaTiO_3$ and $KNbO_3$.

		Cubic — Tetragonal	Tetragonal — Orthorhombic	Orthorhombic — Rhombohedral
$BaTiO_3$	ΔE	47∼50[a,b,c]	16∼26[a,b,c,d]	8∼14[b,c,d]
	ΔS	0.12∼0.13	0.06∼0.09	0.04∼0.07
$KNbO_3$	ΔE	190±15	85±10	32±5
	ΔS	0.28	0.17	0.12

[a] Blattner, Kaenzig, and Merz, Helv. Phys. Acta **22**, 35 (1949).
[b] G. Shirane and A. Takeda, J. Phys. Soc. Japan **7**, 1 (1952).
[c] J. Volger, Philips Research Repts. **7**, 21 (1952).
[d] S. S. Todd and R. E. Lorenson, J. Am. Chem. Soc. **74**, 2043 (1952).

[5] P. Vousden, Acta Cryst. **4**, 373 (1951).

[6] See for example, J. C. Southard and F. G. Brickwedde, J. Am. Chem. Soc. **55**, 4378 (1933).

[7] S. Nagasaki and Y. Takagi, J. Appl. Phys. Japan **17**, 104 (1948).

[8] A. F. Devonshire, Phil. Mag. (7) **40**, 1040 (1949).

Infrared Lattice Absorption Bands in Germanium, Silicon, and Diamond*

R. J. Collins† and H. Y. Fan
Purdue University, Lafayette, Indiana

(Received November 6, 1953)

Infrared absorption bands characteristic of the crystal lattice were investigated for germanium and silicon. The absorption was found to be insensitive to lattice imperfections due to impurities ($\sim 10^{18}$ cm^{-3}) and due to disorders ($\sim 10^{19}$ cm^{-3}) produced by nucleon irradiation. It did vary with temperature in the same way as the calculated mean-square displacement of the atoms. Variations of absorption with temperature were also studied for two specimens of type I diamond. The bands characteristic of type II diamonds showed similar temperature dependence, whereas the long-wavelength bands were temperature insensitive. It appears that the observed absorption in germanium and silicon corresponds to the absorption characteristic of type II diamond and is made possible by the thermal vibration of the atoms. The long-wavelength bands in type I diamonds may be due to impurities.

INFRARED absorption bands in silicon and germanium, which are characteristic of the crystal lattice, were reported independently by the authors[1] and Lord.[2] Previous to these reports Oberly and Burstein,[3] and Briggs[4] have observed an absorption band in high-resistivity silicon at 8.9 microns and ascribed it to the lattice. Subsequently Fan and Becker[5] had shown that this band is in fact characteristic of the silicon lattice, being present in the same strength in all samples. On extending the measurement to 40 microns a number of such bands were found.

Both germanium and silicon have diamond type lattice. Infrared absorption in diamond reported first by Robertson, Fox, and Martin[6] has received considerable attention and has caused controversy in its explanation. A reasonable suggestion[7] is that the absorption is due to lattice imperfections either chemical or physical, but no explanation has yet been established. Aside from the question of availability diamond specimens, being natural crystals, have impurity contents which cannot be controlled. With the modern techniques developed for the preparation of silicon and germanium, it is comparatively easy to obtain large single crystals of known and controllable impurity content. An investigation of the effect of different factors on the lattice absorption in these crystals should contribute to the understanding of absorption in diamond type lattices.

EXPERIMENTAL RESULTS

The absorption studies were carried out on two instruments; a Perkin-Elmer double-pass monochromator which was used for all measurements above 77°K and a Leiss monochromator used for the measurements at 5°K. The cryostat used for the 5°K measurements had polyethylene windows and made measurements from 750–650 cm^{-1} impossible. Furthermore the aperture of the cryostat was small and the accompanying decrease in signal as well as resolution could easily have resulted in an error in the 5°K data of as large as 20 percent. The results obtained are summarized in the following.

(A) The lattice absorption bands of germanium and silicon are shown in Fig. 1. Besides these bands there is absorption due to free carriers, which is proportional to the carrier concentration. These curves are taken on samples with sufficiently small carrier concentration, so

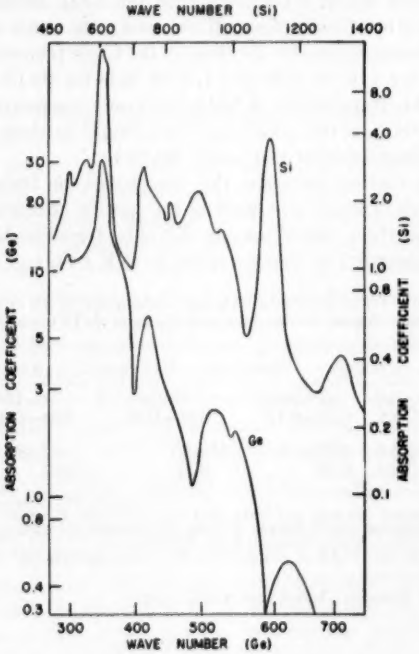

FIG. 1. Lattice absorption in germanium and silicon.

* Work supported by a Signal Corps Contract.
† Now at Bell Telephone Laboratories, Murray Hill, New Jersey.
[1] R. J. Collins and H. Y. Fan, Phys. Rev. **86**, 648 (1952).
[2] R. C. Lord, Phys. Rev. **85**, 140 (1952).
[3] J. J. Oberly and E. Burstein, Phys. Rev. **78**, 642 (1950).
[4] H. B. Briggs, Phys. Rev. **77**, 727 (1950).
[5] H. Y. Fan and M. Becker, *Proceedings of Reading Conference* (Butterworths Scientific Publications, London, 1951).
[6] Robertson, Fox, and Martin, Trans. Roy. Soc. (London) **A263**, 463 (1934).
[7] D. E. Blackwell and G. B. B. M. Sutherland, J. chim. phys. **46**, 9 (1949).

that carrier absorption is negligible. For samples with large carrier concentration, the carrier absorption is superimposed on the lattice bands. When separated the latter are found to be the same in all samples measured. The frequency scale for the germanium curve is 0.56 times that for the silicon. This ratio of the scales is chosen to make the strongest bands for the two materials coincide. It is seen that the band structures for the two substances have considerable similarity.

(B) Impurity and lattice defects. The introduction of impurities affect the carrier concentration of semiconductors. For accurate measurements of lattice absorption the carrier concentration must be kept low. Using donor and acceptor impurities together, large amounts of impurities can be introduced while the carrier concentration remains small. A germanium specimen was cut from such a melt doped with indium and antimony to an impurity concentration of about 10^{18} cm^{-3}. The resistivity of the sample was about 2 ohm cm which corresponds to a small enough carrier concentration to give negligible absorption. The lattice absorption of this sample is the same as that of purest samples with impurity concentration $\sim 10^{14}$ cm^{-3}. Although the purest samples may have more impurities than is indicated by the electrical properties, an addition of 10^{18} cm^{-3} should appreciably affect the total impurity content.

In an attempt to introduce lattice defects a germanium sample was heated to 900°C and rapidly quenched.[8] This treatment did not change the lattice absorption. It has been shown by Gallagher that at temperatures above 500°C germanium may be plastically deformed with slip lines in 111 planes.[9] A specimen was heated to 550°C and subjected to a load producing a 5° bend. The dislocations introduced by this process had no effect on the lattice absorption.

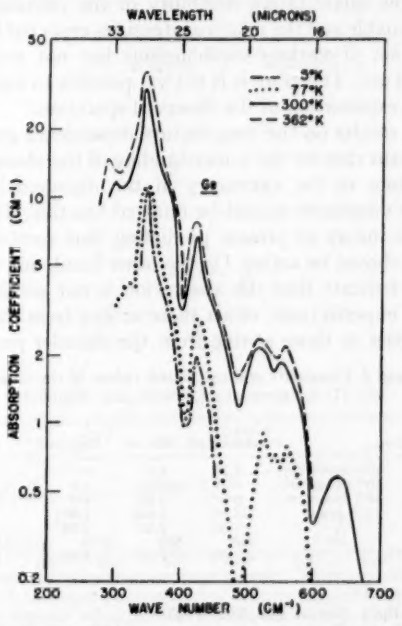

FIG. 2. Lattice absorption in germanium at different temperatures.

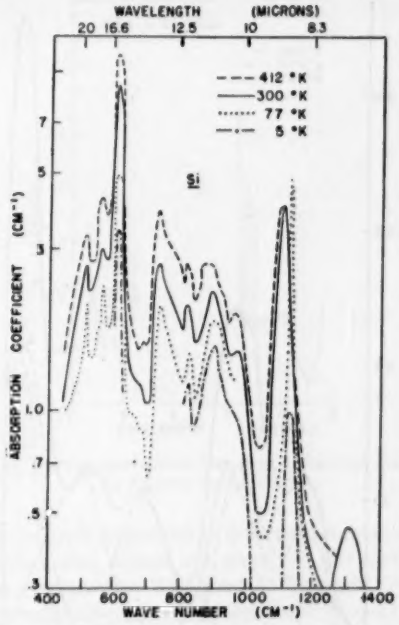

FIG. 3. Lattice absorption in silicon at different temperatures.

It has been reported that, upon irradiation with high-energy nucleons, the resistivity of silicon increases and may reach very high values not obtainable otherwise.[10] Large carrier concentration and high carrier absorption associated with large impurity content can thus be made negligible by nucleon irradiation, making it possible to study the lattice absorption. *P*-type silicon samples of 0.03-ohm cm resistivity with an impurity concentration about 3×10^{18} cm^{-3} were bombarded in the Oak Ridge pile until the resistivity had increased to over 10^3 ohm cm. From Hall effect and resistivity measurements it was estimated that about 10^{19} cm^{-3} lattice defects were produced. These specimens with high concentrations of impurities and lattice defects gave the same lattice absorption as the purest silicon samples.

(C) Temperature dependence. The effect of temperature on the lattice absorption was determined for germanium and silicon from 5°K to 400°K. For temperatures above 400°K the absorption of the thermally excited carriers was too large for the lattice absorption to be studied reliably.

[8] W. E. Taylor and K. Lark-Horovitz, Purdue Semiconductor Research Progress Report, February, 1950 (unpublished); W. E. Taylor, Ph.D. thesis, Purdue University, 1950 (unpublished).

[9] C. G. Gallagher, Phys. Rev. **88**, 721 (1952).

[10] K. Lark-Horovitz, *Proceedings of Reading Conference* (Butterworths Scientific Publications, London, 1951); Becker, Fan, and Lark-Horovitz, Phys. Rev. **85**, 730 (1952).

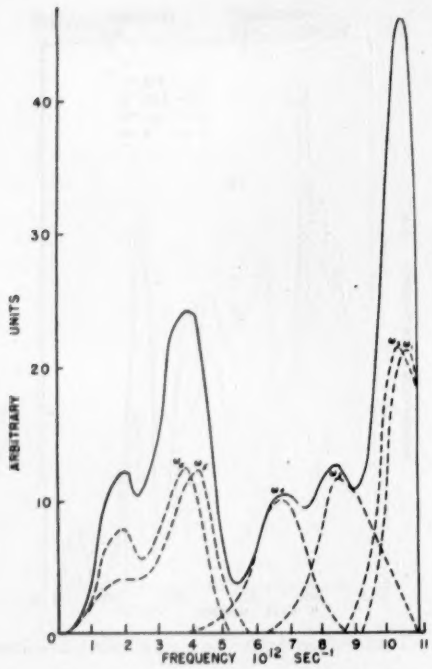

FIG. 4. Frequency distribution of the vibrational modes for germanium calculated by Y. S. Hsieh.

In germanium the lattice absorption increases with increasing temperature (Fig. 2). Within the experimental error all the bands change in the same manner.

For silicon (Fig. 3) except for the 1110 cm^{-1} band the absorption increases with increasing temperature. The exceptional behavior of the 1110 cm^{-1} band as shown by the 77°K curve has been carefully checked. However, at 5°K the band could have sharpened still more but not observed due to insufficient resolution of our equipment. The 1110 cm^{-1} band was the only band in either germanium or silicon which with our resolution showed a clear shift of the peak with temperature.

DISCUSSION

Born's work on the diamond-type lattice based on the interaction of first neighbors was extended by Nagendra Nath[11] to include second-neighbor interactions. The following relation was derived

$$\frac{(8\times 4\pi^2c^2m\nu_0^2/a)[4\pi^2c^2m\nu_0^2/a+8c_{11}-16c_{44}]}{[3\times 4\pi^2c^2m\nu_0^2/a-8c_{11}+16c_{12}]^2}=1, \quad (1)$$

where ν_0 is the limiting frequency of vibration, $2a$ is the lattice constant, m is the atomic mass, c is the velocity of light, and c_{11}, c_{12}, c_{44} are the elastic constants. The values of the constants are given in Table I. Using the frequency ν_1 of the strongest absorption peak for ν_0, the calculated values of the ratio in (1) come out close to unity (fifth row, Table I). This seems to indicate that the strongest absorption band corresponds to the excitation of optical modes of vibration. However, in the case of diamond ν_0 is known from the frequency shift of the first-order Raman line to be $\nu_0=1332$ cm^{-1}. Using this value, the ratio in (1) is 1.40 (Table I), rather poor agreement. Born[12] has pointed out three possible explanations for this discrepancy: (a) interaction of more distant neighbors is appreciable, (b) second-neighbor forces are not central as assumed in (1), (c) experimental error in the values of elastic constants. The relation (1) loses its validity if (a) and (b) are true. On the other hand, in her calculations for diamond Smith[13] adjusted the value of c_{44} from the experimental value 4.3×10^{12} to 5.0×10^{12} dynes/cm^2, which gives 1.04 for the ratio in (1).

The various bands in the absorption might correspond to the excitation of combination modes.[14] Calculations for germanium have been made by Hsieh[15] following Smith's[13] method but using only first-neighbor interaction. The calculated frequency distribution of vibrational modes is given in Fig. 4. The curve is a composite of three acoustical branches (dotted curves 1, 2, and 3) and three optical branches (4, 5, and 6). Any two modes with wave-number vectors equal and opposite in sign, for example one optical and one acoustical mode, could be excited if they are not forbidden by other selection rules. Thus a continuous absorption with various peaks could be expected. However, the quantitative reliability of the calculation is questionable and the relative intensities expected for the excitation of various combinations has not yet been worked out. Therefore it is not yet possible to elaborate on the explanation of the observed spectrum.

The results on the temperature dependence gives an important clue for the understanding of the absorption. According to the symmetry of the diamond lattice, optical vibrations should be infrared inactive. There is also no theory at present predicting that combination modes should be active. On the other hand, our experiments indicate that the absorption is not sensitive to lattice imperfections, either those arising from chemical impurities or those arising from the disorder produced

TABLE I. Constants and calculated values of the ratio in Eq. (1) for germanium, silicon, and diamond.

		Germanium	Silicon	Diamond	
c_{11}	10^{12} dynes/cm^2	1.29	1.67	9.5	
c_{12}	10^{12} dynes/cm^2	0.48	0.65	3.9	
c_{44}	10^{12} dynes/cm^2	0.67	0.80	4.3	
m	10^{-22} gram	12.05	4.658	1.995	
a	Å	5.65	5.42	3.56	
ν_1	cm^{-1}	340	610	2175	($\nu_0=1332$ cm^{-1})
Ratio (1)		1.06	1.12	1.05	1.40

[11] N. S. Nagendra Nath, Proc. Indian Acad. Sci. **1**, 333 (1934).

[12] M. Born, Nature **157**, 582 (1946).

[13] H. Smith, Trans. Roy. Soc. (London) **A241**, 105 (1948–49).

[14] E. Teller, in *Hand- und Jahrbuch der Chemische Physik* (Akademische Verlagsgesellschaft, Leipzig, 1934), Vol. 9, II, p. 161.

[15] Y. S. Hsieh, Phys. Rev. **85**, 730 (1952).

by nucleon bombardment. Moreover, an absorption due to lattice imperfection may become sharper at low temperature but would not be expected to show an over-all decrease as found experimentally. The observed temperature dependence seems to indicate that the absorption is made possible by the thermal vibrations of the atoms. One might assume that the dipole moment induced by a vibrational mode is in the first approximation proportional to the root-mean-square thermal displacement $(\langle r^2\rangle_{Av})^{\frac{1}{2}}$. The absorption should then be proportional to $\langle r^2\rangle_{Av}$. Lonsdale[16] has shown that

$$\langle r^2\rangle_{Av}=\frac{4.364\times10^{-14}}{A\theta}\left\{\frac{\phi(\beta)}{\beta}+\frac{1}{4}\right\}, \tag{2}$$

where θ is the Debye temperature, A is the atomic weight,

$$\beta=\theta/T,$$

$$\phi=\frac{1}{\beta}\int_0^\beta\frac{\xi d\xi}{e^\xi-1}. \tag{3}$$

Figure 5 gives the calculated curves for germanium, silicon, and diamond. The values of θ used are 363°K, 658°K, and 2340°K[16] for the three substances, respectively. The curves are plotted with $\langle r^2\rangle_{Av}$ for 5°K normalized to unity. The relative magnitudes of the strongest absorption peak measured at different temperatures for germanium and silicon are given by the circles and crosses, respectively. The good fit between the points and corresponding curves confirms the proportionality between the absorption and $\langle r^2\rangle_{Av}$. The 5°K points show some deviation, being low for silicon and somewhat high for germanium. However, as explained above, the accuracy of the measurements for this temperature was not as good as for the higher-temperature measurements.

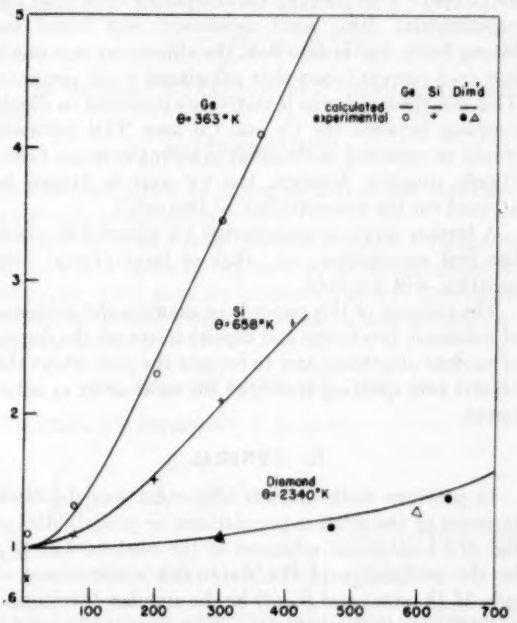

FIG. 5. Calculated curves of mean-square displacement of atoms due to thermal vibrations for germanium, silicon, and diamond. The points give the relative magnitudes of the strongest absorption peak at different temperatures. The 2175-cm^{-1} peak is used for diamond.

[16] K. Lonsdale, Acta. Cryst. 1, 142 (1948).

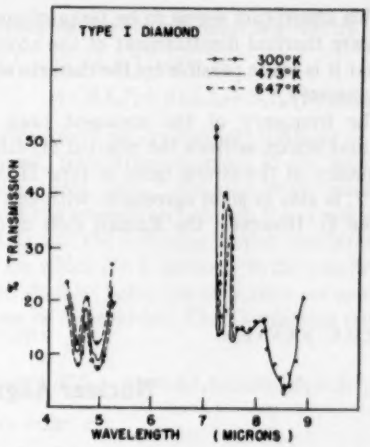

FIG. 6. Transmission curves for a type I diamond specimen at different temperatures.

In the case of diamond Robertson, Fox, and Martin[6] found no significant variation of absorption in the temperature range 80°K to 300°K. The curve for diamond in Fig. 5 shows that we should expect the change of absorption in this temperature range to be small as a result of the high Debye temperature. Consequently measurements were made at higher temperatures on two specimens of type I diamond. Figure 6 gives the transmission curves showing the prominent absorption peaks for one of the samples. It is known that the group of absorption bands at shorter wavelengths is present in all diamonds and is the only one present in type II, whereas the group of bands at longer wavelengths varies from specimen to specimen. It is seen that the short-wavelength group varied with temperature while the long-wavelength group was temperature-insensitive. The second specimen showed the same behavior. The triangles in Fig. 5 gives the relative absorption at different temperatures for the 2175-cm^{-1} band in the short-wavelength group taken on one specimen and the filled circles gives the data taken on the other specimen. The points are seen to be in fair agreement with the calculated curve.

The results of these measurements lead to the following conclusions:

(A) The absorption observed in germanium and silicon is similar in nature to the absorption in type II diamond.

(B) This absorption seems to be proportional to the mean-square thermal displacement of the atoms, indicating that it is made possible by the disturbance of the lattice symmetry.

(C) The frequency of the strongest peak in germanium and silicon satisfies the relation (1) fairly well. The frequency of the strong band in type II diamond, 2175 cm^{-1}, is also in good agreement with this relation (see Table I). However, the Raman shift in diamond gives a quite different value for ν_0, 1332 cm^{-1}, which does not satisfy (1). It would seem that rather than arising from errors in the values of the elastic constants, the discrepancy is due to the inaccuracy of relation (1) for reasons pointed out by Born.

(D) The long-wavelength absorption bands in diamond, which varies from specimen to specimen and is temperature-insensitive, seems to be due to lattice imperfections, e.g., impurities.

PHYSICAL REVIEW VOLUME 93, NUMBER 4 FEBRUARY 15, 1954

Nuclear Alignment at Low Temperatures

N. R. STEENBERG*
Division of Physics, National Research Council, Ottawa, Canada
(Received November 9, 1953)

The population distribution of nuclei aligned at low temperatures is derived by means of an expansion of the density matrix in powers of A/kT with an arbitrary external field. It is shown how this is related to the angular distribution of emitted γ radiation. The influence of interionic exchange and dipole coupling is examined to order $(A/kT)^3$ and is found to be generally small and cannot account for some experimental results. The case of finite crystal field interaction is considered as it applies to the angular distribution.

I. INTRODUCTION

FOR the interpretation of early experiments on nuclear alignment at low temperatures it was found sufficient to assume a rather simple picture of the process.[1,2] However, recent experiments at Oxford[3] have made further study of the problem necessary. It will be recalled that radioactive isotopes are substituted in a salt whose low-temperature properties are known and nuclear alignment is detected through the anisotropic distribution of the emitted γ radiation.

The early experiments[4] depended on the anisotropic hfs shown by some salts in their microwave absorption spectra. Among the assumptions made in the theory of this effect were: (a) that the crystalline field splitting of the ionic states was large enough that at low temperatures only the ground state doublet was occupied and the ion could be described by a fictitious "ionic spin," $S=\frac{1}{2}$, and anisotropic g values; (b) that interionic forces between neighboring ions could be ignored insofar as nuclear alignment was concerned.

The recent series of experiments[3] were done on a Ce—Co salt containing Co^{60}. These depended on the above effect and also on the application of an external magnetic field to polarize part of the ions which then in turn through the (nearly isotropic) hfs coupling polarized their nuclei. Theoretical curves were drawn, for various values of field, of the variation with temperature of the anisotropy ϵ in the emitted radiation.[5] If $F(\beta)$ is the angular distribution, ϵ is defined as $\epsilon=[F(\frac{1}{2}\pi)-F(0)]/F(\frac{1}{2}\pi)$. On comparing these with the experimental data, good agreement was found for strong fields, but in zero field the anisotropy was much less (~5 percent) than that calculated (~25 percent). This disagreement was tentatively attributed to dipole coupling between the Ce and Co ions. This influence would be expected to diminish in strong external fields. Dipole coupling between the Ce ions is known to account for the susceptibility of this salt.[6]

A further series of experiments are planned in which the first assumption, i.e., that of large crystal field splitting, will not hold.

The purpose of this paper is to examine the influence of interionic (exchange and dipole) forces on the degree of nuclear alignment and to include the case where the crystal field splitting is only of the same order as other forces.

II. GENERAL

In previous work[1] nuclear alignment was discussed in terms of the relative populations, or probabilities of the $2I+1$ magnetic substates of the nucleus. Let W_M be the probability of the state with z component of spin M ($\hbar$ units) and $F_M(\beta)$ be the angular distribution of radiation from that state, then the total angular distribution is $F(\beta)=\Sigma_M W_M F_M(\beta)$.

To obtain W_M, a general approach is to consider the

* National Research Laboratories Postdoctorate Fellow.
[1] N. R. Steenberg, Proc. Phys. Soc. (London) **A65**, 791 (1952); Proc. Phys. Soc. (London) **A66**, 399 (1953).
[2] H. A. Tolhoek and J. A. M. Cox, Physica **19**, 101 (1953).
[3] E. Ambler *et al.*, Phil. Mag. **44**, 216 (1953).
[4] Daniels, Grace, and Robinson, Nature **168**, 780 (1951).
[5] N. R. Steenberg, thesis, Oxford University, 1953 (unpublished).
[6] J. M. Daniels, Proc. Phys. Soc. (London) **A66**, 673 (1953).

density matrix ρ of the system at thermal equilibrium[7] given by

$$\rho=\exp\{-\mathcal{H}/kT\}, \tag{1}$$

where $\mathcal{H}$ is the Hamiltonian for the system. The mean value $\langle O\rangle$ of any quantum observable, O, can then be calculated from the formula

$$\langle O\rangle=\mathrm{Tr}[O\rho]/\mathrm{Tr}[\rho]. \tag{2}$$

From this point of view $F_M(\beta)$ is an expression involving the matrix elements of a number of tensor spin operators, $\Pi_k(M)$, of even order.[1] Where the ionic degeneracy is greater than two the calculation of the exact value of each $\langle\Pi_k\rangle$ is impractical. However, at "high" temperatures ρ can be expanded in powers of $1/kT$, and neglecting high powers, $F(\beta)$ is then found to depend in a simple fashion on $\langle\Pi_2\rangle$ alone,

$$\Pi_2(M)=3M^2-I(I+1).$$

To express W_M in terms of ρ, we write $\mathrm{Tr}\rho$ as $\sum_M(M|\mathrm{Tr}'\rho(I_2)|M)$, where Tr′ implies a sum over electronic states only. Then

$$W_M=(M|\mathrm{Tr}'\rho|M)[\textstyle\sum_M(M|\mathrm{Tr}'\rho|M)]^{-1}; \tag{3}$$

that is, the sum of those diagonal elements of ρ which belong to the several electronic states but to the same nuclear state, normalized so that $\sum_M W_M=1$. In this notation the mean value of any nuclear observable becomes, e.g.,

$$\langle\Pi_2\rangle=\textstyle\sum_M W_M\Pi_2(M). \tag{4}$$

The expansion of ρ can be done in the straightforward way

$$\rho=1-\mathcal{H}/kT+\tfrac{1}{2}\mathcal{H}^2/(kT)^2-+\cdots, \tag{5}$$

provided all terms in $\mathcal{H}$ are such that the expansion converges satisfactorily.

However, Simon *et al.*[7] have shown how $\mathrm{Tr}'\rho$ can be expanded in terms of one part of the Hamiltonian $\mathcal{H}_1$ while the other part $\mathcal{H}_0$ is kept arbitrary. $\mathcal{H}_0$ and $\mathcal{H}_1$ do not in general commute. Thus, where $\mathcal{H}=\mathcal{H}_0+\mathcal{H}_1$ and $\tau=-1/kT$,

$$\mathrm{Tr}'\rho=\mathrm{Tr}'\exp\{\mathcal{H}_0\tau\}\textstyle\sum_n R_n. \tag{6}$$

R_n, which will involve τ^n, is given by

$$R_n=\int_0^\tau\int_0^{\tau_1}\cdots\int_0^{\tau_{n-1}}\mathcal{H}_1'(\tau_1)\mathcal{H}_1'(\tau_2)\cdots\mathcal{H}_1'(\tau_n)d\tau_n\cdots d\tau_1,$$

and

$$\mathcal{H}_1'(\tau)=\exp\{-\mathcal{H}_0\tau\}\mathcal{H}_1\exp\{\mathcal{H}_0\tau\}.$$

This technique is employed here since we generally require the external field to be arbitrary. The notation of Simon will be followed except where noted.

Consider now a crystal having an axis of magnetic symmetry along which the external field H is applied.

[7] Simon, Rose, and Jauch, Phys. Rev. **84**, 1155 (1951).

For our purpose the Hamiltonian is given by

$$\mathcal{H}=D[S_z^2-\tfrac{1}{3}S(S+1)]+\beta Hg_{\parallel}S_z+[AS_zI_z+B(S_xI_x+S_yI_y)]+G(SS'). \tag{7}$$

Term 1 represents the crystal field splitting of the electronic states, term 2 the coupling of the ionic spin to the external field, term 3 the anisotropic hfs coupling, and term 4 the interaction between S and a neighboring ion. In this and the following section our interest is in systems for which $S=\frac{1}{2}$ (either $\frac{1}{2}$ in fact, or because of the lowest doublet being the only state occupied), then term 1 can be disregarded. Then neglecting term 4 and taking

$$\mathcal{H}_0=\beta g_{\parallel}HS_z,\quad \mathcal{H}_1=AS_zI_z+B(S_xI_x+S_yI_y),$$

we find to order τ^2:

$$(M|\mathrm{Tr}'\rho|M)=Z[1+\tau AGM+\tau^2A^2(a_0+a_1M+a_2M^2)+\cdots], \tag{8}$$

where, for

$$S=\tfrac{1}{2},$$
$$G=-\tfrac{1}{2}\tanh\tfrac{1}{2}\theta,$$
$$a_1=x^2G(1-\tfrac{1}{2}\theta\coth\tfrac{1}{2}\theta)/\theta^2,$$
$$a_2=(\theta-2x^2\tanh\tfrac{1}{2}\theta)/8\theta,$$
$$\theta=\alpha/kT,\quad x=B/A.$$

From Eq. (3) it then follows that

$$W_M=(2I+1)^{-1}\{1+AGM\tau+\tau^2A^2[a_1M+\tfrac{1}{3}a_2\Pi_2(M)]+\cdots\}. \tag{9}$$

Our primary interest is in the angular distribution $F(\beta)=\sum_M W_MF_M(\beta)$, and since $F_{-M}(\beta)=F_M(\beta)$ it is sufficient to consider the expression:

$$W_M{}^E=\tfrac{1}{2}(W_M+W_{-M})=(2I+1)^{-1}\{1+\tfrac{1}{3}A^2a_2\Pi_2(M)/(kT)^2+\cdots\}, \tag{10}$$

which will be termed the even-population function. The function $a_2(\theta)$ varies rather slowly with temperature in the range where the approximation is valid. Given this expression, the angular distribution and anisotropy can be approximated as follows:

$$F(\beta)\simeq 1+A^2a_2(\theta)I(I+1)(2I-1)(2I+3)\times XP_2(\cos\beta)/15(kT)^2. \tag{11}$$

X is a function of the multipole order and nuclear transition involved,[1] β is the angle between the axis of alignment and the line of observation,

$$\epsilon=[F(\tfrac{1}{2}\pi)-F(0)]/F(\tfrac{1}{2}\pi)\simeq -A^2a_2I(I+1)(2I-1)(2I+3)X/10(kT)^2. \tag{12}$$

The degree of nuclear alignment has been defined[7] as

$$\Delta=\textstyle\sum_M W_M\Pi_2(M)/3I^2,$$

which becomes, under the above circumstances,

$$\Delta\simeq A^2a_2(I+1)(2I-1)(2I+3)/45I(kT)^2. \tag{13}$$

It should be observed how all these quantities are determined in this approximation by the coefficient of Π_2 in $W_M{}^E$.

For the angular distribution, only the even-population function is required. However, other nuclear properties depend on the odd spin moments, for example the degree of circular polarization of γ radiation[8] or the degree of nuclear polarization defined by Simon *et al.* as $f_N=\sum_M W_M M/I$. In this case we need only the odd-population function given by $W_M{}^O=\frac{1}{2}(W_M-W_{-M})$.

III. INTERIONIC FORCES

(a) Exchange Coupling

In considering exchange coupling, it is assumed that the ion S whose nucleus is to be aligned is coupled to one neighboring ion S' of a different type by the $G(SS')$ term in the Hamiltonian given by

$$G(SS')=J_{\parallel}S_zS_z'+J_{\perp}(S_+S_-'+S_-S_+'), \qquad (14)$$

where $S_\pm=(S_x\pm iS_y)/\sqrt{2}$. We will later put both S and $S'=\frac{1}{2}$. The exchange is isotropic if $J_{\parallel}=J_{\perp}$. Taking

$$\mathcal{H}_0=\alpha S_z+\alpha' S_z', \quad \alpha'=g_{\parallel}'\beta H,$$
$$\mathcal{H}_1=AS_zI_z+B(S_+I_-+S_-I_+)+G(SS'),$$

and following the procedure outlined above, it is found that $W_M{}^E$ is unaffected by the interaction to order τ^2. That is, either due to cancellation or taking the symmetric average, no new terms are added to the expression for $W_M{}^E$ given by Eq. (10). Thus, to obtain the first correction due to the interaction, it is necessary to compute $\mathrm{Tr}'\exp\{\mathcal{H}_0\tau\}R_3$, whence with S and $S'=\frac{1}{2}$ we obtain:

$$W_M{}^E=(2I+1)^{-1}\{1+\tfrac{1}{3}A^2\tau^2\Pi_2(M) \times[a_2-\tau(AP-J_{\parallel}Q)]+\cdots\}, \qquad (15)$$

where the correction terms are

$$P=x^2(3\tanh\tfrac{1}{2}\theta+\tfrac{1}{4}\theta^2\tanh\tfrac{1}{2}\theta-3\theta/2),$$
$$Q=\tfrac{1}{2}x^2(\theta\tanh^2\tfrac{1}{2}\theta-\theta+2\tanh\tfrac{1}{2}\theta)(\tanh\tfrac{1}{2}\theta')/8\theta^2,$$
$$\theta'=\alpha'/kT.$$

It should be recalled that the proper convergence of this of this approximation demands that $J_{\parallel}$ be of the same order as A. The influence of the interaction is to diminish the degree of alignment if the exchange integral, $J_{\parallel}$, is positive and to enhance it if it is negative.

Only $W_M{}^E$ and $W_M{}^O$ are quoted, since W_M itself contains very complicated third-order corrections to the odd spin moments which are of no interest. $W_M{}^O$ is now given by[9]

$$W_M{}^O\simeq\tfrac{1}{2}AM\{\tanh\tfrac{1}{2}\theta-\tau(2a_1A-J_{\parallel}K)\}/kT(2I+1), \qquad (16)$$

where

$$K=\tfrac{1}{4}\tanh\tfrac{1}{2}\theta'(1-\tanh^2(\tfrac{1}{2}\theta),$$
$$a_1=-\tfrac{1}{2}x^2\tanh\tfrac{1}{2}\theta(1-\tfrac{1}{2}\theta\coth\tfrac{1}{2}\theta)/\theta^2.$$

The ion S may be influenced by interaction with a number of such ions, that is, in place of $G(SS')$ in the Hamiltonian we may need to consider $\sum_i G^i(SS^i)$, $G^i(SS^i)=J_{\parallel}{}^iS_zS_z{}^i+J_{\perp}{}^i(S_+S_-{}^i+S_-S_+{}^i)$. Then the above results are modified only by replacing $J_{\parallel}$ by $\sum_i J_{\parallel}{}^i$.

(b) Dipole Coupling

For dipole-dipole coupling it is assumed that the ion S is situated at the origin of a set of coordinates and interacts with S', situated at a point $\mathbf{r}$ through the $G(SS')$ term given by

$$G(SS')=[r^2(\boldsymbol{\mu}\cdot\boldsymbol{\mu}')-3(\boldsymbol{\mu}\cdot\mathbf{r})(\boldsymbol{\mu}'\cdot\mathbf{r})]/r^5, \qquad (17)$$

where

$$\boldsymbol{\mu}=\beta[g_{\perp}(S_x\mathbf{i}+S_y\mathbf{j})+\mathbf{k}S_zg_{\parallel}].$$

$G(SS')$ can be put into a form which is sometimes more convenient as follows:

$$G(SS')=\lambda[aS_zS_z'+b(S_+S_-'+S_-S_+') +S_z(cS_+'-\bar{c}S_-')+(dS_+-\bar{d}S_-)S_z' +eS_+S_+'+\bar{e}S_-S_-'], \qquad (18)$$

where

$$\lambda=-\beta^2(4\pi)^{\frac{1}{2}}/5^{\frac{1}{2}}r^3,$$
$$a=2g_{\parallel}g_{\parallel}'Y_2{}^0(\theta\varphi),$$
$$b=-g_{\perp}g_{\perp}'Y_2{}^0(\theta\varphi),$$
$$c=\sqrt{3}g_{\parallel}g_{\perp}'Y_2{}^{-1}(\theta\varphi),$$
$$d=\sqrt{3}g_{\perp}g_{\parallel}'Y_2{}^{-1}(\theta\varphi),$$
$$g=6^{\frac{1}{2}}g_{\perp}g_{\perp}'Y_2{}^{-2}(\theta\varphi),$$

and the Y's are spherical harmonics in the polar angles of S'. The similarity of Eq. (18) to Eq. (14) should be noted for, taking $\mathcal{H}_0$ and $\mathcal{H}_1$ as before, results of identical form are obtained for this interaction as for the exchange interaction, at least to order τ^3. That is, Eq. (15) and Eq. (16) apply equally to this type of interaction except that $\sum_i J_{\parallel}{}^i$ is replaced by $\sum_i\lambda^ia^i$. Now

$$\lambda^ia^i=-\beta^2g_{\parallel}g_{\parallel}{}^i(3\cos^2\theta^i-1)/(r^i)^3, \qquad (19)$$

so that nuclear alignment is enhanced if $\theta=0$ or π and is diminished if $\theta=\pi/2$.

Since the dipole term Eq. (17) depends on the orientation of the second dipole, it is evident that this interaction may introduce another preferred direction into the problem. Where one dipole S' interacts with S, $\langle I_x\rangle$ and $\langle I_y\rangle$ will not in general vanish. However, if a pair (or pairs) of dipoles S' and S'' are symmetrically placed with respect to the z axis, i.e., S' at xy and S'' at $-x-y$ it is found that $\langle I_x\rangle$ and $\langle I_y\rangle$ vanish.

(c) Discussion and Application

Because of the equivalence of the two interactions they can be discussed together. It should be borne in

[8] N. R. Steenberg, Proc. Phys. Soc. (London) **A66**, 391 (1953).

[9] Note this expression will not yield f_N' as given by A. Simon *et al.*, Phys. Rev. **84**, 1155 (1951), Eq. (35), on placing $x=1$ and $S=S'=\frac{1}{2}$, since their results Eqs. (34) are in error.

mind that all the remarks to follow refer to an approximation which is only valid where $(A/kT)^3 \gg (A/kT)^4$.

The first point to be noted is the limits of these expressions for large and small field. As $H\to\infty$, P, Q, K, and a_1 all approach zero, and $a_2\to(1-x^2)/8$ leaving

$$W_M{}^E \simeq (2I+1)^{-1}\{1+\tfrac{1}{6}(A/2kT)^2(1-x^2)\Pi_2(M)\}. \quad (20)$$

This means that, as antipcated, the nuclear alignment becomes independent of interactions in strong external fields.

For small fields, as $H\to 0$,

$$\begin{aligned} a_2 &\to (1-x^2+x^2\theta^2/12)/8, \\ P &\to x^2\theta^2/960, \\ Q &\to x^2\theta\theta'/192. \end{aligned} \quad (21)$$

Thus it can be seen that for zero field the nuclear alignment is independent of interactions. Furthermore reference to Eq. (20) shows that the nuclear alignment is again independent of interactions of $x=B/A=0$ in any field (this is not true if $S>\frac{1}{2}$).

Since only $\sum_i J_{11}{}^i$ or $\sum_i \lambda^i a^i$ is involved, the influence of the interaction does not depend on its anisotropic nature.

Lastly, the interaction term Q is in competition with the term P and thus $\sum_i J_{11}{}^i$ or $\sum_i \lambda^i a^i$ must be at least of the order of A in order that the interaction term be influential.

In general, it can be said that such interactions will only be effective under rather restricted circumstances, *viz.* (a) in moderate fields, (Q is a maximum and much greater than P for $\theta\simeq 5$), (b) $\sum_i \lambda^i a^i$ is at least of the order of A or greater, (c) in particular, where the hfs is nearly isotropic, $x\simeq 1$ where a_2 is small. Otherwise this influence on nuclear alignment is negligible at least at "high" temperatures.

If we now consider the experiment referred to earlier, it will be seen that dipole interactions cannot account for the lack of agreement in zero field since ϵ is then independent of interactions up to at least $1/T=50$. Furthermore, for the Ce ions (S') $g_{11}{}'$ is very nearly zero so that even in moderate fields this influence cannot account for the disagreement.

The crystal constants for this salt, g_{11}, $g_\perp$, A, etc., were measured[9] at 20°K and the alignment experiments were done at about 0.01°K. This, coupled with the conclusions above, leads to the reluctant suggestion that further structural changes occur between 20° and 0.01° making these constants temperature-dependent.

IV. FINITE CRYSTAL FIELD SPLITTING

For this problem S is arbitrary and we take

$$\mathcal{H}_0=\alpha S_z,$$

$$\mathcal{H}_1=AS_zI_z+B(S_+I_-+S_-I_+)+D[S_z{}^2-\tfrac{1}{3}S(S+1)].$$

[9] R. S. Trenam, Proc. Phys. Soc. (London) **A66**, 118 (1953).

Again we must compute $\mathrm{Tr}'\exp\{\mathcal{H}_0\tau\}R_3$ in order to get a correction to $W_M{}^E$. This is less formidable in this case since the D term is diagonal. Our result is

$$W_M{}^E=(2I+1)^{-1}\{1+\tfrac{1}{3}\tau^2A^2\Pi_2(M) \times[a_2+A\tau P+D\tau E]+\cdots\}, \quad (22)$$

where

$$\begin{aligned} E &= \tfrac{1}{2}d_2-\tfrac{1}{8}[2S(S+1)+3bG]a_2, \\ d_2 &= S(S+1)[\tfrac{2}{3}S(S+1)-1+2b^2] \\ &\quad +bG[3b^2+(5/3)S(S+1)-2]+d_0, \\ d_0 &= \tfrac{1}{2}x^2[\chi(\cosh\theta-1)+\psi(\theta-\sinh\theta)], \\ \chi &= 2bG[3b^2+\tfrac{2}{3}S(S+1)-2]+2S(S+1)(2b^2-1), \\ \psi &= \tfrac{1}{3}G(2S+3)(2S-1)+3Gb^2+2S(S+1)b, \\ a_2 &= \tfrac{1}{2}[\theta S(S+1)+G(x^2+\theta b)], \\ G &= \tfrac{1}{2}[b-(2S+1)\coth(S+\tfrac{1}{2})\theta], \quad b=\coth\tfrac{1}{2}\theta. \end{aligned}$$

It can be verified that the function E vanishes if S is put equal to $\frac{1}{2}$. Furthermore, $E\to 0$ as $H\to\infty$, so that in large fields the nuclear alignment is again independent of this perturbation. As $H\to\infty$,

$$W_M{}^E\to(2I+1)^{-1}\{1+\tau^2A^2S^2\Pi_2(M)/6\}. \quad (23)$$

In small fields, ignoring terms of order τ^4,

$$A^2E\to S(S+1)(2S+3)(2S-1)(2A^2+B^2)/180$$

as $H\to 0$, so that

$$W_M{}^E\to\frac{1}{(2I+1)}\left\{1+\frac{A^2S(S+1)\Pi_2}{18(kT)^2} \times\left[(1-x^2)-\frac{D(2S+3)(2S-1)(2+x^2)}{30kT}\right]\right\}. \quad (24)$$

Note that this is independent of field (the correction due to field is of order τ^4) and thus holds in zero field. Furthermore, even for isotropic hfs ($x=1$) nuclear alignment will arise in the absence of field through the D term, although this will be of opposite sign, i.e., the nuclei will tend to lie in the equatorial plane.

These calculations would apply to the Mn ions in the manganese bismuth nitrate reported by Trenam.[9]

V. ACKNOWLEDGMENT

The author is indebted to the National Research Council of Canada for a Special Scholarship held at Oxford where this work was commenced and for a Postdoctorate Fellowship under which it was completed.

Microwave Resonance Absorption in Nickel Ferrite-Aluminate*

THOMAS R. MCGUIRE
United States Naval Ordnance Laboratory, White Oak, Maryland
(Received November 12, 1953)

Magnetic resonance measurements on $NiOAl_tFe_{2-t}O_3$ gave g values which shifted from $g>2$ to $g<2$ at approximately $t=0.7$. At this composition the dominant magnetic moment changes from the B to the A sites and the shift in g values is believed to be correlated with the vanishing of the magnetic moment and angular momentum at different points close to $t=0.7$. The g values have the general characteristic of decreasing in magnitude as the temperature is raised. At $t=1.75$ and $-196°C$ two resonant peaks were observed, one with $g=1.4$ and a new peak with $g=4.0$, while for $t=2$ (nickel aluminate) no resonance absorption was observed. The half-widths of the resonance curves increased to a maximum value at $t=0.5$ and went through a minimum in the region of $t=1.25$.

INTRODUCTION

ELECTRONIC magnetic resonance absorption at microwave frequencies in nickel ferrite where a magnetic atom is partially replaced by a nonmagnetic one has been investigated[1,2] only for the case of Ni^{++} replaced by Zn^{++}. For this substitution the saturation magnetization[3] increases in a regular manner when zinc is first added, while the g values obtained from microwave resonance measurements of corresponding zinc content samples decrease slightly below the value found for pure nickel ferrite. At first glance this is not an unexpected behavior since the g values are all close to two.

Recently Maxwell and Pickart[4] and also Gorter[5] have found that when Al^{+++} is substituted for Fe^{+++} in nickel ferrite the magnetization decreases rapidly and exhibits the unusual effect of going through a zero magnetization point at a small percentage of aluminum. These nickel ferrite-aluminate compounds are identified as $NiOAl_tFe_{2-t}O_3$ where t takes on values from 0 to 2. Zero magnetization is approached at $t=0.7$ and for greater values of t the magnetization again increases. In the present paper the experimental results of magnetic resonance in nickel ferrite-aluminates are presented with particular attention given to the region of aluminum content where the magnetic moment approaches zero.

EXPERIMENTAL

The resonance measurements were made on spherical specimens made from the same batches used by Maxwell and Pickart[4] in their work. Spheres, ranging in diameter from 0.020 in. to 0.065 in. were ground to size by allowing sintered pieces to tumble in an air stream with abrasive powder, a method used by Bond[6] and Healy.[7] Two sets of measurements were made, the first after the samples were annealed and the second set following quenching. The annealed heat treatment consisted of heating the spheres to 1050°C and then allowing them to cool slowly over a 24-hour period, while quenching was done from 1400°C by plunging the specimens, enclosed in quartz tubes, into cold water.

The resonance apparatus has been described in some detail in a previous paper.[8] It is a microwave bridge that operates at a frequency of approximately 9300 Mc/sec, arranged so that a full-resonance curve is traced out as the dc magnetic field sweeps from 50 to 10 000 gauss. This arrangements facilitates the measurement of line shapes. A specimen of diphenyl trinitro-

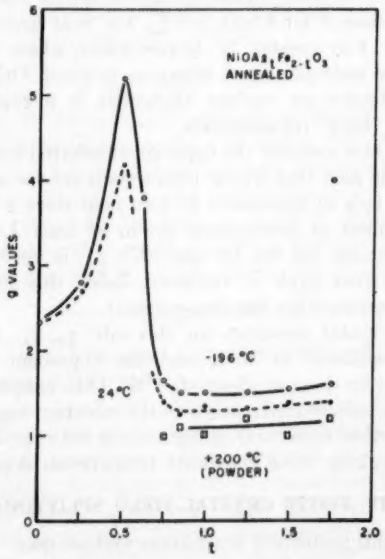

FIG. 1. g values as a function of aluminum content shown for 200°C, 24°C, and −196°C.

* A preliminary report of this work was given at the North Carolina meeting of the American Physical Society [Phys. Rev. **91**, 206 (1953)].

[1] H. G. Beljers and D. Polder, Nature **165**, 800 (1950).
[2] T. Okamura (private communication to R. K. Wangsness).
[3] E. W. Gorter, Nature **165**, 798 (1950).
[4] L. R. Maxwell and S. J. Pickart, Phys. Rev. **92**, 1120 (1953).
[5] E. W. Gorter, private communication to L. R. Maxwell (to be published).
[6] W. L. Bond, Rev. Sci. Instr. **22**, 344 (1951).
[7] D. W. Healy, Jr., Harvard University Technical Report No. 135, Aug. 15, 1951 (unpublished); Phys. Rev. **86**, 1009 (1952).
[8] L. R. Maxwell and T. R. McGuire, Revs. Modern Phys. **25**, 279 (1953).

phenyl hydrazyl, with the known g value[9] of 2.004, was usually added to the cavity for calibration purposes.

The resonance frequency of the cavity containing the specimen will vary appreciably, as a function of the intensity of the dc magnetic field, because of magnetic dispersion. In order to obtain the absorption at the true resonance frequency, the reflector potential of the klystron (Varian V50) was modulated (6 cps) by a small alternating potential. In this way it is possible to pass through the resonance frequency of the cavity a hundred times or more in the course of one sweep. The specimens were mounted with Duco cement on the surface of a rotating platform about 0.070 in. in diameter which formed a part of the terminating end of the resonant cavity. The Duco cement provided an insulating layer between the specimen and the wave

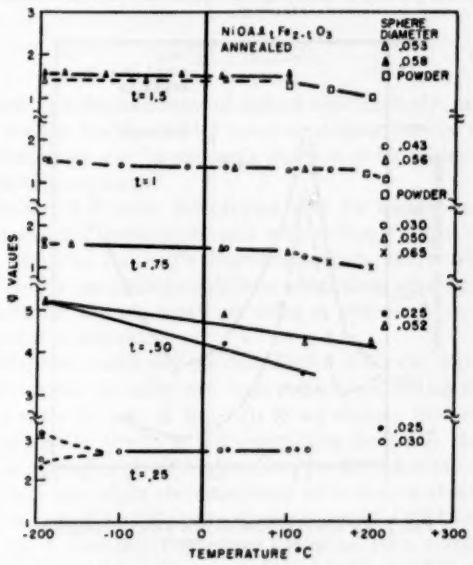

FIG. 2. g values as a function of temperature for specimens of different composition and sphere diameter.

guide while the platform allowed the specimen to be rotated in order to detect demagnetization effects due to departures from spherical shapes. Measurements were made on samples of two or three different diameters to see if there was any change in the resonance magnetic field value as a function of sphere size. Size effects were first observed in nickel ferrite and nickel zinc ferrite by Beljers and Polder,[1] who found that the g factors increased as sphere size became smaller although this is not necessarily a general behavior.

In addition to the size effect, the resonance behavior may be affected by the chemical composition and also the heat treatment. When measurements are repeated on a new group of samples variation is found in the experimental data probably because of the above factors. It is estimated that the accuracy of both the g values and the half-widths is within ± 3 percent.

[9] C. H. Townes and J. Turkevich, Phys. Rev. 77, 148 (1950).

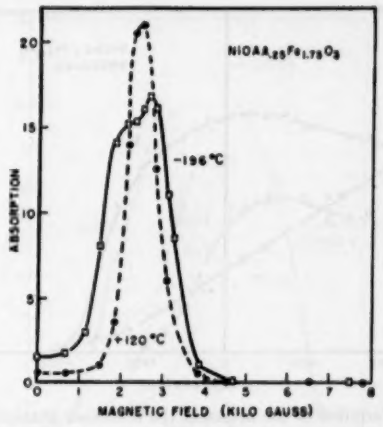

FIG. 3. Resonance curves for $t=0.25$ at 120°C and −196°C.

EXPERIMENTAL RESULTS AND DISCUSSION

The g values, shown in Figs. 1–9, are calculated using Kittel's[10] resonance condition for a ferromagnetic sphere:

$$\omega=\gamma H, \qquad (1)$$

where $\gamma=ge/2mc$. The g value for a free electron spin is 2, while values larger than 2 are attributed to the nonquenched magnetic moment of orbital electron motion.

Figures 1 and 2 show g as a function of composition and temperature. For $t=0.25$ a slight splitting which has been plotted as a single mean value in Fig. 1 but as two different values in Fig. 2 was observed at −196°C. The shape of the corresponding resonance curve ($t=0.25$) is illustrated in Fig. 3.

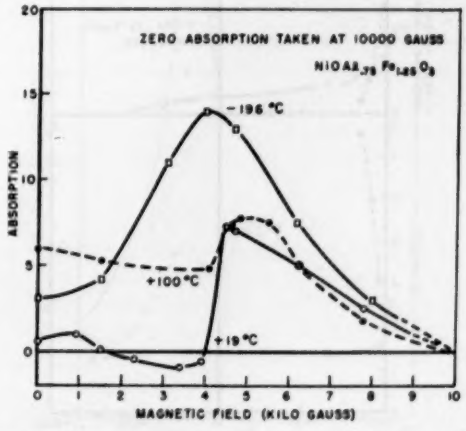

FIG. 4. Resonance curves for $t=0.75$ at 19°C, 100°C, and −196°C.

[10] C. Kittel, Phys. Rev. 73, 155 (1948).

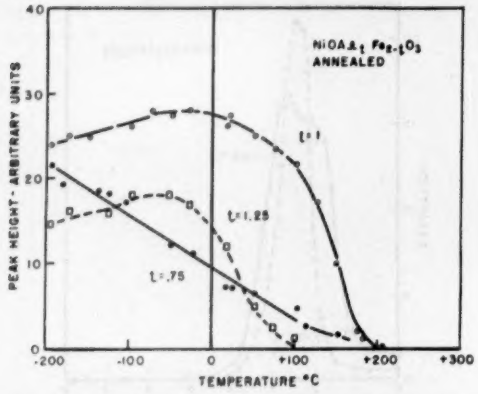

FIG. 5. Variation of the height of the resonance absorption with temperature for three different compositions.

The specimens of composition $t=0.5$ were the only ones that showed a g value dependent upon the sphere size. This dependence (Fig. 2) was most pronounced at room temperature but it disappeared at -196°C. From Figs. 1 and 7 it is seen that this composition had the greatest g value and half-width of the annealed group. It is possible, however, that the accuracy of these values is somewhat less than the measurements on other compositions because, at the low applied fields (1000 gauss) at which resonance took place, the specimen might not be magnetically saturated.

Samples of composition $t=0.75$ through 1.50 all had similar behavior with the exception of the absorption curve of $t=0.75$ (Fig. 4) which showed a lack of symmetry at the higher temperatures and seemed to indicate a second resonance peak at low fields. For this same range of compositions, Curie temperatures are well defined by the gradual disappearance of the absorption in the spherical specimens as a function of the temperature (see Fig. 5). In general they follow the shape of the magnetization curves given by Maxwell and Pickart.[4] Above the Curie temperatures measurements made on powder samples gave g values of approximately unity. This unexpected low value of g bears further investigation.

Nickel aluminate ($t=2$) exhibited no resonance absorption at any temperature from -196°C to $+250$°C. This result might be expected since the half-width curve (Fig. 7) is increasing rapidly as t approaches 2.

When the samples are quenched from 1400°C an entirely new ionic distribution occurs which gives rise to the g values and half-widths shown in Figs. 8 and 9. Both g and the half-width remain large in the region of $t=0.5$ to 0.85. Thus we see that the shift in g from above 2 to less than 2 that was present in the annealed material does not occur when the specimens are quenched. For higher aluminum content than $t=1$, resonance absorption was very weak and it was not possible to estimate half-widths with any reasonable degree of accuracy.

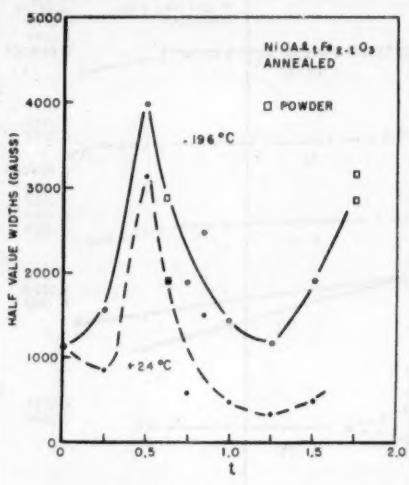

FIG. 7. Variation of half-widths with composition at 24°C and -196°C.

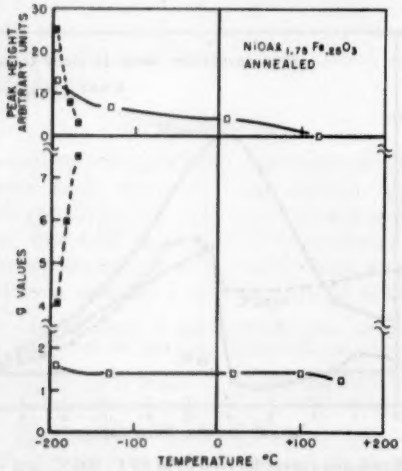

FIG. 6. g values and height of the resonance absorption curve for sample $t=1.75$ showing two resonant peaks at low temperatures.

The unusual behavior of the g values as a function of composition in the annealed condition can best be understood by considering the nature of the saturation magnetization of this group of compounds. The Néel theory[11] considers two types of interstices or magnetic sites in the spinel structure. These sites are designated Type A (tetrahedral holes) and Type B (octahedral holes) in which the magnetic atoms are surrounded by 4 and 6 oxygen ions, respectively. As aluminum atoms are added in the nickel ferrite aluminates, the resultant magnetic moment of the ions on the B sites decrease until a composition is reached ($t=0.7$) where the

[11] L. Néel, Ann. phys. 3, 137 (1948).

moments on the A and B sites are approximately equal and opposite. For aluminum content greater than $t=0.7$ there is evidence that the magnetic moment of the ions on the A sites becomes greater than those on the B. We see that the shift in g values and half-widths occurs at the particular composition where the dominant magnetic moment shifts from the ions on the B sites to those on the A sites.

Wangsness[12] and Tsuya[13] have both examined sublattice effects in magnetic resonance, and their work shows that the effective g is given simply by the algebraic sum of the ion-magnetic moments divided by the algebraic sum of the spin angular momentum of the system. This can be written for a single molecule as

$$g_{eff}=\frac{\sum_n\sum_i g_{ni}f_{ni}S_n}{\sum_n\sum_i f_{ni}S_n}, \tag{2}$$

$$\mu=\sum_n\sum_i g_{ni}f_{ni}S_n, \tag{3}$$

where S_n is the spin value of the nth type ion and f_{ni} and g_{ni} are the fraction and g value of this ion on the ith lattice, while μ is the magnetic moment of the molecule in Bohr magnetons.

Smart[14] has made the propsal that for ferrites such as the nickel ferrite-aluminate system Eqs. (2) and (3) can be solved for the f's thus obtaining the distribution of ions. He has made calculations which show reasonable results for the ion locations using g_i values obtained from other sources.

Without considering the distribution of ions in detail, it is possible to make two observations concerning the data with the use of Eq. (2). If we assume that the nickel ferrite ($t=0$) is not completely inverted, then on an average a small fraction x of an Ni^{++} ion will be on an A site while the remainder $1-x$ is on a B site. In the case of nickel ferrite the fractions of Fe^{+++} ions on the A sites and B sites are $1-x$ and $1+x$, respectively. Using 1 for the spin value of Ni^{++} and $5/2$ for the spin of Fe^{+++} Eq. (2) may be written

$$x=\tfrac{1}{2}[(\mu/g_{eff})-1]. \tag{4}$$

The measured values for nickel ferrite are $\mu=2.2$ Bohr magnetons and $g_{eff}=2.35$ which when substituted in (4) lead to a negative value of x. We see that for any positive value of x, g_{eff} must be less than μ.

A possible solution to the difficulty outlined above, that g_{eff} must be no greater than μ in nickel ferrite, has been given by Okamura[15] and his colleagues who have found that g_{eff} as given by Eq. (1) is frequency dependent. At low frequencies (9000 Mc/sec) g_{eff} is much larger than it should be because there is an internal field (H_i) present which aids the applied field H, and

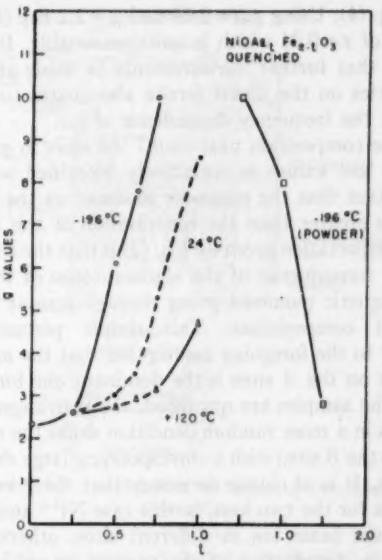

FIG. 8. g values for quenched samples as a function of composition at 120°C, 24°C, and −196°C.

Eq. (1) should be written as

$$\omega=\gamma(H+H_i). \tag{5}$$

Okamura has made measurements at four different frequencies from 9400 to 47 000 Mc/sec and solved Eq. (5) to find a value of $H_i=510$ gauss and $g_{eff}=2.05$ for nickel ferrite at room temperature. This new g_{eff} calculated from Eq. (5) is less than μ in agreement

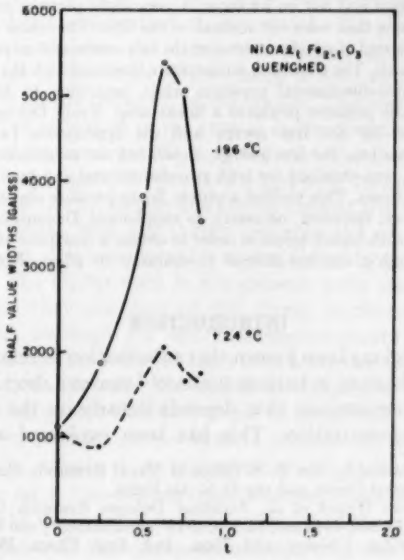

FIG. 9. Variation of half-widths for quenched samples at 24°C and −196°C as a function of composition.

[12] R. K. Wangsness, Phys. Rev. **91**, 1085 (1953).
[13] N. Tsuya, Progr. Theoret. Phys. Japan **7**, 263 (1952).
[14] J. Samuel Smart, private communication (to be published).
[15] Okamura, Torizuka, and Kojima, Phys. Rev. **88**, 1425 (1952).

with Eq. (4). Using $g_{eff}=2.05$ and $\mu=2.2$ Eq. (4) gives a value of $x=0.24$ which is quite reasonable. It is important that further measurements be made at higher frequencies on the nickel ferrite aluminates to obtain data on the frequency dependence of g_{eff}.

At the composition near $t=0.7$ the shift in g_{eff} from high to low values is tentatively identified with the assumption that the magnetic moment on the A sites becomes greater than the contribution of the B sites. The interpretation given by Eq. (2) is that the change in g_{eff} is a consequence of the algebraic sum of the spins and magnetic moments going through zero at slightly different compositions. This simple picture lends validity to the foregoing assumption that the magnetic moment on the A sites is the dominant one for $t>0.7$. When the samples are quenched, the rearrangement of the ions in a more random condition shifts the moment back to the B sites with a corresponding large change in g values. It is of course necessary that the g values be different for the two ions, in this case Ni^{++} and Fe^{+++}, or for the same ion in different sites, otherwise the change in distribution of the various magnetic atoms either due to heat treatment or chemical composition would not alter the ratio which gives g_{eff}.

CONCLUSIONS

It is seen from this work that there can be large variations in the resonance behavior of a substitutional ferrite and that for any particular composition further changes can be effected depending on the particular heat treatment the specimen has undergone. With the aid of Eq. (2) a simple interpretation of both very large and small g values is possible, and this in turn bears on the broader question of the exact distribution of ions for the specimen.

ACKNOWLEDGMENTS

I wish to thank both Dr. R. K. Wangsness and Dr. J. S. Smart for many helpful discussions of this work, and Dr. L. R. Maxwell for his advice on experimental problems which have arisen. I am indebted to Mr. E. P. Wenzel for his cooperation in the recording of the resonance curves.

PHYSICAL REVIEW VOLUME 93, NUMBER 4 FEBRUARY 15, 1954

Effect of a Two-Dimensional Pressure on the Curie Point of Barium Titanate*

P. W. FORSBERGH, JR.
Laboratory for Insulation Research, Massachusetts Institute of Technology, Cambridge, Massachusetts

(Received November 9, 1953)

By hydraulic means, a single crystal of barium titanate in the shape of a flat circular disk was subjected to a pressure exerted on its edges and not on its faces. A very slight pressure removed all domains that were not normal to the disk. The stress system then consisted of equal pressures on the two a axes, and no pressure on the c axis. The transition temperature increased with the square of the two-dimensional pressure, while, according to Merz, a hydrostatic pressure produces a linear drop. Using Devonshire's expansion for the free energy and the appropriate Legendre transformation, the free energy, depending on polarization and pressure, was obtained for both two-dimensional and hydrostatic stress systems. This yielded a purely linear-pressure dependence, and it was, therefore, necessary to supplement Devonshire's expansion with higher terms in order to obtain a quadratic effect.

Although it was too difficult to evaluate the effect of pressure on the transition temperature itself when higher terms were included, it was easy to determine the effect on the Curie-Weiss temperature T_0. This is the temperature at which the inverse susceptibility of the cubic phase extrapolates to zero, and its pressure dependence will be the subject of a future paper. For both two-dimensional and hydrostatic pressures, the linear part of the shift of the Curie-Weiss temperature was found to depend only on the lower terms in the free energy, and provide two independent relations for determining the two g coefficients. The quadratic shift of the Curie-Weiss temperature depends on the higher terms with which Devonshire's expansion was supplemented, and a reasonable interpretation of these higher terms gave an upward direction to the quadratic shift of the Curie-Weiss temperature.

INTRODUCTION

IT has long been known that substitution of strontium for barium in barium titanate[1,2] causes a drop in the Curie temperature that depends linearly on the strontium concentration. This has been explained as the result of an effective decrease of the unit-cell size caused by the smaller strontium ions. If, instead, the unit-cell size is reduced by application of hydrostatic pressure, the transition temperature decreases with decreasing unit-cell size at about the same rate.[3] The substitution of lead for barium, on the other hand, raises the transition temperature at a rate depending linearly on the lead concentration.[2] Lead titanate itself has a much higher Curie temperature (490°C) and is much more

* Sponsored by the U. S. Office of Naval Research, the U. S. Army Signal Corps, and the U. S. Air Force.

[1] A. von Hippel *et al.*, National Defense Research Council Reports 14-300, 1944 and 14-540, 1945 (unpublished); von Hippel, Breckenridge, Chesley, and Tisza, Ind. Eng. Chem. **38**, 1097 (1946).

[2] D. F. Rushman and M. A. Strivens, Trans. Faraday Soc. **A42**, 231 (1946).

[3] W. J. Merz, Phys. Rev. **78**, 52 (1950).

strongly tetragonal.[4] In fact, optical observations on crystals grown in the laboratory[5] show that it remains tetragonal all the way down to liquid helium temperatures, although with a rapid drop of the birefringence. The effect of hydrostatic pressure has been discussed by Slater[6] in terms of his statistical model of barium titanate. In this model, the local potential seen by the Ti ion, that is, the potential exclusive of dipole interaction, is represented by *one* harmonic potential well of cubic symmetry, supplemented by a small, fourth-power term to keep the spontaneous polarization finite. If the lattice size is reduced by hydrostatic compression (or strontium substitution), the oxygen ions that surround the Ti ion tetrahedrally are pressed more tightly against the Ti ion. The consequent stiffening of the local harmonic potential well requires a greater local field caused by dipole interaction to displace the Ti ion a given distance.

A two-dimensional pressure, however, should have quite a different effect, for the crystal will contract along two axes but expand along the third. If the two axes undergoing compression are cubic axes, the local potential well will acquire tetragonal symmetry and will become football shaped, or possibly even dumbbell shaped. The latter would mean that the single local potential well has become a double well, which would result in an order-disorder type of transition if the barrier between the two wells were comparable to kT. The way in which a two-dimensional pressure affects the Curie transition in barium titanate will depend very critically on how the z expansion is related to the x contraction, and particularly on how the internal field is affected by these strains. One may say that the change in the local potential well produced by a two-dimensional pressure should allow the Ti ion to displace more freely in the z direction. On the other hand, an expansion of the lattice in the polarization direction and contractions across the polarization direction should reduce the local field.

APPLICATION OF TWO-DIMENSIONAL PRESSURES

Bridgman[7] has made studies of plastic flow and fracture of a number of substances under two-dimensional compression. One method was to use a specially constructed steel die that could actually push on a ductile material in two directions at once, and the other method was to exert a pull in one direction on a sample subjected to hydrostatic pressure. The latter method amounts to a two-dimensional pressure superposed on a hydrostatic compression that is less than the applied hydrostatic pressure by the strength of the pull. In the present work, we have developed a method of exerting a uniform two-dimensional compression on the edges of a disk-shaped sample with pressures up to, and probably well above, 1000 atmospheres. While this is small compared to the range of two-dimensional pressure obtainable by Bridgman's second method, our technique has the advantage of leaving the faces of the disk exposed, so that one can make optical and x-ray measurements and apply electric fields.

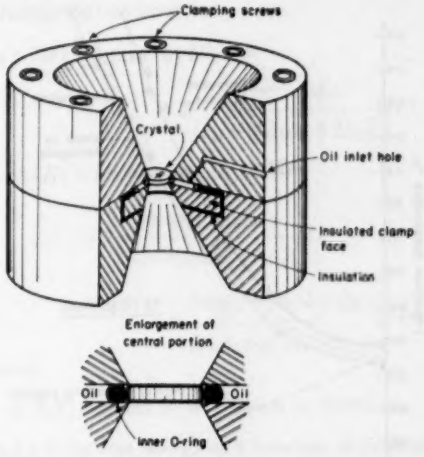

FIG. 1. Details of crystal holder for applying two-dimensional pressure.

The method relies on a rubber "O-ring," which is a circular ring of soft rubber with a circular cross section. The O-ring is placed around the disk-shaped sample and the combination is clamped in a steel clamp as shown in Fig. 1. The faces of the clamp have openings to permit direct observation of the crystal. The clamp is tightened, thereby flattening the O-ring, until the separation of the faces of the clamp is only *ca* 2 mils greater than the thickness of the crystal. This clearance allows free expansion of the crystal in the direction not subjected to pressure. Oil is forced into the clamp as shown in the figure by means of a hydraulic pump. The pressure of the oil pushes the O-ring against the edges of the crystal, and the O-ring prevents the oil from leaking out. The outside seal is accomplished by another O-ring. The clamp used in the present work was designed so that one face of the clamp is electrically insulated, although the electrical measurements have not yet been made. Observation with a microscope was sufficient to determine the transition temperature. By introducing quartz windows, it will be possible to apply a different pressure to the faces of the crystal, and to study the effect of a superposition of hydrostatic pressure on a two-dimensional pressure. Since a soft rubber has a low shear modulus, sticking of the rubber to the faces of the clamp should not create a large pressure correction at the pressure used. However, if the O-ring is lubricated before clamping, the rubber can

[4] Shirane, Hoshino, and Suzuki, Phys. Rev. **80**, 1105 (1950); G. Shirane and E. Sawaguchi, Phys. Rev. **81**, 458 (1951).
[5] H. H. Rogers, Technical Report 56, Laboratory for Insulation Research, Massachusetts Institute of Technology, 1952 (unpublished).
[6] J. C. Slater, Phys. Rev. **78**, 748 (1950).
[7] P. W. Bridgman, *Large Plastic Flow and Fracture* (McGraw-Hill Book Company, Inc., New York, 1952).

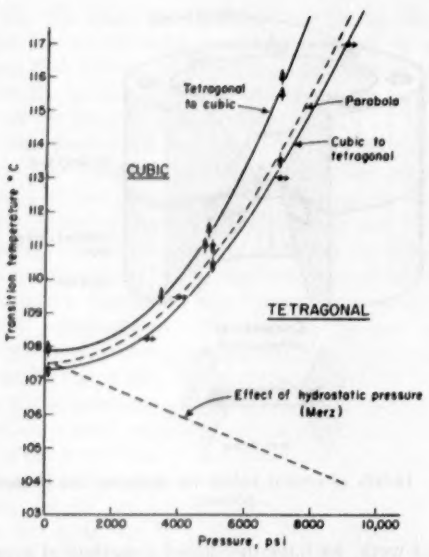

FIG. 2. Effect of two-dimensional pressure on the Curie transition in barium titanate.

relax back and forth between the faces of the clamp fairly rapidly under changes in pressure. The data can be taken in such a manner as to allow a check on the presence or absence of a frictional correction in the pressure, which is read by means of a Bourdon gauge in the oil line.

EFFECT ON TRANSITION TEMPERATURE

The disk-shaped crystal was cut from a strain-free crystal plate of cubic-growth habit and of uniform thickness. Its diameter was a little over $\frac{1}{8}$ in. and its thickness, *ca* 20 mils. The thickness to diameter ratio of about 1:8 should be sufficient to prevent elastic buckling. The clamp was wound with nichrome ribbon and well insulated with glass cloth. Temperatures were measured by means of a mercury thermometer embedded deeply in the massive metal of the clamp. The transition was observed with a polarizing microscope, which revealed a considerable disturbance at the transition point. The transition was reasonably sharp at all pressures. The effect of pressure on the transition was followed by zigzagging isothermally and isobarically along the transition curve. The agreement of the downgoing transition temperatures taken isothermally and isobarically shows that the rubber transmitted the pressure without appreciable frictional correction (Fig. 2). Unfortunately, the upgoing transition could be taken only isobarically due to the insensitive needle valve in the hydraulic pump. The results show a purely quadratic dependence of the transition temperature on two-dimensional pressure. The width of thermal hysteresis increases with two-dimensional pressure. The results of Merz,[8] using hydrostatic pressure, show a purely linear pressure dependence. If, for convenience, the two-dimensional and hydrostatic pressure effects are symbolized by 2-H and 3-H, respectively, the results can be described as follows, where H is the oil pressure in atmospheres and T_c the transition temperature:

$$2\text{-}H: \qquad T_c = T_{c0} + 3.1\times 10^{-5} H^2,$$

$$3\text{-}H \text{ (Merz}^3\text{)}: \quad T_c = T_{c0} - 0.0058 H.$$

EFFECT OF PRESSURE ON DEVONSHIRE'S FREE-ENERGY EXPANSION

Devonshire[9] has expressed the free energy of barium titanate in terms of polarization and strain, with respect to the cubic unpolarized configuration, as

$$\begin{aligned} A(\mathbf{x},\mathbf{P}) = {} & \tfrac{1}{2}c_{11}{}^{P}(x_x^2+y_y^2+z_z^2)+c_{12}{}^{P}(y_yz_z+z_zx_x+x_xy_y) \\ & +\tfrac{1}{2}c_{44}{}^{P}(x_y^2+y_z^2+z_x^2)+\tfrac{1}{2}\chi''(P_x^2+P_y^2+P_z^2) \\ & +\tfrac{1}{4}\xi_{11}''(P_x^4+P_y^4+P_z^4) \\ & +\tfrac{1}{2}\xi_{12}''(P_y^2P_z^2+P_z^2P_x^2+P_x^2P_y^2) \\ & +g_{11}(x_xP_x^2+y_yP_y^2+z_zP_z^2) \\ & +g_{12}\{x_x(P_y^2+P_z^2)+y_y(P_z^2+P_x^2) \\ & +z_z(P_x^2+P_y^2)\}+g_{44}(y_zP_yP_z+z_xP_zP_x \\ & +x_yP_xP_y)+\tfrac{1}{6}\zeta''(P_x^6+P_y^6+P_z^6). \end{aligned} \quad (1)$$

The boldface symbols mean the stress or strain tensors and the vector polarization, the components of all of which are in the above expression. For the present purposes, we need not consider configurations involving shears or any components of polarization aside from that in the z direction. We are thus considering the dependence of the free energy on x_z, y_y, z_z, P_z (which we shall abbreviate x, y, z, P), all other strain components (the shears) and the x and y components of polarization being kept equal to zero:

$$\begin{aligned} A(\mathbf{x},\mathbf{P}) = {} & \tfrac{1}{2}c_{11}{}^{P}(x^2+y^2+z^2)+c_{12}{}^{P}(yz+zx+xy) \\ & +\tfrac{1}{2}\chi''P^2+\tfrac{1}{4}\xi_{11}''P^4+g_{11}zP^2 \\ & +g_{12}(x+y)P^2+\tfrac{1}{6}\zeta''P^6. \end{aligned} \quad (2)$$

Using the convention that a positive stress shall be a compression and a positive strain an extension, we find that the three stress components are $X=-\partial A/\partial x$, $Y=-\partial A/\partial y$, $Z=-\partial A/\partial z$, and thus for a two-dimensional pressure:

$$\begin{aligned} -H &= c_{11}x+c_{12}(y+z)+g_{12}P^2, \\ -H &= c_{11}y+c_{12}(z+x)+g_{12}P^2, \\ 0 &= c_{11}z+c_{12}(x+y)+g_{11}P^2, \end{aligned} \quad (3)$$

where the superscripts P of the elastic coefficients at constant polarization have been dropped for convenience. For a hydrostatic pressure, the stress equations (3) are the same except that the zero in the third line is replaced by $-H$.

To discuss the Curie point and the properties asso-

[9] A. F. Devonshire, Phil. Mag. 40, 1040 (1949); 42, 1065 (1951).

ciated with the z direction, we need only compare cubic and tetragonal configurations, so that the strains x and y are equal, and the stress relations become

$$3\text{-}H:\begin{cases}-H=\\ -H=\end{cases},\quad 2\text{-}H:\begin{cases}-H=(c_{11}+c_{12})x+c_{12}z+g_{12}P^2,\\ 0=2c_{12}x+c_{11}z+g_{11}P^2,\end{cases}\tag{4}$$

which can be solved for x and z, giving

$$\begin{aligned}2\text{-}H:\quad x&=-\frac{c_{11}}{(c_{11}-c_{12})(c_{11}+2c_{12})}H\\&\quad-\frac{c_{11}g_{12}-c_{12}g_{11}}{(c_{11}-c_{12})(c_{11}+2c_{12})}P^2,\\ z&=\frac{2c_{12}}{(c_{11}-c_{12})(c_{11}+2c_{12})}H\\&\quad+\frac{2c_{12}g_{12}-(c_{11}+c_{12})g_{11}}{(c_{11}-c_{12})(c_{11}+2c_{12})}P^2;\\ 3\text{-}H:\quad x&=-\frac{(c_{11}-c_{12})}{(c_{11}-c_{12})(c_{11}+2c_{12})}H\\&\quad-\frac{c_{11}g_{12}-c_{12}g_{11}}{(c_{11}-c_{12})(c_{11}+2c_{12})}P^2,\\ z&=-\frac{(c_{11}-c_{12})}{(c_{11}-c_{12})(c_{11}+2c_{12})}H\\&\quad+\frac{2c_{12}g_{12}-(c_{11}+c_{12})g_{11}}{(c_{11}-c_{12})(c_{11}+2c_{12})}P^2.\end{aligned}\tag{5}$$

If we now substitute these expressions for the strains into the free energy [Eq. (2)], remembering that $x=y$, we obtain for both cases

$$\begin{aligned}A(\mathbf{x},\mathbf{P})=&\text{ terms in }H^2+\text{terms in }HP^2+\text{terms in }P^2\\&+\text{terms in }P^4+\text{terms in }P^6.\end{aligned}\tag{6}$$

We can now determine the free energy $A(\mathbf{X},\mathbf{P})$ expressed in terms of stress and polarization, and see how it compares with the free energy as a function of polarization at zero stress,[8] for which the most recent coefficients have been given by Merz.[9] The free energy in terms of stress and polarization is related to that in terms of strain and polarization by the usual Legendre transformation:[10]

$$A(\mathbf{X},\mathbf{P})=A(\mathbf{x},\mathbf{P})+\mathbf{x}\cdot\mathbf{X},\tag{7}$$

where $\mathbf{x}\cdot\mathbf{X}$ is a scalar product, and is the transformation term that must be added to Eq. (6) to obtain the free energy expressed in terms of polarization and pressure.

[9] W. J. Merz, Phys. Rev. **91**, 513 (1953).

[10] See, for instance, L. Tisza, *Phase Transformations in Solids* (John Wiley and Sons, Inc., New York 1951), pp. 1–38.

The transformation term is

$$\begin{aligned}\mathbf{x}\cdot\mathbf{X}_{2\text{-}H}&=2Hx=\text{a term in }H^2\\&\quad-2\frac{c_{11}g_{12}-c_{12}g_{11}}{(c_{11}-c_{12})(c_{11}+2c_{12})}HP^2,\\ \mathbf{x}\cdot\mathbf{X}_{3\text{-}H}&=2Hx+Hz=a\text{ term in }H^2\\&\quad-2\frac{c_{11}g_{12}-c_{12}g_{11}}{(c_{11}-c_{12})(c_{11}+2c_{12})}HP^2\\&\quad+\frac{2c_{12}g_{12}-(c_{11}+c_{12})g_{11}}{(c_{11}-c_{12})(c_{11}+2c_{12})}HP^2.\end{aligned}\tag{8}$$

Therefore,

$$A(\mathbf{X},\mathbf{P})=\text{terms in }H^2+\text{terms in }HP^2+A_P,\tag{9}$$

where A_P is the free energy as a function of polarization for zero stress, the coefficients of which have recently been given by Merz as

$$A_P=3.7\times10^{-5}(T-T_0)P^2-1.7\times10^{-13}P^4+3.8\times10^{-23}P^6.$$

T_0 is the Curie-Weiss temperature at atmospheric pressure and is about 11°C below the transition temperature, and the units are electrostic cgs units.

The only terms through which the pressure can affect the dependence of the free energy on the polarization are terms containing both H and P, in this case [Eq. (9)], the terms in HP^2. If these terms add up to a positive quantity, pressure will raise the free energy of the polarized configurations faster than that of the unpolarized phase, and so lower the transition temperature; if they add up to a negative quantity, it is raised.

Having found the transformation terms [Eq. (8)], we now need to calculate the contribution of $A(\mathbf{x},\mathbf{P})$ to terms containing both H and P. The terms in $A(\mathbf{x},\mathbf{P})$ that give terms in H and P (*viz.*, HP^2) are as follows, where we have set $x=y$ since we are only interested in comparing cubic and tetragonal configurations:

$$(c_{11}+c_{12})x^2+\tfrac{1}{2}c_{11}z^2+2c_{12}xz+g_{11}zP^2+2g_{12}xP^2.$$

For a two-dimensional pressure the sum of the terms in HP^2 in $A(\mathbf{x},\mathbf{P})$ is

$$\begin{aligned}&\{(c_{11}+c_{12})2[c_{11}(c_{11}g_{12}-c_{12}g_{11})]\\&\quad+(\tfrac{1}{2}c_{11})2[2c_{12}(2c_{12}g_{12}-(c_{11}+c_{12})g_{11})]\\&\quad+2c_{12}[-2c_{12}(c_{11}g_{12}-c_{12}g_{11})]+2c_{12}[-c_{11}(2c_{12}g_{12}\\&\quad-(c_{11}+c_{12})g_{11})]\}HP^2/(c_{11}-c_{12})^2(c_{11}+2c_{12})^2\\&\qquad+(g_{11}2c_{12}-2g_{12}c_{11})HP^2/(c_{11}-c_{12})(c_{11}+2c_{12}).\end{aligned}$$

The second and fourth terms within the braces cancel, and the first and third terms, when added together and factored, become $2(c_{11}g_{12}-c_{12}g_{11})(c_{11}-c_{12})(c_{11}+2c_{12})$, which, when multiplied by the quantity outside braces, exactly cancels the last term in the whole expression, which means that for a two-dimensional pressure, $A(\mathbf{x},\mathbf{P})$ contributes no terms in HP^2.

However, for hydrostatic pressure the free energy $A(\mathbf{x},\mathbf{P})$ contributes $-2c_{12}g_{11}/(c_{11}-c_{12})(c_{11}+2c_{12})HP^2$. Therefore, when we add on the transformation terms [Eq. (8)], the HP^2 term in $A(\mathbf{X},\mathbf{P})$ is

$$\frac{-2g_{12}(c_{11}-c_{12})-g_{11}(c_{11}+c_{12})}{(c_{11}-c_{12})(c_{11}+2c_{12})}HP^2 \text{ for 3-}H$$

and (11)

$$-2\frac{c_{11}g_{12}-c_{12}g}{(c_{11}-c_{12})(c_{11}+2c_{12})}HP^2 \text{ for 2-}H.$$

The free energy in terms of polarization and pressure is then

$$2\text{-}H: \quad A(\mathbf{X},\mathbf{P})=A_e+\left[3.7\times10^{-5}(T-T_0)-2\frac{c_{11}g_{12}-c_{12}g_{11}}{(c_{11}-c_{12})(c_{11}+2c_{12})}H\right]P^2-1.7\times10^{-13}P^4+3.8\times10^{-23}P^6,$$

$$3\text{-}H: \quad A(\mathbf{X},\mathbf{P})=A_e+\left[3.7\times10^{-5}(T-T_0)-\frac{2(c_{11}-c_{12})g_{12}+(c_{11}+c_{12})g_{11}}{(c_{11}-c_{12})(c_{11}+2c_{12})}H\right]P^2-1.7\times10^{-13}P^4+3.8\times10^{-23}P^6. \quad (12)$$

From this it is seen that the dependence of free energy on polarization, for a given applied pressure, is unaltered only if there is a corresponding change in temperature ΔT:

$$2\text{-}H: \quad \Delta T=\frac{1}{3.7\times10^{-5}}\left[2\frac{c_{11}g_{12}-c_{12}g_{11}}{(c_{11}-c_{12})(c_{11}+2c_{12})}\right]H,$$

$$3\text{-}H: \quad \Delta T=\frac{1}{3.7\times10^{-5}}\left[\frac{2(c_{11}-c_{12})g_{12}+(c_{11}+c_{12})g_{11}}{(c_{11}-c_{12})(c_{11}+2c_{12})}\right]H. \quad (13)$$

Since a purely linear dependence of the transition temperature on two-dimensional pressure is thus predicted, it is necessary to supplement Devonshire's expansion with higher terms in order to account for the quadratic effect. While it is too difficult to evaluate the effect of pressure on the transition temperature itself in the presence of the higher terms, it will be shown that the effect on the Curie-Weiss temperature T_0 is easy to determine. This may be determined experimentally by extrapolating to zero the inverse susceptibility of the cubic phase. Its dependence upon two-dimensional and hydrostatic pressure will be the subject of a future paper. It will be shown in the following section that the linear part of the shift in the Curie-Weiss temperature for two-dimensional and hydrostatic pressures gives two independent linear relations connecting the coefficients g_{11} and g_{12}, and the quadratic shifts give two linear relations connecting the 9 coefficients in the higher terms with which Devonshire's expansion may be supplemented.

EFFECT OF HIGHER TERMS IN THE FREE ENERGY ON THE CURIE-WEISS TEMPERATURE

As a result of the symmetry of the crystal, the strains with respect to the cubic phase depend on even powers of the polarization. Since there is a P^2 term in the strain, the P^6 term in the free energy as a function of stress and polarization [given by Eq. (10) for zero stress] will be partially made up of terms not included in Devonshire's expansion Eq. (1). These are terms in strain $\times P^4$, strain^2 $\times P^2$, and strain^3. For the present case of no shears and no polarization other than P_z, the free energy including these higher terms will be

$$\begin{aligned}A(\mathbf{x},\mathbf{P})=&\tfrac{1}{2}c_{11}{}^P(x^2+y^2+z^2)+c_{12}{}^P(yz+zx+xy)\\&+\tfrac{1}{2}\chi''P^2+\tfrac{1}{4}\xi_{11}''P^4+g_{11}zP^2+g_{12}(x+y)P^2\\&+\tfrac{1}{6}\zeta''P^6+\beta_{11}zP^4+\beta_{12}(x+y)P^4\\&+\gamma_{11}z^2P^2+\gamma_{12}(x^2+y^2)P^2+\gamma_{13}xyP^2\\&+\gamma_{14}(yz+zx)P^2+\delta_{11}(x^3+y^3+z^3)+\delta_{12}xyz\\&+\delta_{13}[y(z^2+x^2)+z(x^2+y^2)+x(y^2+z^2)]. \quad (14)\end{aligned}$$

There is not enough accurate information to evaluate any of these higher terms, but it is easy to show that the terms with coefficients γ and δ give rise to a quadratic dependence of the Curie-Weiss temperature T_0 on the pressure.

The isotherms of polarization *vs* electric field, that Merz[9] calculates from the free energy, are reproduced in Fig. 3, where t is proportional to $(T-T_0)$, T_0 being the Curie-Weiss temperature. It is easy to show that the transition temperature occurs at the point $t=0.75$ and in Fig. 4 the free energies corresponding to $t=0$, $t=0.75$ and $t=1$ are shown schematically. The Curie-Weiss temperature $t=0$, is clearly the temperature to which the cubic phase could be supercooled in the absence of thermal fluctuations, and the tetragonal phase could be overheated to $t=1$ in the absence of thermal fluctuations. The Curie-Weiss temperature $t=0$ is determined by the condition $(\partial P/\partial E)=\infty$ taken

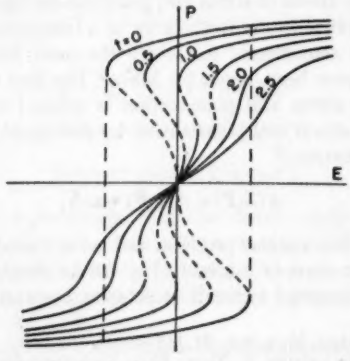

FIG. 3. Merz's isotherms of the electric field.

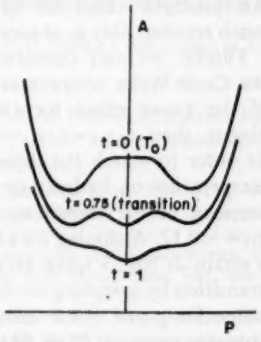

FIG. 4. Schematic representation of free-energy isotherms in vicinity of transition.

at zero polarization, where the strain polarization relations will be those for very small values of these variables and will, therefore, be given by Eqs. (5), which may be written

$$x=C_1H+G_{12}P^2, \quad z=C_2H+G_{11}P^2. \tag{5}$$

When the above strains are substituted into Eq. (14) and the Legendre transformation terms included, the terms in the free energy as a function of polarization and pressure $A(\mathbf{X},\mathbf{P})$ that contain P^2 and hence determine the slope $\partial P/\partial E$ at $P=0$ and the Curie-Weiss temperature, will be

$$\begin{aligned}\tfrac{1}{2}\chi''P^2+\Big\{&[2(c_{11}+c_{12})C_1G_{12}+c_{11}C_2G_{11}\\&+2c_{12}(C_1G_{11}+C_2G_{12})+g_{11}C_2+2g_{12}C_1]\\&+\begin{matrix}2G_{12}\text{ (for }2H)\\2G_{12}+G_{11}\text{ (for }3H)\end{matrix}\Big\}HP^2+[\gamma_{11}C_2^2+2\gamma_{14}C_1C_2\\&+(2\gamma_{12}+\gamma_{13})C_1^2+3(2\delta_{11}+2\delta_{13})C_1^2G_{12}\\&+3\delta_{11}C_2^2G_{11}+(\delta_{12}+2\delta_{13})(C_1^2G_{11}+2C_1C_2G_{12})\\&+2\delta_{13}(2C_1C_2G_{11}+C_2^2G_{12})]H^2P^2. \end{aligned}\tag{15}$$

Thus the linear dependence of the Curie-Weiss temperature depends entirely on the coefficients g (and, of course, c, which are known) and is given by Eqs. (13). The quadratic dependence is determined by the coefficients γ and δ, and depends, of course, also on the g and c coefficients.[11]

For two-dimensional pressure, the linear part of the pressure shift [Eqs. (13)] is seen to be proportional to the coefficient G_{12}. If one can assume that the Curie-Weiss temperature changes in more or less the same way as the transition temperature, which has yet to be checked, one would conclude that G_{12} is zero, and, therefore, that the x strain has no P^2 dependence at all. In Fig. 5 are plotted the strains from the x-ray data of Kay and Vousden[12] against the fourth power of the polarization, as recently measured by Merz;[9] within 25°C of the transition temperature the x strain is directly proportional to P^4 rather than P^2. One may object to using the results of Kay and Vousden on crystals that gave much too low values for the spontaneous polarization. But Merz has shown that the reason for these low values in crystals that are not exceedingly good is that some tendency to antiparallel domain formation persists to fairly appreciable fields. The x-ray parameters, however, are not affected by the existence of domains. The crystals of Merz have a somewhat lower transition temperature than those of Kay and Vousden, so the data were plotted for corresponding temperatures below the transition temperature.

The nature of the terms with coefficients γ and δ is immediately apparent upon differentiation of the free energy [Eq. (14)]:

$$\begin{aligned}-\partial Z/\partial z&=c_{11}{}^PP+2\gamma_{11}P^2+3\delta_{11}z+2\delta_{13}(x+y),\\-\partial X/\partial x&=c_{11}{}^PP+2\gamma_{12}P^2+3\delta_{11}x+2\delta_{13}(y+z),\\-\partial X/\partial y&=c_{12}{}^PP+\gamma_{13}P^2+\delta_{12}z+2\delta_{13}(x+y),\\-\partial Z/\partial x&=c_{12}{}^PP+\gamma_{14}P^2+\delta_{13}y+2\delta_{13}(y+z).\end{aligned}\tag{16}$$

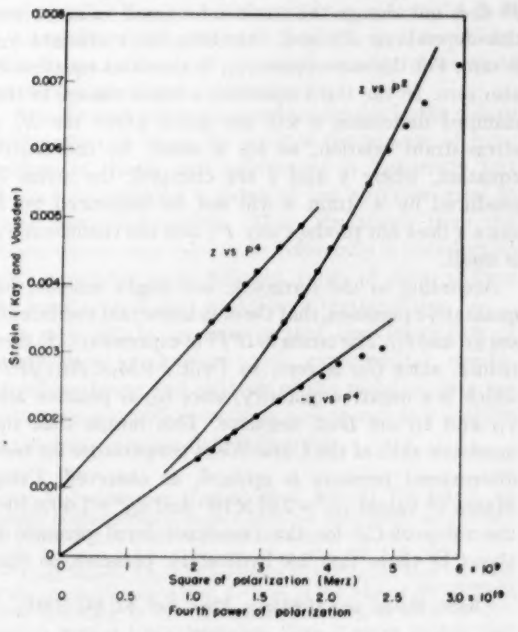

FIG. 5. Plots of the tetragonal strains against powers of the polarization.

[11] As has been pointed out by Tisza (reference 10), the validity of thermodynamics in the vicinity of a point such as ($t=0$, $P=0$) in Fig. 4 is questionable, since the statistical fluctuations about one of the macroscopic variables will be large. The expression (15), when divided by $P^2/2$, is the inverse susceptibility of the cubic phase as a function of temperature and pressure. As prescribed by Devonshire, the temperature dependence arises only from the coefficient $\chi''=\chi_0(T-T_0)$, which is a straight line passing through zero at the temperature T_0. Equation (15) states that the application of pressure shifts the straight line up or down. What we call the shift in the Curie-Weiss temperature, ΔT_0, is simply the amount of the shift of this straight line in the direction of the temperature axis. The fact that the validity of thermodynamics is questionable when one is very close to the crossing point, does not enter the picture.

[12] H. F. Kay and P. Vousden, Phil. Mag. **40**, 1019 (1949).

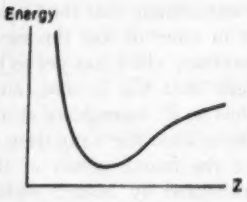

FIG. 6. Typical dependence of energy on an interatomic distance.

For the small polarization and strains involved in the present discussion, one can make some qualitative statements about the γ and δ coefficients. Considering the first of the above equations, it states that the mechanical stiffness in the z direction departs from Hooke's law by the quantity $3\delta_{11}z$ when the x and y directions are clamped and the polarization is not allowed to change (since the partial derivatives are taken at constant x, y, P in the first line). This is to be expected, since, with x, y, and P clamped, the energy as a function of extension in the z direction is not a parabola, but is rather as shown in Fig. 6, which to a second approximation has a negative z^3 term in addition to the z^2 term. Hence the coefficient δ_{11} must be a negative quantity. For small changes in the clamped dimensions x and y, the shape of the energy curve in the z direction will probably not change much except to be shifted, so one would expect δ_{12} to be rather small. If one increases the fixed value of the polarization, z will be increased since $z=G_{11}P^2$, and thus γ_{11} must have the same sign as δ_{11}, i.e., negative.

Considering the second of Eqs. (16), the polarization P^2 does not change the strain x for small values, since this depends on P^4, and, therefore, the coefficient γ_{12} is zero. For the same reason γ_{13} in the third equation is also zero. In the third equation, a small change in the clamped dimension z will not much affect the X, y stress-strain relation, so δ_{12} is small. In the fourth equation, where y and z are clamped, the stress Z produced by a strain x will not be influenced by P since x does not produce any P^2, and the coefficient γ_{14} is small.

According to the foregoing, one might assume, for qualitative purposes, that the only important coefficients are γ_{11} and δ_{11}. The terms in H^2P^2 in expression (15) then reduce, since G_{12} is zero, to $[\gamma_{11}C_2^2+3\delta_{11}C_2^2G_{11}]H^2P^2$ which is a negative quantity, since G_{11} is positive and γ_{11} and δ_{11} are both negative. This means that the quadratic shift of the Curie-Weiss temperature for two-dimensional pressure is upward, as observed. Using Mason's[13] values $c_{11}^P=2.07\times10^{12}$ and $c_{12}^P=1.40\times10^{12}$, the value of C_2^2 for the two-dimensional pressure is about 18 times that for hydrostatic pressure, so that the quadratic effect for hydrostatic pressure is very much smaller, also as observed.

Finally, we may consider the linear dependence of the Curie-Weiss temperature on hydrostatic pressure. If the linear effect for two-dimensional pressure is absent, then $c_{11}g_{12}-c_{12}g_{11}=0$ from which $g_{12}=0.68g_{11}$. In order to match the dependence of the Curie-Weiss temperature on hydrostatic pressure to Merz's[3] measurement of the transition, it is necessary to assume $g_{11}=-0.17$. Assuming $z=aP^2+bP^4$, one can match the z strain in Fig. 5 quite accurately within 25°C of the transition by assuming $a=0.57\times10^{-12}$, which requires a value for g_{11} of -1.2. However, the curve in Fig. 5 suggests negative P^6 or P^8 terms in the strains, and, in fact, the z strain can be accurately represented by $z=2\times10^{-13}P^2+3.4\times10^{-22}P^4-2.9\times10^{-32}P^6$, where the coefficient of P^2 requires a value of $g_{11}=-0.42$. This gives a linear dependence on hydrostatic pressure about twice that observed.

PROBABLE EFFECT ON THE HYSTERESIS LOOP

If the shift remains quadratic to much higher pressures, a two-dimensional pressure of 2000 atmos should raise the transition by more than 100°C. This should result in a marked increase of the coercive field at room temperature. Furthermore, it is possible that at room temperature the hysteresis loop is affected by the proximity of the orthorhombic transition around 5°C, since the direction of the polarization might well reverse by a rotation through the orthorhombic configurations rather than by direct passage through the cubic configuration. In this case, the effect of the two-dimensional pressure on the orthorhombic transition would enter into the picture. It is expected that the two-dimensional pressure, as presently applied to two of the pseudo-cubic axes, will cause a very large depression of the orthorhombic transition. The reason for expecting this is that the elongation that accompanies the spontaneous polarization would be working in part against a component of compression, when the polarization direction snaps into a new direction at 45° to the direction in which there is no component of stress. The rhombohedral phase would likewise be suppressed by the two-dimensional pressure as applied at present. From the magnitudes of the effects of two-dimensional and of hydrostatic[3] pressures on the orthorhombic transition, it will be possible to obtain information about the shear terms in Devonshire's expansion.

ACKNOWLEDGMENT

The present work was made possible by the use of a barium titanate crystal of suitable size, obtained through the courtesy of Dr. S. O. Morgan of the Bell Telephone Laboratories.

[13] Bond, Mason, and McSkimin, Phys. Rev. 82, 442 (1951).

Electrical Properties of *N*-Type Germanium*

P. P. DEBYE,† *Bell Telephone Laboratories, Murray Hill, New Jersey*

AND

E. M. CONWELL,‡ *Sylvania Electric Products, Bayside, New York*

(Received August 3, 1953)

Measurements of conductivity and Hall effect from 11°K to 300°K on a set of *n*-type germanium samples covering the range from intrinsic to degenerate are reported. The purity and uniformity of the samples and extensiveness of the data permit a more thorough-going comparison with theory than has been possible in previous work.

The theory of mobility is reviewed briefly. The treatment of impurity scattering by Brooks and Herring is presented, and their formula for the impurity mobility is used throughout. An analytical formula for obtaining the mobility from lattice and impurity mobilities is included. The effect of electron-electron collisions on the mobility is considered in a qualitative manner.

The principal conclusions concerning the mobility are as follows: (1) Over the range 20.4°K to 300°K the lattice mobility varies as $T^{-1.61}$ rather than the theoretically predicted $T^{-1.5}$. (2) The impurity mobility increases with temperature less rapidly than the theoretical formula predicts, the exponent of T in the numerator being apparently between 1.0 and 1.5. (3) The Erginsoy formula for neutral impurity scattering appears to fit the experimental data reasonably well for a value of effective mass about one-third the free electron mass. (4) Dislocation scattering is negligible, leading to the conclusion that the density of edge-type dislocations is less than $10^4/cm^2$.

In fitting the concentration data, the parameters involved are activation energy, acceptor concentration, and effective mass. An effective mass in the neighborhood of one-quarter the free electron mass gives the best fit for all samples. The values of acceptor concentration obtained in this way for this effective mass agree well with those calculated from the low-temperature mobility values. The activation energy obtained for the purer samples is 0.0125 ev, in agreement with the value calculated from the hydrogen-like model for one-quarter the free electron mass.

The variation of activation energy with concentration does not agree with that observed by Pearson and Bardeen for *p*-type silicon. The effects which have been proposed to explain the variation are: residual potential energy of attraction between free electrons and ionized donors, screening of trapping centers by the free electrons, polarization of neutral centers by free electrons. It is concluded that a combination of the three effects will probably be required to explain the results.

The ratio of Hall to drift mobility is shown to agree with the theoretically predicted value within about 10 percent in the range 78°K to 300°K.

I. INTRODUCTION

MEASUREMENTS of conductivity and Hall effect have been made on a new set of germanium samples with widely varying amounts of added arsenic in the temperature range from 11°K to 300°K. The room temperature resistivities of these samples varied from 43 ohm cm to 0.005 ohm cm. Special precautions were taken in the growing of the crystals to ensure uniformity of the impurity distribution and a minimum of impurities other than the arsenic. The fact that the Hall mobilities of these samples at 300°K are higher than any previously reported[1] is presumably evidence for the greater perfection of these crystals.

From the measurements carrier concentration and Hall mobility were computed, and the results so obtained compared with existing semiconductor theory. This theory is based on a number of simplifying assumptions, of which the major one is that of spherical surfaces of constant energy in the conduction band. There is now a considerable body of evidence, experimental and theoretical, that this is untrue. Magnetoresistance data for *n*-type germanium cannot be explained in terms of spherical energy surfaces.[2] Calculation of the band structure of germanium[3] yields the result that the edge of the conduction band is not at $k=0$, in which case the constant energy surfaces are not spherical.[4] It is nevertheless significant, and perhaps not surprising, that in many respects the simple theory gives quite good agreement with experiment.

A parameter which appears throughout in the theory is the effective mass. In practice the process of comparison of theory and experiment is frequently just that of determining a value of the effective mass in some particular context. Thus, deviations from the simple theory may show up as differences in the effective mass computed from different types of data, or from the same type of data at different temperatures.

In this article we first present the description of experimental techniques and experimental results. Mobility theory and analysis of the mobility data are in the two succeeding sections, and theory and analysis of the concentration data follow this.

---

* Presented at the North Carolina Meeting of the American Physical Society, March, 1953.

† Now at Raytheon Manufacturing Company, Waltham, Massachusetts.

‡ Work partly done at Bell Laboratories. On leave from Brooklyn College, Brooklyn, New York.

[1] Hall mobilities of these samples at 300°K have been reported by P. P. Debye and E. M. Conwell, Phys. Rev. **87**, 1131 (1952).

[2] G. L. Pearson and H. Suhl, Phys. Rev. **83**, 768 (1951). Although magnetoresistance data have not been taken for this new set of samples, it is unlikely that the results will be very different.

[3] F. Herman and J. Callaway, Phys. Rev. **89**, 518 (1953).

[4] These results might be incorrect to the extent that the edge of the conduction band is at $k=0$, or at the edge of the Brillouin zone. According to the calculations, however, at $k=0$ the conduction band is triply degenerate. Since it seems unlikely that these calculations would give the symmetry type incorrectly, it seems definite that wherever the edge of the conduction band the constant energy surfaces are nonspherical.

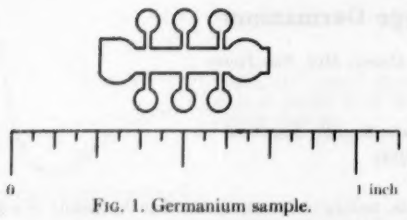

FIG. 1. Germanium sample.

II. EXPERIMENTAL PROCEDURES AND RESULTS

The single crystals from which the samples were cut were grown from germanium which had been very carefully purified by either zone refining[5] or repeated crystallization with subsequent discarding of the crystal end containing most of the impurities. A few of the purer crystals were grown by zone leveling.[6] The remainder were pulled from the melt by the method reported by Teal.[7] In the case of the doped crystals a small amount of arsenic was added in the melt before the final crystal was grown.[8]

The germanium samples were prepared in the standard manner by cutting with a diamond wheel a slice of about 0.050 inch thickness perpendicular to the long axis of the single crystal.[9] This orientation was chosen because it gives the smallest over-all change in resistivity. This slice was lapped to a specified thickness (0.015–0.045 in.), and mounted on a glass plate with sealing wax. The desired "bridge" shape (Fig. 1) was then obtained by cutting away the unwanted portions of the germanium with a vibrating steel dye.[10] The large areas on both ends of the bridge were used for the current leads, the center arms for the Hall measurements and either pair of outside arms on the same side for resistivity measurements.[11] The ends for the current leads were made unequal for easy identification. Some of the advantages claimed for this configuration are that the actual contact areas are far removed from the area of measurement and that the unbalance voltage across the Hall arms due to the sample current is always practically zero.

The bridge was probed at 0.05-cm intervals along its center line to measure the room temperature resistivity and check uniformity. If there was any nonuniformity in the immediate Hall area, its resistivity was corrected accordingly.

The completed bridge was mounted in the sample holder. This consisted essentially of a hollow brass block at the inside of which the bridge was clamped into place. The large mass of the holder (about 300 g) served to give good temperature stability. The brass block also contained the platinum resistance thermometer and a small heater. The block was suspended on thin (0.004-in. wall) Monel tubing which also supported two radiation shields. All lead wires ran inside this tube. The complete assembly was enclosed by a glass Dewar 18 in. long, which was surrounded by a vacuum-tight brass casing. By connecting a vacuum pump to the Dewar, it was possible to reduce the pressure over the refrigerant and, therefore, the temperature of its boiling point. With liquid hydrogen as the refrigerant, this arrangement gave a minimum temperature of about 10.8° Kelvin.

The temperature range of the measurements usually extends from about 11° to somewhat above 300° Kelvin. At the boiling points of nitrogen and hydrogen and below the latter the sample was substantially in temperature equilibrium with the holder and thermometer. For the regions from 20.4° to 78° and 78° to

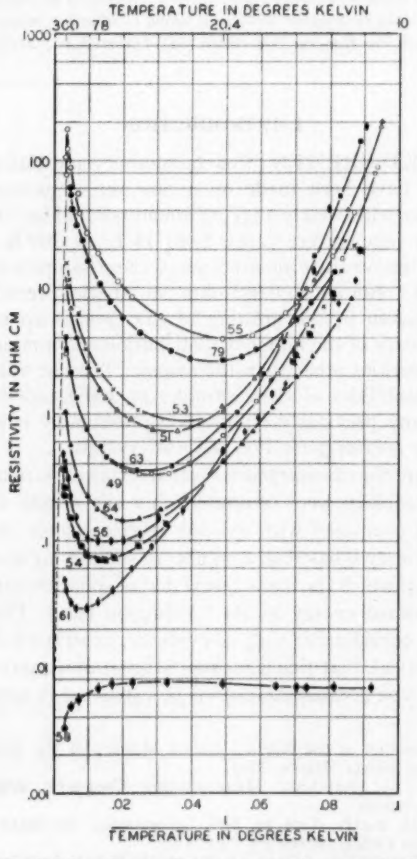

FIG. 2. Resistivity of a set of *n*-type germanium samples (arsenic-doped) as a function of inverse absolute temperature.

[5] W. G. Pfann, J. Metals 4, 747 (1952); W. G. Pfann and K. M. Olsen, Phys. Rev. 89, 322 (1953).

[6] The zone-melted materials were supplied by W. G. Pfann and K. M. Olsen of Bell Laboratories.

[7] G. K. Teal and J. B. Little, Phys. Rev. 78, 647 (1950).

[8] The pulled crystals were supplied by E. Buehler and W. W. Bradley of Bell Laboratories.

[9] Much of the sample preparation work, to be described in the succeeding paragraphs, was carried out by J. P. Maita of Bell Laboratories who also made many contributions to the techniques used.

[10] This is described by W. L. Bond, Phys. Rev. 78, 646 (1950).

[11] Germanium samples of this shape had been used previously for Hall and resistivity measurements by G. L. Pearson of Bell Laboratories.

300° Kelvin, where the sample holder was allowed to warm up slowly in vacuum, it was shown that the temperature differential between sample and thermometer was also insignificant. The resistance of the platinum thermometer was measured with a Mueller bridge, and then converted into temperature according to a calibration made by the National Bureau of Standards.

The field strength of the electromagnet (gap $2\frac{1}{8}$ in.) was measured by comparison with a secondary standard which had also been calibrated at the National Bureau of Standards. The Hall effect was measured with fields of up to about 4000 gauss, the field being always low enough to stay within the linear range. The dc measurements were made with a type $K2$ potentiometer and galvanometer. The sample current was measured with a vacuum-tube microammeter. All the wiring and batteries with the exception of the potentiometer were shielded.

The resistivities of eleven samples as a function of the inverse absolute temperature are shown in Fig. 2. The intrinsic behavior is indicated by a dashed line. For relatively pure materials the resistivity goes

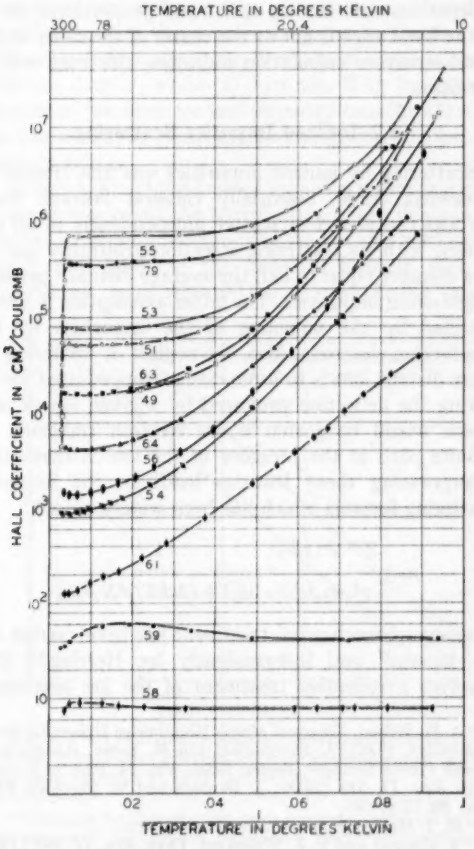

FIG. 3. Hall coefficient of a set of n-type germanium samples (arsenic-doped) as a function of inverse absolute temperature.

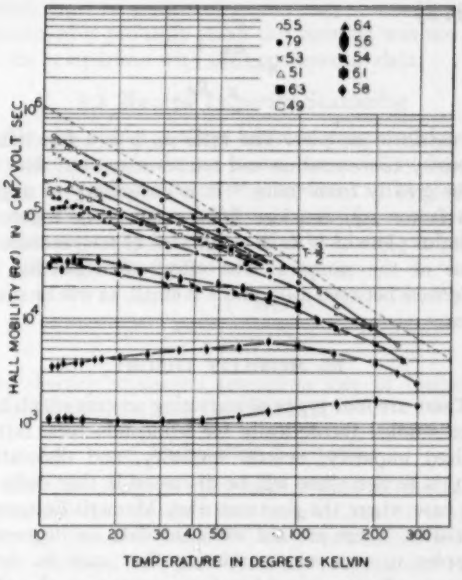

FIG. 4. Hall mobility of a set of n-type germanium samples (arsenic-doped) as a function of absolute temperature.

through a broad minimum when the temperature is lowered and reaches in the range 10°–13°K values which are comparable to those at room temperature. When more impurities are introduced, the resistivity minimum moves to higher temperatures and its values in the 10°–13°K range lie appreciably above those at ambient temperatures. Finally, sample 58, which contains enough impurities to make it degenerate over most of the temperature range, shows almost no change in resistivity with temperature.

The Hall coefficient R in cm³/coulomb was obtained from the equation[12]

$$R = tV \times 10^8 / HI, \tag{1}$$

and is plotted as a function of the inverse absolute temperature in Fig. 3. In this equation t represents the thickness of the bridge in cm, V is one-half the sum of the Hall voltages in volts measured with the magnetic field in the normal and in the reversed direction, and I is the current in amperes. While most of the samples in their low-temperature behavior fall into a more or less consistent pattern, samples 56 and 63 show a much larger slope than their neighbors. Both these samples had been cut from near the tip end of the crystal and therefore probably contained a larger total impurity concentration.

Resistivity and Hall data were combined to give Hall mobility, defined as R/ρ. This is plotted as a function of temperature in Fig. 4. From the definition of Hall mobility it follows that electron concentration n is

[12] See, for example, W. Shockley, *Electrons and Holes in Semiconductors* (D. Van Nostrand Company, Inc., New York, 1950), p. 213.

given by

$$n=\frac{\mu_H}{\mu}\frac{1}{Re} \tag{2}$$

for extrinsic samples. The ratio μ_H/μ is a function of impurity concentration and temperature, but does not differ greatly from unity.[13] It is customary to neglect this factor and consider $1/Re$ equal to n. Figure 10 contains plots of $1/Re$ as a function of temperature for some of the samples. The effect of neglecting the difference between μ_H/μ and 1 is small, as will be shown later.

III. MOBILITY THEORY

There are four types of scattering process which have been studied theoretically for semiconductors: lattice, ionized impurity, neutral impurity, and dislocation. In this section these will be discussed in that order for the case where the electrons obey Maxwell-Boltzmann statistics. There are not sufficient data on degenerate samples to warrant considering that case in detail. Some qualitative considerations concerning the effect of electron-electron collisions on the mobilities so obtained will also be presented. The following notation will be used:

σ = conductivity (ohm^{-1} cm^{-1})
R = Hall coefficient
μ = mobility (cm^2/volt sec)
$\mu_H = R\sigma$ = Hall mobility (cm^2/volt sec)
μ_L = lattice mobility (cm^2/volt sec)
μ_I = ionized impurity mobility (cm^2/volt sec)
μ_N = neutral impurity mobility (cm^2/volt sec)
μ_D = dislocation mobility (cm^2/volt sec)
n = density of conduction electrons (/cm^3)
N_D = density of donors (/cm^3)
N_A = density of acceptors (/cm^3)
N_I = density of ionized impurities (/cm^3)
N_N = density of neutral impurities (/cm^3)
e = magnitude of charge on the electron = 1.60×10^{-19} coulombs
m = mass of the electron in free space = 9.03×10^{-28} g
m_n = effective mass of a conduction electron (g)
k = Boltzmann's constant = 1.37×10^{-16} erg/degree
T = absolute temperature (°K)
$\hbar$ = Planck's constant/2π = 1.04×10^{-27} erg sec
$\mathcal{E}$ = kinetic energy (ergs)
τ = relaxation time (sec)
κ = dielectric constant, 16.1 for germanium
l_L = mean free path for lattice scattering (cm)
c_{ll} = average longitudinal elastic constant
$\mathcal{E}_{1n}$ = shift of edge of conduction band per unit dilation (ev)
$\mathcal{E}_{1p}$ = shift of edge of filled band per unit dilation (ev)

[13] See Eq. (17) and accompanying text.

3.1 Lattice Scattering

Several theoretical treatments of scattering by lattice vibrations have been carried out[14] with essentially equivalent results. In the Bardeen-Shockley derivation the lattice mobility is given by

$$\mu_L=\frac{(8\pi)^{\frac{1}{2}}\hbar^4 c_{ll}}{3\mathcal{E}_{1n}^2 m_n^{5/2}(kT)^{\frac{3}{2}}}. \tag{3}$$

It is usually considered that the temperature variation of $\mathcal{E}_{1n}$, m_n, and c_{ll} can be neglected. This has been substantiated for the last of these three in the case of germanium. It has been found experimentally that in the temperature range from 78°K to 293°K the elastic constants of germanium decrease about 3 percent,[15] which is negligible for the present purposes. The lattice mobility should then vary with temperature as $T^{-\frac{3}{2}}$. It should be mentioned, however, that underlying the $\frac{3}{2}$-power dependence is the assumption that the band edge is located at the center of the Brillouin zone. For the band edge at $k=0$ the electron interacts with low-energy lattice quanta, for which equipartition is satisfied, and this leads to a matrix element for the transition independent of electron speed and proportional to T. If the band edge is not at the center of the zone, as the band structure calculation indicates, this may not be the case.

3.2 Ionized Impurity Scattering

Scattering by ionized impurities was first treated in somewhat crude, essentially classical fashion. Each ion was considered to scatter independently of all the others, with its scattering x section arbitrarily cut off at a distance equal to half the average distance between neighboring impurities. The latter assumption is partly justified by the screening of the impurities by the conduction electrons. Also, the neglect of scattering by more distant ions is to some extent compensated for by taking the deflection produced by a given ion as that which would be gotten if the electron traversed an infinite path in the presence of the ion. A derivation incorporating these features leads to the impurity scattering formula which has been widely used,[16]

$$\mu_I=\frac{2^{7/2}}{\pi^{\frac{1}{2}}}\frac{\kappa^2(kT)^{\frac{3}{2}}}{m_n^{\frac{1}{2}}e^3N_I}\frac{1}{\ln[1+(3\kappa kT/e^2N_I^{\frac{1}{3}})^2]}. \tag{4}$$

A quantum-mechanical treatment has been carried out by Brooks[17] and independently by Herring.[18] This involves a collective treatment of the ion scattering.

[14] A. H. Wilson, *Theory of Metals* (Cambridge University Press, Cambridge, 1936); A. Sommerfeld and H. Bethe, *Handbuch der Physik* (Julius Springer, Berlin, 1933), Vol. 24, Part 1; F. Seitz, Phys. Rev. **73**, 549 (1948); J. Bardeen and W. Shockley, Phys. Rev. **80**, 72 (1950).
[15] H. J. McSkimin (private communication).
[16] E. Conwell and V. F. Weisskopf, Phys. Rev. **77**, 388 (1950).
[17] H. Brooks, Phys. Rev. **83**, 879 (1951).
[18] C. Herring (private communication).

The potential due to each ion is taken as a screened Coulomb potential. A Fourier analysis of the potential due to a random distribution of screened ions is carried out, and the results used in computing the matrix elements of the perturbing potential. This leads to a mobility which differs from (4) only in the replacement of the logarithmic term, e.g.,[18]

$$\mu_I=\frac{2^{7/2}}{\pi^{\frac{1}{2}}}\frac{\kappa^2(kT)^{\frac{1}{2}}}{m_n^{\frac{1}{2}}e^3N_I}\frac{1}{\ln(1+b)-b/(1+b)}, \tag{5}$$

where

$$b=\frac{6}{\pi}\frac{\kappa m_n k^2T^2}{nh^2e^2}. \tag{6}$$

For $n=N_I$, the two formulas give closely the same results; this is shown in Fig. 5, where the two mobilities are plotted as a function of impurity concentration at 300°K and 78°K. For this plot the effective mass has been taken as one-quarter the free-electron mass.[19] The two formulas give quite different results, however, when the conduction electron density is appreciably less than the ionized impurity density, the Brooks-Herring formula giving a lower mobility for the same concentration of ionized impurities. It has been pointed out by Herring that this is essentially due to the fact that (5) takes into account the decrease in screening when n is less than N_I while (4) does not. With less effective screening the same ionized impurity concentration will of course scatter more effectively, giving smaller electron mobilities.

A derivation of the ionized impurity scattering which takes into account the contribution of the dilatation of the lattice around the impurity ion has also been carried out.[20] This leads to the previous formula with the logarithmic term replaced by a complicated integral which must be evaluated numerically. Since the effect concerned is probably small this formula was not used in the comparison with the experimental data.

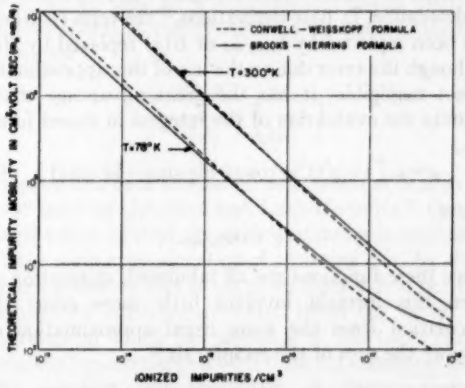

FIG. 5. Plots of impurity mobility *vs* ionized impurity concentration from Conwell-Weisskopf and Brooks-Herring impurity scattering formulas at 78°K and 300°K.

3.3 Neutral Impurity Scattering

Because of the analogy between a neutral donor or acceptor and a hydrogen atom, the mobility for scattering by neutral donors or acceptors can be obtained by suitable modification of the results for scattering of slow electrons by hydrogen. This has been carried out by Erginsoy,[21] leading to

$$\mu_n=\frac{1}{20}\frac{m_n e^3}{N_N\kappa h^3}. \tag{7}$$

The density of neutral impurities can, of course, be obtained directly from the Hall data.

3.4 Dislocation Scattering

The scattering of dislocations due to the lattice dilatation they produce has been calculated theoretically by Dexter and Seitz.[22] This gives a mobility which is proportional to T and inversely proportional to the number of dislocation lines per cm², which of course is unknown. For what would appear to be a reasonable dislocation density in germanium this process would only be of importance at low temperatures. There it would be difficult to separate from the ionized impurity scattering since the density of acceptors, which are all ionized, is unknown. Neglect of the dislocation scattering is more adequately justified, however, by the fact that it appears quite possible to account for the observed mobilities over the entire temperature range by the action of the scattering mechanisms previously cited. In sample 55, for example, the acceptor concentration required to account for the mobility observed at 11.5° is about $10^{12}/\text{cm}^3$ if it is assumed that only lattice and impurity scattering are operative. Since this is already quite small it is unlikely that there is appreciable dislocation scattering in this sample. From this it can be concluded, with the use of the Dexter-Seitz formula, that the dislocation density in this sample is less than $10^6/\text{cm}^2$.[23] Since there appears no reason why dislocation density should increase with impurity concentration, this estimate should be valid for all these samples.

3.5 Effect of Electron-Electron Collisions

In the previously mentioned derivations of mobility only the interaction of the electrons with the particular scattering mechanism was considered. The interaction of the electrons with each other may, however, prevent these mobilities from being realized.[24] The effect can be

[18] Evidence for this effective mass has been presented by P. P. Debye and E. M. Conwell, reference 1. Further evidence will be considered in the course of the present paper.

[20] C. Horie, Sci. Repts. Tôhoku Univ. 34, 29 (1950).

[21] C. Erginsoy, Phys. Rev. 79, 1013 (1950).

[22] D. L. Dexter and F. Seitz, Phys. Rev. 86, 964 (1952).

[23] This estimate is based on an effective mass of $m/4$ with ε_{11} corrected accordingly. See Sec. 4.1.

[24] To the authors' knowledge this was first demonstrated for the case of ion scattering, by Cohen, Spitzer, and Routly, Phys. Rev. 80, 230 (1950).

understood as follows. The current density for a given value of electric field intensity depends on the total electron momentum developed by the field. This in turn depends on the rate of momentum transfer to the scattering mechanism. Electron-electron collisions do not affect the current density directly since they cannot alter the total momentum. They do, however, tend to randomize the way in which this total is distributed among the different velocity groups. When the scattering mechanism is such as to lead to a nonuniform distribution, electron-electron collisions will give rise to a net transfer of momentum from electrons which dissipate it less efficiently to those which dissipate it more efficiently, resulting in an over-all greater rate of momentum transfer and lower mobility. Conversely, if the scattering mechanism is such as to lead to a uniform distribution, electron-electron collisions will not, as in the previous case, provide a more efficient mechanism for momentum transfer to the scatterers, and the mobility will be unaffected.

On the basis of this discussion it is apparent that the size of the effect of electron-electron collisions on the mobility is a function of the velocity dependence of the relaxation time. Thus, in particular, for neutral impurity scattering where the relaxation time is not a function of velocity, the mobility will not be affected by electron-electron collisions. Also, ion scattering should be much more affected than lattice scattering since in the former case τ is proportional to v^3, while in the latter it is proportional to v^{-1}.

It has been pointed out by Herring that it is possible to compute simply an upper limit for the size of this effect under the usual simplifying assumptions about the band structure. If the electron-electron collisions were completely effective in randomizing the drift velocities, the electron distribution in an electric field would be a Maxwell-Boltzmann distribution centered about $v=v_d$, the drift velocity. It can then be calculated that the maximum effect of these collisions would be to multiply μ_I by a factor 0.3, μ_L by 0.88. A calculation of the effect on μ_I has been carried out classically and leads to a factor 0.6.[25] This should be reasonably accurate for low electron densities and high temperatures. No calculation has been made for the case of lattice scattering. It is reasonable to expect here a factor of perhaps 0.95 for low electron densities. With increasing electron density this should decrease toward the limiting value 0.88 because of the increased frequency of electron-electron collisions compared to the electron-lattice collisions.

3.6 Combination of Mobilities

For a Maxwell-Boltzmann distribution of the electron energies and spherical surfaces of constant energy it can be shown[26] that the mobility, with electron-electron interaction neglected, depends on the relaxation time,

$$\mu=\frac{e}{m_n}\frac{\langle v^2\tau\rangle}{\langle v^2\rangle}. \tag{8}$$

If dislocation scattering is neglected the relaxation time can be written

$$\frac{1}{\tau}=\frac{1}{\tau_L}+\frac{1}{\tau_I}+\frac{1}{\tau_N}. \tag{9}$$

We shall consider first the case in which neutral impurity scattering can also be neglected. If we introduce the notation

$$v_T=(2kT/m_n)^{\frac{1}{2}}, \tag{10}$$

$$x=v^2/v_T^2=\mathcal{E}/kT, \tag{11}$$

the relaxation times can be written

$$\tau_L=l_L/v_Tx^{\frac{1}{2}}, \tag{12}$$

$$\tau_I=B(x)v_T^3x^{\frac{3}{2}}, \tag{13}$$

where $B(x)$ is a slowly varying function of x. Substitution of these expressions for the relaxation times in (8) leads to

$$\mu=\mu_L\int_0^\infty\frac{x^3e^{-x}}{(l_L/B(x)v_T^4)+x^2}dx. \tag{14}$$

Since $B(x)$ varies slowly with x it would be quite satisfactory to replace it in this integral by a constant which is its value at the maximum of the integrand. This is what is done in the evaluation of μ_I from (8). In that case the maximum of the integrand occurs at $x=3$. It can then be shown that

$$l_L/B(3)v_T^4=6\mu_L/\mu_I. \tag{15}$$

Since the maximum of the integrand of (14) is not easy to determine, in past derivations,[27] the term $l_L/B(x)v_T^4$ has been replaced by $6\mu_L/\mu_I$ or $B(x)$ replaced by $B(3)$. Although the error due to the use of this approximation is not negligible, it has the great advantage that it permits the evaluation of the integral in closed form,[28] e.g.,

$$\mu=\mu_L[1+q^2\{\mathrm{Ci}q\cos q+\mathrm{Si}q\sin q-\tfrac{1}{2}\pi\sin q\}], \tag{16}$$

where

$$q^2=6\mu_L/\mu_I.$$

Since these functions are all tabulated, calculation of μ from this formula involves little more effort than calculation from the more usual approximation employing the sum of the reciprocals.[29]

[25] L. Spitzer, Jr., and R. Härm, Phys. Rev. **89**, 977 (1953).
[26] Reference 12, p. 276.
[27] H. Jones, Phys. Rev. **81**, 149 (1951) and V. A. Johnson and K. Lark-Horovitz, Phys. Rev. **82**, 977 (1951).
[28] This was pointed out by H. Jones, reference 27.
[29] A graph of μ/μ_L as a function of μ_L/μ_I, computed from (16) has been published by E. Conwell, Proc. Inst. Radio Engrs. **40**, 1331 (1952). Percent difference between the mobilities computed from (14) and from the sum of the reciprocals, which may be quite appreciable, is plotted by V. A. Johnson and K. Lark-Horovitz, reference 27.

It can be seen that the approximation (16) will always lead to too small values of μ for a given μ_L and μ_I. The electrons which make the maximum contribution to μ_I are relatively fast ones. It has already been stated that they have energy of about $3kT$. These are just the ones, however, which are more effectively scattered by the lattice vibrations. When both scattering mechanisms are operative, therefore, the group of electrons which makes the maximum contribution to the mobility will certainly have energy less than $3kT$. The maximum of the integrand of (14) will, therefore, always occur at smaller values of x than $x=3$. Since B is a monotonically decreasing function of x the mobility calculated using $B(3)$ will, as previously stated, always be too small. The error will clearly be negligible, however, if $\mu_L \gg \mu_I$ or $\mu_L \ll \mu_I$.

Numerical integration of (14) was carried out for a number of cases to determine the magnitude of the error. For μ_I taken from (4), at 78°K the error was found to be about 9 percent at $N_I=10^{15}$ ($\rho \simeq 0.3$ ohm cm), 13 percent at $N_I=10^{17}$ ($\rho \simeq 0.01$ ohm cm), while for μ_I from (5), at this temperature it was 3 percent at 10^{15}, 6 percent at 10^{17}. It is to be expected that the error would be smaller in the latter case; the logarithmic term of (4) contains x to the second power, while that of (5) is linear in x. If, as was done in the calculations, values of μ computed from (16) are used to compute ρ for comparison with the experimental μ vs ρ the error is, of course, magnified. As will be seen later, it does affect somewhat the conclusions which can be drawn about effective mass from comparison of experiment and theory. These are also affected somewhat by electron-electron collisions, as will be demonstrated in a later section.

For comparison with experimental data it is necessary to compute the Hall mobility $R\sigma$, rather than μ. It can be shown that for a Maxwell-Boltzmann distribution and spherical energy surfaces the ratio of μ_H to μ is given by[30]

$$\frac{\mu_H}{\mu}=\frac{\langle v^2\tau^2\rangle}{\langle v^2\rangle}\div\left(\frac{\langle v^2\tau\rangle}{\langle v^2\rangle}\right)^2. \tag{17}$$

This ratio has been calculated as a function of μ/μ_I by Jones[31] and by Johnson and Lark-Horovitz,[32] for the case in which neutral impurity scattering is negligible, with the same approximation of replacing $B(x)$ by $B(3)$. The error due to this is no more than a few percent, however, for small μ_L/μ_I which turns out to be the only range in which the precision of this correction is important for comparison with these experimental data.

We consider now the effect of electron-electron collisions. As previously indicated, this will multiply the mobility by a factor, to be denoted by γ which is less than 1. The size of this factor depends on the relative frequency of collisions of electrons with each other and with the scatterers, and on the relative importance of lattice and impurity scattering, or μ_L/μ_I. It is possible to make some qualitative predictions about the effect of the latter which are useful. To this end consider the variation of relaxation time with μ_L/μ_I. For $\mu_L/\mu_I=0$, τ is proportional to $1/v$ and slow electrons develop much greater drift velocities than fast ones. The initial effect of increasing μ_L/μ_I is to reduce this asymmetry, i.e., make τ less velocity-dependent, because ionized impurities scatter slow electrons much more strongly than fast ones. It is in general at least a fair approximation to represent τ as a constant$\times v^n$, where n is, of course, a function of μ_L/μ_I. In this range, n would vary from -1 to 0. As μ_L/μ_I increases beyond this, impurity scattering begins to dominate. Fast electrons then develop greater drift velocities than slow ones, this asymmetry becoming more marked as μ_L/μ_I grows. In this range the values of n are positive, increasing from 0 to 3, the latter obtained at $\mu_L/\mu_I=\infty$. This variation of the velocity dependence of the relaxation time is substantiated by the variation with μ_L/μ_I of μ_H/μ, which according to (17) is the weighted average of τ^2 divided by the square of the weighted average of τ. This ratio is 1.18 for $\mu_L/\mu_I=0$, decreases initially with μ_L/μ_I reaching a minimum of 1.03 around $\mu_H/\mu=0.1$, and then increases until it reaches 1.93 at $\mu_L/\mu_I=\infty$.

From what has been said previously, it can be seen that as μ_L/μ_I starts to increase from 0, γ can either increase or decrease, depending on whether the decreasing velocity dependence or the increasing frequency of electron-electron collisions is the more important effect. In either case, the change in γ up to $\mu_L/\mu_I=0.1$ should not be more than a few percent. Around $\mu_L/\mu_I=0.1$, γ can have a value at most a few percent higher than its value at $\mu_L/\mu_I=0$. Beyond 0.1, γ will decrease consistently, and more rapidly, as μ_L/μ_I increases. It will not get as small as 0.6, however, because the degenerate region will be reached before impurity scattering dominates the situation to this extent. When Maxwell-Boltzmann statistics cease to be valid the interaction of electrons with ones of different velocity groups is limited by the Pauli principle and electron-electron collisions decrease in importance.

In the case in which neutral impurity scattering is also important, calculation of the mobility to the accuracy of (16) would involve considerably more numerical effort. Under the circumstances, it was considered that a sufficiently good approximation could be obtained by computing μ from

$$1/\mu=(1/\mu_{LI})+(1/\mu_N), \tag{18}$$

where μ_{LI} is the mobility computed from μ_L and μ_I according to (16). A sum of reciprocals should yield a considerably better approximation in this case than it does for the combination of μ_L and μ_I. In that case the electrons which boost the value of μ_I are discriminated

[30] See reference 12, p. 277.
[31] H. Jones, reference 27.
[32] V. A. Johnson and K. Lark-Horovitz, reference 27.

against by the lattice scattering, those which boost μ_L are discriminated against by the impurity scattering, and neither group will make the contribution to the mobility implied by the values of the separate μ's. The neutral impurity scattering, however, is not velocity-dependent and does not therefore discriminate against any particular velocity group.

The presence of an appreciable amount of neutral impurity scattering will also affect the values of μ_H/μ and γ. Again, the effort involved in making any quantitative calculations here was not considered justified. It is apparent, however, that the presence of neutral impurity scattering will make τ less velocity dependent and thus in general decrease μ_H/μ and increase γ. In the limit of all neutral impurity scattering, both μ_H/μ and γ equal 1.

IV. ANALYSIS OF MOBILITY DATA

Before undertaking a detailed analysis of the mobility data we shall consider briefly some of the gross features of the variation with impurity content and temperature. The mobilities, as expected, decrease with increasing carrier concentration until very low temperatures, where the residual impurity concentration is large enough to take over in some cases. The temperature variation of the Hall mobility for these samples shows the wide range of behavior characteristic of the wide range of impurity concentrations. Sample 55 is so pure the mobility scarcely departs from the negative slope characteristic of lattice mobility down to the lowest temperatures observed. With increasing impurity concentration this departure appears at higher temperatures due to the greater importance of ionized impurity scattering relative to lattice scattering. It can be observed, however, that in most of the samples at temperatures below that for which the initial flattening of the slope appears, the slope again gets steeper, giving μ_H *vs* T an s shape. This is displayed well by sample 64, for example. Apparently the effect of impurity scattering is decreasing even though the temperature is decreasing. This can be explained by the fact that the ionized impurity content of these samples is decreasing as the temperature decreases due to electrons dropping back into donor centers. It indicates that N_A is much smaller than the saturation value of N_D-N_A, which is borne out by later calculations. Sample 61 is sufficiently impure to show a positive slope over a long temperature range. The fact that this never becomes as steep as predicted for ionized impurity scattering, however, suggests that this sample has large neutral impurity scattering as well. Sample 58 exhibits the approximately constant mobility characteristic of a degenerate sample.

For more quantitative comparison of experiment and theory the data are usefully broken down into the following parts:

1. Data for the range of temperatures and impurity concentrations for which impurity scattering is negligible. These afford a check on the theory of lattice scattering, mainly on the theoretically predicted temperature dependence since μ_L involves two unknown parameters m_n and $\mathcal{E}_{1n}$.

2. Data for the range of temperatures, 300°K to 78°K roughly, for which N_I is known and neutral impurity scattering is small or negligible; from these it is possible to obtain a check of much of the foregoing theory, and in particular of that for ionized impurity scattering.

3. Data for the temperature range below 78°; a rough check of the theory, now including neutral impurity scattering, can be obtained. The theory can be used to compute an approximate density of acceptors in the individual samples.

The three parts will be considered in that order.

4.1 Lattice Scattering Range

For the purer samples in the temperature range from about 78°K to where the samples become intrinsic it is seen that μ_H decreases more steeply than $T^{-1.5}$, going as $T^{-1.66}$ for the purest sample, approximately as $T^{-1.6}$ for the next several samples in order of purity. Since impurity scattering would only make the mobility go less steeply than $T^{-1.5}$, this section of the data must represent lattice mobility. In that case the theory of the preceding section predicts that μ_H/μ will be a constant, 1.18, over the temperature range concerned for these samples. It would then follow that the lattice mobility varies with temperature essentially as $T^{-1.6}$.

New drift mobility measurements on high-resistivity samples in the range 150°K to 300°K do indicate that μ_H/μ is constant and approximately equal to 1.1 in this range.[33] The difference between this value and 1.18 is within the limits of experimental error. Additional support for theory is provided by the carrier concentration data. In the range 78° to 300° $1/Re$ is essentially constant for the purer samples. Since $n=(\mu_H/\mu)\cdot(1/Re)$ and should furthermore be constant to within a few percent in this range, μ_H/μ must remain constant to within a few percent down to 78°K.

It follows that the observed temperature dependence is essentially that of μ_L and that the latter can reasonably be computed from the Hall mobility taking $\mu_H/\mu=1.18$. The values of μ_L which gave the best fit to the experimental data at a number of temperatures are shown in Fig. 6. A 20.4° value is included although this is in somewhat more doubt than the others since a correction had to be made for impurity scattering. From this plot μ_L varies with temperature as $T^{-1.64}$. As stated previously, this may result from the edge of the conduction band not being located at $k=0$.

It is interesting to note that effective masses of $m/4$ for electrons and holes in the deformation potential formulas for μ_L give about as good agreement with experiment for germanium as m. The values of $\mathcal{E}_{1n}$ and $\mathcal{E}_{1p}$ computed from (3) using the known room temperature mobilities of electrons and holes and effective

[33] M. Prince (private communication).

masses of $m/4$ are 9.4 and 13.6 ev, respectively. The difference of these agrees reasonably well with the experimentally determined shift of the energy gap per unit dilation.[34]

4.2 78°K to 300°K Range

We consider now the temperature range 78° to 300°. For these samples the acceptor concentration is sufficiently small that in this range, where ionization of donors is practically complete, the density of ionized impurities can be taken equal to the density of conduction electrons. Also, neutral impurity scattering can be neglected in all but a couple of instances. Mobility is then a unique function of resistivity which can be calculated theoretically and compared with experimental values at any given temperature. This makes it unnecessary to compute for the individual samples, which is quite advantageous in view of the scatter of experimental results.

For the theoretical calculation μ_L was taken from the fit for the purest samples (see Fig. 6) and μ_I from the Brooks-Herring formula, Eq. (5). The mobility was then computed from the approximate formula (16). This was in turn used to compute ρ from $\rho=1/ne\mu$. The mobility was converted to Hall mobility by use of (17), with the approximation discussed in the last section.

The values of μ_H/μ calculated from (17) were shown in the last section to be at least approximately correct for pure samples in this temperature range. By similar arguments this can be extended to less pure samples. Mobilities have been obtained at 300°K for resistivities ranging from 30 ohm cm to 0.05 ohm cm by drift mobility measurements.[35] These lead to a variation of μ_H/μ with resistivity or impurity concentration which is quite similar to that predicted by (17), but everywhere about 10 percent too low.[36] Again, it is felt that the discrepancy is within the limits of experimental

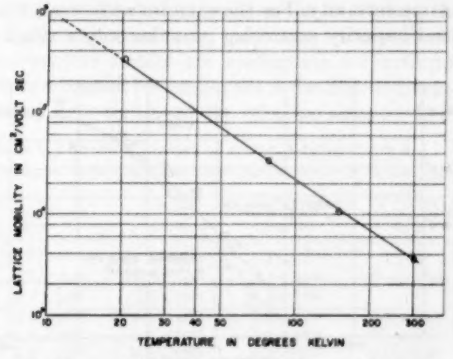

FIG. 6. Lattice mobility obtained from fits to the experimental data plotted vs absolute temperature.

[34] For a discussion of this subject see J. Bardeen and W. Shockley, reference 14.

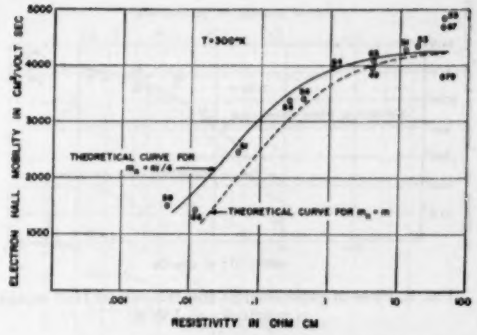

FIG. 7. Plots of experimental and theoretical Hall mobility vs resistivity at 300°K.

error and use of μ_H/μ from (17) is justified.[35] An experimental determination of this kind is not available at temperatures below 300°K. For these temperatures, however, a demonstration of the approximate validity of (17) is provided by the concentration data. Consider the experimentally determined variation of $1/Re$ with temperature in the range 78° to 300° for moderately impure samples such as 64. Although carrier concentration should be constant or increasing slightly with temperature, $1/Re$ for such samples reaches a maximum below 300° and then decreases. μ_H/μ calculated from (17), however, is increasing with temperature in this neighborhood in just such a way as to give approximately constant or increasing n for these samples. Incorporation of μ_H/μ determined from the theoretical formula was therefore considered justified.

In the calculations described, the correction for electron-electron collisions is automatically included at the high resistivity end by choosing μ_L to fit the purest samples. This, however, applies to the whole curve some amount of correction. For the region up to and a little beyond the minimum of μ_H/μ the amount should be correct within a few percent. Right around the minimum the curve is possibly overcorrected and thus low by a few percent. Use of (16) will cause the theoretical curve to be low; this will amount to a few percent around the minimum of μ_H/μ.

Plots of the experimental data and theoretical curves for various values of m_a in (5) at temperatures of 300°, 150°, and 78° are shown in Figs. 7 through 9, respectively. The 300° situation will be considered first.[36] The minimum of the μ_H/μ curve occurs around 0.03 ohm cm, between samples 61 and 66. Because of the scatter of samples at this end of the resistivity scale it is difficult to apply the ideas of the preceding paragraphs

[35] Drift measurements give directly the mobility of minority carriers in a sample. Conversion of this to majority carrier mobility introduces uncertainty because of the approximations involved.

[36] A similar pair of curves for 300° was published by P. P. Debye and E. M. Conwell, reference 1. They differ from those in Fig. 7, however, in that the impurity mobility was calculated from (4) in that case. The use of (5) raises the curve at the low-resistivity end (see Fig. 5), making the effective mass larger.

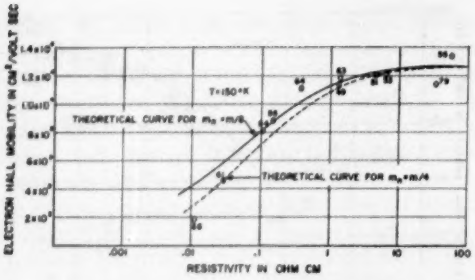
ELECTRON HALL MOBILITY IN CM²/VOLT SEC
T=150°K
THEORETICAL CURVE FOR m_n = m/8
THEORETICAL CURVE FOR m_n = m/4
RESISTIVITY IN OHM CM

FIG. 8. Plots of experimental and theoretical Hall mobility *vs* resistivity at 150°K.

and to determine an effective mass. It does, however, seem reasonable to say that $m/4$ is a lower limit, with the best value lying between $m/4$ and $m/2$.

At 78° impurity scattering is beginning to affect even the purest samples, and better fits are obtained by using slightly different lattice mobilities with different effective masses. Determination of the effective mass at this temperature is complicated by the presence of neutral impurity scattering in the more heavily doped samples, e.g., 56, 54, 61. Since $1/Re$ at 78° is not much less than $1/Re$ at 300° for these samples, and the presence of neutral impurity scattering makes the published values of μ_H/μ inaccurate, the density of neutral impurities cannot be determined with any precision. It can nevertheless be shown that the correction to the mobility from this source should be of the order of 10 percent for samples 54 and 56, and much larger for 61. These samples should then lie quite perceptibly below the theoretical curve for lattice and impurity scattering. Samples 54 and 56 are, however, well above the $m/4$ curve. The minimum of μ_H/μ at 78° occurs at about 0.2 ohm cm, near sample 64. It is expected then that this sample will lie above the theoretical curve about 5 percent. It is about 20 percent above the $m/4$ curve, however. This sample does tend to lie higher than the others but only by about 8 percent. On the basis of these considerations, it can be seen that an effective mass of about $m/8$ provides a satisfactory fit at 78°. The same type of reasoning applied to the 150° data leads to an effective mass at that temperature between $m/6$ and $m/8$.

On the basis of the relative insensitivity of the fit to the effective mass value and the scatter of the data, it is apparent that not too much significance is to be attached to the particular effective mass values obtained. In particular, if the μ_H/μ values used are somewhat too high, as indicated by the drift mobility results, the m_n values stated are all high. This, however, will not wipe out the trend to increasing effective mass with temperature.

Since there is no other reason to believe that effective mass as such is changing in this way, these results are more significantly interpreted as indicating that μ_I does not vary with temperature as predicted by (4) or (5) but somewhat less rapidly. According to these results, the exponent of T in the numerator should be closer to 1.0 than 1.5.

It would appear desirable to check this result by computing $\mu_I(T)$ directly from $\mu(T)$ for the individual samples. Such a procedure would at first sight seem to have the additional advantage of being independent of μ_H/μ. Actually, however, this is not the case because it is necessary to know n to compute μ from σ. In any case, this type of approach is not useful because ionized impurity scattering is generally considered smaller than lattice scattering in these samples throughout this temperature range. Small errors in μ, therefore, whether experimental or from inaccuracy in μ_H/μ, lead to large errors in μ_I.

4.3 Temperature Range Below 78°K

In the temperature range below 78° detailed consideration was given to the data for 20.4°K and for 11.5°K, the latter being about the lowest temperature attained for most samples. At these temperatures lattice scattering, ionized, and neutral impurity scattering are all important. The relevant quantities about which information is desired are acceptor density and effective masses to be used in ionized and neutral impurity scattering formulas. We shall consider first the information which can be obtained about the latter. At 11.5° for all but the two purest samples carrier concentration is down to less than one percent of its 300° value, and the density of neutral donors is quite accurately equal to the saturation value of N_D-N_A. This enables one to set fairly accurately a lower limit for the effective mass to be used in neutral impurity scattering. The values of μ computed from the Erginsoy formula for m_n less than $m/4$ are less than the experimental Hall mobilities for the samples with large N_N, e.g., 64, 54, 56, 61. If lattice and ionized impurity scattering are also taken into account for these samples, this lower limit is pushed up to about $m/3$. An upper limit for the effective mass to be used in μ_N cannot be set with the same certainty. For the samples with small N_N the neutral impurity scattering provides only a small cor-

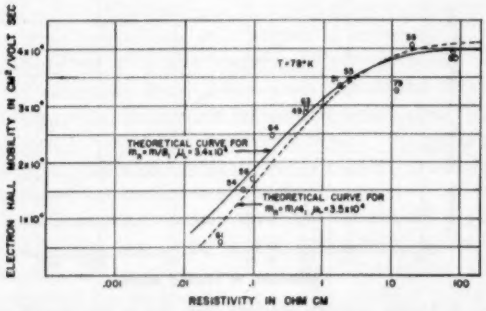

FIG. 9. Plots of experimental and theoretical Hall mobility *vs* resistivity at 78°K. Note, however, that the theoretical curves do not include neutral impurity scattering, which does affect samples 54, 56, and 61.

rection for m_n greater than $m/4$. In the samples with large N_N the observed mobilities can be fitted for any m_n greater than $m/4$ simply by adjusting the N_A values, which are of course unknown. For large enough m_n, however, these become unreasonably large. An upper limit to the effective mass can therefore be set by consideration of what is plausible in the way of acceptor concentration in these samples.

In the undoped, high-resistivity samples, such as 55, the temperature-dependence and the high mobility suggest that compensation of impurities is not taking place, and N_A should be somewhat less than the saturation value of N_D-N_A, or at most that order of magnitude. In the doped samples it is reasonable to expect N_A's of the same order of magnitude, or larger by perhaps a factor of 10 because the starting material before doping is not always purified to quite the same extent. On the basis of the stated chemical purity of the doping arsenic it is not expected that the doping process would add an amount of p-type impurity comparable to this residual concentration. Thus it appears reasonable to expect acceptor concentrations in the range 10^{12}/cm^3 to 10^{14}/cm^3 in all samples, with no particular correlation appearing between acceptor concentration and resistivity.

On this basis m_n should certainly be taken less than m in the Erginsoy formula. For $m_n=m$ there is a definite trend to increasing N_A with increasing N_N; the three most heavily doped nondegenerate samples requiring much larger values than the others to explain the observed mobilities. The values of m_n which lead to N_A values which best fit the criteria set up in the preceding paragraph are in the neighborhood of $m/3$.

In computing N_A the μ_N values were first obtained using an effective mass of $m/3$. These were used in (18) to calculate μ_{LI} from the observed mobilities. The impurity mobility was then computed from (16) with the lattice mobility taken as 8.0×10^5 cm^2/volt sec, the value obtained by extrapolation of the high-temperature results (see Fig. 6). Because of the number of unknowns it is not possible to determine from the 11.5° data the value of effective mass to be used in μ_I. Although the high-temperature results are inadequate for extrapolation, it is a reasonable guess that if the high-temperaature trend were continued the effective mass at 11.5° would be $m/16$ or less. N_I values were calculated from μ_I using effective masses of $m/16$ and $m/4$. With n taken from the Hall data, N_I values were finally obtained from $(N_I-n)/2$. The deviation of μ_H/μ from 1 was neglected throughout in the calculation described.

TABLE I. Calculated values of acceptor concentration.

Sample	Saturation N_D-N_A	N_A from mobility ($m/4$)	N_A from mobility ($m/16$)	N_A from concentration data
	1/cm^3	1/cm^3	1/cm^3	1/cm^3
55	1.0×10^{13}	4.8×10^{11}	1.3×10^{12}	2×10^{12}
53	9.4×10^{13}	5.9×10^{11}	1.8×10^{12}	
51	1.4×10^{14}	9.6×10^{12}	2.2×10^{13}	7.3×10^{12}
63	4.6×10^{14}	2.5×10^{13}	5.8×10^{13}	7×10^{13}
49	4.8×10^{14}	9.8×10^{12}	2.3×10^{13}	2.5×10^{13}
64	1.7×10^{15}	3.0×10^{11}	6.0×10^{12}	1.9×10^{13}
56	5.1×10^{15}	1.0×10^{14}	2.4×10^{14}	
54	7.5×10^{15}	3.6×10^{13}	1.0×10^{14}	1.5×10^{14}
61	5.5×10^{16}	1.3×10^{15}	4.7×10^{15}	2.0×10^{15}

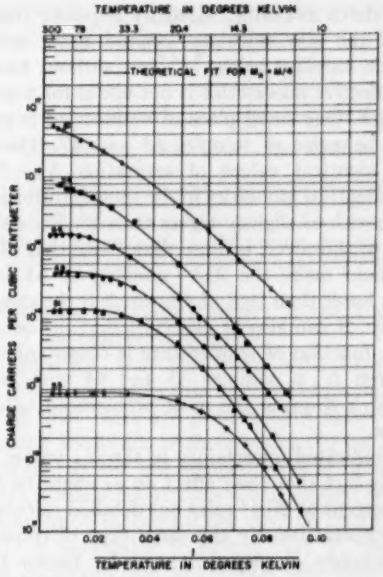

FIG. 10. Electron concentration as a function of inverse absolute temperature for a number of samples. The points are computed from the Hall data, and the solid lines are theoretical fits for an effective mass of $m/4$.

This is sufficiently accurate for the purer samples because μ_H/μ values are quite close to 1 anyway. It would also be so for the less pure samples if their mobility were mainly determined by neutral impurity scattering. It was found, however, that ionized impurity scattering was quite important in some of the more heavily doped samples. In some cases, μ_H/μ values might be 1.5 or greater, and their inclusion would affect the N_A values considerably. A rough correction was made for this by computing another set of N_A values incorporating μ_H/μ values determined from μ_L/μ_I, and interpolating between the two sets according to the value of μ/μ_{LI} for the sample. This probably results in somewhat too large N_A for the more heavily doped samples. The N_A values so obtained are listed in Table I. Detailed consideration of the different samples shows that, despite uncertainties in the effective masses, the values listed for $m/16$ can be expected to be good within a factor 10 with the possible exception of samples 54 and 64. In the case of samples 51, 63, and 49 the N_A's are better determined, being probably correct within a factor 5. Semiquantitative verification of this set of N_A values is provided by comparison with the set obtained from carrier concentration data, which are also listed in Table I. These will be considered in the next section. This is unfortunately the only quantitative

type of check available. Minority impurity concentrations of the size calculated should quite noticeably affect the mobility below 78°, but without knowledge of the effective masses this is not useful for a quantitative check. One small piece of verification is provided by the behavior of samples 63 and 49. These have almost identical values of saturation N_D-N_A and almost identical mobilities in the temperature range 78° to 300°, with 63 slightly higher than 49. The calculated N_A for 63, however, is more than twice that of 49 and this should make the 20.4° mobility of 63 about 10 percent lower than that of 49, which is the case experimentally. It can also be observed that the behavior of μ_H as a function of temperature is consistent with the calculated N_A's, samples 53 and 64 with relatively small N_A's showing the most pronounced s-shape, for example.

The indicated uncertainty in the N_A values coupled with the fact that their effect on μ_I might be as much as 40 percent at 20.4° rules out detailed calculations at that temperature. By the same type of consideration as previously employed it can be shown that the effective mass to be used in the ionized impurity scattering is less than $m/4$, while that for neutral impurity scattering lies between $m/6$ and m.

V. THEORY AND ANALYSIS OF CONCENTRATION DATA

5.1 Evaluation of Parameters Involved in Fit

The relation between electron concentration and temperature in the extrinsic region is given by[37]

$$\frac{n(N_A+n)}{N_D-N_A-n}=\left(\frac{2\pi m_n kT}{h^2}\right)^{\frac{3}{2}}\exp(-\mathcal{E}_D/kT), \quad (19)$$

where $\mathcal{E}_D$ is the amount of energy required to raise an electron from a donor level to the conduction band. For samples with impurity content of perhaps 10^{16}/cm³ or greater, $\mathcal{E}_D$ may be expected to vary somewhat with concentration and temperature. As is customary, however, the assumption that $\mathcal{E}_D$ is constant for a given sample was made in fitting all samples. The validity of this assumption will be examined later.

In attempting to fit the data, it was found that for a given sample the activation energy is determined within fairly narrow limits but the other two parameters are not. Since m_n is expected to be the same for all samples, outside the degenerate and near-degenerate ranges at any rate, the criterion of best fit for all samples was used to choose an m_n value. This gave a value of $m/4$.

[37] J. H. DeBoer and W. C. van Geel, Physica 2, 186 (1935). This form takes into account trapping of the electrons by the ground state of the donors only, $\mathcal{E}_D$ being the distance of the ground state below the edge of the conduction band. On the hydrogen-like model, the excited states all lie within $\mathcal{E}_D/4$ of the conduction band. At temperatures such that $kT\ll\mathcal{E}_D$, trapping by these excited states will be negligible compared to trapping by the ground state and (19) is valid. In what follows only this temperature range is used in determining the parameters in (19).

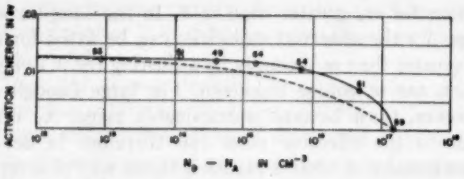

FIG. 11. Activation energy as a function of uncompensated donor concentration. The solid line represents the variation found experimentally, the dashed line the type of variation found experimentally for silicon: $\mathcal{E}_D(N_D)=\mathcal{E}_D(0)-\alpha N_D^{\frac{1}{3}}$.

The fitted curves for this mass are shown in Fig. 10. Curves which do not fit too badly can be obtained for values of m_n in the range from $0.2m$ to $0.5m$, but masses in the neighborhood of $m/4$ give the best results.[38] The N_A values used in the curves shown are listed in Table I. They are all within a factor 3 of those determined for $m/16$ in the low-temperature mobility. Since the latter are only good within a factor 5 or 10, this constitutes reasonable agreement and additional support for a value in the neighborhood of $m/4$. The $\mathcal{E}_D$ values obtained from fitting these curves are plotted *vs* N_D-N_A in Fig. 11.[39] As previously mentioned, the $\mathcal{E}_D$ values are not very sensitive to the effective mass value chosen.

As mentioned in a previous section, the experimental data in Fig. 10 represent $1/Re$ rather than carrier concentration. It can be shown that the effect on the activation energy of neglecting μ_H/μ is small for these samples. The activation energy is essentially determined by the slope of n *vs* $1/T$ over a small range of temperatures, roughly 15°K to 11°K. For the purer samples the change in μ_H/μ in this range can be calculated with reasonable accuracy from (15), and is less than 15 percent. Inclusion of μ_H/μ would thus lead to alteration of the slope and $\mathcal{E}_D$ of less than 15 percent for these samples. For more impure samples the error would be much larger if it were not for the presence of appreciable neutral impurity scattering. This will cut down the μ_H/μ values, and therefore the correction to the slope.

According to the hydrogen-like model of a donor, the binding energy of an electron is given by

$$\mathcal{E}_D=\frac{13.6}{\kappa^2}\frac{m_n}{m}=0.052\frac{m_n}{m} \quad (20)$$

for germanium. From the curve-fitting described, an $\mathcal{E}_D$ value of 0.0125 ev is obtained for the purer samples.

[38] Note, however, that sample 56 showed anomalous behavior in that it could not be fitted well with any set of parameters, but better-fitting curves were obtained with effective masses of the order of m than with $m/4$. This sample was cut from near the tip end of a single crystal, had a relatively large N_A, and may have been quite nonuniform in impurity distribution.

[39] Sample 59, the lowest concentration sample for which $\mathcal{E}_D$ was zero, was unfortunately not prepared as were the others discussed and may not have been arsenic-doped. The lowest concentration sample in the series which had vanishing $\mathcal{E}_D$ had a concentration of about 3×10^{17}/cm³. This sample is not included because, unfortunately, complete data are not available.

Substituted in (20) this gives an m_n of $m/4$, which is just in the range of m_n values found to give the best agreement with the concentration data. It can thus be said that at least approximate equality of these effective masses has been established. This is significant in that equality is what would be expected on the usual simple picture of the band structure and energy surfaces but was not necessarily expected for the more complicated case.

5.2 Variation of Activation Energy with Concentration

Before comparing the observed variation of activation energy with theoretical predictions, it is worth noting that these results do not agree with those found by Pearson and Bardeen for p-type silicon.[40] In that case it was found that the variation of activation energy with concentration followed closely an equation of the type

$$\mathcal{E}_D(N_D)=\mathcal{E}_D(0)-\alpha N_D^{\frac{1}{3}}, \qquad (21)$$

where $\alpha=4.3\times10^{-8}$. In checking whether these data follow such an equation, it is necessary to take $\alpha=2.35\times10^{-8}$ to make $\mathcal{E}_D$ vanish at $1.5\times10^{17}/\text{cm}^3$. The resulting $\mathcal{E}_D(N_D)$ is plotted in Fig. 11. (Actually it is plotted *vs* N_D-N_A rather than N_D, but this makes little difference.) It is apparent that it does not agree well with these experimental results. It can furthermore be shown that this conclusion is not dependent on the value of effective mass chosen for fitting within the range of reasonably good fitting, of course.

There are three types of effect which have been considered to explain the variation of activation energy with concentration. We shall first consider the mechanism investigated by Pearson and Bardeen and subsequently by Castellan and Seitz,[41] in attempting to explain the empirical result (21). They suggested that the decrease of activation energy with concentration was due to the potential energy of attraction between the ionized donors and conduction electrons. This mechanism, they considered, would lead to a lowering of activation energy inversely proportional to the average distance between an electron and an ion, thus essentially proportional to the $\frac{1}{3}$-power of the density of ionized donors. It is apparent that this leads to a variation of activation energy with degree of ionization, in which case the assumption of constant $\mathcal{E}_D$ is of course not valid. Since the $\mathcal{E}_D$ values are determined by the fit to the low-concentration part of the experimental curve, they must represent values characteristic of the low-concentration region. The previous theory would then predict that the $\mathcal{E}_D$ values vary according to an equation of the form (21) with N_D replaced by the average density of ionized donors in the low-concentration or low-temperature region.[42]

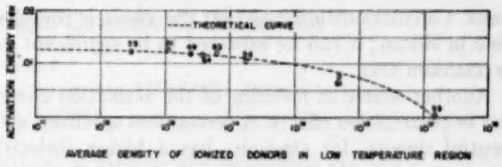

FIG. 12. Activation energy as a function of the average density of ionized donors in the temperature interval used for fitting. The dashed line represents the theoretical variation predicted by Eq. (21) with N_D replaced by the average density of ionized donors in the fitting interval, and repulsion of acceptors neglected.

In comparing this prediction with experimental results it is necessary to take account of the fact, so far neglected, that there are present both ionized donors and ionized acceptors, with densities N_A+n and N_A, respectively. At the low temperatures in question N_A is, in fact, usually larger than n and ionized donor and ionized acceptor concentrations may be approximately equal. It is reasonable to expect that N_A negatively charged acceptors will not cancel the effect of N_A positively charged donors. In the presence of both, an electron would tend to concentrate around the positive charges and avoid the negative charges, particularly at low temperatures, and thus obtain a lowering of its average potential energy.

Some information about the relative importance of this mechanism can be obtained by neglecting the repulsion of the acceptors and plotting $\mathcal{E}_D$ *vs* average density of ionized donors in the region from which the $\mathcal{E}_D$ value was obtained. Such a plot is shown in Fig. 12. N_A values were taken as the mean of those obtained from mobility and concentration data. The average value of n over the region involved in fitting, obviously a poorly defined quantity, is fortunately small compared to N_A in almost all cases. Also shown is a plot of $\mathcal{E}_D$ from the theoretical equation (21) with N_D replaced by the average density of ionized donors. The value of α required for fit at the high-concentration end is about that obtained in a crude estimate of the effect by Pearson and Bardeen and by Castellan and Seitz. Although this curve certainly overestimates the lowering predicted by the previous theory, the significant experimental points lie a little lower than the curve. It would appear that this mechanism can account for part of, but not all, the observed decrease in activation energy.

It was pointed out by Pincherle,[43] and by James and Lehman, that free carriers will also give rise to a decrease in activation energy by screening the field around a trapping center. The effectiveness of screening and therefore the amount of the decrease will be greater at lower temperatures and higher electron concentra-

[40] G. L. Pearson and J. Bardeen, Phys. Rev. **75**, 865 (1949).
[41] G. W. Castellan and F. Seitz, "On the energy states of impurities in silicon," published in *Semi-Conducting Materials* (Butterworths Scientific Publications, London, 1951).
[42] For this reason, it was pointed out by Castellan and Seitz, this mechanism does not explain the Pearson and Bardeen experimental result (21).
[43] L. Pincherle, Proc. Phys. Soc. (London) **A64**, 663 (1951).

tions. Calculations indicate that the effect is considerable in silicon; it can be expected to be significant for germanium also.

Another source of lowering of the activation energy lies in polarization effects. A germanium specimen with neutral donors, for example, has a higher dielectric constant than a pure one. A free electron in the impure specimen can give rise to a greater polarization, lowering the edge of the conduction band and consequently the activation energy. A crude evaluation of the size of these effects was carried out for the case of silicon by Castellan and Seitz.[41] They assumed that the polarizability of a neutral donor was that of a hydrogen atom with effective nuclear charge equal to the reciprocal of the dielectric constant of silicon. The hydrogen-like model can be modified quite analogously to allow for an effective mass different from the free-electron mass. An m_n/m ratio less than 1 increases the polarizability, and thus the size of the effect. The analysis of Castellan and Seitz applied to germanium, with an effective mass of $m/4$, leads to a lowering of $\mathcal{E}_D$ for sample 61, which has an N_D-N_A of $5\times10^{16}/\text{cm}^3$, of about 0.001 ev. For samples with higher impurity concentration the effect would be greater. This indicates that polarization effects, although probably smaller than the others, must also be taken into account in explaining the experimental results.

It is of interest to consider the variation of activation energy with temperature to which the three effects cited give rise. In the case of the screening effect the temperature dependence arises from the dependence on carrier concentration and from the fact that the fraction of the time spent by electrons around the positive charges depends on their kinetic energy. The variation in activation energy due to this effect might be considerable over the temperature interval important in determining $\mathcal{E}_D$. In the limit of low temperature and vanishing concentration the decrease in $\mathcal{E}_D$ arising from this mechanism will vanish. The attraction of electrons to ionized donors will depend on temperature for the same reasons that the screening effect does, but will also depend greatly on the minority impurity concentration in the individual sample. The variation of $\mathcal{E}_D$ with temperature due to this mechanism should be relatively small at temperatures such that the conduction electron concentration is less than N_A. This is the case, for example, over the temperature interval from which the $\mathcal{E}_D$ value is determined and at all lower temperatures in the case of sample 61. This mechanism gives a decrease in activation energy which does not vanish in the limit of low-temperature and low-electron concentration. Polarization effects differ from the other two in that they will be largest in this limit and will vary significantly with temperature only at temperatures higher than those involved in obtaining the $\mathcal{E}_D$ values. It can be seen that the way in which $\mathcal{E}_D$ varies with temperature will depend on the relative importance of the three effects, which in turn may be different in different temperature ranges. Study of the Hall constant at lower temperatures may be useful in separating the effects.

It is usually considered that metallic conduction, or the vanishing of activation energy, will set in around concentrations such that half the average distance between donor impurities is equal to the radius of the bound electron orbit.[41] This statement can be somewhat refined by assuming the impurities uniformly spaced so they can be surrounded by imaginary spheres all of the same radius r_s chosen so that the spheres fill all space. In terms of this, the criterion for vanishing $\mathcal{E}_D$ could be stated thus: r_s must equal the average distance of the bound electron from the center of the sphere. This condition is not at all satisfied in the case of p-type silicon,[40] where for the lowest concentration at which metallic conduction is observed r_s is approximately five times this distance. For n-type germanium and an effective mass of $m/4$, r_s for the lowest concentration at which metallic conduction is observed is approximately twice this distance. To satisfy the criterion stated previously a concentration of $2\times10^{18}/\text{cm}^3$ would be required. It is to be expected that randomness of the impurity distribution will cause the onset of metallic conduction at lower concentrations than required by the above criterion; it is possible that this effect can account for this discrepancy.

ACKNOWLEDGMENTS

The authors are indebted to numerous groups at Bell Laboratories who helped in the preparation of the crystals and to Miss D. Oxman and Mrs. M. F. Shearer for some of the calculations. It is a pleasure to acknowledge indebtedness to Dr. C. Herring for many valuable discussions, particularly on the subject of electron-electron collisions. A special acknowledgment is due J. P. Maita for carrying out much of the labor of sample preparation and measurements, and for contributions throughout the experimental work.

Infrared Optical Properties of Single Crystals of Tellurium*

JOSEPH J. LOFERSKI†
Randal Morgan Laboratory of Physics, University of Pennsylvania, Philadelphia, Pennsylvania
(Received November 13, 1953)

The fundamental optical absorption and photoconductivity of single crystals of tellurium has been investigated. Tellurium crystals exhibit dichroism in the infrared, i.e., the absorption constant depends on the polarization of the incident radiation. At 300°K for radiation polarized perpendicular to the C axis the absorption edge, located by means of an arbitrary criterion, is at 3.82 microns (0.324 ev); for the case of polarization parallel to the C axis the same criterion locates the second edge at 3.29 microns (0.374 ev). The difference between absorption constants survives at wavelengths beyond the edges and is ascribable to the effective masses of the carriers, which depend on their direction of motion relative to the crystal axis. The variation of the energy gaps with temperature has been observed to be -2×10^{-4} ev/°C, i.e., the energy gaps decrease with increasing temperature. Comparison is made with existing theories. The photoconductivity which is barely detectable at room temperature is considerably enhanced by a reduction of the temperature to 90°K. The spectral response indicates the presence of two peaks corresponding in position to the absorption edges. Measurements of the dependence of photoresponse on voltage, light intensity, and shuttering speed indicate that the photoresponse is at least partially in conformity with a monomolecular model. Selenium-tellurium alloys containing 2.7 percent and 11 percent selenium by weight and therefore possessing a considerably reduced lattice volume show a shift of photoconductivity and transmission toward shorter wavelengths, i.e., larger energy gaps.

I. INTRODUCTION

THIS investigation is concerned with the infrared optical properties of single crystals of tellurium, and in particular with the effects of temperature, of the addition of selenium, and of the crystalline anisotropy on the transmission and photoconductivity of the element.

The optical properties of semiconductors have proven to be an important tool in the determination of the band structure appropriate to these materials.[1–3] From the location of the fundamental absorption edge and the corresponding threshold of photoconductivity it is possible to establish the width of the forbidden energy gap; the value so obtained is in reasonable agreement with the values determined by measuring the conductivity as a function of temperature in the intrinsic range.[4] Furthermore the movement of these thresholds when the lattice volume is changed is directly related to the change in energy gap due to the dilation.

Other information can be extracted from the absorption beyond the edge, i.e., from the absorption of radiation whose energy is too low to induce direct transitions from the filled to the conduction band. It is postulated that such residual absorption is due to the free conduction electrons in the material, and consequently some of the properties of these electrons can be inferred from this absorption.

II. SOME GENERAL PROPERTIES OF TELLURIUM (AND SELENIUM)

Tellurium occupies the fifty-second place in the periodic table, its ground state being $5s^25p^4$. It belongs to the VIb group, which comprises in order of increasing atomic number the insulators oxygen and sulfur, the semiconductors selenium and tellurium, and the metal polonium.[5]

Selenium and tellurium share a peculiar hexagonal crystal structure, illustrated in Fig. 1.[6] The atoms are arranged in spiral chains which are oriented along the C axis, each atom sharing covalent bonds with its two nearest neighbors in the chain. The chains are held together by a combination of Van Der Waals and metallic binding. Every third atom is directly above another atom in its chain, so that looking down the C axis a chain appears triangular in shape. The hexagonal lattice is finally achieved by locating a chain at the center and at each of the six corners of the hexagon. This hexagonal structure is readily revealed in tellurium by cleaving a crystal, since the relatively weak binding between chains generates planes of easy cleavage parallel to the C axis.

Because of the difference in atomic radii the lattice constants of selenium are smaller than those of tellurium as shown in Table I.[7]

The similarities between selenium and tellurium suggest that the two elements might form a complete series of solid solutions for all concentrations, and indeed corroborating evidence can be found in the

* This work was supported by contracts with the U. S. Office of Naval Research. The work on Te-Se alloys was supported by an Air Force contract.
† Now at RCA Laboratories, Princeton, New Jersey.
[1] *Semiconducting Materials* (Butterworths Publishing Company, London, 1951), p. 132.
[2] N. F. Mott and R. W. Gurney, *Electronic Processes in Ionic Crystals* (Clarendon Press, London, 1940), Chap. V.
[3] F. Seitz, *Modern Theory of Solids* (McGraw-Hill Book Company, Inc., New York, 1940), Chap. XVII.
[4] K. Lark-Horovitz and K. W. Meissner, Phys. Rev. **76**, 1530 (1949); M. Becker and H. Y. Fan, Phys. Rev. **76**, 1530 (1949).
[5] A. von Hippel, J. Chem. Phys. **16**, 372 (1948).
[6] *Landolt-Bornstein Phys.-Chem. Tabellen* (Julius Springer, Berlin, 1929), 5. Aufl. 1. Erg.-Bd, p. 394.
[7] E. Grison, J. Chem. Phys. **19**, 1109 (1951).

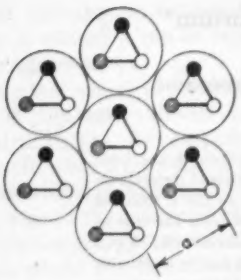

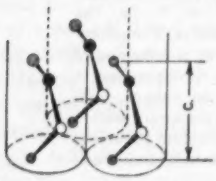

FIG. 1. The crystal structure of tellurium and selenium. Similarly shaded atoms are at the same level in neighboring chains and above each other in the same chain (after Grison).

literature.[7] The most recent x-ray investigation indicates that both lattice constants decrease in a linear fashion as selenium is added to tellurium. The volume of the crystal lattice is reduced, thus markedly affecting the properties of the material. Part of this investigation is consequently devoted to a preliminary study of two alloys of selenium and tellurium.

The electrical properties of tellurium have undergone an intensive investigation in recent years by the groups at Purdue University and at Tôhoku University in Japan.[8,9] An analysis of the available data by Fukuroi indicates that the thermal energy gap is 0.34 ev,[10] which suggests that the fundamental optical absorption ought to begin at a wavelength of about 3.6 microns. Thus tellurium should possess a photoconductive threshold farther in the infrared than any other element with the possible exception of grey tin.[11]

As for the optical properties of tellurium, early investigators reported that the conductivity of tellurium was unaffected by radiation.[12] The existence of a photoconductive effect in tellurium films was reported by Bartlett,[13] although he does not discuss spectral sensitivity except to remark that the wavelength of the exciting radiation had to be less than 4500A. The presence of a photovoltaic effect was observed by Bergmann and Hausler who indicated that the effect was too small to have its spectral dependence established.[14]

Recently Moss[15] observed photoconductivity in evaporated films of tellurium at 195°K and at 90°K. The spectral response reached a maximum at 1.1 microns while the photoconductive threshold lay at about 3.5 microns. The shift of threshold with temperature was 2×10^{-4} ev/°C.[16] Subsequently, he also published data on the transmission of such films. The absorption constant at 1 micron was 10^5 cm^{-1}; it falls to 5×10^4 cm^{-1} at 3 microns. He reported that transmission measurements were possible on bulk samples although he does not indicate whether he used single crystals.[17]

III. EXPERIMENTAL ARRANGEMENT

A. Preparation of the Samples

Much of the work on transmission has been performed using single crystals of tellurium kindly supplied to us by the Anaconda Copper Refining Company. These appear to have been grown unintentionally from the melt, their dimensions varying up to a maximum of about 2 cm×1 cm×0.2 cm. The crystals are prepared for use by grinding and polishing them according to metalographic techniques and subsequently by optical techniques. Spectroscopic analysis of the samples failed to indicate any impurities although a determination of the Hall coefficient as a function of temperature indicated that the impurity concentration was about 10^{18}/cc. The samples were barely in the intrinsic range at room temperature.[18] Uniformity of the samples was established by probing their surface to determine the resistivity from a plot of the potential drop *versus* distance from an electrode. The resistivity was about 0.3 ohm-cm parallel to the C axis.

These crystals were however unsuitable for measurement of photoconductivity. Because of their dimensions, their resistance was so small that the change in voltage across the sample was not detectable, *viz.*, with an incident energy of 10^{-4} watt and a wavelength of 3 microns the rms change in voltage across a sample was less than 10^{-6} volt with a dc bias of 4.5 volts. Consequently in order to obtain samples of a size suitable for measuring photoconductivity and in general to improve on the purity of the tellurium it was necessary to produce single crystals. These were obtained using an adaptation of the Bridgman technique.[19] Crystals of random orientations and dimensions varying in diameter from about 0.2 mm to 1.5 cm, were successfully produced. The orientation of the crystals was determined by visual examination after the ends had been cleaved and the crystals had been etched by concentrated HNO_3.

TABLE I. Lattice constants of Te and Se in angstroms.

	C	A	C/A
Se	4.944	4.337	1.14
Te	5.912	4.495	1.32

[8] Fukuroi, Tanuma, and Tobisawa, Sci. Repts. Research Inst. Tôhoku Univ. **A1**, 373 (1951).
[9] V. E. Bottom, Science **115**, 570 (1952).
[10] T. Fukuroi, Sci. Repts. Research Inst. Tôhoku Univ. **A3**, 175 (1951).
[11] T. S. Moss, Proc. Phys. Soc. (London) **A64**, 590 (1951).
[12] L. Gmelin, *Gmelins Handbuch der Anorganischen Chemie, Tellur* (Verlag Chemie, Berlin, 1940), Vol. 11, p. 215.
[13] P. S. Bartlett, Phys. Rev. **26**, 247 (1925).
[14] L. Bergmann and J. Hausler, Z. Physik **100**, 50 (1936).
[15] T. S. Moss, Proc. Phys. Soc. (London) **A62**, 264 (1949).
[16] T. S. Moss, Phys. Rev. **79**, 1011 (1950).
[17] T. S. Moss, Proc. Phys. Soc. (London) **B65**, 62 (1952).
[18] A. Nussbaum (private communication).
[19] P. A. Bridgman, Proc. Am. Acad. Sci. **60**, 305 (1925).

The crystals were spectroscopically analyzed; again no impurities were indicated. The measurement of the Hall coefficient and the conductivity indicated that the impurity concentration was about 10^{15}/cc in the exhaustion region.[18]

The samples were further prepared for photoconductive experiments by etching in nitric acid. Electrical contact to the sample was provided by electroplating nickel to the ends and soldering copper leads to the nickel.

B. Apparatus

The source of monochromatic radiation was a Beckman infrared monochromator equipped with rock salt optics; it was used in conjunction with a Nernst glower. Most of the measurements were made with radiation interrupted at the rate of 10 cps. The radiation emerging from the monochromator was incident on a plane mirror set at 45 deg to the face of the instrument so that the beam was deflected outward through a polarizer onto a front surface spherical mirror. The latter in turn formed an image of the slit on the sample

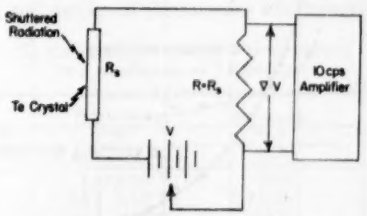

FIG. 2. Circuit used to measure photoconductivity.

whose photoconductivity or optical absorption was being measured. When the optical absorption was under observation, the radiation transmitted by the sample was collected by an elliptical mirror. The mirror formed an image on the target of a Perkin-Elmer radiation thermocouple whose output was fed into a suitable amplifier.

On the other hand the photoconductivity was observed using the simple series circuit of Fig. 2. Due to the radiation the resistance of the sample changes by an amount ΔR. The resulting change in voltage ΔV across the fixed resistor R, when expressed in terms of the constant dc voltage across the sample V, the change in conductivity $\Delta\sigma$, and the dark conductivity σ, is given by:

$$\Delta V = -V\Delta\sigma/\sigma.$$

This signal ΔV is normalized to constant incident energy by using the output of the radiation thermocouple to provide a normalization curve. It is the ratio of ΔV to the output of the thermocouple $V_{T.C.}$ which is recorded as the relative photoresponse.

The transmission polarizer was constructed following the method of Elliott *et al.*[20] It consisted of five unsupported films of amorphous selenium about 50 microns thick mounted so that the radiation to be polarized was incident on the films at Brewster's angle.

[20] Elliott, Ambrose, and Temple, J. Opt. Soc. Am. 38, 212 (1948).

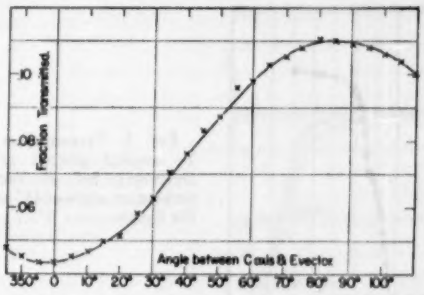

FIG. 3. Transmission of a typical Te crystal plotted *vs* angle between the *C* axis and *E* vector of the incident polarized radiation. $\lambda = 5$ microns.

IV. OPTICAL ABSORPTION: EXPERIMENTAL RESULTS

The transmission of a typical crystal as function of the angle between the *C* axis and the plane of vibration of the electric vector for a wavelength beyond the absorption edge, *viz.*, 5 microns, is shown in Fig. 3. The transmission is largest when the plane of polarization is perpendicular to the *C* axis; it is smallest when the plane of polarization is parallel to the *C* axis. Figure 4 shows the transmission as a function of λ for these extreme positions. It is evident that the threshold of transmission as well as the transmission in the region beyond the edge depends markedly on polarization. For an angle intermediate between the two extreme polarizations the transmission is as shown in Fig. 5. The results shown in Fig. 5 can be computed from those shown in Fig. 4 in the conventional way, i.e., by resolving the incident radiation into two components one parallel to, and the other perpendicular to the *C* axis and adding the resulting transmissions vectorially. Thus the plane of electric vibration always experiences a rotation toward the direction perpendicular to the *C* axis.

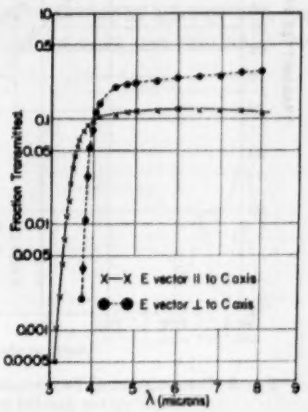

FIG. 4. Transmission plotted *vs* wavelength for a typical Te crystal showing the effect of polarizing the incident radiation.

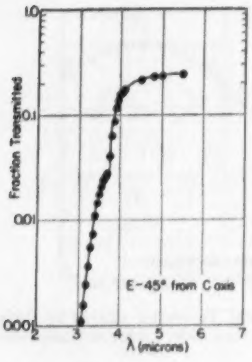

FIG. 5. Transmission of Te crystal plotted *vs* λ (microns) for *E* vector making an angle of 45° with the *C* axis.

In order to determine the value of the absorption constant, i.e., to separate the absorption from the reflection loss, the transmission of a number of samples, of differing thickness was determined as a function of wavelength (Fig. 6). The results are analyzed according to the expression:

$$I/I_0=(1-R)^2e^{-Kx},$$

where I_0 and I are the incident and transmitted intensities, respectively, K is the absorption constant, x is the thickness of the sample, and R is the reflection loss at a surface. From a plot of $\ln(I/I_0)$ *vs* x, both K and $(1-R)^2$ can be determined. The results for K are shown in Fig. 7. It is evident that there are two separate absorption edges dependent on the polarization of the incident radiation, and that even beyond the edge the absorption is different for each direction of polarization. Thus tellurium exhibits dichroism in the infrared.

Because a satisfactory theory of the absorption edge has not been developed, somewhat arbitrary criteria must be used for the location of this edge. If that value of wavelength for which the transmission has fallen to, say, 20 percent of its value in the transparent region is chosen, the two edges are 3.91 microns (which corresponds to 0.316 ev) for **E** perpendicular to the *C* axis and at 3.45 microns (0.358 ev) for **E** parallel to the *C* axis. If the point where the transmission is 5 percent of its long wavelength value is used, these edges are at 3.82 microns (0.324 ev) and 3.29 microns (0.374 ev).

The dependence of transmission on temperature is illustrated in Fig. 8, where the transmission is plotted against λ for **E** parallel to the *C* axis. The results indicate

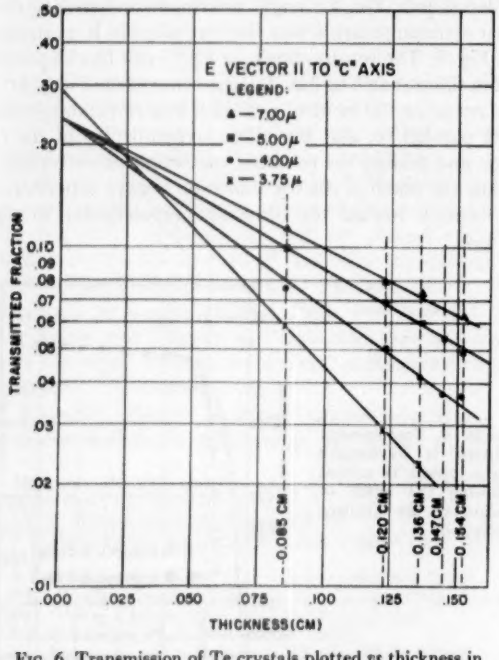

FIG. 6. Transmission of Te crystals plotted *vs* thickness in cm, *E* vector parallel to the *C* axis.

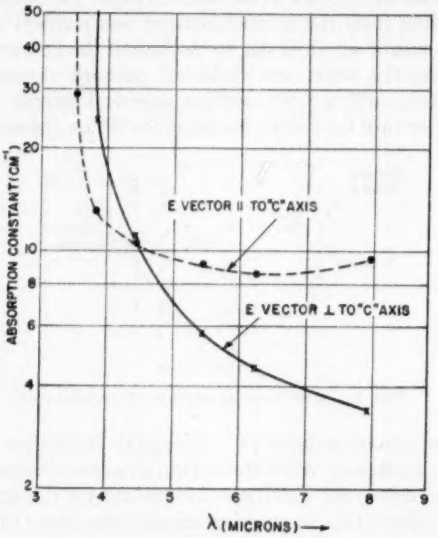

FIG. 7. Absorption constants (cm^{-1}) plotted *vs* (microns) for Te crystals.

that the edge shifts by an amount approximately -2×10^{-5} ev/°C between 100°K and 300°K and -5×10^{-5} ev/°C between 300°K and 400°K, independent of the criterion used to locate the edge. These shifts were barely detectable, i.e., they were at the limit of resolution available in our optical system. The absorption edge for **E** perpendicular to the *C* axis shifted by approximately the same amount.

V. PHOTOCONDUCTIVITY: EXPERIMENTAL RESULTS

The dependence of photoconductive response on temperature, voltage, light intensity, shuttering speed, wavelength, and polarization has been examined.

(A) Temperature

With the particular circuit chosen to measure photoconductive response, the signal ΔV is proportional to

the ratio $\Delta\sigma/\sigma$ as indicated above. Consequently ΔV is expected to be largest at 90°K where σ has decreased by a factor of 18 to 25, depending on the purity of the sample, from its room temperature value. In Table II we have tabulated $(\Delta V/V)V_{\text{T.C.}}$, i.e., the response per volt at constant incident energy, the resistance of the sample, and the ratio $\Delta\sigma_T/\Delta\sigma_{300°}$ at four temperatures. The wavelength chosen was 3.6 microns.

Because of the enhanced response in the low-temperature region most measurements of the spectral dependence were limited to these temperatures, where it was possible to work with smaller band widths.

(B) Voltage

The response for a given light intensity proved to be a linear function of the voltage. In spite of shielding the contacts, there was a residual photovoltaic effect which persisted after the voltage across the sample had vanished. At 100°K its magnitude was 6 μv as compared to a signal of 200 μv with a 1-volt bias across the sample. No saturation of the response was observed. Attempts to increase the voltage toward saturation ended in destruction of the samples which melted away.

TABLE II. Photoresponse *vs* temperature, at a wavelength of 3.6 microns.

Temp., °K	$(\Delta V/V)V_{\text{T.C.}}$ volts	Resistance ohms	$\Delta\sigma_T/\Delta\sigma_{300°}$
302	0.78×10^{-6}	20.7	1.00
273	2.33×10^{-6}	29.9	2.20
195	14.4×10^{-6}	122.0	3.10
100	56.7×10^{-6}	295.0	5.16

(C) Shuttering Speed

A large-diameter disc which contained twenty openings was driven by a variable-speed motor to provide a means of interrupting the incident radiation at various frequencies. White light of high intensity was focused on the sample and the signal generated across a series resistor was fed into a wide band amplifier and read off a (Ballantine) ac voltmeter. For the range of shuttering speeds available, i.e., up to 1000 cps the photoresponse was independent of shuttering speed at 300°K and at 90°K.

(D) Light Intensity

The light intensity was reducible by means of a set of grey filters which consisted of wire screens of different meshes. The results indicated that at 90°K the response was linear with light intensity, L_0, for $\lambda=3.6$ microns, and is proportional to $\sqrt{L_0}$ for $\lambda=2.2$ microns. At 300°K the response was approximately linear with light intensity when white light was used.

(E) Spectral Response and Polarization

In order to improve its accuracy, much of the data on spectral sensitivity was gathered by continuously

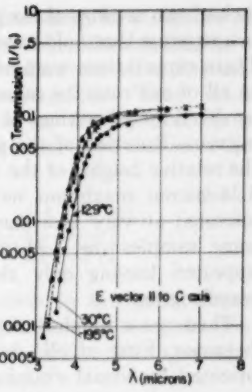

FIG. 8. Transmission of Te crystal plotted *vs* (microns) at three temperature E vector parallel to the C axis.

scanning the spectrum with the help of an automatic wavelength drive attached to the monochromator. The amplified signal, after rectification, was fed into an automatic recorder. A constant slit width was maintained throughout a run; its size was chosen so as to yield a maximum resolution in the region of the photoconductive threshold.

The results at 100°K will be discussed first since at this temperature the enhanced photoconductivity permitted the use of a band width of no more than 0.05 micron for all wavelengths on the curve. The normalized photoresponse is shown in Fig. 9. The most remarkable feature of these curves is the appearance of two separate maxima at wavelengths just short of the threshold. An average of thirty trials on five samples at 100°K places the maxima at 3.24 microns (0.381 ev) and at 3.72 microns (0.332 ev) while the threshold of photoconductivity (that value of the wavelength for which the normalized response has fallen to one-half its maximum value) lies at 4.02 microns (0.307 ev). These values should be compared to the positions of the absorption edges as given above, *viz.*, 3.27 microns (0.377 ev) and 3.77 microns (0.328 ev).

The coexistence of the two maxima was ascribed to the unpolarized quality of the incident radiation. Consequently for subsequent experiments the radiation was polarized. It was expected that by analogy with the transmission there would be only one maximum for

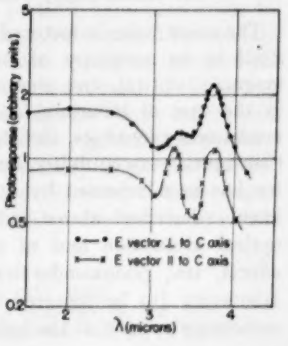

FIG. 9. Photoresponse plotted *vs* λ for Te crystal at 90°K.

each of two settings of the polarizer 90° apart and that two separate threshold wavelengths would be observed. These expectations were only partly realized (Fig. 9). In all of our runs the same long wavelength threshold persisted for all settings of the polarizer, i.e., $\lambda_1 = 4.02$. microns. Rotation of the polarizer did however affect the relative heights of the two maxima. In general the 3.24-micron maximum never exceeded that at 3.72 microns; at very best they were equal. However on some samples the 3.24-micron peak practically disappeared leaving only the one at longer value of wavelengths.

There are a number of possible explanations of this behavior. First of all, the thin needle crystals were oriented by visual examination and may never have been so oriented that the plane of polarization had no components perpendicular to the C axis. Furthermore the "crystals" may have consisted of more than one crystal, these being oriented at small angles to each other.

At the sublimation temperature of CO_2(195°K) the smallest practicable band width at the photoconductive threshold was 0.25 micron, so that the results obtained at this temperature are not as conclusive as those at 100°K. Here again two separate maxima appeared and their average positions were at 3.30 microns (0.374 ev) and 3.75 microns (0.329 ev). The threshold was at 3.94 microns. Comparing results at these two temperatures, the threshold of photoconductivity shifted by 7×10^{-5} ev/°C while the positions of the maxima shifted by -7×10^{-6} ev/°C and -3×10^{-5} ev/°C. The shifting of the maxima was in the same direction as the motion of the absorption edges. On the other hand the thresholds moved in the opposite direction. However, closer examination indicated that the shape of the curve near the threshold had changed with the temperature, so that different criteria for the location of the threshold yielded shifts of different signs as well as different magnitudes. It was concluded therefore that the position and shifting of the maxima bear a closer connection to the same properties of the absorption edges, and consequently to that of the energy gap.

VI. DISCUSSION OF THE EXPERIMENTAL RESULTS

(A) Anisotropy, General Discussion

The anisotropic character of a crystal lattice manifests itself in an anistropy of its mechanical, electrical, magnetic, optical, and photoelectric properties. Thus, in the case of tellurium, anisotropy of some of the mechanical properties, the electrical conductivity, the diamagnetic susceptibiltiy, and the thermal conductivity has been reported by other workers. The experiments described above indicate the anisotropy of optical absorption and of one of the photoelectric effects, *viz.*, photoconductivity. Other work in this laboratory (to be reported soon) indicates that the anisotropy extends to the index of refraction.

Because the electrical conductivity, the index of refraction, and the optical absorption for wavelengths longer than those at the absorption edge depend on the properties of the conduction electrons in a relatively simple fashion, the theory of these properties should indicate what effect anisotropy has on them and what correlations can be expected between them.

Thus the electrical conductivity σ is given by the expression

$$\sigma = neb = ne^2\tau/m^*,$$

where n is the number of carriers, e is the electronic charge, b is their mobility, τ is the mean lifetime between collisions, and m^* is the effective mass. In an anisotropic crystal, $1/m^*$ and consequently b and σ are tensor quantities which tensor reduces to three diagonal components for a hexagonal lattice. The ratio of σ parallel to, and perpendicular to, the C axis, as reported by Bottom, is 1.9.[9]

Secondly the classical Drude-Zener theory of the optical absorption caused by free carriers in solids leads to the following expression for the absorption constant K:

$$K = \frac{2\pi\mu_0 c}{N}\sigma_{dc}\left[\frac{\gamma^2}{\gamma^2+\nu^2}\right],$$

where σ_{dc} is the dc conductivity, ν is the frequency of the exciting radiation, N is the index of refraction, and $\gamma = e/2\pi m^* b$. From this expression it is possible to compute the value of K, say parallel to the C axis, using these values: $\sigma_{dc} = 0.3$ ohm^{-1} cm^{-1}, $N = 4.8$, $\lambda = 5$ microns. The result is 8.9×10^{-3} cm^{-1} compared to a measure value of $\sim$20 cm^{-1}. Such a discrepancy in magnitude between theory and experiment has also been observed in germanium and silicon.[11]

In the case of an anisotropic lattice σ_{dc}, N, and consequently K are tensors and the analysis leads to the following result:

$$(NK)_{11}/(NK)_{33} = (\sigma_{dc})_{11}/(\sigma_{dc})_{33}.$$

Here the subscripts 11 and 33 refer to quantities perpendicular to the C axis and parallel to it, respectively. Since $\sigma_{dc} \propto b \propto 1/m^*$, the theory predicts that by measuring the optical constants of an anisotropic crystal, it should be possible to arrive at a value for the ratio of effective masses therein. In the case of tellurium, the ratio N_{11}/N_{33} as measured by Miss P. Hartig in this laboratory is 0.78 for $\lambda = 5$ microns. Furthermore Bottom measured the ratio $(\sigma_{dc})_{11}/(\sigma_{dc})_{33}$ as 0.52. Thus the theory predicts that $K_{11}/K_{33} < 1$ which is in agreement with the results shown in Fig. 7. Closer quantitative comparison is not possible because the values of the absorption constant shown in Fig. 7, do not appear to be in accord with the Drude-Zener theory, *viz*, K is not proportional to λ^2 in the range of wavelengths shown, which was limited by the available equipment. An extension of the observation to longer

wavelengths is necessary before one can make any conclusive comparison with the theory.

(B) Anisotropy and the Energy Gaps of Tellurium

The location of the optical absorption edge of a semiconductor corresponds closely to the longest wavelength of radiation energetically capable of exciting an electron from the filled to the conduction band. Theory, however, does not indicate what criterion should be used for the exact location of this edge on the experimental curve. Consequently the exact evaluation of the gap width is not possible from transmission data. In the case of tellurium the significant fact is that no matter what criterion is used for the location of the absorption edge, there are two separate edges, each corresponding to a different value of the energy gap.

The presence of two gap widths was inferred from the transmission of the sample without correcting for the reflection loss; this procedure is questionable. However, even after such correction, two edges remain, as shown in Fig. 7. Furthermore, photoconductivity offers a means of observing the dependence of the absorption constant on wavelength for a large value of $K(>100\ \text{cm}^{-1})$ so that the existence of two maxima in the dependence of photoresponse on the wavelength indicates that the two edges do not coalesce for values of K larger than those shown in Fig. 7. Thus the experiments demonstrate that the minimum energy required to induce an optical transition from the filled to the conduction band is a function of the polarization of the incident radiation. The probability of such a transition is proportional to $|\langle\psi_i\xi\cdot\nabla\psi_f\rangle|^2$ where ψ_i and ψ_f are the wave functions of the initial and final states, respectively, ξ is a unit vector parallel to the electric vector of the exciting radiation, and ∇ is the operator representing the instantaneous momentum of the electron. Thus the experimental results imply that if the electrons are all in the same initial state, changing the direction of ξ will induce transitions into final states of different minimum energies. This in turn suggests a multiplicity of bands which are less than 0.4 ev above the valence band. Further speculation on the significance of the optical selection rules must be deferred, however, until a satisfactory band model becomes available.[21] Such a band model must also explain the anomolous double reversal in the sign of the Hall coefficient reported by Bottom and Fukuroi.

(C) Variation of the Energy Gap with Temperature

The dependence on the lattice parameter of the forbidden gap between the valence and the conduction bands can be studied experimentally in a number of ways. One of the most direct is an observation, as a function of pressure, of the conductivity of an intrinsic semiconductor at two temperatures. Then since $\sigma=\sigma_\infty\exp(-E_G/2KT)$, where we assume that σ_∞ is relatively insensitive to temperature, we can solve for E_G:

$$E_G=[2K\ln(\sigma_2/\sigma_1)]\left[\frac{1}{T_2}-\frac{1}{T_1}\right]^{-1}.$$

Such an experiment was performed by Bridgman, whose results were analyzed by Bardeen[22,23] to yield the following value for the slope of the line relating energy gap to pressure in tellurium:

$$\partial E_G/\partial P)_T=-1.6\times10^{-5}\ \text{ev}-\text{cm}^2/\text{kg}.$$

Thermodynamically, temperature is equivalent to pressure in changing the lattice parameter, and for changing temperature the result is

$$\partial E_G/\partial T)_P=1.7\times10^{-4}\ \text{ev}/^\circ\text{C},$$

where we have used Bridgman's values of the thermal expansion coefficient and for the compressibility[23] to convert from one set of parameters to the other.

Bardeen and Shockley[24] have related this shift in lattice parameter to the mobilities of holes and electrons, so that from an experimental determination of the mobilities and the elastic constants of the material it is possible to determine the variation of energy gap with dilation of the lattice. Fukuroi[10] has used their results to compute this variation and his result is

$$\partial E_G/\partial P)_T=-2.2\times10^{-5}\ \text{ev}-\text{cm}^2/\text{kg},$$

which is in fair agreement with Bridgman's result. He used values of the mobility and the effective mass ratios for holes and electrons determined at Tôhoku University. However he did not take into account the anistropy of the tellurium lattice.

Now there is another way of obtaining information about changes in the gap width of a semiconductor, *viz.*, by measuring the shift in the fundamental absorption band under the influence of pressure and of temperature. No measurements of the movement of the absorption edge with pressure have been made for an elementary semiconductor, but it would be expected that since a pure compression would be involved the results should agree with the movement of the energy gap determined by a Bridgman type experiment. Measurements of the shift of the edge with temperature had been made, however, notably in germanium and silicon, and the results so obtained did not agree quantitatively with the value measured by other methods.[1]

[21] By using group theory, H. B. Callen has made a qualitative theoretical analysis of the energy band structure of a tetragonal crystal composed of atoms whose ground state is $5s^25p^4$. There is a close analogy between such a hypothetical solid and tellurium, so that this model successfully explains many of the properties of tellurium discussed in this paper. The results are being prepared for publication. Work is also in progress to extend this treatment to a lattice having the spiral chain structure of tellurium.

[22] J. Bardeen, Phys. Rev. **75**, 1777 (1949).
[23] P. W. Bridgman, Proc. Am. Acad. Sci. **60**, 366 (1925).
[24] J. Bardeen and W. Shockley, Phys. Rev. **80**, 72 (1950).

Fan[25] has proposed an explanation for this discrepancy based on the fact that temperature not only affects the volume of the lattice, but also increases thermal vibrations. The interaction between the new spectrum of lattice vibrations and the conduction electrons will result in a shift of the valence and the conduction bands with a consequent decrease of the forbidden band between them. Fukuroi[26] used Fan's results to compute the magnitude of this effect in tellurium and the result was -0.68×10^{-4} ev/°C. However, it should be emphasized that the expression he used was applicable to the diamond lattice and modification must be made before it is applied to the anisotropic tellurium lattice. Addition of these two terms yields a value of approximately 1.0×10^{-4} ev/°C as compared to the experimentally determined shift of approximately -3×10^{-5} ev/°C.

The effect of lattice contraction on the energy gap is quite solidly established by Bridgman's experiment and Hall's confirmation thereof in the lower pressure range.[27] Consequently, in order that there be closer conformity between theory and experiment, it is necessary that the negative, i.e., the Fan term, be of a larger absolute value. Fan found this same difficulty in germanium, where theory and experiment would agree if the effective mass of the electron were reduced by a factor of 3.0. In the case of tellurium, such agreement would result if the effective mass were reduced by a factor of 3.5. There is no experimental basis for such an assumption.

(D) Photoconductivity: Discussion

All of our measurements of photoconductivity were made with shuttered radiation partly to avoid the effects of background radiation and consequent drifting, but mostly to take advantage of the relative ease of amplifying the resulting signal. In the case of tellurium we are dealing with a high dark-current semiconductor, in which the photoconductivity is a small perturbation on the dark current. Under these conditions the rate of change of carrier concentration while the sample is uniformly illuminated by light of intensity L_0 is given by

$$dn(t)/dt=\alpha L_0-BNn(t),$$

where $n(t)$ is the density of photoelectrons, N is the density of carriers in the dark $[N\gg n(t)]$, α is a constant which is related to the excitation efficiency, and B is a constant which expresses the probability for recombination of the electron and a hole in the filled band.

This equation can be solved for $n(t)$, and since experimentally we measure the rms voltage due to the shuttered light, we will ignore the transient terms and compute the rms value of $n(t)$. The result is:

$$n_{\rm rms}=\frac{\alpha L_0}{\sqrt{2}}\left[\frac{1}{(BN)^2+\omega^2}\right]^{\frac{1}{2}},$$

and the measured

$$\Delta V_{\rm rms}=\frac{ebRAV}{l}n_{\rm rms},$$

where e is the electron charge, b is the mobility, R is the resistance of the matching resistor, l is the length of the sample, V is the voltage impressed across it, and A is the cross-sectional area. Thus the so-called monomolecular model predicts that the ac response should be directly proportional to V and L_0, and either insensitive to the shuttering frequency or else inversely proportional to it, depending on whether $BN\gg\omega$ or $BN\ll\omega$, respectively.

Our experiments at 300°K indicate that $\Delta V_{\rm rms}\propto VL_0$ and that it is insensitive to shuttering speeds up to 1000 cps for a square-wave input.

At 90°K the photosignal was large enough to permit its observation on an oscilloscope. Here again the response followed the shape of the signal up to the highest shuttering speeds available, *viz.*, 1000 cps. The time-constant or the photoconductive process is therefore shorter than 10^{-3} sec.

Using monochromatic light, $\Delta V_{\rm rms}$ is proportional to L_0 for $\lambda=3.6$ microns, i.e., in the vicinity of the absorption edge, whereas it is proportional to $L_0^{\frac{1}{2}}$ for $\lambda=2.2$ microns, i.e., in the region where absorption takes place within the surface layer. Thus the surface has different photoconductive properties from the bulk material. The experiments therefore indicate that at 90°K the bulk material photoconductivity is in accord with the monomolecular model, while the surface follows either a bimolecular process or else it exhibits complications due to trapping.

The difference in the properties of the surface and of the volume can be used to explain qualitatively the presence of a maximum in photoresponse at the absorption edge. There may be a larger number of traps in the surface layer which would decrease the sensitivity as the absorption was confined to a greater degree in the surface material.

An alternative explanation for the existence of the maximum is afforded by a model similar to Fassbender's,[28] where the optical absorption is included in the analysis of the resulting photocurrent. In this case we modify the basic monomolecular equation by writing

$$L_0=a_0Ke^{-Kz},$$

where L_0 is the light absorbed in a thickness dz, a_0 is the intensity of the incident radiation, K is the absorption constant, and z is the sample thickness. The analysis leads to the result that the total number of electrons liberated by radiation of wavelength λ is

$$N(\lambda)=\frac{a_0K(\lambda)}{B}[1-e^{-K(\lambda)D}],$$

[25] H. Y. Fan, Phys. Rev. **82**, 900 (1951).
[26] T. Fukuroi, Sci. Repts. Research Inst. Tôhoku Univ. **A3**, 175 (1951).
[27] H. Hall (private communication from the author).
[28] J. Fassbender, Ann. Physik **5**, 33 (1949).

where D is the total thickness of the sample. It is necessary to assume some functional relation between K and λ. Reasonable considerations suggest that at the absorption edge $K=\gamma/\lambda$, where γ is a constant, while in the short wavelength region $K=$const. These assumptions lead to a maximum response at the absorption edge, if the response is proportional to $L_0^{\frac{1}{2}}$. This condition is fulfilled, at least partially, in tellurium.

An explanation for the temperature dependence of the photoresponse shown in Table III, is based on the observation that, although each incident photon liberates a pair of carriers, the observed photocurrent depends on the number of times these liberated carriers traverse the circuit before they experience recombination. Thus the ratio of photocurrent to photon current, Q, is not necessarily unity. In our case, Q was about 0.1 for $\lambda=2$ microns at 90°K. Rose[29] shows that the measured increment in the current ΔI, is related to the photon current F, through the expression

$$\Delta I=eQF=(e\tau/T_\tau)F,$$

where e is the electronic charge, τ is the lifetime of the carriers, and T_τ is their transit time between electrodes, which is related to the mobility b, the voltage V, and sample length l, thus

$$T_\tau=l^2/bV.$$

Therefore the ratio $\Delta\sigma_T/\Delta\sigma_{302^\circ}$ recorded in Table III, which is essentially $\Delta I_T/\Delta I_{302^\circ}$, is given by

$$\Delta\sigma_T/\Delta\sigma_{302^\circ}=(\tau b)_T/(\tau b)_{302^\circ}.$$

This expression is greater than unity, since the mobility is greater at the lower temperature, whereas τ should not change very much. This is in qualitative agreement with our experimental results, although quantitative comparison is not feasible since none of the quantities on the right side of the equation is known.

VII. THE OPTICAL PROPERTIES OF TELLURIUM-SELENIUM ALLOYS

As mentioned previously, we have also examined the photoconductivity and optical transmission of two alloys of tellurium and selenium. Our main purpose was to observe the spectral sensitivity of these properties and to observe the magnitude of the photoconductive effect.

Single crystals of alloys containing 2.7 percent selenium by weight, (hereafter referred to as alloy No. 1) and 11 percent selenium by weight (hereafter alloy No. 2) were grown in a manner similar to that used for growing tellurium crystals. The selenium was obtained from the Canadian Copper Refining Company and their spectroscopic analysis indicated about 7 parts/million impurities. The alloy No. 1 crystals looked very much like Te, although the alloy No. 2 had lost much of the metallic luster characteristic of Te. Uniformity of an alloy No. 2 crystal was established by probing the surface to determine a plot of the potential drop against distance from an electrode. The resistivity as computed from the slope of this curve was 4.1 ohm-cm as compared to 0.6 ohm-cm for tellurium. This is in qualitative agreement with the results of Haken[30] for the resistivity of these alloys. The resistivity of alloy No. 1 was 0.75 ohm-cm. Measurement of the Hall constant and conductivity leads to values of 150 cm²/volt sec for the mobility in alloy No. 1 and 25 cm²/volt sec in alloy No. 2 at 300°K.

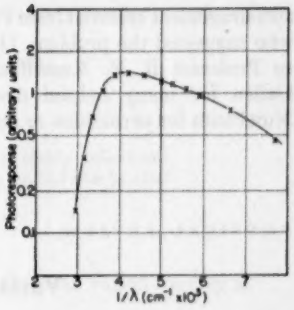

FIG. 10. Photoresponse of alloy No. 2 (89 Te-11 Se) plotted *vs* λ (cm^{-1}).

The transmission of alloy No. 1 exhibits two absorption edges as in tellurium, but these have shifted to shorter wavelengths and are now located (at 300°K) at $\lambda_{1/8}=3.29\mu$ (0.375 ev) for **E** parallel to the C axis and at $\lambda_{1/8}=3.57\mu$ (0.346 ev) for **E** perpendicular to the C axis as compared to 3.45μ (0.358 ev) and 3.91μ (0.316 ev) for the corresponding quantities in tellurium. The photoconductivity at 90°K exhibited two peaks at 3.33μ (0.372 ev) and 3.59μ (0.344) and the threshold of photoconductivity was at 3.75μ (0.330 ev).

The photoconductivity of alloy No. 2 is shown in Fig. 10. It was impossible to decide whether two peaks and two edges existed since the maximum photoresponse and the absorption coincide in location with the position of the atmospheric absorption band between 2.6 and 3.0 microns. The data shows however that the response has virtually disappeared at 3.1 microns and the maximum photoresponse occures at about $\lambda=2.8$ microns.

Thus the reduction of lattice parameter accompanying the addition of selenium to tellurium increases the energy gap of the resulting alloy over that of pure tellurium. This conclusion is in agreement with the values for energy gap of the alloys derived by plotting $\ln\sigma$ *vs* reciprocal temperature by Mr. Nussbaum of this laboratory and is in qualitative agreement with the unpublished results of H. Hall,[31] who found that the gap increased with addition of selenium up to concentrations of 30 percent.

The author gratefully acknowledges the advice and

[29] A. Rose, RCA Rev. **12**, 362 (1951).

[30] W. Haken, Ann. Physik **32**, 330 (1910).

[31] H. Hall (private communication).

encouragement received from Professor P. H. Miller, Jr., who suggested the problem. He is very much indebted to Professor B. R. Russell and to Professor H. B. Callen for many helpful discussions; to Mr. Allen Nussbaum for permission to refer to unpublished work; to all his colleagues for their advice and assistance; to Mr. H. Mohr for his excellent work in constructing the necessary apparatus, and to the U. S. Office of Naval Research, Bureau of Ships, who supported this investigation financially.

PHYSICAL REVIEW VOLUME 93, NUMBER 4 FEBRUARY 15, 1954

Variation of the *l*-Type Doubling Constant in HCN

J. F. WESTERKAMP*
Columbia University, New York, New York
(Received July 16, 1953)

Microwave measurements on six transitions between the *l*-type doublets of HCN show that the *l*-type doubling constant depends on rotational angular momentum J as follows:

$$q=224.471-0.002613J(J+1) \text{ Mc/sec.}$$

MICROWAVE transitions directly between the two levels of HCN, which have been split by *l*-type doubling, have been reported[1] and a variation noticed in the value of the *l*-type doubling constant q with the rotational quantum number J. However, discrepancies in the nature of this variation and uncertainties[1,2] in its functional dependence on J stimulated the present measurement of *l*-type doubling in HCN for a number of different values of J.

Measured frequencies for microwave transitions between the *l*-doubled levels of HCN in the first excited bending mode ($v_2=1$) for a wide range of values of J are listed in Table I. These frequencies are expected to have the form

$$\nu=qJ(J+1)=[q_{J=0}-\epsilon J(J+1)]J(J+1). \quad (1)$$

The small quantity ϵ is expected to be of the order $q(B/\omega_2)^2\approx 10^{-5}q$, where B is the rotational constant and ω_2 the bending frequency. It is shown in Table I that the measured frequencies can be fitted fairly well to an expression of the form (1) with $q_{J=0}=224.471$ and $\epsilon=0.002614$. The form (1) and the positive sign of ϵ are in accordance with calculations of Nielsen.[3]

TABLE I. Transitions between *l*-type doublets of HCN in excited bending mode ($v_2=1$) for various rotational states, and the *l*-type doubling constant q.

J	Frequency ν in Mc/sec	$q=\dfrac{\nu}{J(J+1)}$	$q=224.471-0.002614J(J+1)$
6	9423.3	224.365	224.361
8	16147.8	224.274	224.283
9	20181.4	224.238	224.236
10	24660.4	224.185	224.184
11	29585.1	224.129	224.126
12	34953.5	224.061	224.063

These results are essentially in agreement with those of Weatherly and Williams,[2] although these authors did not measure enough transitions to determine critically the dependence of q on J. Evaluation of ϵ from the earlier measurements of Shulman and Townes[1] is inaccurate apparently because misidentification of frequency markers gave errors in some of the measured frequencies which were multiples of 30 Mc/sec.

The author is grateful to Professor Townes for suggesting these measurements, and to Mr. A. Javan and Mr. J. Lotspeich for considerable help in carrying them out.

* Present address: Juncal 2114, Buenos Aires, Argentina.
[1] R. G. Shulman and C. H. Townes, Phys. Rev. 77, 421 (1950).
[2] T. L. Weatherly and D. Williams, Phys. Rev. 87, 517 (1952).
[3] H. H. Nielsen (private communication).

Magnetic Resonance in αFe_2O_3

P. W. ANDERSON, F. R. MERRITT, J. P. REMEIKA, AND W. A. YAGER
Bell Telephone Laboratories, Murray Hill, New Jersey
(Received October 21, 1953)

Magnetic resonance experiments performed on αFe_2O_3 confirm the existence of a highly anisotropic, weak ferromagnetism which disappears below −15°C. The anisotropy energy has been studied as a function of orientation.

I. INTRODUCTION

WITH the use of fields up to 24 000 gauss, αFe_2O_3 single crystals were studied by magnetic resonance at 1.25-cm wavelength. A range of temperatures, including the Morin transition at −14°C,[1] was investigated. A strong line was observed above this transition, which is probably a ferromagnetic resonance due to the "parasitic ferromagnetism" of Néel.[2] We were able to study in some detail the marked anisotropy known to be exhibited by this ferromagnetism.[3–5] However, we unexpectedly found that this anisotropy does not vary appreciably with temperature near the transition at −14°C, but rather that all observable resonances simply disappear completely below this temperature. It seems, then, that these observations do not, as had been hoped, indicate that the ferromagnetism turns, with the antiferromagnetism, from the basal plane to the (magnetically) hexagonal axis at this temperature. Thus we do not confirm Néel's hypothesis[2] on this point, although our measurements do not necessarily exclude this hypothesis.

The resonance fields were studied as a function of the orientation of the external field with respect to the crystal. These observations have been fitted to a phenomenological ferromagnetic anisotropy energy. The *ad hoc* character of this fitting must, however, be emphasized; in view of the rather mysterious nature of all the phenomena in this substance it is not even certain that such a description of them is correct.

II. OBSERVATIONS

A number of flat plates parallel to the basal plane were grown. They were rather impure, analyzing about 3 percent Fe^{++}. The one used in most experiments was about 21 square mm in area and about 0.35 mm thick. The single plate gives a strong resonance at room temperature (losses several times the nonmagnetic losses in a cavity of $Q \sim 2000$) at a field which is about 2300 gauss when the dc and rf fields are both perpendicular to the hexagonal axis. The half-power full width of the line was 600 gauss, and the line is plotted in Fig. 1. The position of the peak varied roughly as

$$H_{res} = (2270 + 60 \sin 6\varphi) \text{ gauss} \quad (1)$$

as the angle φ between the dc field and some undetermined direction, both in the plane perpendicular to the axis, is varied. This rather small anisotropy has not been observed previously.

The very low resonance field (for a g factor of 2 it should be 8600 gauss) confirms the large anisotropy observed previously for the parasitic ferromagnetism.[3,4] We note that the usual magnetization of αFe_2O_3, of the order of a few emu/cc, can lead to macroscopic demagnetizing fields of at most a few hundred gauss so that we can neglect any ordinary demagnetizing effects. The usual formula,[6] assuming that the small anisotropy in the plane [Eq. (1)] can be neglected, is

$$H_0^2 = H_{res}(H_A + H_{res}). \quad (2)$$

Here H_0 is the normal resonance field, H_{res} the observed resonance field, and H_A the anisotropy field. This equation gives for the anisotropy field (if we assume $H_0 \simeq 8600$ gauss):

$$H_A \cong 30\,000 \text{ gauss}. \quad (3)$$

The resonance field was observed at room temperature as a function of the angle between the field and the basal plane in order to find out more about the anisotropy energy. If one writes the anisotropy energy as

$$U_A = MH_A f(\sin\theta), \quad (4)$$

where θ is the angle between the magnetization and the basal plane, the resonance fields are given by the

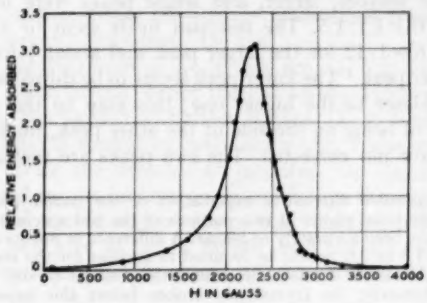

FIG. 1. The absorption line in the "normal" position (H parallel to hexagonal plane).

[1] F. J. Morin, Phys. Rev. **78**, 819 (1950).
[2] L. Néel and R. Pauthenet, Compt. rend. **234**, 2172 (1952); L. Néel, Revs. Modern Phys. **25**, 58 (1953).
[3] T. Townsend Smith, Phys. Rev. **8**, 721 (1916).
[4] R. Chevallier and S. Mathieu, Ann. Physik **18**, 258 (1943).
[5] L. Néel, Ann. Physik **4**, 249 (1949).
[6] C. Kittel, Phys. Rev. **73**, 155 (1948).

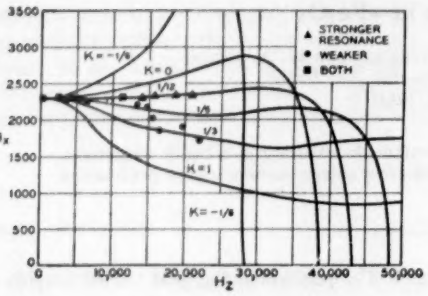

FIG. 2. H_x vs H_z for resonance: theoretical curves and experimental points.

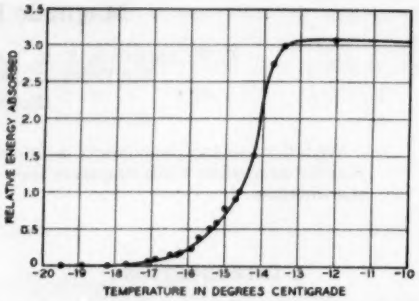

FIG. 3. Peak intensity in the "normal" position as a function of temperature.

equations

$$\frac{M_{x0}}{M_{z0}}=\tan\theta=\frac{H_z-H_A f'/2}{H_x},$$
$$H_0^2=H_x^2\sec^2\theta+H_A H_z\cos\theta(\tfrac{1}{2}f''). \tag{5}$$

Here θ is the angle of the static magnetization with the basal plane, given that the external field is H_z, H_x (x is in the plane, z along the axis). We assume that

$$f(\sin\theta)=\sin^2\theta+K\sin^4\theta, \tag{6}$$

and the components of the resonant field H_x and H_z are plotted against each other for a number of values of K in Fig. 2.

The observed behavior of the resonance as the angle between H and the basal plane was increased was the following: until H was 70° or more from this plane, the resonance shifted in such a way that H_x was approximately constant, thus deviating appreciably from the behavior for $K=0$ at the higher angles. The maximum intensity did not change much; the breadth increased proportionally to the central field, as one would expect. At the higher fields and angles, a second resonance slowly split off from the main one toward lower fields. The intensities indicated that the two new resonances had both been part of the original one: the intensities of the smaller, larger, and single peaks were in the ratio 0.3:1.2:1.5. The resonant fields seem to fit (5) with $K=1/12$ for the larger peak and about $\frac{1}{8}$ for the smaller peak.[7] The lower peak seems to be shifted where it is closer to the higher one; this may be the usual effect of being on the side of the other peak, for which we have not corrected. The two peaks are plotted as triangles for the stronger, circles for the weaker on Fig. 2. Note that the second peak, in spite of its lower resonant field, fits an anisotropy energy which is *higher* at the axis.

The effect of varying the temperature was surprisingly small. At no temperature from −50°C to room temperature could any signal at all be detected, up to 19 000 gauss, with the dc field along the axis. At all temperatures at which a signal could be detected in the plane position of H, the field was 2300±50 gauss. The intensity of this resonance varied sharply at the lower transition point, as shown in Fig. 3, disappearing below it as mysteriously as does the parasitic ferromagnetism, without shifting or broadening appreciably.

One very minor effect was observed near the transition. It was found that the lower one of the two resonances at high angles θ shifted noticeably to lower fields in the transition region. This effect was difficult to pin down quantitatively but was definitely there, since at some orientations in which, at room temperature, no absorption whatever was observed, absorptions as high as 1/10 to 2/10 of the usual maximum showed up in the region −14 to −16°C. These phenomena occurred only at the angles closest to the axis and at the highest fields. A rough estimate of the effect of temperature on line position would be that, whereas at $H_x=10\,000$ no shift could be observed, in the region $H_x=15\,000$–$20\,000$ the value of H_z for resonance is 500–1000 gauss lower than previously. Unfortunately, according to our formulas such behavior indicates a *higher* total anisotropy energy, if anything. We repeat that when H was accurately parallel to the axis, no signal was ever observed; computations show that this condition eliminates larger negative values of K from consideration and thus indicates that the position parallel to the axis is always highly unfavorable energetically.

We should like to acknowledge helpful suggestions from F. J. Morin on growing the crystals and to thank J. P. Wright for performing the analysis of the crystals for Fe^{++}.

[7] A possible alternative explanation of the double peaks is that the basal planes of two portions of the test specimen may not have been accurately co-planar. A difference in orientation of about 1.5 to 2.0° would be required to account for the observations. Hematite is known to exhibit this type of crystal habit. Unfortunately, the crystal was broken before this hypothesis could be checked.

Sputtering of Alkali Atoms by Inert Gas Ions of Low Energy

RICHARD C. BRADLEY
Department of Physics, University of California, Berkeley, California

(Received September 28, 1953; revised manuscript received November 5, 1953)

Direct measurements of sputtering have been made using alkali metal targets bombarded by inert gas ions in high vacuum, the sputtered atoms being counted by a surface ionization detector. Measurements were made in the range 0–1800 ev ion energy for the ions He^+, Ne^+, A^+, and Xe^+ incident upon Na and K target surfaces. Secondary electron coefficients γ were measured simultaneously. It was found that over most of the energy range covered, the measured sputtering coefficient θ' (number of sputtered atoms reaching the detector per positive ion incident on the target) was linear in $\ln E$ for He^+ and Ne^+ and in $\sqrt{E}$ for A^+ and Xe^+, where E is the ion energy. At energies less than about 150 volts the sputtering rate appeared to be controlled by the amount of kinetic energy which could, on the average, be transferred to a single surface atom in a direct two-body collision. Thus at low energies Ne^+ produced the most sputtering from a Na surface, whereas A^+ produced the most from a K surface. At high energies, the sputtering rate was in the same order as (but not proportional to) the mass of the ion. The effect of surface contamination was also studied. An old surface showed a lower sputtering coefficient than a fresh surface and a higher and more erratic secondary electron coefficient, the effect being most pronounced for the light ions. The absolute sputtering coefficient θ (total number of sputtered atoms per incident ion) could not be measured directly, but it was estimated from the geometry that for 1000-volt ions the value of the coefficient ranged from about 1.0 for Xe^+ on K to 0.05 for He^+ on Na.

INTRODUCTION

SPUTTERING, the phenomenon of the disintegration of metal surfaces under the impact of gaseous positive ions, has been known for nearly a century. However, even though a great many investigations of the phenomenon have been conducted, relatively little is known concerning the mechanism involved. The trouble is that most of the early experiments were conducted in glow discharges where the uncertainties inherent in the method make quantitative interpretation of the data difficult. The early studies have been well summarized by Massey and Burhop.[1]

With the improvement in vacuum techniques and the development of good positive ion sources, it is now possible to study sputtering in vacuums with monoenergetic ion beams. Such studies have been made by Timoshenko[2] and Keywell[3] for several ion-target combinations. The target weight loss method used by them gives absolute sputter rates θ (number of sputtered atoms per incident ion) and is applicable whenever the rate is reasonably high—that is, for ion beams of hundreds or thousands of electron volts energy and tens or hundreds of microamperes intensity. It is not, however, a sufficiently sensitive method for low-energy measurements. Evidence of sputtering due to ions of very low energy ($\sim$10 ev) has been reported by Loeb,[4] Wehner and Medicus,[5] and others, but under conditions not suitable for an accurate evaluation of the sputtering rate.

Several theories on sputtering exist,[3,6–8] but the evidence thus far is not conclusive in favor of any of them. Actually, the process is probably sufficiently complicated so that no single theory would be applicable under all conditions.

The purpose of the present experiment was to apply the ion-beam vacuum technique to a study of sputtering at low energy. In order to have sufficient sensitivity, an electrical method of counting the sputtered atoms was used. The apparatus consisted of an ion source and gun, an alkali metal target, and a surface ionization detector to measure the sputtered alkali atoms. Aside from its sensitivity, the method has also the advantage of giving direct measurements of the sputtering rate θ' (number of sputtered atoms reaching the detector per positive ion incident on the target). With a given target, one can rapidly run through the available energy range for several different types of ions without ever having to expose the system to air; reproducibility checks are possible at any time to see if the surface has changed its characteristics. If at the end of a run the initial measurements were repeated and found to be unchanged, it was assumed that the surface maintained constant characteristics throughout the run.

The disadvantages of the method are: (1) it is limited to the alkali metals; hence there is no opportunity for a direct comparison with other studies. (2) It does not give absolute sputtering rates, since only those atoms which strike the detector are counted. On the other hand, unless one has reason to think that the angular distribution of sputtered atoms may change, relative values can give as much insight into the sputtering mechanism as absolute values. (3) There is no way of

* This research was supported under a grant from the U. S. Office of Naval Research.

[1] H. S. W. Massey and E. H. S. Burhop, *Electronic and Ionic Impact Phenomena* (Clarendon Press, Oxford, 1952).
[2] Gregory Timoshenko, J. Appl. Phys. **12**, 69 (1941).
[3] Frank Keywell, Phys. Rev. **87**, 161 (1952).
[4] Loeb, Kip, and Hudson, Phys. Rev. **60**, 714 (1941).
[5] G. Wehner and G. Medicus, Phys. Rev. **89**, 339 (1953).
[6] K. H. Kingdon and I. Langmuir, Phys. Rev. **20**, 108 (1922).
[7] A. V. von Hippel and E. Blechschmidt, Ann. Physik **81**, 1043 (1926).
[8] E. S. Lamar and K. T. Compton, Science **80**, 541 (1934).

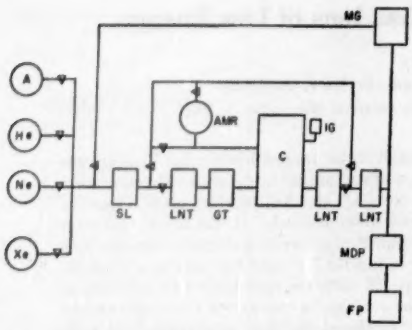

FIG. 1. Schematic diagram of the vacuum system. *C*, chamber; *AMR*, alkali metal reservoir; *IG*, ionization gauge; *MG*, MacLeod gauge; *SL*, variable slow leak; *LNT*, liquid nitrogen trap; *GT*, gold trap; *MDP*, mercury diffusion pump; *FP*, mechanical fore pump.

ensuring a really clean surface since it is not possible to "flash" the surface to a high temperature before each measurement. With a possible background pressure of oxygen of 1×10^{-8} mm of Hg, an oxide monolayer would form on a fresh alkali surface in a matter of minutes, whereas the time required to make a complete series of measurements was several hours.

The effect on sputtering of an aging surface was studied at some length, and it was found possible to slow up the aging process sufficiently so that reproducibility could be maintained over the period required to make a complete series of measurements.

DESCRIPTION OF APPARATUS AND EXPERIMENTAL PROCEDURE

A. The Vacuum System

The experimental chamber, which is shown as *C* in Fig. 1, was evacuated by a mercury diffusion pump *MDP* backed by a mechanical pump *FP*. Liquid nitrogen traps *LNT* were installed between the chamber and the rest of the system so that during actual operation there were no stopcocks directly exposed to the chamber.

The outgassing procedure consisted of baking the chamber in an oven at 400°C for forty-eight hours, induction heating the electrodes to a cherry-red temperature for several hours, running all filaments at a higher-than-operating temperature for several days, and thoroughly torching all the glass tubing of the vacuum system. All this was done, of course, before any alkali metal was admitted to the chamber. The vacuum obtained was such that with all filaments at their operating temperatures the pressure in the chamber was about 5×10^{-8} mm of Hg as read by an ionization gauge.

Spectroscopically pure inert gases He, Ne, A, or Xe could be admitted to the system through a mercury-ceramic variable slow leak *SL*.[9] The normal operating pressure in the chamber ranged from 2×10^{-5} mm for Xe to 3×10^{-4} mm for He. Aside from furnishing ions for the beam, the inert gases could also be used to move the liquid alkali metals into the chamber.

[9] H. D. Hagstrum and H. W. Weihart, Rev. Sci. Instr. **21**, 394 (1950).

B. The Alkali Metals

The two target metals used in this experiment were sodium and potassium. While in principle any alkali metal would have served, these two were chosen because of their low vapor pressures at room temperature and because they can readily be distilled in Pyrex vessels.

Several ounces of each metal were distilled through six stages under high vacuum. A vacuum breakoff seal between the fifth and sixth stages *D* and *R* of Fig. 2 made it possible to distill through the first five stages, using an auxiliary vacuum system and thus without exposing the chamber to the distillation products. In the sixth distillation the alkali metal was allowed to flow down into the horizontal intake tube and, while still liquid, pushed into the chamber. When the alkali appeared in the mouth of the intake tube it was allowed to solidify, and the solid surface formed the first target. Subsequent fresh targets could be obtained by reliquefying the metal, overflowing the old surface using pressure from behind, and allowing the new surface to freeze.

The liquid alkalis were pushed either by a magnetic slug *MS* sealed in a quartz envelope which could slide in the intake tube and be moved by a magnet outside the system or else by a slight pressure of inert gas. The magnetic slug technique was used whenever possible as it afforded better control. Greater force was possible using gas pressure, but the flow tended to be more erratic. The difficulty lies in the strong adhesion between the alkali metals and Pyrex glass.

C. The Electrode System of the Chamber

A schematic diagram of the electrode system of the chamber is shown in Fig. 3. The essential elements are (1) the ion source and gun, (2) the target and secondary

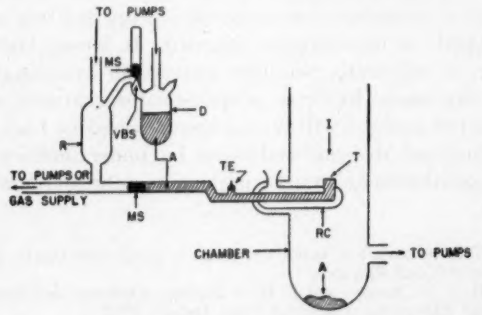

FIG. 2. Alkali metal system. *A*, alkali metal; *D*, distillation bulb; *MS*, magnetic slug; *VBS*, vacuum-breakoff-seal; *R*, alkali metal reservoir; *TE*, target electrode; *RC*, refrigeration chamber; *TE*, target electrode; *T*, target; *I*, ion beam.

electron collector, and (3) the surface ionization detector. Except for the target and the filaments all electrodes were of tantalum.

1. *The Ion Source and Gun*

The ion source was of the Finkelstein type.[10] Such a source was well suited for this study since (a) it gives an ion beam of low-energy spread, (b) it can be operated at pressures so low (10^{-4}–10^{-5} mm of Hg) that the kinetic mean free paths of the ions and sputtered atoms are long compared to interelectrode distances, thus obviating any need for differential pumping, and (c) it can be operated at source voltages so low that the ionizing electrons have insufficient energy to produce doubly charged ions—thus giving assurance that there are only singly charged atomic ions in the beam. (Singly charged molecular ions are ruled out by the low pressures.)

The operation of the source was roughly as follows: electrons emitted by the hot tungsten cathode C were attracted by the anode cylinder A and repelled by the electrodes RP and L_1. An axial magnetic field H of about 200 gauss caused the electrons to follow tight helical trajectories back and forth along the axis between C and L_1, giving them long free paths in a small volume, accounting for the high efficiency of the source. Eventually, as a result of inelastic impacts, space charge fields, or otherwise, the electrons were collected by A.

In the meantime a fraction of the positive ions, which were created in this region by electron collisions with gas atoms, were drawn out by the extraction electrode L_1 into the gun. The voltages used on the various electrodes L_1-L_4 of the gun to give best operation were determined experimentally. Best extraction was obtained when L_1 and L_2 were maintained at the same potential, approximately 350 volts negative with respect to the anode A. L_4 and T were kept at the same potential (aside from a contact potential difference) so that electrons from the target could be separately collected. Highest beam intensity was achieved when L_3 was highly negative (~2 kv) but this led to difficulties, for at low ion energies secondary electrons produced at the walls of the gun were being accelerated by the high field between L_3 and L_4 and were reaching the target in appreciable numbers. This difficulty was largely removed if L_3 were maintained at the same potential as L_4 and T, even though this meant an over-all reduction

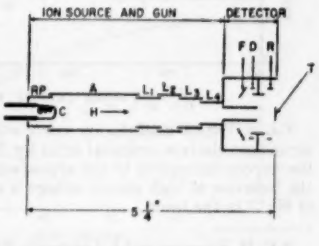

FIG. 3. Schematic diagram of electrode system. C, hot tungsten cathode; RP, electron repeller plate; A, anode; H, magnetic field; L_1-L_4, ion lenses; F, hot platinum filament; D, alkali ion collector; R, secondary electron collector; T, target.

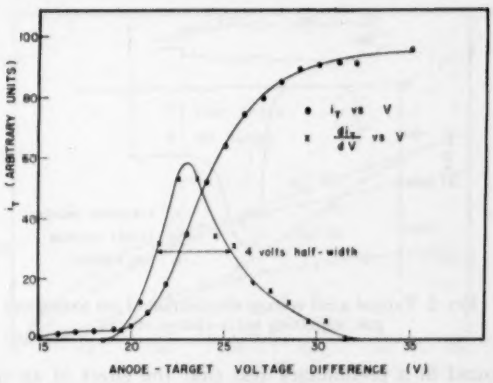

FIG. 4. Typical retarding potential measurement to determine energy spread of primary beam.

of beam intensity. The extraneous electron current could only be measured when the anode-target potential was less than the cutoff potential for the ion beam, but above cutoff its effect could be inferred by noting whether γ, the secondary electron coefficient of the target, showed a reasonable behavior on the basis of the independent researches of Hagstrum,[11] Parker,[12] and others.

The ion energy as well as the energy spread of the beam was determined by retarding potential measurements. Figure 4 is a typical curve. Although the apparent half-width of the beam was 4 volts, there are two reasons for believing that the actual half-width was less than this. In the first place it is seen that the geometry of the electrode system was unsuitable for accurate retarding potential measurements; an isolated potential hill produced by a target of this shape would deflect the ions to the side unless they were approaching the hill normally to the equipotentials. Thus, even a perfectly monoenergetic ion beam would show an apparent energy spread. The second reason for believing that the measured energy spread was exaggerated lies in the work of Parker,[12] who, using a similar source and gun, but having better geometry, found the half-width not to exceed two volts. On this basis, then, it was assumed that the actual half-width of the beam was two volts and that the peak of the distribution was one volt from the high-energy limit. Aside from this one-volt correction, the ion energy was assumed to be the difference in potential between the target potential and the cutoff potential (Fig. 5).

From the cutoff potential one could infer the energy of the electrons which produced the ions V_e. This is the difference between the cutoff potential (corrected for contact potential) and the cathode potential. In order that only singly charged ions be produced, this potential was adjusted for each gas to lie between the first and second ionization potentials of that gas. It was

[10] A. Theodore Finkelstein, Rev. Sci. Instr. 11, 94 (1940).

[11] Homer D. Hagstrum, Phys. Rev. 89, 244 (1953).

[12] J. H. Parker, Phys. Rev. 92, 536 (1953).

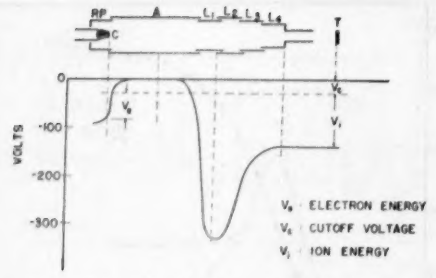

FIG. 5. Typical axial voltage distribution of ion source and gun neglecting space-change effects.

found in a preliminary test that the effect of an unknown admixture of doubly charged ions (which were created when the anode-cathode voltage was sufficiently high) was to cause a decrease in the apparent sputtering coefficient and an increase in the apparent secondary electron coefficient (Fig. 6). This is understandable when one considers the relative importance of the following factors in contributing to sputtering and secondary electron emission: (a) the doubly charged ions arrive with half the mass-to-charge ratio of the singly charged ions, and, therefore, for a given ion current to the target there are fewer incident ions; (b) they arrive with twice the kinetic energy and will hence produce more sputtering per ion but in general not twice as much; (c) they arrive with nearly three times the potential energy and will accordingly produce more secondary electrons. The apparent sputtering rate would be lower with the mixed beam because the effect of (a) overshadows the effect of (b), but the apparent secondary electron emission would be higher because the effect of (c) more than cancels out the effect of (a).

2. *The Target and Secondary Electron Collector*

The solidified alkali metal in the mouth of the intake tube served as a target. By magnetic control a substitute tantalum target could be swung into position between this tube and L_4 so that the ion beam could be measured in the absence of the alkali target.

L_4 and T were maintained at the same potential, and the secondary electron collector ring R was biased 40 volts positive with respect to T. The bias on the ring necessary to achieve a nearly saturated electron current was determined experimentally (Fig. 7). It was possible to read the target current (i_T), the ring current (i_R), or the combination of the two (i_{TR}). Ideally, i_{TR} is the ion current alone, i_R the secondary electron current alone, and i_T the sum of the two or $i_+(1+\gamma)$, where i_+ is the ion current and γ is the secondary electron coefficient. Admittedly the geometry was unsuitable either for 100 percent collection of the target secondaries or 100 percent removal of the extraneous secondaries produced in the gun so that i_R and hence i_{TR} were both subject to error. (Measurements of i_T below ion cutoff indicated that only a negligible number of extraneous electrons were reaching T so that i_T at least was accurately given by the above expression.) However, if a Faraday cage sort of arrangement had been used to remove this trouble, it would have been difficult to install the surface-ionization detector to measure sputtering. On the basis of the curves obtained for γ (actually the ratio i_R/i_{TR}), it was felt that above about 50 volts ion energy i_+ could be assumed to equal i_{TR} quite closely, and below 50 volts i_+ was obtained from the relation $i_T=i_+(1+\gamma)$, where γ was gotten by extrapolating the γ curves obtained above 50 volts back to zero. Justification for this extrapolation again lies in the work of Hagstrum[11] and Parker.[12]

3. *The Surface Ionization Detector*

It is known from both theory and experiment[13] that a neutral alkali atom striking a hot metal surface will lose its valence electron to the surface and will boil off as an ion provided only that the work function of the surface exceeds the ionization potential of the atom. For Na and K atoms incident on hot platinum there is effectively 100 percent ionization by the surface. The emerging positive ions can be collected by an electrode negatively biased with respect to the platinum surface.

Sputtering is a diffuse process (the angular distribution of sputtered atoms, according to Seeliger,[14] follows a cosine law) so that in applying this type of detector to a sputtering problem it is desirable that the filament subtend a fairly large solid angle with respect to the target to ensure adequate sensitivity. In this case it was achieved by using a conical-shaped annular ring (F of Fig. 3) of 0.6-mil platinum foil, 0.25 in. wide at a distance of 0.8 in. from the target. It was heated to an orange color by a conduction current of a few amperes carried by 0.060-in. tungsten leads that served also to

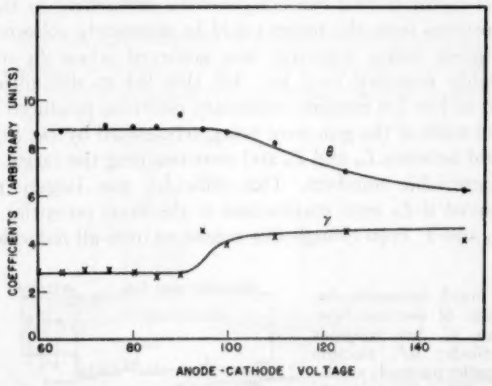

FIG. 6. The effect of the ion source voltage on the sputtering and secondary electron emission rates for He^+ on Na. The breaks in the curves correspond to the appearance potential for He^{++}, and the behavior at high source voltage is attributed to an admixture of He^{++} in the beam.

[13] K. H. Kingdon and I. Langmuir, Phys. Rev. **21**, 380 (1923).
[14] R. Seeliger and K. Sommermeyer, Z. Physik **93**, 692 (1935).

support the electrodes of the ion gun. The collector (*D* of Fig. 3) was a tantalum ring placed below the foil and shielded from the ion beam. The collector current was measured by a Kiethley electronic electrometer which read the voltage drop across a Victoreen high resistor.

There were several sources of background current to the collector, the principal one being due to vapor from deposits of sputtered alkali metal in the vicinity of the filament. For the purpose of bucking out the general dc background, an opposing voltage across a low resistance potentiometer was put in series with the Victoreen high resistance, the electrometer being shunted across the combination of the two. The limit to the sensitivity of the detector was set by the "noise" level, the amplitude of which was about 10^{-11} ampere for sodium and somewhat higher for potassium.

The contribution to the collector current due to sputtering (i_D) was measured by switching the ion beam on and off. In order that temperature-dependent background currents be unaffected in the process, the switching was done on an electrode voltage (anode-cathode voltage of the ion source) rather than on the source filament.

It is to be noted that the geometry of the detector was unsuitable for 100 percent collection of the ions from the filament, but if a Faraday cage arrangement had been used it would have been difficult to shield the collector from reflected ions of the primary beam, and moreover one might expect a higher vapor pressure of alkali metal and hence a higher background current in such an enclosure.

A bias of 45 volts gave a reasonably saturated collection current (Fig. 7) and was maintained at this value throughout the experiment. Since the objective of this study was to measure relative sputtering rates, lack of total collection would introduce no serious error; but it could cause an error in any estimates of absolute sputtering rates.

One further correction was still necessary. It was found that even when the platinum filament was cold, there was a small change in the ion current to the collector when the primary beam was switched on and off. The problem was to decide whether this change was due to charged sputtered particles or whether it was due to reflected ions from the primary beam. Using a high-energy primary beam, a retarding potential was put on the detector assembly to ascertain the energy of the ions which were reaching the detector. It was found that most of the ions were of high energy. Since it might be expected that an appreciable fraction of sputtered particles would be of low energy, it was assumed that this current was due solely to reflected beam ions, and it was therefore subtracted from the measured sputtering current. Mass spectrographic analysis would be desirable to prove the point conclusively. All sputtering coefficients at ion energies larger than 150 volts are affected by this correction. At 1000 volts the correction ranged from approximately 50 percent for He^+ to 5 percent for Xe^+.

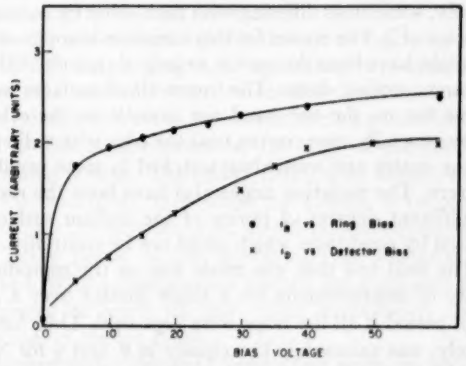

FIG. 7. Collector currents *versus* bias voltages.

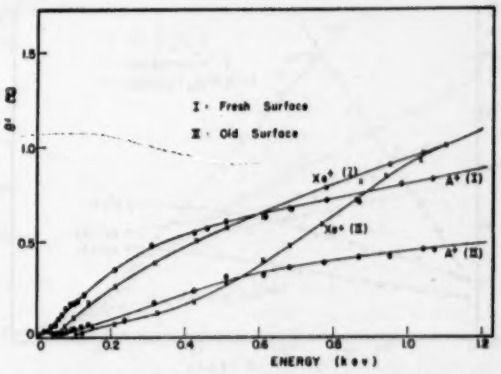

FIG. 8. The sputtering coefficients for A^+ and Xe^+ for a fresh sodium surface (I) and for a 5-day-old surface (II).

DISCUSSION OF RESULTS

A. Effect of an Aging Surface

When the first sodium surface was obtained, several runs were made over the available energy range for A^+ ions to determine the degree of reproducibility that might be expected. It was found that if all traps were maintained at liquid nitrogen temperatures, the morning and afternoon runs would agree within the limits of accuracy of the experiment, showing that the aging process was proceeding at a negligibly slow rate. Several hours of bombardment with the most energetic ions (1900 ev) produced no change, indicating that the rate of energy transfer to the surface was insufficient to effect any degree of "cleanup." On the other hand, if only the trap next to the mercury diffusion pump was kept cold overnight and the other traps were allowed to warm up, the result was that each day the sputtering rates were lower than the day before and the secondary electron emission rates were higher and more erratic. Thus, the effect of an aging sodium surface for A^+ ions was to decrease the measured sputtering coefficient θ'

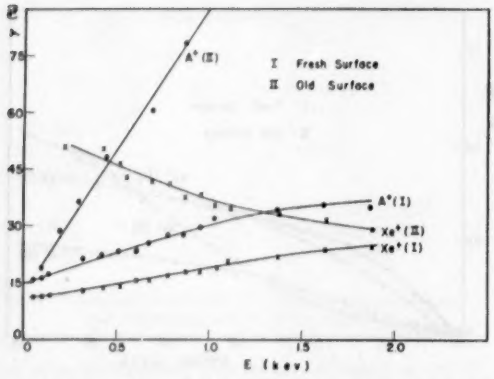

FIG. 9. The secondary electron coefficients for A^+ and Xe^+ for a fresh sodium surface (I) and for a 5-day-old surface.

and to increase the secondary electron coefficient γ. This is not surprising. It has long been known that a layer of oxide or other impurity on a surface inhibits sputtering. As for the secondary electron emission, since it is a process which depends on the nature of the metal, the surface layer, and the incident ions, various workers have observed different effects due to surface contamination. Oliphant[15] and Timoshenko[2] found lower γ's for clean surfaces, whereas Hagstrum[11] and Parker[12] found the reverse.

The effect on θ' and γ due to an aging sodium surface for He^+ and Ne^+ were similar in all respects to the effect for A^+, except that γ values were if anything even more erratic. The effect for Xe^+ seemed to be quite different. Whereas θ' for A^+ decreased over the entire energy spectrum available, θ' for Xe^+ showed a marked decrease only at the lower energies; at 1500 volts there was relatively little change, as is seen in Fig. 8. In like manner, γ was less affected at high energies than at low, as is shown in Fig. 9. A possible interpretation of this is that only the fast, heavy ions were able to blast their way through the surface layer and react with the underlying sodium metal. Of the other ions, a fraction would lose their energy in the surface layer, producing a more copious electron emission (causing a higher γ) and sputtering the surface impurity atoms or molecules which would not be detected by the detector (causing a lower θ').

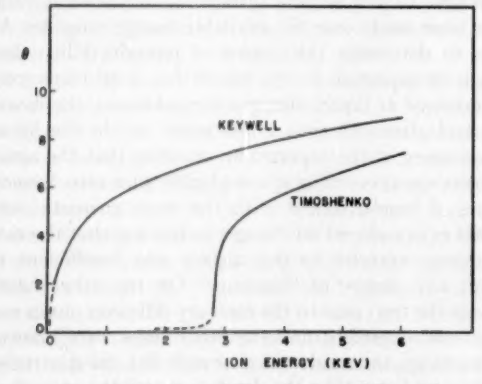

FIG. 10. The data of Timoshenko and Keywell for argon ions on silver.

[15] M. L. E. Oliphant, Proc. Roy. Soc. (London) **A127**, 373 (1930).

There is an interesting point concerning the θ' curves for Xe^+: The difference in curves I and II is reminiscent of the difference observed by Timoshenko and Keywell for argon ions on silver, as seen in Fig. 10, suggesting that perhaps their difference can be explained by a difference in cleanliness of their target specimens. Such a conclusion may not be justified in view of the qualitative nature of the present study.

The next test was made on the reproducibility of initial values for several fresh sodium surfaces. In each case the same procedure was followed, namely: (1) flashing all filaments until the background pressure under operating conditions was 5×10^{-8} mm or less, (2) filling all liquid nitrogen traps, (3) overflowing the old surface and allowing the fresh surface to freeze, and (4) making measurements immediately. Unfortunately it was found that such measurements would not repeat themselves closely, sometimes differing with each other by as much a factor of 2. The reason for this variation is not known. It might have been due partly to lack of reproducibility of target surface shape. The frozen alkali surfaces were never flat on the one hand nor smooth on the other. They generally were convex near the edge with a dimple in the center and were always etched in some peculiar pattern. The variation might also have been the result of different degrees of purity of the sodium surfaces, caused by conditions which could not be controlled.

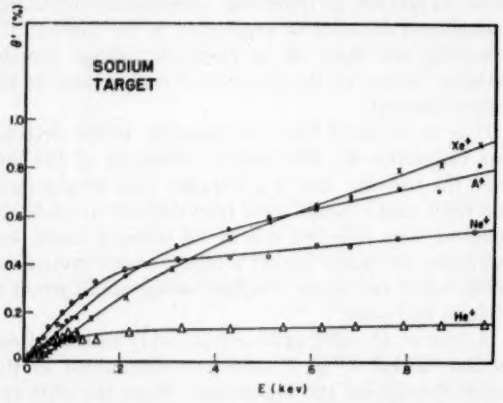

FIG. 11. Results of measurements of the sputtering coefficients for He^+, Ne^+, A^+, and Xe^+ on a fresh sodium surface.

The final test that was made was on the reproducibility of measurements for a single surface over a 24-hour period if all the traps were kept cold. This, fortunately, was successful. The change in θ' and γ for Ne^+ and He^+ was less than 5 percent in this period.

Having established, then, the conditions under which it was necessary to operate, four series of runs were made to determine the effect of ion mass and energy on relative sputtering rates. Before each series a fresh surface was obtained using the method described above. Then runs were made over the available energy range for He^+, Ne^+, A^+, and Xe^+. The time required to do this, allowing for evacuation to 5×10^{-5} mm between runs, was 18 hours. At the end of one of these runs, a check was made using the initial gas to see if the surface characteristics had changed, and again the change proved to be less than 5 percent (approximately the accuracy of the measurements). It was assumed, then, that all runs within each series were made on surfaces of constant characteristics.

As was expected, the absolute values did not check from series to series, nor were relative values always in the same ratio. However, each series showed similar characteristics which will be discussed in the next section.

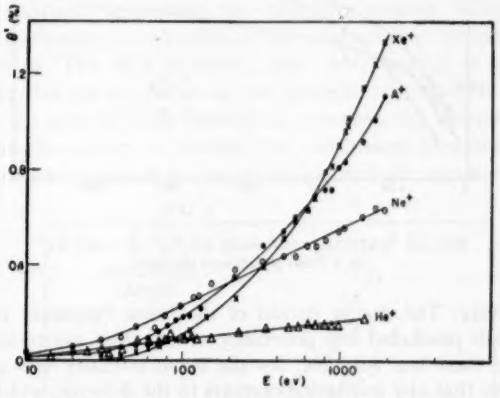

FIG. 12. The data of Fig. 11 plotted on a semilog scale.

B. Effect of Ion Mass and Energy for a Sodium Target

Figures 11, 12, 13, and 14 are plots of the sputtering data from one of the series of runs, using a sodium target. Figure 15 shows the corresponding curves for the secondary electron coefficient.

In the momentum-transfer theory, as first proposed by Kingdon and Langmuir,[6] sputtering is presumed to arise as a result of an ion rebounding from the bottom of a microscopic pit in the surface, striking from behind one of the lattice atoms on the edge of the pit and knocking it loose. The theory predicts an initial period of low sputtering rate while the surface is becoming pitted by the incoming ions. In the present experiment, no initial period of low sputtering rate was ever observed. With a fresh sodium surface the sputtering rate appeared to reach its final value immediately upon turning on the ion beam.

Lamar and Compton,[8] from their work on accommodation coefficients, suggested that the same sort of mechanism could occur for the case of an ion penetrating the surface since there would then be a chance of the ion striking a surface atom from behind after colliding with subsurface lattice atoms. They predicted that this mechanism would predominate for the small, light ions whereas for the heavy ions surface penetration would be less likely and another mechanism ("local heating"[7]) would predominate.

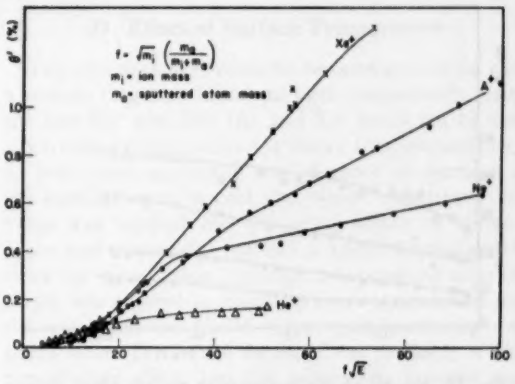

FIG. 13. The data of Fig. 11 plotted on a momentum scale.

Keywell[3] has recently proposed that the theory of neutron cooling by a moderator is applicable to the case of an ion penetrating a metal lattice. The ion loses its energy to the lattice atoms, some of which in turn are able to escape. The theory predicts a relationship of the form

$$\theta = A \ln E - B,$$

where A and B are constants characteristic of the ion-metal combination.

From the theories of Lamar and Compton and of Keywell one might expect Keywell's equation to hold for the light ions and von Hippel's "local heating" equation ($\theta = CE$, where C is a constant characteristic

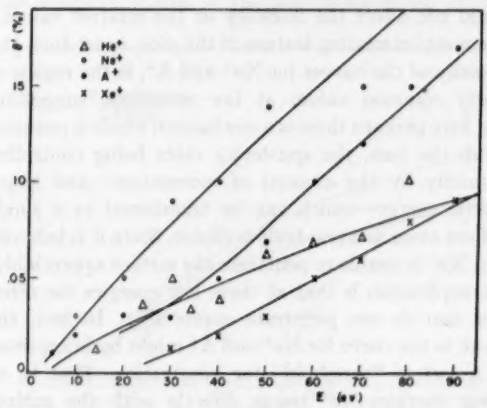

FIG. 14. The data of Fig. 11 plotted on an expanded energy scale.

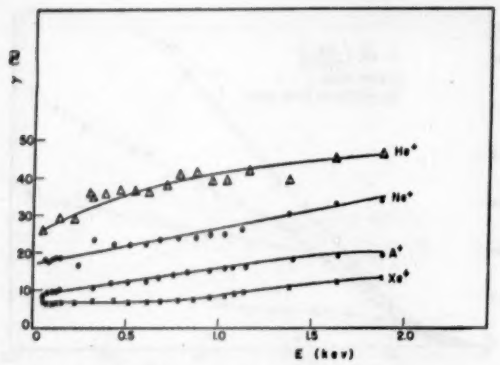

FIG. 15. Results of measurements of the secondary electron coefficients for He^+, Ne^+, A^+, and Xe^+ on a fresh sodium surface.

of the metal surface, its temperature, etc.) to hold for the heavy ions. It is seen from Fig. 12 that the sputtering rates for He^+ and Ne^+ can indeed be satisfactorily represented by straight lines on a semilog plot over most of the energy range in agreement with Keywell's equation, whereas the curves for A^+ and Xe^+ are seen to be of a different form. The form, however, for A^+ and Xe is not that predicted by von Hippel's theory, as can be seen from Fig. 11. In fact, the sputtering rates for these two ions, instead of being linear in E, appear to be much more nearly linear in the square root of E, as seen in Fig. 13. This suggests that the momentum of the ion is a more meaningful parameter than its energy, which theory is further borne out when one notes that at high energy and for a given energy the order of mass and, for a given energy, the order of sputtering for the four ions is the same as the order of mass and hence momentum. What actually is plotted in Fig. 13 is θ' *vs* the momentum relative to the center-of-mass system in a direct two-body collision involving a stationary sodium atom and an incident ion. (The square root of 2 factor has been omitted since it would merely change the abscissa scale by this factor but would not affect the linearity or the relative values.) The most interesting feature of the plot, apart from the linearity of the curves for Xe^+ and A^+, is the region of nearly common values at low momenta, suggesting that here perhaps there is a mechanism which is common to all the ions, the sputtering rates being controlled primarily by the amount of momentum—and hence kinetic energy—which can be transferred to a single sodium atom in a two-body collision. Since it is believed that Xe^+ is unable to penetrate the surface appreciably, the implication is that at these low energies the other ions also do not penetrate appreciably. In fact, the break in the curve for Ne^+ and A^+ might be interpreted as a sort of "threshold" for penetration. That is, at lower energies Ne^+ reacts directly with the surface atoms whereas at higher energies it buries itself in the lattice and by a "neutron cooling" process is able to transfer some of its energy back to the surface atoms.

The momentum-transfer theory also predicts a sputtering *threshold* when

$$\frac{4mm'}{(m+m')^2}E=q,$$

where m and m' are masses of the target atom and incident ion; E, the ion energy; and q, the atomic heat of sublimation. For sodium, $q=1.1$ electron volts so that the sputtering threshold for Ne^+, A^+, He^+, and Xe^+ should be 1.1, 1.2, 2.2, and 2.2 electron volts, respectively. The energy spread of the beam (apparent or real) precluded any possibility of detecting sputtering at these low voltages; for the beam intensity was so low that any sputtering currents to the detector, which would have been small even with a beam of normal intensity, were completely out of range below the noise level of the detector. Furthermore, this noise level made it impossible to make precise measurements of sputtering currents at a few volts above threshold, thus ruling out the possibility of being able to make accurate extrapolations. Sputtering could first be detected for Ne^+ at 5 volts, for He^+ and A^+ at 10 volts, and for Xe^+ at 30 volts. Up to about 200 volts, Ne^+ showed the highest sputtering rate, with A^+ next. This is consistent with the theory, since Ne^+, having most nearly the same mass as Na, is able to transfer the most kinetic energy in a collision with a sodium atom. Figure 14 represents the data for θ' at less than 100 volts. In consideration of the uncertainties in the measurements, it is felt that the extrapolations come reasonably close to the theoretical values for Ne^+ and He^+ but are doubtful for A^+ and completely unsatisfactory for Xe^+. Apparently below 30 volts it was impossible for Xe^+ to transfer its energy effectively to a sodium atom. Whether this is a significant feature in the sputtering mechanism or whether it was caused by the surface oxide layer is not

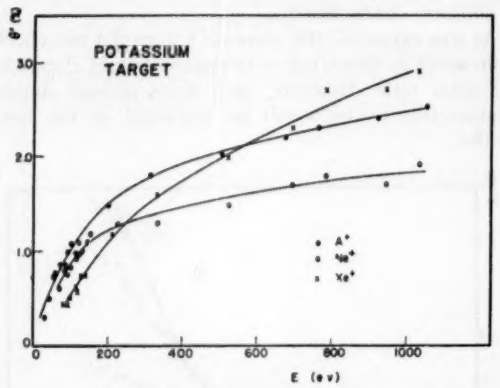

FIG. 16. Sputtering coefficients for Ne^+, A^+, and Xe^+ on a fresh potassium surface.

known. That it might have been the latter is suggested by Fig. 8.

C. Effect of Ion Mass and Energy for a Potassium Target

Figures 16, 17, and 18 represent the data for a potassium surface. Because of its high vapor pressure, potassium proved to be a more troublesome metal than sodium with the present experimental setup. In the first place, the general background noise level to the detector was an order of magnitude higher than for sodium so that even though the sputtering rates were somewhat higher, the over-all sensitivity was considerably lower. For this reason no measurements could be made at very low energies, and no reliable measurements could be made at all with helium. In addition, the overflow technique of obtaining successive fresh surfaces was not readily applicable, because reliquefying the metal resulted in a deposition of potassium on the insulators supporting the detector, making further measurements impossible without dismantling the apparatus. The data obtained, then, were neither as extensive nor as reliable as that obtained with sodium.

In spite of these drawbacks, however, the measurements appear to confirm the conclusions previously drawn for sodium in that (a) at low energies sputtering

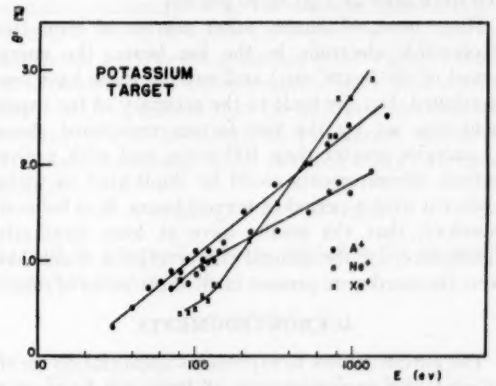

FIG. 17. The data of Fig. 16 plotted on a semilog scale.

is greatest for the ions with mass most nearly equal to the mass of the target atoms (A^+ ions in this case), and (b) at high energies the order of sputtering is the same as (but not proportional to) the mass, and, hence, the momentum of the ion. The plot of θ' *vs* $f\sqrt{E}$ also shows a region of relatively common values at low energy, again indicating that here the sputtering rate is controlled by the amount of energy which can be transferred to a target atom in a two-body collision.

As for the form of the sputtering curves, those for A^+ and Ne^+ seem to be reasonably linear on a semilog plot, whereas that for Xe^+ appears to be most nearly linear on a $\sqrt{E}$ plot.

D. Effect of Surface Temperature

Two attempts were made to measure sputtering with a sodium target at liquid nitrogen temperature, using the ions He^+ and Ne^+ (A^+ and Xe^+ could not be used since their boiling points are above this temperature). In both cases sputtering was observed to decrease as the surface began to cool, but before any steady low value was reached the sputtering began to increase again and eventually reached a value approximately twice the initial value. The high rate persisted after the target was allowed to return to room temperature and did not reach the initial value again until over two hours later. The initial decrease was probably a true temperature effect, but the subsequent increase may well have been due to sodium vapor coming from the region of the hot detector and condensing on the cold target as a "clean" sodium layer. It was thus not possible to get meaningful data on the temperature dependence of the sputtering rate.

E. Secondary Electron Emission

The theory of secondary electron emission has been rather completely worked out by Hagstrum[11] and others. Basically the mechanism is believed to consist of neutralization of an incoming positive ion by an electron from the metal, the energy of neutralization being carried off as kinetic energy by a second electron which may then escape. The curves of Fig. 15 seem to be consistent with this theory of potential energy ejection, in that (a) the relative values of the emission are in the same order as the relative values of the potential energy of the ions, and (b) there is apparently only a small dependence on the kinetic energy of the ions.

No attempt was made to measure the energy distribution of these electrons since the geometry was unsuitable for this.

F. Absolute Sputtering Rates

Only the roughest sort of estimate can be made for the absolute values of the sputtering rates. At least

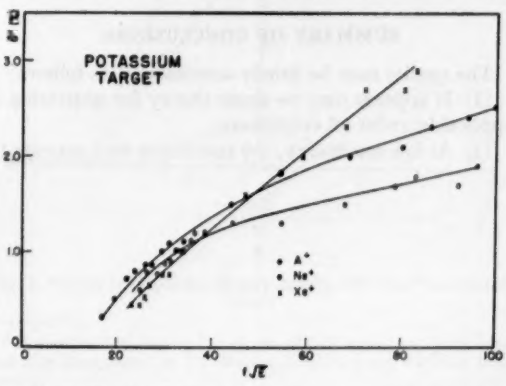

FIG. 18. The data of Fig. 16 plotted on a momentum scale.

four factors must be taken into account: the ratio of the solid angle subtended by the detector to the total solid angle available for sputtering, the angular distribution of the sputtered atoms, the ratio of the collector current to a saturated collector current (saturated with respect to both the bias and the temperature), and the degree to which sputtering has been reduced as a result of surface impurities. The effect of the last item is difficult to reckon since at no time was there ever a guarantee that the metal surface was clean. On the basis of the attempted temperature variation measurement previously discussed, it is felt that in general sputtering was diminished for He^+ and Ne^+ by at least a factor of 2 as a result of the oxide layer. There are no such data available for A^+ and Xe^+. Neglecting, then, this effect as incalculable, it is estimated from the geometry (using a cosine distribution law for the sputtered atoms) and also from the electrical characteristics of the assembly that about 3 percent of the total number of sputtered atoms were counted. Thus, absolute sputtering rates may be deduced approximately by multiplying the ordinate scales by 33.

It is seen that for 1000-ev ions, θ, the absolute sputtering coefficient, ranges from 1.0 for Xe^+ on K to 0.05 for He^+ on Na. In view of the studies of Timoshenko and Keywell, θ seems surprisingly low, especially since the alkalis, having low sublimation energies, might be expected to sputter quite easily. It is felt that the discrepancy cannot be entirely attributed to an error in the estimate of the absolute coefficient but that in fact the alkali surfaces used did indeed show a low sputtering rate. Certainly surface impurities—which were not "cleaned up" by ion bombardment in the present experiment—account for a part of it. Timoshenko and Keywell both used high energy and high intensity beams, and not only were their surfaces probably cleaner as a result of this, but also the sputtering mechanism itself might have been quite different. However, any conclusions which might be drawn would be little more than speculation until such time as the present study is repeated under conditions which have been modified to simulate those of the other authors.

SUMMARY OF CONCLUSIONS

The results may be briefly summarized as follows:

(1) It appears that no single theory for sputtering is applicable under all conditions.

(2) At low ion energy, the sputtering rate appears to depend only on the amount of energy which can on the average be transferred to a single surface atom in a two-body collision. What the sequence of events is between this collision and the emergence of a sputtered atom is a matter of conjecture.

(3) At high energy the sputtering rate is in the same order as (but not proportional to) the mass of the ions.

(4) No evidence was found in favor of the theory of local heating, at least insofar as a linear dependence of θ' on E is concerned. It appears instead that for the light ions θ' is linear in $\ln E$, and for the heavy ions in $\sqrt{E}$.

(5) Sputtering, being a surface phenomenon, is greatly effected by surface conditions, the effect of an oxide layer being to reduce the sputtering rate.

DISCUSSION OF ERRORS

The principal uncertainties in this experiment resulted from:

(1) Lack of control over the initial characteristics of a fresh surface, causing θ' to vary by as much as a factor of 2 for two different surfaces of the same metal but otherwise similar conditions.

(2) Fluctuating background currents to the detector, limiting its sensitivity, and thus making impossible accurate measurements at very low energy. The probable limit of error at ion energies less than 30 ev may well have been as high as 50 percent.

There were, of course, other sources of error (unaccountable electrons in the ion beam, the energy spread of the beam, etc.) and most of these have been mentioned, but the limit to the accuracy of the experiment was set by the two factors mentioned above. At energies greater than 100 volts, and with a given surface, measurements could be duplicated to within 5 percent over a period of several hours. It is believed, therefore, that the results have at least qualitative significance, for the general characteristics which have been discussed were present in all of the series of runs.

ACKNOWLEDGMENTS

The author wishes to express his appreciation for the support and encouragement of Professor Leonard B. Loeb, who proposed the problem and under whose direction it was carried out. He would also like to thank Dr. J. H. Parker for the loan of his induction heater and Mr. W. M. Brower and Mr. M. R. Corbett for their assistance in constructing the apparatus.

Microwave Spectrum of $N^{14}O^{16}$†

J. J. GALLAGHER, F. D. BEDARD, AND C. M. JOHNSON
Radiation Laboratory, The John Hopkins University, Baltimore, Maryland

(Received October 5, 1953)

The $J=1/2\rightarrow 3/2$ ($v=0$) rotational transition of the $^2\pi_{1/2}$ state of $N^{14}O^{16}$ has been measured. This transition occurs at 150 372.30 Mc/sec and is split into two groups of five lines due to Λ-type doubling and a large magnetic hyperfine interaction. The value of B_0 is found to be 1.69510 cm^{-1} and $r_0=1.1539$A. The Λ-doubling constant p is determined as 355.2 Mc/sec, and a spin of 1 is again confirmed for N^{14}. A preliminary analysis of the magnetic hyperfine structure is given, based on the interaction Hamiltonian $aI_{z'}L_{z'}+b\mathbf{I}\cdot\mathbf{S}+cI_{z'}S_{z'}$, where a, b, and c are constants.

INTRODUCTION

NITRIC oxide, quite unlike the usual molecule observed in the microwave region, has both electron spin and orbital angular momentum different from zero in its ground state. From optical spectra this ground state is known to be a $^2\Pi_{\frac{1}{2},\frac{1}{2}}$ with the $^2\Pi_{\frac{1}{2}}$ levels lying lower in energy. Also, since the doublet separation[1] is large (124.2 cm^{-1}) compared to the separations of the rotational energy levels (5 cm^{-1}), Hund's case (*a*) best describes the coupling of the various angular momentum vectors of the molecule. In the $^2\Pi_{\frac{1}{2}}$ state, which is the one of interest here, the spin and orbital angular momentum vectors are coupled to the internuclear axis with their components along this axis opposed. A net axial angular momentum $\mathbf{\Omega}$ of $\frac{1}{2}\hbar$ results which is combined vectorially with the angular momentum $\mathbf{N}$ due to rotation of the molecule to give the total angular momentum $\mathbf{J}$ (exclusive of nuclear spin). Figure 1 shows the arrangement of these vectors. Since Ω is a component of $\mathbf{J}$, it follows that for this case J cannot be less than $\frac{1}{2}$, and the rotational transitions, neglecting centrifugal stretching, occur between energy terms of the form:

$$F_v(J)=B_vJ(J+1)+(A-B)\Omega^2, \qquad (1)$$

where B_v is the usual constant related to the molecular moment of inertia, I_v, by

$$B_v=h/8\pi^2cI_v, \qquad (2)$$

and A is a constant (defined later) for a given electronic state. With the selection rule $\Delta J=0, \pm 1$ and $\Delta\Omega=0$ holding, it follows that a series of transitions similar to that for a diatomic molecule in a $^1\Sigma$ state is obtained. However, for the $^2\Pi_{\frac{1}{2}}$ case, the J values are half-integers and the lowest transition, which is the one observed in this experiment, is the $J=1/2\rightarrow 3/2$.

When $\Omega\neq 0$ each of the rotational energy levels given by Eq. (1) is doubly degenerate. However, due to the interaction of the electronic angular momentum with the rotational motion, this degeneracy is broken down, and each J level is split into two components of slightly different energy. This splitting known as Λ doubling (Ω doubling) increases with increasing J, thus causing two lines of slightly different frequency for each rotational transition.

The spectrum of $N^{14}O^{16}$ is further complicated by the nuclear spin of N^{14}. A nuclear magnetic moment is associated with this spin and serves to couple the nuclear spin $\mathbf{I}$ to the angular momentum vector $\mathbf{J}$ to give the resultant $\mathbf{F}$. The vector $\mathbf{F}$ can take values $(J+I)$, $(J+I-1)$, $\cdots|J-I|$, and, since each combination is of slightly different energy, the Λ-doublet components are split into a hyperfine pattern.

Nitric oxide is one of the very few molecules in which Λ doubling and magnetic hyperfine structure can be studied under the high resolution of microwave spectroscopy. It is the purpose of this paper to describe the observed spectrum[2] of the $J=1/2\rightarrow 3/2(v=0)$ transition of the $^2\Pi_{\frac{1}{2}}$ state of $N^{14}O^{16}$ and to give a preliminary correlation of the data with existing theory.

MEASUREMENTS AND APPARATUS

The $J=1/2\rightarrow 3/2$ transition occurs at approximately 2-mm wavelength, and the spectrum consists of ten lines split into two groups of five each. In the group occurring

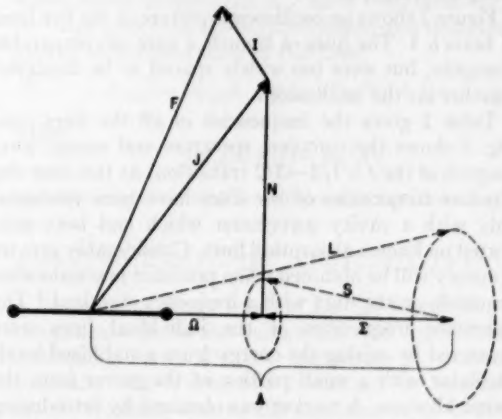

FIG. 1. Vector diagram for Hund's case (*a*) for the $^2\Pi_{1/2}$ state of $N^{14}O^{16}$.

† This research was supported by the U. S. Navy, Bureau of Ordnance.

[1] R. H. Gillette and E. H. Eyster, Phys. Rev. **56**, 1113 (1939).

[2] It was learned during the course of this work that these lines had also been found by Dr. Walter Gordy's group at Duke University.

FIG. 2. Oscilloscope picture of the branch 1 lines of the $J=1/2\rightarrow3/2$ rotational transition of $N^{14}O^{16}$.

at the lower frequency, the $F=3/2\rightarrow1/2$ line is at the high-frequency end, and the $F=3/2\rightarrow5/2$ line is at the low-frequency end with a total separation of 69.1 Mc/sec. Somewhat surprisingly, this group bears little similarity to the other group at a slightly higher frequency. The separations between the components of this higher-frequency group are much larger with a total spread between end lines of 269.1 Mc/sec. Also, in contrast to the other case, the $F=3/2\rightarrow1/2$ line lies at the low-frequency end, and the $F=3/2\rightarrow5/2$ line occurs at the center of the group. Thus, the $F=3/2\rightarrow1/2$ transitions of the two groups lie closest together and are separated by 129.6 Mc/sec. These assignments were made on the basis of observed intensities. Although accurate intensity measurements even on a relative basis are difficult to make in microwave spectroscopy, there was no difficulty in the case of the $F=3/2\rightarrow1/2$ and $F=3/2\rightarrow5/2$ lines, since these two are the weakest and strongest, respectively, and differ by a factor of 25. All the other lines are about 30 to 40 percent as strong as the $F=3/2\rightarrow5/2$ line. Hereafter, the lines of the low-frequency group will be referred to as branch 1 and those of the high-frequency group as branch 2.

Figure 2 shows an oscilloscope picture of the five lines of branch 1. The lines of branch 2 were of comparable strengths, but were too widely spaced to be displayed together on the oscilloscope.

Table I gives the frequencies of all the lines, and Fig. 3 shows the complete spectrum and energy level diagram of the $J=1/2\rightarrow3/2$ transition. At this time the absolute frequencies of the lines have been measured only with a cavity wavemeter which had been calibrated on known absorption lines. Considerably greater accuracy will be obtained when precision measurements are made on the lines with a frequency standard.* The difference frequencies of the individual lines were measured by mixing the energy from a stabilized local-oscillator with a small portion of the power from the swept klystron. A marker was obtained by introducing the mixed output of the two oscillators into a communication receiver tuned to a frequency coinciding with the difference frequency of the klystrons at some point within the sweep range. When the output of the receiver was applied to the oscilloscope, a pip was produced each time the difference frequency coincided with the receiver frequency. This marker pip could be moved from one absorption peak to another by tuning the receiver, and the frequency separation of two lines was given directly by the difference in the receiver dial readings. All frequency separations, except the interval between the two groups, were also checked by producing sidebands on the klystron local oscillator with a variable-frequency (1 to 20 Mc/sec) oscillator. These sidebands were adjusted to coincide with a pair of lines, and the line separation was then given directly by the reading of the variable frequency oscillator.

Both the receiver and variable-frequency oscillator were calibrated with a crystal-controlled oscillator at the time of the measurements.

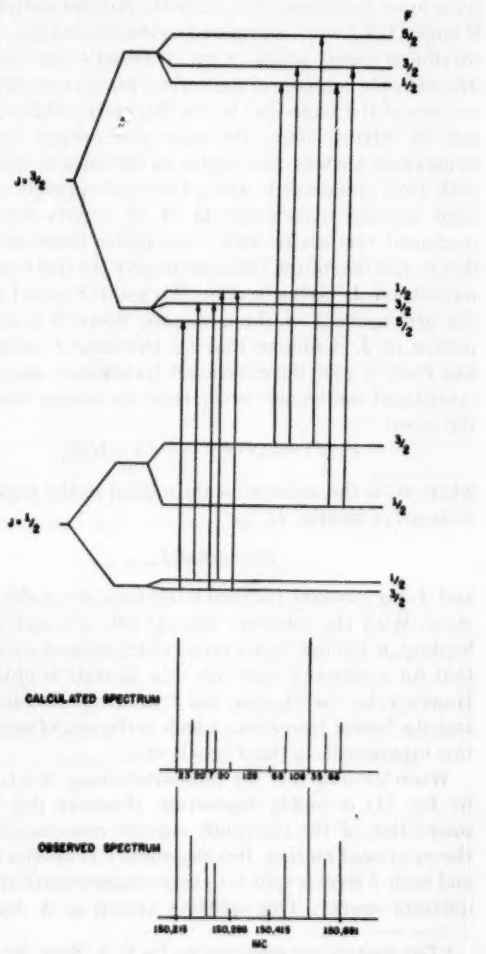

FIG. 3. Energy level diagram and complete spectrum of the $J=1/2\rightarrow3/2$ rotational transition of the $^3\Pi_{1/2}$ state of $N^{14}O^{16}$.

* Our frequency standard has been completed since this paper was submitted, and the measurements given here have been made using this standard rather than the less accurate method mentioned above.

TABLE I. Observed and calculated lines for the $J=1/2\rightarrow3/2$ transition of the $^2\Pi_{1/2}$ state of $N^{14}O^{16}$.

Transition	Measured frequency Absolute Mc/sec	Line separations Mc/sec	Calculated line separations Mc/sec	Relative intensities Measured	Calculated
Branch 1					
$F=3/2\rightarrow5/2$	150 176.30±0.25			100	100
		22.22	24.21		
$F=1/2\rightarrow3/2$	150 198.52			65	37.1
		20.05	19.98		
$F=3/2\rightarrow3/2$	150 218.57			43	29.6
		6.90	6.53		
$F=1/2\rightarrow1/2$	150 225.47			43	29.6
		19.91	19.98		
$F=3/2\rightarrow1/2$	150 245.38			5	3.7
		129.64			
Branch 2					
$F=3/2\rightarrow1/2$	150 375.02			5	3.7
		63.90	63.55		
$F=3/2\rightarrow3/2$	150 438.92			50	29.6
		107.33	105.91		
$F=3/2\rightarrow5/2$	150 546.25			100	100
		34.13	35.71		
$F=1/2\rightarrow1/2$	150 580.38			40	29.6
		63.73	63.55		
$F=1/2\rightarrow3/2$	150 644.11			60	37.1

The microwave energy at 150 kMc/sec (2-mm wavelength) was obtained by employing a silicon crystal multiplier to generate the fifth harmonic of the output of a 30-kMc/sec reflex klystron. For detection, a silicon crystal rectifier was also used. In both the multiplier and the detector, the cat whisker and crystal were mounted inside the wave guide as an integral part of the unit.

The absorption cell containing the NO gas was a seven-foot length of silver wave guide 0.280 in.×0.140 in. in cross section. Since we wished to observe the lowest rotational transition in the $^2\Pi_{\frac{1}{2}}$ state, a considerable increase in absorption intensity could be obtained by cooling the gas. The freezing point of NO is −163.6°C, and it still has a considerable vapor pressure at liquid nitrogen temperature. Therefore, the cell was enclosed in a one-inch diameter brass tube insulated with two inches of Styrofoam and kept immersed in liquid nitrogen during these measurements.

At this low temperature the lines were strong enough to be observed under high resolution with a simple video receiver. The $F=3/2\rightarrow1/2$ line, which is only about four percent as strong as the $F=3/2\rightarrow5/2$ line, appeared as a pip about three times noise when the tuning was optimized on its frequency.

INTERPRETATION OF DATA

Equation (1) is not a sufficiently accurate expression for the rotational energy levels when the measurements are made in the microwave region. The effect of rotational distortion on the spin multiplet must be included. Because of this interaction, the off-diagonal matrix elements belonging to pairs of rotational levels in different multiplet components are significant, and the expression for the rotational energy levels of the doublet becomes[3]

$$F_v(J)=B_v[(J+\tfrac{1}{2})^2-\Lambda^2]\pm\tfrac{1}{2}[4B_v^2(J+\tfrac{1}{2})^2+A\Lambda^2(A-4B_v)]^{\frac{1}{2}}+D_vJ^2(J+1)^2. \quad (3)$$

Here A and B_v are the same constants as in Eq. (1), and D_v is the centrifugal stretching constant. The constant A is a measure of the coupling between the electron spin S and the orbital angular momentum Λ. For large A/B_v, which holds for our case ($A/B_v\approx75$), Eq. (3) reduces to

$$F_v(J)=B_v\left(1\pm\frac{B_v}{\Lambda^2A}+\cdots\right)J(J+1)-D_vJ^2(J+1)^2, \quad (4)$$

where terms independent of J have been omitted. The (−) sign goes with the $^2\Pi_{\frac{1}{2}}$ component and thus, for the ground vibrational state of this case,

$$F_0(J)=B_{0\,\mathrm{eff}}J(J+1)-D_0J^2(J+1)^2, \quad (5)$$

where

$$B_{0\,\mathrm{eff}}=B_0(1-B_0/A), \quad (6)$$

and the frequency of the rotational transitions is given by

$$\nu_0=F_0(J+1)-F_0(J)=2B_{0\,\mathrm{eff}}(J+1)-4D_0(J+1)^3. \quad (7)$$

Each of the energy levels of Eq. (5) is split into two components since the symmetric and antisymmetric Λ-doubling states are not degenerate in a rotating molecule. Van Vleck[4] has calculated the perturbing matrix elements due to the components of electronic angular momentum perpendicular to the internuclear axis and has shown that the splitting of an energy level

[3] E. Hill and J. H. Van Vleck, Phys. Rev. 32, 250 (1928).
[4] J. H. Van Vleck, Phys. Rev. 33, 467 (1929).

in a $^2\Pi_{\frac{1}{2}}$ state due to Λ-type doubling is given by

$$F_c(J)-F_d(J)=p(J+\tfrac{1}{2}), \tag{8}$$

where

$$p\approx 4AB/\nu(\Pi\rightarrow\Sigma). \tag{9}$$

The subscript 0 has been dropped from the $F(J)$, and the new subscripts c and d are the usual spectroscopic notation for the levels of the Λ doublet. The frequency separation of the Λ-doublet lines is given by

$$\Delta\nu_\Lambda=[F_c(J+1)-F_c(J)]-[F_d(J+1)-(J)], \tag{10}$$

and, if Eq. 8 is substituted into this expression, then for any transition

$$\Delta\nu_\Lambda=p. \tag{11}$$

Van Vleck[4] has also shown theoretically that for small J values the Λ doubling in the $^2\Pi_{\frac{1}{2}}$ state is much greater than in the $^2\Pi_{\frac{3}{2}}$ state. Mulliken and Christy[5] have verified this difference experimentally, giving a value of 0.01 cm^{-1} (300 Mc/sec) for p or $\Delta\nu_\Lambda$ in the $^2\Pi_{\frac{1}{2}}$ state and a negligible splitting for the $^2\Pi_{\frac{3}{2}}$ state. Beringer and Rawson[6] in their work on the Zeeman transitions of NO have recently resolved Λ doubling in the $^2\Pi_{\frac{1}{2}}$ state and give a value of about 1.7 Mc/sec for the splitting.

The value of the splitting $\Delta\nu_\Lambda$, as well as the absolute frequencies of the Λ-doublet transitions ν_1 and ν_2, can be determined from Eqs. (24) and (25) that follow. Thus, from our data,

$$\Delta\nu_\Lambda=p=355.2 \text{ Mc/sec},$$
$$\nu_1=150\,194.70 \text{ Mc/sec},$$

and

$$\nu_2=150\,549.90 \text{ Mc/sec}$$

before hyperfine splitting.

If values of $D_0=0.53\times10^{-6}$ cm^{-1}, $A=124.2$ cm^{-1}, and $\alpha_e=0.0178$ cm^{-1} are taken from Gillette and Eyster,[1] then $B_{0\,eff}$ and B_0 can be determined from Eqs. (6) and (7) and B_e from the relation:

$$B_e=B_0+\tfrac{1}{2}\alpha_e. \tag{12}$$

Table II contains all the molecular parameters determined wholly or partially from this experiment. Our value of $B_0=1.69510$ cm^{-1} agrees quite well with the value 1.6957 cm^{-1} determined by Gillette and Eyster.[1]

It is well established that the nuclear spin of N^{14} is 1, and this experiment offers an additional verification of this value. Each of the Λ-doublet components was observed to be split into five lines. Any value of spin greater than one coupled to the angular momentum vector **J** would have produced six lines for the $J=1/2\rightarrow3/2$ transition. Nuclei with spins 1/2 or 0 would have given rise to three lines, and one line, respectively.

TABLE II. Molecular constants $N^{14}O^{16}$.

ν_0	150 372.30 Mc/sec
p	355.2 Mc/sec
$B_{0\,eff}$	50 124.17 Mc/sec = 1.67196 cm^{-1}
B_0	50 817.73 Mc/sec = 1.69510 cm^{-1}
I_0	16.5089×10^{-40} gm-cm^2
r_0	1.1539A
B_e	1.70400 cm^{-1} = 51 084.5 Mc/sec
I_e	16.4226×10^{-40} gm-cm^2
r_e	1.1509A

The quadrupole coupling constant of N^{14} in NO has been determined previously by Beringer and Castle[7] as approximately −1.7 Mc/sec. When the hyperfine splitting for the $J=1/2\rightarrow3/2$ transition of NO is calculated from such a coupling value, it comes out orders of magnitude smaller than the separations observed here.

The only other known mechanism available for coupling the nuclear spin to the angular momentum **J** is the interaction of the nuclear magnetic moment with the electronic orbital and spin magnetic moments. (The splitting due to interaction of the nuclear magnetic moment with the magnetic moment associated with the rotating nuclei is, in all cases previously examined by microwaves, much smaller than that due to quadrupole coupling.)

In the analysis presented here, the work of Frosch and Foley[8] on magnetic hyperfine structure will be employed. These authors derive the magnetic hyperfine interaction for a diatomic molecule from the Dirac equation of an electron in the field of the nucleus. After performing a series of unitary transformations on the Dirac equation and retaining only matrix elements diagonal in Λ, they arrive at the expression,

$$H=aI_{z'}L_{z'}+b\mathbf{I}\cdot\mathbf{S}+cI_{z'}S_{z'}, \tag{13}$$

for the magnetic hyperfine interaction Hamiltonian. The z' direction is along the internuclear axis, and

$$a=2g_I\mu_0\mu_N(1/r_1^3)_{Av},$$
$$b=2g_I\mu_0\mu_N\left[\frac{2}{3}\frac{\delta(r_1)}{r_1^2}-\frac{3\cos^2\chi-1}{2r_1^3}\right]_{Av}, \tag{14}$$
$$c=2g_I\mu_0\mu_N\left[\frac{3\cos^2\chi-1}{r_1^3}\right]_{Av}.$$

Here, r_1 is the distance from the nucleus with the spin to the electron, χ is the angle between r_1 and the internuclear axis, g_I the nuclear g factor, μ_N the nuclear magneton, μ_0 the Bohr magneton and $\delta(r_1)$ a coefficient that arises because of the quasi-relativistic treatment.

The quantities in brackets $[\ ]_{Av}$ are to be averaged over the electronic space coordinates for the particular state.

Equation (13) holds for both Hund's case (a) and case (b) and may be written

$$H=aI_{z'}L_{z'}+b(I_{x'}S_{x'}+I_{y'}S_{y'})+(b+c)I_{z'}S_{z'}. \tag{15}$$

[4] R. S. Mulliken and A. Christy, Phys. Rev. **38**, 87 (1931).
[5] R. A. Beringer and E. B. Rawson, Phys. Rev. **86**, 607 (1952).
[7] R. A. Beringer and J. G. Castle, Jr., Phys. Rev. **78**, 581 (1950).
[8] R. A. Frosch and H. M. Foley, Phys. Rev. **88**, 1337 (1952).

For a good case (a) molecule, the second term has only nonzero matrix elements which are off-diagonal in Λ and can be neglected. Hence,

$$H=[a\Lambda+(b+c)\Sigma]I_{s'}.$$

When Λ doubling is taken into account by considering the effect of matrix elements nondiagonal in Λ, Frosch and Foley obtain

$$W_{S/A}=(+|H|+)\pm(+|H|-) \tag{16}$$

for the hyperfine energy perturbations of the symmetric and antisymmetric Λ-doublet components of a case (a) $^2\Pi_{\frac{1}{2}}$ state.

Here,

$$(+|H|+)=D\frac{\mathbf{I}\cdot\mathbf{J}}{2J(J+1)}$$

$$=D\frac{F(F+1)-J(J+1)-I(I+1)}{4J(J+1)}, \tag{17}$$

where

$$D=[a\Lambda+(b+c)\Sigma]=a-(b+c)/2, \tag{18}$$

and

$$(+|H|-)=d(J+\tfrac{1}{2})\frac{F(F+1)-J(J+1)-I(I+1)}{4J(J+1)} \tag{19}$$

where

$$d=\frac{g_I\mu_0\mu_N}{2}\left[\frac{3}{r_1^3}\sin^2\chi\right]_{Av}. \tag{20}$$

The symmetric and antisymmetric Λ-doubling states are linear combinations of the degenerate electronic wave functions; i.e.,

$$(\psi_e)_S=[f(\Lambda,\Sigma)+f(-\Lambda,-\Sigma)](\tfrac{1}{2})^{\frac{1}{2}}, \tag{21}$$

$$(\psi_e)_A=[f(\Lambda,\Sigma)-f(-\Lambda,-\Sigma)](\tfrac{1}{2})^{\frac{1}{2}}. \tag{22}$$

As mentioned in the discussion of Λ doubling, these states have different interaction energies with the rotational motion thus causing each rotational level to be split into two components. Since for symmetry considerations the total wave function of a state can be written as a product,

$$\psi_{\text{total}}=\psi_e\psi_V\psi_R; \tag{23}$$

one of these component levels is positive (ψ_{total} symmetric) and one negative (ψ_{total} antisymmetric). The vibrational wave function, ψ_V, is always symmetric, and ψ_R is alternately symmetric and antisymmetric; therefore, $(\psi_e)_S$ will be the + component of one rotational level and − component of the next and likewise for $(\psi_e)_A$. Transitions occur only between + and − levels. Thus, the levels with ψ_e symmetric form one series and those with ψ_e antisymmetric form another series.

Since the constant d of Eq. (20) is positive ($g_I=+0.4$), the $(\psi_e)_A$ state must be the lower of the two components for each rotational state in order to fit the observed spectrum. Therefore, when the hyperfine perturbations of Eq. (16) are taken into account the line frequencies are given by

$$\nu=\nu_1+W_A(J=\tfrac{3}{2})-W_A(J=\tfrac{1}{2}) \tag{24}$$

for branch 1, and

$$\nu=\nu_2+W_S(J=\tfrac{3}{2})-W_S(J=\tfrac{1}{2}) \tag{25}$$

for branch 2. Here, ν_1 and ν_2 are the frequencies of the Λ-doublet lines without hyperfine splitting. Since the line separations were measured more accurately than the absolute frequencies, pairs of equations of the form (24) and/or (25) were solved in terms of the measured difference frequencies for the constants D and d as well as the Λ-doublet constant p. These constants are, of course, overdetermined by this group of equations, and hence have to be adjusted for best fit. Values of $D=92.6$ Mc/sec and $d=112.6$ Mc/sec give the calculated difference frequencies listed in Table I. The agreement between the observed and calculated spectra is very good but not quite within the experimental error. This difference is thought to be due to the effect of nuclear quadrupole coupling. Upon completion of our frequency standard more accurate measurements will be made on these lines, from which it may be possible to determine the quadrupole coupling of N^{14} in this molecule.

The magnetic hyperfine parameters evaluated here will be used in a later paper to obtain information on the electronic structure of NO.

It is hoped that enough sensitivity at 250 kMc/sec can be attained to observe the $J=3/2\rightarrow5/2$ transition in both the $^2\Pi_{\frac{1}{2}}$ and $^2\Pi_{\frac{3}{2}}$ states. Also, a spectroscope to measure the Zeeman splitting is being planned.

We are indebted to Dr. C. H. Townes for pointing out an error in our interpretation of a symmetry condition in the work by Frosch and Foley.

Nuclear Quadrupole Coupling in Polar Molecules*

H. M. FOLEY,† *Columbia University, New York, New York*
R. M. STERNHEIMER, *Brookhaven National Laboratory, Upton, New York*
AND
D. TYCKO,† *Columbia University, New York, New York*
(Received November 2, 1953)

The effect of an external charge on the nuclear electric quadrupole coupling has been investigated for various ions. These results presumably apply to the case of polar molecules. The quadrupole moment induced by the nuclear quadrupole moment Q is $46.5Q$, $8.7Q$, $50.2Q$, and $86.8Q$ for the Cl^-, Cu^+, Rb^+, and Cs^+ ions, respectively. When an external charge interacts with the ion as in a polar molecule, the induced moment is added to Q, so that the quadrupole coupling is multiplied by a factor of order 10–100. This model of a polar molecule disregards the exchange repulsion between the ions. Evidence is presented from several molecules which seems to confirm the existence of the induced quadrupole moment, although there is only partial agreement with the experimental values. It is shown that the contribution to the quadrupole coupling due to the induced dipole moment in second order is small compared to the induced quadrupole effect.

I. INTRODUCTION

IT has been previously shown[1,2] that the nuclear quadrupole moment induces a quadrupole moment in the electron distribution of the atom. This induced moment interacts with the valence electron and contributes to the hyperfine splitting. The same effect is expected to take place for molecules where the atom core around the nucleus whose quadrupole coupling is considered interacts both with the valence electrons and the other atom cores and nuclei in the molecule. Consider, for simplicity, the case of a polar diatomic molecule, e.g., NaCl. The quadrupole coupling at the Cl nucleus includes the interaction of the moment induced in the Cl^- ion with the Na^+ ion. Since the Na^+ ion is almost wholly external to the Cl^- electron distribution, the effect of penetration is small and the interaction energy due to the Cl^- core is of the order of the interaction of the total Cl^- induced moment with a unit charge placed at the position of the Na nucleus. The total induced moment $|Q_{iT}|$ has been calculated for the Cl^-, Cu^+, Rb^+, and Cs^+ ions, as representative examples, and was found to be very large, having values $46.5Q$, $8.7Q$, $50.2Q$, and $86.8Q$, respectively. Here Q is the nuclear quadrupole moment, and the sign of Q_{iT} is such as to reinforce the effect of the nuclear Q. The largest contribution to Q_{iT} is due to the radial excitations of the p and d shells, i.e., to the excitation of p electrons into higher p states and similarly to $nd \rightarrow d$ terms. These modes of excitation have been described previously[1] as antishielding effects, and are distinguished from the angular excitations such as $ns \rightarrow d$ and $np \rightarrow f$ which tend to shield the nuclear Q.

The purpose of this paper is to point out the existence of the antishielding effect for molecules and to describe the calculations which give the order of magnitude of this effect. In general, if the magnitude of the induced moment is $|\gamma_\infty|Q$, the quadrupole coupling q will be of order $2e(1+|\gamma_\infty|)/R^3$ rather than $2e/R^3$, which would be its value without the induced moment; here R is the internuclear distance. Since $|\gamma_\infty|$ is of order 10–100 for medium and heavy ions, the order of magnitude of the experimental values of q can be compared with the present calculations. At present q can be deduced for only very few cases. It will be shown that for some of these q is much larger than $2e/R^3$. This fact may be taken as an indication of the presence of antishielding, although other effects may also play a role in determining q. We also discuss the contributions from the dipole perturbation of the wave functions to the nuclear quadrupole coupling and show that these terms are generally small.

II. CALCULATION OF THE INDUCED QUADRUPOLE MOMENT

The calculation of the radial modes of excitation by the nuclear Q has been described previously in I. Here we will merely summarize the procedure of the calculation by taking the $3p$ shell of Cl^- as an example. For the $m=0$ states (m = magnetic quantum number) it was shown that the nuclear Q gives rise to the following $3p \rightarrow p$ perturbation:

$$u_{1,p} = (2/5)(3/2)^{\frac{1}{2}} Q u'_{1,p} \cos\theta, \tag{1}$$

where $u_{1,p}$ is r times the perturbation of the wave function, θ is the angle which the radius vector (of length r) makes with the axis of Q, and $u'_{1,p}$ is the solution of

$$-\frac{d^2u'_{1,p}}{dr^2} + \left[\frac{2}{r^2} + V_0 - E_0\right] u'_{1,p} = u'_0 \left(\frac{1}{r^3} - \left\langle \frac{1}{r^3} \right\rangle_{3p}\right). \tag{2}$$

Here V_0 is the effective potential for the $3p$ electrons, E_0 is the unperturbed energy, $\langle 1/r^3 \rangle_{3p}$ is the average

* The work carried out at Brookhaven National Laboratory was done under the auspices of the U. S. Atomic Energy Commission.
† Supported by a grant from the National Science Foundation.
[1] R. M. Sternheimer, Phys. Rev. **80**, 102 (1950); **84**, 244 (1951). The second paper will be referred to as I.
[2] R. M. Sternheimer and H. M. Foley, Phys. Rev. **92**, 1460 (1953).

value of $1/r^3$ for the $3p$ state, and u_0' is r times the radial part of the unperturbed wave function, normalized according to $\int_0^\infty u_0'^2 dr = 1$. For u_0' we took the Hartree-Fock function[3] for Cl^- which gives $\langle 1/r^3\rangle_{3p} = 5.7 a_H^{-3}$. Equation (2) was integrated numerically starting from $r=0$ by means of the power series,

$$u_{1,p}' = a_1 r + a_2 r^2 + a_3 r^3 + \cdots + b_2 r^2 \log r + b_3 r^3 \log r + \cdots, \quad (3)$$

where the a_i and b_i are constant coefficients which are determined by inserting Eq. (3) into (2) and equating powers of r. a_2 is arbitrary and was taken as 0. This coefficient corresponds to the part of $u_{1,p}'$ proportional to u_0' (solution of the homogeneous equation) which is determined below. The resulting values of $u_{1,p}'$ for two radii near $r = 0.02 a_H$ are used to start the numerical integration. In order to be consistent with u_0', the square bracket on the left-hand side of (2), which will be denoted by P, was obtained from u_0' as follows:

$$P(r_n) = [u_0'(r_n+\delta) - 2u_0'(r_n) + u_0'(r_n-\delta)]/\delta^2 u_0'(r_n), \quad (4)$$

where r_n is a selected radius and δ is the interval of integration. The values of $u_{1,p}'$ are obtained from

$$u_{1,p}'(r_n+\delta) = \{2 + \delta^2[P(r_n) - I(r_n)/u_{1,p}'(r_n)]\} \times u_{1,p}'(r_n) - u_{1,p}'(r_{n-1}), \quad (5)$$

where $I(r) = u_0'(r^{-3} - \langle r^{-3}\rangle_{3p})$ is the expression on the right-hand side of (2). It can be shown that the resulting $u_{1,p}'$ should be well-behaved for large r, because of the property $\int_0^\infty I u_0' dr = 0$. In actual cases, this is not true because of the finite δ used in the integration, and it is necessary to use a suitable cut-off procedure. No serious error is introduced by this treatment. The perturbation must be made orthogonal to u_0'. As shown in I, this is achieved by subtracting a suitable multiple of u_0'. One obtains

$$\bar{u}_{1,p}' = u_{1,p}' - \alpha u_0', \quad (6)$$

where

$$\alpha = \int_0^\infty u_{1,p}' u_0' dr. \quad (6a)$$

$\bar{u}_{1,p}'$ together with u_0' is shown in Fig. 4 of I. The total induced moment $Q_{iT}(3p\to p)$ due to $3p\to p$ is given by[1]

$$Q_{iT}(3p\to p) = (48/25) Q \int_0^\infty u_0' \bar{u}_{1,p}' r^2 dr = -46.4Q, \quad (7)$$

where the $-$ sign indicates that, in view of $Q(Cl^{35,37}) < 0$, there is an excess of electrons near $\theta = 0°$ and 180° at large r. Thus the effect of $Q_{iT}(3p\to p)$ at large r is to reinforce the nuclear Q. The sign of $Q_{iT}(3p\to p)$ can be explained in terms of the orthogonality of $\bar{u}_{1,p}'$ and u_0'. Near $r=0$, there is a lack of electrons for $\theta \cong 0°$ and 180° in view of the positive potential energy $-e^2 Q(3\cos^2\theta - 1)/4r^3$ in the field of Q. Hence $Q u_0' \bar{u}_{1,p}'$ is negative near $r=0$, and because of the orthogonality, $Q u_0' \bar{u}_{1,p}' > 0$ for large r. Thus $Q_{iT}(3p\to p)$ is positive.

[3] D. R. Hartree, Proc. Roy. Soc. (London) **A156**, 56 (1936).

TABLE I. Induced quadrupole moment for the Cl^-, Cu^+, Rb^+, and Cs^+ ions. γ_∞ is the ratio of the total induced moment to Q, and the values listed above γ_∞ are the contributions of the radial and angular modes to γ_∞.

Ion	Cl^-	Cu^+	Rb^+	Cs^+
$\gamma_\infty(2p\to p)$	−1.5	−0.60	−0.47	−0.21
$\gamma_\infty(3p\to p)$	−46.4	−6.4	−3.4	−1.6
$\gamma_\infty(3d\to d)$		−3.7	−1.2	−0.38
$\gamma_\infty(4p\to p)$			−47.3	−8.4
$\gamma_\infty(4d\to d)$				−3.4
$\gamma_\infty(5p\to p)$				−75.7
γ_∞(ang)	+1.4	+2.0	+2.2	+2.9
γ_∞	−46.5	−8.7	−50.2	−86.8

The calculation of the $2p\to p$ excitation for Cl^- proceeds in the same manner as $3p\to p$ and gives $Q_{iT}(2p\to p) = -1.5Q$. It may be noted that these calculations for Cl^- are identical with those reported in I, except that we have integrated over the induced moment distribution to find the total induced moment. The wave function calculations for the angular modes[4] ($ns\to d$, $np\to f$) give $Q_{iT,\text{ang}} = +1.42Q$ (shielding). Thus the total induced moment is $Q_{iT} = -46.5Q$, so that the effect of Q is increased at large distances by a factor $1 + |Q_{iT}|/Q = 47.5$. In the following Q_{iT}/Q will be denoted by γ_∞. The terms of γ_∞ due to various modes will be written $\gamma_\infty(2p\to p)$, $\gamma_\infty(3p\to p)$, $\cdots$, where the parenthesis indicates the mode of excitation. For convenience these terms are listed in Table I. The large magnitude of $Q_{iT}(3p\to p)$ is due partly to the factor r^2 in the induced moment density. Since $u_0' \bar{u}_{1,p}' r^2$ has its maximum at $r = 3.4 a_H$, r^2 contributes roughly a factor 12 to the result.

The same procedure as for Cl^- was used for Cu^+, Rb^+ and Cs^+. For Cu^+, we used the Hartree-Fock functions obtained by Hartree.[5] The radial modes for the p shells are found from the same equations as for Cl^-. Figure 1 shows the $3p\to p$ wave $\bar{u}_{1,p}'$ and the induced moment $Q_i(3p\to p)/Q = (48/25) u_0' \bar{u}_{1,p}' r^2$ together with the unperturbed $3p$ function u_0'. It is seen that $\bar{u}_{1,p}'$ has one more node than u_0' and that the induced moment is antishielding ($Q_i < 0$) outside the last node of $\bar{u}_{1,p}'$. For $3d$, the $3d\to d$ excitation is obtained by a calculation similar to that given in I for the $np\to p$ waves. After summing over the states in the $3d$ shell, one finds for the induced moment

$$Q_{iT}(3d\to d) = (16/7) Q \int_0^\infty u_0' \bar{u}_{1,d}' r^2 dr, \quad (8)$$

where u_0' is r times the radial $3d$ function, normalized

[4] A small error was found in the earlier calculations of the angular modes. The values of $\bar{q}_0(r)$ shown in Fig. 5 of I are too large for $r > 1.2 a_H$. These values should be: $\bar{q}_0(2.0) = 0.528$, $\bar{q}_0(3.0) = 0.279$, $\bar{q}_0(4.0) = 0.113$. The quadrupole correction factor given in reference 17 is practically unchanged.

[5] D. R. Hartree, Proc. Roy. Soc. (London) **A157**, 490 (1936).

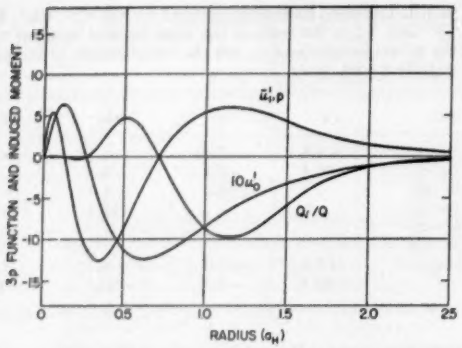

FIG. 1. $3p\rightarrow p$ perturbation $\bar{u}'_{1,p}$ for Cu^+, induced moment density Q_i/Q and unperturbed $3p$ function u_0'. The induced moment is $-6.4Q$.

according to $\int_0^\infty u'^2_0 dr=1$, and $\bar{u}'_{1,d}$ is that solution of

$$-\frac{d^2\bar{u}'_{1,d}}{dr^2}+\left(\frac{6}{r^2}+V_0-E_0\right)\bar{u}'_{1,d}=u_0'\left(\frac{1}{r^3}-\left\langle\frac{1}{r^3}\right\rangle_{3d}\right), \quad (9)$$

which is orthogonal to u'_0. Here E_0 is the unperturbed $3d$ energy and $\langle 1/r^3\rangle_{3d}$ is the average of $1/r^3$ over the $3d$ wave function. The contributions of the $m=0, \pm1$ and ±2 states to Eq. (8) are $Q\int_0^\infty u'_0\bar{u}'_{1,d}r^2dr$ times 32/49, 16/49, and 64/49, respectively.

The shielding due to the angular modes was obtained by interpolation of the result for Cl^- mentioned previously and similar wave function calculations for Cs^+ which will be reported soon. These calculations give $Q_{iT,\text{ang}}=2.95Q$ for Cs^+. In order to obtain $Q_{iT,\text{ang}}$ for Cu^+ by interpolation, we have considered besides $Q_{iT,\text{ang}}/Q$ for $Cl^-(1.42)$ the values for[1] Al(1.06) and Na(0.62). One thus obtains $Q_{iT,\text{ang}}\cong 2.0Q$ for Cu^+.

In order to obtain the induced moment distribution $Q_{i,\text{ang}}(r)$ which is needed below, we used the Thomas-Fermi model according to which[1]

$$Q_{i,\text{ang}}(r)dr=0.2998Q(\chi x)^{\frac{1}{2}}(x/r)dr, \quad (10)$$

where χ and x are the Thomas-Fermi function and variable, respectively, and $x=(Z^{\frac{1}{2}}/0.8853)r$, where r is in units a_H. Since the Thomas-Fermi model is not valid for large r, an exponential decrease of $Q_{i,\text{ang}}$ was assumed for $x\gtrsim 9$, in place of Eq. (10). The exponential was adjusted so that the total induced moment is $\cong 2.0Q$. We note that the precise treatment of $Q_{i,\text{ang}}(r)$ is not important in the present problem, because $Q_{iT,\text{ang}}$ is generally small compared to the induced moment due to the radial modes.

The various terms of γ_∞ for Cu^+ are given in Table I. γ_∞ is smaller than for Cl^-, although it still represents a large effect. An important reason for this difference is that the Cu^+ $3p$ function is more internal than the Cl^- $3p$ function; the outermost maximum of u'_0 is at $r=0.6a_H$ as compared to $1.5a_H$ for Cl^-. As a result the maximum of $u'_0\bar{u}'_{1,p}r^2$ is at a smaller value of r, $1.15a_H$ as compared to $3.4a_H$, and the difference in the effective r^2 explains in part the smaller $Q_{iT}(3p\rightarrow p)$ for Cu^+.

For Rb^+ and Cs^+ the Hartree functions[6] were used. These functions are presumably not as accurate as the Hartree-Fock functions used for Cl^- and Cu^+, but should give the correct order of magnitude of the effect. The results are listed in Table I. The large value of $Q_{iT}(4p\rightarrow p)$ for Rb^+ and $Q_{iT}(5p\rightarrow p)$ for Cs^+ is again correlated with the position of the outermost maximum of $u'_0\bar{u}'_{1,p}r^2$ which occurs at $r=2.7a_H$ and $3.1a_H$, respectively.

The contribution of the induced moment to the quadrupole coupling q at a nucleus (A) of a polar diatomic molecule can be easily obtained if the molecule is completely ionic and if the ion centered at the other nucleus (B) can be represented by a unit point charge. q is then given by $(2e/r^3)[1-\gamma(R)]$, where

$$\gamma(r)\equiv(1/Q)\left[\int_0^r Q_i dr'+r^5\int_r^\infty Q_i r'^{-5}dr'\right]. \quad (11)$$

Here $Q_i dr$ is the induced moment due to all modes between r and $r+dr$. γ is 0 at $r=0$ and approaches $Q_{iT}/Q=\gamma_\infty$ for large r. The general behavior of $1-\gamma(r)$ is the same for the four cases studied, as shown by Fig. 2. $1-\gamma(r)$ is generally less than 1 up to some radius $r\sim 1.5a_H$ where the antishielding by the outermost (and possibly next to outer) p shell becomes effective. Then $1-\gamma$ increases rapidly to the asymptotic value $1-\gamma_\infty$. At the common internuclear distances $(R\sim 5a_H)$, $1-\gamma$ is $\gtrsim 90$ percent of the asymptotic value. Thus the γ_∞ given in Table I can be used to estimate the effect of the induced moment on q.

The effect of the extent of the charge distribution of the ion centered at nucleus B is expected to be small if γ is close to γ_∞ and does not vary appreciably over the dimensions of the ion at B. The general expression

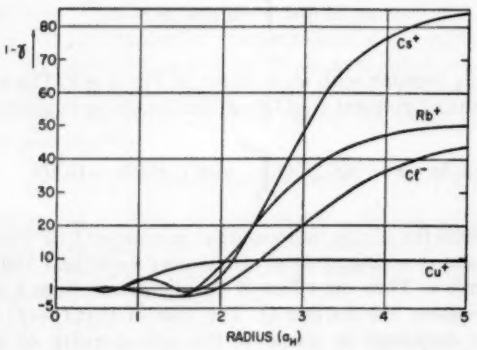

FIG. 2. $1-\gamma(r)$ for Cl^-, Cu^+, Rb^+ and Cs^+. The function $(1-\gamma)Q(3\cos^2\vartheta-1)/2r^3$ gives the total quadrupole potential.

[6] D. R. Hartree, Proc. Roy. Soc. (London) **A143**, 506 (1934); **151**, 101 (1935).

for q is

$$q=2e\left\{\frac{Z_B[1-\gamma(R)]}{R^3}-\int\frac{(1-\gamma)(3\cos^2\theta_A-1)\rho_B}{2r_A^3}dV\right\}, \tag{12}$$

where Z_B is the charge of nucleus B, r_A and θ_A are polar coordinates with origin at A and with respect to the internuclear axis, ρ_B is the charge density of the ion at B, and dV is the volume element. In the following we will frequently use q' defined as $q'\equiv q/2e$.

The numerical integration to obtain the perturbed wave functions introduces some error, although a large number of intervals δ ($\sim$50 for the external shells) was used. It is estimated that the values of Table I are accurate within $\pm$25 percent for Cl^- and $\pm$50 percent for the other ions.

The effect of the polarization of the closed shells can also be obtained by considering the perturbation of the ion by the external charge and calculating the contribution of the perturbed wave functions to the electric field gradient at nucleus A. The equivalence of this result with that obtained from the induced moment has been shown previously[2] and can be used as a check on the calculations.

The values of Q_{iT} obtained above are not exactly self-consistent. In order to obtain self-consistent values of the perturbations $\bar{u}'_1$ one must replace the right-hand sides of Eqs. (2) and (9) by

$$I'=u'_0\left[\frac{1-\gamma}{r^3}-\left(\frac{1-\gamma}{r^3}\right)\right], \tag{13}$$

and solve the resulting equations. This was done for Cl^-. The effect of using I' was found to be small and reduces the total induced moment Q_{iT} by only $\sim$10 percent. The reason for the smallness of this effect is that $\bar{u}'_{1,p}$ is largely determined by the inner parts of the atom where γ is relatively small and positive (shielding). A similar result was found for the $5p\rightarrow p$ wave of Cs^+ where the use of I' leads to $Q_{iT}(5p\rightarrow p)=-72.2Q$ as compared to $-75.7Q$ obtained from Eq. (2). Thus it can be concluded that the values of Table I are self-consistent to the accuracy of the calculations.

The data for the polar molecules for which q can be obtained appear to give support to the existence of a strong antishielding. For $K^{39}Br^{81}$ the values[7] $(eqQ)_{Br}/h=8.555$ Mc/sec and[8] $Q(Br^{81})=0.280\times10^{-24}$ cm^2 give $q'=0.0650a_H^{-3}$. Without the induced moment one would expect $q'=1/R^3$ which is $0.00660a_H^{-3}$ (using[7] $R=2.82$A). If κ denotes the ratio $q'/(1/R^3)$, we have $\kappa=9.85$. κ may be compared with $1-\gamma_\infty$ for the neighboring ion Rb^+, which is 51.2. These values differ considerably, showing that other effects besides the antishielding must play a role. On the other hand the fact that κ is $\sim$10 indicates that a large amplifying effect of the type of the antishielding probably does exist.

[7] Fabricand, Carlson, Lee, and Rabi, Phys. Rev. **91**, 1403 (1953).
[8] J. G. King and V. Jaccarino, Phys. Rev. **91**, 209 (1953).

For $NaCl^{35}$, the values[9] $(eqQ)_{Cl}/h=5.6$ Mc/sec and[10] $Q(Cl^{35})=-0.07894\times10^{-24}$ cm^2 lead to $q'=0.151a_H^{-3}$, as compared to $1/R^3=0.01127a_H^{-3}$ (using[11] $R=2.36$A). Thus one obtains $\kappa=13.4$ which is again of order 10 but considerably smaller than $1-\gamma_\infty=47.5$. For[9] NaI^{127}, $(eqQ)_I/h=-260$ Mc/sec and[12] $Q(I^{127})=-0.59\times10^{-24}$ cm^2 lead to $q'=0.938a_H^{-3}$, whereas $1/R^3=0.00744a_H^{-3}$ (with[11] $R=2.71$A). The resulting value of κ is 126. This ratio agrees fairly well with $1-\gamma_\infty=87.8$ for the neighboring ion Cs^+. The antishielding by the outer p electrons represents the effect of a small covalency, as is discussed below.

For $K^{39}Cl^{35}$ the quadrupole coupling[13] is close to zero for the state with vibrational quantum number $v=0$. Upon using[13] $(eqQ)_{Cl}/h=-0.075$, -0.237, and -0.393 Mc/sec for $v=1$, 2, and 3, respectively, one obtains $q'=0.00202$, 0.00639, and $0.0106a_H^{-3}$ for $v=1$, 2, and 3, respectively. We remark that q' for $v=3$ exceeds $1/R^3$ which is $0.00778a_H^{-3}$ (using[13] $R=2.67$A).[14] These data for KCl seem to indicate that another effect which tends to cancel the antishielding is of importance for this molecule.

Concerning the use of calculations for a positive ion, e.g., Cs^+, to obtain the induced quadrupole moment for the neighboring negative ion with the same electron core (I^-) one may expect that Q_{iT} will be larger for the negative ion since the outermost electrons ($5p$) are more loosely bound and hence can be polarized more easily in the latter case. In order to obtain an estimate of this effect, the $3p\rightarrow p$ wave for K^+ was calculated, in order to compare it with $3p\rightarrow p$ for Cl^-. Using the Hartree-Fock[15] $3p$ function for K^+, we found $\gamma_\infty(3p\rightarrow p)=-18.2$ as compared to -46.4 for Cl^-. Thus the effect of the additional binding of the positive ion reduces $\gamma_\infty(3p\rightarrow p)$ by more than a factor of 2. Referring to the cases of Br^- and I^- which are involved in the comparison with the experimental data, it is likely that $1-\gamma_\infty$ is larger than the values obtained for Rb^+ and Cs^+, respectively. This would improve the agreement with experiment for NaI where the theoretical value of $1-\gamma_\infty$ for Cs^+ is 87.8 as compared to $\kappa=126$. For KBr an increase of $1-\gamma_\infty$ above the value for Rb^+ (51.2) would lead to a worse disagreement with $\kappa=9.85$.

III. HYDROGENIC WAVE FUNCTIONS

It is of interest that the radial and angular perturbations of the wave functions can be obtained exactly for

[9] Professor P. Kusch (private communication).
[10] V. Jaccarino and J. G. King, Phys. Rev. **83**, 471 (1951).
[11] Stitch, Honig, and Townes, Phys. Rev. **86**, 813 (1952); Honig, Mandel, and Townes, Columbia Radiation Laboratory Quarterly Report, June, 1953 (unpublished).
[12] J. E. Mack, Revs. Modern Phys. **22**, 64 (1950).
[13] Lee, Fabricand, Carlson, and Rabi, Phys. Rev. **91**, 1395 (1953).
[14] We note that although q' is close to zero, the variation of q' with v is of the same order of magnitude ($\sim$2/3 as large) as for q' at the Br nucleus in KBr. From the data of reference 7 for $(eqQ)_{Br}/h$ in $K^{39}Br^{79}$ one finds $q'=0.0651$, 0.0713, and $0.0775a_H^{-3}$ for $v=0$, 1 and 2, respectively.
[15] D. R. Hartree, Proc. Roy. Soc. (London) **A166**, 450 (1938).

the case of a hydrogenic potential $V_0=-2Z/r$, where Z is the atomic number. This will be done first for the radial modes for $2p$ and $3p$ which give rise to the antishielding. Instead of obtaining this effect from the induced quadrupole moment, we consider the perturbation of the core wave functions by the field of the external charge and the resulting contribution to the field gradient at the nucleus.[2] For a unit charge placed at a distance R, the contribution to q' is $(48/25)R^{-3}\times\int_0^\infty u'_0\bar{u}'_1/r^3dr$, where $\bar{u}'_1$ is that solution of

$$-\frac{d^2\bar{u}'_1}{dr^2}+\left[\frac{l(l+1)}{r^2}-\frac{2Z}{r}+\frac{Z^2}{n^2}\right]\bar{u}'_1=u'_0(r^2-\langle r^2\rangle) \quad (14)$$

which is orthogonal to the unperturbed p function u'_0; n and l are the principal and orbital quantum numbers, respectively; $\langle r^2\rangle$ is the average of r^2 over u'_0. The normalization is $\int_0^\infty u'^2_0dr=1$.

For $2p\rightarrow p$, we have

$$u'_0=(Z^{5/2}/24^{1/2})r^2\exp(-Zr/2), \quad (15)$$

whence $\langle r^2\rangle=30/Z^2$. Equation (14) is solved by assuming that $\bar{u}'_1$ has the form

$$\bar{u}'_1=(Z^{5/2}/24^{1/2})(c_3r^3+c_4r^4+c_5r^5)\exp(-Zr/2). \quad (16)$$

The coefficients c_4 and c_5 are determined from Eq. (14) and c_3 is chosen such as to make $\bar{u}_1'$ orthogonal on u'_0. One finds

$$\bar{u}'_1=\frac{Z^{5/2}}{24^{1/2}}\left[-\frac{160}{Z^4}r^2+\frac{3}{Z^2}r^4+\frac{1}{3Z}r^5\right]\exp(-Zr/2). \quad (17)$$

This gives

$$\int_0^\infty(u'_0\bar{u}'_1/r^3)dr=-67/(12Z), \quad (18)$$

so that the contribution to q' is

$$\Delta q'=(48/25)R^{-3}\int_0^\infty(u'_0\bar{u}'_1/r^3)dr=-268/(25ZR^3). \quad (19)$$

$\gamma_\infty(2p\rightarrow p)$ is given by $\Delta q'/(1/R^3)=-268/25Z$. The negative sign corresponds to the antishielding.

In a similar manner, the perturbation due to the $3p\rightarrow p$ mode was obtained. We find

$$\bar{u}'_1=\frac{(2Z/3)^{5/2}}{3}\left[-\frac{3645r^2}{2Z^4}+\frac{1215r^3}{4Z^3}+\frac{18r^4}{Z^2}-\frac{r^5}{Z}-\frac{r^6}{12}\right]\exp\left(-\frac{Zr}{3}\right), \quad (20)$$

and $\gamma_\infty(3p\rightarrow p)=-1008/25Z$.

An attempt was made to correlate this result for $3p$ with the Hartree function values of Table I. We can obtain an effective Z such that the formula for $\gamma_\infty(3p\rightarrow p)$ gives the same value as the calculation by means of the Hartree functions. Thus the values of Table I lead to $Z_{eff}=0.87$, 6.3, 11.9, and 25.2 for Cl^-, Cu^+, Rb^+, and Cs^+, respectively. One may expect that Z_{eff} is related to the charge of the nucleus screened by the electron distribution. Using Slater's screening constants,[16] one finds $Z_0=Z-11.25$ for the effective charge of the central field for $3p$. One thus obtains $Z_0=5.75$, 17.75, 25.75, and 43.75 for Cl^-, Cu^+, Rb^+, and Cs^+, respectively. These values of Z_0 are considerably larger than the Z_{eff} required to give the results obtained from the Hartree functions. This lack of agreement is perhaps not surprising since the Hartree $3p$ wave functions have only a remote similarity to hydrogenic functions. On the other hand, the main features of the hydrogenic perturbed functions $\bar{u}'_1$ such as the sign and the number of nodes, are in agreement with the Hartree function calculations.

For the angular excitations of the internal shells we obtain the induced quadrupole moment from the following equation for the perturbation due to the nuclear Q,

$$-\frac{d^2u'_1}{dr^2}+\frac{l(l+1)u'_1}{r^2}-\frac{2Zu'_1}{r}+\frac{Z^2u'_1}{n^2}=\frac{u'_0}{r^3}. \quad (21)$$

For the $1s\rightarrow d$ wave the result has been given previously,[2]

$$u_1'=(Z^{3/2}/3)[1+(Z/3)r]\exp(-Zr), \quad (22)$$

and the contribution to γ_∞ is

$$\gamma_\infty(1s\rightarrow d)=\frac{8}{5}\int_0^\infty u'_0u'_1r^2dr=\frac{2}{3Z}. \quad (23)$$

For $2s\rightarrow d$, one finds

$$u'_1=\frac{Z^{5/2}}{6\sqrt{2}}\left[1-\frac{Z}{6}r-\frac{Z^2}{24}r^2\right]\exp(-Zr/2), \quad (24)$$

whence $\gamma_\infty(2s\rightarrow d)=4/3Z$. For $2p\rightarrow f$, the perturbation is

$$u'_1=\frac{Z^{5/2}}{24\sqrt{6}}\left[r+\frac{Z}{10}r^2\right]\exp(-Zr/2), \quad (25)$$

so that $\gamma_\infty(2p\rightarrow f)=48/25Z$. For $3p\rightarrow f$ one finds

$$u'_1=\frac{(2Z/3)^{5/2}}{36}\left[r-\frac{Z}{15}r^2-\frac{Z^2}{135}r^3\right]\exp(-Zr/3), \quad (26)$$

so that $\gamma_\infty(3p\rightarrow f)=78/25Z$.

For $3s\rightarrow d$, the degeneracy of the $3s$ and $3d$ states makes it necessary to use a more refined treatment. Since the hydrogenic case is at best only a very crude representation for $3s$, a solution was not obtained.

We note that the hydrogenic results for the angular modes are in quite good agreement with the values

[16] J. C. Slater, Phys. Rev. **36**, 57 (1930).

obtained from the Hartree wave functions, if one uses Z_{eff} equal to the screened Z_0 defined above. Thus for Cl^-, the induced moment is $0.113Q$ for $2s\rightarrow d$ and $0.157Q$ for $2p\rightarrow f$, as obtained from the Hartree functions. These values lead to $Z_{eff}=11.8$ for $2s\rightarrow d$ and 12.2 for $2p\rightarrow f$, in good agreement with $Z_0=12.85$ derived from Slater's screening constants.[16]

IV. INDUCED DIPOLE EFFECT

Aside from the induced quadrupole moment, there is a further induced effect which contributes to the quadrupole coupling for polar molecules. This effect arises by virtue of the dipole moment induced near nucleus A by the ion surrounding B. In second order the dipole perturbation contributes to q.

We first consider the perturbation of an s state. The complete Schroedinger equation to second order is

$$(H_0+H_1)(u_{0,ns}+w_1+w_2)=(E_0+E_2)(u_{0,ns}+w_1+w_2), \tag{27}$$

where H_0 and E_0 are the unperturbed Hamiltonian and energy, respectively, H_1 is the dipole perturbation, $u_{0,ns}$ is the ns function (times r), w_1 is the first-order perturbation of the wave function, w_2 and E_2 are the second-order terms in the wave function and the energy, respectively. Assuming that the ion at B acts as a positive point charge, H_1 is given by $-(2r/R^2)\cos\theta$ (Rydberg units) for $r<R$. Upon equating the first- and second-order terms in (27), one obtains

$$(H_0-E_0)w_1=-H_1u_{0,ns}, \tag{28}$$

$$(H_0-E_0)w_2=-H_1w_1+E_2u_{0,ns}. \tag{29}$$

The contribution to q arises from the two second-order terms in the density, w_1^2 and $2u_{0,ns}w_2$. Since w_1 is a p wave, Eq. (28) becomes

$$-\frac{d^2w_1}{dr^2}+\left(\frac{2}{r^2}+V_0-E_0\right)w_1=\frac{2}{R^2}u_{0,ns}r\cos\theta, \tag{30}$$

where V_0 is the effective spherical potential. Here and in the following the wave functions are normalized to a volume element $r^2dr\sin\theta d\theta$. Upon introducing $u'_{0,ns}\equiv u_{0,ns}\sqrt{2}$, w_1 can be written

$$w_1=w'_1\sqrt{2}\cos\theta/R^2, \tag{31}$$

where w'_1 satisfies

$$-\frac{d^2w'_1}{dr^2}+\left(\frac{2}{r^2}+V_0-E_0\right)w'_1=u'_{0,ns}r. \tag{32}$$

Note that

$$\int_0^\infty u'^2_{0,ns}dr=1. \tag{33}$$

The contribution $\Delta q'_1$ due to the w_1^2 terms for both s electrons is

$$\Delta q'_1=-2\int_0^\infty\int_0^\pi\frac{w_1^2(3\cos^2\theta-1)}{2r^3}dr\sin\theta d\theta$$

$$=-\frac{16}{15R^4}\int_0^\infty\frac{w_1'^2}{r^3}dr. \tag{34}$$

In order to obtain w_2, we substitute the expressions for H_1 and w_1 in Eq. (29), giving

$$(H_0-E_0)w_2=\left[\frac{E_2u'_{0,ns}}{\sqrt{2}}+\frac{2\sqrt{2}w'_1r}{3R^4}\right]+\frac{2\sqrt{2}w'_1r(3\cos^2\theta-1)}{3R^4}, \tag{35}$$

where the right-hand side has been written as a sum of s and d functions. Thus w_2 has both an s and a d part. Only the d part is of interest here since the overlap of the s part with $u_{0,ns}$ does not contribute to q. If we write the d function part of w_2, as

$$w_{2,d}=(2\sqrt{2}/3R^4)w'_{2,d}(3\cos^2\theta-1), \tag{36}$$

the radial function $w'_{2,d}$ is determined by

$$-\frac{d^2w'_{2,d}}{dr^2}+\left(\frac{6}{r^2}+V_0-E_0\right)w'_{2,d}=w'_1r. \tag{37}$$

In view of Eq. (36), the density due to the overlap of $w_{2,d}$ and $u_{0,ns}$ for both s electrons is

$$\rho_2=(8/3R^4)u'_{0,ns}w'_{2,d}(3\cos^2\theta-1). \tag{38}$$

The contribution to q' is

$$\Delta q'_2=-\int\rho_2[(3\cos^2\theta-1)/2r^3]dV$$

$$=-(32/15R^4)\int_0^\infty(u'_{0,ns}w'_{2,d}/r^2)dr. \tag{39}$$

For the dipole perturbation of $1s$ states, Eqs. (32) and (37) can be solved exactly if one assumes that $u'_{0,1s}$ is a hydrogenic function,

$$u'_{0,1s}=2Z^{\frac{1}{2}}r\exp(-Zr). \tag{40}$$

w'_1 is then given by

$$w'_1=Z^{-\frac{1}{2}}r^2\exp(-Zr)[1+(Z/2)r], \tag{41}$$

and Eq. (31) yields

$$\Delta q'_1=-19/(30Z^2R^4). \tag{42}$$

Upon inserting w'_1 into Eq. (37), one can easily verify that the solution is

$$w'_2=Z^{-1}\left(\frac{15}{32Z^2}r^3+\frac{5}{16Z}r^4+\frac{1}{16}r^5\right)\exp(-Zr). \tag{43}$$

Eq. (39) now gives

$$\Delta q'_2 = -14/(15Z^3R^4), \tag{44}$$

so that the complete term for the dipole excitation of $1s$ is

$$\Delta q'_{1s,D} = -47/(30Z^3R^4). \tag{45}$$

The ratio of $\Delta q'_{1s,D}$ to the ionic term will be denoted by $\rho_{1s,D}(=-47/30Z^3R)$. For q at the Cl nucleus in NaCl ($R=4.46a_H$), $\rho_{1s,D}=-7.2\times10^{-5}$. Although the terms due to $1s$ (and other inner shells) are negligible for Cl^-, it will be seen below that the term due to the outermost shell ($3p$) is quite appreciable. We note that for the perturbation of ns, the normalization condition and the determination of E_2 enter only into the calculation of the s part of w_2, but do not affect $w'_{2,d}$.

For the electrons in a p shell, the dipole perturbation gives rise to excited d and s states in first order, and in second order gives excited p and f states, as shown in Fig. 3. In this figure an arrow corresponds to the application of the perturbation. The subscripts indicate the unperturbed state and the type of perturbation (dipole or quadrupole) which is being considered. Primes are used to distinguish the various s, p, d, f functions from each other. The contributions to q arise from the terms of type $(d_{np,D}, d_{np,D})$, $(np, p_{np,D})$, $(np, f_{np,D})$ and $(np, p'_{np,D})$, where $(np, p_{np,D})$ is the density due to the overlap of np with $p_{np,D}$, and the notation for the perturbed wave functions is the same as in Fig. 3. For brevity, the subscript np will be omitted in the following.

By a procedure similar to that used for the s states, one finds, for the total contribution of a p shell,

$$\Delta q'_{np,D} = -\frac{1}{R^4}\left[\frac{16}{15}J(d_D,d_D)+\frac{32}{75}J(3p,p_D) + \frac{96}{125}J(f_D,f_D)+\frac{32}{15}J(3p,p'_D)\right]. \tag{46}$$

Here $J(a,b)$ is defined as

$$J(a,b)=\int_0^\infty [w'_i(a)w'_j(b)]/r^3dr, \tag{47}$$

where $w'_i(a)$ and $w'_j(b)$ are the radial functions (times r) for the perturbed waves a and b, respectively. The subscript (i,j) indicates the order of the perturbation. The w'_i are determined by the equations,

$$M_2w'_1(d_D)=u'_{0,np}r, \tag{48}$$

$$M_0w'_1(s_D)=u'_{0,np}r, \tag{49}$$

$$M_1w'_2(p_D)=w'_1(d_D)r-\lambda_1u'_{0,np}, \tag{50}$$

$$M_2w'_2(f_D)=w'_1(d_D)r, \tag{51}$$

$$M_1w'_2(p'_D)=w'_1(s_D)r-\lambda_2u'_{0,np}, \tag{52}$$

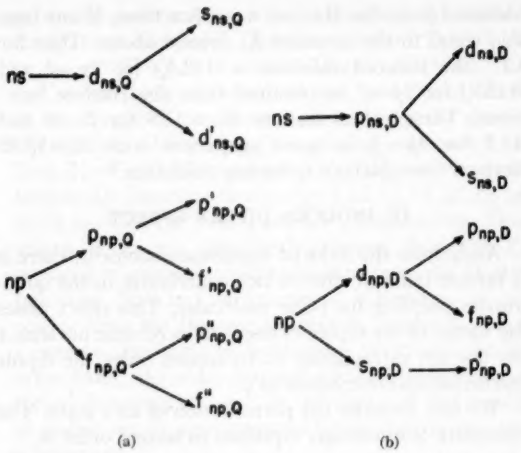

FIG. 3. Perturbations arising in first and second order from dipole and quadrupole parts of potential produced by external charge. (a) Quadrupole perturbation. (b) Dipole perturbation.

where

$$M_l=-\frac{d^2}{dr^2}+\frac{l(l+1)}{r^2}+V_0-E_0, \tag{53}$$

and $u'_{0,np}$ is r times the radial np function, normalized according to

$$\int_0^\infty u'^2_{0,np}dr=1. \tag{53a}$$

The parameters λ_i are proportional to the second-order energy terms (E_2) and are given by

$$\lambda_1=\int_0^\infty w'_1(d_D)ru'_{0,np}dr, \tag{54}$$

$$\lambda_2=\int_0^\infty w_1'(s_D)ru'_{0,np}dr. \tag{55}$$

It is seen that the right hand sides of Eqs. (50) and (52) are orthogonal on $u'_{0,np}$. These equations determine $w'_2(p_D)$ and $w'_2(p'_D)$, respectively, except for the addition of an arbitrary multiple of $u'_{0,np}$. This part of the perturbation is determined by the normalization conditions which are

$$\int_0^\infty\{[w_1'(d_D)]^2+2u'_{0,np}w'_2(p_D)\}dr=0, \tag{56}$$

$$\int_0^\infty\{[w'_1(s_D)]^2+2u'_{0,np}w'_2(p'_D)\}dr=0. \tag{57}$$

The calculation of these perturbed wave functions and of the resulting $\Delta q'_{3p,D}$ [Eq. (46)] was carried through for the $3p$ shell of Cl^-. The first-order perturbations $w'_1(d_D)$ and $w'_1(s_D)$ were obtained by numerical integration of Eqs. (48) and (49), and then

the second-order perturbations were found from Eqs. (50)–(52). We give here the contributions to $\Delta q'_{3p,D}R^3$, which is the ratio of $\Delta q'_{3p,D}$ to the ionic term. These values are proportional to $1/R$ and pertain to NaCl ($R=4.46a_H$); they will be called $\rho_D(a,b)$. We have: $\rho_D(d_D,d_D)=-0.2$, $\rho_D(3p,p_D)=+4.8$, $\rho_D(3p,f_D)=-0.2$, $\rho_D(3p,p'_D)=+6.5$.

The principal reason for calculating the induced dipole effect was to determine whether it tends to cancel the first-order antishielding discussed earlier. The total contribution $\sum(a,b)\rho_D(a,b)$ is $+10.9$. It should be noted that the sign of the ρ_D is independent of the sign of the external charge, since ρ_D involves the square of H_1. For an external positive charge the induced dipole effect has the same sign as the antishielding, while for an external negative charge (e.g., Na coupling in NaCl) the induced dipole effect tends to reduce the magnitude of q (shielding). Thus the possibility of cancellation would occur only in the latter case. However, the results for Cl^- appear to indicate that the induced dipole effect will be rather small compared to the first-order terms (10.9 as compared to 46.5). Moreover, the values of ρ_D given above are probably overestimates for the following reason. The perturbation was taken as $-(2r/R^2)\cos\theta$ for all r, whereas for $r>R$, we have $H_1=-(2R/r^2)\cos\theta$. The outermost maximum of $w'_2(p_D)$ is at $r=4.7a_H$ which is outside $R(=4.46a_H)$ for NaCl. Thus the perturbing potential is effectively too large, resulting in an overestimate of $w'_2(p_D)$ and hence of $J(3p,p_D)$. The same remark applies for the other perturbed functions.

V. SECOND-ORDER QUADRUPOLE EFFECT

Besides the induced dipole effect, there is another second-order contribution to q which arises from applying twice the quadrupole part of the potential of the external charge. This term is $-(r^2/R^3)(3\cos^2\theta-1)$ for $r<R$, and in first order gives rise to the induced quadrupole effect. The second-order term is evaluated in the same manner as the induced dipole effect.

For the excitation of an s state, one obtains the functions shown in Fig. 3. In first-order ns is excited to a d wave ($d_{ns,Q}$) and in second order one obtains s, d, and g functions. The contribution to q' is given by

$$\Delta q'_{ns,Q}=-\frac{1}{R^6}\left[\frac{16}{35}J(d_{ns,Q},d_{ns,Q})+\frac{32}{35}J(ns,d'_{ns,Q})\right], \quad (58)$$

where $J(a,b)$ is defined by Eq. (47). The radial functions $w'_1(d_{ns,Q})$ and $w'_2(d'_{ns,Q})$ are determined by

$$M_2w'_1(d_{ns,Q})=u'_{0,ns}r^2, \quad (59)$$

$$M_2w'_2(d'_{ns,Q})=w'_1(d_{ns,Q})r^2. \quad (60)$$

For the excitation of a p state, Fig. 3 shows the perturbed wave functions which arise in first and second order. In the following the subscript np of these functions will be omitted. One finds for the complete p shell,

$$\Delta q'_{np,Q}=-\frac{1}{R^6}\left[\frac{48}{125}J(p_Q,p_Q)+\frac{576}{875}J(f_Q,f_Q)+\frac{96}{125}J(np,p'_Q)+\frac{288}{875}J(np,f'_Q)+\frac{288}{875}J(np,p''_Q)+\frac{1152}{875}J(np,f''_Q)\right]. \quad (61)$$

The radial functions which are involved in the $J(a,b)$ are determined by the equations:

$$M_1w'_1(p_Q)=u'_{0,np}(r^2-\langle r^2\rangle_{np}), \quad (62)$$

$$M_2w'_1(f_Q)=u'_{0,np}r^2, \quad (63)$$

$$M_1w'_2(p'_Q)=w'_1(p_Q)(r^2-\langle r^2\rangle_{np})-\lambda_3u'_{0,np}, \quad (64)$$

$$M_2w'_2(f'_Q)=w'_1(p_Q)r^2, \quad (65)$$

$$M_1w'_2(p''_Q)=w'_1(f_Q)r^2-\lambda_4u'_{0,np}, \quad (66)$$

$$M_2w'_2(f''_Q)=w'_1(f_Q)r^2, \quad (67)$$

where

$$\lambda_3=\int_0^\infty w'_1(p_Q)r^2u'_{0,np}dr, \quad (68)$$

$$\lambda_4=\int_0^\infty w'_1(f_Q)r^2u'_{0,np}dr. \quad (69)$$

The normalization conditions are

$$\int_0^\infty\{[w'_1(p_Q)]^2+2u'_{0,np}w'_2(p'_Q)\}dr=0, \quad (70)$$

$$\int_0^\infty\{[w'_1(f_Q)]^2+2u'_{0,np}w'_2(p''_Q)\}dr=0. \quad (71)$$

Equations (62)–(67) were solved numerically for the $3p$ state of Cl^-, and the second-order quadrupole effect was calculated from Eq. (61). We will give the values of $\rho_Q(a,b)$ defined as the ratio of the terms of Eq. (61) to $1/R^3$. ρ_Q varies as $1/R^3$ and the following values pertain to NaCl: $\rho_Q(p_Q,p_Q)=-0.6$, $\rho_Q(f_Q,f_Q)=-0.003$, $\rho_Q(3p,p'_Q)=+9.8$, $\rho_Q(3p,f'_Q)=-0.006$, $\rho_Q(3p,p''_Q)=+1.1$, $\rho_Q(3p,f''_Q)=-0.016$. The complete second-order quadrupole term $\sum(a,b)\rho_Q(a,b)$ is $+10.3$. However, as for the induced dipole effect, the perturbed waves are overestimated because of the use of the perturbing potential $-(r^2/R^3)(3\cos^2\theta-1)$ for all r. Thus it is likely that the actual second-order effect for $Cl^-[(\Delta q'_{3p,D}+\Delta q'_{3p,Q})R^3]$ is considerably smaller than the value 21.2 obtained from the ρ_D and ρ_Q given above. A value of ~ 10 would be hardly outside the limits of error of the first-order antishielding. Aside from $3p$, only the $3s$ shell is expected to give an appreciable second-order

term. The inner shells make a very small contribution to the second-order effects.

It can be concluded that the induced dipole and second-order quadrupole effects for Cl^- are rather small compared to the first-order antishielding. This result seems to indicate that at least for the case of Cl^- the first-order antishielding should give a good approximation to the effect of an external charge on the quadrupole coupling.

VI. CONCLUSIONS

While the experimental values of the quadrupole coupling give some support to the present calculations of the antishielding, it should be stressed that the case of KCl and the rather poor agreement for NaCl and KBr show that other effects are of importance for at least some molecules. In fact, the strong repulsive exchange forces which exist between ions at short internuclear distances may be expected to produce distortions of the charge distribution which contribute to the quadrupole coupling. The possible importance of this effect is suggested by the fact that the repulsive forces are as important as the Coulomb attraction between the ions treated as point charges in determining the internuclear distance. Hence one might expect that the exchange repulsion has a similarly large effect on the quadrupole coupling.

The present calculations are essentially concerned with a model of polar molecules and correspond to a weak valence bond. Thus the radial distortion ($np \rightarrow p$) for Cl^- in NaCl may be regarded as a pulling away of the Cl^- p electrons by the Na^+ ion. As a result there are fewer p electrons of Cl^- near $r=0$ along the internuclear axis, and this results in a positive contribution to q'. If there is a strong valence bond so that the electron has an appreciable probability to be localized on the other ion, the model is expected to be a poor representation. However, with the exception of the exchange forces, it should be well suited for polar molecules.

It should be emphasized that the antishielding effects which predominate for the case of an external charge are quite different in character from the shielding effects discussed previously[1] for atomic valence electrons. The former are due to the radial modes of excitation, while the latter involve the angular modes. The essential difference between the molecular and the atomic case arises from the penetration of the atomic valence electrons. Thus, as shown by Fig. 2, the total induced effect for Cl is very small ($1-\gamma \sim 1$) and in fact shielding up to $r \sim 1a_H$ where most of the quadrupole coupling for the $3p$ electron takes place. This accounts for the small shielding effect[1] found for $3p$ of Cl, and the same effect occurs in other atomic cases. From the previous calculations for Cl it was believed that the antishielding is generally small compared to the shielding for the atomic ground states.[17] This problem is being investigated at present by one of us (R.M.S.) using the results for heavy ions obtained here and some additional calculations. It appears that the shielding generally predominates for the light atoms ($Z \lesssim 30$) for which quadrupole correction factors have been given.[17] For medium and heavy atoms the antishielding may be larger than the shielding due to the angular modes. These considerations do not affect the previous results[17] for Cl and Al in which the effect of the radial modes was taken into account.

For excited atomic states, preliminary calculations have shown that there is a weak net antishielding due the external distribution of these wave functions. Thus even for the lowest excited (p) states of the alkalis, one obtains a weak antishielding, because of the small penetration. For the Na $3p$ state, a preliminary calculation gives ~ 10 percent antishielding.

For the case of a polar molecule, in contrast to atomic states, the other ion is at a distance $R \sim 5a_H$ and the large magnitude of the antishielding can be understood in terms of the rapid increase of $1-\gamma(r)$ with r (see Fig. 2). However, it should be noted that even a contribution of $100/R^3$ is considerably smaller than the atomic value of q' which would be involved in molecules having a typical valence bond. Thus the present considerations hardly affect the discussion of covalent molecules.[18]

It should be noted that the induced quadrupole moment is fairly small for the light elements for which the $3p$ shell is not occupied. For Al, the $2p \rightarrow p$ antishielding is[1] $\gamma_\infty(2p \rightarrow p) = -2.19$ while the angular modes give $\gamma_\infty(\text{ang}) = 1.06$ so that the total induced moment is $-1.13Q$. For Na a calculation of the $2p \rightarrow p$ and the angular perturbations gives $\gamma_\infty(2p \rightarrow p) = -2.73$ and $\gamma_\infty(\text{ang}) = 0.62$ so that $Q_{iT} = -2.11Q$. Q_{iT} is also expected to be small for the elements between B and F for which the $2p$ shell is not complete.

The Thomas-Fermi model gives a fairly good approximation to the angular (shielding) modes of excitation, but appears not to include the radial (antishielding) modes. As has been shown here, the latter arise mostly from the valence electrons and depend on the position of the ion in the periodic table. It is well known that the Thomas-Fermi model does not generally include effects of this kind.

[17] R. M. Sternheimer, Phys. Rev. **86**, 316 (1952).

[18] C. H. Townes and B. P. Dailey, J. Chem. Phys. **20**, 35 (1952). The quoted statement by one of us (H.M.F.) that a shielding takes place in the presence of external charges was based on the Thomas-Fermi results together with preliminary calculations for the s electrons of Cl^-.

Energy Levels in Lu^{176} and Hf^{176}†

JAMES R. ARNOLD
Institute for Nuclear Studies, University of Chicago, Chicago, Illinois
(Received November 5, 1953)

The energies of the three gamma rays in cascade with the β^- emission of Lu^{176} have been determined to be 306, 203, and 89 kev. Peak intensity and conversion x-rays suggest the assignment of all transitions as $E2$. The energies support the theory of Bohr and Mottelson. The total K x-ray intensity shows no excess to be ascribed to a K-capture branch setting a limit of $K/\beta^- < 0.1$. The half-life of Lu^{176} is $(2.15 \pm 0.10) \times 10^{10}$ years.

EARLIER experimental work on the nuclides Lu^{176} and Hf^{176} has indicated the decay scheme shown in Fig. 1.[1,2] The question of the existence of an orbital capture branch could not be definitely settled, although it was not prominent. The great interest in this nuclide derives not only from its own high spin and moment, but from the fact that its decay makes accessible Hf^{176} in states of high spin. The theory of Bohr and Mottelson[3] can now be compared with experiment for several levels.

Through the kindness of Dr. Frank H. Spedding we have obtained a 4.974-gram sample of highly purified Lu_2O_3. This sample was used for measurements on our low-level scintillation spectrometer. A typical spectrum is shown in Fig. 2. The gamma-ray energies are found to be 306, 203, and 89 kev by comparison with a series of known radiations, chief weight being placed on the 279-kev transition in Hg^{203}. The 122-kev peak is due to backscattering.

In order to convert the peak areas to absolute intensities, corrections were made for the following factors: (1) Geometry. The source was spread over a rectangular area of 26.4 cm^2 to minimize self-absorption. Its geometry was determined by comparison of the 306- and 203-kev photo-peak areas in the geometry used to those at a distance of 10.1 cm from the crystal face, where the geometry could be calculated easily. Scattered gamma rays from the shield do not affect this result. The geometry was 5.4 percent. (2) Self-absorption. This was corrected for by interpolation from the tables of Davisson and Evans.[4] Absorption by the aluminum can was also corrected for in this way. (3) Stopping power of the crystal and fraction of pulses appearing in the "photo-peak." These were obtained from the data of Novey[5] on a crystal of the same dimensions; in the case of the latter effect these were checked by our own measurements. The agreement was satisfactory. (4) Escape of the iodine K x-ray. This factor is of importance for the 55-kev peak. Novey's value[5] was used.

The values obtained for the total intensity of each radiation in the sample appear in Table I. The first column shows the actual intensities. The second shows gamma-ray intensities corrected for K conversion assuming all are $E2$ transitions. The tables of Rose *et al.*[6] were used for the more energetic gammas, while the experimental value of McGowan[7] was used for the 89-kev transition. The intensity of this peak is the least accurate; values obtained using Bohr and Mottelson's value for α_{total} are given in parentheses. L and M conversion has been neglected except for the 89-kev line; this may cause an appreciable error for the 203-kev line.

The calculated intensities for the K x-ray assume a fluorescent yield of 0.92 in this region. X-rays of hafnium appear due to internal conversion, while those of lutetium appear due to self-absorption in the sample,

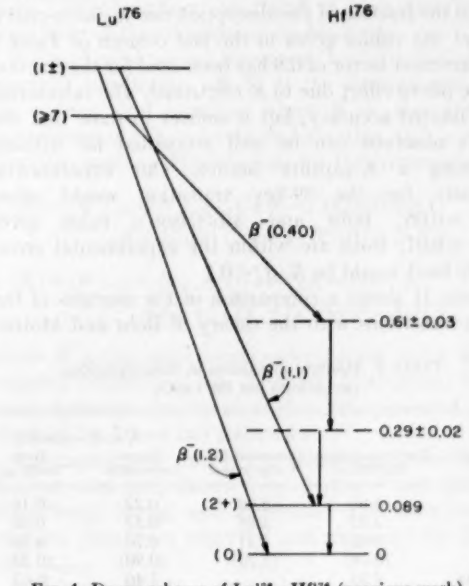

FIG. 1. Decay scheme of Lu^{176}–Hf^{176} (previous work).

† This work was supported under contract by the U. S. Office of Ordnance Research.

[1] G. Scharff-Goldhaber, as reported in M. Goldhaber and R. D. Hill, Revs. Modern Phys. **24**, 179 (1952).

[2] J. R. Arnold and T. Sugihara, Phys. Rev. **90**, 332 (1953).

[3] A. Bohr and B. R. Mottelson, Phys. Rev. **89**, 316 (1953); Kgl. Danske Videnskab. Selskab, Mat.-fys. Medd. **27**, 16 (1953).

[4] C. M. Davisson and R. Evans, Revs. Modern Phys. **24**, 79 (1952).

[5] T. B. Novey, Phys. Rev. **89**, 672 (1953).

[6] M. Rose *et al.*, Phys. Rev. **83**, 79 (1951).

[7] F. K. McGowan, Phys. Rev. **87**, 542 (1952).

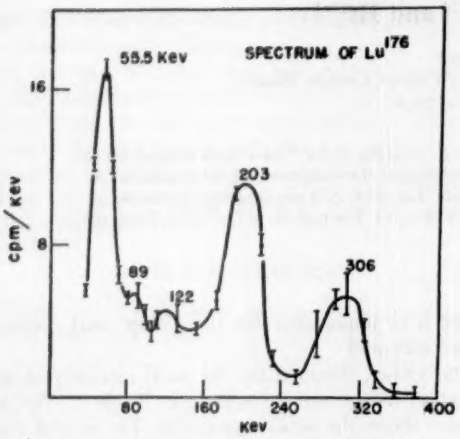

FIG. 2. Example of spectrum of Lu^{176}.

which occurs largely by photoeffect. This results in a "build-up" of K x-rays in a sample of finite thickness. We calculated the "build-up" intensity by assuming a uniform source of infinite extent and finite depth. For exponential absorption the fraction absorbed is given by

$$f_{abs}=(\tfrac{1}{2}x)[(2x-3)+(x+3)e^{-x}-x^2\mathrm{Ei}(-x)], \quad (1)$$

where x is the source thickness in terms of the mean absorption length. If we now assume that the absorption occurs uniformly through the source (which is not a bad assumption), make a small correction for edge effects, and from the tables of Davisson and Evans obtain the fraction of the absorption due to photo-effect, we get the values given in the last column of Table I (a correction factor of 0.8 has been used for the fraction of the photo-effect due to K electrons). The calculation is of limited accuracy, but it suffices to show that the x-rays observed can be well accounted for without assuming a K-capture branch. Our experimental intensity for the 89-kev transition would allow $K/\beta^-\approx 0.06$; Bohr and Mottelson's value gives $K/\beta^-\approx 0.01$. Both are within the experimental error. A safe limit would be $K/\beta^-<0.1$.

Table II shows a comparison of the energies of the three transitions with the theory of Bohr and Mottelson.[3] The agreement is seen to be very good, with a tendency to a lower value of B for the high energies, which is also in accord with theory.[8] The next higher transition is estimated as 420 kev, which is to be compared with the value of 400 kev found by Suttle[9] for the energy of the β^- transition. The drop in the value of B and the experimental uncertainties leave open the possibility that there may be a small contribution of a singly forbidden β^- transition of very low energy. No gamma ray of corresponding energy has been seen, however. Hf^{176}, then, becomes one of the best cases yet recorded in favor of the model of Bohr and Mottelson.

The half-life of Lu^{176} has been determined from the data given above, assuming an isotopic abundance of 2.6 percent in natural lutetium. The value obtained is $(2.15\pm0.1)\times10^{10}$ years. This value is probably independent of the presence of a minor orbital capture branch, which would give rise to Yb^{176}, if the theory is to be believed, with about the same series of gamma transitions.

It appears that this half-life is short enough for geochemical usefulness. Despite the rarity of lutetium, the fact that Hf^{176} is a 5 percent species and the great difference in geochemistry of the two elements bring this nuclide into the range of modern isotope-dilution techniques.

The decay scheme as presently established is shown in Fig. 3. The assignment of a spin to the ground state

TABLE I. Absolute intensities in disintegrations per minute per mg Lu_2O_3.

Energy (kev)	Electromagnetic Radiation	Corrected for K conversion	K x-rays expected from conversion	K x-rays expected from "build-up"
306	3.68	3.92	0.22	0.16
203	3.32	3.88	0.52	0.30
89	0.62	1.41	0.72	0.16
89[a]	(0.78)	(1.76)	(0.90)	(0.20)
K x-ray	2.35		1.46	0.62
			(1.64)	(0.66)

[a] The numbers in parentheses are the values obtained by assuming $\alpha_{total}=4$.

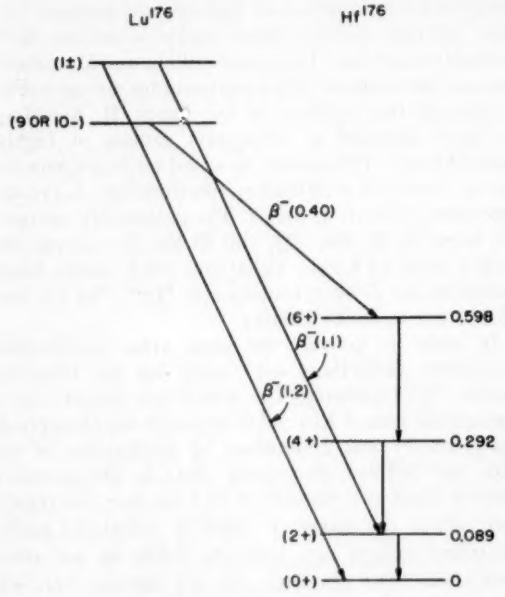

FIG. 3. Decay scheme of Lu^{176}—Hf^{176} (present work).

[3] A. Bohr and B. R. Mottleson, Kgl. Danske Videnskab. Selskab, Mat.-fys. Medd. 27, 16 (1953), see p. 91.
[9] A. D. Suttle, Ph.D. thesis, University of Chicago, 1952 (unpublished).

TABLE II. Energies of Hf^{176} transitions.

Energy (kev)	I_{upper}	$4I+2$	B (kev)
89	2	6	14.8
203	4	14	14.5
306	6	22	13.9
(420)[a]	(8)	(30)	(14)

[a] Estimated value.

of Lu^{176} is based on Klinkenberg's[10] theoretical statement that the parity is odd, and the ft value of the β^- decay indicating a third-forbidden transition.[9]

One may infer the possible presence of other odd-odd nuclei of high spin in this region. Such species, if their half-lives were too short for occurrence in nature, would be difficult to excite by ordinary means. Even first-forbidden transitions would be of rather long life, with correspondingly low intensity. Thus a number of the activities now known in this region may be isomeric states.

[10] P. F. A. Klinkenberg, Revs. Modern Phys. **24**, 63 (1952).

ACKNOWLEDGMENTS

The author is indebted to Dr. Frank H. Spedding for the loan of the sample which made this work possible and to Dr. Murray Gell-Mann and Dr. V. L. Telegdi for valuable discussions of the theoretical aspects of the problem. Mrs. Margery Bryant assisted with the experimental measurements. The U. S. Office of Ordnance Research contributed generous support.

PHYSICAL REVIEW VOLUME 93, NUMBER 4 FEBRUARY 15, 1954

Microwave Spectrum of O_2†

MASATAKA MIZUSHIMA AND ROBERT M. HILL*

Department of Physics, Duke University, Durham, North Carolina

(Received October 2, 1953)

Twenty-four lines of the microwave spectrum of oxygen molecule have been carefully measured. The theoretical origin of this spectrum is reexamined and the effect of centrifugal distortion is taken into account. The agreement between theory and experiment is satisfactory. It is pointed out that this spectrum is not suitable to determine the velocity of light.

I. INTRODUCTION

THE microwave spectrum of oxygen is due to its $^3\Sigma$ ground state. The rotational levels are split into triplets by the interaction of the spins of the unpaired electrons and the end-over-end rotation. Magnetic dipole transitions within these triplets give rise to 25 observable lines centered near 60 000 Mc/sec and one line at approximately double the center frequency.

An expression for the energy levels of this so-called ρ-type triplet was first given by Kramers,[1] who considered the spin-spin interaction, and showed it to be equivalent to a coupling of the total electron spin S and the figure axis of the molecule proportional to $3\cos^2\theta-1$, where θ is the angle between S and the figure axis.

Hebb[2] considered the interaction of a component of electronic angular momentum, perpendicular to the figure axis and precessing about it, and the electron spin. This interaction was found to have exactly the same form as that considered by Kramers.

Schlapp[3] recalculated the energy levels including the magnetic interaction $\mu\mathbf{K}\cdot\mathbf{S}$, of the electron spin and the end-over-end rotation, where $\mathbf{K}$ is the angular momentum of the end-over-end rotation and μ is the coupling constant. His formulas for the frequencies are

$$\nu_+(K)=(W_{J-K}-W_{J-K+1})/h=-(2K+3)B+\lambda-(K+1)\mu+[(2K+3)^2B^2+\lambda^2-2\lambda B]^{\frac{1}{2}}, \quad (1a)$$

$$\nu_-(K)=(W_{J-K}-W_{J-K-1})/h=(2K-1)B+\lambda+K\mu-[(2K-1)^2B^2+\lambda^2-2\lambda B]^{\frac{1}{2}}, \quad (1b)$$

where B is the usual rotational constant and λ is the coupling constant of the Kramers' interaction. Using these formulas he could explain the infrared data obtained by Dieke and Babcock.[4]

The unresolved microwave transitions near 60 000 Mc/sec were first observed by Beringer[5] and then by Strandberg, Meng, and Ingersoll.[6] The low-pressure, resolved lines were observed and measured by Burk-

† This research was supported by the United States Air Force under a contract monitored by the Office of Scientific Research, Air Research and Development Command. The information contained in this paper is part of a thesis submitted by one of the authors, Robert M. Hill, in partial fulfillment of the requirements for the Ph.D. degree at Duke University.

* Present address: Electronic Defense Laboratory, Sylvania Electric Products, Inc., Mountain View, California.

[1] H. A. Kramers, Z. Physik **53**, 422 (1929).

[2] M. H. Hebb, Phys. Rev. **49**, 610 (1936).

[3] R. Schlapp, Phys. Rev. **51**, 342 (1937).

[4] G. H. Dieke and H. D. Babcock, Proc. Natl. Acad. Sci. U. S. **13**, 670 (1927).

[5] R. Beringer, Phys. Rev. **70**, 53 (1946).

[6] Strandberg, Meng, and Ingersoll, Phys. Rev. **75**, 1524 (1949).

halter, Anderson, Smith, and Gordy.[7] A few of these same lines were also measured by Gokhale and Strandberg.[8] The one high-frequency line was measured by Anderson, Johnson, and Gordy.[9] Burkhalter *et al.*[7] noticed that while Schlapp's formulas (1) give $\nu_+(K-1)+\nu_-(K+1)=2\lambda+\mu$, which does not depend on K, their experimental value of this sum increases with K.

A recent paper by Miller and Townes[10] reexamined the fine structure theory and obtained the formulas:

$$\nu_+(K)=-(2K+3)(B-\tfrac{1}{2}\mu)+\lambda-(K+1)\mu+[(2K+3)^2(B-\tfrac{1}{2}\mu)^2+\lambda^2-2\lambda(B-\tfrac{1}{2}\mu)]^{\frac{1}{2}}, \quad (2a)$$

$$\nu_-(K)=(2K-1)(B-\tfrac{1}{2}\mu)+\lambda+K\mu-[(2K-1)^2(B-\tfrac{1}{2}\mu)^2+\lambda^2-2\lambda(B-\tfrac{1}{2}\mu)]^{\frac{1}{2}}, \quad (2b)$$

which can be obtained from the formulas (1) by replacing B by $B-\frac{1}{2}\mu$. The same formulas were also obtained by one of the present authors.[11]

The revised formulas (2) still give a constant value for $\nu_+(K-1)+\nu_-(K+1)$, namely $2\lambda+\mu$, which does not agree with experiment. Miller and Townes[10] assumed that B and λ in the formulas (2) are not constant but are expressed as

$$B=B_0-0.14K(K+1)\ \text{Mc/sec}, \quad (3a)$$

$$\lambda=\lambda_0-\lambda_1K(K+1), \quad (3b)$$

respectively. Using the values cited in the last column of Table II of this paper, they were able to obtain a satisfactory agreement with experiment. By combining their value of B_0 and the value obtained by infrared[12] work, Miller and Townes arrived at a value of 299 781 $\pm$33 km/sec for the velocity of light. The difference between our theory and that of Miller and Townes will be pointed out in Secs. III and V.

II. EXPERIMENT

The line measurements were made on a Zeeman modulation spectrometer very similar to that described by Burkhalter *et al.*[7] A factor of ten increase in the signal-to-noise ratio was obtained by using Sylvania Type 1-N-53 crystals as detectors. A similar gain was made by slotting the coaxial cavity in the Type 1-N-26 multiplier crystal and matching its doubled output directly into the wave guide of the cell. The standard coaxial probe was used in the wave guide carrying the fundamental frequency. This increased signal-to-noise ratio permitted the use of small time constants with lock-in amplifier and recorder, eliminating any chance of possible shift in the line shape due to the time delay of the recorder network. Frequency measurements were made with a frequency standard monitored by W. W. V. Each line was measured as the tube was mechanically tuned in each direction, as a check on the lock-in time constant. The results are listed in Table I.

III. REEXAMINATION OF THE THEORY

The Hamiltonian for the ρ-type triplet is given as

$$H=B|\mathbf{K}|^2+2\lambda(S_z^2-|\mathbf{S}|^2)+\mu\mathbf{K}\cdot\mathbf{S}, \quad (4)$$

where S_z is the component of S along the molecular axis. The first term is the usual rotational energy, the second term represents the spin-spin interaction averaged over the space coordinates,[1] while the last term is the magnetic interaction between $\mathbf{S}$ and $\mathbf{K}$.[3]

If the constants B, λ, and μ are assumed independent of K, the matrix elements of H for the case $|S|=1$ are found to be:

$$H=B\begin{bmatrix}J(J-1) & 0 & 0\\ 0 & (J+1)(J+2) & 0\\ 0 & 0 & J(J+1)\end{bmatrix}+\lambda\begin{bmatrix}-2J/(2J+1) & 2\{J(J+1)\}^{\frac{1}{2}}/(2J+1) & 0\\ 2\{J(J+1)\}^{\frac{1}{2}}/(2J+1) & -2(J+1)/(2J+1) & 0\\ 0 & 0 & 0\end{bmatrix}+\mu\begin{bmatrix}J & 0 & -(J-1)(J+1)^{\frac{1}{2}}\\ 0 & -(J+1) & -J\{J(2J+3)/(2J+1)\}^{\frac{1}{2}}\\ -(J-1)(J+1)^{\frac{1}{2}} & -J\{J(2J+3)/(2J+1)\}^{\frac{1}{2}} & 0\end{bmatrix},$$

$$J=|\mathbf{K}+\mathbf{S}|, \quad (5)$$

where the bases are chosen so as to make $|\mathbf{K}|^2$ diagonal.

For a homonuclear diatomic molecule like $(O^{16})_2$ the nuclear functions for $K=$odd and $K=$even states have different symmetry properties for the permutation of the nuclei. Therefore, the matrix element between $K=$even and $K=$odd states vanishes, and the last term in the formula (5) becomes[13]

$$\mu\begin{bmatrix}J & 0 & 0\\ 0 & -(J+1) & 0\\ 0 & 0 & 0\end{bmatrix}. \quad (6)$$

The secular equation given by the formulas (5) and (6) can be easily solved and gives the formulas (2) for the absorption frequencies.

The constants B, λ, and μ can depend on K, since the molecule is deformed by the centrifugal force. Since the perturbation due to the centrifugal potential is proportional to $K(K+1)$, the electronic and vibrational part of the wave function can be expanded as follows under

[7] Burkhalter, Anderson, Smith, and Gordy, Phys. Rev. **79**, 651 (1950).
[8] B. V. Gokhale and M. W. P. Strandberg, Phys. Rev. **84**, 844 (1951).
[9] Anderson, Johnson, and Gordy, Phys. Rev. **83**, 1061 (1951).
[10] S. L. Miller and C. H. Townes, Phys. Rev. **90**, 537 (1953).
[11] M. Mizushima, Phys. Rev. **91**, 222 (1953).
[12] H. D. Babcock and L. Herzberg, Astrophys. J. **108**, 167 (1948).
[13] For the case of $O^{16}O^{17}$ or $O^{16}O^{18}$ formula (5) should be used.

the adiabatic assumption:

$$\psi(K)=\psi_0+AK(K+1)\psi_1+\cdots, \tag{7}$$

where ψ_0 and ψ_1 are the unperturbed wave functions and A is a small numerical factor. Thus, the rotational constant B becomes

$$B(K)=B_0+B_1K(K+1)+\cdots, \tag{8}$$

and B_1 is known from infrared data[14] to be approximately 5×10^{-6} cm^{-1}.

From the expansion (7), the matrix elements of the coupling constant λ are seen to be

$$\int\psi(K)\lambda\psi(K)=\int\psi_0\lambda\psi_0+2AK(K+1)\int\psi_1\lambda\psi_0$$
$$\equiv\lambda_0+K(K+1)\lambda_1, \tag{9}$$

and

$$\int\psi(K-1)\lambda\psi(K+1)=\lambda_0+(K^2+K+1)\lambda_1. \tag{10}$$

TABLE I. Experimental and calculated frequencies (Mc/sec).

K	ν_+obs	ν_+calc	ν_-obs	ν_-calc
1	56 265.6±0.6	56 264.7	118 750.5±0.5	118 750.0
3	58 446.2±0.2	58 446.7	62 487.2±0.4	62 485.7
5	59 591.4±0.2	59 591.1	60 308.0±0.2	60 305.4
7	60 433.4±0.2	60 435.0	59 163.4±0.2	59 163.6
9	61 149.6±0.2	61 150.8	58 323.2±0.1	58 323.3
11	61 799.8±0.4	61 800.4	57 611.4±0.2	57 612.1
13	62 413.8±0.4	62 411.4	56 970.8±0.4	56 968.0
15	62 996.6±0.2	62 998.0	56 364.0±0.4	56 363.5
17	63 567.2±0.2	63 568.3	55 784.6±0.4	55 784.3
19	64 128.0±0.8	64 127.2	55 221.6±0.4	55 222.4
21	64 678.2±0.2	64 677.9		54 672.8
23	65 224.2±0.8	65 222.6	54 129.4±0.4	54 132.4
25			53 599.4±0.8	53 599.0

The coupling constant μ may be also K dependent, but a small K-dependent term of a function as small as μ may be neglected. Thus, considering centrifugal distortion the matrix of the Hamiltonian (4) becomes, for $(O^{16})_2$,

$$H=\begin{bmatrix} B_0J(J-1)+B_1J^2(J-1)^2 & 0 & 0 \\ 0 & B_0(J+1)(J+2)+B_1(J+1)^2(J+2)^2 & 0 \\ 0 & 0 & B_0J(J+1)+B_1J^2(J+1)^2 \end{bmatrix}$$
$$+\begin{bmatrix} -2\{\lambda_0+\lambda_1J(J-1)\}J/(2J+1) & 2\{\lambda_0+(J^2+J+1)\lambda_1\}\{J(J+1)\}^{\frac{1}{2}}/(2J+1) & 0 \\ 2\{\lambda_0+(J^2+J+1)\lambda_1\}\{J(J+1)\}^{\frac{1}{2}}/(2J+1) & -2\{\lambda_0+\lambda_1(J+1)(J+2)\}(J+1)/(2J+1) & 0 \\ 0 & 0 & 0 \end{bmatrix}$$
$$+\begin{bmatrix} J\mu & 0 & 0 \\ 0 & -(J+1)\mu & 0 \\ 0 & 0 & 0 \end{bmatrix}. \tag{11}$$

When the secular equation obtained from the above formula is solved, the following expressions for the absorption frequencies are found:

$$\nu_+(K)=-B_0(2K+3)-B_12(2K+3)(K^2+3K+3)$$
$$+\lambda_0+\lambda_1(K+1)(K-2)+\tfrac{1}{2}\mu+f(K+1), \tag{12a}$$

$$\nu_-(K)=B_0(2K-1)+2B_1(2K-1)(K^2-K+1)$$
$$+\lambda_0+\lambda_1K(K+3)+\tfrac{1}{2}\mu+f(K-1), \tag{12b}$$

where

$$f(K)=[(B_0-\tfrac{1}{2}\mu)^2(2K+1)^2-2(B_0-\tfrac{1}{2}\mu)\lambda_0$$
$$+\lambda_0^2+6(B_0-\tfrac{1}{2}\mu)\lambda_1K(K+1)$$
$$+4(B_0-\tfrac{1}{2}\mu)B_1(2K+1)^2(K^2+K+1)$$
$$-4\lambda_0B_1(K^2+K+1)+2\lambda_0\lambda_1K(K+1)$$
$$+4B_1^2(2K+1)^2(K^2+K+1)^2$$
$$+\lambda_1^2K(K+1)(K^2+K+4)$$
$$+12B_1\lambda_1K(K+1)(K^2+K+1)]^{\frac{1}{2}},$$

and

$$\nu_-(1)=2\lambda_0+4\lambda_1+\mu. \tag{12c}$$

For $B_1=\lambda_1=0$, the above formulas reduce to the formulas (2). From the formulas (12) we see that the sum relationship has become

$$\nu_+(K-1)+\nu_-(K+1)=2\lambda_0+\mu+2\lambda_1(K^2+K+2). \tag{13}$$

[14] G. Herzberg, Ann. Physik **19**, 800 (1934).

This formula shows a slight dependence upon K which Schlapp's did not.

If we use the value 299 776 km/sec for the velocity of light, the infrared data[12] give $B_0=43\,100.9$ Mc/sec. Adopting this B_0 value, we obtain the set of values shown in the column 1 of Table II which gives satisfactory agreement between our formulas (12) and experimental data. The comparison between calculated and experimental values is made in Table I.

The present theory differs from that of Miller and Townes in the method of taking into account the centrifugal effect. Miller and Townes have used in the formulas (2) a value of B arrived at from considerations of centrifugal distortion and an empirical value of λ, whereas we have included the effects of centrifugal

TABLE II. Values of the coupling constants (Mc/sec).

	Present paper I[a]	Present paper II[b]	Miller and Townes[c]
B_0	43 100.9	43 097.8	43 101.6
B_1	−0.141	−0.141	−0.14
λ_0	59 501.0	59 501.3	59 501.6
λ_1	0.05996	0.05996	0.0575
μ	−252.29	−252.53	−252.72

[a] This column lists the set of values which gives $c=299\,776$ km/sec and which gives the calculated values shown in Table I.
[b] This column lists one of the other sets which also give good agreement between theory and experiment.
[c] Reference 10.

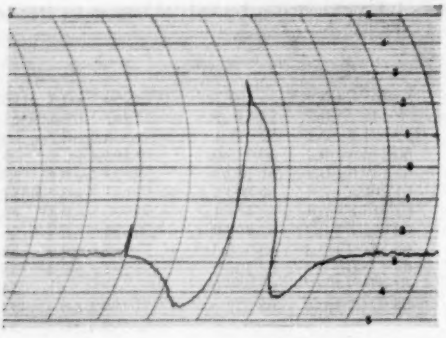

FIG. 1. 9_ line ($p=1.22$-mm Hg).

distortion, under the adiabatic assumption, in the Hamiltonian. It is natural that their values of the coupling constants are different from ours, as can be seen in Table II, since they differ in definition. Numerically, however, they are not so different, due to the fact that in the present case the centrifugal effect is very small. But in other states where this effect is large a marked difference will appear.

IV. INTERPRETATION OF λ_1

Since the centrifugal effect is small in our case, we may start from the harmonic oscillator approximation for the vibrational wave function. Thus, the vibrational parts of ψ_0 and ψ_1 are the harmonic oscillator wave functions of the ground state and first excited state, respectively. Because of the centrifugal potential, which is approximately

$$\frac{-h^2}{8\pi^2 m}K(K+1)\left(\frac{1}{r_e^2}-\frac{2\rho}{r_e^3}\right), \tag{13}$$

where r_e is the equilibrium interatomic distance and $\rho=r-r_e$, ψ_0 and ψ_1 will be mixed to give a distorted wave function:

$$\psi(K)=\psi_0+h^{\frac{1}{2}}(8\pi^2 m^{\frac{1}{2}}\nu^{\frac{1}{2}}r_e^{\,3}2^{\frac{1}{2}})^{-1}K(K+1)\psi_1, \tag{14}$$

where m is the reduced mass and ν is the vibrational frequency.

The coupling constant λ can be expanded at the equilibrium interatomic distance as

$$\lambda=\lambda_e+(\partial\lambda/\partial r)_{r=r_e}\rho+\cdots. \tag{15}$$

Thus

$$\int\psi(K)\lambda\psi(K)=\int\psi_0\lambda\psi_0+2AK(K+1)\int\psi_0\lambda\psi_1$$
$$\equiv\lambda_0+\lambda_1K(K+1), \tag{16}$$

from which we obtain

$$\lambda_0=\int\psi_0\lambda\psi_0=\lambda_e, \tag{17a}$$

$$\lambda_1=2A\int\psi_0\lambda\psi_1=h^2 16(\pi^4 m^2\nu^2 r_e^{\,3})^{-1}(\partial\lambda/\partial r)_{r=r_e}. \tag{17b}$$

If we use the obtained values for the constants, we find

$$(\partial\lambda/\partial r)_{r=r_e}=+2.41\times10^3 \text{ Mc/sec Å}. \tag{18}$$

Thus, we obtain

$$\lambda=59\,501.0+2.41\times10^3\rho \text{ Mc/sec}, \tag{19}$$

with ρ in Å.

V. VELOCITY OF LIGHT

If we combine the B_0 value obtained here with that obtained in infrared spectra,[12] we shall be able to obtain the value of the velocity of light. However, it must be noted that the accuracy of the B_0 value obtained in the microwave spectrum is not so good.

Suppose $B_0+\Delta B_0$ is adopted instead of B_0, where ΔB_0 is very small compared to B_0. Then from our equation (12) we obtain the increase of the calculated frequency as

$$\Delta\nu_+(K)=\Delta B_0[\{(2K+3)^2(B_0-\tfrac{1}{2}\mu)-\lambda_0\}f(K+1)^{-1}$$
$$-2K-3+16K^4B_1]=\Delta\nu_-(K+2), \tag{20}$$

where f is the function defined in the Eq. (12). Using the numerical values obtained in Sec. III, we find that always $0>\Delta\nu/\Delta B_0>-0.1$, except in the $K=1$ case where the ratio is about -0.2. It means that a change of 5 Mc/sec in the value of B_0 amounts to a change of less than 0.5 Mc/sec in the calculated ν values, which is within the error limits. Readjustment of the other constants will make the latter change smaller. As an example, we have shown another set of values in the second column of Table II. This set is as good as the former one in explaining the experimental results. Thus, the value of the velocity of light obtained from the oxygen spectra may have a rather large flexibility. A crude estimation gives $c=299\,776\pm60$ km/sec, corresponding to the experimental error of ±0.5 Mc/sec.

The authors wish to thank Professor W. Gordy for his encouragement.

Mathematical Analysis of the Hahn Spin-Echo Experiment

T. P. Das and A. K. Saha
Institute of Nuclear Physics, Calcutta, India
(Received August 5, 1953)

It was felt that the averaging procedures employed by Hahn in his theory of the "Spin-echoes" requires modification in several respects. A more satisfactory averaging procedure has been introduced here, and gives substantially the same results as those obtained by Hahn.

INTRODUCTION

THE powerful free-induction technique has been introduced into the field of nuclear induction quite recently by Hahn.[1] In contrast to the usual methods of observation, where the motion of magnetic nuclei is studied in the *presence* of a steady or pulsed rf field, the free-induction method confines itself to a study of the motion in the *absence* of the rf field, or rather in the interval following the application of the rf field, which is applied in the form of rectangular pulses of short duration. A theory of the "free induction" process and of a further extension of it, termed the "spin-echo" process, was also given by Hahn,[1] starting from the conventional Bloch equations.[2] Besides taking account of the effects of natural relaxation processes and field inhomogeneity, Hahn has also considered the effect of diffusion processes within the periods of observation. In trying to follow his theory, we found that his arguments regarding the diffusion damping of the free induction and the echo signals did not appear quite convincing. We therefore repeated his calculations using what appeared to us a more satisfactory averaging procedure. We give below the details of our calculations and compare our results with those obtained by Hahn.

THE FUNDAMENTAL EQUATIONS

In the analysis of the spin-echo phenomena, the basic Bloch equations and their solutions, in the presence and absence of the applied rectangular rf-field pulses, are applied successively. However, the following two modifications are introduced:

(a) First, because of the inhomogeneity of the steady magnetic field in the Z direction, the sample under study may be broken up into small groups of nuclei, each characterised by a particular value of ω_s, the angular Larmor frequency about the Z direction. The inhomogeneity of the magnetic field causes a distribution in ω_s and hence in $\Delta\omega=\omega_s-\omega$ (ω being the applied rf frequency) among the groups; and we may call this breakup into groups a division into "isochromatic" groups. We shall then have one set of Bloch equations[2] for each isochromatic group, and in this we shall have to use the natural spin-spin relaxation time T_2 instead of the net transverse relaxation time T_2^*, including the effect of the field inhomogeneity.[3] The effect of the magnetic field inhomogeneity is taken care of by the splitting into isochromatic groups. It will be assumed that $g(\Delta\omega)$, representing the distribution in $\Delta\omega$ among the groups, is Gaussian with a root-mean-square value $1/T_2^*$, and is thus symmetrical about $\Delta\omega=0$.

(b) Secondly, the "self-diffusion" effect has to be introduced. This takes account of the fact that by virtue of the random motion of the molecules carrying the nuclei, especially in liquid samples, each isochromatic group moves into different inhomogeneous parts of the field, so that ω_s is a random function of time and may be written

$$\omega_s(t)=\omega_s(t')+\eta_{tt'}.$$

$\eta_{tt'}$ represents the change in Larmor frequency by diffusion in the interval $t-t'$, so that $\Delta\omega$ is now also a function of time; i.e.,

$$\Delta\omega(t)=\Delta\omega(t')+\eta_{tt'}. \tag{1}$$

When we write $\Delta\omega$ without specifying the time, we shall mean the value at time $t=0$. Thus $\Delta\omega(t')=\Delta\omega+\eta_{t'0}$. Thus, the modified Bloch equations for a isochromatic group $\Delta\omega$ may, for the interval t' to t, be written as

$$\begin{aligned} dU/dt+[\Delta\omega(t')+\eta_{tt'}]V&=-U/T_2,\\ dV/dt-[\Delta\omega(t')+\eta_{tt'}]U&=-(V/T_2)-\omega_1 W,\\ dW/dt&=\omega_1 V+((1-W)/T_1), \end{aligned} \tag{2}$$

where UM_0, VM_0, and WM_0 are the X, Y, and Z components, respectively, of the magnetic moment vector $\mathbf{M}(\Delta\omega)$ of a nucleus, in the group under study, in a coordinate system rotating with the rf field $\mathbf{H}_1$, with frequency equal to the frequency of the rf field, and with $\mathbf{U}$ in the direction of $\mathbf{H}_1$.[2] M_0 corresponds to the intrinsic magnetic moment of the nucleus under study. T_1 and T_2 represent the spin-lattice and spin-spin relaxation times, respectively, because of natural relaxation processes, and $\omega_1=\gamma H_1$, γ being the gyromagnetic ratio of the nucleus under study. Here $\Delta\omega(t')$ has been used instead of $\Delta\omega$ because there will be a spectrum of Larmor frequencies in the originally homogeneous isochromatic group $\Delta\omega$ at the instant t' as a result of the fact that the members of the group will on account of diffusion spread out to different positions.

[1] E. L. Hahn, Phys. Rev. **80**, 580 (1950).
[2] F. Bloch, Phys. Rev. **70**, 460 (1946).
[3] Bloembergen, Purcell, and Pound, Phys. Rev. **73**, 679 (1948).

$\eta_{tt'}$ represents the further shift of Larmor frequency of the cluster $\Delta\omega+\eta_{t'0}$ in the interval $t-t'$.

If the rf field be applied for an interval t_w, very small compared with T_1 and T_2, so that the relaxation processes and diffusion processes have little time to be effective, then we can neglect the terms involving these effects, and the solutions of Eqs. (2) for a isochromatic group $\Delta\omega$ during the pulse are given by

$$\begin{aligned} U(t)&=[\Delta\omega(t')/\Omega]aQ+U(t'),\\ V(t)&=a\sin(\Omega t+\psi),\\ W(t)&=-(\omega_1/\Omega)aQ+W(t'), \end{aligned} \tag{3}$$

where t' refers to the start of the rf-field pulse, and

$$\begin{aligned} a&=\{[V(t')]^2+[U(t')\cdot\cos\Theta-W(t')\cdot\sin\Theta]^2\}^{\frac{1}{2}},\\ \psi&=\tan^{-1}\left(\frac{V(t')}{U(t')\cdot\cos\Theta-W(t')\sin\Theta}\right),\\ \Delta\omega(t')&=\Delta\omega+\eta_{t'0},\\ \cot\Theta&=\Delta\omega(t')/\omega_1,\\ Q&=\cos[\Omega(t-t')+\psi]-\cos\psi,\\ \Omega&=\{\omega_1^2+[\Delta\omega(t')]^2\}^{\frac{1}{2}}. \end{aligned} \tag{4}$$

If we further have the condition that

$$\omega_1\gg(\Delta\omega)_{\frac{1}{2}}, \tag{5}$$

where $(\Delta\omega)_{\frac{1}{2}}$ is the half-width of the distribution in $\Delta\omega$ and is proportional to $1/T_2^*$, then we can write the solutions at the end of the pulse approximately as

$$\begin{aligned} U(t'+t_w)&=U(t'),\\ V(t'+t_w)&=V(t')\cos\xi-W(t')\sin\xi,\\ W(t'+t_w)&=V(t')\sin\xi+W(t')\cos\xi, \end{aligned} \tag{6}$$

with $\xi=\omega_1 t_w$ representing the angle of nutation of the magnetic moment vector about the direction of the rf field.[1] The rf pulse may be referred to by specifying the angle ξ. Thus in Purcell's qualitative explanation [Sec. III(B) of Hahn's paper[1]] of the spin-echo phenomena, a 90° pulse was used.

In the absence of the rf field pulse, $\omega_1=0$, and the Eqs. (2) reduce to

$$\begin{aligned} dU/dt+[\Delta\omega(t'')+\eta_{tt''}]V&=-U/T_2,\\ dV/dt-[\Delta\omega(t'')+\eta_{tt''}]U&=-V/T_2,\\ dW/dt&=(1-W)/T_1, \end{aligned} \tag{7}$$

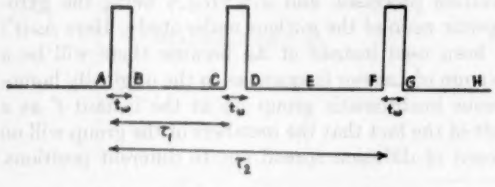

FIG. 1. Applied radio-frequency pulses.

where t'' refers to the instant when the previous rf pulse was cut off and free precession started. From the first two equations of (7) we get, putting $f=U+iV$, (compare Jacobsohn and Wangsness[4])

$$f(t)=f(t'')\cdot\exp\left[-\frac{t-t''}{T_2}+i\left\{\Delta\omega(t'')\cdot(t-t'')+\int_{t''}^{t}\eta_{tt'''}dt'''\right\}\right]. \tag{8}$$

Separating (8) into real and imaginary parts, we have

$$\begin{aligned} U(t)&=\exp\left(-\frac{t-t''}{T_2}\right)\\ &\quad\times[U(t'')\cos\{\Delta\omega(t'')\cdot(t-t'')+\phi_{tt''}\}\\ &\quad-V(t'')\sin\{\Delta\omega(t'')\cdot(t-t'')+\phi_{tt''}\}],\\ V(t)&=\exp\left(-\frac{t-t''}{T_2}\right)\\ &\quad\times[V(t'')\cos\{\Delta\omega(t'')\cdot(t-t'')+\phi_{tt''}\}\\ &\quad+U(t'')\sin\{\Delta\omega(t'')\cdot(t-t'')+\phi_{tt''}\}]. \end{aligned} \tag{9}$$

From the third equation of (7), we have

$$W(t)=1+\{W(t'')-1\}\exp\left(-\frac{t-t''}{T_1}\right). \tag{10}$$

Now, in (9), we have a phase factor involved, *viz.*,

$$\phi_{tt''}=\int_{t''}^{t}\eta_{tt'''}dt''', \tag{11}$$

giving the phase accumulation by the precessing group owing to the random diffusion process. Now, because of the random nature of this diffusion process we have to average over the different possible $\phi_{tt''}$ values. For this purpose we need a distribution function in $\phi_{tt''}$, which we may denote by

$$P[\phi_{tt''},t-t'']. \tag{12}$$

This has been evaluated by Slichter (see reference 1), and is shown in the appendix to be

$$P[\phi_{tt''},t-t'']=\frac{1}{\left[\frac{4\pi}{3}k(t-t'')^3\right]^{\frac{1}{2}}}\times\exp\left(-\frac{3\phi_{tt''}^2}{4k(t-t'')^3}\right), \tag{13}$$

where $k=(\gamma G)^2D$; G refers to the field gradient, assumed constant over the sample, and D is the self-

[4] B. A. Jacobsohn and R. K. Wangsness, Phys. Rev. **73**, 942 (1948).

diffusion coefficient of the liquid containing the nuclei. There is an important difference between our method of averaging over ϕ and that of Hahn. This point will be taken up later and leads to results somewhat different in nature from those of Hahn. Furthermore, to average over the Larmor frequency shift $\eta_{t'''t'''}$, we need a distribution function in $\eta_{t'''t'''}$, *viz.*, $P[\eta_{t'''t'''}, t''-t''']$, which is shown in the appendix to be

$$P[\eta_{t'''t'''}, t''-t'''] = \frac{1}{[4\pi k(t''-t''')]^{\frac{1}{2}}} \times \exp\left[-\frac{\eta_{t'''t'''}^2}{4k(t''-t''')}\right]. \quad (14)$$

CONDITIONS AT SUCCESSIVE STAGES OF APPLICATIONS TO THE PULSES

Using these results, we pass on to an analysis of the nature of nuclear signals to be expected when the rf field is applied in the form of successive pulses of the type indicated in Fig. 1. The pulses satisfy the following conditions regarding the intervals between the first and second and between the second and third pulses:

$$\tau_1 \gg t_w, \quad \tau_1 \gg T_2^*, \quad \text{and} \quad \tau_2 > 2\tau_1, \quad (15)$$

together with the following conditions regarding the width and amplitude:

$$t_w \ll T_2, T_1 \quad \text{and} \quad \omega_1 \gg 1/T_2^*. \quad (16)$$

Using Eqs. (6), (9), and (10), we shall now tabulate the values of U, V, and W for a group, at successive stages of application of the pulses, *viz.*, at A, B, C, D, F, G, and H (see Fig. 1). The equations at E are obtained from those at F by writing t in place of τ_2. In this connection, it is to be noted that at A, as well as at B, the isochromatic group has its precessing frequency equal to $\Delta\omega$. In the first free precession interval, i.e., from B to C, diffusion occurs; and a phase accumulation ϕ_{10}, given by $\int_0^{\tau_1}\eta_{t'''0}dt'''$, and with a distribution given by Eq. (31), takes place in the U and V terms, W remaining independent of the diffusion. At C, the isochromatic group $\Delta\omega$ breaks up into clusters, each with a Larmor frequency $\Delta\omega+\eta_{10}$, whose spectrum is given by (33). In the second free precession interval, i.e., from D to F, a further phase accumulation ϕ_{21}, equal to $\phi_{\tau_2\tau_1}$, occurs in U and V, and the cluster $\Delta\omega+\eta_{10}$ again breaks up at F into further clusters of Larmor frequencies $\Delta\omega+\eta_{10}+\eta_{21}$. The quantity W, belonging to the isochromatic group $\Delta\omega$, still remains unaffected by the diffusion at the end of the second free precession interval, as is apparent from the equations in Table I. On this point we disagree with Hahn, who expected a spectrum in W at this stage depending on η. Finally, as the positions reached by the cluster at C and again at F, starting from C, are quite independent of each other, η_{10} and η_{21} will be independent of each other and may be separately averaged by using the probability that a cluster may collect a Larmor frequency shift η_{10} in the interval between 0 and τ_1, and

TABLE I. Values of U, V, and W at instants A, B, C, D, F, G, and H.

Instant / Larmor frequency	$0(A)$	$t_w(B)$	$\tau_1(C)$	$\tau_1+t_w(D)$	$\tau_1(F)$	$\tau_1+t_w(G)$	$t>\tau_1+t_w(H)$
	$\Delta\omega$	$\Delta\omega$	$\Delta\omega+\eta_{10}$	$\Delta\omega+\eta_{10}$	$\Delta\omega+\eta_{10}+\eta_{21}$	$\Delta\omega+\eta_{10}+\eta_{21}$	$\Delta\omega+\eta_{10}+\eta_{21}+\eta_{32}$
U	0	0	$\sin\xi\sin(\Delta\omega\tau_{10}+\phi_{10})$ $\times\exp(-\tau_{10}/T_2)P(\phi_{10},\tau_{10})$	$U(C)$	$[U(D)\cos\{(\Delta\omega+\eta_{10})\tau_{21}+\phi_{21}\}$ $-V(D)\sin\{(\Delta\omega+\eta_{10})\tau_{21}+\phi_{21}\}]$ $\times\exp(-\tau_{21}/T_2)P(\phi_{21},\tau_{21})P(\eta_{10},\tau_{10})$	$U(F)$	$[U(G)\cos\{(\Delta\omega+\eta_{10}+\eta_{21})(t-\tau_2)+\phi_{21}\}$ $-V(G)\sin\{(\Delta\omega+\eta_{10}+\eta_{21})(t-\tau_2)+\phi_{21}\}]$ $\times\exp\left(-\frac{t-\tau_2}{T_2}\right)P(\phi_{21},t-\tau_2)P(\eta_{21},\tau_{21})$
V	0	$-\sin\xi$	$-\sin\xi\cos(\Delta\omega\tau_{10}+\phi_{10})$ $\times\exp(-\tau_{10}/T_2)P(\phi_{10},\tau_{10})$	$V(C)\cos\xi$ $-W(C)\sin\xi$	$[U(D)\sin\{(\Delta\omega+\eta_{10})\tau_{21}+\phi_{21}\}$ $+V(D)\cos\{(\Delta\omega+\eta_{10})\tau_{21}+\phi_{21}\}]$ $\times\exp(-\tau_{21}/T_2)P(\phi_{21},\tau_{21})P(\eta_{10},\tau_{10})$	$V(F)\cos\xi$ $-W(F)\sin\xi$	$[U(G)\sin\{(\Delta\omega+\eta_{10}+\eta_{21})(t-\tau_2)+\phi_{21}\}$ $+V(G)\cos\{(\Delta\omega+\eta_{10}+\eta_{21})(t-\tau_2)+\phi_{21}\}]$ $\times\exp\left(-\frac{t-\tau_2}{T_2}\right)P(\phi_{21},t-\tau_2)P(\eta_{21},\tau_{21})$
W	1	$\cos\xi$	$1+(\cos\xi-1)\exp(-\tau_{10}/T_1)$	$V(C)\sin\xi$ $+W(C)\cos\xi$	$1+\{W(D)-1\}\exp(-\tau_{21}/T_1)$	$V(F)\sin\xi$ $+W(F)\cos\xi$	$1+\{W(G)-1\}\exp\left(-\frac{t-\tau_2}{T_1}\right)$

η_{21} in the interval $\tau_2-\tau_1$, *viz.*, $P(\eta_{10}, \tau_{10})\cdot P(\eta_{21}, \tau_{21})$ given by Eqs. (38) and (39). After the third pulse, free precession starts again and we use ϕ_{t2} to denote the phase difference accumulated in U and V between G and H, the latter corresponding to instant $t>\tau_2+t_w$. It is our aim to calculate $V(t)$ explicitly in the second and third free precession intervals, because the signal expected will only depend on V.

PRIMARY ECHO

Using the solutions in Table I, we shall now investigate the conditions after passage of the second pulse at $t=\tau_1$. In this case, we have to consider the solutions at E for U and V, which can be obtained, as pointed out before, from the solutions at F, by substituting t for τ_2, with $\tau_1+t_w<t<\tau_2$. It has, of course, to be remembered that since we shall ultimately integrate over a Gaussian distribution in $\Delta\omega$, we need only retain the terms with even parity with respect to $\Delta\omega$. In this respect, the U term at E may easily be seen to be entirely of odd parity with respect to $\Delta\omega$, and so it does not contribute to the total signal from the sample under study. And even in the V term, we have to retain only that part which is even with respect to $\Delta\omega$.

In this connection we need the even terms in x in products of the form $\sin(ax+p)\sin(bx+q)$ and $\cos(ax+p)\cos(bx+q)$, and it may be easily seen that, in these products, the parts even with respect to x are given by:

$$[\sin(ax+p)\sin(bx+q)]_{\text{even}} = \sin ax \sin bx \cos p \cos q + \cos ax \cos bx \sin p \sin q.$$

$$[\cos(ax+p)\cos(bx+q)]_{\text{even}} = \cos ax \cos bx \cos p \cos q + \sin ax \sin bx \sin p \sin q. \quad (17)$$

Now, at E, we find, substituting the values of U, V, and W in previous instants, the total signal to be proportional to

$$V(E)=\int_{-\infty}^{\infty}\iiint\Big[\sin\xi\sin(\Delta\omega\tau_{10}+\phi_{10}) \times\exp\Big(-\frac{\tau_{10}}{T_2}\Big)\sin\{(\Delta\omega+\eta_1)(t-\tau_1)+\phi_{t1}\} + \Big\{-\sin\xi\cos(\Delta\omega\tau_{10}+\phi_{10}) \times\exp\Big(-\frac{\tau_{10}}{T_2}\Big)\cos\xi - W(c)\sin\xi\Big\} \times\cos\{(\Delta\omega+\eta_{10})(t-\tau_1)+\phi_{t1}\}\Big] \times\exp\Big(-\frac{t-\tau_1}{T_2}\Big)P(\phi_{10},\tau_{10})P(\phi_{t1},t-\tau_1) \times P(\eta_{10},\tau_{10})g(\Delta\omega)d\phi_{10}d\phi_{t1}d\eta_{10}d(\Delta\omega).$$

Since the distributions over η_{10} and ϕ_{10} are Gaussian, we have to retain only that part of V which is even in η_{10} and ϕ_{10}. Applying the symmetry conditions (17) we have, for the part of the integrand which is of even parities in $\Delta\omega$, η_{10} and ϕ_{10},

$$\Big[\sin\xi\{\sin^2\tfrac{1}{2}\xi\cos\Delta\omega(t-2\tau_1)\cos(\phi_{t1}-\phi_{10}) - \cos^2\tfrac{1}{2}\xi\cos\Delta\omega t\cos(\phi_{t1}+\phi_{10})\} \times\cos\eta_1(t-\tau_1)\exp(-t/T_2) - W(C)\sin\xi\cos\Delta\omega(t-\tau_1)\cos\phi_{t1} \times\cos\eta_1(t-\tau_1)\exp\{-(t-\tau_1)/T_2\}\Big] \times P(\phi_{10},\tau_{10})P(\phi_{t1},t-\tau_1)P(\eta_{10},\tau_{10})g(\Delta\omega). \quad (19)$$

Using for $g(\Delta\omega)$ the normalized Gaussian distribution,

$$g(\Delta\omega)=\frac{T_2^*}{(2\pi)^{\frac{1}{2}}}\exp\Big[-\frac{(\Delta\omega T_2^*)^2}{2}\Big], \quad (20)$$

and using Eqs. (31), (33), and (34) of the appendix, we get the total signal at E proportional to

$$V(E)=\sin\xi\sin^2\frac{\xi}{2}\exp\Big[-\frac{t}{T_2}-\frac{(t-2\tau_1)^2}{2T_2^{*2}}\Big] \times\exp\Big[-\frac{k}{3}\{(t-\tau_1)^3+\tau_1^3+3\tau_1(t-\tau_1)^2\}\Big] -\sin\xi\cos^2\frac{\xi}{2}\exp\Big[-\frac{t}{T_2}-\frac{t^2}{2T_2^{*2}}\Big] \times\exp\Big[-\frac{k}{3}\{(t-\tau_1)^3+\tau_1^3+3\tau_1(t-\tau_1)^2\}\Big] -W(c)\sin\xi\exp\Big[-\frac{t-\tau_1}{T_2}-\frac{(t-\tau_1)^2}{2T_2^{*2}}\Big] \times\exp\Big[-\frac{k}{3}\{(t-\tau_1)^3+3\tau_1(t-\tau_1)^2\}\Big]. \quad (21)$$

This equation may be compared with the corresponding Eq. (17) of Hahn's paper. The first and third terms give, respectively, the *primary echo* at $t=2\tau_1$, and the *free-induction signal* following the second pulse. The middle term is a continuation of the *free-induction signal* following the first pulse and, on account of the smallness of T_2^*, is almost zero in the second free precession interval. There is complete agreement between our results and those of Hahn regarding the trigonometric part of the amplitude of the various terms, the damping due to the natural relaxation processes, and the position of the maxima. But, there is disagreement in the diffusion terms. We compare our diffusion terms with those of Hahn, in Table II.

SECONDARY ECHOES

In this case, we have to consider the conditions at H, after the passage of the third pulse. Here again we need

TABLE II. Our diffusion damping terms for the primary echo, compared with those of Hahn.

Term	Position of maximum	Hahn's results: Value of the diffusion term	Hahn's results: Value of the diffusion term at echo maximum	Our results: Value of the diffusion term	Our results: Value of the diffusion term at echo maximum
Primary echo	$2\tau_1$	$\exp(-\frac{1}{3}k\delta^2)$	$\exp\left(-\frac{8k\tau_1^3}{3}\right)$	$\exp\left[-\frac{k}{3}\{(t-\tau_1)^3+\tau_1^3+3\tau_1(t-\tau_1)^2\}\right]$	$\exp\left(-\frac{5k\tau_1^3}{3}\right)$
Free induction signal following second pulse	τ_1	$\exp\left[-\frac{k}{3}(t-\tau_1)^3\right]$		$\exp\left[-\frac{k}{3}\{(t-\tau_1)^3+3\tau_1(t-\tau_1)^2\}\right]$	

consider only the terms even in $\Delta\omega$, and the U term may again be seen to have no contribution to the total signal. Further, we have also to find the terms in V even in $\Delta\omega$. For this purpose, in addition to conditions (17) we need the terms even in x from the products

$$\sin(ax+p)\sin(bx+q)\cos(cx+r)$$

and

$$\cos(ax+p)\cos(bx+q)\cos(cx+r).$$

Thus,

$$\begin{aligned}
&[\sin(ax+p)\sin(bx+q)\cos(cx+r)]_{\text{even}}\\
&\quad=\sin ax\sin bx\cos cx\cos p\cos q\cos r\\
&\qquad-\sin ax\sin bx\sin cx\cos p\sin q\sin r\\
&\qquad-\cos ax\sin bx\sin cx\sin p\cos q\sin r\\
&\qquad+\cos ax\cos bx\cos cx\sin p\sin q\cos r.\\
&[\cos(ax+p)\cos(bx+q)\cos(cx+r)]_{\text{even}}\\
&\quad=\cos ax\cos bx\cos cx\cos p\cos q\cos r\\
&\qquad+\cos ax\sin bx\sin cx\cos p\sin q\sin r\\
&\qquad+\sin ax\cos bx\sin cx\sin p\cos q\sin r\\
&\qquad+\sin ax\sin bx\cos cx\sin p\sin q\cos r. \qquad (22)
\end{aligned}$$

From the solutions for V at H, we get, after applying the values of U, V, and W at previous instants A, B, C, D, F, and G, the total signal, as proportional to

$$\begin{aligned}
V(H)=\int\int\int_{-\infty}^{\infty}\int\int\int\Big[&\sin\{(\Delta\omega+\eta_{10}+\eta_{21})(t-\tau_2)+\phi_{t2}\}\\
&\times\Big(\cos\{(\Delta\omega+\eta_{10})\tau_{21}+\phi_{21}\}\sin\xi\sin(\Delta\omega\tau_{10}+\phi_{10})\\
&\times\exp\left(-\frac{\tau_{10}}{T_2}\right)P(\phi_{10},\tau_{10})\\
&-\sin\{(\Delta\omega+\eta_{10})\tau_{21}+\phi_{21}\}.\\
&\times\Big\{-\cos\xi\sin\xi\cos(\Delta\omega\tau_{10}+\phi_{10})\\
&\times\exp\left(-\frac{\tau_{10}}{T_2}\right)P(\phi_{10},\tau_{10})-\sin\xi W(C)\Big\}\Big)\\
&\times\exp\left(-\frac{\tau_{21}}{T_2}\right)P(\phi_{21},\tau_{21})P(\eta_{10},\tau_{10})\\
&+\cos\{(\Delta\omega+\eta_{10}+\eta_{21})(t-\tau_2)+\phi_{t2}\}\\
&\times\Big(\cos\xi\sin[(\Delta\omega+\eta_{10})\tau_{21}+\phi_{21}]\\
&\times\sin\xi\sin(\Delta\omega\tau_{10}+\phi_{10})\exp\left(-\frac{\tau_{10}}{T_2}\right)\\
&\times P(\phi_{10},\tau_{10})+\cos[(\Delta\omega+\eta_{10})\tau_{21}+\phi_{21}]\\
&\times\Big\{-\cos^2\xi\sin\xi\cos(\Delta\omega\tau_{10}+\phi_{10})\\
&\times\exp\left(-\frac{\tau_{10}}{T_2}\right)P(\phi_{10},\tau_{10})-\sin\xi\cos\xi W(C)\Big\}\\
&\times\exp\left(-\frac{\tau_{21}}{T_2}\right)P(\phi_{21},\tau_{21})P(\eta_{10},\tau_{10})\\
&-\sin\xi-\sin\xi\exp\left(-\frac{\tau_{21}}{T_1}\right)\\
&\times\Big\{-1-\sin\xi\sin\xi\cos(\Delta\omega\tau_{10}+\phi_{10})\\
&\times\exp\left(-\frac{\tau_{10}}{T_2}\right)P(\phi_{10},\tau_{10})+\cos\xi W(C)\Big\}\Big)\Big]\\
&\times\exp\left(-\frac{t-\tau_2}{T_2}\right)P(\phi_{t2},t-\tau_2)P(\eta_{21},\tau_{21})g(\Delta\omega)\\
&\times d\phi_{10}d\phi_{21}d\eta_{10}d\phi_{t2}d\eta_{21}d(\Delta\omega). \qquad (23)
\end{aligned}$$

Retaining, as before, the part of the integrand which is of even parity in $\Delta\omega$, η_{10}, η_{21}, ϕ_{10}, ϕ_{21}, and ϕ_{t2}, we get,

using Eqs. (31), (33), and (34) of the appendix,

$$V(H)=\frac{\sin^3\xi}{2}\exp\left[-(\tau_2-\tau_1)\left(\frac{1}{T_1}-\frac{1}{T_2}\right)-\frac{t}{T_2}\right]$$
$$\times\exp\left[-\frac{\{t-(\tau_2+\tau_1)\}^2}{2T_2^{*2}}\right]\exp[-\tfrac{1}{3}k\{(t-\tau_2)^3$$
$$+\tau_1^3+3\tau_1(t-\tau_1)^2+3(\tau_2-\tau_1)(t-\tau_2)^2\}]$$
$$+\sin\xi\sin^4\frac{\xi}{2}\exp\left[-\frac{t}{T_2}\right]$$
$$\times\exp\left[-\frac{\{t-(2\tau_2-2\tau_1)\}^2}{2T_2^{*2}}\right]$$
$$\times\exp[-\tfrac{1}{3}k\{(t-\tau_2)^3+(\tau_2-\tau_1)^3+\tau_1^3$$
$$+3\tau_1(t-2\tau_2+\tau_1)^2+3(\tau_2-\tau_1)(t-\tau_2)^2\}]$$
$$+W(c)\sin\xi\sin^2\frac{\xi}{2}\exp\left[-\frac{t-\tau_1}{T_2}\right]$$
$$\times\exp\left[-\frac{\{t-(2\tau_2-\tau_1)\}^2}{2T_2^{*2}}\right]$$
$$\times\exp[-\tfrac{1}{3}k\{(t-\tau_2)^3+(\tau_2-\tau_1)^3$$
$$+3\tau_1(t-2\tau_2+\tau_1)^2+3(\tau_2-\tau_1)(t-\tau_2)^2\}]$$
$$+\frac{\sin^3\xi}{4}\exp\left[-\frac{t}{T_2}\right]\exp\left[-\frac{\{t-2\tau_2\}^2}{2T_2^{*2}}\right]$$
$$\times\exp[-\tfrac{1}{3}k\{(t-\tau_2)^3+(\tau_2-\tau_1)^3+\tau_1^3$$
$$+3(\tau_2-\tau_1)(t-\tau_2)^2+3\tau_1(t-2\tau_2+\tau_1)^2\}]. \quad (24)$$

We have not included in the above equation those terms which represent the continuations of the primary echo and the free induction terms arising in the previous free precession intervals, because these will be almost totally damped out in the interval H. The first term in (24) represents the *stimulated echo* occurring at the instant $t=\tau_2+\tau_1$. The remaining terms represent the *secondary echoes* occurring, respectively, at $t=2(\tau_2-\tau_1)$, $2\tau_2-\tau_1$, $2\tau_2$. Our results agree again with those of Hahn [reference 1, Eqs. (22-A) to (22-D)] for the positions, trigonometric dependence on ξ, and damping due to natural relaxation processes. But there appears again a discrepancy in the diffusion damping terms. We tabulate in Table III our results, together with those of Hahn for comparison.

DISCUSSION

The physical picture explaining the mechanism of formation of the various echoes has been given in great detail by Hahn.[1] We shall here confine ourselves mainly to a discussion on the origin and magnitude of the discrepancies between Hahn's diffusion terms and ours.

The origin of the discrepancy is in the different procedures used for averaging over ϕ and η. Hahn applies the averaging procedure for η merely to the W term as indicated in his Eq. (14). For the U and V terms [see reference 1, Eq. (11-A)], he collects the phase difference accumulated in the interval $t-t''$, *viz.*, $\phi(t)-\phi(t'')$, and in the term $\exp[i\{\phi(t)-\phi(t'')\}]$ he applies the averaging procedure to $\phi(t)$, regarding $\phi(t'')$ as a constant and with $\phi(t)$ now representing the phase difference accumulated in the interval from t to the start. Our method, on the other hand, is somewhat different. In our procedure terms like $\phi(t)$ and $\phi(t'')$, by themselves, have no meaning; only terms like $\phi_{tt''}$, representing the phase difference accumulated by diffusion in the interval t to t'', are important. This is because, as mentioned before, we divide the entire interval of application of pulses, into successive free precession intervals. Starting with a single isochromatic group characterized by $\Delta\omega$, we take account both of the entire Larmor frequency shifts for calculations of U, V, and W, and the phase differences that U and V undergo in the successive intervals, applying suitable distribution functions for these (given in appendix); ultimately, at the position of formation of the echoes, as in Eqs. (18) and (23),

TABLE III. Our diffusion damping terms for the secondary echoes, compared with those of Hahn.

		Hahn's results		Our results	
Term	Position of echo maximum	Value of the diffusion term	Value of the diffusion term at echo maximum	Value of the diffusion term	Value of the diffusion term at echo maximum
Stimulated echo	$\tau_2+\tau_1$	$-\frac{1}{3}k[\tau_1^3+(t-\tau_2)^3+3\tau_1^2(\tau_2-\tau_1)]$	$-\frac{1}{3}k(3\tau_1^2\tau_2-\tau_1^3)$	$-\frac{1}{3}k[(t-\tau_2)^3+\tau_1^3+3\tau_1(t-\tau_2)^2+3(\tau_2-\tau_1)(t-\tau_2)^2]$	$-\frac{1}{3}k(3\tau_1^2\tau_2+2\tau_1^3)$
First secondary echo	$2\tau_2-2\tau_1$	$-\frac{1}{3}kt^3$	$-(8k/3)[\tau_2^3-3\tau_2^2\tau_1+3\tau_1^2\tau_2-\tau_1^3]$	$-\frac{1}{3}k[(t-\tau_2)^3+(\tau_2-\tau_1)^3+\tau_1^3+3\tau_1(t-2\tau_2+\tau_1)^2+3(\tau_2-\tau_1)(t-\tau_2)^2]$	$-\frac{1}{3}k[5\tau_2^3-23\tau_1^3+39\tau_1^2\tau_2-29\tau_1\tau_2^2]$
Second secondary echo	$2\tau_2-\tau_1$	$-\frac{1}{3}k(t-\tau_1)^3$	$-(8k/3)(\tau_2-\tau_1)^3$	$-\frac{1}{3}k[(t-\tau_2)^3+(\tau_2-\tau_1)^3+3(\tau_2-\tau_1)(t-\tau_2)^2+3\tau_1(t-2\tau_2+\tau_1)^2]$	$-\frac{1}{3}k[5(\tau_2-\tau_1)^3]$
Third secondary echo	$2\tau_2$	$-\frac{1}{3}kt^3$	$-(8k/3)\tau_2^3$	$-\frac{1}{3}k[(t-\tau_2)^3+\tau_1^3+(\tau_2-\tau_1)^3+3(\tau_2-\tau_1)(t-\tau_2)^2+3\tau_1(t-2\tau_2+\tau_1)^2]$	$-\frac{1}{3}k[5\tau_2^3-6\tau_1\tau_2^2+3\tau_1^2\tau_2+3\tau_1^3]$

we average over the entire frequency shift and phase difference accumulated. This procedure has been accepted by Dr. Hahn as more rigorous.[5]

The magnitude of the discrepancies is apparently serious, when we consider the expressions for any general time t. But we must remember that the damping of the echoes is primarily determined by T_2^*, which is usually very short, so that we have to evaluate these expressions by taking the values of t near the echo maxima. The discrepancy now appears less serious, and the qualitative dependence pointed out by Hahn, *viz.*, that the stimulated echo is much less damped than the others, is also clearly borne out, as the stimulated echo only involves τ_2 and the others involve τ_2^3. For the special condition of experiment, *viz.*, $\tau_2 \gg \tau_1$ (in fact in his experiment for measuring the damping of the stimulated echo, Hahn uses $\tau_2/\tau_1 \approx 50$), we get the diffusion term for the stimulated echo by both Hahn's method and our method to be $\exp(k\tau_1^2\tau_2)$. Thus. the experimental result, *viz.*, the linear dependence of the diffusion damping of the stimulated echo on τ_1^2 (see Fig. 8 of reference 1), also receives support from our calculations.

However, a uniform discrepancy appears in the damping effect because of diffusion for the other terms. For $\tau_2 \gg \tau_1$, Hahn's treatment gives $\exp[-(8/3)k\tau_2^3]$ for all the other secondary echoes, while ours gives $\exp[-(5/3)k\tau_2^3]$. An exactly similar discrepancy occurs in the primary echo. Unfortunately, Hahn has published no exact quantitative measurements on the damping effect due to diffusion of the other echoes. Of course, this numerical coefficient is quite unimportant in measurements of k, and therefore of γ, G, and D by comparison methods, but we feel that the above analysis puts the interpretation of the echoes on a firmer footing.

We are grateful to Dr. E. L. Hahn for pointing out to us that Carr[6] has arrived at results in agreement with ours for the primary echo. We have not yet had the opportunity to procure a copy of Carr's work. The authors are indebted to Professor M. N. Saha for his constant interest during the progress of the work.

APPENDIX

The distribution functions $P[\phi_{tt''}, t-t'']$ may be evaluated as follows. If we assume that there is a field gradient G outwards from the center of the magnet, then if $\Delta\omega(t'')$ refers to the start of the self-diffusion process, then at instant t''' we shall have in its place, $\Delta\omega(t'')+\gamma G[l(t''')-l(t'')]=\Delta\omega(t'')+\gamma G l_{t'''t''}$, where $l_{t'''t''}$ represents the displacement in the direction of the field-gradient $t'''-t''$ (because the change in field involved in the diffusion process $=G[l(t''')-l(t'')]$). Therefore,

$$\eta_{t'''t''}=\gamma G l_{t'''t''},$$

and

$$\phi_{tt''}=\gamma G\int_{t''}^{t} l_{t'''t''}dt'''; \tag{25}$$

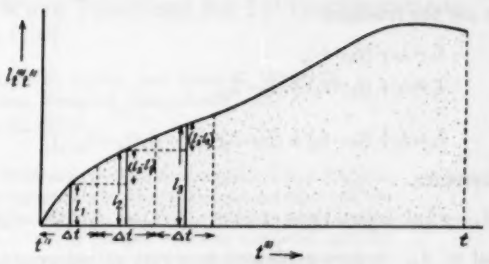

FIG. 2. Area covered in the $l-t$ plane.

i.e., $\phi_{tt''}$ depends on the area covered by the $l_{t'''t''}$ *versus* t''' curve. Now, the distribution in $l_{t'''t''}$ is well known to be given by the expression

$$P[l(t'''), t'''; l(t''), t''] = \frac{1}{[4\pi D(t'''-t'')]^{\frac{1}{2}}}\exp\left[-\frac{l_{t'''t''}^2}{4D(t'''-t'')}\right], \tag{26}$$

D referring to the coefficient of self-diffusion. Therefore, mean square value of $l_{t'''t''}$ is given by

$$\langle l_{t'''t''}^2\rangle_{\text{Av}} = \int_0^\infty\int_0^\pi\int_0^{2\pi} \frac{1}{[4\pi D(t'''-t'')]^{\frac{1}{2}}} \times\exp\left[-\frac{l^2}{4D(t'''-t'')}\right] l^2\sin\theta\, dl\, d\theta\, d\phi$$

$$=6D(t'''-t'').$$

As we are interested in only the component of the displacement along the field gradient direction,

$$\langle l_{t'''t''}^2\rangle_{\text{Av}} = (6D/3)(t'''-t'') = 2D(t'''-t''). \tag{27}$$

Now, to get the distribution in ϕ, we have to find the root-mean-square value of $\phi_{t'''t''}$, which we denote by $(\langle\phi_{tt''}^2\rangle_{\text{Av}})^{\frac{1}{2}}$; this depends on the shaded area in Fig. 2. We have to find the mean square value of this shaded area $A_{tt''}$. To do so, we divide the time interval $t-t''$ into n equal parts Δt, where

$$n\Delta t = t-t'',$$

so that if $n\to\infty$, then $\Delta t\to 0$. We evidently have from Fig. 2,

$$A_{tt''}=l_1\Delta t+l_2\Delta t+\cdots+l_n\Delta t.$$

Now, l_1 and l_2 are not independent quantities, because

$$l_2=l_1+\Delta l,$$

where Δl refers to the displacement in the interval between Δt and $2\Delta t$, but Δl is itself independent of l_1 and l_2. So, to get $A_{tt''}$ as a sum of independent quantities,

[5] E. L. Hahn (private communication).
[6] H. Carr, thesis, Harvard University, 1952 (unpublished).

we use the relations

$$l_2=l_1+(l_2-l_1),$$
$$l_3=l_1+(l_2-l_1)+(l_3-l_2),$$
$$\cdots\cdots\cdots\cdots\cdots\cdots$$
$$l_n=l_1+(l_2-l_1)+(l_3-l_2)+\cdots+(l_n-l_{n-1}).$$

Therefore,

$$A_{tt'}=[nl_1+(n-1)(l_2-l_1)+\cdots+(l_n-l_{n-1})]\Delta t, \quad (28)$$

and so $A_{tt'}$ is now expressed as a sum of independent quantities. Hence, by the standard deviation theorem,[7]

$$\langle A_{tt'}{}^2\rangle_{Av}=[\langle l_1{}^2\rangle_{Av}n^2+\langle(l_2-l_1)^2\rangle_{Av}(n-1)^2+\cdots+\langle(l_n-l_{n-1})^2\rangle_{Av}](\Delta t)^2.$$

As l_1, l_2-l_1, $\cdots$ all occur in the same time Δt, we have, from (27),

$$\langle l_1{}^2\rangle_{Av}=\langle(l_2-l_1)^2\rangle_{Av}=\cdots=\langle(l_n-l_{n-1})^2\rangle_{Av}=2D\Delta t.$$

Therefore,

$$\begin{aligned}\langle A_{tt'}{}^2\rangle_{Av}&=2D\Delta t[1^2+2^2+\cdots+n^2]\\&=2D(\Delta t)^3n(n+1)(2n+1)/6\\&\approx\tfrac{2}{3}D(\Delta t)^3n^3\\&\approx\tfrac{2}{3}D(t-t'')^3,\end{aligned} \quad (29)$$

remembering that n is large. Therefore,

$$\begin{aligned}\langle\phi_{tt'}{}^2\rangle_{Av}&=\gamma^2G^2\langle A_{tt'}{}^2\rangle_{Av}\\&=\tfrac{2}{3}(\gamma G)^2D(t-t'')^3=\tfrac{2}{3}k(t-t'')^3,\end{aligned} \quad (30)$$

where $k=(\gamma G)^2D$. Hence, assuming a Gaussian distribution for $\phi_{tt'}$ also, we have

$$\begin{aligned}P(\phi_{tt'},t-t'')&=\frac{1}{(2\pi\langle\phi_{tt'}{}^2\rangle_{Av})^{\frac{1}{2}}}\exp\left[\frac{-\phi_{tt'}{}^2}{2\langle\phi_{tt'}{}^2\rangle_{Av}}\right]\\&=\left(\frac{3}{4\pi k(t-t'')^3}\right)^{\frac{1}{2}}\exp\left[-\frac{3\phi_{tt'}{}^2}{4k(t-t'')^3}\right].\end{aligned} \quad (31)$$

Further, we need the distribution function in $\eta_{tt'}$. From Eq. (25), we have

$$\begin{aligned}\langle\eta_{tt'}{}^2\rangle_{Av}&=(\gamma G)^2\langle l_{tt'}{}^2\rangle_{Av}\\&=2(\gamma G)^2D(t-t'')=2k(t-t'').\end{aligned} \quad (32)$$

Hence, assuming a Gaussian distribution in $\eta_{tt'}$, we have

$$\begin{aligned}P[\eta_{tt'},t-t'']&=\frac{1}{(2\pi\langle\eta_{tt'}{}^2\rangle_{Av})^{\frac{1}{2}}}\exp\left[-\frac{\eta_{tt'}{}^2}{2\langle\eta_{tt'}{}^2\rangle_{Av}}\right]\\&=\frac{1}{[4\pi k(t-t'')]^{\frac{1}{2}}}\exp\left[-\frac{\eta_{tt'}{}^2}{4k(t-t'')}\right].\end{aligned} \quad (33)$$

Using these distribution functions for $P[\phi_{tt'},t-t'']$ and $P[\eta_{tt'},t-t'']$, we can evaluate the various integrals over ϕ and η involved in (18) and (23), making suitable substitutions for t and t''. For these integrations as well as those over $\Delta\omega$ we need the standard integrals:

$$\begin{aligned}&\int_{-\infty}^{\infty}\cos ax\exp(-b^2x^2)dx=\frac{\sqrt{\pi}}{b}\exp\left(-\frac{a^2}{4b^2}\right),\\&\int_{-\infty}^{\infty}\sin ax\exp(-b^2x^2)dx=0.\end{aligned} \quad (34)$$

[7] See James V. Uspensky, *Introduction to Mathematical Probability* (McGraw-Hill Book Company, Inc., New York, 1937), p. 270.

A Discussion of Analytic and Hartree-Fock Wave Functions for $1s^2$ Configurations from H^- to C V†

LOUIS C. GREEN, MARJORIE M. MULDER, MARGARET N. LEWIS, AND JOHN W. WOLL, JR.
Strawbridge Observatory, Haverford College, Haverford, Pennsylvania

(Received October 30, 1953)

Two simple analytic expressions are presented, both of which are excellent approximations to a Hartree-Fock $1s$ wave function in a $1s^2$ configuration. One of these expressions is a two-parameter function and the other a three-parameter one. The parameters were chosen variationally and their values are given for the various members of the isoelectronic sequence from H^- to C V. The energies were also computed, and the energies and the wave functions are compared with the corresponding Hartree-Fock quantities where the latter are known. Both the two- and the three-parameter functions approximate the numerical functions closely and give energies as low, or almost as low, as the more reliable of the Hartree-Fock energies. The three-parameter wave function proves to be the better, particularly in the case of H^-. Some comments are made on the existing numerical functions and their energies.

ANALYTIC expressions which are approximations to the one-electron wave functions for the different atoms and ions have proved to have a variety of applications in physical, astrophysical, and chemical problems. Usually these expressions have been found by choosing the values of certain parameters either variationally or so that the expressions will approximate existing Hartree or Hartree-Fock numerical functions. Morse, Young, and Haurwitz[1] determined variationally the values of the parameters in determinants of one-electron wave functions for various configurations involving $1s$, $2s$, and $2p$ electrons. This work was extended by Goldberg and Clogston[2] to include the $3p$ and $3d$ electrons. Improved results have been given by Duncanson and Coulson.[3] Approaching the problem in the second of the ways mentioned above, Slater[4] showed that it was possible to obtain a good approximation to the Hartree functions by using a sum of terms of the form $c_k r^n e^{-\alpha_k r}$. Recently Löwdin[5] has fitted a number of Hartree-Fock numerical functions very closely by using slightly more generalized sums of functions of the Slater type than those originally employed by Slater himself. Löwdin has also shown that when the values of the parameters have been determined for a few atoms, one may interpolate, and even extrapolate, to neighboring atoms with considerable accuracy. The present work deals in some detail with two simple analytic expressions for the Hartree-Fock function of a $1s$ electron in a $1s^2$ configuration. For both expressions the values of the parameters have been chosen variationally. One of the expressions used is of the Löwdin form. The interest in these functions arises from the low energies which they give and the closeness with which they reproduce the numerical functions.

The present investigation was begun when, in the course of some work on correlation energies in the ground states of H^-, He I, and Li II,[6] it became desirable to have the Hartree-Fock wave function, or a close approximation to it, for the ground state of H^-. Since the Hartree-Fock wave function itself was not available, it was decided to try a simple analytic function as an approximation. In the end two analytic wave functions of somewhat different type were tried. The first was a two-parameter function and the second a three-parameter one. The parameters were chosen to give the minimum energy. To obtain some idea of the accuracy of these functions for H^-, the corresponding functions were determined for the ground states of all the members of the isoelectronic sequence from He I through C V. These wave functions were then compared directly, and by way of the energy which they yielded, with the Hartree-Fock wave functions where the latter were known. The similarity of the analytic wave functions to the numerical ones proved to be surprisingly close. Since such functions have a variety of uses, it seemed wise to discuss them separately from the work on correlation energies. In particular, $1s$ functions of the present type could be obtained readily for any of the elements and might serve as excellent first or second approximations from which to start the regular Hartree-Fock calculations.

Other work by two of us on He I[7] suggested that a two-parameter function of the form

$$R^N(r)=Nre^{-Zr}(1+cZ^2r^2)=Nre^{-Zr}(1+kr^2) \quad (1)$$

should give a good representation of the radial part of the Hartree-Fock wave function for a $1s$ electron in a $1s^2$ configuration. The normalized ground-state wave function is then

$$\Psi^N=\frac{1}{4\pi}\frac{1}{r_1}R^N(r_1)\frac{1}{r_2}R^N(r_2). \quad (2)$$

† This research was supported in part by the United States Air Force under a contract monitored by the Office of Scientific Research, Air Research and Development Command. This contract was administered by the University of Pennsylvania.

[1] Morse, Young, and Haurwitz, Phys. Rev. 48, 948 (1935).
[2] L. Goldberg and A. M. Clogston, Phys. Rev. 56, 696 (1939).
[3] W. E. Duncanson and C. A. Coulson, Proc. Roy. Soc. (Edinburgh) 62, 37 (1944); Nature 164, 1003 (1949).
[4] J. C. Slater, Phys. Rev. 42, 33 (1932).
[5] P. O. Löwdin, Phys. Rev. 90, 120 (1953).
[6] Green, Lewis, Mulder, Wyeth, and Woll, Phys. Rev. 93, 273 (1954).
[7] L. C. Green and M. M. Mulder (unpublished).

TABLE I. Values of the constants in the 2-parameter function, Eq. (1), which give the lowest ground-state energies.

	Z	c	k	N
H^-	0.892171	0.0885	0.07044	1.289902
He I	1.986653	0.0550	0.2171	4.736406
Li II	2.960529	0.0322$_8$	0.2827	9.235412
Be III	3.932785	0.0214	0.3310	14.61756
B IV	4.918830	0.0160	0.3871	20.78640
C V	5.910933	0.0128	0.4472	27.65059

Equation (2) was substituted into the energy integral and the values of the parameters c and Z giving the lowest energy were obtained. The results are given in Table I. In the first column is given the atom and its state of ionization. In the second and third columns are listed the values of the parameters in the first form of the function given in Eq. (1) which yield the minimum energy for the $1s^2$ configuration. In column four is the value of the product $k=cZ^2$ for use in the second form of the function. Column five gives the normalization constant. In determining the values of the parameters, values of k were chosen, and the energy expression for each k was then minimized with respect to Z. From a table of k *versus* the energy, the particular k which gave the lowest energy to five decimals was selected. This k and the corresponding Z are given in Table I.

The values of the constants in Table I have been used to compute the energies of the various $1s^2$ configurations and to compare the radial part of the wave function given by Eq. (1) with the numerical Hartree-Fock function. These results and the energies given by a one-parameter function, the simple exponential

$$R^N(r)=2Z^{\frac{1}{2}}re^{-Zr}, \tag{3}$$

the Hartree-Fock energies, and the energies found from experiment are given in Table II. All of the energies given in Table II are expressed in units of hc times the Rydberg constant for the particular element. In the second column is given the energy for the $1s^2$ configuration as found from the simple exponential, Eq. (3). In the third column is the energy found from the two-parameter function, Eq. (1). In the fourth column is the Hartree-Fock energy as given by various authors, or as computed from their data. The Hartree-Fock energy for He I is taken from Wilson.[8] The energy for Li II is taken from Fock and Petrashen.[9] For Be III the $F_0(1s1s)$ integral[10] was computed from the $1s$ wave function given by Hartree.[11] This integral together with the $1s$ eigenvalue given by Hartree[11] yielded the energy given in Table II. The same procedure was followed for C V using the wave function and eigenvalue given by Jucys.[12] In the fifth column of Table II is the experimental energy[13] for the various atoms with the exception of H^-. For H^- the experimental energy is not very accurately known. Therefore in this case Table II gives the theoretical value as determined by Henrich[14] from an eleven-parameter function involving powers of the interelectron distance r_{12}. Finally, in the sixth column is given the integral of the square of the difference between the Hartree-Fock function and the two-parameter function. The wave function used for He I was taken from Wilson and Lindsay.[15]

A number of comments must now be made about the figures in Table II. First, one notes that both the one- and the two-parameter functions give lower energies for Li II than that quoted for the Hartree-Fock function. The Hartree-Fock function, however, should give the lowest energy obtainable. For the $1s^2$ configuration the Hartree-Fock solution reduces to a single product of the form given in Eq. (2) and therefore becomes identical with the ordinary Hartree solution. In the trial form of this solution, the function R is arbitrary except for certain very general requirements placed on all wave functions. The form of R is then chosen to give the lowest energy. Since the one- and two-parameter functions are only a subclass of the class of all functions R, the minimum energy obtainable from them cannot be lower than the minimum obtainable from the functions R. Furthermore, it is improbable that there is any error in the energies of the one- or two-parameter functions because the differences of these energies from one another and from the experimental energies run so smoothly, with the possible exception of H^-, which is discussed below. The value given for the Hartree-Fock energy is, therefore, too high. This situation could be the result of an error in the published energy, or it could arise if the wave function were not a very precise self-consistent field solution. Several arguments suggest that the former is the case. In the first place, the numerical wave function is very similar to the two-parameter function, as indicated by the small size of the integral of the square of their difference. The numerical function is even more similar to the better three-parameter wave function described below. One may compute the difference ΔE between the energy E_{HF}, given by the Hartree-Fock $1s$ function $R_{HF}{}^N$, and the energy E_A, given by one of

[8] W. S. Wilson, Phys. Rev. **48**, 536 (1935).
[9] V. Fock and M. J. Petrashen, Physik. Z. Sowjetunion **8**, 547 (1935).
[10] D. R. Hartree and W. Hartree, Proc. Roy. Soc. (London) **A156**, 45 (1936).
[11] D. R. Hartree and W. Hartree, Proc. Roy. Soc. (London) **A149**, 210 (1935).
[12] A. Jucys, Proc. Roy. Soc. (London) **A173**, 59 (1939).
[13] The values of the ionization energies and Rydberg constants were taken from Charlotte E. Moore, *Atomic Energy Levels*, National Bureau of Standards Circular 467 (U. S. Government Printing Office, Washington, D. C., 1949).
[14] L. R. Henrich, Astrophys. J. **99**, 59 (1944).
[15] W. S. Wilson and R. B. Lindsay, Phys. Rev. **47**, 681 (1935). The authors wish to thank Professor Lindsay for supplying them with the wave function to one more figure and at half the interval of the published values.

TABLE II. Comparison of the 2-parameter functions and energies with those of the Hartree-Fock solutions.

	Energies				
	1-param.	2-param.	Hartree-Fock	Exp.	$\int_0^\infty (R_{HF}{}^N - R_{2-p}{}^N)^2 dr$
H^-	− 0.94531	− 0.96534		− 1.05512[a]	
He I	− 5.69531	− 5.72294	− 5.723[b]	− 5.80752	0.000100[c]
Li II	−14.44531	−14.47242	−14.42[d]	−14.56079	0.000012[d]
Be III	−27.19531	−27.22160	−27.245[e]	−27.31443	0.000024[e]
B IV	−43.94531	−43.97104		−44.07130	
C V	−64.69531	−64.72065	−64.967[f]	−64.83415	0.000021[f]

[a] Lowest theoretical value, see reference 14.
[b] See reference 8.
[c] See reference 15.
[d] See reference 9. This is the value given in the original paper. It is clearly too high; see discussion which follows.
[e] Computed from the data in reference 11.
[f] Computed from the data in reference 12. The value is impossibly low; see discussion which follows.

the analytic $1s$ functions, $R_A{}^N$:

$$\Delta E=\frac{1}{16\pi^2}\left\{\int (R_{HF}{}^N R_{HF}{}^N)^* H(R_{HF}{}^N R_{HF}{}^N)d\tau - \int (R_A{}^N R_A{}^N)^* H(R_A{}^N R_A{}^N)d\tau\right\}.$$

The difference of these two integrals may be estimated by writing $R_{HF}{}^N=R_A{}^N+\Delta R$, making use of the Hermitian character of H, and dropping all terms in the integrand involving more than the first power of ΔR. We then have

$$\Delta E\approx 4E_{HF}\int_0^\infty R_{HF}{}^N \Delta R d\tau \approx 4E_A\int_0^\infty R_A{}^N \Delta R dr. \quad (4)$$

The value of ΔE estimated from Eq. (4) is 0.00 whether one uses the two-parameter function or the three-parameter function for $R_A{}^N$. Since both of these functions yield $-14.47R_yhc$ for the energy, it seems probable that the energy associated with this numerical function is approximately 0.05 lower than the value given in Table II. As an additional argument it should be pointed out that Löwdin has used the Li II $1s$ function given by Fock and Petrashen as one of those from which he interpolated and extrapolated the wave functions for neighboring systems with excellent results. In conclusion, it would seem that the wave function given by Fock and Petrashen is an acceptable Hartree-Fock solution but that their published value for the energy is incorrect.

For C V the difference between the computed Hartree-Fock energy and the experimental energy is out of line with that which is found for the other atoms. Indeed, the computed energy is lower than the experimental. It is well known, however, that no approximate solution of the Schrödinger equation can give a lower energy than that yielded by the exact solution. On the other hand, one should be careful about identifying the experimental energy with the energy of an exact solution, since the Schrödinger equation which is dealt with here is not the true Schrödinger equation of the problem because it does not include relativistic effects. However, such effects should be small, and the experimental energy must therefore be very close to the energy which would be obtained from an exact solution of the Schrödinger equation considered. It appears, therefore, that the Hartree-Fock energy for C V given in Table II is probably in error. An alternative possibility would be that the experimental energy is in error. However, the estimated uncertainty in the experimental energy[13] amounts to only 1 percent of the change which would be necessary in the experimental value if the difference between the computed and experimental values for C V were to be brought into line with that for the other atoms. Another possibility would be that an error was made by the present authors in their computation of $F_0(1s1s)$, which is not given by Jucys but which is necessary for a determination of the energy. However, the values of this quantity as found using Jucys' numerical wave function and as found from the present two-parameter analytic wave function differ by only $0.010R_yhc$. It would therefore seem that there is an error in the published eigenvalue for the $1s$ function of CV. This eigenvalue cannot be associated with the given wave function, which itself seems to be all right. The similarity of the Hartree-Fock wave function for CV to the two- and three-parameter functions suggests that this wave function is of equal accuracy with those for other atoms.

In view of the errors in the Hartree-Fock energies for Li II and C V, which have just been discussed, any evaluation of the success of the two-parameter function as an approximate representation of the Hartree-Fock functions should be based on the energies which it yields for He I and Be III and on the values of the integrals given in the final column of Table II. Judged on the basis of the energies, the two-parameter function is remarkably good. In the case of He I it yields the same energy as the Hartree-Fock solution to four figures, and in the case of Be III the difference is only 0.09 percent. The wave functions themselves may be compared in a variety of ways. The integral of the square of the difference of the functions, which appears in the last column of Table II, is one such comparison. As a better measure of the similarity of the functions,

one may define the "root-mean-square difference":

$$\bar{\Delta}=\left\{\frac{1}{l}\int_0^{\infty}(R_{HF}{}^N-R_A{}^N)^2dr\right\}^{\frac{1}{2}}. \tag{5}$$

Here $R_{HF}{}^N$ is the normalized Hartree-Fock function, $R_A{}^N$ is the normalized analytic wave function, and l is the range of r in which either function differs from zero by as much as 0.001. With this definition the root-mean-square difference for He I is found to be 0.0038. It is interesting to note also that the maximum difference between the two functions in the case of He I is 0.0071. The corresponding quantities for Li II are 0.0016 and 0.0032, for Be III 0.003 and 0.005, and for C V 0.003 and 0.006.

If one subtracts the experimental energies in Table II from the energies given by the two-parameter function, one obtains a quantity which has a minimum at He I. Since the present work was begun in the hope of obtaining a good analytic approximation to the Hartree-Fock wave function for H^-, it seemed unfortunate that the two-parameter function yielded an energy farther from the experimental value in the case of H^- than for either He I or Li II. However, in view of the general excellence of the two-parameter function of Eq. (1), it seemed possible that some closely related function might do as well or better. Perhaps the two most obvious functions to try might be considered to be

$$R^N(r)=Nre^{-Zr}(1+cZr) \tag{6}$$

and

$$R^N(r)=Nre^{-Zr}(1+cZ^3r^3). \tag{7}$$

However, one can show that for the range of nuclear charges considered here, the lowest energies obtainable with Eq. (6) are given by $c=0$; that is, they are identical with those found from the simple exponential of Eq. (3). Attention was therefore turned to Eq. (7). In this case the energies from He I through C V were found to be from 0.006 to 0.008 above those found using Eq. (1). On the other hand, for H^- with $Z=0.868183$, $c=0.0219$, and $N=1.330082$, the energy was found to be $-0.97391R_yhc$. This value is an improvement of -0.00857 or about 1 percent over that found from Eq. (1).

At this point it seemed worth while to try to determine whether a still lower energy and a closer fit to the Hartree-Fock function might not be obtained with a three-parameter function of the form

$$R^N(r)=Nr(e^{-Zr}+ce^{-kZr}). \tag{8}$$

A function of this type was used by Löwdin[8] to fit the Hartree-Fock 1s functions for Li II and C V. When he had found the values of the parameters giving the best fit, he interpolated and extrapolated these parameters to obtain values to be used for H^-, He I, Be III, B IV, N VI, and O VII. He was able to represent the normalized Li II and C V functions with maximum errors below $1.0\cdot10^{-3}$, and his interpolated Be III function was equally good. Excellent as these results were, it nevertheless seemed that it would be desirable to choose the parameters in Eq. (8) by the minimum principle. This was particularly to the point in the case of H^-, for which Löwdin extrapolated two steps. The expression for the energy E of the ground state of an ion of nuclear charge A in terms of the parameters in Eq. (8) was found to be

$$E=Zf_4^{-1}\{f_1Z+f_2A+f_3f_4^{-1}\}, \tag{9}$$

where

$$f_1=\frac{1}{2}\left\{1+\frac{16k}{(1+k)^3}c+\frac{1}{k^3}c^2\right\},$$

$$f_2=-\left\{1+\frac{8}{(1+k)^2}c+\frac{1}{k^2}c\right\},$$

$$f_3=\frac{1}{64}\left\{5+256\frac{11+8k+k^2}{(1+k)^2(3+k)^3}c+16\frac{1+5k+48k^2+5k^3+k^4}{k^2(1+k)^5}c^2+256\frac{1+8k+11k^2}{k^3(1+k)^2(1+3k)^3}c^3+5\frac{1}{k^5}c^4\right\},$$

$$f_4=\frac{1}{4}\left\{1+\frac{16}{(1+k)^3}c+\frac{1}{k^3}c^2\right\},$$

and E is given in units of hc times the Rydberg constant for the particular element. The relation of the normalization constant N to the parameters of the wave function is given by the expression $N^2=Z^3f_4^{-1}$. The results of minimizing E are given in Table III. In the second, third, and fourth columns are given the values of the parameters in Eq. (8) which yield the minimum energy for the $1s^2$ configuration, and in column five is given the associated normalization constant. In determining the values of the parameters, values of c and k were chosen, and the energy expression for each pair of values was then minimized with respect to Z. From a table of the energy *versus* c and k, the particular pair of values of c and k giving the lowest energy to five decimals was selected. This pair of values together with the corresponding Z is given in Table III.

A comparison of the quantities in Table III with the corresponding figures computed from Löwdin's results

TABLE III. Values of the constants in the 3-parameter function, Eq. (8), which give the lowest ground-state energies.

	Z	k	c	N
H^-	0.461519	2.63	2.04	0.453593
He I	1.455799	2.00	0.60	2.968466
Li II	2.448599	1.87	0.36	6.817469
Be III	3.444520	1.81	0.258	11.68495
B IV	4.442959	1.78	0.200	17.42020
C V	5.440003	1.75$_5$	0.165	23.85844

TABLE IV. Comparison of the 3-parameter functions and energies with those of the Hartree-Fock solutions.

	Energies			$\int_0^\infty (R_{HF}{}^N - R_{3-P}{}^N)^2 dr$
	Löwdin	3-param.	Hartree-Fock	
H^-	− 0.97236	− 0.97565		
He I	− 5.72305	− 5.72334	− 5.723[a]	298 ×10⁻⁸ [b]
Li II	−14.47274	−14.47280		172 ×10⁻⁸
Be III	−27.22257	−27.22260	−27.245[c]	22.2×10⁻⁸
B IV	−43.97224	−43.97246		
C V	−64.72157	−64.72238		707 ×10⁻⁸

[a] See reference 8.
[b] See reference 15.
[c] Computed from the data in reference 11.

shows that the difference decreases with increasing atomic number, the decrease being more rapid for the smaller nuclear charges. Thus the differences in Z, k, and c for H^- are, respectively, 8 percent, 12 percent, and 63 percent of the values in Table III. For Li II the corresponding numbers are 0.6 percent, 3 percent, and 7 percent, and for C V −0.2 percent, −0.3 percent, and 2 percent.

The values of the constants in Table III have been used to compute the energies of the various $1s^2$ configurations and to compare the radial part of the wave functions given by Eq. (8) with the numerical Hartree-Fock functions. For the sake of further comparison, energies computed from Löwdin's values of the parameters in Eq. (8) are included, as are the Hartree-Fock energies for He I and Be III. All of the energies given in Table IV are expressed in units of hc times the Rydberg constant for the particular element. In the second column is given the energy of the $1s^2$ configuration as found from Löwdin's values of the parameters in Eq. (8). In the third column is the energy found from the values of the parameters listed in Table III. In the fourth column is given the Hartree-Fock energy for the two cases in which these energies are thought to be reliable (see the discussion following Table II above). In the fifth column is given the integral of the square of the difference between the Hartree-Fock function and the three-parameter function.

One sees at once that the energies yielded by the three-parameter function are lower than any of the corresponding values given by the two-parameter function. The improvement is small but definite, about 0.004 percent, except in the case of H^-, for which the improvement is about 1 percent relative to the two-parameter function of Eq. (1) and about 0.2 percent relative to the function of Eq. (7). Furthermore, the functional form of the three-parameter expression appears to be such that it approximates the Hartree-Fock function much more closely than does the two-parameter expression. One may again take the "root-mean-square difference," $\bar{\Delta}$, as defined in Eq. (5), as a measure of the similarity of the two functions. For He I, $\bar{\Delta}$ so defined proves to be 0.0006, and the maximum difference between the two functions is 0.0012. The corresponding quantities for Li II are 0.0006 and 0.0011, for Be III 0.0003 and 0.0008, and for C V 0.002 and 0.005. In the average, therefore, the three-parameter function gives a five-fold improvement over the two-parameter function as a representation of the Hartree-Fock function.

It is interesting to note that in the case of Be III the root-mean-square difference is just what it would be if we assumed a random rounding error in the third and last decimal place of the wave function which Hartree gives.[11] One should say, however, that the signs of the differences do not seem to be random in character. The analytic function tends to be the smaller for $r<0.70$ atomic units, and the reverse is the case for larger r. In view of the close similarity of the numerical and the analytic wave functions for Be III, the question arises as to the reality of the difference of −0.022 in their energies as listed in Table IV. Since the difference of the two functions is of the order of that to be expected from rounding error, and since, in view of the size of the function, rounding in the third decimal place can only increase the average magnitude of the differences, an estimate of the energy difference from Eq. (4) should yield an upper limit to this quantity. The value of ΔE found from Eq. (4) was −0.012, about 50 percent of the difference of the tabulated values. Since it is a relatively simple matter to obtain the minimum energy for the three-parameter function from Eq. (8), this result with regard to the size of ΔE would suggest that there might be a small error in the Hartree-Fock energy for the ground state of Be III as given in Tables II and IV. Since the values of $F_0(1s1s)$ as computed from the numerical and the analytic functions agree to 3 in the fourth decimal, the error, if any, would have to be in the eigenvalue of the $1s$ wave function.

Finally, the run of the differences between the Hartree-Fock and the analytic functions as one passes from He I to Li II to Be III suggests that the differences found for C V are too large. If once again one maintains one's confidence in the correctness of the analytic functions because of the simplicity of their derivation, one is led to believe that the Hartree-Fock wave function for the ground state of C V is slightly less accurate than those for the other atoms.

In summary, the present work describes a two-parameter and a three-parameter function, Eqs. (1) and (8), both of which are excellent approximations to the Hartree-Fock $1s$ wave function in the $1s^2$ configuration. The values of the parameters for the various members of the isoelectronic sequence from H^- to C V are given in Tables I and III. The energies are computed and in Tables II and IV the energies and the wave functions are compared with the corresponding Hartree-Fock quantities where the latter are known. The three-parameter wave function proves to be the better, particularly in the case of H^-. Some comments are made on the existing numerical functions and their energies.

Energy Levels in N^{14} from the Scattering of Protons by C^{13}†

EDMUND A. MILNE
Kellogg Radiation Laboratory, California Institute of Technology, Pasadena, California
(Received November 2, 1953)

The differential cross section for the elastic scattering of protons by C^{13} has been determined in the energy range from 0.45 to 1.60 Mev at angles of 50, 90, 120, 140, and 160 degrees in the center-of-mass system. Marked anomalies were found in the scattering at 0.55, 1.16, 1.47, and 1.55 Mev corresponding to excited states in N^{14} at 8.06, 8.62, 8.90, and 8.98 Mev. The spins and parities of these states have been determined from a preliminary analysis of the data which also indicates an effect due to the broad resonance at 1.25 Mev in $C^{13}(p,\gamma)N^{14}$ corresponding to an excited state in N^{14} at 8.70 Mev. The assignment for the 8.06-Mev level is $J=1^-$, for the 8.62-Mev level $J=0^+$ and for the broad 8.70 Mev level $J=0^-$. The probable assignment for the 8.90-Mev level is $J=3^-$ and for the 8.98-Mev level $J=1^+$.

The elastic scattering of protons by C^{13} was also measured from 300 kev to 550 kev at angles of every ten degrees in the center-of-mass system from 30 to 160 degrees.

I. INTRODUCTION

FIVE levels were reported by Seagrave[1] in the nucleus N^{14} from a study of the excitation curve of the reaction $C^{13}(p,\gamma)N^{14}$. The spins and parities of these states were not completely determined in this experiment nor in the study of the radiative cascade transitions made by Woodbury, Day, and Tollestrup.[2] In order to obtain more information, we have measured the differential cross section for the $C^{13}(p,p)C^{13}$ at several different scattering angles.

Before measuring the $C^{13}(p,p)C^{13}$ differential cross section we measured the $C^{12}(p,p)C^{12}$ differential cross section. In a previous article Jackson and Galonsky[3] reported the results of a partial wave analysis of the differential cross section for the $C^{12}(p,p)C^{12}$ obtained by Goldhaber and Williamson.[4] Their analysis led to values of the resonance energies and widths that differed somewhat from the proton capture data.[1,5,6] In addition, the experimental and calculated scattering cross section could not be brought into agreement below 1 Mev. We have measured the differential cross section for $C^{12}(p,p)C^{12}$ at thirteen different angles from 300 to 600 kev to investigate these discrepancies at the low energy. Jackson *et al.*[7] have more recently remeasured the $C^{12}(p,p)C^{12}$ differential cross section and analyzed[8] their new data; this new measurement has resolved their previous discrepancies.

This paper describes the experiments on the elastic scattering of protons by C^{13} and C^{12} and presents the data obtained. It also discusses the probable assignments of the levels in N^{14} from a preliminary analysis of the data. A more complete theoretical analysis of the $C^{13}(p,p)C^{13}$ data will be presented in a forthcoming paper.

The 2-Mv electrostatic accelerator recently reconstructed at the Kellogg Radiation Laboratory provided a steady source of protons which is maintained homogeneous to better than 0.05 percent by an 80 degree electrostatic analyzer of 1-meter radius and 1-millimeter entrance and exit slits. The target was placed at the "object" position of the 180-degree, double-focusing, magnetic, proton spectrometer described by Snyder *et al.*,[9] It has been remounted so as to allow a continuously variable scattering angle from 0–160 degrees with the incident beam.

The magnetic field of the spectrometer was measured by a null reading magnetometer similar to that described previously.[10] It consisted of a coil carrying a current, measured by a Leeds and Northrup potentiometer, suspended in the magnetic field. The restoring torque which just balanced the torque produced by the field acting on the coil was produced by a quartz fiber. The indicator was a beam of light reflected from a mirror on the coil to a 920 phototube. The signal from the phototube was converted into 60-cycle ac, the phase of which depended on which half of the phototube received the most light and the amplitude depended on the difference of the illumination of the two halves of the phototube. This signal was amplified and then fed into an amplidyne through a phase detector. The field of the spectrometer generator was controlled by the output of the amplidyne. Thus any error of the field was automatically corrected. It was possible to reproduce the magnetic field measurements to an accuracy of better than 0.1 percent over extended periods of time and to regulate the magnetic field to about 0.02 percent for short periods.

A scintillation counter placed at the "image" position of the magnetic spectrometer was used to count the scattered protons. It consisted of a 931-A photomulti-

† Assisted by the joint program of the U. S. Office of Naval Research and U. S. Atomic Energy Commission.

[1] J. D. Seagrave, Phys. Rev. **85**, 197 (1952).
[2] Woodbury, Day, and Tollestrup, Phys. Rev. **92**, 1199 (1953).
[3] H. L. Jackson and A. I. Galonsky, Phys. Rev. **84**, 401 (1951).
[4] G. Goldhaber and R. M. Williamson, Phys. Rev. **82**, 495 (1951).
[5] W. A. Fowler and C. C. Lauritsen, Phys. Rev. **76**, 314 (1949).
[6] D. M. Van Patter, Phys. Rev. **76**, 1264 (1949).
[7] Jackson, Galonsky, Eppling, Hill, Goldberg, and Cameron, Phys. Rev. **89**, 365 (1953).
[8] H. L. Jackson and A. I. Galonsky, Phys. Rev. **89**, 370 (1953).
[9] Snyder, Rubin, Fowler, and Lauritsen, Rev. Sci. Instr. **21**, 852 (1950).
[10] C. C. Lauritsen and T. Lauritsen, Rev. Sci. Instr. **19**, 916 (1948).

plier tube and a scintillating screen prepared by dusting zinc sulfide powder on the end of a Lucite cylinder.

II. EXPERIMENTAL PROCEDURE

The targets used were made by a method developed by Seagrave[1] by cracking C^{13} enriched methyl iodide on a tantalum strip heated to a bright orange. This method was used for making thin targets for the $C^{13}(p,\gamma)N^{14}$ experiments. The targets used in the scattering experiments were made by cracking a thick layer of normal carbon from methane on the heated tantalum strip in order to provide a light element backing, then cracking the C^{13} enriched carbon on top of the normal carbon. This was done in order to conserve the relatively expensive C^{13} enriched methyl iodide. The methyl iodide enriched to 61 percent C^{13} was obtained from Eastman Kodak Company. When the tantalum strip was cooled the carbon layer usually formed a large blister which was then removed from the strip as a foil. One can obtain foils 1 cm×3 cm or larger in this manner. The carbon foils thus obtained were mounted on a copper target blank.

The first targets used for the scattering experiments on C^{12} were made by holding a copper target blank in the flame of benzene until a thick layer of soot was deposited. No difference could be detected in the scattering from the two kinds of targets.

A profile or momentum spectrum curve of the protons scattered by each target was made at a selected energy not near any resonance before using the target for a yield curve to check it for contaminations on the surface.

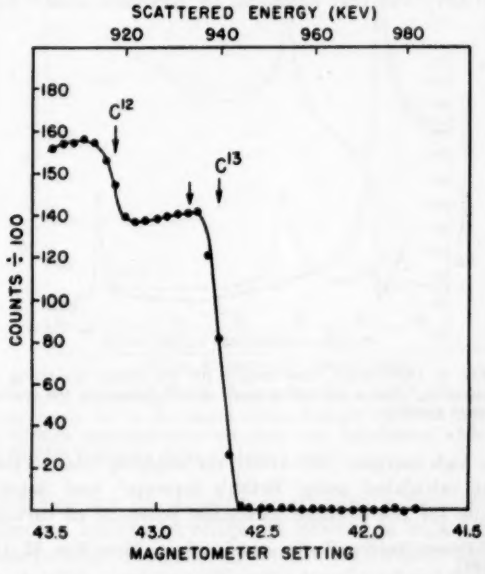

FIG. 1. A profile or $H\rho$ plot for a C^{13} enriched target at a scattering angle of 160 degrees in the center-of-mass system and the proton bombarding voltage of 1272 kev. The arrow indicates the point used for a yield curve.

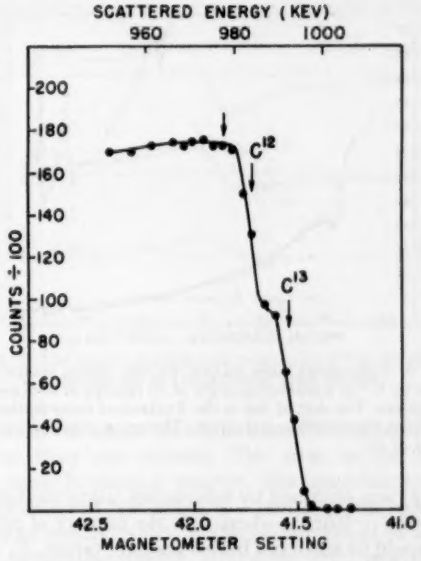

FIG. 2. Profile for a C^{13} enriched target at a scattering angle of 90 degrees in the center-of-mass system and a proton energy of 1150 kev. The separation of the steps from the two isotopes of carbon approaches the resolution of the spectrometer for the slit width employed.

A profile is a curve of the number of counts plotted against the magnetometer setting (inversely proportional to momentum) with the bombarding energy and scattering angle held constant. Figure 1 shows a typical profile at a scattering angle of 160 degrees in the center-of-mass system for $C^{13}(p,p)$. At this angle the protons scattered by the two isotopes differ enough because of the different recoil energy to be easily separated by the spectrometer. Each point of the yield curves at the large scattering angles was taken with the spectrometer field set so as to measure the full number of counts from C^{13} but not to count the protons scattered from C^{12}. Each point represents the scattering by a thin lamina in the thick target which is determined by the energy interval accepted by the spectrometer and the energy loss of the incident and scattered particles in this lamina.

Figure 2 shows another profile at 90 degrees. At this angle the separation of the protons scattered from the two isotopes approaches the resolution of the spectrometer for the slit width employed to give sufficient counts and, hence, the protons scattered from the two isotopes of carbon cannot be separated for the scattering angles of less than 90 degrees. Since the C^{12} and C^{13} scattered protons could not be separated at the small scattering angles the number of counts had to be corrected for the C^{12} present. Both a normal carbon target and C^{13} enriched target were placed on the target backing. The target backing could be raised or lowered so that the two foils could be alternately placed in the proton beam. Each point of the yield curves for

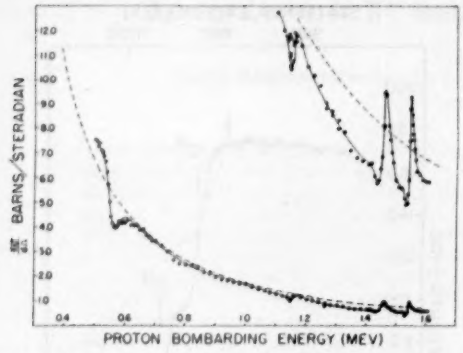

FIG. 3. Differential cross section for the elastic scattering of protons by C^{12} at a scattering angle of 50 degrees in the center-of-mass system. The dotted line is the Rutherford cross section. The solid line is the experimental curve. The upper curve is scaled by a factor of 10.

$C^{13}(p,p)$ was obtained by subtraction using the formula $N=1.65N_1-0.65N_2$, where N is the number of protons that would be scattered from a pure C^{13} target, N_1 is the number of protons scattered from the C^{13} enriched target (61 percent C^{13}+39 percent C^{12}) and N_2 is the number of protons scattered from a normal carbon target (1 percent C^{13}+99 percent C^{12}).

III. EXPERIMENTAL RESULTS

In the region covered by the yield curves (0.45–1.60 Mev) four anomalies were found. These correspond to the 0.556- and 1.16-Mev resonances observed by Seagrave[1] in the $C^{13}(p,\gamma)N^{14}$ reaction and the 1.46- and 1.55-Mev resonances observed by Seagrave but not definitely attributed to the $C^{13}(p,\gamma)N^{14}$ reaction because of the very low gamma-ray yield. These scattering experiments definitely show that excited states corresponding to these resonance energies occur in N^{14}. The very broad resonance at 1.25 Mev in the $C^{13}(p,\gamma)N^{14}$ reaction was not observed as a pronounced anomaly in the scattering measurements but was indicated in the theoretical analysis of the yield curve. Figures 3–8 show the results obtained.

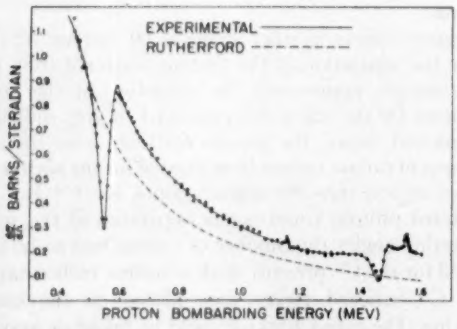

FIG. 4. Differential cross section for the elastic scattering of protons by C^{13} at a scattering angle of 90 degrees in the center-of-mass system.

An attempt was made to study the scattering at the 1.7-Mev resonance, but the resonance is so narrow that it could not be resolved. The resonance is about 2 kev wide, and the over-all resolution of the experimental procedure is about 3–4 kev at this energy.

The differential cross section for $C^{12}(p,p)C^{12}$ was measured from 300 to 600 kev at thirteen different angles. Figures 9–13 show the results obtained. The data for $C^{12}(p,p)C^{12}$ are presented as the ratio of the observed cross section divided by the Rutherford cross section.

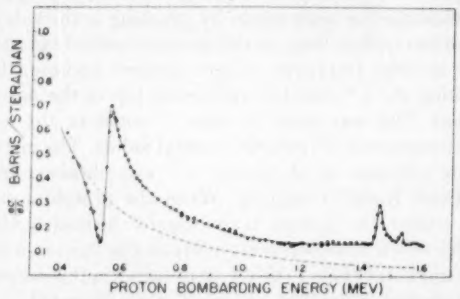

FIG. 5. Differential cross section for the elastic scattering of protons by C^{13} at a scattering angle of 120 degrees in the center-of-mass system. Note that the 1.16-Mev resonance has no effect at this angle.

The differential cross section for the elastic scattering of protons by C^{13} and C^{12} was calculated using the formulas of Brown *et al.*[11] and Snyder *et al.*[9] The stopping cross section of carbon used for the low energies (400–600 kev) was that measured by Reynolds *et al.*[12] For the high energies (500–1700), the stopping cross section was calculated using Bethe's formula[13] and Segrè's value for the average ionization potential of carbon,

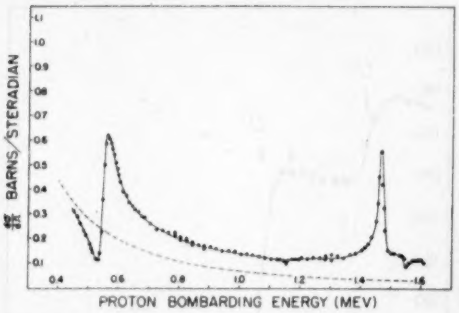

FIG. 6. Differential cross section for the elastic scattering of protons by C^{13} at a scattering angle of 140 degrees in the center-of-mass system.

[11] Brown, Snyder, Fowler, and Lauritsen, Phys. Rev. **82**, 159 (1951).

[12] Reynolds, Whaling, Wenzel, and Dunbar, Phys. Rev. **92**, 742 (1953).

[13] M. Stanley Livingston and H. A. Bethe, Revs. Modern Phys. **9**, 264 (1937).

$I=74.4$ ev.[14] The stopping cross sections agree to less than one percent in the overlapping region but are lower than the stopping cross section calculated by Hirshfelder and Magee[15] by about 6 percent.

The efficiency of the counter was calculated by scattering protons from copper and assuming that the scattering from copper obeys the Rutherford scattering

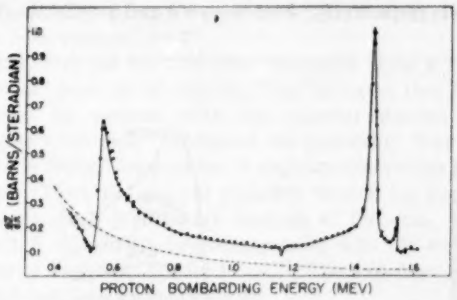

FIG. 7. Differential cross section for the elastic scattering of protons by C^{13} at the scattering angle of 160 degrees in the center-of-mass system.

law. The stopping cross section of copper used is that measured by Whaling and Wenzel.[16]

At least 10 000 counts were taken at each point so that the statistical uncertainty given by the coefficient of variation $\pm 1/\sqrt{N}$ is 1 percent or less except at the smaller angles where the C^{13} scattering was subtracted,

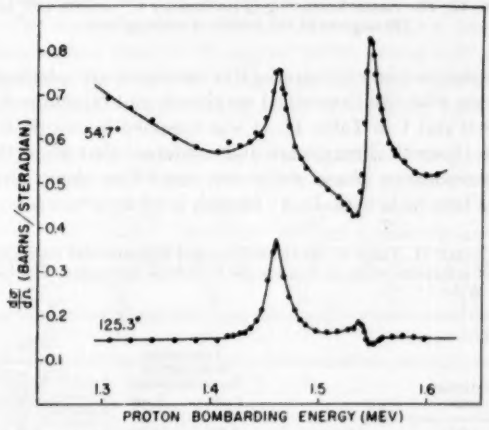

FIG. 8. Differential cross section for the elastic scattering of protons by C^{13} at the angles where $P_3(\cos\theta)=0$. Note that the 1.47-Mev resonance does not show any interference while the 1.55-Mev resonance does.

in which case the statistical uncertainty is about 2 or 3 percent. Systematic errors are believed to be less than one percent. The probable error in the absolute magnitude of the various solid angles is assumed to be about

[14] J. Mather and E. Segrè, Phys. Rev. 84, 191 (1951).
[15] J. Hirshfelder and J. Magee, Phys. Rev. 73, 207 (1948).
[16] W. Whaling and W. A. Wenzel (private communication).

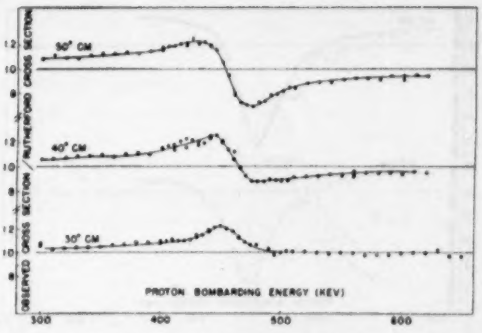

FIG. 9. The elastic scattering of protons by C^{13} at 30, 40, and 50 degrees in the center-of-mass system.

3 percent[17] whereas the relative error in the solid angles is less than one percent. The error in the current integrator is about 1 percent. The uncertainty in the composition of the target is 2 percent. The reproducibility of results, which is affected by errors in settings and target smoothness, straggling, etc., was in most cases within 1 percent at the large scattering angles, 2–3 percent at 90 degrees, and 4–5 percent at 50 degrees. The error in the stopping cross section of carbon is assumed to be about 3 percent. This gives an uncertainty in the absolute magnitude of a little less than 5 percent for the large scattering angles and 8 percent for 50 degrees.

IV. DISCUSSION

A quantitative comparison of the values E_r and Γ with those derived from the proton-capture data awaits a detailed theoretical fit of the scattering data. However, the parities and in some cases the spins of the states can be determined from the scattering data without a detailed theoretical analysis. The states formed by partial waves of odd orbital angular momentum cannot show interference, i.e., a decrease, at 90 degrees, whereas those formed by even angular mo-

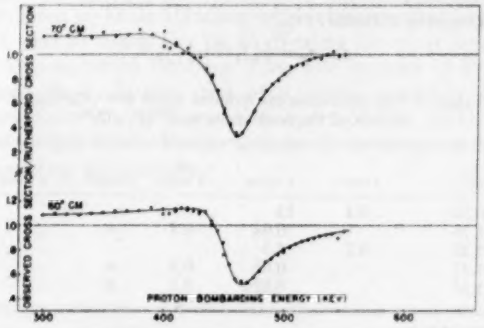

FIG. 10. The elastic scattering of protons by C^{13} at 60 and 70 degrees in the center-of-mass system.

[17] The efficiency of the counter is included in the effective solid angle; hence, this error is the assumed error in the stopping cross section for copper.

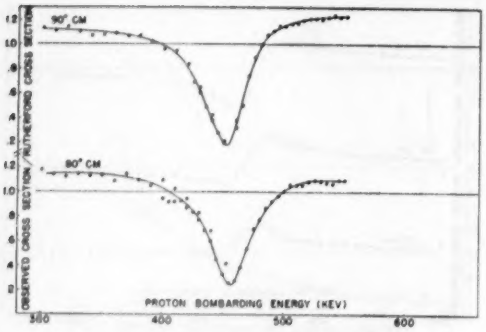

FIG. 11. The elastic scattering of protons by C^{13} at 80 and 90 degrees in the center-of-mass system.

mentum will usually show interference. Hence, if the parity of the target nucleus is known the parity can usually be determined from a study of the scattering at 90 degrees.

The dimensionless reduced width, $\theta^2=\gamma^2(\hbar^2/2Ma)^{-1}$, where γ^2 is the reduced level width of Wigner and Eisenbud,[18] has been calculated by Woodbury[19] employing the Coulomb tables of Block *et al.*,[20] with an interaction radius of $1.41(13^{\frac{1}{3}}+1)\times10^{-13}$ cm. The quantity $1/\theta^2$ may be interpreted as the number of nuclear transversals of the incident particle in the compound system. Wigner's criterion[21] places an upper limit on θ^2 of 3, and with this criterion one is able to place an upper limit on the possible l value of the incident particle. See Table I.

The capture gamma-ray work of Seagrave[1] and the radiative cascade measurements of Woodbury, Day, and Tollestrup[2] show that the 8.06-Mev level in N^{14} formed by protons of 0.56 Mev is formed by s-wave protons. The scattering agrees with this finding. However, they were unable to assign a definite J value to this state. The proton has a spin of $\frac{1}{2}^+$ and C^{13} has a spin of $\frac{1}{2}^-$, thus the state can be either $J=0^-$ or 1^-. The theoretical scattering formula reduces to a relatively simple form when only s-wave phase shifts are taken into account, *viz.*,

$$d\sigma/d\omega=\tfrac{3}{4}|f_1|^2+\tfrac{1}{4}|f_0|^2,$$

TABLE I. The dimensionless reduced width $\theta^2=\gamma^2(\hbar^2/2Ma)^{-1}$ of five of the resonances in $C^{13}(P,\gamma)N^{14}$.

E_R (Mev)	θ^2 s wave	p wave	d wave	f wave	g wave
0.55	0.4	13			
1.16		0.04	0.3	∞	
1.25	0.7	4.5			
1.47		0.05	0.5	∞	
1.55		0.016	0.1	4	

[18] E. P. Wigner and L. Eisenbud, Phys. Rev. 72, 29 (1947).
[19] H. H. Woodbury, Ph.D. thesis, California Institute of Technology, 1953 (unpublished).
[20] Block, Hull, Broyles, Bouricius, Freeman, and Breit, Revs. Modern Phys. 23, 147 (1951).
[21] E. P. Wigner, Am. J. Phys. 17, 99 (1949).

where

$$f_1=(1/k)[-\tfrac{1}{2}\eta(\csc^2\tfrac{1}{2}\theta)\exp(i\eta\ln\csc^2\tfrac{1}{2}\theta)+\sin\delta_0{}^1\exp(i\delta_0{}^1)],$$

$$f_0=(1/k)[-\tfrac{1}{2}\eta(\csc^2\tfrac{1}{2}\theta)\exp(i\eta\ln\csc^2\tfrac{1}{2}\theta)+\sin\delta_0{}^0\exp(i\delta_0{}^0)].$$

$\delta_0{}^0$ and $\delta_0{}^1$ are the s-wave phase shifts for channel spin 0 and 1, respectively; $k=1/\lambda=\mu v/\hbar$ and $\eta=zZe^2/\hbar v$. The

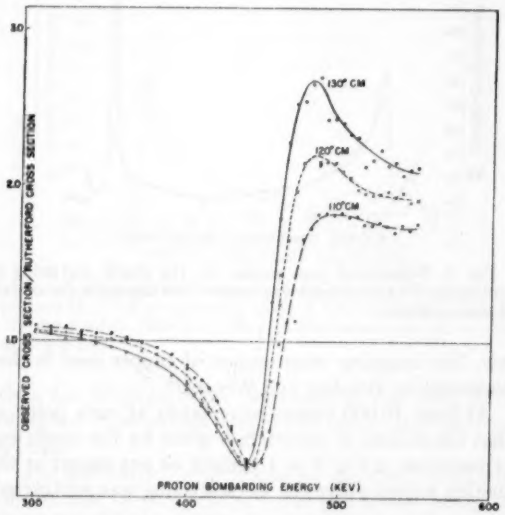

FIG. 12. The elastic scattering of protons by C^{13} at 110, 120, and 130 degrees in the center-of-mass system.

maximum and minimum of this resonance are tabulated along with the theoretical maximum and minimum for $J=0$ and 1 in Table II. It was assumed in calculating the theoretical maximum and minimum that all of the nonresonance phase shifts are zero. This shows that the best fit is with $J=1^-$ for this level in N^{14}.

TABLE II. Table of the theoretical and experimental maximum and minimum cross section for the 0.56-Mev resonance. The best fit is $J=1^-$.

Scattering angle		Theoretical cross section (barns/steradian) $J=1^-$	$J=0^-$	Experimental cross section (barns/steradian)
50	Max	4.85	4.76	4.3
	Min	3.47	4.63	4.0
90	Max	0.77	0.66	0.87
	Min	0.25	0.57	0.30
120	Max	0.63	0.40	0.70
	Min	0.12	0.26	0.14
140	Max	0.61	0.35	0.62
	Min	0.10	0.20	0.11
160	Max	0.59	0.31	0.64
	Min	0.08	0.16	0.10

The broad level in N^{14} at 8.70 Mev is also formed by s-wave protons at 1.25 Mev. This level does not show up in our measurements explicitly. This would indicate that if there is a resonance here the state must be $J=0^-$ because the effect is so small. Mr. Gerald Speisman has calculated the s-wave phase shifts from the data in the neighborhood of this resonance and has found that the $J=0$ s-wave phase shift appears indeed to be passing through a resonance. This state therefore has been assigned $J=0^-$.

The data for the 1.16-Mev resonance show a symmetrical peak at 90 degrees. This indicates that it is formed by protons with odd angular momentum. Wigner's criterion[21] eliminates the possibility that the state is formed by protons of angular momentum 3 or larger. Thus, the state is probably formed by p-wave protons. In a preliminary analysis of the data, Professor R. F. Christy found agreement with the assignment of $J=0^+$ but not for 1^+ or 2^+. The 8.06-Mev level in N^{14} has been assigned $J=0^+$.

Because of the dip in the scattering at 90 degrees, the 8.90-Mev level in N^{14} is formed by either s, d, or g-wave protons at 1.47 Mev. Wigner's criterion eliminates the possibility of g-wave and complexity of the angular distribution of the scattering rules out s-wave. The scattering at 54.7 degrees and 125.3 degrees [the angles where $P_2(\cos\theta)=0$] show symmetrical peaks which indicates that the state is formed by d-wave protons (see Fig. 8). The maximum of the resonance is best fitted with the assignment $J=3^-$.

The scattering near the 1.55-Mev resonance has a symmetrical peak at 90 degrees which would indicate formation by p- or f-wave protons. The parity is therefore probably even. The f wave is excluded by the Wigner criterion. The peak of the scattering could not be fitted with the assignments of $J=0^+$ or 2^+. It cannot be formed by d-wave protons because the scattering at 54.7 and 125.3 degrees shows interference. By a process of elimination, this state has been assigned $J=1^+$. A perfect fit to simple theory cannot be expected in view of nonresonance potential scattering.

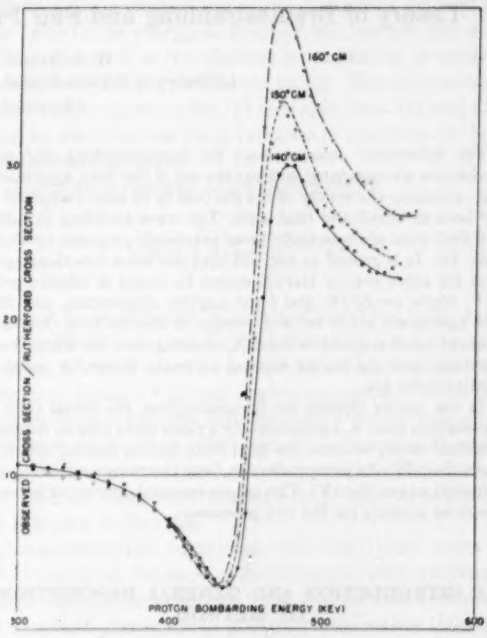

FIG. 13. The elastic scattering of protons by C^{13} at 140, 150, and 160 degrees in the center-of-mass system.

TABLE III. Parameters for the 460-kev resonance in $C^{13}(p,\gamma)$.

Investigator:	Milne (present paper)	Jackson and Galonsky[a]	Jackson and Galonsky[b]	Fowler and Lauritsen[c]	Seagrave[d]
Reaction:	$C^{13}(p,p)$	$C^{13}(p,p)$	$C^{13}(p,p)$	$C^{13}(p,\gamma)$	$C^{13}(p,\gamma)$
E_p (kev)[e]	462	470	461	456	450
(kev)[e]	35	36	34	35	36
E_γ (Mev)	2.370	2.379	2.369		
(kev)	32	33	31	32	32.5

[a] See reference 3.
[b] See reference 8.
[c] See reference 5.
[d] See reference 1.
[e] Laboratory system.

I wish to thank Dr. W. D. Warters for many hours of help in taking the data. I am also grateful to Professor R. F. Christy and Mr. Gerald Speisman for discussions of the theoretical aspect of this problem and to Dr. W. A. Fowler and Dr. J. D. Seagrave for suggesting this problem.

PHYSICAL REVIEW VOLUME 93, NUMBER 4 FEBRUARY 15, 1954

Theory of Bremsstrahlung and Pair Production. I. Differential Cross Section

H. A. BETHE AND L. C. MAXIMON*
Laboratory of Nuclear Studies, Cornell University, Ithaca, New York
(Received October 29, 1953)

The differential cross sections for bremsstrahlung and pair production are calculated without the use of the Born approximation, assuming the energy of the electron to be large compared to mc^2 both in initial and final state. The wave functions in initial and final state are essentially those previously proposed by Furry (Sec. II). It is proved in Sec. III that our wave functions agree with the exact ones of Darwin except for terms of relative order a^2/l^2, where $a=Ze^2/\hbar c$ and l the angular momentum, and that this agreement holds for any energy of the electron. An independent proof is given in Sec. IX, showing that the Furry wave functions give the matrix element correctly except for terms of relative order $1/\epsilon$.

In the matrix element for bremsstrahlung, the initial state of the electron must be represented by a plane wave plus an outgoing spherical wave, whereas the final state has an ingoing spherical wave (Sec. IV). In pair production, both electrons contain ingoing spherical waves (Sec. V). This causes essential differences between the cross sections for the two processes.

The cross section for pair production is calculated in Sec. VI; the result consists of the Bethe-Heitler formula multiplied by a relatively simple factor, plus another term of similar structure. A simplified derivation is given, which is valid for the important case of small angles between electrons and quantum (Sec. VII); it provides a useful check of the cross section of Sec. VI. In Sec. VIII, the bremsstrahlung cross section is calculated and found to be the Bethe-Heitler result multiplied by a factor. This factor is different from that encountered in pair production and becomes important only for very small momentum transfer q. In the limit of complete screening, these small q do not contribute and the cross section goes over into that of the Born approximation.

The error in the cross sections calculated in this paper is estimated (Sec. X) to be of order $1/\epsilon$, where ϵ is the energy of the final electron in bremsstrahlung, or that of the less energetic electron in pair production, in units of mc^2. The total cross section for pair production by a quantum of energy k may be in error by $\log k/k$.

I. INTRODUCTION AND GENERAL DESCRIPTION OF METHOD

THE exact calculation of bremsstrahlung and pair production is a problem of long standing. For nonrelativistic energies, the bremsstrahlung problem was solved exactly by Sommerfeld.[1] For relativistic energies, a solution has been obtained only in Born approximation, by Bethe and Heitler.[2] The total cross section for pair production by high-energy x-rays has been repeatedly tested by experiment[3–9] and the Bethe-Heitler cross section was found to be correct for light elements, but too high (by about 10 percent) for heavy elements. This discrepancy is less than might have been expected since the error in the Born approximation should be of the order of magnitude $(Z/137)^2$ which is 36 percent for lead. Still it is reasonable to assume that the discrepancy is due to failure of the Born approximation, and it was attributed to this cause in the experimental papers.

Sommerfeld's success in the nonrelativistic case was due to the fact that the Schrödinger equation for an electron in the Coulomb field can be separated in parabolic coordinates. This provides a wave function for an electron traveling in a definite direction so that, for instance, the problem of Rutherford scattering can be solved directly and in closed form.[10] This is not possible in relativistic theory, whether Dirac or Klein-Gordon; in this case only a separation in polar coordinates is possible. This makes even the simple problem of electron scattering very cumbersome.[11,12]

If we tried to use wave functions separated in polar coordinates for the bremsstrahlung problem, the calculation would become incredibly cumbersome. We should have to calculate the transition matrix element from any initial angular momentum l_1 of the electron to any final l_2. Now the important values of l extend somewhat beyond $l_0=b/\lambda$, where b is the atomic radius and λ the de Broglie wavelength of the electron divided by 2π; b/λ is about 137ϵ, where ϵ is the electron energy in units of mc^2, so that for a 100-Mev electron l_0 is nearly 30 000 and the number of matrix elements required about 10^9. Worse than that, in each of these matrix elements the retardation factor for the light quantum, $e^{i\mathbf{k}\cdot\mathbf{r}}$, has to be expanded in spherical harmonics, and l_2 terms in this expansion will contribute to the matrix element if $l_2<l_1$. Presumably, these various contributions will interfere partly destructively. The whole calculation would have to be carried out for any pair of initial and final energies, ϵ_1 and ϵ_2. Even if many shortcuts should prove feasible, it is clear that this calculation would be an essentially impossible task.[13]

* Now at Graduate Division of Applied Mathematics, Brown University, Providence, Rhode Island.
[1] A. Sommerfeld, Ann. Physik 11, 257 (1931).
[2] H. A. Bethe and W. Heitler, Proc. Roy. Soc. (London) A146, 83 (1934).
[3] G. P. Adams, Phys. Rev. 74, 1707 (1948).
[4] R. L. Walker, Phys. Rev. 76, 527 (1949).
[5] J. L. Lawson, Phys. Rev. 75, 433 (1949).
[6] DeWire, Ashkin, and Beach, Phys. Rev. 83, 505 (1951).
[7] C. R. Emigh, Phys. Rev. 86, 1028 (1952).
[8] Rosenblum, Schrader, and Warner, Phys. Rev. 88, 612 (1952).
[9] A. I. Berman, Phys. Rev. 90, 210 (1953).
[10] N. F. Mott and H. S. W. Massey, *The Theory of Atomic Collisions* (Clarendon Press, Oxford, 1949), second edition, p. 47.
[11] N. F. Mott and H. S. W. Massey, *The Theory of Atomic Collisions* (Clarendon Press, Oxford, 1949), second edition, p. 74.
[12] W. A. McKinley and H. Feshbach, Phys. Rev. 74, 1759 (1948).
[13] It is true that Harvey Hall, Phys. Rev. 38, 622 (1934), and Revs. Modern Phys. 8, 358 (1936), was able to solve the related problem of the photoelectric effect in the K shell by considering each angular momentum l_1 of the final electron state separately. However, in this case the angular momentum of the initial state

It is therefore essential to find at least an appropriate solution in parabolic coordinates, sufficiently accurate for the calculation of the radiative matrix element. We shall show that a slight modification of Furry's wave function[14] satisfies this condition. Indeed, it will be shown in Sec. III that this wave function is obtained from the exact wave function (i.e., from the expansion in terms of spherical harmonics times radial functions) if in the latter we neglect[15] $a^2=(Z/137)^2$ as compared with l^2. Thus the large values of l which were disturbing in the solution by expansion in spherical harmonics, turn out to be helpful in this approach. Small values of l are known to be unimportant: both from the Born approximation solution,[2] and from the Weizsäcker-Williams[16] method, it can be shown that impact parameters less than the Compton wavelength, and thus values of l less than ϵ, give relatively little contribution, the contribution in this region being proportional to ldl. The error due to neglect of a^2 would therefore appear to be of order a^2/ϵ^2. Actually, a more detailed consideration of the error in the wave function, along the lines of Sec. III of this paper, shows that the error is of order $a^2/\epsilon \log\epsilon$). A similar result, a^2/ϵ, will be found from a discussion of the matrix element in Sec. IX. Assuming the latter behavior, the total cross section, integrated over all energies of the final state, will then have an error of order $a^2\epsilon_1^{-1}\log\epsilon_1$ [see Eq. (10.6)]. Thus our theory will be satisfactory for energies of 50 Mev or more (error less than 2 percent) but will give appreciable errors below 20 Mev.

We propose, then, to use the Furry wave function, which was indeed originally developed for the bremsstrahlung problem. The same wave function, for the same purpose, was developed by Sommerfeld and Maue,[17] but neither they nor Furry used it to calculate the bremsstrahlung itself. The first serious attempt at an exact calculation of bremsstrahlung was made by Bess,[18] who used a wave function of similar structure as Furry's but containing one additional term which Bess believed necessary for the purpose. Unfortunately, as Nordsieck pointed out to us,[19] this additional term is incorrect (see Sec. II) and so is, therefore, Bess' result for the cross section. However, Bess' work is still valuable for the integration of the matrix element and also because he wrote the Furry wave function in a much more convenient form than Furry had done, namely,

$$\psi=Ne^{i\mathbf{p}\cdot\mathbf{r}}[1-(i/2\epsilon)\boldsymbol{\alpha}\cdot\boldsymbol{\nabla}]F(ia\epsilon/p;1;ipr-i\mathbf{p}\cdot\mathbf{r}), \quad (1.1)$$

where $\mathbf{p}$ is the momentum of the electron in units of mc, $\epsilon=(p^2+1)^{\frac{1}{2}}$ its energy in units of mc^2, $a=Ze^2/\hbar c$, $\boldsymbol{\alpha}$ the Dirac operator, $\mathbf{r}$ the electron's coordinate in units of $\hbar/mc$, and N a normalization factor. The derivation of (1.1) will be given in Sec. II (see also Secs. III and IX), and we shall use the wave function in this form for both initial and final state.

The matrix element to be calculated is

$$M=\int\psi_2^*\alpha_\lambda\psi_1 e^{-i\mathbf{k}\cdot\mathbf{r}}d\tau, \quad (1.2)$$

where λ is the direction of polarization of the light wave, α_λ the Dirac α matrix in this direction, and the subscripts 1 and 2 refer to initial and final state of the electron. Using (1.1) and neglecting certain terms discussed in Sec. IX, the integral may then be written in the form (6.2), (6.3). (See Sec. VI.) Now the integrals in (6.3) can be evaluated exactly, which is done in Sec. VI, and all other contributions to M can be neglected as is shown in Sec. IX.

It is somewhat surprising that the three terms in (6.2) are all of the same order of magnitude, whereas it might be expected that the term 1 in the wave function (1.1) would give a much greater contribution than the term $(i/2\epsilon)\boldsymbol{\alpha}\cdot\boldsymbol{\nabla}$ which at least *seems* to be of relative order $1/\epsilon$. In other words, I_1 of (6.3) may be expected to be much larger than I_2 and I_3. This is indeed the case, as is shown in Sec. VI and VII; I_1 is of order ϵ, I_2 and I_3 of order 1. Nevertheless, the three integrals give contributions of the *same* order to the matrix element M. This is due to the matrix factors in (6.2): the matrix $(u_2^*\alpha_\lambda u_1)$ is of order $1/\epsilon$ whereas the matrix vector $(u_2^*\alpha_\lambda\boldsymbol{\alpha}u_1)$ has a component of order unity. This makes the contributions of I_1, I_2 and I_3 all of order unity.

The statement about the order of magnitude of the matrix factors can be seen as follows: In the first term of (6.2), the matrix factor $(u_2^*\alpha_\lambda u_1)$ represents essentially the velocity of the electron (in units of c) perpendicular to the direction of propagation of the quantum, $\mathbf{k}$. But the differential cross section is known to be large only if the angles θ_1, θ_2 between the electron directions $\mathbf{p}_1$, $\mathbf{p}_2$ and the quantum $\mathbf{k}$ are small, of order $1/\epsilon$. Then the electron velocities perpendicular to $\mathbf{k}$ will also be small of this order, and so will the matrix factor $(u_2^*\alpha_\lambda u_1)$. On the other hand, in the second and third term in (6.2), we may, for instance, choose the component of the vector $\boldsymbol{\alpha}$ in the direction λ. This makes the matrix factor equal to $(u_2^*u_1)$ and this is nearly equal to unity because the electron momenta in states 1 and 2 are nearly parallel. This proves the statement above. This fact that I_2 and I_3 give contributions of the same order as I_1, although they look at first sight much smaller, has been a major cause for obscuring this entire problem in the past.

The contributions to the matrix element M which are *not* contained in (6.2) might be expected to fall into three classes: (a) terms which contain an integral of

is $l_2=0$ so that only one (actually a few) terms of the expansion of $e^{i\mathbf{k}\cdot\mathbf{r}}$ in spherical harmonics contribute. Therefore, at least the individual matrix elements are rather simple; only the summation of the cross section over l_1 is laborious.

[14] W. H. Furry, Phys. Rev. **46**, 391 (1934).

[15] This proof goes beyond that of Furry, who had to neglect also terms of order $1/\epsilon^2$.

[16] C. F. v. Weizsäcker, Z. Physik **88**, 612 (1934); E. J. Williams, Kgl. Danske Videnskab. Selskab. Mat.-fys. Medd. **13**, 4 (1935).

[17] A. Sommerfeld and A. W. Maue, Ann. Physik **22**, 629 (1935).

[18] L. Bess, Phys. Rev. **77**, 550 (1950).

[19] A. Nordsieck (private communication).

order 1, and a matrix factor of order $1/\epsilon$, (b) terms containing an integral of order $1/\epsilon$ and a matrix factor of order 1, and (c) terms of order $\epsilon^{-2}\log\epsilon$ or smaller. The term which Bess tried to take into account[20] is of type (a), as is shown in Sec. IX-c. Examination shows that there is no term of type (b). The term $\nabla F_2^*\nabla F_1$ which naturally must occur is of type (c) and is shown to be small of order $\epsilon^{-2}\log\epsilon$ in Sec. IX-d; this term could not easily be evaluated by analytical methods. Generally, the proof that (6.2) determines the matrix element with sufficient accuracy, is given in Sec. IX, and we regard this proof as a central part of our calculation. The most important consequence of this proof is that it is unnecessary to calculate the wave function to a better accuracy than the Furry wave function.

Once the Furry wave function is established as sufficient, the evaluation of the matrix elements is possible using the method of Bess or a similar one of Nordsieck. The resulting differential cross section differs from that of Bess only by the correction of minor algebraic mistakes and the omission of terms arising from the spurious term in Bess' wave function. It is therefore simpler than that of Bess and more similar to the Bethe-Heitler cross section.

In the accompanying paper by Davies and ourselves, the differential cross section is integrated over angles and furthermore it is shown that screening can be taken into account easily.

II. WAVE FUNCTION

We start with the first-order Dirac equation for an electron in a Coulomb field,

$$(E+Ze^2/\rho)\psi=\beta mc^2\psi-i\hbar c\boldsymbol{\alpha}\cdot\nabla\psi. \tag{2.1}$$

Introducing $\hbar/mc$ as the unit of length, mc^2 as that of energy, $a=Ze^2/\hbar c$ and the other notations as described below Eq. (1.1), we get

$$(\epsilon+a/r-\beta+i\boldsymbol{\alpha}\cdot\boldsymbol{\nabla}_r)\psi=0, \tag{2.2}$$

where $\boldsymbol{\nabla}_r$ denotes the gradient with respect to the coordinate $\mathbf{r}$, no longer with respect to $\boldsymbol{\rho}=(\hbar/mc)\mathbf{r}$ as in (2.1). In (2.2), ψ is the usual four-row unicolumnar matrix, and $\boldsymbol{\alpha}$ and β the four-row four-column matrices of the Dirac equation.

Since we wish to derive wave functions which are the relativistic generalization of the exact solution of the Schrödinger equation with a Coulomb potential, we transform (2.2) into a second-order equation which reduces to the Schrödinger equation when spin and relativity effects are neglected, i.e., for $a\ll1$ and $v\ll c$. This may be accomplished by applying the operator $[(\epsilon+a/r)+\beta-i\boldsymbol{\alpha}\cdot\boldsymbol{\nabla}_r]$ to (2.2), which results in

$$[\nabla_r^2+p^2+2\epsilon a/r]\psi=[i\boldsymbol{\alpha}\cdot\boldsymbol{\nabla}_r(a/r)-a^2/r^2]\psi, \tag{2.3}$$

after making use of the commutation relations for $\boldsymbol{\alpha}$ and β. Here $\mathbf{p}$ is the momentum of the electron in units of mc and $\epsilon^2=p^2+1$. The terms on the right-hand side of (2.3) are negligible for $a\ll1$ and $v\ll c$, in which case we are left with the Schrödinger equation

$$[\nabla_r^2+p^2+2\epsilon a/r]\psi=0. \tag{2.4}$$

As is well known,[1,10] the exact solution of this is

$$\psi=Ne^{i\mathbf{p}\cdot\mathbf{r}}uF, \tag{2.5}$$

where N is a normalization constant, F is the confluent hypergeometric function

$$F=F(ia\epsilon/p;1;ipr-i\mathbf{p}\cdot\mathbf{r}), \tag{2.6}$$

and $u=u(\mathbf{p})$, the normalized Dirac matrix coefficient for a free electron of momentum $\mathbf{p}$. This factor, which is independent of $\mathbf{r}$, is the only one by which (2.5) differs from the purely nonrelativistic solution; it insures that (2.5) satisfies also the first order Eq. (2.2) asymptotically for large r. The asymptotic behavior of (2.5), (2.6) is a plane wave plus outgoing spherical waves.

Following Bess[18] and starting with the wave function $Ne^{i\mathbf{p}\cdot\mathbf{r}}uF$, we try to find a solution of the form

$$\psi=Nei^{\mathbf{p}\cdot\mathbf{r}}(1+\Omega)uF, \tag{2.7}$$

where Ω is an operator to be determined. Then, remembering that (2.5) is an exact solution of (2.4), substitution of (2.7) in (2.3) gives

$$(\nabla_r^2+2i\mathbf{p}\cdot\boldsymbol{\nabla}_r+2\epsilon a/r)\Omega uF$$
$$=[ia\boldsymbol{\alpha}\cdot\boldsymbol{\nabla}_r(1/r)-a^2/r^2](1+\Omega)uF. \tag{2.8}$$

If we now assume that Ω commutes with the operator $\nabla_r^2+2i\mathbf{p}\cdot\boldsymbol{\nabla}_r$, then (2.8) becomes

$$(2\epsilon a/r)\Omega uF-\Omega(2\epsilon auF/r)$$
$$=[ia\boldsymbol{\alpha}\cdot\boldsymbol{\nabla}_r(1/r)-a^2/r^2](1+\Omega)uF. \tag{2.9}$$

Since the simplest operators that commute with $\nabla_r^2+2i\mathbf{p}\cdot\boldsymbol{\nabla}_r$ are those which are made up of any number of differentiations with respect to x,y,z and of Dirac matrices, we assume Ω to be of the form

$$\Omega=\textstyle\sum_n\sigma_n,$$

where

$$\sigma_0=a_{01},$$

$$\sigma_1=a_{11}\partial/\partial x+a_{12}\partial/\partial y+a_{13}\partial/\partial z,$$

$$\sigma_2=a_{21}\partial^2/\partial x^2+a_{22}\partial^2/\partial y^2+\cdots+a_{24}\partial^2/\partial x\partial y+\cdots, \tag{2.10}$$

and the a_{nm} are constants or Dirac matrices. In particular, σ_0 would merely affect the asymptotic behavior of the wave function. However, since $u(\mathbf{p})$ is already the correct asymptotic Dirac amplitude, σ_0 must not contain any Dirac operators, but must merely be a constant, and as such can be absorbed in the normalizing factor N. Therefore we may set $\sigma_0=0$ and find that Ω contains at least one differentiation with respect to coordinates.

[20] With the incorrect wave function used by Bess, this term appeared to be of order 1 instead of $1/\epsilon$.

Substituting (2.10) in (2.9) we may attempt to satisfy (2.9) to terms of $O(1/r^2)$, and hence obtain

$$-2\epsilon a[\sigma_1(1/r)]uF = [ia\boldsymbol{\alpha}\cdot\boldsymbol{\nabla}_r(1/r)-a^2/r^2]uF+O(1/r^3). \quad (2.11)$$

Mere inspection shows that if we set

$$\sigma_1=-i\boldsymbol{\alpha}\cdot\boldsymbol{\nabla}_r/2\epsilon, \quad (2.12)$$

then the first of the terms on the right is canceled. Furthermore, it may be noted that there is no σ_1 of the form assumed in (2.10) such that $\sigma_1(1/r)\sim 1/r^3$, and thus we cannot satisfy (2.3) to $O(1/r^2)$ with Ω of the form assumed in (2.10).[21] Actually, as will be shown in Sec. IX, it is unnecessary to solve (2.3) with the term involving a^2/r^2 on the right; the solution so far obtained, i.e., with $\Omega=\sigma_1$ as given in (2.12), is sufficient.

We consider now the wave function $Ne^{i\mathbf{p}\cdot\mathbf{r}}(1+\Omega)uF$, where $\Omega=-(i/2\epsilon)\boldsymbol{\alpha}\cdot\boldsymbol{\nabla}_r$, and see to what extent it satisfies (2.3), forgetting that we were led to Ω by consideration of the terms in (2.9) which contain the lowest power of $1/r$. Denoting the wave function that satisfies (2.3) *exactly* by ψ, we may write

$$\psi=\psi_a+\psi_b+\psi_c, \quad (2.13)$$

where

$$\psi_a=Ne^{i\mathbf{p}\cdot\mathbf{r}}uF, \quad (2.14)$$

$$\psi_b=-(i/2\epsilon)Ne^{i\mathbf{p}\cdot\mathbf{r}}\boldsymbol{\alpha}\cdot\boldsymbol{\nabla}Fu, \quad (2.15)$$

and ψ_c remains undetermined. Thus we wish to see how satisfactory ψ_b is as a correction to ψ_a, i.e., to what extent we can neglect ψ_c. Substituting (2.13), (2.14), (2.15) in (2.3) and noting that

$$[\nabla_r^2+p^2+2a\epsilon/r]\psi_a=0, \quad (2.16)$$

we have

$$[\nabla_r^2+p^2+2\epsilon a/r](\psi_b+\psi_c) = [ia\boldsymbol{\alpha}\cdot\boldsymbol{\nabla}_r(1/r)-a^2/r^2](\psi_a+\psi_b+\psi_c). \quad (2.17)$$

Substituting (2.15) and using (2.16), we find

$$[\nabla_r^2+p^2+2\epsilon a/r]\psi_b=ia\boldsymbol{\alpha}\cdot\boldsymbol{\nabla}_r(1/r)\psi_a, \quad (2.18)$$

so that

$$[\nabla_r^2+p^2+2\epsilon a/r]\psi_c=ia\boldsymbol{\alpha}\cdot\boldsymbol{\nabla}_r(1/r)(\psi_b+\psi_c) -(a^2/r^2)(\psi_a+\psi_b+\psi_c). \quad (2.19)$$

We shall return to (2.19) in Sec. IXc when showing that the contribution to the differential cross section coming from ψ_c may be neglected when compared with that arising from ψ_a and ψ_b.

III. COMPARISON OF THE WAVE FUNCTION WITH THE SOLUTION IN RADIAL WAVES

In this section, we intend to show that our solution to the wave equations (2.14, 2.15) agrees with the exact solution within terms of the order a^2/l^2 for *any* energy. Since the matrix element of bremsstrahlung comes mostly from impact parameters equal to $\hbar/mc$ or larger, the values of l contributing most are of order ϵ or greater. Therefore, the calculations in this section give an added proof that the error in our cross section becomes negligible for large ϵ.

The exact solution of the Dirac equation in a Coulomb field has been given by Darwin[22] in the form of an infinite series. Starting from the Darwin solution, Furry[14] has derived wave functions in closed form by neglecting, in each of the terms of the summation, terms of $O(1/\epsilon^2)$ and of $O(a^2/l^2)$ compared to those kept, where l is the angular momentum. We shall show that the wave function which we have been using here, namely $\psi_a+\psi_b$, Eq. (2.14, 2.15), may be obtained directly from the Darwin solution by neglecting only terms of $O(a^2/l^2)$ in the infinite series, not those of $O(1/\epsilon^2)$. Thus the wave function $\psi_a+\psi_b$ is actually valid for *all* energies, and, moreover, satisfies [up to terms of $O(a^2/l^2)$] the more restrictive first-order Dirac equation as well as the second-order equation.

Since the Darwin solution is given as an expansion in spherical harmonics, we shall first expand $\psi_a+\psi_b$ in spherical harmonics and then show that, apart from a different normalization factor, this is identical with Darwin's series solution when one neglects terms of $O(a^2/l^2)$ in the latter. We shall indicate the steps for the initial state wave function; the procedure for the final state is identical.

From the work of Gordon[23] we have, directly,

$$\psi_a\equiv N_1e^{i\mathbf{p}\cdot\mathbf{r}}uF=u\sum_l(2l+1)i^lL_l(r)P_l(\cos\theta), \quad (3.1)$$

where

$$L_l(r)=e^{\frac{1}{2}\pi a_1}[\Gamma(l+1-ia_1)/(2l+1)!](2pr)^l \times e^{ipr}F(l+1-ia_1;\,2l+2;\,-2ipr), \quad (3.2)$$

and

$$a_1=a\epsilon/p=Ze^2/\hbar v. \quad (3.3)$$

Solving (3.1) for uF and substituting in ψ_b, Eq. (2.15), we obtain

$$\psi_b=-\frac{i\alpha_x u}{2\epsilon}\sum i^le^{\frac{1}{2}\pi a_1}\frac{(2l+1)\Gamma(l+1-ia_1)}{(2l+1)!}(2pr)^le^{ipr} \times\{\cos\theta P_l[ipF(l+1-ia_1;\,2l+2;\,-2ipr) +(l/r)F(l+1-ia_1;\,2l+2;\,-2ipr) -2ip[(l+1-ia_1)/(2l+2)] \times F(l+2-ia_1;\,2l+3;\,-2ipr)] +(\sin\theta/r)P_l^{(1)}F(l+1-ia_1;\,2l+2;\,-2ipr) -ipP_lF(l+1-ia_1;\,2l+2;\,-2ipr)\}$$

(continued on next page)

[21] It should be noted that Bess, in the paper referred to, assumes that (2.9) is satisfied to $O(1/r^2)$ by choosing $\sigma_1=-(i/2\epsilon)\boldsymbol{\alpha}\cdot\boldsymbol{\nabla}_r +(a/2\epsilon)\partial/\partial r$. As pointed out by Dr. Nordsieck this is incorrect, for although $(a/2\epsilon)\partial/\partial r(2\epsilon a/r)=-a^2/r^2$, the operator $\partial/\partial r$ does not commute with $\nabla_r^2+2i\mathbf{p}\cdot\boldsymbol{\nabla}_r$.

[22] C. G. Darwin, Proc. Roy. Soc. (London) **A118**, 654 (1928).

[23] W. Gordon, Z. Physik **48**, 180 (1928).

$$-i(\alpha_x\cos\varphi+\alpha_y\sin\varphi)(u/2\epsilon)\sum i^l e^{i\pi a_1}(2l+1)$$
$$\times[\Gamma(l+1-ia_1)/(2l+1)!](2pr)^l e^{ipr}$$
$$\times\{\sin\theta P_l[ipF(l+1-ia_1;\,2l+2;\,-2ipr)$$
$$+(l/r)F(l+1-ia_1;\,2l+2;\,-2ipr)$$
$$-2ip[(l+1-ia_1)/(2l+2)]$$
$$\times F(l+2-ia_1;\,2l+3;\,-2ipr)]-(\cos\theta/r)P_l^{(1)}$$
$$\times F(l+1-ia_1;\,2l+2;\,-2ipr)\},\quad(3.4)$$

where we have defined $P_l^{(1)}=\sin\theta(dP_l/d\cos\theta)$, and note that $\boldsymbol{\alpha}\cdot\mathbf{r}/r=\alpha_x\sin\theta\cos\varphi+\alpha_y\sin\theta\sin\varphi+\alpha_z\cos\theta$ and $\boldsymbol{\alpha}\cdot\mathbf{p}=\alpha_z p$, since the z axis has been chosen in the direction of $\mathbf{p}$.

In order to obtain an expansion of ψ_b in spherical harmonics, we make use of the following recurrence relations involving the Legendre polynomials P_l and the associated Legendre functions $P_l^{(1)}$:

$$\begin{aligned}
\sin\theta P_l^{(1)}&=l[P_{l-1}-\cos\theta P_l],\\
(2l+1)\sin\theta P_l&=P_{l+1}^{(1)}-P_{l-1}^{(1)},\\
(2l+1)\cos\theta P_l&=(l+1)P_{l+1}+lP_{l-1},\\
(2l+1)\cos\theta P_l^{(1)}&=lP_{l+1}^{(1)}+(l+1)P_{l-1}^{(1)},
\end{aligned}\quad(3.5)$$

in which we define $P_0^{(1)}=0$ and $P_{-1}^{(1)}=0$ in order that these recurrence relations will also be valid for $l=0$. We also make use of the following recurrence relations for the confluent hypergeometric function:

$$\begin{aligned}
xF(a+1;b+1;x)&=b[F(a+1;b;x)-F(a;b;x)],\\
xaF(a+1;b+1;x)&=b(b-1)[F(a;b-1;x)\\
&\quad-F(a;b;x)],\\
aF(a+1;b+1;x)&=(a-b)F(a;b+1;x)\\
&\quad+bF(a;b;x).
\end{aligned}\quad(3.6)$$

The last of these three relations can be derived directly from the first two.

By straightforward but tedious application of (3.5) and (3.6), we may obtain

$$\psi_b=(a_1/2\epsilon)\alpha_z u\sum e^{i\pi a_1}(2l+1)i^l$$
$$\times[\Gamma(l+1-ia_1)/(2l+1)!](2pr)^l(e^{ipr}/r)P_l$$
$$\times[F(l+1-ia_1;\,2l+2;\,-2ipr)$$
$$+ia_1(l-ia_1)^{-1}F(l-ia_1;\,2l+2;\,-2ipr)]$$
$$+(a_1/2\epsilon)(\alpha_x\cos\varphi+\alpha_y\sin\varphi)u\sum e^{i\pi a_1}$$
$$\times(2l+1)i^l[\Gamma(l+1-ia_1)/(2l+1)!]$$
$$\times(2pr)^l(e^{ipr}/r)P_l^{(1)}(l-ia_1)^{-1}$$
$$\times F(l-ia_1;\,2l+2;\,-2ipr).\quad(3.7)$$

Having obtained the expansions of ψ_a and ψ_b in spherical harmonics, we turn now to the Darwin solution as given in Mott and Massey,[24] where the following two components of the wave function are given:

$$\begin{aligned}
\psi_3&=\sum[(l+1)e^{i\eta_l}G_l+le^{i\eta_{-l-1}}G_{-l-1})i^lP_l,\\
\psi_4&=\sum[-e^{i\eta_l}G_l+e^{i\eta_{-l-1}}G_{-l-1})i^lP_l^{(1)}e^{i\varphi},
\end{aligned}\quad(3.8)$$

where

$$e^{i\eta_{-l-1}}G_{-l-1}=\frac{\Gamma(\rho_l+1-ia_1)ie^{\frac{1}{2}\pi a_1}e^{\frac{1}{2}i\pi(l-\rho_l)}}{2\Gamma(2\rho_l+1)(\rho_l-ia_1)}(2pr)^{\rho_l}\frac{e^{ipr}}{pr}$$
$$\times\{-(l-ia_1/\epsilon)F(\rho_l-ia_1;\,2\rho_l+1;\,-2ipr)$$
$$+(\rho_l-ia_1)F(\rho_l+1-ia_1;\,2\rho_l+1;\,-2ipr)\},\quad(3.9)$$

and $\rho_l=(l^2-a^2)^{\frac{1}{2}}$ (positive square root implied). $e^{i\eta_l}G_l$ may be obtained directly from (3.9) by replacing l by $-l-1$ everywhere except in the factor $e^{\frac{1}{2}i\pi(l-\rho_l)}$ which is replaced by $e^{\frac{1}{2}i\pi(l-\rho_{-l-1})}$. In obtaining (3.9) from Mott and Massey, we have replaced n, $\alpha=Ze^2/\hbar c$, $\gamma=Ze^2/\hbar v$, and $\gamma'=\gamma(1-v^2/c^2)^{\frac{1}{2}}$, by their corresponding symbols in the notation that we have been using, namely l, a, a_1, and a_1/ϵ, respectively. We have also divided G_{-l-1} and G_l (as given in Mott and Massey) by p in order that they have the same asymptotic behavior as $L_l(r)$, given in (3.1). Further, the relation

$$F(a;b;x)=e^xF(b-a;b;-x)$$

has been substituted in the Darwin solution in order that the arguments of the confluent hypergeometric functions be the same as those in (3.1) and (3.2) for ψ_a and ψ_b.

If we assume $a^2/p^2\ll1$ in each term of the sum, then ρ_l and ρ_{-l-1} may be replaced by l and $l+1$, respectively, so that we have then, from (3.9),

$$e^{-i\eta_{-l-1}}G_{-l-1}=-\frac{i\,\Gamma(l+1-ia_1)e^{\frac{1}{2}\pi a_1}}{2\;\Gamma(2l+1)(l-ia_1)}(2pr)^l\frac{e^{ipr}}{pr}$$
$$\times\{-(l-ia_1/\epsilon)F(l-ia_1;\,2l+1;\,-2ipr)$$
$$+(l-ia_1)F(l+1-ia_1;\,2l+1;\,-2ipr)\},\quad(3.10)$$

and

$$e^{i\eta_l}G_l=\frac{\Gamma(l+2-ia_1)e^{\frac{1}{2}\pi a_1}}{2\Gamma(2l+3)(l+1-ia_1)}(2pr)^l\frac{e^{ipr}}{pr}$$
$$\times\{(l+1+ia_1/\epsilon)F(l+1-ia_1;\,2l+3;\,-2ipr)$$
$$+(l+1-ia_1)F(l+2-ia_1;\,2l+3;\,-2ipr)\}.\quad(3.11)$$

By substituting (3.10) and (3.11) in (3.8) we may obtain, after numerous applications of the relations given in (3.6),

$$\psi_3=\sum(2l+1)(2l+1)!^{-1}i^le^{\frac{1}{2}\pi a_1}\Gamma(l+1-ia_1)(2pr)^l$$
$$+e^{ipr}F(l+1-ia_1;\,2l+2;\,-2ipr)P_l$$
$$+(a_1p/2\epsilon)(\epsilon+1)^{-1}\sum(2l+1)(2l+1)!^{-1}i^le^{\frac{1}{2}\pi a_1}$$
$$\times\Gamma(l+1-ia_1)(2pr)^l(e^{ipr}/r)P_l$$
$$\times\{F(l+1-ia_1;\,2l+2;\,-2ipr)$$
$$+ia_1(l-ia_1)^{-1}F(l-ia_1;\,2l+2;\,-2ipr)\},\quad(3.12)$$

[24] N. F. Mott and H. S. W. Massey, *The Theory of Atomic Collisions* (Clarendon Press, Oxford, 1949), second edition, p. 76, Eq. (25); p. 79, Eqs. (35), (37), and (38).

and

$$\psi_4=(a_1p/2\epsilon)(\epsilon+1)^{-1}e^{i\sigma}\sum(2l+1)(2l+1)!^{-1}i^le^{\frac{1}{2}\pi a_1}\times\Gamma(l+1-ia_1)(2pr)^l(e^{ipr}/r)P_l^{(1)}\times(l-ia_1)^{-1}F(l-ia_1;2l+2;-2ipr). \quad (3.13)$$

We note first that, apart from the matrix factors, the terms in the summation for ψ_3 [Eq. (3.12)] are identical to those in (3.1) for ψ_a and in (3.7) for the part of ψ_b with the factor α_z. Further, apart from the matrix factors, the terms in the summation for ψ_4 (Eq. (3.13)) are identical to those with the factors α_x and α_y in the summation for ψ_b in (3.7).

Now, if u represents the state with positive energy and "spin up," then, since we have chosen the z axis in the direction of $\mathbf{p}$, we have $p_x=p_y=0$, $p_z=p$, and

$$u=[1+p^2/(\epsilon+1)^2]^{-\frac{1}{2}}\begin{pmatrix}1\\0\\p/(\epsilon+1)\\0\end{pmatrix}. \quad (3.14)$$

Thus with

$$\alpha_x=\begin{pmatrix}0&0&0&1\\0&0&1&0\\0&1&0&0\\1&0&0&0\end{pmatrix},\quad \alpha_y=\begin{pmatrix}0&0&0&-i\\0&0&i&0\\0&-i&0&0\\i&0&0&0\end{pmatrix},$$
$$\alpha_z=\begin{pmatrix}0&0&1&0\\0&0&0&-1\\1&0&0&0\\0&-1&0&0\end{pmatrix}, \quad (3.15)$$

and numbering the Dirac components of our wave function (3.1) by ψ_{a1}, ψ_{a2}, ψ_{a3}, ψ_{a4}, we have, from (3.1), (3.7), (3.12), and (3.13),

$$\psi_{a1}+\psi_{b1}=[1+p^2/(\epsilon+1)^2]^{-\frac{1}{2}}\psi_3,$$
$$\psi_{a2}+\psi_{b2}=[1+p^2/(\epsilon+1)^2]^{-\frac{1}{2}}\psi_4, \quad (3.16)$$

where ψ_3 and ψ_4 refer to the function of Mott and Massey. The wave function used here, $\psi_a+\psi_b$, is, therefore, apart from a difference of normalization factor,[25] identical with that of Darwin after neglecting terms of $O(a^2/l^2)$ in the latter.*

It may be noted that since we have assumed only $a^2/l^2\ll 1$ rather than $a^2\ll 1$ in each of the terms, further corrections to $\psi_a+\psi_b$ may be obtained fairly easily. We need only write

$$\psi=\psi^{(1)}+\Sigma_l[f_l(r,\theta,\phi;a^2)-f_l(r,\theta,\phi;0)], \quad (3.17)$$

where $\psi^{(1)}$ is our old solution of Sec. II, $f_l(r,\theta,\phi;a^2)$ is the component of the exact Darwin solution for a given l, and $f_l(r,\theta,\phi;0)$ is the same component with a^2/l^2 replaced by zero. In practice, the sum is extended over a *finite* number of terms according to the accuracy desired.

IV. THE MATRIX ELEMENT IN BREMSSTRAHLUNG

It is well known[26] that the matrix element for bremsstrahlung is

$$H_{12}'=C\int\psi_2^*\alpha_\lambda e^{-i\mathbf{k}\cdot\mathbf{r}}\psi_1 d\tau, \quad (4.1)$$

where

$$C=-e\hbar c(2\pi/k)^{\frac{1}{2}}, \quad (4.2)$$

and α_λ is the component of the Dirac matrix operator $\boldsymbol{\alpha}$ in the direction of polarization, λ, which is perpendicular to the propagation vector $\mathbf{k}$. The wave functions ψ_1 and ψ_2 of the initial and final state of the electron are taken in the Coulomb potential and are given by the expressions in Secs. II and III.

The wave function of a continuum state, however, is not fully defined until its asymptotic behavior is given. In the case of ψ_1, it is clear that it has to be represented by a plane wave propagating in the direction of the initial momentum $\mathbf{p}_1$, plus outgoing spherical waves. In the past,[1,18,27] ψ_2 has often been chosen in the same manner. That this is incorrect was recognized first by Mott and Massey[28] in a more general context and then by Sommerfeld[29] in relation to our particular problem. A physical argument was given by us in an earlier paper.[30] The correct theory was used for internal conversion by Rose *et al.*[31] who give references to several previous papers in which the incorrect assumption was made, as well as to Rarita and Schwinger[32] who were familiar with the correct treatment.

A mathematical argument which leads to that of Mott and Massey is as follows. The Hamiltonian of our system is

$$H=H_e+H_r+H', \quad (4.3)$$

where H_r is the Hamiltonian of the pure radiation field, H_e that of the electron including its Coulomb interaction with the nucleus, and H' the interaction between electron and radiation. The latter is to be regarded as a small perturbation, and to be treated only in first approximation. The Schrödinger equation is

$$H\Psi=E_1\Psi, \quad (4.4)$$

where E_1 is the energy of the incident electron. In zero order, we have no radiation present, and the wave function therefore satisfies

$$H_e\Psi^{(0)}=E_1\Psi^{(0)}. \quad (4.5)$$

[25] Darwin, Mott, and Massey, take the particle density to be $|\psi_3|^2+|\psi_4|^2$ and consider ψ_1 and ψ_2 as expressed in terms of ψ_3, ψ_4. We take the density to be $|\psi_1|^2+|\psi_2|^2+|\psi_3|^2+|\psi_4|^2$; this explains the difference in normalization.

* *Note added in proof:*—Closer examination shows that our wave function (3.2) differs from Darwin's true wave function by terms of order a^2/l rather than a^2/l^2. This will be shown in a forthcoming paper by one of us (L. C. M.). It has the consequence of making the error in our matrix element of order $a^2/(\epsilon\log\epsilon)$, as mentioned in Sec. I.

[26] See Heitler, *The Quantum Theory of Radiation* (Oxford University Press, London, 1944), second edition, p. 96.

[27] L. Maximon and H. A. Bethe, Phys. Rev. 87, 156 (1952).

[28] Reference 24, pp. 111–13.

[29] A. Sommerfeld, *Atombau und Spektrallinien* (F. Vieweg and Son, Braunschweig, 1939), Vol. 2, pp. 457 and 502.

[30] Bethe, Maximon, and Low, Phys. Rev. 91, 417 (1953).

[31] Rose, Biedenharn, and Arfken, Phys. Rev. 85, 5 (1952).

[32] W. Rarita and J. Schwinger, Phys. Rev. 59, 436 (1941).

The solution of this equation is the initial electron wave function, ψ_1.

In first order, we have to solve

$$(H_e+H_r-E_1)\Psi^{(1)}=-H'\Psi^{(0)}. \tag{4.6}$$

Now if we take the part of $\Psi^{(1)}$ in which there is a quantum k present, $H_r\Psi^{(1)}=k\Psi^{(1)}$ and

$$(H_e-E_2)\Psi^{(1)}=-H'\Psi^{(0)}=-H'\psi_1, \tag{4.7}$$

since $E_2=E_1-k$. Now if we take the factor of $\Psi^{(1)}$ which describes the electron and denote it by ϕ, then

$$(H_e-E_2)\phi=C'\alpha_\lambda\psi_1 e^{-i\mathbf{k}\cdot\mathbf{r}}\equiv S, \tag{4.8}$$

where C' is a constant closely related to C, Eq. (4.2). The right-hand side of (4.8) will be called "the source" and denoted by S. Our task is now to solve (4.8) by a wave function ϕ which consists exclusively of outgoing spherical waves, without any plane wave, because there is no incident electron having the final momentum $\mathbf{p}_2$.

Writing the left-hand side of (4.8) more explicitly, we seek a solution of

$$[\nabla^2+p_2^2+U(r)]\phi=S, \tag{4.9}$$

where $U(r)$ is the "potential operator" occurring in (2.3), *viz.*,

$$U(r)=2\epsilon a/r-ia\boldsymbol{\alpha}\cdot\nabla(1/r)+a^2/r^2, \tag{4.10}$$

and the solution ϕ is supposed to contain only outgoing spherical waves. Exactly the same problem is solved by Mott and Massey, with somewhat different notation and with the restrictive assumption that

$$rU(r)\to 0, \text{ as } r\to\infty.$$

This restriction is not satisfied by our potential (4.10) but can be satisfied by introducing a screening factor $e^{-\alpha r}$ in (4.10) and letting α go to zero in the end.

Mott and Massey show that ϕ behaves asymptotically, as

$$\phi(\mathbf{r})=-(4\pi r)^{-1}e^{ip_2r}\int d\tau' S(\mathbf{r}')\mathfrak{F}(r',\pi-\Theta), \tag{4.11}$$

where

$$\mathfrak{F}(r',\theta)=\sum(2l+1)i^l e^{i\eta_l}L_l(r')P_l(\theta) \tag{4.12}$$

is the well-known solution of the ***homogeneous*** wave equation in the given potential, i.e., of (4.9) with zero on the right-hand side. The asymptotic behavior of $\mathfrak{F}$ is the usual one, *viz.*, plane wave plus outgoing spherical waves. L_l is the regular (and real) solution of the radial wave equation and η_l the phase shift for angular momentum l in the given potential. According to (4.11), $\mathfrak{F}$ must be taken in the integrand at the angle $\pi-\Theta$, where Θ is defined by Mott and Massey as the angle between the vectors $\mathbf{r}$ and $\mathbf{r}'$. Now we are interested in the asymptotic behavior of $\phi(\mathbf{r})$ in the direction $\mathbf{p}_2$; therefore we must choose $\mathbf{r}$ in (4.11) in the direction of $\mathbf{p}_2$, and $\pi-\Theta=\chi$ is the angle between $-\mathbf{p}_2$ and $\mathbf{r}'$. Therefore $\mathfrak{F}(r',\pi-\Theta)$ is a function which behaves asymptotically like a plane wave propagating in the direction $-\mathbf{p}_2$, plus the outgoing spherical waves associated with it by the potential $U(r)$; thus,

$$\mathfrak{F}(r,\pi-\Theta)\to e^{-ip_2\cdot r}+r^{-1}e^{ip_2r}f(\chi), \tag{4.13}$$

where $\chi=\pi-\Theta$ is the angle between $-\mathbf{p}_2$ and $\mathbf{r}$, and $f(\chi)$ is the amplitude of the wave scattered through an angle χ from the direction of the plane wave, $-\mathbf{p}_2$.

It should be noted that in (4.11) $\mathfrak{F}$ occurs, not $\mathfrak{F}^*$. Therefore $\mathfrak{F}$ must be identified with ψ_2^* in the matrix element (4.1). Therefore ψ_2 itself[33] will be

$$\psi_2=\mathfrak{F}^*(r,\pi-\Theta)=e^{+ip_2\cdot r}+r^{-1}e^{-ip_2r}f^*(\chi). \tag{4.14}$$

In other words, ψ_2 is a plane wave propagating as usual in the direction $+\mathbf{p}_2$, plus a spherical wave which is *ingoing* rather than outgoing. The amplitude of the ingoing wave is large near $\chi=0$, or $\Theta=\pi$, i.e. on the side *from which the plane wave is coming*, as is reasonable for an ingoing spherical wave associated with the plane wave $e^{ip_2\cdot r}$.[34]

We can prove more explicitly that ψ_2 is just the solution of the homogeneous equation which satisfies the boundary condition of having no *outgoing* spherical waves added to the plane wave $e^{ip_2\cdot r}$. Inserting $\theta=\pi-\Theta$ in (4.12), we note that $P_l(\pi-\Theta)=(-1)^lP_l(\Theta)$ and $i^l(-1)^l=i^{-l}$; in fact, this is the way in which $\mathfrak{F}(r',\pi-\Theta)$ is first introduced in the derivation by Mott and Massey. Therefore

$$\begin{aligned}\psi_2(\mathbf{r}')&=\mathfrak{F}^*(r',\pi-\Theta)\\&=\sum(2l+1)i^l e^{-i\eta_l}L_l(r')P_l(\Theta).\end{aligned} \tag{4.15}$$

This differs from the usual expression for the wave function, (4.12), only by having $e^{-i\eta_l}$ instead of $e^{i\eta_l}$. By considering the asymptotic behavior of $L_l(r')$, it is easily seen[35] that

$$\psi_2=e^{ip_2\cdot r}+r^{-1}e^{-ip_2r}g(\theta), \tag{4.16}$$

with

$$\begin{aligned}g(\theta)&=(-2ik)^{-1}\sum(2l+1)(e^{-2i\eta_l}-1)(-1)^lP_l(\theta)\\&=f^*(\pi-\theta)=f^*(\chi).\end{aligned} \tag{4.17}$$

For the actual evaluation of the matrix element, it is more convenient to use $\mathfrak{F}$ than ψ_2. As is seen from (4.13), $\mathfrak{F}$ is the usual solution, plane wave plus outgoing spherical waves, only with $-\mathbf{p}_2$ instead of $+\mathbf{p}_2$. Therefore, if we consider only the part of the matrix element (4.1) arising from the "main" part ψ_a, defined in (2.13),

[33] There is of course no need to go to ψ_2; the actual calculation could be done equally well directly with $\mathfrak{F}$.

[34] It is good to note that in the Born approximation one doesn't need to pay attention to the incoming wave because one doesn't consider any spherical waves at all in the wave function. This was recognized by Mott and Massey, p. 356, reference 10.

[35] As in Mott and Massey, pp. 22–24, reference 10.

of the wave functions ψ_1 and ψ_2, we get

$$H_{12}'=CN_1N_2^*(u_2^*\alpha_\lambda u_1)\int d\tau e^{-i\mathbf{k}\cdot\mathbf{r}}e^{i(\mathbf{p}_1-\mathbf{p}_2)\cdot\mathbf{r}}$$

$$\times F(ia_1;1;ip_1r-i\mathbf{p}_1\cdot\mathbf{r})F(ia_2;1;ip_2r+i\mathbf{p}_2\cdot\mathbf{r}) \quad (4.18)$$

with

$$a_1=a\epsilon_1/p_1, \quad a_2=a\epsilon_2/p_2. \quad (4.19)$$

The usual choice of ψ_2, with outgoing spherical waves, would replace the last factor in (4.18) by

$$F(-ia_2;1;-ip_2r+i\mathbf{p}_2\cdot\mathbf{r}). \quad (4.20)$$

The evaluation of the matrix element will be given in Sec. VIII.

V. WAVE FUNCTION AND MATRIX ELEMENT IN PAIR PRODUCTION

In the case of pair production, *both* the electron and the positron are produced, and therefore both should be represented by plane waves with convergent spherical waves. Thus, in contrast to the Born approximation theory, there is a significant difference between the matrix element for bremsstrahlung and pair production. The latter is

$$H_{12}'=C\int\psi_-^*\alpha_\lambda\psi_+^*e^{i\mathbf{k}\cdot\mathbf{r}}d\tau, \quad (5.1)$$

where ψ_+ is the wave function of the positron.

The spinor factor u_+^* in the wave function ψ_+^* of a positron of momentum $\mathbf{p}_+$ is the same as the spinor factor u_1 (not conjugate) in the wave function of an electron of momentum $-\mathbf{p}_+$ and negative energy $-\epsilon_+$. The matrix element (5.1) thus contains the matrix factor

$$b=(u_-^*\alpha_\lambda u_1). \quad (5.2)$$

The spatial part of ψ_+ differs from that of an electron by having the sign of the Coulomb interaction reversed. This can be accomplished by changing the sign of $a\epsilon/p$ in the first argument of the hypergeometric function (2.6), thus obtaining

$$\psi_{+a}'=N_+e^{i\mathbf{p}_+\cdot\mathbf{r}}u_+F(-ia\epsilon_+/p_+;1;ip_+r-i\mathbf{p}_+\cdot\mathbf{r}) \quad (5.3)$$

for a positron going in the direction $\mathbf{p}_+$ plus *outgoing* spherical waves. For ψ_+ in (5.1) we must again take ingoing spherical waves, so that ψ_+^* is represented, in analogy with (4.18), by

$$\psi_{+a}^*=N_+^*e^{-i\mathbf{p}_+\cdot\mathbf{r}}u_1F(-ia_1;1;ip_+r+i\mathbf{p}_+\cdot\mathbf{r}), \quad (5.4)$$

with

$$a_1=a\epsilon_+/p_+. \quad (5.5)$$

Similarly, the negaton is described by a wave function ψ_-^* exactly like the last factor of (4.18), and the "main" part of the matrix element (5.1) becomes

$$H_{12}'=CN_+^*N_-^*(u_-^*\alpha_\lambda u_1)\int d\tau e^{i(\mathbf{k}-\mathbf{p}_1-\mathbf{p}_2)\cdot\mathbf{r}}$$

$$\times F(-ia_1;1;ip_+r+i\mathbf{p}_+\cdot\mathbf{r})$$

$$\times F(ia_-;1;ip_-r+i\mathbf{p}_-\cdot\mathbf{r}). \quad (5.6)$$

Asymptotically for large r, the hypergeometric function gives a large scattered wave where its argument is small. The scattered waves of *both* electron and positron in (5.6) are therefore large when $\mathbf{r}$ is in the direction $-\mathbf{p}$ (convergent waves), whereas in (4.18) one scattered wave (for the incident electron) is large in the direction $+\mathbf{p}$, the other (outgoing electron) in the direction $-\mathbf{p}$. This will make a considerable difference in the matrix element.

As is well known, ψ_+^* can also be considered as the wave function (not conjugate) of a negative energy, negatively charged electron. The usual prescription for obtaining this is to take the electron wave function

$$\psi_1=N_1e^{i\mathbf{p}_1\cdot\mathbf{r}}F(ia\epsilon_1/p_1;1;ip_1r-i\mathbf{p}_1\cdot\mathbf{r})u(\mathbf{p}_1,\epsilon_1), \quad (5.7)$$

and substitute $\epsilon_1=-\epsilon_+$, $\mathbf{p}_1=-\mathbf{p}_+$, while leaving $p_1=+p_+$. It is easily seen that this leads to the correct function

$$\psi_1=N_1e^{-i\mathbf{p}_+\cdot\mathbf{r}}$$

$$\times F(-ia\epsilon_+/p_+;1;ip_+r+i\mathbf{p}_+\cdot\mathbf{r})u(-\mathbf{p}_+,-\epsilon_+), \quad (5.8)$$

which is exactly the function occurring in (5.6).

VI. EVALUATION OF THE PAIR MATRIX ELEMENT AND CROSS SECTION

We proceed now to the evaluation of the matrix element (5.1). For ease of writing, we shall denote the quantities referring to the positron by the subscript 1 rather than +, and those referring to the electron by 2. Thus $\mathbf{p}_1=\mathbf{p}_+$ in the next two sections, F_1 is the hypergeometric function relating to the positron and F_2^* that for the electron.

We substitute $d^3\rho=(\hbar/mc)^3d^3\mathbf{r}$ and $\psi_1=\psi_{1a}+\psi_{1b}+\psi_{1c}$, as in (2.13), and similarly for the negaton. Of the resulting integrals we will show that three may be evaluated in closed form, and those remaining will be shown in Sec. IX to give contributions to the differential cross-section which may be neglected when the energies of the positive and negative electron are much larger than mc^2.

We proceed then to those integrals that may be evaluated in closed form and to the differential cross-section determined from them alone. These integrals are

$$C\int\psi_{2a}^*\alpha_\lambda e^{i\mathbf{k}\cdot\mathbf{r}}\psi_{1a}d^3\rho+C\int\psi_{2a}^*\alpha_\lambda e^{i\mathbf{k}\cdot\mathbf{r}}\psi_{1b}d^3\rho$$

$$+C\int\psi_{2b}^*\alpha_\lambda e^{i\mathbf{k}\cdot\mathbf{r}}\psi_{1a}d^3\rho. \quad (6.1)$$

Using (2.14), (2.15), the matrix element which we will use may be written in the form

$$H_{12}'=C'[(u_2^*\alpha_\lambda u_1)I_1+(u_2^*\alpha_\lambda\boldsymbol{\alpha}\cdot\mathbf{I}_2u_1)+(u_2^*\boldsymbol{\alpha}\cdot\mathbf{I}_3\alpha_\lambda u_1)], \quad (6.2)$$

where

$$I_1=\int e^{i\mathbf{q}\cdot\mathbf{r}}F_2^*F_1d^3r, \quad (6.3)$$

$$\mathbf{I}_2=-(i/2\epsilon_1)\int e^{i\mathbf{q}\cdot\mathbf{r}}F_2^*\nabla F_1d^3r, \quad (6.3a)$$

$$\mathbf{I}_3=(i/2\epsilon_2)\int e^{i\mathbf{q}\cdot\mathbf{r}}(\nabla F_2^*)F_1d^3r, \quad (6.3b)$$

and

$$C'=C(\hbar/mc)^3N_2^*N_1, \quad (6.4)$$

$$\mathbf{q}=\mathbf{k}-\mathbf{p}_1-\mathbf{p}_2. \quad (6.5)$$

N_1 and N_2 will be determined so that ψ_1 and ψ_2 are normalized to unit amplitude asymptotically. Following Bess again, the integrals in (6.3) may be obtained from the integral

$$I_0=\int e^{-\lambda r}e^{i\mathbf{q}\cdot\mathbf{r}}F_2^*F_1d^3r/r \quad (6.6)$$

by differentiation with respect to parameters. Thus

$$I_1=-\partial I_0/\partial\lambda|_{\lambda=0}. \quad (6.7)$$

Further, according to (5.6),

$$F_1=F(-ia_1;\,1;\,ip_1r+i\mathbf{p}_1\cdot\mathbf{r}),$$

and differentiation of the argument gives

$$\nabla_r(p_1r+\mathbf{p}_1\cdot\mathbf{r})=(p_1/r)\nabla_{p_1}(p_1r+\mathbf{p}_1\cdot\mathbf{r}), \quad (6.8)$$

where

$$\nabla_{p_1}\equiv(\partial/\partial p_{1x},\,\partial/\partial p_{1y},\,\partial/\partial p_{1z}), \quad (6.9)$$

and F_2 is independent of $\mathbf{p}_1$. Therefore we have

$$\mathbf{I}_2=-(ip_1/2\epsilon_1)\nabla_{p1}\int e^{i\mathbf{q}\cdot\mathbf{r}}F_2^*F_1d^3r/r$$

$$=-(ia/2a_1)\nabla_{p1}I_0|_{\lambda=0}, \quad (6.10)$$

in which both a_1 and $\mathbf{q}$ are to be considered independent of $\mathbf{p}_1$ when operating with ∇_{p1}. Similarly, since $F_2^*=F(ia_2;\,1;\,ip_2r+i\mathbf{p}_2\cdot\mathbf{r})$,

$$\mathbf{I}_3=(ia/2a_2)\nabla_{p2}I_0|_{\lambda=0}. \quad (6.11)$$

The method used in the evaluation of I_0 (involving contour integration) is due to Dr. A. T. Nordsieck.[36] The authors are indebted to Dr. Nordsieck for his generous communication of the essential steps of this evaluation. By a calculation entirely analogous to that in the accompanying paper,[36] we obtain

$$I_0=\frac{2\pi}{\alpha}\left(\frac{\gamma}{\alpha}\right)^{i\omega_1}\left(\frac{\alpha}{\alpha+\beta}\right)^{i\omega_2}F(-ia_1,\,ia_2;\,1;\,x), \quad (6.12)$$

where

$$\alpha=\tfrac{1}{2}(q^2+\lambda^2),\qquad \beta=\mathbf{p}_2\cdot\mathbf{q}-i\lambda p_2,$$
$$\gamma=\mathbf{p}_1\cdot\mathbf{q}-i\lambda p_1+\alpha,\quad \delta=\mathbf{p}_1\cdot\mathbf{p}_2-p_1p_2+\beta, \quad (6.13)$$

$$x=(\beta\gamma-\alpha\delta)/[\gamma(\alpha+\beta)]. \quad (6.14)$$

For small λ, the three quantities α, $\alpha+\beta$, and γ are all real; in fact we have

$$D_1\equiv 2(\alpha+\beta)_{\lambda=0}=2\mathbf{q}\cdot\mathbf{p}_2+q^2$$
$$=(\mathbf{k}-\mathbf{p}_1)^2-p_2^2=2k(\epsilon_1-p_1\cos\vartheta_1);$$
$$D_2\equiv 2(\gamma)_{\lambda=0}=2\mathbf{q}\cdot\mathbf{p}_1+q^2 \quad (6.15)$$
$$=(\mathbf{k}-\mathbf{p}_2)^2-p_1^2=2k(\epsilon_2-p_2\cos\vartheta_2).$$

Therefore the two powers with imaginary exponent in (6.12) will be of absolute magnitude unity. The argument of the hypergeometric function, x, can be shown to be between 0 and 1. For most calculations, it is preferable to consider

$$y\equiv 1-x=\left.\frac{\alpha(\gamma+\delta)}{\gamma(\alpha+\beta)}\right|_{\lambda=0}. \quad (6.16)$$

Some algebra yields

$$y=q^2\mu/D_1D_2, \quad (6.17)$$

where

$$\mu=2(\gamma+\delta)_{\lambda=0}=k^2-(p_1+p_2)^2 \quad (6.18)$$

is a positive quantity (since $k=\epsilon_1+\epsilon_2$), independent of angles. It is convenient to introduce the abbreviations:

$$K=4\pi a(D_2/q^2)^{ia_1}(D_1/q^2)^{-ia_2},\quad |K|=4\pi a, \quad (6.19)$$

$$V_{12}(x)=F(-ia_1,\,ia_2;\,1;\,x), \quad (6.20)$$

$$W_{12}(x)=(a_1a_2)^{-1}dV_{12}/dx$$
$$=F(1-ia_1,\,1+ia_2;\,2;\,x). \quad (6.21)$$

We now differentiate (6.12) as required in (6.7), (6.10), and (6.11). For this purpose, $\mathbf{q}$ must be kept constant, i.e., (6.15) and (6.18) must not be used until *after* the differentiation. We note that, for $\lambda=0$,

$$-p_1\nabla_{p1}\delta=p_2\mathbf{p}_1-p_1\mathbf{p}_2\equiv\mathbf{P},\quad \nabla_{p2}\delta=\mathbf{P}/p_2+\mathbf{q}. \quad (6.22)$$

We obtain

$$I_1=2K\left\{\frac{V_{12}}{q^2}\left(\frac{\epsilon_2}{D_1}-\frac{\epsilon_1}{D_2}\right)+\frac{iW_{12}}{D_1D_2}\left[a_1\epsilon_2\left(\frac{\mu}{D_1}-1\right)+a_2\epsilon_1\left(\frac{\mu}{D_2}-1\right)\right]\right\},$$

$$\mathbf{I}_2=K\left\{-\frac{V_{12}}{D_2}\frac{\mathbf{q}}{q^2}+ia_2\frac{W_{12}}{D_1D_2}\left[\mathbf{q}\left(\frac{\mu}{D_2}-1\right)+\frac{\mathbf{P}}{p_1}\right]\right\}, \quad (6.23)$$

$$\mathbf{I}_3=K\left\{\frac{V_{12}}{D_1}\frac{\mathbf{q}}{q^2}+ia_1\frac{W_{12}}{D_1D_2}\left[\mathbf{q}\left(\frac{\mu}{D_1}-1\right)-\frac{\mathbf{P}}{p_2}\right]\right\}.$$

[36] A. T. Nordsieck, following paper in this issue. The integration was already carried out by Bess, but it is somewhat more difficult to follow the complex arguments of all the quantities involved in Bess' paper.

In the limit of high energies, $a_1=a_2=a$ with an error of the relative order $1/\epsilon^2$. We may therefore replace V_{12} and W_{12}, respectively, by

$$V(x)=F(-ia, ia; 1; x)$$
$$=1+\frac{a^2}{1!^2}x+\frac{a^2(1+a^2)}{2!^2}x^2+\frac{a^2(1+a^2)(2^2+a^2)}{3!^2}x^3+\cdots, \quad (6.24)$$

$$W(x)=a^{-2}dV/dx$$
$$=1+\frac{1+a^2}{1!2!}x+\frac{(1+a^2)(2^2+a^2)}{2!3!}x^2+\cdots. \quad (6.25)$$

Both of these functions are real so that the expressions for I_1 to $\mathbf{I}_3$, (6.23), fall into a real part proportional to V and an imaginary part proportional to W. The resulting cross section therefore contains only V^2 and W^2, not VW.

In the cross section we require the absolute square of the matrix element H_{12}', Eq. (5.1), summed over the spin directions of electron and positrons, and averaged over the directions of polarization of the incident quantum. Since the spin sums of $|H_{12}'|^2$ involve the free-electron Dirac matrix coefficients u_1 and u_2 we may use the spur and closure theorems. From (6.2) we have then

$$\Sigma|H_{12}'|^2=|C'|^2(\epsilon_1\epsilon_2)^{-1}$$
$$\times\sum_{\nu=1}^{2}\{I_{1\nu}^2(\epsilon_1\epsilon_2+1-p_1p_2\cos\theta_1\cos\theta_2)$$
$$+(\mathbf{I}_{2\nu}^2+\mathbf{I}_{3\nu}^2)(\epsilon_1\epsilon_2-1+p_1p_2\cos\theta_1\cos\theta_2)$$
$$-2I_{2\nu z}I_{3\nu z}(\epsilon_1\epsilon_2-1+\mathbf{p}_1\cdot\mathbf{p}_2)$$
$$+2(\mathbf{I}_{2\nu}-\mathbf{I}_{3\nu})\cdot(\mathbf{p}_2I_{3\nu z}p_{1z}-\mathbf{p}_1I_{2\nu z}p_{2z})$$
$$+2\mathbf{I}_{3\nu}\cdot\mathbf{p}_2\mathbf{I}_{2\nu}\cdot\mathbf{p}_1-2\mathbf{I}_{2\nu}\cdot\mathbf{p}_2\mathbf{I}_{3\nu}\cdot\mathbf{p}_1$$
$$+2I_{1\nu}\epsilon_2(\mathbf{I}_{2\nu}\cdot\mathbf{p}_1-I_{3\nu z}p_{1z})$$
$$+2I_{1\nu}\epsilon_1(\mathbf{I}_{3\nu}\cdot\mathbf{p}_2-I_{2\nu z}p_{2z})$$
$$+2(\mathbf{p}_1\cdot\mathbf{p}_2-p_{1z}p_{2z})\mathbf{I}_{2\nu}\cdot\mathbf{I}_{3\nu}\}, \quad (6.26)$$

where $I_{k\nu}$, with $\nu=1$ and 2, denote the real and imaginary part, respectively, of the integral I_k, $k=1$ to 3 (see remarks following Eq. (6.25)). The subscript z used in the expression above denotes the z component of the vector to which it applies, i.e., the component in the direction of $\mathbf{k}$.

The results (6.23), (6.26) do not differ greatly from Bess' results (37) and (36). In (6.26), the only difference is that Bess omitted the last line which is in fact not important for small angles θ_1, θ_2. In (6.23), $\mathbf{I}_2$ and $\mathbf{I}_3$ differ from Bess' expression only by the denominators p_1 and p_2 in the last terms which are needed for dimensional reasons. I_1 is much simpler than the corresponding expression of Bess which contains a number of additional terms arising from the incorrect part of his wave function.[21] It is reasonable that the results should differ only in I_1 because Bess' additional term in ψ, $(a/2\epsilon)\partial F/\partial r$, involves no matrix operator and should have the same matrix factor as the contribution of ψ_a. A minor change is in the coefficient K for which Bess has $4\pi a(D_1/D_2)^{ia}$; this does not affect the result.

The transition probability per unit time is

$$w=(2\pi/\hbar)\rho_f\Sigma|H_{12}'|^2, \quad (6.27)$$

where $\Sigma|H_{12}'|^2$ is given by (6.26) and ρ_f is the density of final states for the two emitted electrons, i.e.,

$$\rho_f=(mc^2)^4p_1\epsilon_1p_2\epsilon_2d\Omega_1d\Omega_2(2\pi\hbar c)^{-6}, \quad (6.28)$$

where $d\Omega_1$, and $d\Omega_2$ are the solid angles.

The differential cross section, $d\sigma$, is equal to the transition probability normalized to unit current of the incident particle. Thus we must divide w by the velocity of the incident quantum, c, and obtain

$$d\sigma=\frac{(2\pi)^2}{\hbar c}\frac{(mc^2)^4}{(2\pi\hbar c)^6}p_1p_2\epsilon_1\epsilon_2\Sigma|H_{12}'|^2d\epsilon_1$$
$$\times\sin\theta_1d\theta_1\sin\theta_2d\theta_2d\phi, \quad (6.29)$$

where $\phi=\phi_1-\phi_2$ and the integration over ϕ_2 has been carried out, yielding a factor 2π.

The factor $|C'|^2$ in $|H_{12}'|^2$ is given by (6.4) and (4.2) in terms of the normalization factors N_1 and N_2. The wave function of the negative electron is asymptotically $\psi_2=N_2e^{i\mathbf{p}_2\cdot\mathbf{r}}u_2F_2$. Since the exponential and u_2 are normalized to unity we must examine the asymptotic behavior of F_2 which is

$$F_2\sim[\Gamma(1+ia_2)]^{-1}e^{-\pi a_2/2}e^{ia_2\log(p_2r+\mathbf{p}_2\cdot\mathbf{r})}. \quad (6.30)$$

Thus, normalizing ψ_2 to unit amplitude, we have

$$|N_2|^2=|\Gamma(1+ia_2)|^2e^{\pi a_2}=\pi a_2e^{\pi a_2}/\sinh\pi a_2, \quad (6.31)$$

whereas for the positive electron the sign of a is reversed, yielding

$$|N_1|^2=\pi a_1e^{-\pi a_1}/\sinh\pi a_1, \quad (6.32)$$

with positive a_1.

Substituting (4.2), (6.4), (6.19), (6.31), and (6.32), we have

$$|C'K|^2=(4\pi a)^2\frac{2\pi e^2\hbar^2c^2}{k}\left(\frac{\hbar}{mc}\right)^6\frac{\pi^2a_1a_2e^{\pi(a_2-a_1)}}{\sinh\pi a_1\sinh\pi a_2}. \quad (6.33)$$

Upon making the approximations $a_1\approx a$, $a_2\approx a$ [involving errors of $O(1/\epsilon^2)$], this becomes

$$|C'K|^2=\frac{(2\pi a)^4}{(\sinh\pi a)^2}\frac{2\pi e^2\hbar^2c^2}{k}\left(\frac{\hbar}{mc}\right)^6. \quad (6.34)$$

Substituting (6.23), (6.26), and (6.34) in (6.29), we

have the differential cross-section for pair production:

$$d\sigma = -\left(\frac{\pi a}{\sinh \pi a}\right)^2 \frac{a^2}{2\pi}\left(\frac{\hbar}{mc}\right)^2 \frac{e^2}{\hbar c}\frac{p_- p_+}{k^3} d\epsilon_+ \times \sin\theta_- \sin\theta_+ d\theta_- d\theta_+ d\phi$$
$$\times\left\{\frac{V^2(x)}{q^4}\left[\frac{p_-^2 \sin^2\theta_-(4\epsilon_+^2-q^2)}{(\epsilon_- - p_- \cos\theta_-)^2} + \frac{p_+^2 \sin^2\theta_+(4\epsilon_-^2-q^2)}{(\epsilon_+ - p_+ \cos\theta_+)^2} + \frac{(4\epsilon_-\epsilon_+ + q^2 - 2k^2)2p_- p_+ \sin\theta_- \sin\theta_+ \cos\phi}{(\epsilon_- - p_- \cos\theta_-)(\epsilon_+ - p_+ \cos\theta_+)} - \frac{2k^2(p_-^2 \sin^2\theta_- + p_+^2 \sin^2\theta_+)}{(\epsilon_- - p_- \cos\theta_-)(\epsilon_+ - p_+ \cos\theta_+)}\right]\right.$$
$$+ \frac{a^2[k^2 - (p_- + p_+)^2]^2 W^2(x)}{[4k^2(\epsilon_- - p_- \cos\theta_-)(\epsilon_+ - p_+ \cos\theta_+)]^2}$$
$$\times\left[\frac{p_-^2 \sin^2\theta_-(4\epsilon_+^2-q^2)}{(\epsilon_- - p_- \cos\theta_-)^2} + \frac{p_+^2 \sin^2\theta_+(4\epsilon_-^2-q^2)}{(\epsilon_+ - p_+ \cos\theta_+)^2} - \frac{(4\epsilon_-\epsilon_+ + q^2 - 2k^2)2p_- p_+ \sin\theta_- \sin\theta_+ \cos\phi}{(\epsilon_- - p_- \cos\theta_-)(\epsilon_+ - p_+ \cos\theta_+)} + \frac{2k^2(p_-^2 \sin^2\theta_- + p_+^2 \sin^2\theta_+)}{(\epsilon_- - p_- \cos\theta_-)(\epsilon_+ - p_+ \cos\theta_+)}\right.$$
$$\left.\left. - 4k^2(\epsilon_-\epsilon_+ + p_- p_+ \cos\theta_- \cos\theta_+)\right]\right\}. \quad (6.35)$$

It will be recognized that the first group of terms, those proportional to $V^2(x)$, is identical with the Bethe-Heitler cross section except for the factor

$$[V(x)\pi a/\sinh \pi a]^2. \quad (6.36)$$

It can be shown that[37]

$$V(x=1) = \sinh \pi a/\pi a, \quad (6.37)$$

so that the cross section is simply multiplied by

$$[V(x)/V(1)]^2. \quad (6.38)$$

In addition, there is another group of terms proportional to $W^2(X)$. These terms have a form very similar to that of the Bethe-Heitler terms, but the deviations from the latter are real, as will be further demonstrated in the next section.

The pair-production cross section (6.35) may be compared with Bess's result (38) for bremsstrahlung. When the translation from one phenomenon to the other is made in the usual way, the main difference is that (6.35) does not contain those terms which arise from Bess' spurious terms in I_1, i.e., all his terms containing a^2V^2, a^2VW or a^4W^2. In addition, Bess omitted the q^2 terms in the first square bracket, which is not serious. The second bracket has been completely rewritten to make its similarity with the first bracket evident; apart from this, it differs from Bess' appreciably in content.

[37] Davies, Bethe, and Maximon, Eq. (24), this issue [Phys. Rev. 93, 788 (1954)].

VII. SMALL-ANGLE APPROXIMATION

It is well known that the main contribution to the *integral* cross section for either pair production or bremsstrahlung comes from *small* angles, θ_1 and θ_2 of order $1/\epsilon$. Moreover, our whole approximation, i.e., the representation of the electron wave functions by the contributions a and b, alone, Eqs. (2.14), (2.15), is only justified for small angles. It is therefore interesting to investigate the behavior of our matrix elements and cross sections in the limit of small angles. This will permit a considerable simplification, and thereby better insight into the orders of magnitude and the structure of the expression. Furthermore, this simplification is an essential first step in the integration of the cross section over angles.[38]

We introduce the vectors $\mathbf{u}$ and $\mathbf{v}$ to denote the components of $\mathbf{p}_1$ and $\mathbf{p}_2$, respectively, perpendicular to $\mathbf{k}$. Their magnitudes are

$$u = p_1\theta_1, \quad v = p_2\theta_2, \quad (7.1)$$

if we make the approximation $\sin\theta_1 = \theta_1$, $1-\cos\theta_1 = \frac{1}{2}\theta_1^2$ which we shall use generally. It is convenient to split $\mathbf{q}$ into the part in the z direction and the part perpendicular to $\mathbf{k}$ which are, respectively,

$$q_z = (1+u^2)/2\epsilon_1 + (1+v^2)/2\epsilon_2, \quad (7.2)$$

$$\mathbf{q}_\perp = -(\mathbf{u}+\mathbf{v}),$$
$$q_\perp^2 = u^2 + v^2 + 2uv\cos\phi. \quad (7.3)$$

Here, and in the following, we neglect consistently terms of relative order $1/\epsilon^2$. The minimum value of q, for $u=v=0$, is

$$q_{\min} = q_{z\,\min} \equiv \delta = k - p_1 - p_2 \approx k/2\epsilon_1\epsilon_2. \quad (7.4)$$

If u and v are of order 1, q is of the same order; but q_z is generally of order $1/\epsilon$ and q *can* be of that order if the vectors $\mathbf{u}$ and $\mathbf{v}$ are nearly equal and opposite.

The quantities introduced in (6.15) to (6.18) are, in our approximation and notation,

$$D_1 = (k/\epsilon_1)(1+u^2), \quad D_2 = (k/\epsilon_2)(1+v^2), \quad (7.5)$$

$$\mu = 2k\delta = k^2/\epsilon_1\epsilon_2, \quad (7.6)$$

$$y = q^2/[(1+u^2)(1+v^2)]. \quad (7.7)$$

It will be convenient in the following to use the further

[38] We are indebted to Dr. Handel Davies who carried out the angular integration, for some of the calculations reported in this section.

abbreviations:

$$\xi=1/(1+u^2), \quad \eta=1/(1+v^2), \tag{7.8}$$

in terms of which (7.5) and (7.7) can easily be rewritten. If k and ϵ_1, ϵ_2 are regarded as of the same order of magnitude (order ϵ), and are large compared with 1, then D_1, D_2, μ, y, u, v, ξ, and η are all of order unity.

The vector $\mathbf{P}$ introduced in (6.22) has the components

$$\mathbf{P}_\perp=\epsilon_2\mathbf{u}-\epsilon_1\mathbf{v}, \quad P_z=(\epsilon_1/2\epsilon_2)v^2-(\epsilon_2/2\epsilon_1)u^2. \tag{7.9}$$

Since p occurs only with the denominators p_1, p_2 in (6.23), the component P_z (which is of order 1) gives a negligible contribution compared with either $P_\perp$ (order ϵ) or the remaining terms in (6.23).

Inserting into (6.23), we obtain

$$\begin{aligned} I_1&=2K(\epsilon_1\epsilon_2/k)[q^{-2}(\eta-\xi)V+ia(\xi+\eta-1)W], \\ \mathbf{I}_2&=K(\epsilon_2/k)[-\mathbf{q}q^{-2}\eta V+ia(\mathbf{u}+\eta\mathbf{q})W], \\ \mathbf{I}_3&=K(\epsilon_1/k)[\mathbf{q}q^{-2}\xi V+ia(\mathbf{v}+\xi\mathbf{q})W]. \end{aligned} \tag{7.10}$$

These expressions are very much simpler than (6.23). They show clearly that I_1 is of order ϵ, while I_2 and I_3 are of order 1. This is to be expected from the definitions (6.3) in which $\mathbf{I}_2$, $\mathbf{I}_3$ have extra denominators ϵ_1, ϵ_2. It can also be shown by the methods of Sec. IX.

The spin sum (6.26) contains many terms which are negligible in the limit of high energies and small angles. Clearly, the factor of I_2^2 inside the braces of (6.26) is of order ϵ^2, therefore the complete expression in the braces must be expected to be (and turns out to be) of this order. This means that we should retain coefficients of order 1 multiplying I_1^2, of order ϵ multiplying I_1I_2 or I_1I_3, and of order ϵ^2 multiplying I_2^2, I_2I_3, or I_3^2; all lower powers of ϵ can be neglected. Doing this, (6.26) becomes after some algebra,

$$\begin{aligned} \Sigma|H_{12}'|^2=|C'|^2(\epsilon_1\epsilon_2)^{-1}\sum_\nu\{&(2\epsilon_1\epsilon_2)^{-1} \\ &\times(k^2+\epsilon_2^2u^2+\epsilon_1^2v^2)I_{1\nu}^2 \\ &+2I_{1\nu}(\epsilon_2\mathbf{u}\cdot\mathbf{I}_{2\nu\perp}+\epsilon_1\mathbf{v}\cdot\mathbf{I}_{3\nu\perp}) \\ &+2\epsilon_1\epsilon_2(I_{2\nu\perp}^2+I_{3\nu\perp}^2)\}. \end{aligned} \tag{7.11}$$

This can also be written

$$\begin{aligned} \Sigma|H_{12}'|^2=|C'|^2\sum_\nu\{&(k^2/2\epsilon_1\epsilon_2)I_{1\nu}^2 \\ &+2(I_{1\nu}\mathbf{u}/2\epsilon_1+\mathbf{I}_{2\nu\perp})^2+2(I_{1\nu}\mathbf{v}/2\epsilon_2+\mathbf{I}_{3\nu\perp})^2\}. \end{aligned} \tag{7.12}$$

The simplification achieved in (7.11), (7.12) is quite remarkable. The result can also be understood directly by evaluating approximately the matrix elements occurring in (6.2), *viz.*,

$$b=(u_2^*\alpha_\lambda u_1), \quad \mathbf{c}=(u_2^*\alpha_\lambda\boldsymbol{\alpha}u_1), \tag{7.13}$$

between an initial state of energy $-\epsilon_1$, momentum $-\mathbf{p}_1$, and a final state ϵ_2, $\mathbf{p}_2$. Taking the λ component of $\mathbf{c}$, we obtain the operator $\alpha_\lambda^2=1$ whose matrix element is very nearly 1 if the spins of electron and positron are parallel. There are two possibilities of achieving this, *viz.*, both spins up or both down; hence the factor of I_2^2 and I_3^2 should be 2, as indeed it is in (7.12). Only the components of $\mathbf{I}_2$ and $\mathbf{I}_3$ perpendicular to $\mathbf{k}$ can come in because λ is perpendicular to $\mathbf{k}$. If the electron and positron have opposite spin, the matrix element of c_λ is of order $1/\epsilon$.

The matrix element b, for parallel spin of electron and positron, represents the sum of the velocities of the two particles in the direction of λ (or, after summing over polarization, the velocity component perpendicular to $\mathbf{k}$). The velocity of the positron perpendicular to $\mathbf{k}$ (in units of c) is $\mathbf{u}/\epsilon_1$, that of the electron $\mathbf{v}/\epsilon_2$. It is at least plausible that the positron velocity $\mathbf{u}/\epsilon_1$ will interfere only with $\mathbf{I}_2$ which is due to the correction to the positron wave function, and *vice versa*. The first term in (7.12) arises from the matrix elements of b which correspond to a reversal of spin.

From (7.12) and from the last two paragraphs, we can see clearly what has already been said in the introduction: $\mathbf{I}_2$ and $\mathbf{I}_3$ have matrix factors of order unity, thanks to the extra operator $\boldsymbol{\alpha}$ occurring in $\mathbf{c}$, while I_1 has a matrix factor of order $1/\epsilon$. Therefore, even though I_1 itself is much larger than I_2, *viz.*, of order ϵ rather than 1, its contribution to the complete matrix element is only of the same order as that of I_2 or I_3.

With the simplified expressions (7.10), (7.11), it is now easy to calculate the differential cross section which becomes

$$\begin{aligned} d\sigma=8\left(\frac{\pi a}{\sinh\pi a}\right)^2\frac{a^2}{2\pi}\left(\frac{\hbar}{mc}\right)^2\frac{e^2}{\hbar c}\frac{\epsilon_1^2\epsilon_2^2}{k^3}d\epsilon_1\theta_1d\theta_1\theta_2d\theta_2d\phi \\ \times\{q^{-4}V^2(x)[k^2(u^2+v^2)\xi\eta-2\epsilon_1\epsilon_2(u^2\xi^2+v^2\eta^2) \\ +2(\epsilon_1^2+\epsilon_2^2)uv\xi\eta\cos\phi]+a^2W^2(x)\xi^2\eta^2 \\ \times[k^2(1-(u^2+v^2)\xi\eta)-2\epsilon_1\epsilon_2(u^2\xi^2+v^2\eta^2) \\ -2(\epsilon_1^2+\epsilon_2^2)uv\xi\eta\cos\phi]\}. \end{aligned} \tag{7.14}$$

This result can also be obtained by making the high-energy, small-angle approximations in (6.35) and taking out a factor $8\epsilon_1\epsilon_2$ from the braces. However, the fact that (7.14) can also be deduced from the simple theory of this section gives confidence that no algebraic error has been made on its derivation, and that the difference in structure between the factors of V^2 and W^2 is real.

The result (7.14) is also the most suitable starting point for the integration over angles.

VIII. THE CROSS SECTION FOR BREMSSTRAHLUNG

The matrix element for bremsstrahlung is given in (4.18). Its evaluation is quite similar to that for pair production, with the result, analogous to (6.12),

$$\begin{aligned} I_0=\frac{2\pi}{\alpha}e^{-\pi a_2}\left(\frac{\alpha}{\gamma+\delta}\right)^{ia_1}\left(\frac{\gamma+\delta}{\gamma}\right)^{i(a_1-a_2)} \\ \times F(1-ia_1, ia_2; 1; x), \end{aligned} \tag{8.1}$$

where the meaning of α and β is the same as in (6.13)

but the other parameters are changed to

$$\gamma=\mathbf{p}_1\cdot\mathbf{q}+i\lambda p_1-\alpha, \quad \delta=p_1p_2+\mathbf{p}_1\cdot\mathbf{p}_2-\beta. \tag{8.2}$$

Also,

$$\mathbf{q}=\mathbf{p}_1-\mathbf{p}_2-\mathbf{k}, \tag{8.3}$$

and the argument of F is

$$x=(\alpha\delta-\beta\gamma)/[\alpha(\gamma+\delta)]. \tag{8.4}$$

It is again more convenient to use

$$y=1-x=\gamma(\alpha+\beta)/(\gamma+\delta)\alpha. \tag{8.5}$$

The reason for the appearance of the factor $e^{-\pi a_1}$ is explained in the paper by Nordsieck following this.

The most important change is that δ, Eq. (8.2), now contains the sum of p_1p_2 and $\mathbf{p}_1\cdot\mathbf{p}_2$ rather than their difference, as in (6.13). This change can be traced directly to the form of the matrix element (4.18) for bremsstrahlung which contains $\mathbf{p}_1\cdot\mathbf{r}$ and $\mathbf{p}_2\cdot\mathbf{r}$ with *opposite* signs while in the pair matrix elements (5.6) they occur with the same sign. The effect of the changed expression for δ is to make this quantity very large, of order ϵ^2, if $\mathbf{p}_1$ and $\mathbf{p}_2$ have nearly the same direction, as is usual. The three other parameters, α, β, γ in bremsstrahlung, and all four parameters in pair production, are of order 1. Since δ is now so large, the definition (6.14) of x is no longer convenient because it would make x larger than 1. The changed argument x in turn causes a change of the first parameter of the hypergeometric function, from $-ia_1$ to $1-ia_1$. The new definition (8.4) of x keeps $x<1$; in fact it is easy to show that $y=1-x$ is in general very small (see below). Since for small angles between $\mathbf{p}_1$ and $\mathbf{p}_2$ we may replace δ by $2\epsilon_1\epsilon_2$, we get

$$y=D_1D_2/4\epsilon_1\epsilon_2q^2, \tag{8.6}$$

where D_1 is the same as in (6.15), and

$$D_2=2(\gamma)_{\lambda=0}=2\mathbf{p}_1\cdot\mathbf{q}-q^2=p_1^2-(\mathbf{k}+\mathbf{p}_2)^2 \\ =2k(\epsilon_2-p_2\cos\vartheta_2) \tag{8.7}$$

is given by the same final expression as in (6.15) even though intermediate steps are different. Since D_1 and D_2 are of order 1, y will in general be of order $1/\epsilon^2$ (i.e., where q is of order 1) but will be larger for small q. In particular, if both $\mathbf{p}_1$ and $\mathbf{p}_2$ are in the direction $\mathbf{k}$, then q attains its minimum value (7.4); u and v, Eq. (7.1), are zero and this makes $y=1$ and $x=0$. Thus the argument of F in (8.1) is extremely close to one except for very small q: this is the essential difference between the results for bremsstrahlung and pair production.

We must now differentiate (8.1) with respect to λ, $\mathbf{p}_1$, and $\mathbf{p}_2$ as required by (6.7), (6.10), and (6.11). Consider first the differentiation of the factors in front of F. Of these, α does not depend on λ in first order, nor on the $\mathbf{p}$'s; γ has the exponent $i(a_1-a_2)$ which is of order $1/\epsilon^2$, and δ is so large that $\partial\log(\gamma+\delta)/\partial\lambda$, and the other derivatives, are small of order $1/\epsilon$ or less. Thus one can show that the differentiation of the factors outside of F in (8.1) contributes only a term of relative order $1/\epsilon$ which may be neglected.

It is then only necessary to differentiate with respect to the argument x of the hypergeometric function, and we obtain

$$I_1=\frac{2K}{a}\frac{1}{q^2}\frac{dF}{dx}yi\left(\frac{p_1}{D_2}-\frac{p_2}{D_1}\right), \tag{8.8}$$

where

$$K=4\pi ae^{-\pi a_1}(q^2/4\epsilon_1\epsilon_2)^{ia_1}(4\epsilon_1\epsilon_2/D_2)^{i(a_1-a_2)}. \tag{8.9}$$

We now transform the hypergeometric function. Setting $a_1=a_2=a$, it can easily be shown that

$$F\equiv F(1-ia, ia; 1; x)=F(-ia, ia; 1; x) \\ +iaxF(1-ia, 1+ia; 2; x)=V(x)+iaxW(x), \tag{8.10}$$

with V and W defined in (6.24), (6.25). One of the terms occurring in (8.8) is then

$$y\frac{d}{dx}(xW)=a^{-2}(1-x)\frac{d}{dx}\left(x\frac{dV}{dx}\right). \tag{8.11}$$

Now the hypergeometric function $F(a,b;c;x)$ satisfies the differential equation[39]

$$x(1-x)F''+[c-(a+b+1)x]F'-abF=0. \tag{8.12}$$

For $V=F(-ia, ia; 1; x)$, this becomes

$$x(1-x)V''+(1-x)V'-a^2V=0, \tag{8.13}$$

and, therefore,

$$(1-x)\frac{d}{dx}\left(x\frac{dV}{dx}\right)=a^2V. \tag{8.14}$$

Inserting in (8.8), (8.10), (8.11) gives

$$I_1=2Kq^{-2}(p_2/D_1-p_1/D_2)[V-iayW]. \tag{8.15}$$

This is just the first part I_1 in (6.23), with $V(x)$ replaced by $V-iayW$. Similarly, $\mathbf{I}_2$ and $\mathbf{I}_3$ also become equal to the first term in the respective formulas (6.23), with the same replacement.[40] This result is very similar to the Born approximation which corresponds to taking the limit $a=0$. Doing this in Eq. (6.23) removes the second term which is proportional to aW, and replaces V by 1. Thus our result agrees with the Born approximation except for a factor.

To determine this factor, we must consider the normalization factors of the initial and final electron wave function, N_1 and N_2. N_2 is given by (6.31) and, in our case, N_1 will be given by a similar formula because the initial state is now also an electron of positive energy, whereas the normalization factor (6.32) applied to a negative-energy electron. The two normalization factors $|N_1N_2|^2$ together yield a factor $e^{\pi(a_1+a_2)}$, but our ex-

[39] E. T. Whittaker and G. N. Watson, *A Course of Modern Analysis* (The Macmillan Company, New York, 1946), p. 283.

[40] There are also some changes of sign, due to the difference between pair production and bremsstrahlung; these are the same as in Born approximation.

pression (8.9) shows that $|C'K|^2$ now contains a factor $e^{\pi(a_2-a_1)}$, just as in (6.33), and for high energies this factor goes to one. This leaves the same factor as compared with the Born approximation as in (6.34), *viz.*,

$$\mathfrak{R}=(\pi a/\sinh\pi a)^2. \tag{8.16}$$

This expression is closely related to the hypergeometric function $V(x)$ for $x=1$. In fact, we have[41] for argument 1:

$$F(a, b, c, 1)=\frac{\Gamma(c)\Gamma(1-a-b)}{\Gamma(1-a)\Gamma(1-b)}, \tag{8.17}$$

and therefore from the definition (6.24)

$$V(1)=\frac{\Gamma^2(1)}{\Gamma(1-ia)\Gamma(1+ia)}=\frac{\sinh\pi a}{\pi a}. \tag{8.18}$$

Therefore, when the normalization factor is included, the matrix element for bremsstrahlung differs from that in Born approximation by the factor

$$[V(x)-iayW(x)]/V(1), \tag{8.19}$$

and the cross section by the factor

$$R=[V^2(x)+a^2y^2W^2(x)]/V^2(1). \tag{8.20}$$

As we have already mentioned after (8.7), the argument x of the hypergeometric function is almost always very close to one. Whenever this is so, we may use the result of Davies, Bethe, and Maximon, *viz.*, that for $y=1-x$ near zero,

$$W(x)=-V(1)\log y. \tag{8.21}$$

Then $yW(x)\sim y\log y$ is very small, and the factor (8.20) becomes equal to unity. Thus, for most of the possible angles, θ_1, θ_2, and ϕ, the differential cross section for bremsstrahlung *is given exactly by the Born approximation*. This is in contrast to the cross section for pair production, and is probably due to the fact that the scattered waves for the initial and final electron do not overlap appreciably in bremsstrahlung (see Sec. IV) while they do for pair production (Sec. V).

An exception is the case of q very close to its minimum value, δ. Then, as shown below Eq. (8.7), the argument x is substantially below 1, and then R, Eq. (8.20), will differ from unity. In fact, it can easily be shown to be always less than 1. For this purpose, we take the derivative of the numerator of (8.20) with respect to x (note $y=1-x$):

$$dR'/dx=VdV/dx-a^2yW^2+a^2y^2WdW/dx. \tag{8.22}$$

Using (8.14), we find

$$dR'/dx=a^2yWdW/dx. \tag{8.23}$$

But from the power series expansion (6.25) it is clear that both W and dW/dx are positive for all x between 0 and 1. Therefore (8.20) increases monotonically with x, and since it reaches 1 at $x=1$, it is less than 1 for any other value of x.

Thus we have shown that the bremsstrahlung cross section is always less than the Born approximation value. Concerning the integration over angle, there is one limiting case for which the result is obvious, namely that of complete screening: in this limit, the differential cross section for small q is essentially eliminated by the atom form factor $F(q)$. Then q cannot come close to its lower limit δ, which was the only region in which we obtained a deviation from the Born approximation. Therefore, in the limit of complete screening, the Born approximation is valid for bremsstrahlung.

The integration in the absence of screening has been carried out and will appear shortly. For this limit the correction to the Born approximation turns out to be the same as for pair production [see DBM Eq. (35)]. Experimental cross sections, in which screening is incomplete should therefore (for high energies) be less than the Born approximation value. However, the reduction will be less than that for pair production, where the influence of screening is only in the region of small momentum transfer, for which the Coulomb correction is unimportant.

This has consequences for the theory of cascade showers in heavy elements: the cross section for pair production is reduced by about 10 percent (for lead) while that for bremsstrahlung is unchanged. Therefore the ratio of high-energy photons to electrons in the shower is increased by about 10 percent compared with the conventional theory, and the radiation length is increased by about 5 percent.[42]

IX. THE NEGLIGIBLE MATRIX ELEMENTS

(a) General

It remains for us to prove that the approximate wave function derived in Secs. II, III is really sufficient for the calculation of the matrix element. In particular, we must consider the correction to the wave function which arises from the term a^2/r^2 in the wave equation, i.e., the function ψ_a defined by

$$(\nabla^2+p^2+2\epsilon a/r)\psi_a=-a^2r^{-2}\psi_a, \tag{9.1}$$

and we must show that its contributions to the matrix element, such as (in the case of bremsstrahlung)

$$I_4=\int\psi_{2a}^*e^{-i\mathbf{k}\cdot\mathbf{r}}\psi_{1a}d\tau, \tag{9.2}$$

are actually negligible. It was just this contribution I_4 which Bess tried to take into account, and by which his theory differs from ours. That the contribution from I_4 is negligible will be shown by considering the orders of magnitude of the various contributions to the matrix element.

[41] E. T. Whittaker and G. N. Watson, *A Course of Modern Analysis* (The MacMillan Company, New York, 1946), p. 282, reference 39.

[42] We are indebted to R. R. Wilson for this remark.

We have discussed orders of magnitude already in Sec. VII. As in that section, we consider $\epsilon \gg 1$, and the angles θ_1, θ_2 of order $1/\epsilon$. Then, as is shown above Eq. (7.9), D_1, D_2, μ, u, v, etc., are of order unity. Also q is in general of this order but it can be as small as $O(1/\epsilon)$.

The integral I_1, involving the main part of the wave function, ψ_a, is of order ϵ, while the integrals $\mathbf{I}_2$, $\mathbf{I}_3$, involving the correction ψ_b to the wave function, are of order 1, Eq. (7.10). The matrix factor b, multiplying I_1, is of order $1/\epsilon$, as shown below (7.13), while the matrix factor $\mathbf{c}$, multiplying $\mathbf{I}_2$ and $\mathbf{I}_3$, is of order 1.

Now ψ_b satisfies the differential equation

$$(\nabla^2+p^2+2\epsilon a/r)\psi_b = ia\boldsymbol{\alpha}\cdot\nabla(1/r)\psi_a, \tag{9.3}$$

which is similar to (9.1) in that the right-hand side is of order ψ_a/r^2 in both equations. The order of magnitude of ψ_a must therefore be expected to be the same as that of ψ_b, and the order of I_4 the same as I_2 and I_3, namely unity. In Subsection *c*, we shall prove this statement in detail; but in Bess's paper I_4 comes out to be of order ϵ, like I_1, which is an unreasonable result.

Now the wave function ψ_a, like ψ_a, obviously contains no operators $\boldsymbol{\alpha}$, and therefore the integral I_4 will simply be multiplied by the matrix factor b, Eq. (7.13).[43] In Sec. VII, b was shown to be of order $1/\epsilon$; therefore, if I_4 is of order 1, its contribution to the matrix element is of order $1/\epsilon$ and hence negligible.

(b) The Order of Magnitude of I_1 and I_2

It is useful to discuss in a simple way the orders of magnitude of the principal integrals I_1 and $\mathbf{I}_2$. The first purpose is to check the validity of order-of-magnitude arguments which will later (Subsection c) be used to estimate I_4. Secondly, we shall show that there are no unsuspected cancellations by interference, and finally the arguments will give added insight into the mathematics.

We shall use for the integration variables both polar coordinates r, θ and cylindrical coordinates z, ρ, and use the fact that $q_z \approx \delta \approx O(1/\epsilon)$, while $q_0 \equiv q_\perp$ is in general of order 1. It can be shown that the main contribution to the integral I_1 comes from regions of space in which the hypergeometric functions F in the matrix element (5.6) can be replaced by their asymptotic expressions. This is permitted if the arguments of the hypergeometric functions are large compared with 1, *viz.*,

$$p_1 r + \mathbf{p}_1\cdot\mathbf{r} \gg 1. \tag{9.4}$$

Putting the z axis in the direction of $-\mathbf{p}_1$, this means

$$p_1(r-z) \approx \tfrac{1}{2}p_1 r\theta^2 \gg 1, \tag{9.5}$$

or

$$\theta \gg \theta_0 \equiv (p_1 r)^{-\frac{1}{2}}. \tag{9.6}$$

If $r \lesssim \epsilon$, then θ_0 as defined by (9.6) is larger than or equal to $1/\epsilon$, i.e., to the order of magnitude of θ_1 and θ_2. It is then justified, in first approximation, to consider the vectors $\mathbf{p}_1$, $\mathbf{p}_2$ and $\mathbf{k}$ to be essentially in the same direction, $-z$.

If the argument $u_1 = p_1(r-z)$ is large, the hypergeometric function is given by the asymptotic formula

$$F_1 = \frac{e^{\pi a_1/2}}{\Gamma(1+ia_1)} e^{ia_1 \log u_1}\left(1-\frac{ia_1^2}{u_1}\right) - \frac{ie^{\pi a_1/2}}{\Gamma(-ia_1)} - \frac{e^{iu_1 - ia_1 \log u_1}}{u_1} + O\left(\frac{1}{u_1^2}\right). \tag{9.7}$$

Through u_1, this expression depends on

$$\rho = r\theta; \tag{9.8}$$

we have

$$u_1 = p_1(r-z) \approx p_1\rho^2/2z. \tag{9.9}$$

The other factor depending substantially on ρ is

$$G \equiv \exp(iq_\perp \rho). \tag{9.10}$$

It is easy to see that there is no important constructive interferences between F_1, F_2, and G.

The integral over ρ arises mainly from values of ρ up to

$$\rho_1 = 1/q, \tag{9.11}$$

because at larger values of ρ, rapid oscillations of G set in. Since the volume element is $2\pi\rho d\rho dz$ and since the first term of (9.7) does not contain any power of ρ as a factor, the ρ integration gives a result of the order

$$1/q^2. \tag{9.12}$$

The integral over z contains only one important z-dependent factor, *viz.*,

$$\exp(iq_z z), \tag{9.13}$$

which shows that values of $z \approx r$ up to $1/q_z$ contribute, and this quantity is of order ϵ. Hence we find from a very simple consideration of orders of magnitude that

$$I_1 \sim \epsilon/q^2, \tag{9.14}$$

which agrees with the explicit evaluation in (7.10).

In $\mathbf{I}_2$ and $\mathbf{I}_3$, we need the derivative dF/du which is in the region of validity of the asymptotic expression (9.7):

$$\frac{dF_1}{du} = e^{\pi a_1/2}\frac{1}{u_1}\left(\frac{e^{ia_1 \log u_1}}{\Gamma(ia_1)} + \frac{e^{iu_1 - ia_1 \log u_1}}{\Gamma(-ia_1)}\right) + O\left(\frac{1}{u_1^2}\right), \tag{9.15}$$

where the first and second term correspond to the two first terms in (9.7).

We need consider only those components of $\mathbf{I}_2$ and $\mathbf{I}_3$ which have a matrix factor of order unity, i.e., (from (6.2)) are in the x or y direction. We have from (6.3a), for example,

$$I_{2x} \sim \frac{1}{\epsilon_1}\int e^{i\mathbf{q}\cdot\mathbf{r}} F_2^* \frac{dF_1}{du_1}(\nabla u_1)_x d^3r. \tag{9.16}$$

[43] In this point, we agree with Bess.

We use the asymptotic expressions (6.30) and (9.15) for F_2^* and dF_1/du_1 [from which F_2^* is essentially of $O(1)$ and dF_1/du_1 is essentially of $O(1/u_1)$, when $\rho > \rho_0 = r\theta_0 = (r/p_1)^{\frac{1}{2}}$],[44] and the small angle approximations (9.9) and

$$(\nabla u_1)_z \approx p_1\theta \approx p_1\rho/z, \tag{9.17}$$

[note (9.8)]. The integrals over z and ρ are, then, in view of the remark following (9.9),

$$\int \exp(iq_\perp\rho)d\rho \sim 1/q_\perp, \tag{9.18}$$

and

$$\int \exp(iq_z z)dz \sim 1/q_z = O(\epsilon), \tag{9.19}$$

so that

$$I_{2z} \sim 1/q_\perp = O(1), \tag{9.20}$$

in agreement with the explicit result in (7.10).

(c) The Main Term in the Neglected Part of the Wave Function

In this subsection, we shall discuss the integral I_4, Eq. (9.2), which arises from the main term in the neglected part of the wave function. We shall show that this is of order 1, i.e., of the same order as I_2.

We shall evaluate I_4 by replacing ψ_{2a} by the plane wave, $e^{i\mathbf{p}_2\cdot\mathbf{r}}$. This amounts to replacing N_2F_2 by unity, and thus to neglecting some interference effects. The arguments of Subsection b have shown that the elimination of interference effects will not reduce the order of magnitude of the integrals. Furthermore, we take into account that N_1 and N_2 [Eq. (6.31) and remarks preceding Eq. (8.16)] are of order unity.
Then

$$I_4 = \int e^{-i(\mathbf{p}_2+\mathbf{k})\cdot\mathbf{r}}\psi_{1c}d^3r, \tag{9.21}$$

i.e., apart from a constant factor, I_4 is the Fourier component of ψ_{1c}, corresponding to the momentum $\mathbf{p}_2+\mathbf{k}$, or it is the momentum-space wave function. To calculate this, we multiply (9.1) on both sides by $e^{-i(\mathbf{p}_2+\mathbf{k})\cdot\mathbf{r}}$ and integrate over space. One of the integrals thus occurring we integrate by parts:

$$\int e^{-i(\mathbf{p}_2+\mathbf{k})\cdot\mathbf{r}}\nabla^2\psi_{1c}d^3r = -(\mathbf{p}_2+\mathbf{k})^2\int e^{-i(\mathbf{p}_2+\mathbf{k})\cdot\mathbf{r}}\psi_{1c}d^3r. \tag{9.22}$$

Another integral on the left-hand side, *viz.*,

$$2e\mathcal{A}\int e^{-i(\mathbf{p}_2+\mathbf{k})\cdot\mathbf{r}}\psi_{1c}d^3r/r, \tag{9.23}$$

we neglect; this is an approximation similar to the replacement of ψ_{2a} by a plane wave (the error is probably smaller if the Coulomb field is neglected in *both* ψ_1 and ψ_2). Then we get

$$I_4 = -\frac{a^2}{p_1^2-(\mathbf{p}_2+\mathbf{k})^2}\int e^{i(\mathbf{p}_1-\mathbf{p}_2-\mathbf{k})\cdot\mathbf{r}}\frac{d^3r}{r^2}, \tag{9.24}$$

where we have also replaced ψ_{1a} by the plane wave $e^{i\mathbf{p}_1\cdot\mathbf{r}}$ on the right-hand side of (9.1).

Now

$$p_1^2-(\mathbf{p}_2+\mathbf{k})^2 = 2k(\epsilon_2-p_2\cos\theta_2) = D_2, \tag{9.25}$$

and is of $O(1)$, according to (8.7). Therefore, using the definition of $\mathbf{q}$, Eq. (8.3), the order of magnitude is

$$I_4 \sim \int e^{i\mathbf{q}\cdot\mathbf{r}}d^3r/r^2 \sim 1/q. \tag{9.26}$$

As expected, this is of the same order as I_2, namely independent of ϵ, and has also the same q-dependence as I_2. In Bess' calculation, the integral corresponding to I_4 turned out to be of the same order as I_1 which is unreasonable.

Together with the arguments about the matrix factor in Subsection a, this shows that the contribution of I_4 is of order $1/\epsilon$, and that therefore ψ_c can actually be neglected.

(d) Other Contributions

It is rather evident that the contributions from still higher approximations to the wave function are negligible, and that the same is true of cross terms containing "small parts" of both the initial and final wave function, such as

$$I_5 = \int \psi_{2b}^* e^{-i\mathbf{k}\cdot\mathbf{r}}\psi_{1b}d\tau. \tag{9.27}$$

This particular term gives a contribution of order $\epsilon^{-2}\log\epsilon$ to the matrix element, as shown below.

The significant contribution from I_5 will come from those components with matrix factor of order 1, which result from choosing the z component of ψ_{1b} and a component of ψ_{2b}^* perpendicular to z, or *vice versa*. Following the order of magnitude estimation of I_{2z}, we use the asymptotic expression (9.14) and a similar one for dF_2^*/du_2 and consider

$$I_{5zz} \sim \frac{1}{\epsilon_1\epsilon_2}\int e^{i\mathbf{q}\cdot\mathbf{r}}\frac{(\nabla u_1)_z}{u_1}\frac{(\nabla u_2)_z}{u_2}d^3r. \tag{9.28}$$

Noting that

$$(\nabla u_2)_z/u_2 \approx 1/r, \quad (\nabla u_1)_z \approx p_1\theta, \quad u_1 \approx p_1r\theta^2/2, \tag{9.29}$$

[44] Since the integral in (9.16) converges with $dF_1/du_1 \sim 1/u_1$, it will certainly converge in the region $\rho < \rho_0$ where the asymptotic expression (9.15) is not valid and dF_1/du_1 is of order 1 or less.

and using spherical coordinates, we have

$$I_{5zz}\sim\frac{1}{\epsilon^2}\int e^{iq_z r+iq_\perp r\theta\cos\phi}drd\theta d\phi, \tag{9.30}$$

the azimuthal angle ϕ being measured from the direction of $\mathbf{q}$. The integral over ϕ gives $J_0(q_\perp r\theta)$ and that over θ is then $1/q_\perp r$ for $q_\perp r\gtrsim O(1)$, and of $O(1)$ otherwise. The major contribution to the integral over r is thus in the region $1\leqslant r\leqslant 1/q_z$ from which we have

$$\int_1^{1/q_z}(q_\perp r)^{-1}\exp(iq_z r)dr\sim\frac{\log q_z}{q_\perp}=O(\log\epsilon), \tag{9.31}$$

so that I_{5zz} is of order

$$\epsilon^{-2}\log\epsilon. \tag{9.32}$$

This shows that I_5 is smaller than I_4 which we previously discussed.

The integrals which arise from higher corrections have their integrands more and more concentrated at small r. Ultimately, the main contribution to the integrals comes from values of r of the order of one wavelength, i.e., $1/p$. These integrals will then be of order $1/\epsilon^3$. Now it might be possible, with sufficient mathematical skill, to actually calculate the contributions of order $1/\epsilon$, $\epsilon^{-2}\log\epsilon$ and $1/\epsilon^2$ to the matrix element by explicit evaluation of some of the integrals we have neglected. But there would be very little hope for the numerous contributions of order $1/\epsilon^3$; these can probably be evaluated only in polar coordinates.

X. ESTIMATE OF ERROR

In Sec. IX we found that the main term neglected in calculating the matrix element comes from I_4 and is of relative order $1/\epsilon$. We believe that there are no cancellations from other neglected terms and that the error is indeed of order $1/\epsilon$.

Errors are introduced both in the initial and final state wave function. Since $\epsilon_2<\epsilon_1$ for bremsstrahlung, the error in the cross section must be estimated to be of order $1/\epsilon_2$. It has long been known that the Bethe-Heitler treatment is wrong near the upper limit of the bremsstrahlung spectrum, and corrections have been proposed by Heitler.[45] Probably this problem could now be solved, either using the wave function of this paper or a method similar to that of Harvey Hall.[12]

No approximation is made in the wave function of the quantum, $e^{i\mathbf{k}\cdot\mathbf{r}}$. Hence the theory is expected to remain correct for small k.

The total cross section for pair production (or the total energy radiated in bremsstrahlung) is obtained by integration over ϵ_2. Since all energies ϵ_2 between 1 and ϵ_1 contribute about equally, the relative error in the total cross section is about

$$\Phi=\int_1^{\epsilon_1}\varphi(\epsilon_2)d\epsilon_2/\epsilon_1, \tag{10.1}$$

where $\varphi(\epsilon_2)$ is the relative error at ϵ_2. Thus, if

$$\varphi\sim 1/\epsilon_2,\quad \Phi\sim\epsilon_1^{-1}\log\epsilon_1. \tag{10.2}$$

For pair production, k should be substituted for ϵ_1.

[45] W. Heitler, *The Quantum Theory of Radiation* (Oxford University Press, London, 1944).

Reduction of an Integral in the Theory of Bremsstrahlung

A. NORDSIECK
University of Illinois, Urbana, Illinois

(Received January 12, 1953; revised manuscript received October 13, 1953)

A matrix element integral for bremsstrahlung or pair production without Born approximation is reduced to an ordinary hypergeometric function by contour integration methods. The result is stated in Eqs. (1), (2) for bremsstrahlung and in (1′), (2′) for pair production.

IN the theoretical calculation of bremsstrahlung and pair production cross sections without Born approximation,[1-4] i.e., without the assumption that the deflecting forces exerted by the nucleus on the electrons are small, a certain fundamental matrix element integral occurs which can be reduced to an ordinary hypergeometric function. The reduction is carried out in this note by contour integral methods. For the bremsstrahlung case the correct matrix element integral[5] and its value in terms of a hypergeometric function are

$$I\equiv\int d\mathbf{r}e^{-\lambda r}\frac{e^{i\mathbf{q}\cdot\mathbf{r}}}{r}F(ia_1,1,ip_1r-i\mathbf{p}_1\cdot\mathbf{r})\times F(ia_2,1,ip_2r+i\mathbf{p}_2\cdot\mathbf{r})$$
$$=\frac{2\pi}{\alpha}e^{-\pi a_1}\left(\frac{\alpha}{\gamma}\right)^{ia_1}\left(\frac{\gamma+\delta}{\gamma}\right)^{-ia_2}\times F\left(1-ia_1,ia_2,1,\frac{\alpha\delta-\beta\gamma}{\alpha(\gamma+\delta)}\right). \quad (1)$$

In the original expression for I, $\mathbf{q}=\mathbf{p}_1-\mathbf{p}_2-\mathbf{k}$, $\mathbf{p}_1$ is the initial momentum of the electron, $\mathbf{p}_2$ is its final momentum, and $\mathbf{k}$ is the momentum of the radiated quantum. $a_1=Ze^2/\hbar v_1$ and $a_2=Ze^2/\hbar v_2$, where v_1 and v_2 are the initial and final electron speeds. λ is a real positive parameter introduced for the purpose of allowing other integrals to be evaluated by differentiation with regard to it. Only infinitesimal values of λ are pertinent in applications of the result. In the final expression for I,

$$\alpha=\tfrac{1}{2}(q^2+\lambda^2),\qquad \beta=\mathbf{p}_2\cdot\mathbf{q}-i\lambda p_2,$$
$$\gamma=\mathbf{p}_1\cdot\mathbf{q}+i\lambda p_1-\alpha,\quad \delta=p_1p_2+\mathbf{p}_1\cdot\mathbf{p}_2-\beta. \quad (2)$$

The pair-production integral will be discussed separately below.

Although a result of this type has been derived previously by Bess[3] in a manner patterned after Sommerfeld[1] and employing transformations to parabolic coordinates and several theorems on Bessel functions, it is hoped that a more direct evaluation of I by the powerful methods of contour integration may suggest ways of evaluating other similar integrals. The factor $e^{-\pi a_1}$ in (1) is unambiguously determined by the present method, whereas it is not by the method of the Bessel function theorems.

The confluent hypergeometric functions involved in I are special in that the second parameter is unity (Laguerre functions) and a convenient representation for them is

$$F(ia,1,z)=\frac{1}{2\pi i}\oint^{(0+,1+)}dt\,t^{ia-1}(t-1)^{-ia}e^{zt}. \quad (3)$$

The integration contour is closed and encircles each of the two points 0 and 1 once anticlockwise. At the point where the contour crosses the real axis to the right of 1 $\arg t$ and $\arg(t-1)$ are both zero. Let integral representations of this form be inserted into the expression for I and consider carrying out the space integration first:

$$I=-\frac{1}{4\pi^2}\int dt_1\int dt_2 t_1^{ia_1-1}(t_1-1)^{-ia_1}\times t_2^{ia_2-1}(t_2-1)^{-ia_2}V(t_1,t_2), \quad (4)$$
$$V=\int\frac{d\mathbf{r}}{r}\exp\{-\lambda r+i\mathbf{q}\cdot\mathbf{r}+it_1(p_1r-\mathbf{p}_1\cdot\mathbf{r})+it_2(p_2r+\mathbf{p}_2\cdot\mathbf{r})\}.$$

The interchange of order of integrations is justified if the space integration converges uniformly in t_1 and t_2 on the contours, and this will be the case provided the contours are such that

$$-\lambda-2p_1\mathcal{g}(t_1)-2p_2\mathcal{g}(t_2)<0 \quad (5)$$

everywhere on them. This in turn is possible for any positive λ, and we so restrict the contours for the time being.

[1] A. Sommerfeld, Ann. Physik **11**, 257 (1931).
[2] H. Wergeland, Phys. Rev. **76**, 184 (1949).
[3] L. Bess, Phys. Rev. **77**, 550 (1950).
[4] L. Maximon and H. Bethe, Phys. Rev. **87**, 156 (1952); H. Davies and H. Bethe, Phys. Rev. **87**, 156 (1952) and the paper accompanying the present paper.
[5] As pointed out by Bethe, Low, and Maximon, Phys. Rev. **91**, 417 (1953), the wave function for the final state must be taken to behave asymptotically like a plane wave plus an *ingoing* spherical wave, whereas the initial state wave function is asymptotically a plane wave plus an outgoing spherical wave. The function with the ingoing spherical wave may be derived from the one with the outgoing spherical wave by taking the complex conjugate and reversing the vector momentum. Then since the complex conjugate of the final state wave function appears in the matrix element, the two functions appearing in the matrix element are alike in all respects except for the sense of the momentum vector.

The space integral V is a standard integral for real t_1 and t_2, having the value

$$V=4\pi[|\mathbf{q}-t_1\mathbf{p}_1+t_2\mathbf{p}_2|^2-(t_1p_1+t_2p_2+i\lambda)^2]^{-1}$$
$$=-2\pi[(\beta+\delta)t_1t_2+(\alpha+\gamma)t_1-\beta t_2-\alpha]^{-1}. \quad (6)$$

Since both members of Eq. (6) are analytic functions of t_1 and t_2 wherever (5) holds, this result is valid for all complex t_1 and t_2 obeying (5) as well.

Next we carry out the t_1 integration with t_2 fixed at some value not in violation of (5). The quantity (6) considered as a function of t_1 has one singularity, a simple pole, at

$$t_1=t^*\equiv\frac{\alpha+\beta t_2}{\alpha+\gamma+(\beta+\delta)t_2}. \quad (7)$$

Is t^* inside or outside the t_1 contour? Assume that $g(t_2)=0$, a value compatible with (5), and that λ is so small that its square may be neglected. Then calculate the left member of (5) for $t_1=t^*$:

$$-\lambda-2p_1g(t^*)=\frac{\lambda(At_2^2+2Bt_2+C)}{[\alpha+\gamma+(\beta+\delta)t_2]^2}, \quad (8)$$

where A, B, C are best expressed in terms of the angles θ between $\mathbf{p}_1$ and $\mathbf{p}_2$, ψ_1 between $\mathbf{p}_1$ and $\mathbf{q}$, ψ_2 between $\mathbf{p}_2$ and $\mathbf{q}$ and φ between the planes containing $\mathbf{p}_1$, $\mathbf{q}$, respectively $\mathbf{p}_2$, $\mathbf{q}$: $A=p_1^2p_2^2\sin^2\theta$; $B=p_1^2p_2q(\cos\psi_2-\cos\theta\cos\psi_1)$; $C=p_1^2q\sin^2\psi_1$. The quadratic in the numerator of (8) is positive for all real t_2, for $A\geqslant 0$ and

$$AC-B^2=p_1^4p_2^2q^2\sin^2\psi_1\sin^2\psi_2\sin^2\varphi\geqslant 0. \quad (9)$$

Thus under the assumptions $g(t_2)=0$ and λ infinitesimal, we find that t^* violates condition (5) and must therefore lie outside the t_1 contour. But the conclusion that t^* lies outside the t_1 contour cannot depend on any special assumptions made in order to deduce the conclusion because all pairs of contours in keeping with (5) yield the same result for I and because I is an analytic function of λ. Hence t^* lies outside the t_1 contour in any case.

The t_1 integrand in (4) is single-valued and $O(1/t_1^2)$ as $t_1\to\infty$, so that we may expand the complete t_1 contour to infinity, and upon doing so we find that the only contribution to the t_1 integral is from the residue at the pole t^*. We may of course expand the contour thus at this stage, in violation of (5), because the integrand is analytic. The result of the t_1 integration is

$$-2\pi i[\text{residue at } t^*]=\frac{2\pi(t^*)^{i\alpha_1-1}(t^*-1)^{-i\alpha_1}}{\alpha+\gamma+(\beta+\delta)t_2}. \quad (10)$$

The values of $\arg(t^*)$ and $\arg(t^*-1)$ require to be determined. Now for $\lambda=0$ and t_2 on the real interval $(0,1)$ t^* is likewise on the real interval $(0,1)$ because

$$\mathbf{p}_1\cdot\mathbf{q}-\tfrac{1}{2}q^2>0,$$
$$\mathbf{p}_1\cdot\mathbf{p}_2+p_1p_2+\mathbf{p}_1\cdot\mathbf{q}>\mathbf{p}_2\cdot\mathbf{q}+\tfrac{1}{2}q^2>0. \quad (11)$$

These inequalities follow from the conservation laws and the relation between the energy and the momentum of an electron. Furthermore it follows from the arguments above relative to Eq. (8) that for λ positive but small $g(t^*)$ is negative. Thus t^* lies below the t_1 contour opposite the interval $(0,1)$ and having regard to the complex arguments stipulated for (3), we find $\arg(t^*)-\arg(t^*-1)=\pi+O(\lambda)$ for $0<t_2<1$. Consequently it is convenient to recast (10) into the form

$$2\pi e^{-\pi\alpha_1}(\alpha+\beta t_2)^{i\alpha_1-1}(\gamma+\delta t_2)^{-i\alpha_1}. \quad (12)$$

In virtue of (11) both linear factors in (12) are real and positive on the interval $0<t_2<1$ for vanishing λ; they are both assigned arguments $0+O(\lambda)$ on that interval.

The t_2 integrand has now acquired two new singularities, $t_2=-\alpha/\beta$ and $t_2=-\gamma/\delta$, both of which have negative imaginary parts (as follows from (2) and $p_1>p_2$) and are therefore excluded from the t_2 contour. In general the exclusion of the new singularities from the contours in both contour integrations is the only essential consequence of the requirement for uniform convergence of the space integration, and once the contours are laid so as to exclude the new singularities any stronger restrictions on t_1 and t_2, such as (5), may be disregarded.

I has now been reduced to

$$I=-ie^{-\pi\alpha_1}\int dt_2t_2^{i\alpha_2-1}(t_2-1)^{-i\alpha_2}$$
$$\times(\alpha+\beta t_2)^{i\alpha_1-1}(\gamma+\delta t_2)^{-i\alpha_1}. \quad (13)$$

Again the integrand is single valued and $O(1/t_2^2)$ as $t_2\to\infty$, and this makes the integral reducible to one with only three linear factors, i.e., to an ordinary hypergeometric function. We set $t=1/t_2$ and find:

$$I=-ie^{-\pi\alpha_1}\oint^{(-\beta/\alpha+,-\delta/\gamma+)} dt(1-t)^{-i\alpha_2}$$
$$\times(\alpha t+\beta)^{i\alpha_1-1}(\gamma t+\delta)^{-i\alpha_1}, \quad (14)$$

with the point $t=1$ excluded from the contour. Equation (14) is now to be put into a standard form for the hypergeometric function, and as such a form we take

$$F(a,b,c,x)=\frac{\Gamma(c)\Gamma(b-c+1)}{2\pi i\Gamma(b)}\int_{-\infty}^{(0+,x+)} d\tau\tau^{a-c}$$
$$\times(1-\tau)^{c-b-1}(\tau-x)^{-a}, \quad (15)$$

where for x real and <1, $\arg\tau=\arg(1-\tau)=\arg(\tau-x)=0$ on the real axis to the right of 0 and x and to the left of 1, and a cut exists in the τ plane from 1 to $+\infty$. The appropriate change of variable for reducing I to the standard form is a linear fractional transformation which takes $t=1$ into $\tau=1$ and either $t=-\beta/\alpha$ or $t=-\delta/\gamma$ into $\tau=0$. Of the two alternatives we choose the latter because it makes x lie on the interval $(0,1)$.

Thus $\tau=(\gamma t+\delta)/(\gamma+\delta)$ and (14) becomes

$$I=\frac{2\pi}{\alpha}e^{-\pi a_1}\binom{\alpha}{\gamma}^{ia_1}\left(\frac{\gamma+\delta}{\gamma}\right)^{-ia_2}\frac{1}{2\pi i}\int^{(0+,x+)}d\tau\,\tau^{-ia_1}\times(1-\tau)^{-ia_2}(\tau-x)^{ia_1-1}, \quad (16)$$

where $x=(\alpha\delta-\beta\gamma)/\alpha(\gamma+\delta)$. x ix real and positive but less than 1 for vanishing λ, see (2), (11), and one further inequality, namely,

$$1+\cos\theta-2\cos\psi_1\cos\psi_2\geqslant 0, \quad (17)$$

which follows from the fact that θ, ψ_1 and ψ_2 are sides of a spherical triangle. Since x is real and <1 the arguments of the linear factors in (16) are as required in (15). Identifying the parameters a, b, c, we have the final result stated in (1), (2).

In the case of pair production the corresponding integral to be evaluated and the result are as follows:

$$I'=\int d\mathbf{r}e^{-\lambda r}\frac{e^{i\mathbf{q}\cdot\mathbf{r}}}{r}F(-ia_1,1,ip_1r-i\mathbf{p}_1\cdot\mathbf{r})\times F(ia_2,1,ip_2r+i\mathbf{p}_2\cdot\mathbf{r})$$

$$=\frac{2\pi}{\alpha}\left(\frac{\gamma'}{\alpha}\right)^{ia_1}\left(\frac{\alpha}{\alpha+\beta}\right)^{ia_2}\times F\left(-ia_1,ia_2,1,\frac{\beta\gamma'-\alpha\delta'}{\gamma'(\alpha+\beta)}\right). \quad (1')$$

Since the derivation of this result is so similar to the derivation for bremsstrahlung, we shall indicate only the differences for the sake of brevity. $\mathbf{q}=\mathbf{k}-\mathbf{p}_1-\mathbf{p}_2$ is the nuclear recoil momentum, $\mathbf{p}_1$ is the positron momentum and $\mathbf{p}_2$ is the electron momentum. The wave functions for both electron and positron are asymptotic to plane waves plus ingoing waves. In the final expression for I', α and β have the same meaning as in (2) and γ' and δ' are given by

$$\gamma'=\mathbf{p}_1\cdot\mathbf{q}-i\lambda p_1+\alpha; \quad \delta'=\mathbf{p}_1\cdot\mathbf{p}_2-p_1p_2+\beta. \quad (2')$$

The space integral now has the form

$$V'=-2\pi[(\beta-\delta')t_1t_2+(\alpha-\gamma')t_1-\beta t_2-\alpha]^{-1}. \quad (6')$$

The pole of the t_1 integrand appears at

$$t_1=t^*\equiv\frac{\alpha+\beta t_2}{\alpha-\gamma'+(\beta-\delta')t_2}, \quad (7')$$

and this is again outside the t_1 contour by the same arguments as above. The result of the t_1 integration is now

$$-2\pi i[\text{residue at } t^*]=\frac{2\pi(t^*)^{-ia_1-1}(t^*-1)^{ia_1}}{\alpha-\gamma'+(\beta-\delta')t_2}. \quad (10')$$

For $\lambda=0$ and t_2 on the real interval (0,1), t^* is in this case on the real axis *outside* the interval (0,1) because

$$\mathbf{p}_1\cdot\mathbf{q}+\tfrac{1}{2}q^2>0; \quad \mathbf{p}_2\cdot\mathbf{q}+\tfrac{1}{2}q^2>0, \quad \mathbf{p}_2\cdot\mathbf{q}+\tfrac{1}{2}q^2>p_1p_2-\mathbf{p}_1\cdot\mathbf{p}_2-\mathbf{p}_1\cdot\mathbf{q}. \quad (11')$$

Hence $\arg(t^*)-\arg(t^*-1)=0+O(\lambda)$. The convenient form of (10') is then

$$2\pi(\alpha+\beta t_2)^{-ia_1-1}(\gamma'+\delta' t_2)^{ia_1}. \quad (12')$$

Both linear factors in (12') are real and positive on the interval $0<t_2<1$ for vanishing λ on account of (11'); they are assigned arguments $0+O(\lambda)$ on that interval.

The analog of Eq. (14) is

$$I'=-i\oint^{(-\beta/\alpha+,-\delta'/\gamma'+)}dt(1-t)^{-ia_2}\times(\alpha t+\beta)^{-ia_1-1}(\gamma' t+\delta')^{ia_1}. \quad (14')$$

In order to put this into the standard form (15) we may again make $t=1$ go into $\tau=1$ and make either $t=-\beta/\alpha$ or $t=-\delta'/\gamma'$ go into $\tau=0$. In this case we choose the first alternative because it makes x lie on the interval (0,1). Thus $\tau=(\alpha t+\beta)/(\alpha+\beta)$. Identifying the parameters a, b, c we have the result stated in (1') and (2').

Theory of Bremsstrahlung and Pair Production. II. Integral Cross Section for Pair Production

HANDEL DAVIES,* H. A. BETHE, AND L. C. MAXIMON†
Laboratory of Nuclear Studies, Cornell University, Ithaca, New York
(Received October 29, 1953)

The differential cross section for bremsstrahlung and pair production at high energies obtained in the preceding paper by Bethe and Maximon has been integrated over all angles, and formulas are given for the integral cross section for all Z. For small Z, the correction to the Born approximation is proportional to Z^3, and the constant of proportionality is given. The correction for heavier elements is somewhat less than the Z^3 law would indicate. It is shown that the correction is associated only with large recoil momenta of the nucleus whereas screening is important only for small recoil momenta; and, therefore, the same correction is valid in the case of complete, incomplete, or no screening. Agreement of these new predictions with observations of pair-production cross section at 88 and 280 Mev is excellent and not unreasonable at 17.6 Mev.

I. INTRODUCTION

IT is well known that the predictions of pair-production cross sections made by the Born approximation are not verified for the heavy elements, the discrepancy in the case of Pb being of the order of 10 percent at high energies. The error arises because of the fact that in the Born approximation, the Coulomb interaction is treated as a small perturbation. In the paper immediately preceding this, Bethe and Maximon[1] have made a calculation of the bremsstrahlung process in which the Coulomb interaction is included in the *unperturbed* Hamiltonian and which is valid for all Z as long as the energies of all of the particles involved are large compared with the rest energy of the electron.

The purpose of this paper is to carry out the integration of this differential cross section over all angles, and this is done by a method similar to that used by one of us[2] in determining the influence of screening on bremsstrahlung and pair production. The integration is facilitated by the fact that the energies involved are high and, therefore, the angles between the photon and the electrons are small for significant values of the differential cross section. A brief statement of the results has already been published.[3]

The notation employed is that of Bethe and Maximon,[1] and a natural system of units is used in which $m=c=\hbar=1$.

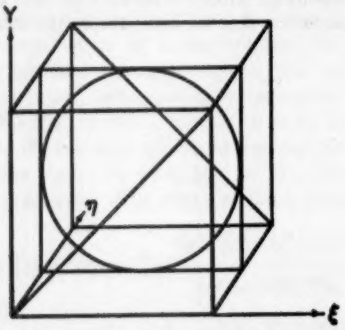

FIG. 1. The domain of integration in the space of ξ, η, and y.

II. THE INTEGRATION

The most convenient starting point is Eq. (7.14) of Bethe and Maximon which gives for the differential cross section

$$d\sigma=8\left(\frac{\pi a}{\sinh\pi a}\right)^2\frac{a^2}{2\pi}\frac{e^2}{\hbar c}\left(\frac{\hbar}{mc}\right)^2\frac{\epsilon_1^2\epsilon_2^2}{k^3}d\epsilon_1$$
$$\times\theta_1 d\theta_1\theta_2 d\theta_2 d\phi\{q^{-4}V^2(x)[k^2(u^2+v^2)\xi\eta$$
$$-2\epsilon_1\epsilon_2(u^2\xi^2+v^2\eta^2)+2(\epsilon_1^2+\epsilon_2^2)uv\xi\eta\cos\phi]$$
$$+a^2W^2(x)\xi^2\eta^2[k^2(1-(u^2+v^2)\xi\eta)$$
$$-2\epsilon_1\epsilon_2(u^2\xi^2+v^2\eta^2)-2(\epsilon_1^2+\epsilon_2^2)uv\xi\eta\cos\phi]\}. \quad (1)$$

The variables of integration are θ_1, θ_2, and ϕ. The other quantities can be expressed in terms of these (see Sec. VII of A):

$$u=\epsilon_1\theta_1, \qquad v=\epsilon_2\theta_2, \quad (2)$$

$$\xi=(1+u^2)^{-1}, \quad \eta=(1+v^2)^{-1}, \quad (3)$$

$$q^2=u^2+v^2+2uv\cos\phi, \quad (4)$$

$$x=1-y, \qquad y=q^2\xi\eta. \quad (5)$$

In all of these expressions, it has been assumed that the angles θ_1, θ_2 are small, of order $1/\epsilon$. In Eq. (4), it has been assumed, furthermore, that q is of order 1 rather than of order $1/\epsilon$. There is an important range of angles, *viz.*, $\epsilon_1\theta_1\approx\epsilon_2\theta_2$, $\phi\approx 0$, for which $q^2=O(1/\epsilon^2)$; and then Eq. (4) is useless, not being of sufficient accuracy. We have found it necessary to consider the two domains (I) $q^2=O(1)$ and (II) $q^2=O(1/\epsilon^2)$ separately. Domain I corresponds to $y=O(1)$ and domain II

* Now at Christ Church College, Oxford, England.
† Now at Graduate Division of Applied Mathematics, Brown University, Providence, Rhode Island.
[1] H. A. Bethe and L. C. Maximon, *Differential Cross Section for Bremsstrahlung and Pair Production*, quoted as A in the following.
[2] H. A. Bethe, Cambridge Phil. Soc. **30**, 524 (1934).
[3] Handel Davies and H. A. Bethe, Phys. Rev. **87**, 156 (1952).

to $y=O(\epsilon^{-2})$. Classically these two domains correspond to small and large impact parameters, respectively.

The minimum value of q is

$$q_{\min}=\delta=k/2\epsilon_1\epsilon_2. \tag{6}$$

The upper limit of q may be taken to be infinite. From Eqs. (4) and (5), the upper limit of y is 1 (which is clear since x is positive); and a more accurate expansion of q^2 shows that the minimum value of y occurs when $q=\delta$ and then $y=\delta^2$.

Domain I: $y=O(1)$

In this domain, Eq. (4) is valid.

Since the hypergeometric functions $V(x)$ and $W(x)$ are complicated functions [see Eq. (6.24) of Bethe and Maximon], the integration over x should be left to the end. We shall therefore transform the integration variables. As a first step, we transform to the variables u, v, and q.

Using Eqs. (2) and (4), we have

$$\frac{\partial(u,v,q^2)}{\partial(\theta_1,\theta_2,\phi)}=2\epsilon_1^2\epsilon_2^2\theta_1\theta_2\sin\phi, \tag{7}$$

so that

$$\theta_1 d\theta_1\theta_2 d\theta_2 d\phi=\frac{uvdudvdq^2}{\epsilon_1^2\epsilon_2^2\{4u^2v^2-(u^2+v^2-q^2)^2\}^{\frac{1}{2}}}. \tag{8}$$

The last term in each of the square brackets of Eq. (1) becomes

$$(\epsilon_1^2+\epsilon_2^2)\xi\eta(q^2-u^2-v^2), \tag{9}$$

and Eq. (1) goes over into

$$\begin{aligned}d\sigma=8Aud&uvdvdq^2[4u^2v^2-(u^2+v^2-q^2)^2]^{-\frac{1}{2}}\\&\times\{q^{-4}V^2(x)[(\epsilon_1^2+\epsilon_2^2)q^2\xi\eta-2\epsilon_1\epsilon_2(u^2\xi-v^2\eta)(\xi-\eta)]\\&+a^2W^2(x)\xi^2\eta^2[k^2-(\epsilon_1^2+\epsilon_2^2)q^2\xi\eta\\&\qquad-2\epsilon_1\epsilon_2(u^2\xi+v^2\eta)(\xi+\eta)]\},\end{aligned} \tag{10}$$

with

$$A=\left(\frac{\pi a}{\sinh\pi a}\right)^2\frac{a^2}{2\pi}\frac{e^2}{hc}\left(\frac{\hbar}{mc}\right)^2k^{-3}d\epsilon_1. \tag{11}$$

Next we change to the variables ξ, η, and y and get

$$\begin{aligned}d\sigma=2Ad\xi d\eta dy&[2y(\xi+\eta-2\xi\eta)-(\xi-\eta)^2-y^2]^{-\frac{1}{2}}\\&\times\{y^{-2}V^2(x)[(\epsilon_1^2+\epsilon_2^2)y+2\epsilon_1\epsilon_2(\xi-\eta)^2]\\&+a^2W^2(x)[k^2-(\epsilon_1^2+\epsilon_2^2)y\\&\qquad-2\epsilon_1\epsilon_2(\xi+\eta)(2-\xi-\eta)]\}.\end{aligned} \tag{12}$$

The limits of integration are 0 and $2p_1$ for u and 0 and $2p_2$ for v; the upper limits can be taken as infinite since only $u, v=0(1)$, and less give significant contributions to the cross section. From Eq. (3), therefore, the limits of ξ, η are 0 and 1. According to Eq. (5),

$$y=q^2\xi\eta=\xi+\eta-2\xi\eta+2\cos\phi[\xi\eta(1-\xi)(1-\eta)]^{\frac{1}{2}}, \tag{13}$$

and the limits of y are obtained by letting ϕ go from 0 to π and doubling the resulting integral. The volume of integration can be conveniently represented in the $\xi\eta y$ space as in Fig. 1.

The volume of integration is contained between two surfaces in the $\xi\eta y$ space, both of which intersect $\eta=0$ in the straight line $y=\xi$, and the plane $\eta=1$ in the straight line $y=1-\xi$, one of which cuts the plane $\eta=\frac{1}{2}$ in the upper half circle and the other in the lower half circle (Fig. 1). When $\xi=\eta$,

$$y=2\xi(1-\xi)(1-\cos\phi), \tag{14}$$

and near $\phi=0$, y is very small. This is precisely the region in which Eq. (4) for q^2 is invalid and must therefore be avoided in our present integration over domain I. It is necessary to insert then a lower cutoff, $y=y_1$, for the present such that

$$\delta^2\ll y_1\ll 1. \tag{15}$$

The integration can now be further simplified by introducing the symmetrical variables:[4]

$$z=\xi+\eta-1, \quad w=\xi-\eta. \tag{16}$$

Then, after some algebra,

$$\begin{aligned}d\sigma=Adzdwdy&[y(1-y)-yz^2-(1-y)w^2]^{-\frac{1}{2}}\\&\times\{y^{-2}V^2[(\epsilon_1^2+\epsilon_2^2)y+2\epsilon_1\epsilon_2w^2]\\&+a^2W^2[(\epsilon_1^2+\epsilon_2^2)(1-y)+2\epsilon_1\epsilon_2z^2]\}.\end{aligned} \tag{17}$$

If we now change the order of integration, integrating first over w and z and finally over y, then the limits of integration over w and z will both be given by the vanishing of the square root in the denominator of (17) which arises from the Jacobian (7) of the original transformation. These limits on z and w suggest the introduction of auxiliary polar coordinates χ, ψ by setting

$$z=(1-y)^{\frac{1}{2}}\sin\chi\cos\psi, \quad w=y^{\frac{1}{2}}\sin\chi\sin\psi. \tag{18}$$

Then

$$\begin{aligned}dzdw&=y^{\frac{1}{2}}(1-y)^{\frac{1}{2}}\sin\chi\cos\chi d\chi d\psi,\\[y(1-y)-yz^2-(1-y)w^2]^{\frac{1}{2}}&=y^{\frac{1}{2}}(1-y)^{\frac{1}{2}}\cos\chi,\end{aligned} \tag{19}$$

and the integral reduces simply to one over the solid angle $\sin\chi d\chi d\psi$. However, it should be noted that the entire domain of w, from $-y^{\frac{1}{2}}$ to $+y^{\frac{1}{2}}$, and the entire domain of z are covered by letting χ go from 0 to $\pi/2$, so that the integral over solid angle gives 2π rather than 4π for the terms independent of χ and ψ. On the other hand, the integral has to be doubled according to the remark after Eq. (13). The averages over solid angle become obviously

$$\langle z^2\rangle=\tfrac{1}{3}(1-y), \quad \langle w^2\rangle=\tfrac{1}{3}y \tag{20}$$

[4] The introduction of $\xi+\eta-1$, rather than $\xi+\eta$ itself, is suggested by the symmetry of the integration volume, Fig. 1, about $\xi=\frac{1}{2}$ and $\eta=\frac{1}{2}$, as well as by the form of the last term in Eq. (12). As is shown by Eq. (17), this procedure leads to the elimination of all linear terms in w and z.

and, after integration,

$$d\sigma = 4\pi A\, dy(\epsilon_1^2+\epsilon_2^2+\tfrac{2}{3}\epsilon_1\epsilon_2)[V^2 y^{-1}+a^2(1-y)W^2]. \quad (21)$$

This exceedingly simple formula is valid for all y down to $y=y_1$, as defined by Eq. (15). It can be shown that all neglected terms are of order $1/\epsilon^2$.

Domain II:[5] $y=O(\delta^2)$

It will now be shown that to the order of approximation in which we are working, the contribution of domain II to the integral cross section is the same as in the Born approximation. The proof depends on the behavior of the functions $V(x)$ and $W(x)$ near $x=1$. It is shown in the Appendix that $V(x)$ is convergent up to and including $x=1$ and that the derivative of $V(x)$ which is related to $W(x)$ by

$$V'(x)=a^2W(x) \quad (22)$$

has a logarithmic singularity at $x=1$, with an expansion of $W(x)$:

$$W(x)=-\frac{\sinh\pi a}{\pi a}[\log y+c_0+O(y\log y)]. \quad (23)$$

When $y=O(\delta^2)$, we can therefore replace $V(x)$ by $V(1)$ with an error of $O(\delta^2\log\delta^2)$ which we will neglect in comparison with unity. Further,[6]

$$V(1)=F(ia,-ia,1,1)=\frac{1}{\Gamma(1-ia)\Gamma(1+ia)}=\frac{\sinh\pi a}{\pi a}, \quad (24)$$

which cancels the first factor in Eq. (1) and subsequent formulas for $d\sigma$.

Again the term in Eq. (1) containing $W(x)$ can be neglected altogether in domain II. This is because W^2, unlike V^2, does not have the denominator q^4 in Eq. (1) or the denominator y in Eq. (21). We therefore need simply the integral over W^2, and, the range of integration in domain II being only δ^2, the contribution to the integral from this domain is $O(\delta^2\log\delta^2)$, which we neglect in comparison with unity.

Therefore, the differential cross section reduces in domain II to that of the Born approximation. Now the integration in the Born approximation has been carried out and yields[2] for the *total* cross section (domains I+II),

$$\sigma_B=4\pi A V^2(1)(\epsilon_1^2+\epsilon_2^2+\tfrac{2}{3}\epsilon_1\epsilon_2)(-\log\delta^2-1), \quad (25)$$

where $V^2(1)$ must be inserted into the cross section to remove that factor $(\pi a/\sinh\pi a)^2$ in the definition of A [Eq. (11)]. The contribution from domain I in the Born limit is obtained by putting $a=0$ in (21), which yields $V(x)=1$, and integrating over y from y_1 to 1; this procedure gives

$$\sigma_{BI}=4\pi A V^2(1)(\epsilon_1^2+\epsilon_2^2+\tfrac{2}{3}\epsilon_1\epsilon_2)(-\log y_1). \quad (26)$$

Therefore, the contribution which comes from domain II in the Born approximation and also in our theory is

$$\sigma_{BII}=4\pi A V^2(1)(\epsilon_1^2+\epsilon_2^2+\tfrac{2}{3}\epsilon_1\epsilon_2)(\log y_1-\log\delta^2-1). \quad (27)$$

III. CROSS SECTION

We now add σ_{BII} of Eq. (27) to the contribution of domain I obtained from Eq. (21) by integrating over y from y_1 to 1; this procedure gives

$$\sigma=4\pi A V^2(1)(\epsilon_1^2+\epsilon_2^2+\tfrac{2}{3}\epsilon_1\epsilon_2)\Big\{\log y_1-\log\delta^2-1+[V(1)]^{-2}\Big[\int_{y_1}^1 V^2(x)y^{-1}dy+a^2\int_{y_1}^1(1-y)W^2(x)dy\Big]\Big\}. \quad (28)$$

The integral in (28) may be written in the form

$$\int_0^{1-y_1}\left(\frac{V^2}{1-x}+a^2xW^2\right)dx. \quad (29)$$

Using the differential equation for the hypergeometric function V which is given in A [Eq. (8.4)], *viz.*,

$$(1-x)\frac{d}{dx}\left(x\frac{dV}{dx}\right)=a^2V, \quad (30)$$

we have, since $dV/dx=a^2W$ [A, Eq. (6.25)],

$$\frac{V}{1-x}=\frac{d}{dx}(xW) \quad (31)$$

and

$$\frac{V^2}{1-x}+a^2xW^2=V\frac{d}{dx}(xW)+xW\frac{dV}{dx}=\frac{d}{dx}(xVW). \quad (32)$$

Thus the integral in Eq. (29) is

$$xVW]_0^{1-y_1}=(1-y_1)V(1-y_1)W(1-y_1)=V(1)W(1-y_1)+O(y_1\log y_1) \quad (33)$$

---

[5] In a paper on the integral cross section for bremsstrahlung to appear shortly, the integration over domain II will be done without using the variables of reference 2. Making the approximations appropriate in domain II and performing the integrations over w and z, we find that the remaining differential cross section is very similar to Eq. (21) in form and equal to it in the region where domains I and II overlap. The differential cross section (in which one has only to integrate over y) valid in both domains may then be written and the integral over the entire range $\delta^2\leq y\leq 1$ performed at one time.

[6] E. T. Whittaker and G. N. Watson, *A Course of Modern Analysis* (Cambridge University Press, Cambridge, 1950), p. 282.

since from Eq. (15) $y_1 \ll 1$. Further, it is shown in the Appendix, Eqs. (A12), (A13), that for y_1 small

$$W(1-y_1) = -V(1)\left[\log y_1 + 2a^2 \sum_{\nu=1}^{\infty} \frac{1}{\nu(\nu^2+a^2)}\right] + O(y_1 \log y_1). \quad (34)$$

Substituting Eqs. (11), (33), and (34) in Eq. (28) gives

$$\sigma = 2a^2 \frac{e^2}{\hbar c}\left(\frac{\hbar}{mc}\right)^2 \frac{d\epsilon_1}{k^3}(\epsilon_1^2+\epsilon_2^2+\tfrac{2}{3}\epsilon_1\epsilon_2) \times\left[2\log\frac{2\epsilon_1\epsilon_2}{k} - 1 - 2f(Z)\right], \quad (35)$$

where

$$f(Z) = a^2 \sum_{1}^{\infty} \frac{1}{\nu(\nu^2+a^2)}. \quad (36)$$

A convenient way to evaluate the sum is to write

$$\sum = (1+a^2)^{-1} + \sum_{n=1}^{\infty} (-a^2)^{n-1}[\zeta(2n+1)-1], \quad (37)$$

or, numerically,[7]

$$\sum = (1+a^2)^{-1} + 0.20206 - 0.0369a^2 + 0.0083a^4 - 0.002a^6. \quad (38)$$

This expression is sufficient to evaluate $\sum$ to 4 decimals up to $a=\frac{2}{3}$, which corresponds to uranium. A curve, going up to $a=0.4$, is given by Jackson and Blatt.[8]

For *small* a, we have

$$\sum = 1.2021, \quad f(Z) = 1.2021a^2. \quad (39)$$

This conclusion means that the correction is proportional to a^2 and hence to Z^2. This has been verified in some[9-16] of the many experimental papers on the absorption of gamma rays by pair production. The coefficient is also in good agreement with experiment (see Sec. V).

For larger a, $\sum$ decreases. For Pb, for instance, $\sum = 0.9250$, which is only about $\frac{3}{4}$ of the low-Z value. Therefore, the correction $f(Z)$ to the Born approximation, as defined by Eq. (36), increases with Z somewhat less rapidly than Z^2.

[7] For accurate numerical values of the Riemann zeta function, see J. P. Gram, Kgl. Danske Videnskab. Selskabs Skrifter, Naturvidenskab. math. Afdel, **10**, 313 (1925).
[8] J. D. Jackson and J. M. Blatt, Revs. Modern Phys. **22**, 77 (1950).
[9] G. D. Adams, Phys. Rev. **74**, 1707 (1948).
[10] R. L. Walker, Phys. Rev. **76**, 527 (1949).
[11] R. L. Walker, Phys. Rev. **76**, 1440 (1949).
[12] J. L. Lawson, Phys. Rev. **75**, 433 (1949).
[13] DeWire, Ashkin, and Beach, Phys. Rev. **83**, 505 (1951).
[14] C. R. Emigh, Phys. Rev. **86**, 1028 (1952).
[15] Rosenblum, Schrader, and Warner, Phys. Rev. **88**, 612 (1952).
[16] A. I. Berman, Phys. Rev. **90**, 210 (1953).

IV. THE EFFECT OF SCREENING

The differential and integral cross sections have been derived under the assumption that the field is a pure Coulomb field. The screening effect of the atomic electrons has been completely neglected. In the Born approximation, the influence of screening on the bremsstrahlung and pair-production processes has been investigated by Bethe,[2] who showed that the screening effect is important only for recoil momenta,

$$q < Z^{\frac{1}{3}}/137. \quad (40)$$

For Pb, therefore, the region of $q > 0.03$ is not seriously affected by the screening.

Because of (8), $y < q^2$; and therefore screening will seriously affect only the region $y < 0.001$. Already in Sec. II (integration over domain II) we have shown that the Born approximation is valid for such small y. Indeed, from the explicit Eq. (28) and from Eq. (23), we find that the contribution of $y < y_1$ to the Coulomb correction $2f(Z)$ is approximately

$$-a^2 \int_0^{y_1} \log^2 y dy = -a^2 y_1[\log^2 y_1 - 2\log y_1 + 2]. \quad (41)$$

For $y_1 = 0.001$, this is about $-0.06a^2$, or 2 percent of the total Coulomb correction. The Coulomb correction is therefore not seriously affected by screening.

We can now make a similar statement about the *differential cross section:* the corrections resulting from screening and resulting from the Coulomb effect are independent; wherever one of them is important, the other is not. This can be seen most easily from Eq. (21) for the differential cross section. As we have already seen, screening is important only for small y, let us say, $y < y_1 = 0.001$. V^2 is multiplied by a factor $1/y$, and V^2 itself is of order 1, Eq. (24). On the other hand, W^2 is multiplied by a factor of order a^2 and is itself of order $(\log y)^2$. Therefore, for small y, the term with W^2 is of relative order

$$y(\log y)^2 a^2,$$

which is small compared with 1. In the same approximation, $V(x)$ may be replaced by $V(1)$, and this factor cancels the factor $(\pi a/\sinh \pi a)^2$ in front of the entire cross section. Therefore, *in the limit of small momentum transfer and in the entire region in which screening can be important, the differential cross sections of Eqs. (21) and (17) reduce to the Born approximation result.*

This is physically reasonable: screening, and small momentum transfer generally, imply large impact parameters of the electron. Under these conditions, the electron wave function should be well represented by a plane wave, and, therefore, the Born approximation should be valid. Only for close collisions with q (and therefore y) of the order of 1, and with impact parameters of the order $\hbar/mc$, will the Coulomb correction be important. The soundness of this physical argument is, however, somewhat doubtful because for

bremsstrahlung[17] the Born approximation breaks down just for small q.

Returning to the integral cross section, we may say that in domain I, the only correction to the Born approximation is the Coulomb correction calculated by Bethe and Maximon, and screening is insignificant, whereas in domain II the Coulomb correction is insignificant and results are sufficiently accurate if the screening effect in the Born approximation is treated as by Bethe.[2] Hence the correction calculated in this paper is valid in the case of screening, partial or complete; and in the latter case, using Bethe's result for a Thomas-Fermi model of the atom, we get, in place of Eq. (35),

$$\sigma=4a^2\frac{e^2}{\hbar c}\left(\frac{\hbar}{mc}\right)^2\frac{d\epsilon_1}{k^3}\{(\epsilon_1^2+\epsilon_2^2+\tfrac{2}{3}\epsilon_1\epsilon_2)\times[\log(183Z^{-\frac{1}{3}})-f(Z)]+\tfrac{1}{9}\epsilon_1\epsilon_2\}, \quad (42)$$

where $f(Z)$ is defined in Eq. (36) and evaluated in Eq. (38).

For partial screening the correction is the same, and Eq. (31) of Bethe and Heitler[18] may be written

$$\sigma=a^2\frac{e^2}{\hbar c}\left(\frac{\hbar}{mc}\right)^2\frac{d\epsilon_1}{k^3}\times\{(\epsilon_1^2+\epsilon_2^2)[\phi_1(\gamma)-(4/3)\log Z-4f(Z)]+\tfrac{2}{3}\epsilon_1\epsilon_2[\phi_2(\gamma)-(4/3)\log Z-4f(Z)]\}, \quad (43)$$

where $\phi_{1,2}(\gamma)$ are the functions given graphically in that paper.

Integration over ϵ_- gives for the total cross section for pair production

$$\sigma=\frac{28}{9}\frac{Z^2r_0^2}{137}\left[\log 2k-\frac{109}{42}-f(Z)\right] \quad (44)$$

without screening. When screening is complete,

$$\sigma=\frac{28}{9}\frac{Z^2r_0^2}{137}\left[\log(183Z^{-\frac{1}{3}})-\frac{1}{42}-f(Z)\right]. \quad (45)$$

At energies at which measurements have been made, the screening effect is incomplete; but the screening calculation in the Born approximation can be done numerically[18] and the Coulomb correction of this paper subtracted. The term to be subtracted is always

$$\Delta\sigma=\frac{28}{9}\frac{Z^2r_0^2}{137}f(Z), \quad (46)$$

no matter whether screening is absent, partial, or complete.

[17] A, Sec. VIII.

[18] H. A. Bethe and W. Heitler, Proc. Roy. Soc. (London) **146A**, 83 (1934).

V. COMPARISON WITH EXPERIMENT

The correction calculated in this paper amounts to a *decrease* of the cross section for pair production, as is in accord with experiment. The magnitude of the theoretical correction is relatively small: although it is of order a^2, as might be expected for a correction to the Born approximation, it has to be compared with a main term which is the logarithm of a large number and is usually of the order 3 to 5: therefore, the Coulomb correction for lead is not $a^2=36$ percent but only about 10 percent. The smallness of the correction as deduced from experiment has often given rise to comment.

One of the remarkable features of the result, Eqs. (35), (36), (42), (43), is that the energy distribution of the pair electrons is essentially unchanged: the major energy dependence is contained in the factor $\epsilon_+^2+\epsilon_-^2+\frac{2}{3}\epsilon_+\epsilon_-$ in Eq. (35), and this is unaltered; only the slowly variable logarithm, $\log(2\epsilon_1\epsilon_2/k)$, is modified by the subtraction of a constant term, $f(Z)$, which is only 10 percent of the logarithm for Pb. Now if the energy of the positron changes from $0.1k$ to $0.5k$, the log changes only by about 1 unit, or about $\frac{1}{4}$ of its value: therefore the relative cross section at these two values of ϵ_1 is changed by the Coulomb correction by only $2\frac{1}{2}$ percent (in the case of no screening). For complete screening, the energy dependence is not changed at all, as shown by Eq. (42); and for partial screening, the change is less than in the absence of screening. This is in agreement with the experimental results of DeWire and Beach[19] who measured the energy distribution of the positrons and electrons produced by 270-Mev photons in a $\frac{1}{2}$-mil gold foil. In this case, screening is *close* to complete, and the experiments give agreement with the Bethe-Heitler distribution within experimental error, as expected from our theory.

Turning now to the total cross section for pair production, the measurements fall into two classes, *viz.*, those of the pair production itself and those of the total cross section for gamma-ray absorption. The former measurements are all relative,[11,12,14] comparing pair production in different targets; for their interpretation, it is necessary that the pair production for one standard element be known. If this standard is chosen to be a very light element, a considerable fraction of the pairs is formed in the field of the atomic electrons, and the cross section for this process is still only approximately known. (This difficulty is absent for energies below $4mc^2$ where the pair formation in the field of an electron is impossible.)[20] For the purpose of minimizing the combined error from this cause and from the Coulomb correction, the standard should be chosen at intermediate Z, e.g., Al or Fe. In any case, measurements of the relative pair cross section are only of moderate accuracy, of the order of 2 percent.

[19] J. W. DeWire and L. A. Beach, Phys. Rev. **83**, 476 (1951).

[20] Experiments in this region have been done by I. E. Dayton, Phys. Rev. **89**, 544 (1953).

The measurement of total absorption cross section[9,10,12,13,15] has the advantage of higher precision which can be as good as ½ percent. It also has the advantage of being absolute, thus avoiding the reference to a standard which itself may not be accurately known. On the other hand, the total cross section must be corrected for other absorption processes. Fortunately, the most important of these, the Compton effect, is very accurately known from theory. The photoelectric effect in the atom is quite unimportant at high energies where our theory of pair production may be tested; its behavior is reasonably well known theoretically[21] and has been studied experimentally at a few Mev by Colgate.[22]

The most troublesome correction to the absorption coefficient arises from the nuclear photoeffect because neither a quantitative theory nor comprehensive experiments on this effect exist. However, it is known that the photoeffect is strong only for photon energies around 20 Mev; in the neighborhood of its maximum, the cross section is about ½ to 1 barn for lead and about proportional to the atomic weight A for other elements. For Pb, this is equal to 2.5–5 percent of the total gamma-ray absorption cross section; for lighter elements, it may be even more. However, at 100 Mev and over, the nuclear photoeffect is probably negligible.

The most careful correction for nuclear photoeffect, by use of both experimental and theoretical information, was applied by Rosenblum, Schrader, and Warner.[15] They find the correction to be 1–1.5 percent of the total cross section at 10.3 Mev and 2–4 percent at 17.6 Mev.

The experimental results for energies above 10 Mev are listed in Table I and compared with theory. We

TABLE I. Percentage reduction of pair-production cross section for lead compared with Born approximation.

Energy Mev	This theory	Experiment	Author	Method[a]	Reference
10.3	28	6.8±1.0	Rosenblum *et al.*	Absol.	c
11.0	26	8.8	Adams	Absol.	d
13.7	23	10.0	Adams	Absol.	d
17.6	20	10.4±0.6	Walker[j]	Absol.	e
17.6	20	12.9±1	Walker[b]	Absol.	e
17.6	20	15.5±2	Walker	Rel.	f
17.6	20	13.5±1.0	Rosenblum *et al.*	Absol.	c
19.0	19	13.5	Adams	Absol.	d
88	11.8	10.7±1.6	Lawson	Absol.	g
280	10.0	9.7±1.2	DeWire *et al.*	Absol.	h
50–300	11.2	11.7±1.7	Emigh	Rel.	i

[a] Absolute measurement of total absorption cross section, or relative measurement of pair production in Pb as compared with a light element.
[b] Corrected for nuclear photoeffect as given in reference 15.
[c] See reference 15.
[d] See reference 9.
[e] See reference 10.
[f] See reference 11.
[g] See reference 12.
[h] See reference 13.
[i] See reference 14.
[j] Uncorrected.

[21] Gladys White, National Bureau of Standards Report NBS-1003 (unpublished).
[22] S. A. Colgate, Phys. Rev. 87, 592 (1952).

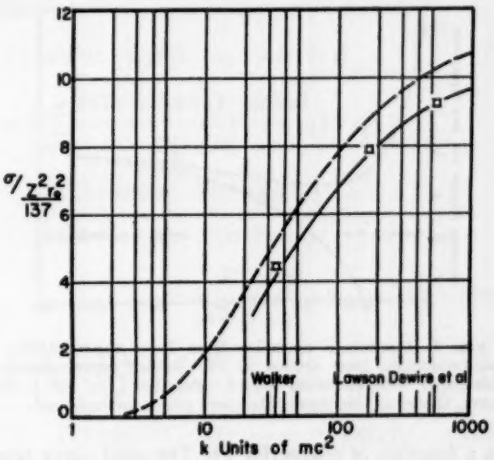

FIG. 2. Total cross section for pair production in Pb. Dotted curve, Born approximation. Solid curve, theory of this paper. Measured points are indicated.

give the percentage reduction of the pair-production cross section for lead relative to that of the Bethe-Heitler theory. The experimental data of references 9 to 12 are also shown in Fig. 2, in which the solid curve represents the theory of this paper and the dashed curve the Born approximation. Both from the table and the figure, it is seen that the agreement is excellent with the absolute cross section measurements of Lawson at 88 Mev and of DeWire *et al.* at 280 Mev. It is equally good with Emigh's experiments in which the continuous gamma rays from a 300-Mev betatron were used to produce pairs in various targets. The pairs were observed in a cloud chamber, and all pairs below 50 Mev combined energy were rejected; Al was used as the standard target. The theoretical value in this case was calculated on the assumption that the photon spectrum behaves like dk/k between 50 and 300 Mev.

Agreement with Walker's measurements at 17.6 Mev is not good, the discrepancy being greater with his absolute absorption coefficient than with his relative measurement of pair production. As we have discussed above, it is probable that the absolute cross section at this energy contains a substantial contribution from nuclear photoeffect. Indeed, if one applies the correction for nuclear photoeffect given by Rosenblum *et al.*[15] for Pb at 17.6 Mev, then Walker's absolute measurement implies a reduction of the cross section compared with Born approximation of 12.9±1 percent, the error including the uncertainty of the correction for the photonuclear effect. This corrected result is not inconsistent with his relative cross section and is in good agreement with the more recent measurement of Rosenblum *et al.* at the same energy. Agreement with Adams'[9] older measurements is not so good since they were not corrected for photonuclear effect.

Figure 3 gives the deviation from Born approximation

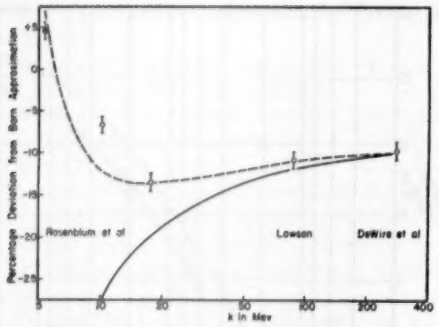

FIG. 3. Percentage deviation from Born approximation of pair-production cross section in Pb. Dashed curve, theory of this paper with empirical second correction [Eq. (48)]. Solid curve, theory of this paper. Measured points are indicated.

as a function of energy for Pb. The solid curve represents the theory of this paper, the points the experiments with probable errors. The good agreement at high energies has already been noted. The discrepancy between theory and experiment below 20 Mev is not surprising. The error in our theory, according to Sec. X of the paper by Bethe and Maximon, should be of the order

$$\delta = a^2\epsilon^{-1}\log\epsilon. \tag{47}$$

At 17.6 Mev we have $\epsilon=35$ giving 3.5 percent from Eq. (47). The actual error is about twice this figure, which is quite understandable considering the roughness of the error estimate. That the experimental points should lie *above* our theoretical curve is consistent with the prediction of the theory of Jaeger and Hulme,[23] who made an exact calculation of the pair-production cross section at 1.53 and 2.55 Mev and found results substantially *higher* than the Born approximation, by 100 and 25 percent, respectively. Their predictions are well confirmed by Colgate's[22] measurement of the absolute total cross section at 2.62 Mev and especially by Dayton's[20] measurement of the relative pair production by various elements at 1.33 and 2.62 Mev. Therefore, one must expect that the correction to the Born approximation crosses zero at some energy. This has been realized by many authors, including Rosenblum *et al.*,[15] who put the crossing point at about 6 Mev. All experiments on Pb above 5 Mev are well represented by the empirical formula

$$\sigma_{\text{pair}}=\sigma_{BH}-4.0+46/\epsilon, \tag{48}$$

where σ_{BH} is the Bethe-Heitler cross section, 4.0 the correction derived in this paper, and the last term an empirical second correction. All cross sections are given in barns. Equation (48) is represented by the dashed line in Fig. 3. The equation is no longer good at energies below 5 Mev.

In summary, we can say that the agreement of our theory with experiment is very satisfactory at high energy (88 Mev and up) and that below 20 Mev deviations exist as should be expected.

[23] J. C. Jaeger and H. R. Hulme, Proc. Roy. Soc. (London) **A153**, 443 (1936); J. C. Jaeger, Nature **148**, 86 (1941).

ACKNOWLEDGMENT

We are indebted to F. J. Dyson for the prevention of a mistake, to R. R. Wilson for helpful discussion, and one of us (H.D.) to the Commonwealth Fund of New York for financial support.

APPENDIX

The arguments involved in the above calculation require a knowledge of the behavior of the hypergeometric functions $V(x)$ and $W(x)$ between $x=0$ and $x=1$.

$V(x)=F(ia,-ia;1;x)$ is convergent at all points in this range, but $W(x)$ is divergent for $x=1$, and the series converges very slowly near $x=1$.

There is a connection[24] between the hypergeometric functions of z and $1-z$,

$$\begin{aligned}&\Gamma(c-a)\Gamma(c-b)\Gamma(a)\Gamma(b)F(a,b;c;z)\\&=\Gamma(a)\Gamma(b)\Gamma(c)\Gamma(c-a-b)F(a,b;a+b-c+1;1-z)\\&\quad+\Gamma(c)\Gamma(c-a)\Gamma(c-b)\Gamma(a+b-c)(1-z)^{c-a-b}\\&\qquad\times F(c-a,c-b;c-a-b+1;1-z),\end{aligned}\tag{A1}$$

which is valid if $c-a-b$ is not an integer.

We wish to investigate $W(x)=F(1+ia,1-ia;2;x)$, for which the above equation is not valid. We proceed in the same way as Whittaker and Watson:[24]

$$\begin{aligned}&\frac{\Gamma(1+ia)\Gamma(1-ia)}{\Gamma(2)}F(1+ia,1-ia;2;z)\\&=\frac{1}{2\pi i}\int_{-i\infty}^{i\infty}\frac{\Gamma(1+ia+s)\Gamma(1-ia+s)\Gamma(-s)}{\Gamma(2+s)}(-z)^s ds.\end{aligned}\tag{A2}$$

Now, by Barnes' lemma,[24]

$$\begin{aligned}&\Gamma(1+ia+s)\Gamma(1-ia+s)/\Gamma(2+s)\\&=\frac{1}{\Gamma(1+ia)\Gamma(1-ia)}\frac{1}{2\pi i}\int_{-i\infty}^{i\infty}\Gamma(1+ia+t)\\&\qquad\times\Gamma(1-ia+t)\Gamma(s-t)\Gamma(-t)dt,\end{aligned}\tag{A3}$$

where the path of integration keeps the poles of $\Gamma(s-t)\Gamma(-t)$ on the right and the poles of $\Gamma(1+ia+t)\Gamma(1-ia+t)$ on the left.

Hence,

$$\begin{aligned}&\Gamma^2(1+ia)\Gamma^2(1-ia)F(1+ia,1-ia;2;z)\\&=\frac{1}{2\pi i}\int_{-i\infty}^{i\infty}\left\{\frac{1}{2\pi i}\int_{-i\infty}^{i\infty}\Gamma(1+ia+t)\Gamma(1-ia+t)\right.\\&\qquad\left.\times\Gamma(s-t)\Gamma(-t)dt\right\}\Gamma(-s)(-z)^s ds.\end{aligned}\tag{A4}$$

[24] E. T. Whittaker and G. N. Watson, *A Course of Modern Analysis* (Cambridge University Press, Cambridge, 1950), fourth edition, p. 290.

If the order of integration is interchanged,

$$\Gamma^2(1+ia)\Gamma^2(1-ia)F(1+ia,1-ia;2;z)$$
$$=\frac{1}{2\pi i}\int_{-i\infty}^{i\infty}\Gamma(1+ia+t)\Gamma(1-ia+t)\Gamma(-t)$$
$$\times\left\{\frac{1}{2\pi i}\int_{i\infty}^{i\infty}\Gamma(s-t)\Gamma(-s)(-z)^s ds\right\}dt \quad \text{(A5)}$$
$$=\frac{1}{2\pi i}\int_{-i\infty}^{i\infty}\Gamma(1+ia+t)\Gamma(1-ia+t)$$
$$\times\Gamma^2(-t)(1-z)^t dt. \quad \text{(A6)}$$

This integral is evaluated by completing the contour with a semicircle to the right. The only poles within the contour are double poles at $t=0,\ 1,\ 2\cdots$. The contribution of the semicircle to the integral goes to zero in the limit of infinite radius. We must find the residue of the integrand at a pole $t=n$. We write $t=n+\zeta$, and, expanding,

$$\Gamma(1+ia+t)\Gamma(1-ia+t)\Gamma^2(-t)(1-z)^t$$
$$=[\Gamma(1+ia+n)+\zeta\Gamma'(1+ia+n)][\Gamma(1-ia+n)$$
$$+\zeta\Gamma'(1-ia+n)]\frac{\pi^2}{\sin^2\pi\zeta}[\Gamma(1+n)+\zeta\Gamma'(1+n)]^{-2}$$
$$\times[(1-z)^n+\zeta\log(1-z)(1-z)^n]. \quad \text{(A7)}$$

The coefficient of $1/\zeta$ is

$$\frac{\Gamma(1+ia+n)\Gamma(1-ia+n)}{\Gamma^2(1+n)}(1-z)^n\left[\frac{\Gamma'(1+ia+n)}{\Gamma(1+ia+n)}\right.$$
$$\left.+\frac{\Gamma'(1-ia+n)}{\Gamma(1-ia+n)}-2\frac{\Gamma'(1+n)}{\Gamma(1+n)}+\log(1-z)\right]. \quad \text{(A8)}$$

Hence,

$$\Gamma^2(1+ia)\Gamma^2(1-ia)F(1+ia,1-ia;2;z)$$
$$=-\sum_{n=0}^{\infty}\frac{\Gamma(1+ia+n)\Gamma(1-ia+n)}{\Gamma^2(1+n)}(1-z)^n$$
$$\times\left\{\frac{\Gamma'(1+ia+n)}{\Gamma(1+ia+n)}+\frac{\Gamma'(1-ia+n)}{\Gamma(1-ia+n)}\right.$$
$$\left.-2\frac{\Gamma'(1+n)}{\Gamma(1+n)}+\log(1-z)\right\}. \quad \text{(A9)}$$

Remembering that

$$\Gamma(1+ia)\Gamma(1-ia)=\frac{\pi a}{\sinh\pi a}=[V(1)]^{-1} \quad \text{(A10)}$$

and neglecting terms of order $1-x=y$ or higher, we get

$$W(x)=-V(1)[\log(1-x)+\Psi(1+ia)$$
$$+\Psi(1-ia)-2\Psi(1)+O(y\log y)], \quad \text{(A11)}$$

where $\Psi(n)=\Gamma'(n)/\Gamma(n)$. This may be written in the form

$$W(x)=-V(1)[\log(1-x)+c_0]+O(y\log y). \quad \text{(A12)}$$

If we use the expression for the Ψ-function, the constant c_0 is found to be

$$c_0=2a^2\sum_{\nu=1}^{\infty}\frac{1}{\nu(\nu^2+a^2)}. \quad \text{(A13)}$$

The Eq. (A12) is used in Eq. (23), and Eq. (A13) in Eq. (34). A practical formula for the sum in Eq. (A13) is given in Eq. (38).

Gamma Rays Excited by the Inelastic Scattering of Neutrons in Lead, Bismuth, Iron, Nickel, and Chromium*

M. A. ROTHMAN AND C. E. MANDEVILLE
Bartol Research Foundation of the Franklin Institute, Swarthmore, Pennsylvania

(Received October 23, 1953)

Using neutrons of the *d*-D reaction at an energy of 3.9 Mev, gamma rays have been excited by the inelastic scattering process in Pb, Bi, Fe, Ni, and Cr. The energies of the gamma rays were measured by scintillation spectrometry.

INTRODUCTION

WHEN neutrons are scattered from nuclei, the inelastic process gives rise to excitation of the target nuclei with the resultant emission of gamma radiation and inelastically scattered neutrons of reduced energy. Measurement of the energies of the inelastically scattered neutron groups locates in energy the nuclear excitation levels. From the level structure, if the knowledge thereof is detailed enough, the gamma-ray spectrum can be predicted. However, very few neutron spectra have been accurately measured, and very little is known of a precise nature concerning the properties of the neutron-excited levels. To determine in a reasonable time the nature of the gamma rays, as well as to study the inelastic cross sections, it has been found more feasible to make direct measurements of the emitted gamma rays, rather than the scattered neutrons.

It has been a general practice to use as sources of primary neutrons the *d*-D or the *d*-T reactions, supplying neutron energies of ~3 Mev and ~14 Mev, respectively. Using Geiger counters and a coincidence technique, the energies of gamma rays excited by fast neutron scattering have been measured by the Oxford group.[1,2] These measurements were confined to the use of *d*-D neutrons of energy 2.5 Mev. A similar technique has been employed at neutron energies of 14 Mev at Los Alamos.[3] Scintillation counting methods have also been applied recently to the problem of the gamma-ray detection.[4–8]

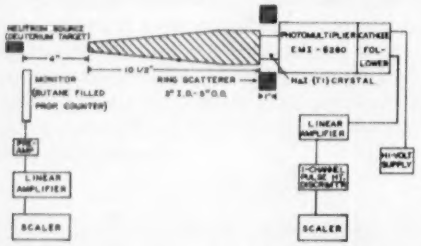

FIG. 1. Geometry and instrumentation for the detection of gamma rays excited by inelastic scattering of neutrons.

EXPERIMENTAL PROCEDURE

Neutrons of energy 3.9 Mev were generated in the smaller Bartol Van de Graaff statitron by passing 1.1-Mev deuterons through a 300-kev thick nickel foil into a chamber containing gaseous deterium. The bombarding beam of magnetically resolved atomic deuterium varied in intensity from 10 to 25 microamperes, half of the beam being lost in striking the supporting grid behind the nickel foil.

The geometry of the scattering measurements is shown in Fig. 1. Neutrons originating in the deuterium target are scattered in the "ring" scatterer surrounding the crystal of NaI-Tl; those scattered inelastically produce gamma rays that are detected in the crystal. The direct beam of neutrons is attenuated by the intervening lead cone. A background counting rate is present which arises from neutrons which are scattered into the crystal by the immediate environment and by the ring scatterer itself. Neutrons which are captured in the crystals of sodium iodide give rise to emissions of gamma rays immediately upon capture, and subsequently to the radiations of the radioactive I^{128}($T_{\frac{1}{2}}$ = 25 min) produced. The radiations of I^{128} are characterized by a hard beta-ray spectrum of maximum energy 2.0 Mev. Since an appreciable fraction of the background with scatterer present was indeed found to arise from neutrons deflected into the crystal by the scatterer, the backgrounds with and without the scatterer were evidently different. Consequently, in order to measure the effective background with scatterer present, a ring of graphite was placed around the crystal. Since the first excited level of C^{12} lies at 4.5 Mev, neutrons of 3.9-Mev energy undergo elastic scattering exclusively, and so produce no gamma rays. From a comparison of the product $n\sigma$ for graphite with the same quantity calculated for the elements employed as scatterers, and from a consideration[9] of the angular distribution of fast

* Assisted by the joint program of the U. S. Office of Naval Research and the U. S. Atomic Energy Commission.

[1] Beghian, Grace, Preston, and Halban, Phys. Rev. **77**, 286 (1950).

[2] Grace, Beghian, Preston, and Halban, Phys. Rev. **82**, 969 (1951).

[3] M. E. Battat, Phys. Rev. **91**, 441 (1953).

[4] Scherrer, Theus, and Faust, Phys. Rev. **89**, 1268 (1953).

[5] L. C. Thompson, Phys. Rev. **89**, 905 (1953).

[6] R. B. Day, Phys. Rev. **89**, 908 (1953).

[7] Garrett, Hereford, and Sloope, Phys. Rev. **91**, 441 (1953).

[8] Scherrer, Smith, Allison, and Faust, Phys. Rev. **91**, 768 (1953).

[9] Huber, Baldinger, and Budde, Helv. Phys. Acta **25**, 444 (1953); A. E. Remund and R. Ricamo, Helv. Phys. Acta **25**, 447 (1953).

neutrons scattered elastically from graphite, it was concluded that graphite should scatter at least as many neutrons into the crystal as do the other scattering elements.

THE MEASUREMENTS

The energy spectrum of the gamma rays excited by 3.9-Mev neutrons on lead is shown in Fig. 2. In Fig. 2(a) are given the pulse height distributions obtained from the NaI crystal, first with the carbon scatterer present to determine the background, and then with

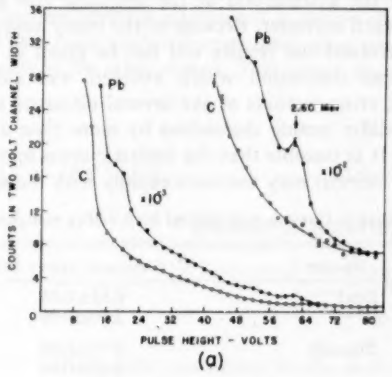

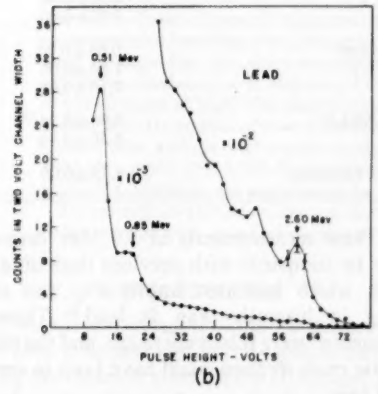

FIG. 2. The energy distribution of pulse heights in the crystal of NaI-Tl with carbon and lead scatterers are shown in Fig. 2(a). Taking the carbon curve as background, the supposed actual contribution of the lead scatterer is shown in Fig. 2(b).

the lead scatterer to determine the gamma rays from the inelastic scattering. The difference curve is given in Fig. 2(b). Although the quantities subtracted are of the same order of magnitude, the experiment was repeated several times, and the results are reproducible in their essential details. Photoelectric peaks corresponding to gamma rays of energies 0.85 and 2.60 Mev are clearly in evidence. Also to be expected are two peaks at 2.1 and 1.6 Mev, caused by pair production in the NaI crystal with the escape of either one or both annihilation quanta from the crystal. These peaks may

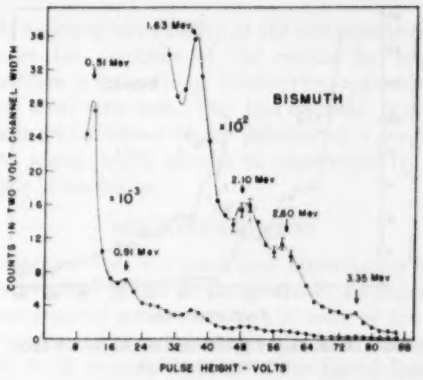

FIG. 3. Pulse-height distribution generated in the crystal of NaI-Tl by the gamma rays resulting from the inelastic scattering of 3.9-Mev neutrons in bismuth.

be superimposed upon a continuum possibly caused in part by low-intensity gamma rays of energy lower than 2.6 Mev. The relatively intense photo peak at 0.51 Mev arises from pair production by the 2.60-Mev gamma ray, and subsequent annihilation occurring within the scatterer itself.

Corroboration of this interpretation of the pulse-height spectrum is obtained by observing the spectrum of the 2.76-Mev gamma ray of Na^{24}. This source, when placed either inside or outside the lead ring, gives a pulse-height distribution which is quite similar in shape to the high-energy region of the spectrum obtained from the lead gamma rays.

An examination of the curves of Fig. 2(a) shows that in the region beyond 2.6 Mev the curves for carbon and lead coincide. Below 2.6 Mev are found the additional contribution of pulses due to the gamma rays from lead. This point is regarded as confirmation of the belief that measurements with the carbon scatterer present yield the true background.

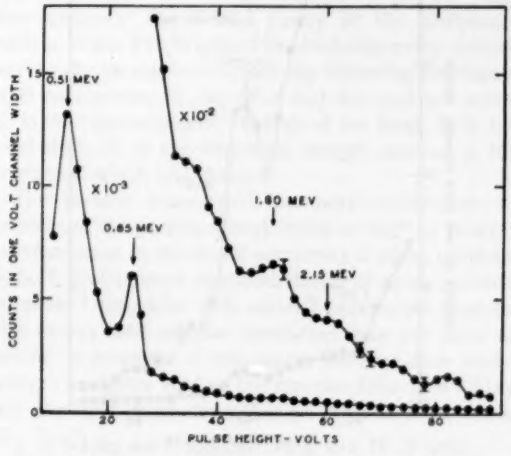

FIG. 4. Gamma-ray spectrum excited by the scattering of 3.9-Mev neutrons in iron.

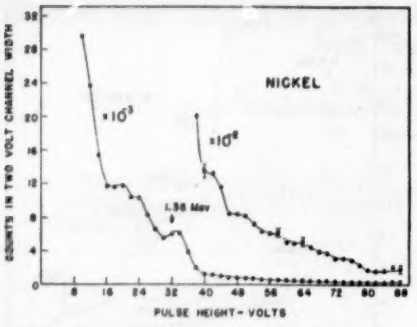

FIG. 5. Gamma-ray spectrum excited by 3.9-Mev neutrons on nickel.

When a scatterer of bismuth was irradiated by 3.9-Mev neutrons, the gamma-ray spectrum of Fig. 3 was obtained. This curve, and those following, have the background observed with the carbon ring already subtracted. The bismuth curve is interpreted to show that gamma rays are emitted at 3.35, 2.60, 1.63, and 0.91 Mev. Again, by comparison with the Na^{24} spectrum, the peak at 2.1 Mev is interpreted as an escape peak of the 2.60-Mev radiation. As in the case of lead, annihilation radiation appears at 0.51 Mev.

The gamma-ray spectrum from neutrons on iron is shown in Fig. 4. The curve can be interpreted as showing the definite presence of the previously reported[5-7] gamma ray at 0.85 Mev as well as gamma rays of quantum energy 1.8 and 2.15 Mev. There is also evidence of gamma rays emitted with quantum energies greater than 2.15 Mev, going up to at least 3.3 Mev. Again, annihilation radiation is seen at 0.51 Mev.

The pulse-height distribution produced by gamma rays from nickel is shown in Fig. 5. There is a clearly identifiable gamma ray at 1.36 Mev, and probably one

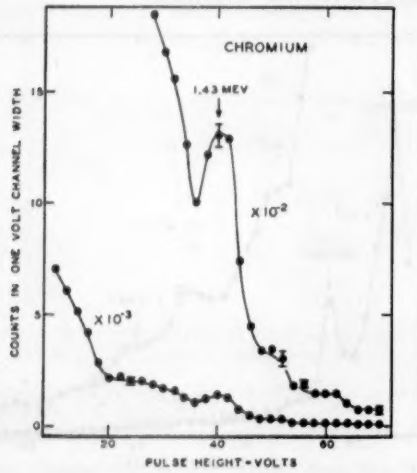

FIG. 6. Gamma-ray spectrum excited by the inelastic scattering of 3.9-Mev neutrons by chromium.

at 0.9 Mev. In addition there are smaller amounts of radiation at intermediate and higher energies.

A scatterer of powdered chromium metal was irradiated by neutrons to give the distribution of Fig. 6. A single, broad photoelectric peak is present corresponding to a quantum energy of 1.43 Mev.

The gamma rays listed above are summarized in Table I.

DISCUSSION

An attempt was made to evaluate the relative intensities of the various gamma rays, taking into account the attenuation of the neutrons and gamma rays in each scatterer. Because of the many approximations involved the results will not be given in detail. A general conclusion which evolved was that the inelastic cross sections of the several elements studied do not differ among themselves by more than a factor of two. It is possible that the inelastic cross section for a given element may fluctuate rapidly with the neutron

TABLE I. Gamma rays excited by 3.9-Mev neutrons.

Element	Gamma-ray energy (Mev)
Lead	0.85±0.06
	2.60±0.06
Bismuth	0.91±0.04
	1.63±0.04
	2.60±0.06
	3.35±0.06
Iron	0.85±0.03
	1.80±0.06
	2.15±0.08
Nickel	0.90±0.04(?)
	1.36±0.04
Chromium	1.43±0.06

energy. These measurements at 3.9 Mev cannot with certainty be compared with previous data obtained at 4.3 Mev, which indicated appreciably less inelastic scattering in bismuth than in lead.[10] These early measurements[10] were relatively rough, and the estimates of inelastic cross sections could have been in error by a factor of two.

Many similarities are found between the gamma rays produced by neutron bombardment and those obtained from radioactive decay. The beta decay of ThC″(Tl^{208}) gives rise to excited states of Pb^{208} which emit well-known 0.86- and 2.61-Mev gamma rays. In like manner the beta decay of Mn^{56} leads to excited states of Fe^{56} which emit gamma rays of 0.85-, 1.8-, and 2.15-Mev energy. Mn^{52} decays by positron emission to excited states of Cr^{52}, with the subsequent appearance of 0.73-, 0.94-, and 1.46-Mev gamma rays. The latter corresponds to the 1.43-Mev gamma ray obtained from the neutron bombardment of chromium. The absence of the 0.73- and 0.94-Mev quanta may be explained by noting that the 1.46-Mev gamma ray arises from a transition

[10] C. E. Mandeville and C. P. Swann, Phys. Rev. 84, 214 (1951).

between the first excited level to the ground state, while the 0.73- and 0.94-Mev quanta come from higher levels. If it is assumed that these higher levels have high spin values, it would not be expected that they would be excited strongly by neutrons of the energy used.

The same argument is applicable in the case of nickel. The radioactive decay of Co^{60} gives two gamma of energy 1.33 and 1.17 Mev, but the neutron bombardment of Ni^{60} produces only one of these, corresponding to the excitation of the first excited state.

It is seen that the pulse-height distributions obtained by neutron scattering in lead, iron, chromium, and nickel are successfully interpreted in terms of gamma rays arising from nuclear energy levels that are known to be excited by other means. This serves as a partial corroboration of the validity of the measurements, and enhances the credence of the results for bismuth, where there is no previous information concerning the energy level structure. The four gamma rays from bismuth give evidence of the presence of a number of excited states which should be observable by other methods of excitation.

ACKNOWLEDGMENT

The writers wish to express their appreciation for the suggestions and advice of Dr. Franz R. Metzger who also participated in accumulation of some of the data. They wish also to acknowledge the kind interest of Dr. W. F. G. Swann, Director of the Bartol Research Foundation.

PHYSICAL REVIEW VOLUME 93, NUMBER 4 FEBRUARY 15, 1954

Elastic Scattering of Alpha Particles by Neon*

E. GOLDBERG,† W. HAEBERLI, A. I. GALONSKY,‡ AND R. A. DOUGLAS
University of Wisconsin, Madison, Wisconsin

(Received November 12, 1953)

Differential cross sections for the elastic scattering of alpha particles by neon have been measured at four angles for alpha energies from 2 to 4 Mev. Absolute values of the cross section are good to ±4 percent. The angles chosen correspond to center-of-mass angles such as to simplify assignments of angular momentum to the scattered resonance wave. Because no nuclear spins are involved, the angular momentum of the scattered wave also fixes the parity and angular momentum of the compound state.

Thirteen resonances were observed. Eleven are attributed to virtual states of Mg^{24} and two are assigned to virtual states of Mg^{26}. The experimental data were analyzed in terms of the Wigner-Eisenbud formalism to determine the additional level parameters: E_r, γ_λ^2 and Δ_λ. The laboratory energies of the $(Ne^{20}+\alpha)$ resonances in Mev, and the total angular momentum and parity assignments of the virtual states are: 2.488(1^-), 2.573 (0^+), 2.652 (2^+), 2.903 (0^+), 3.062 (1^-), 3.184 (2^+), 3.548 (3^-), 3.780 (1^-), 3.801 (2^+), 3.839 (4^+), and 3.923 (2^+). Similarly, the assignments for $(Ne^{22}+\alpha)$ resonances are 3.245 (3^-) and 3.418 (3^-).

The resonances above 3.0-Mev bombarding energy were investigated for competing reactions. No competing reaction with cross sections greater than about one percent of the elastic value were observed.

I. INTRODUCTION

THE elastic scattering of alpha particles by nuclei of zero spin provides a very simple method for classifying the resonant states of the compound nucleus. The method has been discussed in some detail by Cameron[1] and Hill[2] who have studied virtual states of Ne^{20} and O^{16} by alpha scattering on O^{16} and C^{12}. Very briefly stated, the method consists of measuring the elastic scattering cross section as a function of alpha energy at those angles for which the various low-order Legendre polynomials have zeros. The angles at which the resonance scattering vanishes serve to identify clearly the partial waves involved in the resonance scattering. Since no nuclear spins are involved, the angular momentum of the resonance partial wave fixes uniquely the J and parity of the compound nuclear state. The Wigner-Eisenbud dispersion formalism[3,4] may be used to extract the following additional level parameters, E_λ, Δ_λ, $(E_r=E_\lambda+\Delta_\lambda)$, and γ_λ^2, where E_λ is the "characteristic" energy of the level, Δ_λ is the level shift, E_r is the resonance energy, and γ_λ^2 is the "reduced" width of the level.

The present experiment has been undertaken to investigate the nuclear energy levels of Mg^{24} by observing resonances in the elastic scattering of alpha particles by Ne^{20}. Earlier work on the scattering of alpha particles by neon[5,6] was done with natural radioactive sources. The energy and angular resolution was too poor to permit observation of resonances below 5-Mev alpha energy. Brubaker studied the reaction from 4 to 7 Mev and observed broad anomalies in the scattering cross-

* Work supported by the U. S. Atomic Energy Commission and the Wisconsin Alumni Research Foundation.

† U. S. Atomic Energy Commission Predoctoral Fellow. Now at Radiation Laboratory, University of California, Livermore, California.

‡ National Science Foundation Fellow.

[1] J. R. Cameron, Phys. Rev. **90**, 839 (1953).

[2] R. W. Hill, Phys. Rev. **90**, 845 (1953).

[3] E. P. Wigner and L. Eisenbud, Phys. Rev. **72**, 29 (1947).

[4] T. Teichmann and E. P. Wigner, Phys. Rev. **87**, 123 (1952).

[5] G. Brubaker, Phys. Rev. **54**, 1011 (1938).

[6] W. Riezler, Ann. Physik **23**, 198 (1935).

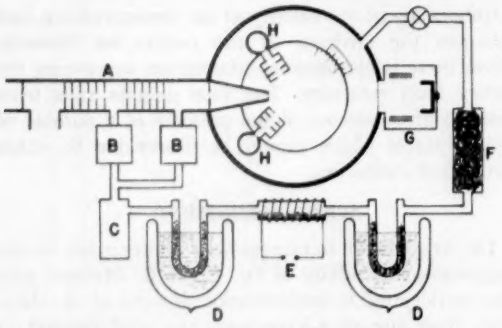

FIG. 1. Schematic diagram of the gas scattering chamber and the gas circulating system. *A*—differential pumping column, *B*—roughing pumps (250 liters/sec), *C*—oil trap, *D*—liquid air trap (with magnesium turnings for better heat contact), *E*—gas purifier (magnesium turnings in inconel tube heated to 600°C), *F*—heat exchanger with copper turnings, *G*—collector cup, *H*—proportional counters with slit systems.

section curves above 5.0 Mev but made no attempt at analysis. Riezler's work was too scanty to permit any conclusions regarding resonances to be drawn.

II. EXPERIMENTAL PROCEDURE

The experimental method has been described previously.[1,2,7] Monoergic (±0.05 percent) alpha particles from an electrostatic generator were scattered by neon in the differentially pumped gas scattering chamber (Fig. 1). The elastically scattered alphas were detected by two proportional counters mounted on a turntable and positioned 114.0° apart. The energy of the alpha particles was varied from 2.0 to 4.0 Mev and yields were recorded for laboratory angles of 78.7°, 114.2°, 131.8°, and 167.3° with respect to the incident beam. In a small region above 3.5 Mev, additional data were taken at 98.5° and 147.5°. The angles chosen correspond roughly to center-of-mass angles for which the Legendre polynomials of order $l=1$ to 4 have zeros.

In order to determine the absolute cross section, neon pressure readings were taken. A beam-current integrator was used[8] to shut off the counting circuits as soon as a predetermined charge (20 microcoulombs) had been collected in the collector cup. Data above 3 Mev were taken with 0.0005-mm nickel foils as counter windows. Below 3.0 Mev, alpha particles scattered through 131.8° and 167.3° had such low energies that a 0.00025-mm window had to be used. Propane was employed as a counter gas. The pulse-height spectrum of the counters showed a well-defined group of pulse heights due to elastically scattered alpha particles and some considerably smaller pulses probably due to γ rays. In order to monitor continuously the number of pulses outside the main group, two discriminator-scalers were used for each counter, the discriminators being adjusted to 30 and 60 percent, respectively, of the pulse height of the main group. The counting rates of the two scalers so set seldom differed by more than one percent. A precision pulser[9] was incorporated in the electronic arrangement to set and check the amplifiers and discriminators.

The neon gas used in the experiment was recirculated by transferring the gas from the exhaust stacks of the forepumps through a purifying stage back to the chamber (Fig. 1). In the purifying stage the gas had to pass over magnesium turnings that were maintained at a near-melting temperature. Tests showed that air leaking into the system was removed efficiently by the purifier. To guarantee neon gas of high purity, frequent mass spectroscopic analyses were made with a Nier-type Consolidated Mass Spectrometer. Nitrogen was the major contaminant but never exceeded 0.2 atom percent. The oxygen content was lower by at least a factor of five. A few other contaminants such as argon were detected but none were greater than 0.1 atom percent. Continuous monitoring of the gas purity was possible by watching the color of the alpha beam in the neon gas. A contamination of several tenths of a percent of air was easily seen as a bluish tinge to the orange color of neon. The neon gas was replaced with fresh gas occasionally and the magnesium was changed once.

The data at $\theta_{lab}=78.7°$ and 167.3° were taken at 3-kev intervals. At $\theta_{lab}=114.2°$ and 131.8° 3-kev steps were taken at the resonances and 15-kev steps off resonances. High-resolution work was done on all of the resonances by changing the resolution of the cylindrical analyzer from its normal setting of ±0.05 percent to ±0.02 percent and reducing the chamber pressure so that the target thickness at one of the angles was approximately equal to the energy spread of the beam. Because of the $\sin\theta$ factor in the thickness of the gas target which the counter sees, the target thickness at 167.3° was almost five times as great as that at 78.7° for the same gas pressure. Consequently the target thickness at 167.3° was normally larger than the cylindrical analyzer resolution.

III. EXPERIMENTAL RESULTS

The cross-section values computed from the data are given in Figs. 2 and 3. The drawings include the results of both the survey work and high-resolution work on the resonances. Not all of the off-resonance data for $\theta_{lab}=78.7°$ and 167.3° have been illustrated. Approximately every other point was plotted to avoid overlapping of the circles. All of the pertinent data for $\theta_{lab}=114.2°$ and 131.8° have been illustrated.

The measured yield of elastically scattered particles Y is related to the cross section by

$$\sigma(\theta_{lab})=Y\sin\theta/NnG.$$

θ is the scattering angle, N and n are the number of

[7] Jackson, Galonsky, Eppling, Hill, Goldberg, and Cameron, Phys. Rev. **89**, 365 (1953).

[8] Worthington, McGruer, and Findley, Phys. Rev. **90**, 899 (1953).

[9] W. C. Elmore and M. Sands, *Electronics* (McGraw-Hill Book Company, Inc., New York, 1949), p. 323.

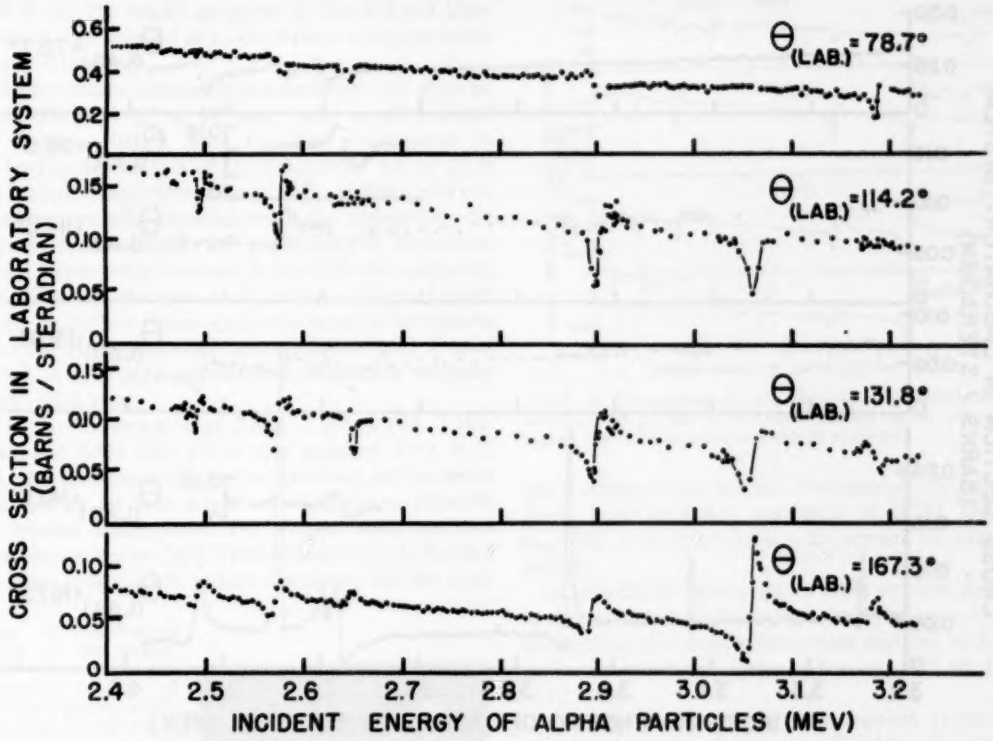
CROSS SECTION IN LABORATORY SYSTEM (BARNS / STERADIAN)
θ(LAB.) = 78.7°
θ(LAB.) = 114.2°
θ(LAB.) = 131.8°
θ(LAB.) = 167.3°
INCIDENT ENERGY OF ALPHA PARTICLES (MEV)

FIG. 2. Experimental cross sections for alpha particles on neon from 2.4 Mev to 3.2 Mev.

incident particles and the number of target nuclei per unit volume, respectively, and G is the geometry factor of the counter slit system.[8] The major error in the cross section was due to the uncertainty in Y. The statistical error was usually about ± 3 percent. The error introduced by the slight dependence of Y upon the discriminator setting of the scalers is estimated to be appreciably less than 1 percent. The uncertainty in θ (± 0.1 degrees) introduces an error of ± 1 percent in the $\sin\theta$ factor at 167.3°. The gas density at the target is known to about ± 1 percent, the G-factor of the slit system to ± 0.2 percent.

The major error in the number of incident particles was not given by the accuracy of the current integrator (better than 0.1 percent) but by the uncertainty in the equilibrium ratio of α^+/α^{++} collected at the Faraday cup. The only experimental data on the equilibrium fraction of singly charged alphas in this energy range is that of Rutherford[10] and is for air. In the present experiment the nickel foil preceding the collector cup determines the α^+/α^{++} ratio. However, at lower energies it has been shown that the equilibrium charge ratio is not strongly dependent on the nature of the medium[11] (with the exception of the very light elements[12]). Therefore Rutherford's data for air was used to correct the measured incident charge. The correction varied from seven percent at $E_\alpha = 2.0$ Mev to one percent at 4.0 Mev. Hence even if the equilibrium ratios for nickel and air are slightly different no appreciable error is introduced into the final cross-section data. It is reasonable to assume that the error will be less than ± 1.0 percent. The arithmetical sum of all uncertainties is 7.0 percent while the rms value of the errors is 3.6 percent. Errors introduced by impurities of the neon gas are not included. Assuming that the impurities scatter classically this error would be of the order of 0.2 percent.

The energy of the alpha particles before entering the chamber was known through the setting of the cylindrical analyzer which was calibrated with the $Li^7(p,n)Be^7$ threshold.[13] The calibration was thought to be reliable to ± 0.1 percent. The major error in the determination of the alpha-particle energy was, however, the uncertainty in the energy loss in the gas. This loss was determined by noting the energy shifts of the resonances as a function of chamber pressure. The correct energy was then found by linear extrapolation to zero pressure. Since the extrapolation method was dependent on energy differences, small fluctuations in energy could affect the final value significantly. The

[10] E. Rutherford, Phil. Mag. **47**, 277 (1924).
[11] M. C. Henderson, Proc. Roy. Soc. (London) **A109**, 157 (1925).
[12] E. Snitzer, Phys. Rev. **89**, 1237 (1953).
[13] Herb, Snowden, and Sala, Phys. Rev. **75**, 246 (1949).

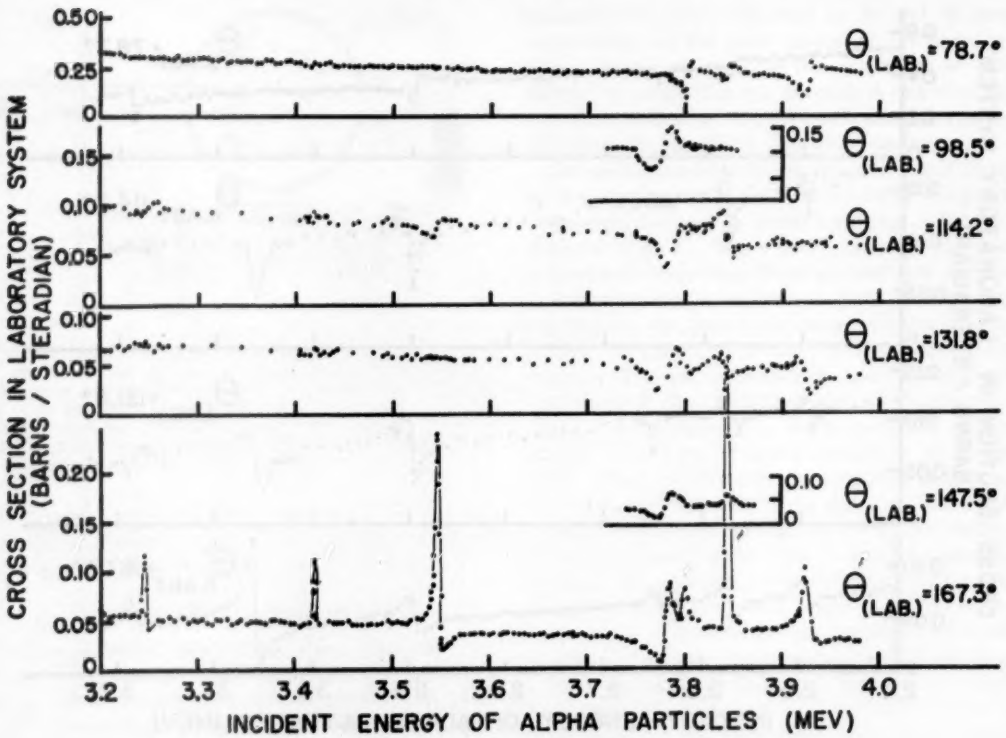

FIG. 3. Experimental cross sections for alpha particles on neon from 3.2 Mev to 4.0 Mev.

data from the thirteen resonances showed that the quantity $\Delta E/\Delta P$ (Mev/cm of oil pressure) fluctuated appreciably over the energy range studied. As a consequence all alpha-particle energies are assigned a ± 5-kev uncertainty.

Ne^{20} is known to have an excited state at 1.634 Mev and Ne^{22} has one at 1.277 Mev.[14] Also the $Ne^{20}(\alpha,p)Na^{23}$ and $Ne^{22}(\alpha,p)Na^{25}$ reactions are energetically possible above 2.4 and 3.4 Mev, respectively.[15,16] To see the degree to which these reactions and inelastic scattering compete with the elastic scattering, the counter angle and counter-window foil were selected to allow possible inelastic groups to appear separated from the main group of pulse heights. An oscilloscope camera of the Land type was employed for quick semiquantitative pulse-height analyses. The response of the photographic emulsion to a given number of alpha pulses seen on the scope was noted in order to place an upper limit on unobserved groups. Photographs of the pulse-height distribution were taken for all resonances above 3.0 Mev. There was no evidence of inelastic scattering at any of the resonances checked. An upper limit of one percent of the elastic cross section may be given. At 3.839 and 3.923 Mev, small pulses thought to be caused by gamma-ray electrons were seen. At the 3.923-Mev resonance, a group about one-fourth the height of the main group was seen. The photograph is shown in Fig. 4. This pulse height is expected for protons from the $Ne^{20}(\alpha,p)Na^{23}$ reaction.

IV. RESULTS OF THE ANALYSIS

Immediate assignments of total angular momenta and parities were possible in most cases by a qualitative examination of the data. Since the angles were chosen to correspond to the zeros of the Legendre polynomials, $P_1(\cos\theta)$ to $P_4(\cos\theta)$, the partial wave responsible for the formation of the compound nucleus was identified by noting the angle or angles at which the anomalies did not appear. The reason for neglecting higher-order partial waves will be discussed later.

Since the main part of the off-resonance cross section is Rutherford scattering, resonance dips in excess of 10 percent could only be associated with anomalies produced by an isotope whose abundance was greater than 10 percent (i.e., Ne^{20}). The experimental results were fitted with the theoretical curves from the Wigner-Eisenbud formalism[3,4,17] to give the parameters E_r, γ_λ^2, and Δ_λ, and as a check on level assignments. The interaction parameter, a, was chosen as $a=1.4(A^{\frac{1}{3}}+4^{\frac{1}{3}})$

[14] F. Ajzenberg and T. Lauritsen, Revs. Modern Phys. 24, 321 (1952).
[15] C. W. Li, Phys. Rev. 88, 1038 (1952) and Li, Whaling, Fowler, and Lauritsen, Phys. Rev. 83, 512 (1951).
[16] E. Bleuler and W. Zünti, Helv. Phys. Acta 20, 95 (1947).
[17] R. K. Adair, Phys. Rev. 86, 155 (1952).

$\times 10^{-13}$ cm. The results are given in Table I and illustrated in Figs. 5 and 6 as a comparison of experimental results to theory.

The formalism also provides a sum rule that gives an upper bound to γ_λ^2 of $3\hbar^2/2\mu a$, which is often called the "Wigner limit". Since $\Gamma_\lambda/\gamma_\lambda^2$ is proportional to the barrier penetration of the l'th partial wave,[4] Γ_λ is also limited. Since resonances with $\Gamma_\lambda < 1$ kev could not be experimentally detected with the apparatus, the Wigner limit excludes the possibility of high-order partial waves being involved in the observed scattering anomalies. For example, at $E_r(\text{lab}) < 4.0$ Mev, J must be <5 if a $Ne^{20}+\alpha$ resonance is to be seen. No resonances should be resolvable much below 2.0 Mev and J must be ≤ 2 to give an experimentally detectable anomaly below ~ 2.4 Mev.

The Ne^{20} resonances at 2.488, 2.573, 2.652, 3.184, 3.548, and 3.839 Mev which were assigned $J=1$, 0, 2, 2, 3, and 4, respectively, are not resolved, but evidence available at all four angles of observation supports the quoted assignments. The Wigner limit restricts these resonances to $J<5$. Their values for Γ_λ in Table I are very approximate values calculated on the basis of the known target thickness and beam resolution and hence are enclosed in parentheses.

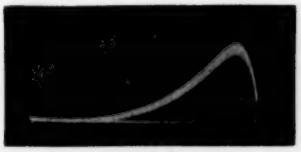

FIG. 4. Oscilloscope picture of the proportional counter pulses at a bombarding energy of 3.923 Mev and $\theta_{\text{lab}}=90°$. The group of large pulses results from elastically scattered alpha particles while the smaller pulses are believed to be caused by protons from the $Ne^{20}(\alpha,p)Na^{23}$ reaction.

The resonances at 3.245 and 3.418 Mev are both thought to be $J=3$ levels in Mg^{26}. The experimental values for cross sections at the peaks are slightly in excess of the calculated values for both resonances. If Nier's values for the isotopic ratios are used,[18] the discrepancy is about 8 percent but if Hibbs' are used,[19] the discrepancy is only 4 percent. However, the resonances appear to be resolved and the magnitudes and shapes of the experimental cross-section curves are in closest agreement to those predicted from the dispersion theory with the $J=3$, Mg^{26} assignment. The resonances at $E=3.780$ and 3.801 Mev involve scattered p and d waves, respectively. The experimental widths (7 ± 2 and 5 ± 1 kev) were assigned from observation of the data at $\theta_{\text{lab}}=78.7°$ and 167.3° where high beam resolution and a thin target were used. The data and theoretical curves are shown in Fig. 7. The level density in this region is sufficiently high that interference from the tails of neighboring levels has a marked effect on the scattering cross section. For example the predicted single level scattering maximum at 3.783 Mev and $\theta_{\text{lab}}=167.3°$ is reduced by ~ 25 percent by this interference.

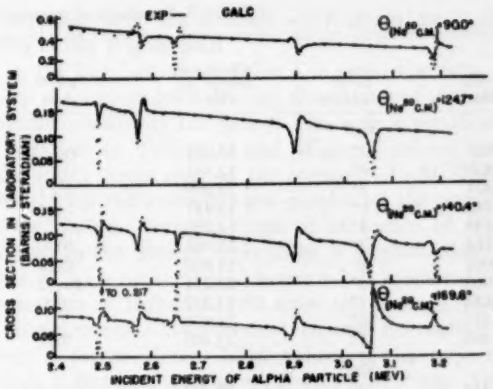

FIG. 5. Comparison of experimental and calculated cross sections from 2.4 Mev to 3.2 Mev. The calculated cross sections neglect the finite experimental energy resolution.

In general the off-resonance cross sections measured in the experiment differ by less than 5 percent from the Rutherford plus hard-sphere cross sections with a the radius of the hard sphere taken as $a=1.40(A^{\frac{1}{3}}+4^{\frac{1}{3}})\times 10^{-13}$ cm.

A marked deviation of experimental points from calculated values above the 3.923-Mev resonance is suggestive of a resonance slightly above 4.0 Mev. The signs of the deviations are those that would be caused by a resonance with $J=1^-$. However, a decrease of the interaction parameter, a, would have the same effect. Considering the expected high density of resonances, it is not unlikely that a neighboring resonance is the cause.

V. DISCUSSION OF RESULTS

The energy level diagram (Fig. 8) and Table I summarize the experimental results. While the alpha

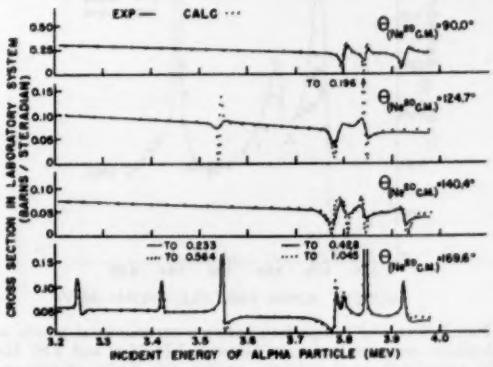

FIG. 6. Comparison of experimental and calculated cross sections from 3.2 Mev to 4.0 Mev. The calculated cross sections neglect the finite experimental energy resolution.

[18] A. O. Nier, Phys. Rev. 77, 789 (1950).
[19] R. F. Hibbs, U. S. Atomic Energy Commission Report AECU-556, August, 1949 (unpublished).

TABLE I. Summary of resonances seen by alpha scattering in neon gas.

E_r(lab) (Mev)	Level assignment	Excitation energy, E_x (Mev)	Γ_λ(lab) (kev)	γ_λ^2(c.m.) (Mev-cm) $\times 10^{15}$	$\frac{\gamma_\lambda^2(\text{c.m.})}{3\hbar^2/2\mu a}$	Δ_λ(c.m.) (Mev)	γ_λ^2(c.m.)/D $\times 10^{13}$, cm
	Mg^{24}						
3.923	2^+	12.601	6±1	8.3	0.03	+0.013	0.22
3.839	4^+	12.531	(1)	(25)	(0.08)		(0.28)
3.801	2^+	12.499	5±1	8.3	0.03	+0.026	0.22
3.780	1^-	12.481	7±2	7.0	0.02	+0.018	0.14
3.548	3^-	12.288	(1)	(10)	(0.03)		(0.08)
3.184	2^+	11.985	(0.5)	(4.2)	(0.01)		(0.11)
3.062	1^-	11.883	8±2	42	0.14	+0.15	0.84
2.903	0^+	11.751	10±2	51	0.16	+0.29	0.60
2.652	2^+	11.542	(0.5)	(25)	(0.08)		(0.67)
2.573	0^+	11.476	(1)	(17)	(0.06)		(0.20)
2.488	1^-	11.405	(0.5)	(18)	(0.06)		(0.36)
	Mg^{26}						
3.418	3^-	13.534	3.2±0.5	34	0.11	+0.070	0.57
3.245	3^-	13.388	2.5±0.5	45	0.15	+0.11	0.75

resonance energy is uncertain by only ±5 kev, the corresponding excitation energy in Mg^{24} has an additional 12-kev systematic uncertainty arising from the uncertainty of the $Ne^{20}+\alpha-Mg^{24}$ energy difference. This energy difference is best calculated by the following cycle: $Na^{23}(d,p)Na^{24}$, $Na^{24}\rightarrow Mg^{24}+\epsilon^-$, $Na^{23}(p,\alpha)Ne^{20}$, $H^2-(H+n)$, $n-H$. In order that our $Ne^{20}+\alpha-Mg^{24}$ difference corresponds to Li's current mass scale,[15] the adjusted Q's of Table I of Li's paper were used.

The only other experimental information concerning the levels of Mg^{24} in this same excitation range comes from the $Na^{23}+p$ reaction. Burling[20] observed $Na^{23}(p,\gamma)Mg^{24}$ and $Na^{23}(p,p')Na^{23*}$ resonances for proton energies from 0.3 to 1.9 Mev. Burling's data below $E_p\sim 1.1$ Mev overlaps the upper portion of the Mg^{24} excitation region studied in the present experiment. For comparison purposes his levels in Mg^{24} are included at the right of the energy-level diagram (Fig. 8). It will be noted that more Mg^{24} levels are seen by the $Na^{23}+p$ reaction than the $Ne^{20}+\alpha$ scattering. This result is not surprising since the scattering of the even parity spin zero particles can only involve Mg^{24} states whose parity is even or odd according as l and hence J is even or odd. Furthermore isobaric spin one ($T=1$) levels of Mg^{24} are forbidden for the alpha scattering but permitted for the $Na^{23}+p$ reactions. The first $T=1$ state of Mg^{24} should occur at ~9.4-Mev[21] excitation.

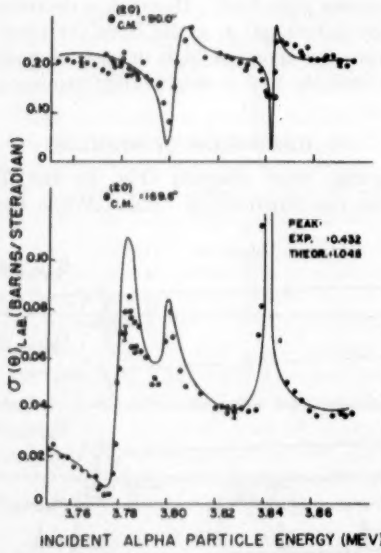

FIG. 7. Detailed comparison between experimental points and calculated cross-section curve between 3.75 Mev and 3.88 Mev. The calculated cross sections neglect the finite experimental energy resolution.

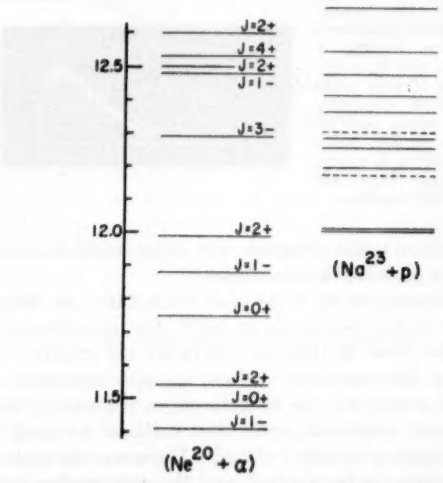

FIG. 8. Energy level diagram of Mg^{24} between 11.4-Mev and 12.6-Mev excitation energy. For comparison the Mg^{24} levels observed by the $Na^{23}(p,\gamma)Mg^{24}$ reaction[20] are indicated at the right.

[20] R. L. Burling, Phys. Rev. 60, 340 (1941).

[21] $(Na^{24}-Mg^{24})+$(Coulomb energy difference $Mg^{24}-Na^{24}$) $-(n-H)=5.33+4.65-0.78=9.4$ Mev.

The density of the $T=1$ states of Mg^{24} should then correspond to that of the excited states of Na^{24} which have been experimentally studied by Sperduto and Buechner.[22] Since for these $T=1$ levels there may be possible shifts of several hundred kilovolts between neighboring isobars, it is not possible to identify which of the $Na^{23}+p$ resonances correspond to the Na^{24} states.

However, *all* the Mg^{24} levels seen by alpha scattering should be accessible also to the $Na^{23}+p$ reaction although the cross section may be low. The first three alpha resonances which overlap Burling's proton data do indeed match within experimental uncertainties the (p,γ) resonances. Such is not the case for the three highest-energy alpha resonances. Perhaps more efficient gamma detectors or observation of the $Na^{23}(p,\alpha)Ne^{20}$ yield function would permit the detection of these states of Mg^{24}.

For each alpha resonance the ratio of γ_λ^2 to the Wigner limit is also given in Table I. If the compound state can be described in terms of an alpha particle in a potential, then the reduced width should be in the order of the Wigner limit.

In the last column of Table I is given the ratio of γ_λ^2 to the average level spacing, D, of states of the same angular momentum and parity. This ratio is significant in relation to Teichman and Wigner's second sum rule[4] which states that on the average $\gamma_\lambda^2 \approx 3D/2\pi K'$, where K' is the average wave number of the particle in the nucleus. For the range of excitation of Mg^{24} covered in the present experiment it is reasonable to treat K' as a constant and hence γ_λ^2/D measures the fluctuation of individual γ^2's from the average given by the sum rule. The observed extreme fluctuation is about a factor of ten. Most values of the ratio lie within a factor of two of $\gamma^2/D=0.4\times10^{-13}$ cm. This fluctuation is perhaps smaller than would be anticipated from the discussion of Teichman and Wigner.[4]

The authors would like to thank Professor H. T. Richards for his interest in the experiment and for several helpful discussions. Mr. K. W. Jones, Mr. M. T. McEllistrem, and Mr. R. E. Benenson kindly assisted in taking the data. The computational aid of Mrs. Helen Ward is gratefully acknowledged.

[22] A Sperduto and W. W. Buechner, Phys. Rev. **88**, 574 (1953).

Double Scattering of High-Energy Protons*†

C. L. OXLEY,‡ W. F. CARTWRIGHT,§ AND J. ROUVINA‖
University of Rochester, Rochester, New York

(Received October 29, 1953)

Measurements of polarization effects in double scattering of protons have been made in the energy range near 200 Mev. With a first scattering angle of 19° and a mean second polar angle of 27°, the azimuthal asymmetry 2ϵ, the fractional difference between second scattered flux at azimuths 0° and 180°, has been determined with several first and second target materials. With a polyethelene second target, an effective hydrogen target was realized by detecting in coincidence the scattered and recoil protons. By successive use of carbon and polyethelene first targets, with an effective hydrogen second target, the asymmetry in double p-p scattering was determined by subtraction to be 9.6 ± 3.5 percent. Since the fractional polarization, P, in a single scatter is related to the asymmetry in a double scatter by $2\epsilon=2PP'$, the polarizations produced in single scatters from hydrogen and carbon were found to be, neglecting energy degradation and angle change, $P_H=22\pm4$ percent and $P_C=43\pm8$ percent. A comparison of the double p-p asymmetry with those calculated by Goldfarb and Feldman using current p-p force models shows that the repulsive core model of Jastrow which best predicts the observed single scattering differential cross sections yields far too little polarization. Considerable singular noncentral force as used in other models seems indicated. The polarized protons produced in scattering from carbon may be useful for other experiments. The polarizations in scattering from several elements in the range from D to Ag, as measured with a hydrogen analyzer, vary from 20 to 50 percent.

I. INTRODUCTION

IN 1951, at the conclusion of proton-proton scattering experiments at 240 Mev,[1] a considerable amount of information on high-energy nucleon-nucleon scattering was available. The theoretical analyses gave no unique information regarding proton-proton forces, but several potential models had been constructed, particularly to fit the proton scattering results from the 32-Mev[2] and early 350-Mev[3] experiments. Christian and Noyes,[4] using singular tensor-force terms, fitted those data, but did not preserve the charge independence of nuclear forces. In an effort to maintain charge independence, Case and Pais[5] used singular triplet spin-orbit interactions of the $\mathbf{L}\cdot\mathbf{S}$ form. Jastrow[6] resorted to the alteration of the singlet well by the introduction of a hard central core, and with some nonsingular tensor interaction was also able to fit the data without sacrifice of charge independence.

Further proton-proton scattering data at small scattering angles which had become available[7] did not fit the predictions of Case and Pais and of Christian and Noyes.

With this as the prevailing situation, we considered the feasibility of an investigation of noncentral forces by measurement of polarization effects in a double-scattering experiment. The interpretation of any measured effect probably would again require computations based on nuclear force models since no common nuclear parameter is directly measured. The only calculations available, those of Wolfenstein,[8] were, unfortunately, based on nuclear models outmoded by high-energy scattering data, and predicted very small polarization effects in double proton-proton scattering.

The experiment was nevertheless undertaken since it was possible that appreciable effects night be present as suggested by the use of sizeable noncentral terms in the models constructed. The measurement of such effects might then allow some choice among proposed models.

II. ASYMMETRY RELATIONS IN DOUBLE SCATTERING

Wolfenstein and Ashkin[9] have given a general derivation of the relation between polarization produced in a single scattering and the asymmetry observed in a double scattering. For purpose of illustration we consider a particular case in which spin flip of the proton in scattering does not occur.

Consider protons scattered at an angle θ in a plane $\phi=0$. If there are noncentral forces involved, the scattered beam will be, in general, partially polarized perpendicular to the plane of scatter. The polarization may be considered as due to a difference in scattering cross sections for the two spin orientations in the incident

* Supported by the U. S. Atomic Energy Commission.

† This work was reported briefly in a letter, Phys. Rev. **91**, 419 (1953).

‡ Now at Institute for Nuclear Studies, University of Chicago, Chicago, Illinois.

§ Now at Naval Ordnance Test Station, China Lake, California.

‖ General Electric Research Laboratory, Schenectady, New York.

[1] C. L. Oxley and R. D. Schamberger, Phys. Rev. **85**, 416 (1952).

[2] W. K. H. Panofsky and F. Filmore, Phys. Rev. **79**, 57 (1950); Cork, Johnston, and Richman, Phys. Rev. **79**, 71 (1950). Later results at this energy are given by F. Filmore, Phys. Rev. **83**, 1252 (1951); B. Cork, Phys. Rev. **90**, 1130 (1953).

[3] O. Chamberlain and C. Wiegand, Phys. Rev. **79**, 96 (1950). More recent data are reported by Chamberlain, Segrè, and Wiegand, Phys. Rev. **81**, 2841 (1951).

[4] R. S. Christian and H. P. Noyes, Phys. Rev. **70**, 85 (1950).

[5] K. M. Case and A. Pais, Phys. Rev. **80**, 203 (1950).

[6] R. Jastrow, Phys. Rev. **81**, 165 (1951).

[7] O. A. Towler, Jr., Phys. Rev. **85**, 1024 (1952); Chamberlain, Segrè, and Wiegand, reference 3.

[8] L. Wolfenstein, Phys. Rev. **75**, 1664 (1949); **76**, 541 (1949).

[9] L. Wolfenstein and J. Ashkin, Phys. Rev. **85**, 947 (1952).

beam. Thus we may write

$$\sigma_+(\theta)=\sigma_0(\theta)\{1+\delta(\theta)\},$$
$$\sigma_-(\theta)=\sigma_0(\theta)\{1-\delta(\theta)\}. \quad (1)$$

For an incident unpolarized beam, the fractional polarization $P(\theta)$ of the scattered beam is

$$P(\theta)\equiv\frac{N_+-N_-}{N_++N_-}=2\langle S_y\rangle=\delta(\theta). \quad (2)$$

If this scattered beam undergoes a second scattering, again limited to this plane, and in the same sense, i.e., at $\phi=0$, relations similar to (1) will hold. Since target-materials, angles, and incident energies of scattering will, in general, be different, primed quantities are used for the second interaction. From the partially polarized beam we will obtain the following fluxes:

$$N_+\propto\sigma_0(\theta)\{1+P(\theta)\}\sigma_0'(\theta')\{1+P'(\theta')\},$$
$$N_-\propto\sigma_0(\theta)\{1-P(\theta)\}\sigma_0'(\theta')\{1-P'(\theta')\}. \quad (3)$$

Adding, the total flux is

$$N'\propto\sigma_0(\theta)\sigma_0'(\theta')\{2+2P(\theta)P'(\theta')\}, \quad (4)$$

and in general it may be shown that

$$N'(\phi)=N_0'(1+PP'\cos\phi)=N_0'(1+\epsilon\cos\phi). \quad (5)$$

Experimentally, this dependence of the flux on the angle ϕ is conveniently measured by the asymmetry,

$$2\epsilon(\theta,\theta')=\frac{N'(0°)-N'(180°)}{\frac{1}{2}\{N'(0°)+N'(180°)\}}. \quad (6)$$

The polarization-asymmetry relations have been proved for the case of two-body collisions. For high-energy disintegrating collisions, we will assume that they hold also in a statistical sense.

III. CONSIDERATIONS IN APPARATUS DESIGN

In a double-scattering experiment, intensity is clearly a major problem. We were therefore led to consider the use of a first target in the circulating cyclotron beam. Sufficient intensity of the first scattered beam is obtainable by locating the second scattering apparatus immediately outside the cyclotron vacuum tank. Since the primary interest was in the double scattering from hydrogen, and a liquid hydrogen target was impractical, it was planned to use a polyethelene, $(CH_2)_n$, first target and to select the proton-proton scatters by the coincidence between the scattered and recoil protons. In order to detect the recoil protons, it is necessary to place a counter below the circulating beam and to use protons scattered at a small upward angle from the median plane. This has the advantage that the scattered protons leaving the cyclotron depart from the median plane and enter a region of lower background. Under these conditions, however, the radial component of the magnetic field may cause depolarizing transitions. Adiabatic conditions do not prevail as the proton leaves the field. A semiclassical calculation yields a transition probability of <2 percent, a negligible amount. Depolarization may also occur as the proton traverses the materials of the scattering equipment. The cross section for this process is given by Wolfenstein[8] as $6\times10^{-30}(Z^2+2Z)$ cm^2, producing negligible depolarization in the thickness of material likely to be involved.

Since the estimates of second scattered intensity were low, we were led to sacrifice angular resolution for intensity. Because of this and other practical considerations, a fixed polar angle experiment was planned. One consideration in choosing this angle was the expected variation of asymmetry with scattering angle. The only available calculations were those of Wolfenstein[8] based on a model which is known to predict incorrectly the nucleon-nucleon single scattering. These calculations predict an asymmetry of less than 1 percent with a maximum near 35° c.m. for 100-Mev protons. An examination of the terms in the asymmetry expression leads one, however, to expect the effects in general to persist over a fairly broad range of angles near 45° c.m. (For identical particles the polarization is zero at 90° c.m.)

Another consideration in the choice of scattering angle is the desirability of a small energy loss in the first scatter and, therefore, of a small scattering angle; to a first approximation the energy difference of protons incident on the first and second targets may then be neglected. It would also be preferable to have first and second scattering angles approximately equal for straightforward interpretation.

In the second scattering a polyethelene target with coincidence detection of the proton-proton scatters is again advantageous. The need for detection of both protons from a thick target, limits second scattering angles to those large enough to give a recoil of at least 30 Mev.

The above requirements are compromised with a first scattering angle of 19° lab. and a median second scattering angle of 27° lab.

In order to measure the scattered flux as a function of the azimuthal angle ϕ, it is necessary to provide means to vary ϕ without changing the geometry or detection efficiency. This may be done by mounting the whole second scattering apparatus in cylindrical geometry and then rotating it as a unit. Provision must then be made to align the mechanical axis with the first scattered beam.

A modification of the above general plan was found necessary because the defocusing effects of the fringing field of the cyclotron reduced the efficiency of detecting the first p-p scatter in coincidence. It was found, however, that of the scattered protons from polyethelene, enough were from the hydrogen to make feasible a

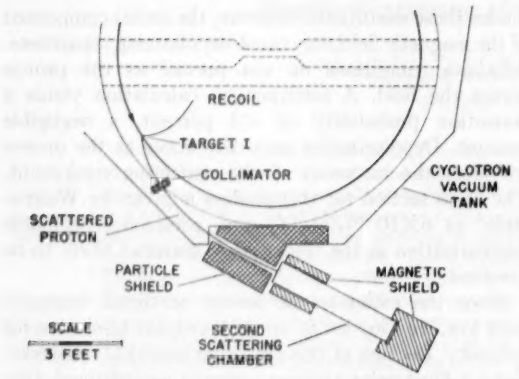

FIG. 1. Plan view of experimental arrangement.

difference determination by comparison with carbon target scattering. Consequently the counter for detection of the first p-p recoil was discarded except for determining the p-p scattered proton trajectory.

IV. APPARATUS

The general arrangement of the apparatus is shown in Fig. 1. The first target intercepts the 220–230 Mev circulating beam of the synchrocyclotron. Protons scattered at about 19° are collimated and selected roughly in energy at the edge of the pole tip, and leave the cyclotron vacuum chamber through a thin window. A broad channel in massive lead and copper shielding allows the protons to enter the second scattering apparatus, which is contained in a cylindrical shell. A magnetic shield reduces the cyclotron fringing field sufficiently to eliminate appreciable distortions of second scattering geometry.

The cylinder is a rigid mechanical structure, supported near each end in order that it may be rotated about its axis. The supports are adjustable so that the mechanical axis may be made to coincide with the beam.

Figure 2 shows the second scattering apparatus as mounted within the cylindrical shell. The useful beam is defined by an axial cylindrical stilbene counter, 0.75 cm in diameter. A target of polyethelene 0.5 cm in diameter, also on the axis, is interchangeable with one of carbon for background evaluation. The targets are suspended from a frame mounted on a carriage providing accurate motion of the targets perpendicular to the plane of the figure. Protons scattered in a range about 27° pass into a two-counter telescope. A copper absorber placed between the counters of the telescope rejects protons of less than about 100 Mev. The recoil proton from the p-p interaction is detected by a single conjugate counter. Because of the large target and need for high efficiency, neither the telescope nor recoil counter was made a defining counter. The effective target thickness–solid angle window is determined by both counter sets. As shown, copper blocks shield the telescope and recoil counters from protons scattered in the axial counter. The auxiliary exploratory counter of the same size as the axial counter was used in coincidence with it to ascertain the direction of the first scattered beam. The mechanical axis was then shifted to coincide with this direction.

In order to place the photomultiplier tubes in a region of low field, long light pipes mounted within the cylindrical shell were used. All photomultipliers were located within a large magnetic shield and in addition were individually shielded with mild steel and Mu metal.

Fourfold coincidences were formed among pulses from the axial counter, the two telescope counters, and the conjugate recoil counter. Figure 3 shows a block diagram of the electronic equipment. Pulses from each counter were amplified by a wide band chain amplier (SKL Model 202) and fed into a coincidence circuit of a modified Garwin[10] type with a resolving time of about 10^{-8} second.

Several types of beam monitor were used during the course of the experiment. One method was to count the

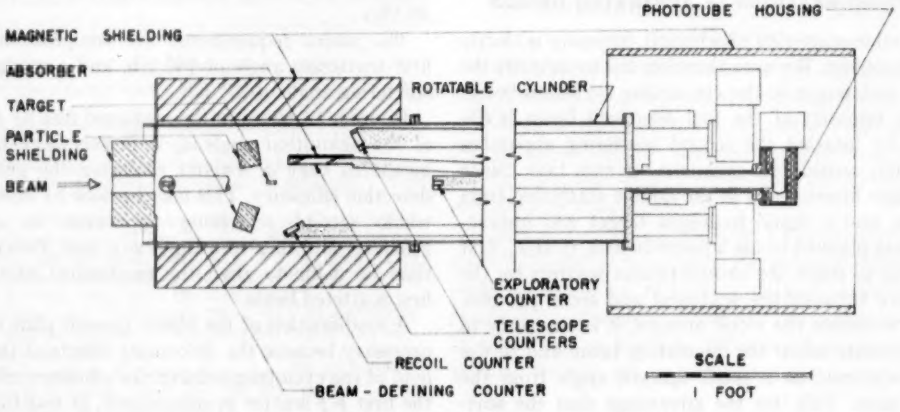

FIG. 2. Second scattering chamber in cross section.

[10] R. L. Garwin, Rev. Sci. Instr. 21, 569 (1950); Phys. Rev. 90, 274 (1953).

useful proton beam as measured by single counts in the axial crystal. Only a negligible fraction of the singles in this counter were from other than beam protons; however, the counting rates, of the order of 10^6 per second instantaneously, could not be counted with complete reliability by the scaling units available. Indirect methods measured either the fast neutron flux from the target or the general slow neutron flux from the cyclotron. In any case the monitor rate used was compared at low beams with the axial crystal counting rate and shown to be proportional to the scattered proton beam flux.

V. EXPERIMENTAL PROCEDURE AND AUXILIARY CHECKS

Alignment

In order to locate the second scattering apparatus, the trajectories of the p-p protons from a polyethelene first

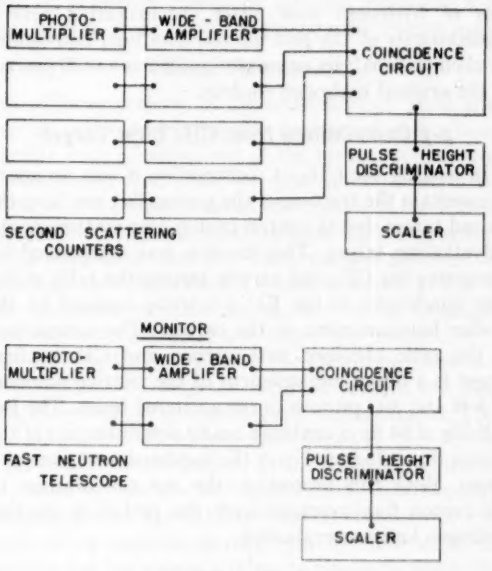

FIG. 3. Block diagram of electronic equipment.

target were traced by using the counter for detection of the p-p recoil near the cyclotron lower pole face in coincidence with a search crystal outside the cyclotron tank. The collimator at the edge of the pole tip was adjusted in position to maximize this beam. The range of the scattered protons was found to agree with that expected from the scattering angle.

Before placing the second scattering apparatus in position the critical components were optically aligned on the mechanical axis. The axial crystal, which fitted snugly in a hole in a Lucite light pipe, was removed to permit sighting along the axis. The polyethelene and carbon second targets were aligned in turn, and motion stops were set so the targets could be returned to axial

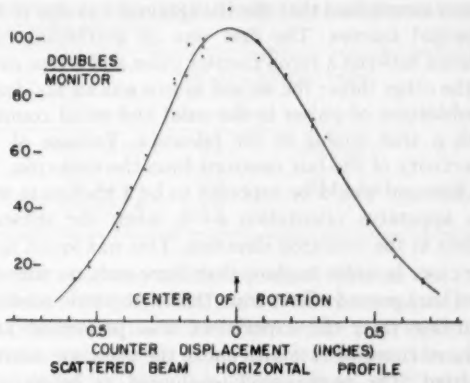

FIG. 4. Profile of scattered beam, as measured by coincidence rate *vs* exploratory counter horizontal translation. Counters were 0.3 inch in diameter and were separated by 20 inches. The profile indicates a beam with angular divergence of 1.8°, full width at half-maximum.

position with the remotely driven carriage. The light-pipe position is adjustable so that the axial counter could also be set on axis. The exploratory beam-aligning counter is movable by a selsyn-driven carriage along a line perpendicular to the cylinder axis. The index reading corresponding to axial position of this crystal is determined during the optical alignment. The alignments of these various elements were made to within 1/10 the radius of the element aligned.

The second scattering apparatus is positioned approximately from the trajectory previously traced. The beam direction relative to the mechanical axis is then found by observing the coincidence rate between axial and exploratory counters as the auxiliary counter is moved. This is done at two rotational positions of the second scattering apparatus, thus tracing across the beam a profile in perpendicular directions. The mechanical axis is then reset to coincide with the beam direction and this alignment is checked by repeating the procedure. The profiles indicate an approximately cylindrically symmetric beam with full width at half-maximum of 1.8° (see Fig. 4). This enabled the mechanical axis to be set within 0.2° of the beam direction.

Background Evaluation

The fourfold coincidence rate included, in addition to the p-p events, a background which was evaluated by replacing the polyethelene second target by an equal-length carbon target. The diameters of these targets were such that they contained the same amounts of carbon. The energy loss of the scattered protons was then approximately the same for the two targets.

The possible sources of background coincidences included actual coincidence scatters from carbon and various chance coincidence combinations which may or may not require the presence of the carbon target. By means of delaying the pulses from the several counters

it was ascertained that the background was due to two principal sources. The first was an accidental coincidence between a recoil counter pulse and a true event in the other three; the second source was an accidental combination of pulses in the axial and recoil counters with a true double in the telescope. Because of the directivity of the fast neutrons from the cyclotron, the background would be expected to be a maximum with the apparatus orientation $\phi=0$, when the telescope points in the cyclotron direction. This was found to be the case. In order to show that there were no unevaluated background effects from this asymmetric telescope counting rate, the experiment was performed at a reduced counting rate with one of the telescope counters omitted. The background, evaluated as before, was then about the same for all azimuthal positions of the scattering chamber, and the asymmetry in the p-p events was found to be the same as determined with both telescope counters in operation. Thus the background evaluated with the carbon second scatterer included all contributions except those due to the presence of the hydrogen in the target.

The contribution to accidental coincidences from singly detected p-p protons is negligible. Another type of background dependent on the presence of the hydrogen is a true p-p scatter involving a proton which does not pass through the front counter. Coincidence in time of such an event with a proton passing through the front crystal (and not making a p-p scatter) would be incorrectly recorded as a true event. The number of such events was evaluated by means of delaying the front pulse. These accidental quadruples were found to be small in number and nearly symmetric with ϕ. Thus the background, including any true coincidences from the carbon itself, was accurately measured by the use of the carbon second scatterer.

Counting Rates

A suitable compromise between adequate counting rates and low background with slow dependence on beam level was obtained with fourfold rates of about 40 counts per minute of which 5 to 15 percent were background. At these rates and with the asymmetries encountered, 10–15 minutes runs gave sufficient statistical accuracy to allow significant comparisons to be made among runs of the same and different rotational position. These run durations were short enough to permit interspersal and repetition of regular and background runs at the several ϕ positions, in order to compensate for any slow time dependent effects. In each of the two independent series of runs carried out, there were approximately ten runs at each rotational position. The variations of counts from run to run, for any given rotational position, were well accounted for by statistical variation.

Further Procedure

Since our primary interest was in the determination of the double p-p asymmetry, we made observations with polyethelene and carbon first targets to determine the effect by difference. (In both cases the effective second target was hydrogen.) Somewhat surprisingly, large asymmetries were found with the carbon first target as a polarizer. For either target, similar counting rates and background were found so that the procedures differed little.

After a series of runs with a carbon target, the first target was changed to polyethelene. No shift of beam direction at the second scattering apparatus was produced in such a target change. As one would expect, the ratio of true quadruple coincidences to neutron monitor counts changed with the first target material, while the ratio of coincidences to scattered beam monitor counts remained the same. In the cyclotron beams used, appreciable chemical decomposition of the polyethelene with loss of hydrogen took place, necessitating several replacements of the first target. The loss, determined by chemical analysis, amounted to as much as 20 percent of the original hydrogen content.

p-p Contribution from CH_2 First Target

In making the CH_2-C subtraction it was necessary to ascertain the fraction of the proton flux reaching the second target due to proton-proton first scatters in the polyethelene target. This fraction was determined by measuring for CH_2 and carbon targets the ratio of the true quadruples to the Be^7 γ activity induced by the proton bombardment of the carbon. The comparison of the ratio obtained with carbon and CH_2 as first target is a direct measurement of the relative numbers of p-H and p-C protons in the scattered beam. The Be^7 half-life of 54 days enables a ready determination of the proton flux integrated over the bombardment time of a target. With this procedure, the p-p contribution to the proton flux averaged over the period of gradual hydrogen loss was evaluated.

Single Rate Effects

The directional neutron beam led to high singles rates in the individual counters, of the order of 10^5/second instantaneously; these varied somewhat with rotation of the apparatus. This led not only to background effects which were evaluated, but also could have produced losses or gains in the recorded p-p counting rates as a result of pile-up or of blocking in the amplifiers or coincidence circuit. The circuits were chosen to avoid these contingencies. In addition, checks were made to determine any asymmetry due to the high singles rates. The first consisted of a measurement of the singles rates in each counter for each azimuthal position. No counter changed counting rate by more than 10 percent; the front counter showed no change, as would be expected from its axial position. The sum

TABLE I. Quadruple coincidences per monitor unit normalized to 100 for average over four ϕ angles, for two independent series of runs. Indicated uncertainties due to counting statistics.

	Carbon first, hydrogen second				CH_2 first, hydrogen second			
	I		II		I		II	
ϕ	True	Background	True	Background	True	Background	True	Background
0°	110.8±1.4	13.0	108.6±1.2	6.3	107.1±1.5	6.2	106.3±1.6	6.7
90°	101.0±1.7	9.0	99.4±2.0	5.8	102.2±2.6	5.1	...	
180°	90.1±1.2	7.3	91.4±1.1	5.8	91.6±1.4	4.8	93.7±1.5	5.0
270°	98.8±1.8	9.3	100.6±2.2	7.0	103.4±2.6	4.3	...	

of the singles rates in one azimuthal position differed from the sum in any other position by less than 1 percent, and thus no serious singles rates effect was expected.

Furthermore, measurements at half the usual beam differed in percent asymmetry by -2.2 ± 3.3 from the full-beam value of 18.3 determined in that series of runs.

Because of the high singles rates, care was taken to insure that the photomultiplier dynode voltages, supplied by a resistor condenser network, remained constant in spite of the charge drained during a beam pulse.

Beam Structure

Possible asymmetry in the scattered flux could arise from an unsymmetric angular divergence of the beam together with misalignment of the target, axial crystal or mechanical axis with the proton beam. A direct estimate of the misalignment effect may be made from the estimated uncertainties in alignment, the geometry of the apparatus, and the beam profiles observed as previously described. Such a profile is shown in Fig. 4. The calculated extreme asymmetry due to misalignment of the front crystal and target is 3 percent.

Due to the fringing field of the cyclotron, there is a correspondence between the energy of protons and their angle of arrival at the second scattering apparatus. This may combine with absorption effects in the second target to give an asymmetry in the observed scattered flux, since in the $\phi=180°$ position the lower-energy incident protons are concentrated on the side of the target which requires traversal through the target in order for the low-energy conjugate proton to reach the counter. For incident protons of about 150 Mev, there will be some loss due to stopping for some angles of scatter. This effect has been estimated on the assumption of a strict correspondence between energy and angle. In that case, with the relation between angle and energy established by floating wire measurements in the field and either the observed angular spread or the observed energy spectrum derived from range measurements, a 1.8-percent asymmetry was calculated. This is an over-estimate, since the finite first target dimensions introduce a spread in angle for a given energy.

Effect of Magnetic Field on Detection Efficiency

It is important to determine the effect of the magnetic field on photomultiplier sensitivy and thus detection efficiency as the apparatus is rotated. We first measured the multiplier sensitivities at the four positions $\phi=0°$, 90°, 180°, and 270° by noise spectrum observations. In the pulse-height region of interest, the extreme variations in pulse height with position were found to be less than 1.5 percent for all counters but one, which showed a variation of 2.5 percent. To convert these pulse-height observations to a measurement of detection efficiency variation, we examined, during each series of runs, the fourfold coincidence rate as the pulses from each counter were, in turn, attenuated 30 percent. Because of the thick second target, the large angular acceptance, and the dispositions of the counters, some deviation from a flat plateau was expected. Typical variations in counting rate with pulse height expressed in terms of the logarithmic derivative, $(dc/c)/(dh/h)$, were found to be, for the four counters, 0.34, 0.33, 0.46, and 0.15. Multiplying, in each case, by the corresponding extreme variations in sensitivity due to the magnetic field, the extreme variations in coincidence rate due to the individual counters were thus found to be 0.44 percent, 0.05 percent, 1.1 percent, and 0.03 percent. Combining the effects in the individual counters, the net variation in coincidence rate with position, due to magnetic field, was calculated to be $+0.7$ percent, $+0.4$ percent, and -1.2 percent for, respectively, 180°, 90°, and 270° referred to the zero degree position. This variation in detection efficiency was substantially independent of the first target material.

VI. PRESENTATION OF DATA

The data is presented in terms of the fourfold to monitor ratios in Table I. The background evaluated with a carbon second target has been subtracted but is indicated in the table. The quadruple to monitor ratio averaged over all four ϕ positions was set equal to 100 so that the percent asymmetries are directly indicated.

The scattered proton flux at each ϕ position is expected to vary as $1+\epsilon\cos\phi$. The fluxes at the 90° and 270° positions are seen to be close to the average value over all ϕ.

From the data of Table I, the asymmetry 2ϵ defined in Eq. (6) is computed and presented in Table II. For a polyethelene first target the fraction, f, of proton flux reaching the second target due to proton-proton first scatters in the polyethelene target was determined, in the manner previously described, and is presented for the two series of runs.

The asymmetry to be expected in an experiment using pure hydrogen as both first and second targets is determined from

$$(f-1)[2\epsilon(\mathrm{C,H})]+f[2\epsilon(\mathrm{H,H})]=2\epsilon(\mathrm{CH_2,H}), \quad (10)$$

where $2\epsilon(\mathrm{C,H})$ is the asymmetry measured in the carbon first, hydrogen second experiment, $2\epsilon(\mathrm{CH_2,H})$ is the asymmetry measured in the CH_2 first, hydrogen second experiment, and $2\epsilon(\mathrm{H,H})$ is the asymmetry to be expected in a pure hydrogen first, hydrogen second experiment. The derived values of $\epsilon(\mathrm{H,H})$ are also presented in Table II.

The first scattering was limited in θ to a range of 4 degrees centered about 20° and the collimator limited the energy of the proton flux impinging on the second target to the range 160–220 Mev. The protons of the 220–230 Mev internal cyclotron beam scattered from hydrogen and passing through the collimator are at $\theta=18.5°-19.5°$ and have energies of 195–205 Mev. In scattering from carbon, because of this energy selection, we have essentially required a nucleon-nucleon collision within the carbon nucleus. (The angle of scatter is sufficiently large that only a small fraction of the scattered protons are those diffracted from the carbon nucleus.[11,12]) Provided the protons incident on the second scattering apparatus exceeded 130 Mev the second p-p scattered protons penetrated the telescope and were detected in coincidence in the angular range 23°–31°. The width in angle ϕ accepted was 44°.

From Eq. (5), $\epsilon(\mathrm{H,H})=P_{\mathrm{H}}(\theta,E)P_{\mathrm{H}}'(\theta',E)$. Assuming a slow variation of P_{H} with θ and E, which decreased from 225 to 200 Mev, we can take $P_{\mathrm{H}}(\theta,E)=P_{\mathrm{H}}(\theta',E')$ and find, for an intermediate energy, the values of P_{H} given in Table III. Under the same assumption we find from $\epsilon(\mathrm{CH})=P_{\mathrm{C}}P_{\mathrm{H}}$ the values of P_{C} also given in Table III.

VII. DOUBLE SCATTERING FROM CARBON

The practical difficulties involved in directly measuring double p-p scattering made a subtraction technique necessary. However, because of the large polarization of protons scattered from carbon, another method is available, in principle, for determining the polarization in proton-proton scattering. If the asymmetry, 2ϵ, in a double scattering from carbon targets is measured, the polarization produced in a single scattering from carbon, P_{C} ($\sqrt{\epsilon}=P_{\mathrm{C}}$, neglecting energy degradation) is obtained directly. Since the product, $P_{\mathrm{C}}P_{\mathrm{H}}$, has been measured from the asymmetry determination in the carbon first, hydrogen second, scattering experiment, this separate determination of P_{C} thus gives a value for P_{H} without recourse to a subtraction experiment.

TABLE II. Comparison of asymmetries for two independent series of runs. Indicated uncertainties are due to counting statistics.

Targets First	Targets Second	Run series	Asymmetry 2ϵ percent	Hydrogen yield: f
Carbon	Hydrogen	I	20.6±2.2	···
		II	17.2±1.6	···
$(CH_2)_n$	Hydrogen	I	15.5±2.2	0.50±0.05
		II	12.6±2.2	0.55±0.05
Hydrogen (derived)	Hydrogen	I	10.4±5	···
		II	8.8±5	···
		Combined	9.6±3.5	···

TABLE III. Derived polarizations from carbon and hydrogen neglecting angle and energy differences in the two scatters. Indicated uncertainties are due to counting statistics.

Run series	I	II	Combined
P_{C}	(45±13)%	(41±11)%	(43±8)%
P_{H}	(23±6)%	(21±6)%	(22±4)%

The apparatus thus far described was changed in order to measure double scattering from carbon targets by omitting the pulse from the recoil counter and recording triple coincidences among the axial and telescope counters. The copper absorber between the telescope counters limited detection to high energy scattered protons. With a reduced beam it was possible to measure these triple coincidences at a rate of 15 per minute with a background of about 25 percent, as evaluated by removing the second target. As in the case of the fourfold arrangement, the rate of change of coincidences with pulse height attenuation in individual channels was slow. The procedure followed in collecting data was similar to that used previously.

Two successive runs using this "triples" coincidence scheme were in significant disagreement among themselves. The source of this defect has not been determined because of limited time available.

For the first set of runs the asymmetry, 2ϵ, was 49.5±8 percent. For the second set of runs the double scattering from carbon yielded $2\epsilon=25.5\pm4$ percent. The polarizations from the two determinations are $P_{\mathrm{C}}=49.8\pm4$ percent and $P_{\mathrm{C}}=36\pm3$ percent, respectively, neglecting energy and angle change. The difference method, which demonstrated reproducibility, gives a polarization of 43±8 percent. Combining these new values of P_{C} with the asymmetry observed in scattering from carbon and then hydrogen, we have ignoring angle and energy effects, $P_{\mathrm{H}}=18.5\pm2$ percent and $P_{\mathrm{H}}=26\pm3$ percent compared with $P_{\mathrm{H}}=22\pm4$ by difference. Neither of the two disagreeing values of P_{C} is inconsistent with that determined by differences, particularly when some allowance is made for the unknown angle and energy dependence of the polarization from carbon. The second measurement of the carbon-carbon asymmetry used a superior geometry for the background evaluation with no second target.

[11] Cladis, Hess, and Moyer, Phys. Rev. **87**, 425 (1950); J. B. Cladis, thesis, University of California, Berkeley, 1952, University of California Radiation Laboratory Report UCRL-1621 (unpublished).

[12] Richardson, Ball, Leith, and Moyer, Phys. Rev. **86**, 29 (1952).

VIII. ACCURACY AND CONSISTENCY OF MEASUREMENTS

The accuracy of the measured asymmetries is limited largely by counting statistics. The quoted uncertainties in asymmetries and polarizations in tables and text are statistical errors only. Several factors which may contribute systematic asymmetries have been examined and discussed in Sec. V. The principal effects are due to the following: (a) a combination of small second target and axial counter misalignments with departure of the beam structure from cylindrical symmetry, (b) changes in polar scattering angle with ϕ due to misalignment, (c) absorption in the target with correlation of energy and angle of arrival, (d) change in circuit loss or pile up with the change of singles counting rates upon rotation. These effects have been estimated to contribute a probable total systematic error of about 3 percent. In several cases direct checks were made, but with accuracy limited by counting statistics.

Several checks which are obvious and desirable have not proved practical. An attempt was made to use the first scattered beam from an internal target placed to give the mirror angle of first scattering, so that the asymmetry would be reversed. This required a traversal of the scattered beam through about 180° in the cyclotron field. The attempt was abandoned when it was found that the intensity was low and that this beam could not be safely assumed to have a small contribution from protons which had struck the cyclotron dee. A change in angle of scatter would have been desirable, but the limitations imposed by the need for a high-energy beam for the second scattering, and the need to bring the scattered beam out of the tank limited the angular range severely.

The proper variation of the second scattered flux with azimuthal angle, and the repeatability of the measurements provide internal checks on the experiment.

Furthermore, several preliminary experiments made at various background levels with different coincidence circuits, target holders, magnetic shielding, second scattering chamber positions and radiation shielding, although of less accuracy than the present experiment, gave results in general agreement with those reported here.

IX. DISCUSSION

During the course of the experiment, Goldfarb and Feldman[13] and Swanson,[14] have made polarization calculations based on specific models of the proton-proton interaction. At 240 Mev the approximate predictions for 2ϵ, considering the angular acceptance of the apparatus, are 0.5 percent[13] for the Jastrow hard core model, 13 percent[13] for the Christian-Noyes tensor model, 30 percent[13] for the Case-Pais $\mathbf{L}\cdot\mathbf{S}$ coupling model, and 3 percent for Swanson's[14] modified Christian-Noyes model. Characteristic of the Christian-Noyes and Case-Pais models which predict the large polarization effects, indicated by our results, is the use of singular noncentral forces. Comparison of these predictions with the experimental results must be made with caution. The models give fits with the observed single scattering which vary from fair to poor; relativistic effects, which have been omitted, may influence the polarization; and the cutoffs used with the singular potentials are to some degree arbitrary.

The calculations of Goldfarb and Feldman made by more exact methods than the Born approximations used by the originators of the several potential models give considerably modified predictions for single proton-proton scattering. Using the results of these calculations Noyes and Camnitz[15] have considered the Coulomb modification of the scattering at small angles. If we now compare the predictions based on the several models with the high-energy proton-proton scattering results now available,[1,7] we find that only the Jastrow model gives the proper flat p-p cross section extending to small scattering angles. The Christian-Noyes and Case-Pais models give results too large there, largely as a result of the singlet scattering from a square of Yukawa well. Single p-p scattering seems therefore to require modification of the singlet potential. The severe modification in the Jastrow model with its accompanying use of smaller, nonsingular, noncentral contributions is, however, inconsistent with our results.

Further information is available in principle from a measurement of the proton-proton polarization as a function of energy and especially as a function of angle of scatter. Such data, in addition to the magnitude of the effect, might yield further indication for a selection between tensor and $\mathbf{L}\cdot\mathbf{S}$ noncentral forces. The higher angular momentum terms in the polarization which are favored by an $\mathbf{L}\cdot\mathbf{S}$ interaction would shift the angle of maximum polarization from the angle predicted by tensor forces; this is indicated, for example, by the calculation of Goldfarb and Feldman. Such experiments would be more practical at somewhat higher energies than we have used, since thick target absorption effects would be less limiting.

The sign of the p-p polarization is undetermined in our experiment, except that it is the same as that in the scattering from carbon. The sign relative to that in the neutron-proton case should be available through experiments with deuterium.

X. POLARIZATION BY D, Be, Li, C, Al, Si, Cu, AND Ag

The observation of the polarization of high-energy protons in scattering from carbon has led us to make an exploratory investigation of the polarization in scattering from several elements. Possible mechanisms will be discussed at the end of the section. It is apparent, however, that the high polarization in scattering from

[13] L. J. B. Goldfarb and D. Feldman, Phys. Rev. **88**, 1099 (1952).

[14] Don R. Swanson, Phys. Rev. **89**, 749 (1953).

[15] H. P. Noyes and H. G. Camnitz, Phys. Rev. **88**, 1206 (1952).

TABLE IV. Polarization in scattering from several elements. Indicated uncertainties are due to counting statistics.

Element	D	Li	Be	B	C	Al	Si	Cu	Ag
Asymmetry with H analyzer[a]	20±3	22±2.5	21±2.5	20±3	18±1.5	9±3	10±2	19±3	12±5
Derived polarization in single scatter[b]	45±11	49±11	49±11	46±12	43±8	21±8	20±6	44±11	28±13

[a] Second scattering from hydrogen at 27°, first scattering from element at 20°.
[b] Based on hydrogen polarization 22±4 percent from Table III.

carbon may result from characteristics of nuclear forces in aggregates, and therefore data regarding the polarization may provide interesting information about nuclear forces if suitable theoretical analyses prove possible.

The present experiments have measured the polarization produced by nine elements in the range from deuterium to silver. We have made these measurements at a fixed polar angle of about 20° and with hydrogen as the analyzer (second scatterer).

Method

The method used to investigate the polarization of high energy protons in collisions with various elements was the same as that employed in the determination of the polarization of protons in collisions with CH_2 and carbon. The fractional polarization of a high energy proton beam scattered at about 20° from the particular element investigated was measured by the asymmetry in the flux of protons scattered from an effective hydrogen target placed in the polarized beam.

The nature of the proton-nucleus collisions which give rise to these high energy scattered protons is discussed later. The energy and angular range of first scatter are such that the process of scattering is the same for all elements; in particular, diffraction scattering contributes a small component to the proton beam, compared with quasi-nucleon-nucleon scattering.

The absorber in the high-energy telescope of the second scattering apparatus put a lower limit of 130 Mev on the energy of first scattered protons that could give rise to a detectable event in the second scattering apparatus. The polarization produced in the first scattering from the element bombarded is immediately derivable from the asymmetry measured in a double scattering, by use of the relation given in Eq. (5). In Sec. VI it is shown that hydrogen produces a polarization of 22±4 percent when protons of about 210 Mev are scattered at an angle of about 25°, roughly the energy and angle of the second scattering. Therefore, the polarization produced in scattering from a first target is approximately determined from the relation $2\epsilon = P_1 P_H$ where 2ϵ is the observed asymmetry in the double scattering, P_1 is the unknown polarization, and P_H is 22 percent. If P_1 differs from P_H in sign, the asymmetry will be negative, the flux being a maximum at $\phi = 180°$ rather than 0°.

Experimental Results

The procedure followed in measuring the asymmetry in the second scattered proton flux corresponded closely to that in the preceding experiments. The background was evaluated by replacing the $(CH_2)_n$ second scatterer by one of carbon, as before, and amounted to 10–14 percent of the true p-p counting rate. Only azimuthal angles of 0° and 180° were usually observed, the 90°–270° fluxes having been observed in the preceding experiment merely to demonstrate the correct behavior of flux variation with ϕ.

The data for each element are presented in terms of the directly measured asymmetry, 2ϵ, and the derived quantity, P_1, the polarization produced in a single collision. The carbon datum from the preceding experiment is included in the table of results (Table IV).

It should be remarked that these data all refer to an incident proton energy of about 230 Mev, a first scattering angle of 18–22° and a second angle of about 25°. In using the relation (5) it is assumed that P_H, the hydrogen polarization, does not vary rapidly over the energy range represented in the beam.

An alternative to using the hydrogen second target as an analyser is the use of a single element as both first and second scatterer. This method was, in fact, used in the case of carbon and aluminum, in addition to the determination of the polarization produced by these elements using the first method with hydrogen as analyzer. The results from such an experiment with carbon as first and second scatterer were presented in Sec. VII. The experiment with aluminum as both first and second scatterer was performed but once, yielding an asymmetry of 11±5 percent. This corresponds to a polarization in a single scatter of 24±4 percent which is to be compared with the value 21±8 percent obtained with the hydrogen analyzer method.

The polarization from deuterium was obtained in a subtraction experiment entirely analogous to the hydrogen polarization experiment. Asymmetries were measured, with hydrogen as analyzer, for carbon first target and $(CD_2)_n$, deutero-paraffin, first target. The subtraction then gave the polarization of the proton beam scattered from deuterium. The scattering processes contributing to the beam included quasi-p-p, quasi-p-n and elastic p-d scattering. It is not possible to determine in such a measurement the polarization produced in these processes separately. The quasi p-p polarization would be expected to be similar to the p-p, modified by

the presence of the lightly bound neutron. A measurement of this effect alone, is, in principle, possible by using a CD_2 second target; requiring detection, as in the *p-p* case, of both scattered protons; the pulse height and angular acceptance of the counters in the second scattering apparatus, however, made separation of the "*p-p*" and elastic "*p-d*" events impractical. The experiment was thus necessarily confined to a measurement of the sum of the effects using the subtraction method alone.

With the exception of deuterium, all elements were in natural isotopic abundance.

Discussion

The strong polarization of protons scattered from carbon (about three quarters of the protons are in one spin state) provides a polarized proton source for other experiments. Fluxes of 5×10^6 protons per cm^2 per minute were available at our second scattering chamber. With polarized target protons prepared by methods discussed by Ross[16] and Overhauser,[17] the triplet and singlet proton-proton scattering might be separated. Since the beam may be slowed in material without appreciable depolarization, nuclear reactions at lower energies might be studied if provisions were made to reduce the energy spread initially present. If the polarization persists to higher energies, studies of meson production from polarized protons may prove of interest.

The nuclear scatterings with which we are dealing here are chiefly internal proton-proton scatterings modified in heavier elements by multiple events. The proton-nucleon scattering in deuterium and carbon has been measured as a function of angle and energy by Cladis, Hess, and Moyer,[11] who found distributions consistent with that predicted by Wolff[18] on the basis of single proton-nucleon collisions within the nuclei for reasonable internal momentum distributions. The diffraction scattering studied by Richardson, Ball, Leith, and Hadley[12] has a strong forward peak falling off at larger angles, so that for carbon, for instance, at about 20°, the diffraction cross section is only a few percent of the observed[19] total cross section for high-energy protons from carbon. The multiple scattering within lead nuclei has been studied theoretically by Goldberger.[20] Although his assumed mean free path should be modified, the calculations indicate that the multiple scattering broadens the energy spectrum by relatively small amounts.

There are no theoretical calculations of which we are aware that treat polarization effects in high-energy scattering from complex nuclei. The sizable polarization effect observed may be of interest in the study of nuclear forces if suitable theoretical analyses become available.

The rise in polarization from 21 percent in hydrogen to about 50 percent in deuterium, and the persistence of the 50 percent level through the light elements to carbon, would be explained most simply by a very strong polarization effect due to the neutrons in the nuclei combining additively with the proton effect as for effectively free collisions. It is not clear that this is a proper interpretation even in the loosely bound deuteron. That is a special case since some of the protons are scattered elastically from the deuteron and in that case interference effects between proton scattering from the proton and neutron may be important. On the basis of published *p-d* scattering results,[11,21] it may be estimated that the ratio of quasi *p-p* to quasi *p-n* to elastic *p-d* contributions at our angle of scatter and incident energy are 1:1:2. The results of Wouters' preliminary experiment[22] on polarization effects in *p-n* scattering may be compared with the indications given by our results. Wouters found an asymmetry of 32 ± 12 percent in *n-p* scattering at 30° laboratory proton angle and within his accuracy no effect at 45°. These were from first scatterings in deuterium and second scatterings in hydrogen. These scatterings are at approximately the supplementary center-of-mass angle to the one in our experiments for the neutron part of the scattering from deuterium and other elements; in Wouters' case an exchange collision occurs, in our experiment a nonexchange. For a Serber mixture of exchange and ordinary forces these two angles would be equivalent in their polarizations,[23,14] but in view of the recent evidence[23] from *n-p* scattering for a different mixture the angles are not equivalent. Wouters also found no polarization effect in the exchange scattering from carbon and lithium. On the basis of a simple nucleon-nucleon collision interpretation it is difficult to see why the polarization effects were found in the proton scattering from nuclei, but not in the neutron scattering.

The downward trend of polarization toward heavier elements may be due to the depolarizing effects of multiple collisions.

The polarization in nuclei may involve factors other than those of a simple impulse nucleon-nucleon interpretation. Theoretical calculations in some detail will be necessary to decide this along with further experiments on the angular and energy dependence of the polarization. One possible enhancement effect in complex nuclei might occur as follows. The calculations of Goldfarb and Feldman indicate that for tensor forces the chief phases important for the polarization are the

[16] M. E. Rose, Phys. Rev. **75**, 213 (1949).
[17] A. W. Overhauser, Phys. Rev. **91**, 476 (1953).
[18] P. A. Wolff, Phys. Rev. **87**, 434 (1952).
[19] C. L. Oxley (unpublished).
[20] M. L. Goldberger, Phys. Rev. **74**, 1269 (1948).
[21] R. D. Schamberger, Phys. Rev. **85**, 424 (1952).
[22] L. F. Wouters, Phys. Rev. **84**, 1069 (1951), thesis, University of California, Berkeley, (1951), University of California Radiation Laboratory Report UCRL-1470 (unpublished).
[23] J. de Pangher, Berkeley report UCRL-2153 (unpublished).

P and coupled $^3F_2$. A mechanism to suppress the scattering associated with the nonpolarizing phases would increase the polarization. Since at this energy the impact parameters for angular momenta of 2–$3\hbar$ become as large as one half the internucleon spacing, the higher waves are more probably associated with momentum transfers to more than one nucleon and thus would not yield protons in the top energy range we selected. Modification of the $^3F_2$ phase by this process might also effect the polarization.

Recent reports by Dickson and Salter[24] and by Marshall, Marshall, and Nedzel[25] cover polarization experiments in which no large effects were found.

[24] J. M. Dickson and D. C. Salter, Proc. Phys. Soc. (London) **A66**, 721 (1953).

XI. ACKNOWLEDGMENTS

We gratefully acknowledge the cooperation and assistance of E. Baskir, D. Klein, J. W. Ring, and W. A. Skillman during the course of the experiment. J. O. Dungan engineered the mechanical construction of the apparatus. We are indebted to Professor S. W. Barnes and several other colleagues at the University of Rochester and elsewhere for helpful discussions and encouragement.

[25] Marshall, Marshall, and Nedzel, Phys. Rev. **92**, 834 (1953).

PHYSICAL REVIEW VOLUME 93, NUMBER 4 FEBRUARY 15, 1954

Angular Distribution of Protons from the Reaction $B^{10}(d,p)B^{11}$†

WILLIAM W. PRATT
Department of Physics, State University of Iowa, Iowa City, Iowa
(Received October 26, 1953)

The angular distributions of the four longest-range proton groups have been measured in the forward direction using a nuclear plate scattering chamber. The deuteron energy was 3.03 Mev. The observed angular distributions were not in agreement with stripping theory, indicating a relatively large contribution from compound nuclear formation.

THE angular distribution of the protons emitted in the $B^{10}(d,p)B^{11}$ reaction has been measured for the four longest-range proton groups. The deuteron energy was 3.03 Mev in the laboratory system of coordinates. Previous measurements on these groups have been made by Endt *et al.*[1] at 0.31 Mev and on the longest-range group by Redman[2] at a variety of energies from 1.06 Mev to 3.68 Mev. It was the purpose of the present work to obtain angular distributions of all four proton groups in the forward direction at a sufficiently high deuteron energy to effect a comparison between the experimental data and the theoretical distributions predicted by Butler[3] for a stripping reaction.

A deuteron beam was obtained from the S.U.I. electrostatic generator. After passing through a magnetic analyzer and a suitable collimating system, the deuterons impinged on a thin target of enriched B^{10} evaporated onto a silver backing of 13.55 mg/cm^2 surface density. Protons from the (d,p) reaction passed through the silver backing into an Eastman NTA nuclear track plate whose surface was inclined at an angle of 5° with respect to the scattering plane. Silver and aluminum foils were inserted between the target and the plate in order to eliminate elastically scattered deuterons and to reduce the proton range in the emulsion to a convenient value (20 to 200 microns) for range measurements. The plates were scanned with a Spencer monocular microscope with a 4-mm achromatic objective and a 10× eyepiece with a calibrated eyepiece scale. It was possible by this method to separate the four proton groups and to determine the number of protons as a function of angle with respect to the direction of the incident deuteron beam.

The resulting angular distributions are shown in Fig. 1 together with the appropriate theoretical curves of Butler's theory.[3] The relative yields at 20° in decreasing order of Q value are 1:0.2:1.2:0.6. The normalization of the theoretical curves is arbitrary. The absence of agreement between the experimental data and the theoretical curves makes it impossible to determine the value of l_n, the orbital angular momentum of the captured neutron. It is customary[3–5] to attribute a lack of agreement between Butler's curves and the experimental data at least in part to the role played by compound nucleus formation (and subsequent proton emission) which is not accounted for in Butler's theory. In this connection it is of interest to consider the proton angular distributions at angles greater than 90°, where the contribution of stripping is presumably small. Figure 2a shows the present data on

† This work was supported in part by the U. S. Atomic Energy Commission.
[1] P. M. Endt *et al.*, Physica **18**, 423 (1952).
[2] W. C. Redman, Phys. Rev. **79**, 6 (1950).
[3] S. T. Butler, Proc. Roy. Soc. (London) **A208**, 559 (1951).
[4] Philip Shapiro, Phys. Rev. **93**, 290 (1954).
[5] W. E. Nickell, Phys. Rev. (to be published).

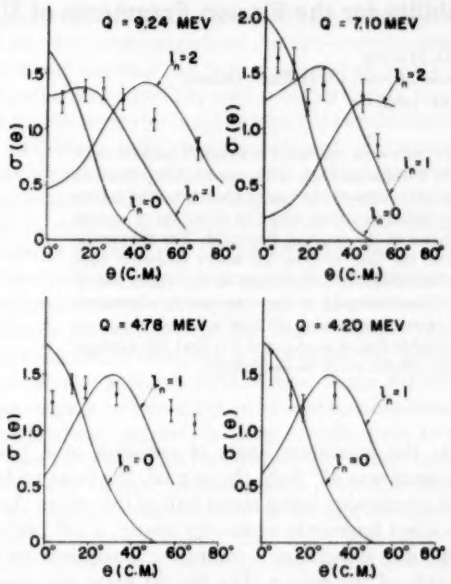

FIG. 1. The angular distribution of four proton groups. The differential cross sections $\sigma(\theta)$ are plotted on arbitrary scales as a function of the center-of-mass angle of scattering θ(C.M.). The errors indicated are statistical errors only.

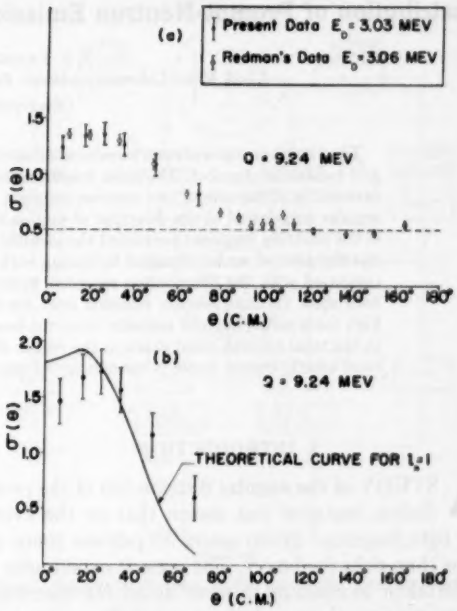

FIG. 2.(a) Comparison of the angular distribution of ground state protons as obtained in the present work with that obtained by Redman[2] at 3.06 Mev. The dotted line indicates the assumed contribution of compound nucleus formation. (b) Angular distribution of ground-state protons with the assumed contribution of compound nucleus formation subtracted. The errors indicated are statistical errors only.

the ground-state transition with that of Redman,[2] who obtained data out to 164°. If it is assumed that the dotted line represents a reasonable approximation to the contribution of compound nucleus formation, then an approximate correction for this effect may be obtained by subtracting this amount from each of the experimental points. This is done in Fig. 2b, and it is seen that the agreement between the experimental points and the theoretical curve for $l_n=1$ is considerably improved.

B^{10} is known[6] to have a spin of 3 and even parity; and the ground state of B^{11} is known[6] to have a spin of $\frac{3}{2}$ and probably (according to the shell model[7]) odd parity. Thus the ground-state proton group would be expected to have a mixture of l_n values of 1, 3, and 5, with the lowest l_n value predominant.[3] The agreement in Fig. 2b could undoubtedly be improved by assuming a mixture of $l_n=1$ and $l_n=3$ for the theoretical curve, although the significance of any such agreement would be open to question.

The proton groups corresponding to the three excited states of B^{11} could presumably be treated in a similar manner, although no data are available at present on the angular distributions at large angles. It does, however, appear from the lack of agreement between the experimental data and Butler's curves that compound nuclear formation is an important effect in these cases also.

The writer is indebted to Professor James A. Jacobs, Philip Malmberg, Philip Shapiro, and W. E. Nickell for much assistance with this work.

[6] F. Ajzenberg and T. Lauritsen, Revs. Modern Phys. **24**, 321 (1952).
[7] P. F. A. Klinkenberg, Revs. Modern Phys. **24**, 63 (1952).

Distribution of Prompt-Neutron Emission Probability for the Fission Fragments of U^{233}

J. S. Fraser and J. C. D. Milton
Chalk River Laboratory, Atomic Energy of Canada Limited, Chalk River, Ontario
(Received November 13, 1953)

The kinetic energies of both members of coincident fragment pairs were measured in a double back-to-back grid ionization chamber. The pulse heights were recorded only when coincident with a prompt fast neutron detected in either one of two neutron counters placed on opposite sides of the fission chamber. The strong angular correlation of the direction of motion of the prompt fission neutrons with the direction of motion of the emitting fragment permitted the identification of the latter as the emitting fragment. The frequency distributions of modes obtained by gating with a neutron from the light or from the heavy fragment were compared with the distribution recorded without a neutron coincidence. Comparison of the three sets of data show (1) that neutron emission from the light fragment predominates at low mass ratios, whereas at high mass ratios neutron emission from the heavy fragment is more probable; (2) that a broad maximum in the total neutron yield exists in the region of the most probable fission mode; and (3) that the average total kinetic energy curve is essentially the same for the three conditions of measurement.

I. INTRODUCTION

A STUDY of the angular distribution of the prompt fission neutrons[1] has shown that on the average the light-fragment group emits 30 percent more neutrons than does the heavy. The present experiment was undertaken to examine in more detail the distribution of prompt-neutron emission probability among the various fission modes.

A "fission mode," as used here, will be defined by the kinetic energies of the two fragments, so that a measurement of the distribution of these energy pairs in coincidence with a prompt neutron is required. The neutron-emitting fragment may be identified as a result of the strong correlation of the direction of motion of the neutron in the laboratory system with the direction of the fragment. If the coincident fragment pairs are collimated and the neutron detector placed on the axis of the collimator, the probability of detecting a neutron from a fragment receding from the neutron counter is completely negligible compared with that for a fragment approaching it.[1] To increase the counting rate, two neutron counters were used, one on each side of the fission chamber. The neutron-emitting fragment was identified as the one approaching the counter which detected the neutron.

II. EXPERIMENTAL ARRANGEMENT

The detectors and their associated electronic circuits are depicted schematically in Fig. 1. The fission chamber is a double back-to-back grid ionization chamber employing electron collection. The thin fissile source of 2 $\mu g/cm^2$ of U^{233} is contained in a collodion film approximately 20 $\mu g/cm^2$. It was prepared after the manner described by Brunton and Hanna.[2] The film was laid on a 0.015-in. thick aluminum plate which had been drilled with an array of equidistant 0.030-in. diameter holes. Over this was placed a similar plate with matching holes. Thus, the fragments were collimated on both sides; the maximum angle of emission of a pair of fragments was 45° from the normal, the most probable angle of emission being about half of this value. As two coincident fragments move very nearly, if not precisely, in opposite directions, a collimator is required on only one side of the source. The second plate was used to minimize the number of noncoincident fragments.

The single counting rate of fission fragment pulses, nearly equal in the two chambers, was approximately 3000 per minute. The rate of counting coincident pairs was about 1100 per minute.

The source was mounted in the grounded cathode common to the two chambers. The grid-cathode spacing was 3.0 cm and the collector was spaced 1.0 cm from the grid. The grid was wound on a brass frame with 0.008-in. diameter nickel wire spaced 0.10 in. center-to-center. According to the theory of Buneman, Cranshaw, and Harvey,[3] this provides a screening of the collector from positive-ion induction of 96 percent efficiency.

The chamber was filled by first admitting 1.5 cm Hg of CO_2 and then argon until the total pressure was 100 cm Hg. Pulse-height saturation of the fission pulses was achieved with 1400 volts on the grid and 2800 volts on the collector. The ratio of the field strengths in grid-collector and cathode-grid regions was thus 3:1, which is adequate to reduce collection of electrons by the grid to a negligible value. The rise time of the pulses was about 0.3 μsec. The purity of gas filling was checked daily on a 30-channel kicksorter by comparing the fission pulse spectrum with pulses from a mercury-switch pulse generator stabilized by OD2 and 5651 regulator tubes in cascade. If the fission pulses drifted by more than one percent, the chamber was refilled.

The neutron counters used were methane-filled cylindrical ionization chambers. They were identical to the type described previously.[1]

Each of the four counters was connected to a preamplifier and provided with a 1-$\mu\mu$f condenser for coupling the signal generator pulses to the input grid. Each of

[1] J. S. Fraser, Phys. Rev. 88, 536 (1952).
[2] D. C. Brunton and G. C. Hanna, Can. J. Research A28, 190 (1950).
[3] Buneman, Cranshaw, and Harvey, Can. J. Research A27, 191 (1949).

the preamplifiers fed a linear amplifier and discriminator. The discriminator outputs of the two neutron counters were mixed together in a twin triode circuit with a common cathode resistor. The output of this circuit, together with the discriminator outputs from the two fission-chamber amplifiers were delay-line-shaped to rectangular pulses approximately 0.8 μsec wide and fed into a triple-coincidence circuit. In this manner a triple coincidence could be registered between a pair of fragments and a neutron in either one of the neutron counters.

The amplified output from each fission chamber was transformed into a flat-topped pulse 15 μsec wide with amplitude proportional to the fission pulse.[2] When a triple coincidence occurred, a gate pulse was generated which allowed a 5-μsec wide portion of the flat-topped pulses to pass to two-stage pulse-lengthening circuits.[4] These produced pulses 3 sec long to deflect the pens of two synchronized Esterline-Angus recording milliammeters. The triple coincidence gate pulse also allowed the appropriate neutron pulse to actuate an operation recorder pen on the edge of that chart associated with the neutron-emitting fragment. The record of an event thus consisted of the pen deflections proportional to the ionization energies of the pair of fragments and a side pen deflection indicating the neutron-emitting fragment.

The energy range was divided arbitrarily into 50 channels by the chart scale. The channel width was 2.75 Mev. The linearity and zero of the complete system from preamplifier to chart was checked daily with the pulse generator. The pulse-lengthening circuits had a tendency to show a slow drift of the base line; in order to facilitate the rejection of any run in which a drift of half a channel or more occurred, the equipment was monitored automatically at regular intervals. It was arranged to have about 15 signal-generator pulses of fixed amplitude recorded on both charts during one minute of each hour. As the coincidence counting rate achieved was about 0.8 per min, no serious loss of true events resulted from the superposition of the monitoring signals.

At intervals throughout the course of the experiment the pulse-height spectra of coincident fragment pairs were recorded without reference to neutron emission. This was done by operating the gate pulse generator by the output of an auxiliary double-coincidence circuit whose resolving time was about 1 μsec. In order to get a large number of evenly spaced pulses on the charts, the fluctuation in the time intervals between pulses was reduced by scaling down the coincidence output by 100 before operating the gate generator. The scaler introduced a delay of 6 μsec between the amplified output and the gate; the peak voltmeter pulses were sufficiently flat, however, that no detectable difference was observed with the gate delayed by this amount.

The discriminator outputs of each of the neutron counters and one of the fission chambers were recorded on scalers.

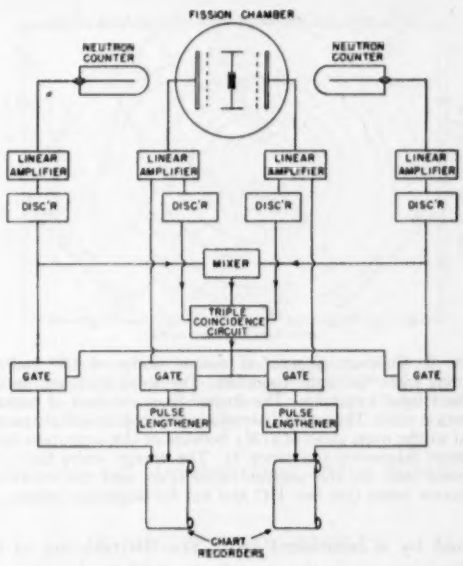

FIG. 1. Schematic diagram of the experimental equipment.

III. CORRECTIONS

Chance Events

The neutron coincidence data recorded on the charts are logically separated into two groups: (1) $N_L(E_L,E_H)$ with the neutron detected in the direction of motion of the light fragment, and (2) $N_H(E_L,E_H)$ with the neutron detected in the heavy-fragment direction. The results of all acceptable runs were thus separated and plotted as number of events on a grid with the light- and heavy-fragment channel numbers as coordinates. The third set of data is that taken without reference to neutron emission. This will be described as the normal distribution, $N_N(E_L,E_H)$.

The first two distributions of events must be corrected for the distribution of random events which comprised ~6 percent of the total. The principal source of the random background was chance coincidences between a neutron count and a true fragment-fragment coincidence. The number of chance counts per minute was computed by taking the product of the resolving time, the sum of the two neutron counting rates and the known fraction of fission-chamber single counting rate which gave fragment-fragment coincidences. The resolving time was obtained by observing the rate of random coincidences between signal-generator pulses fed into one neutron-counter circuit and one of the fission-chamber outputs fed into the other two of the triple-coincidence inputs. The number of chance events is divided equally between the two groups, as there is no preference for the chance neutron count to be associated with either the light or the heavy fragment pulse

[4] J. T. Dewan and K. W. Allen, Rev. Sci. Instr. 21, 823 (1950).

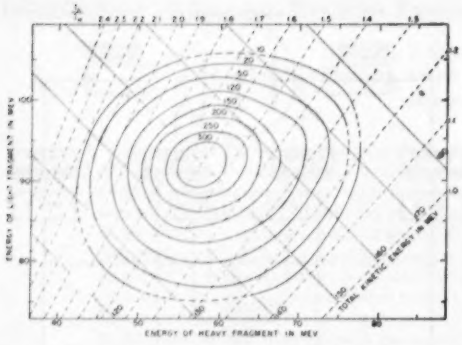

FIG. 2. Contour diagram of fission modes of U^{233} emitting neutrons from the light fragment. The solid lines are lines of constant total ionization. The dashed lines are lines of constant ionization ratio. The ionization ratio is only approximately proportional to the mass ratio M_H/M_L because of the ionization defect of fission fragments (reference 5). The energy scales have been corrected only for the neutron recoil effect and the source and collimator losses (see Sec. III) and not for ionization defect.

formed by a coincident pair. The distribution of the chance events on the coordinate grid is the same as $N_N(E_L,E_H)$. The number of random events, $B(E_L,E_H)$, at each point of the grid is thus computed from the relation $B(E_L,E_H)=\frac{1}{2}N_N(E_L,E_H)\times(B_{FF}/N_{FF})$ where B_{FF} is the total number of background counts, and N_{FF} is the total number in the normal distribution $N_N(E_L,E_H)$.

The random background in $N_N(E_L,E_H)$ is completely negligible. The number of chance fragment-fragment coincidences in the approximately 20 000 recorded events is only 4.

Neutron Recoil Correction

When a fragment emits a neutron, the change in the fragment energy is governed by the conservation of momentum. The assumption has been made that the neutron emission occurs after the fragments have separated. If the emission is assumed to be isotropic in the center-of-mass system and the recoil is averaged

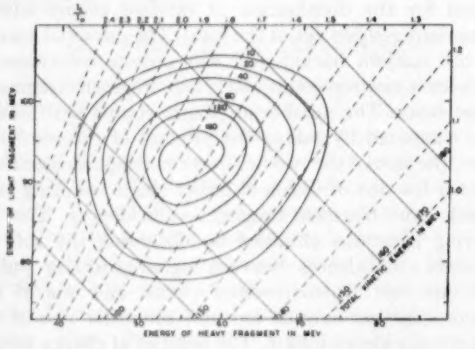

FIG. 3. Contour diagram of fission modes of U^{233} emitting neutrons from the heavy fragment. The energy scales have been corrected only for the neutron recoil effect and the source and collimator losses (see Sec. III) and not for ionization defect.

over all angles, the net reduction in kinetic energy of the fragment is equal to the kinetic energy of one neutron travelling with the velocity of the fragment. The average change in fragment energy ΔE_f is given approximately by $\langle\Delta E_f\rangle_{Av}=\frac{1}{2}M_nV_f^2$. This is the situation prevailing when the fragment energies are measured without reference to neutron emission, since the prompt-neutron emission occurs before the fragment has lost an appreciable amount of energy by ionization.[1]

In the present experiment where the fragment energies are measured in coincidence with a neutron, the range of angles of neutron emission is restricted by the geometry of the apparatus. In this case the average reduction of fragment energy is given by

$$\langle\Delta E_f\rangle_{Av}=\tfrac{1}{2}M_nV_f^2+V_f\langle p_n\cos\theta\rangle_{Av}, \quad (1)$$

where p_n is the momentum of the neutron and θ is the angle between the fragment's initial velocity and the neutron velocity, both p_n and θ being in the center-of-mass system. The average of $p_n\cos\theta$ is taken over the allowed range of angles θ. The details of the calculation and the assumptions involved are described in Appendix I. The results are given in Table I where the two terms of Eq. (1) are shown separately.

TABLE I. Values of $\frac{1}{2}M_nV_f^2$ and $V_f\langle p_n\cos\theta\rangle_{Av}$ in Mev.

	$\frac{1}{2}M_nV_f^2$	$V_f\langle p_n\cos\theta\rangle_{Av}$
Light fragment ($V_f=1.43\times10^9$ cm/sec)	2.12	0.87
Heavy fragment ($V_f=0.933\times10^9$ cm/sec)	0.90	0.80

The second term represents the difference in the energy of the fragment between the two conditions of measurement, *viz.*, with and without the detection of a coincident neutron.

The corrections were applied as follows: for the set of data in which the neutron was associated with the light fragment, 0.87 Mev was added to the measured values of the light-fragment energies; for the other set, 0.80 Mev was added to the heavy-fragment energies.

Ionization Defect Correction

The ionization defect of a fission fragment, which was measured by Leachman,[5] does not have a simple dependence on the energy of the fragment but is rather a function of the mass. No attempt was made to correct the contour diagrams of Figs. 2–6 for this effect. In Figs. 7–9, where the results are given in terms of mass ratios, an approximate correction has been applied to the ionization energy ratios to convert them to mass ratios. The ionization defect was assumed to have, for the sake of simplicity, the form $\Delta E=a+bM$, where a and b are constants and M the mass of the fragment. Using 5.7 and 6.7 Mev for defects of the most probable light and heavy fragments, respectively, gives $a=4.0$ Mev and $b=0.019$ Mev. Average values of 6.0 and 6.8

[5] R. B. Leachman, Phys. Rev. **87**, 444 (1952).

Mev, respectively, were used to correct the energy scales; the error introduced by assuming a constant value of the defect for each fragment group was ≤ 0.4 Mev over the whole range of modes.

Detection Efficiency Correction

Given an equal number of neutrons per fragment, the probability of detecting one from the light fragment is greater than detecting one from the heavy. The larger average velocity of the light fragment throws more neutrons into the cone of detection and at the same time raises the average neutron energy in the laboratory system. Both effects result in a greater detection efficiency for the light fragment. When making a quantitative comparison between the number of events in the two groups this was taken into account. It has not been corrected for in plotting the contours of Figs. 2 and 3.

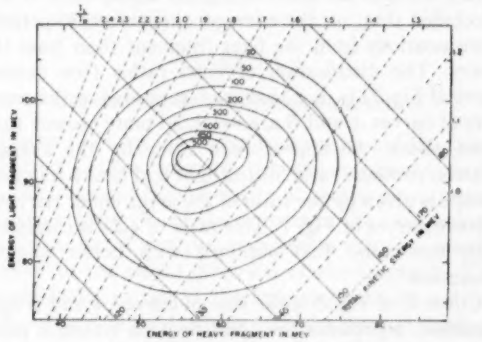

FIG. 4. Contour diagram of fission modes of U^{233} as measured without reference to neutron emission. The energy scales have been corrected only for the source and collimator losses (see Sec. III).

An approximate calculation,[1] which uses the average fragment velocities as measured by Leachman,[6] a reasonable neutron spectrum in the c.m. system, the measured counter efficiency curve, and isotropic neutron emission, yields a ratio $E_L/E_H=1.43$ for the two efficiencies.

Sources and Collimator Losses

The loss of energy in the source is almost entirely due to absorption in the 20-$\mu g/cm^2$ collodion film. Considering that the average fragment traverses slightly more than one-half of this thickness and assuming the rate of energy loss[6,7] as 0.058 Mev/($\mu g/cm^2$) of collodion, one estimates an average energy loss of 0.6 Mev.

The collimator loss arises from the recombination of ions in the low field region inside the collimator holes. An average loss of 1.1 Mev was adopted on the basis of an approximate calculation of the field distribution

[6] N. O. Lassen, Kgl. Danske Videnskab. Selskab, Mat.-fys. Medd. **25**, 11 (1949).

[7] C. Wiegand and E. Segrè, U. S. Atomic Energy Commission Report MDDC-134 (unpublished).

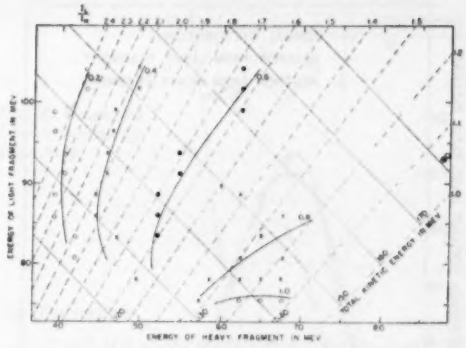

FIG. 5. Contours of constant relative probability per mode of neutron emission from the light fragment of U^{233}. The numbers adjacent to these contours are the ratios of the heights of the contours in Fig. 2 to those in Fig. 4.

in the holes and of measurement of the pulse-height saturation curve.

IV. DISCUSSION OF RESULTS

The net numbers of neutron coincidence events recorded were 12 886 in group 1 (neutrons from light fragment), 7288 in group 2 (neutron from heavy fragment), and 19 481 in group 3 (no neutron coincidence required). The relative numbers in the first two groups are consistent with the ratio expected from the angular distribution of prompt neutrons[1] in U^{233} fission.

Contour diagrams of the fission modes for the three groups are given in Figs. 2–4. The contours are lines of constant frequency of occurrence. The numbers adjacent to the contours are interpolated from the net number recorded in a unit cell of the grid. The group 3 data, Fig. 4, are a remeasurement of the results obtained by Brunton and Hanna[2] for U^{233}. Substantial agreement of the present results with the earlier work is obtained.

The first two diagrams show distinct differences from the third. The peak in Fig. 2 is shifted towards a lower

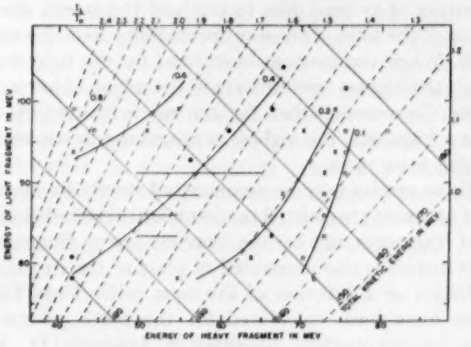

FIG. 6. Contours of constant relative probability per mode of neutron emission from the heavy fragment of U^{233}. The numbers adjacent to these contours are the ratios of the heights of the contours in Fig. 3 to those in Fig. 4. The horizontal bars on the contour labelled 0.4 indicate that the observed neutron emission probability is constant over the length of the bar.

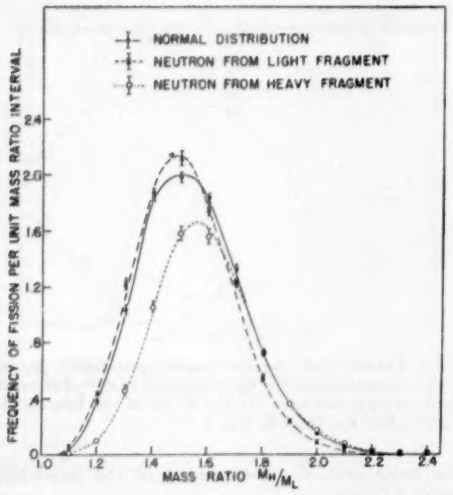
NORMAL DISTRIBUTION
NEUTRON FROM LIGHT FRAGMENT
NEUTRON FROM HEAVY FRAGMENT
FREQUENCY OF FISSION PER UNIT MASS RATIO INTERVAL
MASS RATIO M_H/M_L

FIG. 7. Frequency of fission per unit mass ratio interval for the three groups of data. All of the corrections discussed in Sec. III have been applied in constructing the mass ratio scales of Figs. 7, 8, and 9.

mass ratio, whereas the peak in Fig. 3 is displaced to a higher mass ratio. In Figs. 2 and 3 one has, for a given light- and heavy-fragment energy, i.e., a given mode, a plot of neutron coincidences per unit time. The distribution taken without reference to neutron emission, which may be called the normal distribution, gives the relative frequency of occurrence for that mode. If one divides the coincidence distribution of, say, Fig. 2, by the normal distribution, one gets a number of proportional to the average number of neutrons emitted by the light fragment of that mode, and similarly for the heavy fragment distribution. Then one may construct in each case contours of constant neutron emission probability per mode. Such contours are shown in Figs. 5 and 6.

The interesting features of these diagrams are a variation of at least five to one and the strong correlation of the lines of constant probability with the mass ratio. When the neutron is emitted by the light fragment, the highest contours are in the region of low mass ratios. Conversely, when the neutron is emitted by the heavy fragment, the highest contours are in the region of high mass ratio.

These results may be summarized briefly by stating that neutrons are emitted predominantly by the heaviest light fragments and by the heaviest heavy fragments. This feature is also illustrated in plots of the frequency of fission as a function of the mass ratio. These functions have been calculated for the three groups of data by the method described in Appendix II. The energy scales were first corrected for neutron recoil, ionization defect, and source and collimator losses as described in Sec. III. The results are shown in Fig. 7. The relative areas under the curves of the neutron-fragment coincidence data have been adjusted for the relative neutron detection efficiency. It is evident that there is a mutual displacement of the curves parallel to the mass ratio axis. The curve for the neutron from the light fragment is at a lower mass ratio than the normal, whereas that for the neutron from the heavy fragment is displaced towards higher mass ratios.

It is of interest now to compare the relative frequency of neutron emission which one gets by dividing the ordinates of the coincidence curves in Fig. 7 by the corresponding ordinates of the normal curve. Curves *A* and *B* in Fig. 8 were obtained in this way. Curve *A* gives the relative neutron emission frequency for the heavy fragment and curve *B* the same for the light fragment. This shows in an even more striking way that neutron emission from the light fragment predominates at low mass ratios, whereas at high mass ratios emission from the heavy fragment is greater.

In a study of the neutron angular distribution[1] it was concluded that, on the average, there were 30 percent more neutrons from the light fragment than from the heavy. The distribution of mass ratios (the normal curve of Fig. 7) is such that mass ratios below the crossover of curves *A* and *B* are weighted more heavily than those above. An approximate value for the average neutron emission ratio for the light and heavy fragment groups is given by the ratio of the areas under the coincidence curves of Fig. 7. This ratio of 1.24 is consistent with the value 1.30 obtained with better angular resolution.[1]

Curve *C* of Fig. 8 is the sum of curves *A* and *B* and, therefore, represents the total neutron emission probability. There is evidently a broad maximum in the ν_R value (number of neutrons per fission with mass ratio *R*) in the mass ratio range 1.5 to 1.8. The departure from a constant total neutron yield is not large compared

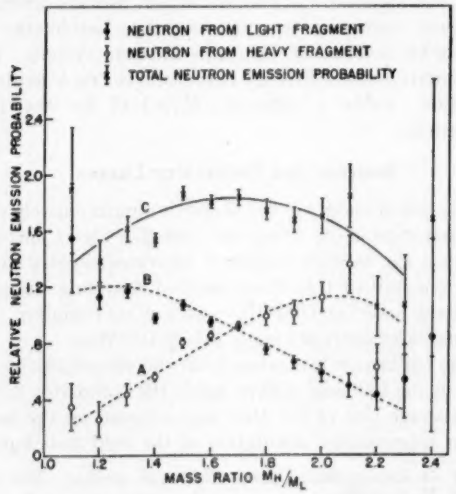

FIG. 8. Relative neutron emission probability as a function of mass ratio for the light and heavy fragments

with the variation exhibited for each fragment group. The predominant effect appears to be the change in neutron emission probability from one fragment group to the other as the mass ratio varies.

The average total kinetic energy for the three sets of data was calculated by the method described in Appendix II. No systematic difference in the three results is discernible in Fig. 9. All three show a significant maximum at a mass ratio of about 1.2. This is in agreement with the results obtained by Brunton and Hanna for the normal distribution.

ACKNOWLEDGMENTS

The authors wish to express their thanks to C. S. Scully and J. Kuehner for performing the rather laborious task of scanning the pulse analyzer records and to Miss A. R. Rutledge and Miss B. J. Sears for carrying out numerical computations. Discussions with Mr. G. C. Hanna, Dr. T. D. Newton and Dr. L. G. Elliott are gratefully acknowledged.

APPENDIX I

Calculation of the Recoil Correction

Figure 10 shows the vector relationships of the initial velocity V_i of the fragment, the final fragment velocity V_f, the fragment recoil velocity V_r in the c.m. system, and the velocity V_n of the neutron in the c.m. system. θ is the angle of neutron emission in the c.m. system relative to the initial direction of the fragment. The initial kinetic energy of the fragment may be written as $E_i=\frac{1}{2}(M+M_n)V_i^2$, where M is the mass of the final fragment and M_n is the neutron mass. The final energy

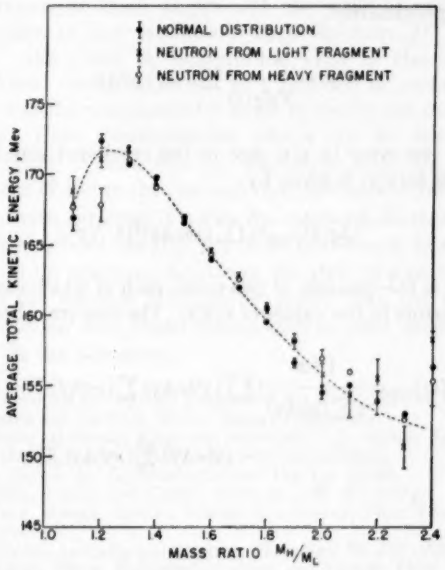

FIG. 9. Average total kinetic energy as a function of the mass ratio for the three groups of data.

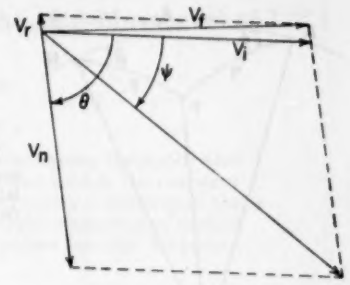

FIG. 10. Fragment and neutron velocity relationships.

of the fragment is

$$E_f=\tfrac{1}{2}MV_f^2=\tfrac{1}{2}M(V_i^2+V_r^2-2V_iV_r\cos\theta). \quad (2)$$

The decrease in fragment energy due to the emission of one neutron of velocity V_n at an angle θ is

$$\Delta E=E_i-E_f=\tfrac{1}{2}M_nV_i^2-\tfrac{1}{2}MV_r^2+MV_iV_r\cos\theta. \quad (3)$$

In the c.m. system, $MV_r=M_nV_n$, so that

$$\Delta E=\tfrac{1}{2}M_nV_i^2-\tfrac{1}{2}(M_n/M)M_nV_n^2+V_iM_nV_n\cos\theta. \quad (4)$$

The average values of V_n and V_i are of the same order, so that the second term may be neglected.

For a given value of V_i the average energy decrease is then

$$\langle\Delta E\rangle_{Av}=\tfrac{1}{2}M_nV_i^2+V_i\langle p_n\cos\theta\rangle_{Av}, \quad (5)$$

where p_n is the neutron momentum in the c.m. system.

When fragment energies are measured without reference to neutron emission, the second term is averaged over all values of θ, whence on the simplest assumption of an isotropic distribution, it becomes equal to zero. If, however, the energies are measured only in coincidence with a neutron detected inside a cone about the direction of motion of the fragment, $p_n\cos\theta$ is averaged only over the range of values of θ allowed by the geometry of the system.

In Fig. 11 the spherical triangle FAN is formed by the angle θ_c between the neutron's direction SN and the collimator axis SA, the angle η between the fragment's direction SF and the collimator axis, and the angle ψ between the neutron and fragment directions. The maximum value of η defined by the collimator was 45°. As the angular resolution of the neutron counter was considerably less than the angular spread introduced by the collimator, it is assumed in the following that its effect on the calculated value of $\langle p_n\cos\theta\rangle_{Av}$ is unimportant. In the measurements reported here $\theta_c=0$ but the formulas are given explicitly for $\theta_c\neq 0$.

The average value of $p_n\cos\theta$ may be written

$$\langle p_n\cos\theta\rangle_{Av}=\frac{\int_0^\infty dp\int_0^{\pi/4}d\psi\, pM(p,\psi)\cos[\theta(p,\psi)]\Theta(\psi)}{\int_0^\infty dp\int_0^{\pi/4}d\psi\, M(p,\psi)\Theta(\psi)}, \quad (6)$$

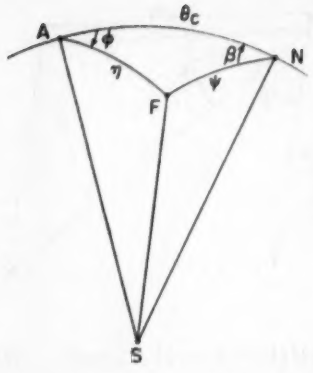

FIG. 11. Spherical triangle used in the calculation of the recoil correction.

where $M(p,\psi)$ is the number of neutrons of momentum p in the c.m. system which emerge at an angle ψ in the laboratory system, and $\Theta(\psi)$ is the distribution of fission fragments in the cone defined by the collimator.

The functions $M(p,\psi)$ were calculated[1] on the basis of isotropic emission, in the c.m. system, of neutrons with an energy spectrum consistent with the observed laboratory spectrum. The distribution of fragments emerging from the collimator is readily calculated in terms of hole dimensions and the angle η,[8] then expressed in terms of ψ. Let $\Omega(\eta)$ be the density of fragments at an angle η. The number in the element of area dA is then

$$\Omega(\eta)dA=\Omega(\eta)\sin\eta d\eta d\varphi=\Omega(\eta)\frac{\sin\eta}{\sin\theta_c\sin\beta}d\eta d\psi. \quad (7)$$

The number between ψ and $\psi+d\psi$ is

$$\Theta(\psi)d\psi=\left\{2\int_{\eta=\theta_c-\psi}^{\eta_{\max}}\Omega(\eta)\frac{\sin\eta}{\sin\theta_c}\times\left[1-\left(\frac{\cos\eta-\cos\psi\cos\theta_c}{\sin\psi\sin\theta_c}\right)^2\right]^{-\frac{1}{2}}d\eta\right\}d\psi. \quad (8)$$

The upper limit, $\eta_{\max}$, of integration is the maximum angle from the axis at which a fragment may emerge from the collimator.

APPENDIX II

Calculation of Frequency of Fission and the Average Total Kinetic Energy as Functions of the Mass Ratio[9]

The experimental data are obtained in the form of frequency of events on a grid whose coordinates are the channel numbers of the recorder chart scale. It is desired to calculate directly from the data the frequency of fission and the average total kinetic energy as functions of the mass ratio and to evaluate the statistical accuracy of the results.

The symbols used are the following:

$x=E_H$ = heavy-fragment channel number,

$y=E_L$ = light-fragment channel number,

$z=y/x=E_L/E_H=M_H/M_L$ = mass ratio,

$g(z)$ = frequency of fission,

$E(z)$ = average total kinetic energy,

N = total number of events,

$\nu(x,y)$ = number of events at (x,y), and

η = transformation variable.

For the frequency distribution one may write

$$g(z)=\frac{1}{N}\int\nu(x,y)\frac{\partial(x,y)}{\partial(\eta,z)}d\eta. \quad (9)$$

Putting $\eta=y$, one gets

$$g(z)=\frac{1}{Nz^2}\int\nu\left(\frac{\eta}{z},\eta\right)\eta d\eta\approx\frac{1}{Nz^2}\sum\nu(x,y)y\Delta y, \quad (10)$$

where the integral is approximated by the summation of the integrand, whose values in the intervals Δy are obtained from the experimental data.

In a similar manner the average total kinetic energy is approximately

$$E(z)\approx\frac{1+z}{Nz^3g(z)}\sum\nu(x,y)y^2\Delta y. \quad (11)$$

The rms error in $g(z)$ due to the combined standard errors $\delta\nu(x,y)$ is given by

$$\langle\Delta g(z)\rangle_{\text{rms}}=\{\sum(y\delta\nu\Delta y)^2\}^{\frac{1}{2}}/Nz^2. \quad (12)$$

$E(z)$ is the quotient of two sums, each of which carries the errors in the values of $\nu(x,y)$. The rms error here is

$$\langle\Delta E(z)\rangle_{\text{rms}}=\frac{1+z}{z\sum(\nu y\Delta y)}\{\sum[(y^2\delta\nu\Delta y)\sum(\nu y\Delta y)-(y\delta\nu\Delta y)\sum(\nu y^2\Delta y)]^2\}^{\frac{1}{2}}. \quad (13)$$

[8] J. Howlett and W. J. Whitehouse, British Atomic Energy Research Establishment Report N/R 473 (unpublished).

[9] The authors are indebted to Dr. T. D. Newton of this laboratory for suggesting this method of treating the data.

Interaction between D^2 and He^3 in the Neighborhood of the 18.6-Mev Level of Li^{5*}†

G. Freier and H. Holmgren
University of Minnesota, Minneapolis, Minnesota
(Received November 2, 1953)

The elastic-scattering differential cross sections and the cross section for the reaction $He^3(d,\alpha)H^1$ have been measured in the neighborhood of energies corresponding to the 18.6-Mev level in the compound nucleus Li^{5*}. The reaction data are essentially in agreement with earlier data having a maximum in the total cross section of approximately 0.94 barn. The interference between the elastic scattering and reaction process make the elastic-scattering cross sections at $\theta_{c.m.}=65.4°$ about 40 percent less than Rutherford scattering.

SEVERAL investigators have measured the cross sections for the reaction $He^3(d,p)He^4$ in the neighborhood of energies corresponding to the 18.6-Mev excited level in the compound nucleus Li^{5*}.[1–5] The more recent measurements of Lillie *et al.*,[3] and Yarnell *et al.*[5] give cross-section values which are in considerable disagreement near the resonance of the reaction. Both of these latter sets of reaction data have been taken with an electrically insulated gas cell connected to the target tube of an accelerator. This target of He^3 gas then served as a source of high-energy protons when bombarded with deuterons. The yield of these protons was then measured externally.

In the present experiment we used the small-volume scattering chamber described earlier[6] but modified it to support entrance, exit, and counter windows of 0.015-mil nickel[7] having a measured thickness of 65 kev for protons with 340 kev of energy. The procedure for taking data was quite similar to the procedure in reference 6 and will not be restated here. This apparatus allowed us to measure the yield of elastically scattered deuterons at small angles and the yield of reaction particles at any laboratory angle between 27° and 163°. We chose to measure the yield of elastically scattered deuterons at 40° as a function of energy as this was the most favorable angle to resolve the desired yields from contamination effects at all energies concerned. Pulses due to scattering from the 5.5 percent of He^4 in the gas could not be resolved and the data were corrected for this by assuming Rutherford scattering from the He^4. We chose to measure, in addition to the scattered deuterons, the yield of α particles from the reaction $He^3(d,p)He^4$ rather than the yield of protons, and these measurements were made at 163° in the laboratory.

The lower limit to the energy of the bombarding deuteron was determined by assuming that there was little charge exchange for deuterons passing through media while they had energies greater than the energy corresponding to the maximum of their dE/dx curve. Our experimental arrangement would then make measurements of the number of incident deuterons by charge collection reliable to ±3 percent at energies greater than 375 kev at the center of the target chamber. This assumption was partially checked by comparing measured values of scattering from argon with calculated Rutherford values. The errors determined here as a function of pressure of the scattering gas and energy of the incident deuterons were consistent with an assumption that they were due to small angle scattering in the gas. The large change in Z in going from argon to helium would give a negligible small-angle scattering error in the case of deuterons scattered from helium.

The calibrations of the electrostatic generator were made at the threshold of the $Li^7(p,n)Be^7$ [8] reaction and the 340.4-kev gamma-ray resonance of the reaction $F^{19}(p,\alpha\gamma)O^{16}$.[9,10] The energy loss in the nickel windows was determined by measuring the energy displacement

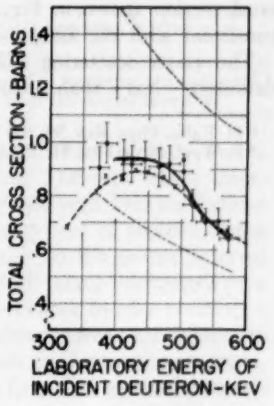

FIG. 1. Total center-of-mass cross sections for the reaction $He^3(d,\alpha)H^1$ as a function of energy. The ordinate values are 4π times the center-of-mass differential cross sections measured at 163° in the laboratory. The dashed line with crossed points shows the results of Yarnell *et al.* The lower and upper dashed lines are the calculated maxima values expected for the $l=0$, $S=\frac{1}{2}$ state and the $l=0$, $S=\frac{3}{2}$ state, respectively, of the D−He^3 wave function. The solid curve through the points is drawn from a best fit of the complex amplitude of the outgoing wave in the D−He^3 wave functions for the $l=0$, $S=\frac{3}{2}$ state.

† Supported by the joint program of the U. S. Office of Naval Research and the U. S. Atomic Energy Commission.

[1] Baker, Holloway, King, and Schreiber, U. S. Atomic Energy Commission Report AECD-2189, 1948 (unpublished).
[2] J. Hatton and G. Preston, Nature **164**, 143 (1949).
[3] Lillie, Bonner, and Conner, Phys. Rev. **88**, 473 (1952).
[4] Tuck, Arnold, Phillips, Sawyer, and Stovall, Phys. Rev. **88**, 159 (1952).
[5] Yarnell, Lovberg, and Stratton, Phys. Rev. **90**, 292 (1953).
[6] Brown, Freier, Holmgren, Stratton, and Yarnell, Phys. Rev. **88**, 253 (1952).
[7] Supplied by Chromium Corporation of America.
[8] Herb, Snowden, and Sala, Phys. Rev. **75**, 246 (1949).
[9] Chao, Tollestrup, Fowler, and Lauritsen, Phys. Rev. **79**, 108 (1950).
[10] A. H. Morrish, Phys. Rev. **76**, 1651 (1949).

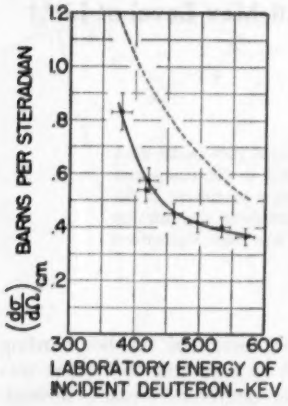

FIG. 2. Differential center-of-mass cross sections for the elastic scattering of deuterons from He^3 as a function of energy at θ cm = 65.4°. The dashed curve shows the Rutherford scattering. The solid curve through the points is drawn from a best fit for the complex coefficient of the outgoing wave in the $D-He^3$ wave function for the $l=0$, $S=\frac{3}{2}$ state.

of the above gamma-ray resonance with and without a window in the path of the incident beam. The relative losses for deuterons at other energies were calculated with the aid of Kahn's dE/dx values[11] for copper. The energy loss in the gas was determined from the atomic stopping cross sections published by Weyl.[12] The largest contribution to the errors in energy was that the entrance-window thickness changed from 65 kev to 90 kev during the course of the experiment. A linear correction with respect to time was made for this change.

When all sources of error are considered, the measured values of the cross sections shown in Fig. 1 and Fig. 2 have errors of about ±8 percent, and the knowledge of the energy for any given point is uncertain to ±15 kev. The reaction data agrees with that of Yarnell *et al.* within experimental error. No angular distribution of the reaction data was made in this experiment, but we have used the spherical-symmetry property measured by Yarnell and multiplied center-of-mass differential cross section by 4π before plotting the total cross section shown in Fig. 1. These results are still consistent with the assignment of a $D_{\frac{3}{2}}$ state in Li^{5*}.

The elastic-scattering differential cross section is definitely less than Rutherford scattering for θ cm = 65.4°. The two sets of data can be fitted with a complex coefficient for the outgoing wave in the $l=0$, $S=\frac{3}{2}$ state of the D^2-He^3 wave function. To analyze these data we followed the methods given by Blatt and Weisskopf.[13] The D^2-He^3 wave function, ψ, was found in terms of a superposition of the two spin states, $S=\frac{1}{2}$ and $S=\frac{3}{2}$, and then resolved into incoming and outgoing waves. To adjust for both reactions and scattering, a complex coefficient was given to the outgoing waves. With the assumption that nuclear interactions are short range, we concluded that only $l=0$ waves would contribute to nuclear effects at the energies used in this experiment. We also assumed that energy levels in the compound nucleus were sufficiently well isolated that only one of the spin states would contribute to the reaction. Then by properly normalizing the probability current associated with ψ and integrating this flux over the surface of a large sphere surrounding the region of the interaction, one can obtain an expression for the total cross section of the reaction. The maximum values of this total cross section for each of the spin states are shown in Fig. 1. If only one spin state is allowed, it then must be an $S=\frac{3}{2}$ state since the experimental values fall between these two maxima. The magnitude of the complex coefficient can be adjusted as a function of energy to obtain a best fit for the total reaction cross section. By subtracting the incident wave, ψ_{inc}, from the above ψ, one then has an expression for the scattered wave, ψ_{scatt}, which contains a phase shift which can be adjusted as a function of energy to fit the elastic-scattering data. The results of this best fit to the experimental data are shown by the solid curves in Fig. 1 and Fig. 2. Since the elastic-scattering data was obtained only at one scattering angle, the fits could not be subjected to further tests. However, the existence of these adjusted curves shows that the data is consistent with an assumption that the reaction results from an $l=0$, $S=\frac{3}{2}$ state.

We wish to extend our sincere thanks to the other members of the electrostatic generator group for help in obtaining these data.

[11] D. Kahn, Phys. Rev. **90**, 503 (1953).
[12] P. Weyl, Phys. Rev. **91**, 289 (1953).
[13] J. M. Blatt and V. F. Weisskopf, *Theoretical Nuclear Physics* (John Wiley and Sons, Inc., New York, 1952), pp. 317–340.

Photodisintegration of the Deuteron by 180-Mev and 260-Mev Gamma Rays*

J. KECK,† R. M. LITTAUER, G. K. O'NEILL,‡ A. M. PERRY,§ AND W. M. WOODWARD
Newman Laboratory of Nuclear Studies, Cornell University, Ithaca, New York

(Received November 2, 1953)

The photodisintegration of the deuteron is observed at gamma-ray energies of 180 Mev and 260 Mev. Both a low-temperature compressed-gas target and a D_2O-H_2O subtraction method are used. The photoprotons are detected in a crystal counter telescope. Their angular distribution shows a fairly marked forward asymmetry. The total cross sections at 165 and 230 Mev (c.m.) are 54 and 66 μb, respectively, with an estimated error of 10 percent on the absolute scale.

STUDIES of deuteron photodisintegration at energies above the meson threshold have been carried out by several groups[1–4] with results which have so far shown some inconsistencies. We have made repeat measurements of the process, using both a low temperature compressed-gas target and a D_2O-H_2O subtraction method. Results obtained by these two methods are in good agreement.

METHOD

Bremsstrahlung from the Cornell electron synchrotron was allowed to strike targets containing deuterium. In the case of the measurements at 260 Mev, the upper limit of the bremsstrahlung spectrum was 310 Mev; for the 180-Mev points, the limit was lowered to 225 Mev in order to reduce the background counting rates.

The bremsstrahlung flux was monitored with a thick copper ionization chamber placed behind the deuterium targets; this chamber has been calibrated in absolute value by comparison with a pair spectrometer and with shower curve measurements,[5] with an estimated error of 5 percent.

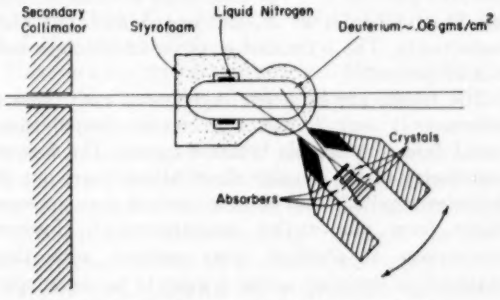

FIG. 1. Diagrammatic view of apparatus with compressed gas target.

Two different types of target were used. The first, a low-temperature compressed-gas target, consisted of a steel chamber 2 in. in diameter, 8 in. long, with 0.025-in. walls, cooled by liquid nitrogen and surrounded by styrofoam for thermal insulation. This target is shown in the diagram of Fig. 1. Deuterium gas was held in it at 1600 psi at a temperature between 77 and 82°K. The second target material was D_2O, with equivalent H_2O targets used to subtract out the photoproton counts due to the oxygen. Since hydrogen cannot give rise to photoprotons in the range of energies selected,

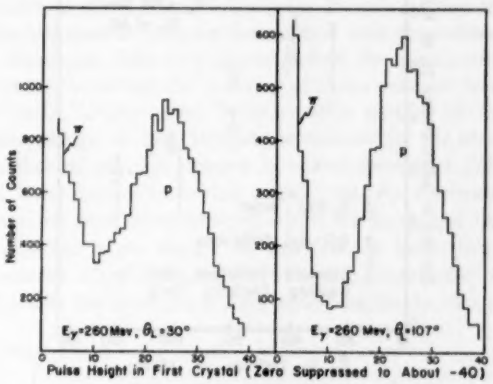

FIG. 2. Differential pulse-height spectra in first crystal for particles of defined residual range. The resolution shown for 107° is typical of that obtained at all other lab. angles except 30°.

the D_2O-H_2O counting rate is due entirely to the photoprotons from deuterium. Different target thicknesses were used in the forward and backward directions, so that the mean energy loss of protons in the target was always comparable to the energy interval accepted by the telescope. Both target thicknesses were used at 90° (c.m.) to obtain a check overlap point.

A three-crystal stilbene telescope was used to identify the photoprotons and define their energy and angle. A coincidence between the first two crystals, in anticoincidence with the third, was required. The resolving time was 0.4 μsec. Charged particles, to be accepted, have to come to rest somewhere between the second and third crystals. With the range interval thus defined, the pulse height in the first crystal serves to identify

* Supported by the joint program of the U. S. Office of Naval Research and the U. S. Atomic Energy Commission.
† Now at California Institute of Technology.
‡ U. S. Atomic Energy Commission Predoctoral Fellow.
§ Now at Oak Ridge National Laboratory, Oak Ridge, Tennessee.
[1] T. S. Benedict and W. M. Woodward, Phys. Rev. **85**, 924 (1952).
[2] R. Littauer and J. Keck, Phys. Rev. **86**, 1051 (1952).
[3] W. S. Gilbert and J. W. Rosengren, Phys. Rev. **88**, 901 (1952).
[4] S. Kikuchi, Phys. Rev. **85**, 1062 (1952).
[5] Details of the calibration of the Cornell bremsstrahlung beam are to be published shortly.

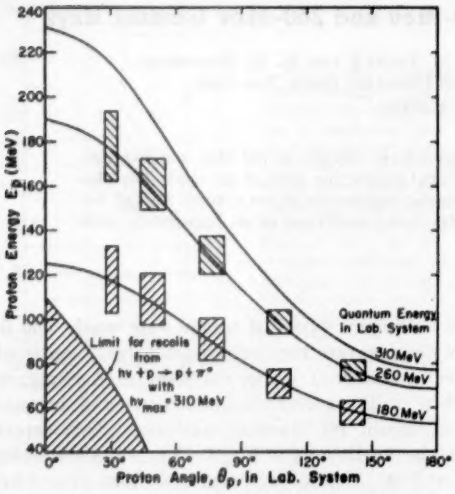
Proton Energy E_p (MeV)
Proton Angle, θ_p, In Lab. System
Quantum Energy In Lab. System
310 MeV
260 MeV
180 MeV
Limit for recoils from $h\nu + p \rightarrow p + \pi^0$ with $h\nu_{max}$ = 310 MeV

FIG. 3. Kinematics of deuteron photodisintegration, showing ranges of proton energy and angle selected.

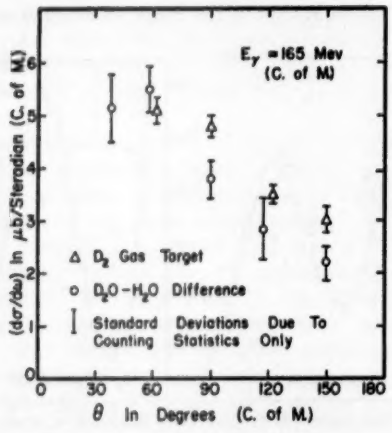
E_γ = 165 Mev (C. of M.)
$(d\sigma/d\omega)$ In μb/Sterodian (C. of M.)
θ In Degrees (C. of M.)
D_2 Gas Target
D_2O-H_2O Difference
Standard Deviations Due To Counting Statistics Only

FIG. 4. Differential cross section for photodisintegration at 165 Mev (c.m.).

their masses. Figure 2 shows differential pulse-height spectra obtained from the first crystal, using a 40-channel mechanical kicksorter. The poorest resolution obtained was at 30°. At all other angles the resolution was better, as typified by the spectrum obtained at 107°.

The energy and angle of the photoproton are sufficient to determine the complete kinematics. The proton energies accepted could be varied by placing suitable copper absorbers between the crystals. Figure 3 shows the range of values selected.

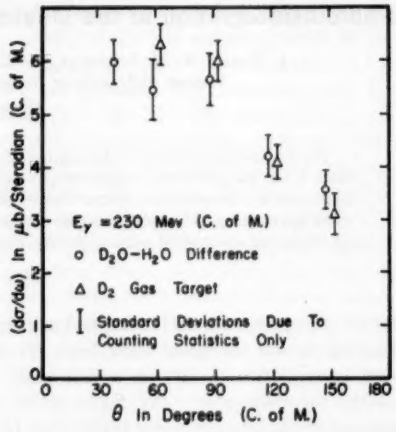
E_γ = 230 Mev (C. of M.)
$(d\sigma/d\omega)$ In μb/Sterodian (C. of M.)
θ In Degrees (C. of M.)
D_2O-H_2O Difference
D_2 Gas Target
Standard Deviations Due To Counting Statistics Only

FIG. 5. Differential cross section for photodisintegration at 230 Mev (c.m.).

In the case of the gas target, defining slits of uranium and tungsten served to exclude particles produced from the end caps of the chamber. An optical model was used to compute the effective target volume and solid angle of detection at each angle.

RESULTS

Figures 4 and 5 show the differential cross sections obtained by the two methods, with fair agreement within the statistical errors. Correction for the nuclear absorption of protons in the absorbers, target walls, and crystals has been made, assuming geometrical cross sections. This correction factor generally ranged from 1.03 to 1.10, but reached the value 1.25 for the 260-Mev point at 30°. The total cross sections obtained are 54 and 66 μb at E_γ(c.m.)=165 and 230 Mev, respectively. The estimated error on an absolute scale is ± 10 percent.

The results are in general agreement with those of references 1 and 2, and with recent (unpublished) work[6] from the Illinois betatron group. The forward asymmetry of the angular distributions bears out the Berkeley results,[3,4] and is more marked than appeared likely from our earlier measurements.[2] However, comparison of absolute cross sections with those obtained at Berkeley would appear to be meaningless at present in view of the uncertainty of the Berkeley beam calibrations.[7]

[6] A. O. Hanson (private communication).
[7] N. Jarmie, University of California Radiation Laboratory Report UCRL-2185, April, 1953 (unpublished).

Inelastic Scattering of Protons by Li^7†

F. Mozer, W. A. Fowler, and C. C. Lauritsen
Kellogg Radiation Laboratory, California Institute of Technology, Pasadena, California

(Received November 9, 1953)

The absolute differential cross section for the inelastic scattering of protons by Li^7 has been measured at ten scattering angles for incident proton energies near the 1030-kev resonance. The differential cross section is nearly isotropic at the resonance whereas at higher energies the scattering shows marked fore-and-aft asymmetry, being predominantly in the backwards direction. The total cross section for inelastic scattering is 41.6±3.0 millibarns at an incident proton energy, $E_1=1050$ kev; 35.4±2.8 millibarns at $E_1=1140$ kev; and 32.0±2.7 millibarns at $E_1=1240$ kev.

THE 18.14-Mev excited state in Be_4 was studied in this laboratory in 1939 by Fowler and Lauritsen[1] who showed its existence by virtue of the resonance occurring in the production of gamma radiation from the reaction $Li^7(p,p'\gamma)$ near an incident proton energy of 1050 kev. In 1949, its energy was more exactly determined to correspond to an incident proton energy of 1030±5 kev.[2] From an analysis of angular distribution data[3] for $Li^7(p,p)$, it was concluded that the excited state in the compound nucleus may have a spin of one, odd parity, and be formed by *s*-wave protons.[4] However, the presence of a broad resonance at a higher energy precluded a detailed agreement, and thus the question of the spin and parity of the 18.14-Mev state in Be^8 remained open.

In an attempt to settle this question, investigations of the excitation curves and angular distributions for the processes $Li^7(p,p)$[5] and $Li^7(p,\gamma)$[6] near an incident proton energy of 1030 kev have recently been completed. With this knowledge, it became desirable to investigate the inelastically scattered protons from $Li^7(p,p')$ near 1030 kev in an attempt to correlate these three sets of data and thus attempt to assign a spin and parity to the 18.14-Mev state in Be^8.

This work was undertaken with a 2-Mev electrostatic generator as the source of the incident protons. These protons were analyzed into a monoenergetic beam to within 0.05 percent by an 80° electrostatic analyzer of one-meter radius and one-millimeter entrance and exit slits.[7] The inelastically scattered protons passed through a variable-angle, double-focusing, magnetic analyzer[8] and were then counted by a scintillation counter.

Targets were prepared by evaporation of natural lithium on thin beryllium foils.[9] Originally it was planned to carry out the experiment using thin targets of lithium. However, it was later found that this method did not yield reliably reproducible results because of contamination layers of oxygen, carbon, and hydrogen on the target and because of deterioration of the thin lithium layer under bombardment. The most consistent results were obtained by use of a thick target of lithium evaporated on a thin beryllium foil and by isolation of the products of reaction which arose in a thin lamina at any desired depth in the target by means of the high resolution of the magnetic analyzer. By this method the absolute cross sections for the reaction were determined.

Aluminum foils were placed before the scintillation counter to prevent the counting of alpha particles from $Li^6(p,\alpha)$, $Li^7(p,\alpha)$, and $Be^9(p,\alpha)$ with protons of the same energy. A correction was introduced for the small number of protons stopped by these aluminum foils. At the forward scattering angles, protons elastically scattered from hydrogen impurities on the target had nearly the same energy as the protons inelastically scattered from lithium. Since it was impossible to eliminate the hydrogen surface layer completely, experi-

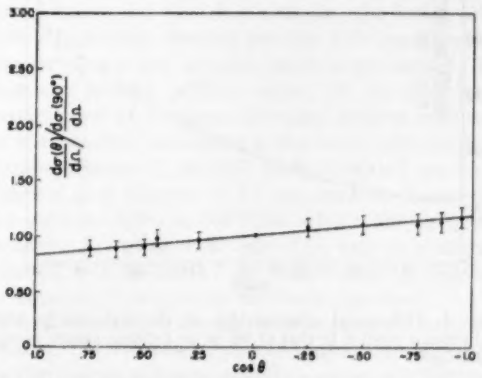

FIG. 1. Differential cross section of the inelastically scattered protons relative to that at 90° at an incident proton energy of 1050 kev.

† Assisted by the joint program of the U. S. Office of Naval Research and the U. S. Atomic Energy Commission.

[1] W. A. Fowler and C. C. Lauritsen, Phys. Rev. **56**, 841 (1939). See also Hudson, Herb, and Plain, Phys. Rev. *57*, 587 (1940); Herb, Kerst, McKibben, Phys. Rev. **51**, 691 (1937).

[2] W. A. Fowler and C. C. Lauritsen, Phys. Rev. **76**, 314 (1949).

[3] Fowler, Lauritsen, and Rubin, Phys. Rev. **75**, 1463 (1949).

[4] E. R. Cohen, Phys. Rev. **75**, 1463 (1949).

[5] Warters, Fowler, and Lauritsen, Phys. Rev. **91**, 917 (1953).

[6] A. A. Kraus, Jr. (to be published).

[7] Fowler, Lauritsen, and Lauritsen, Rev. Sci. Instr. **18**, 818 (1947).

[8] Snyder, Rubin, Fowler, and Lauritsen, Rev. Sci. Instr. **21**, 852 (1950).

[9] For a discussion of some difficulties encountered in making targets as well as the methods used in calibrating the magnetic and electrostatic analyzers, see reference 5.

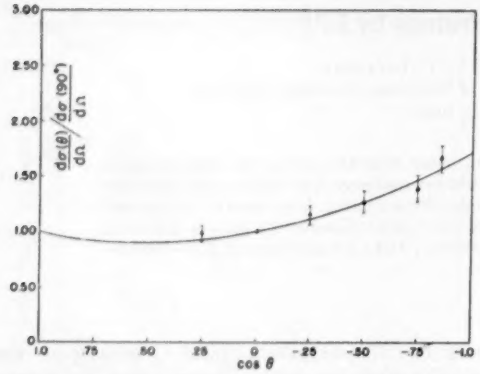

FIG. 2. Differential cross section of the inelastically scattered protons relative to that at 90° at an incident proton energy of 1140 kev.

mental data at the forward angles are somewhat uncertain.

The probable error in the absolute differential cross section due to statistical fluctuations averaged about 4 percent. Combining this with errors due to contamination layers on the target, uncertainties in the analyzer and spectrometer calibrations, angles of observation, and the absolute stopping cross section of protons in lithium, which enters into the reaction cross section formula, there arises a total probable error of about 7 percent. Thus the differential cross sections for $Li^7(p,p')$ at 90° were found to be 3.31 ± 0.24 millibarns per steradian at an incident proton energy E_1 of 1050 kev; 2.51 ± 0.18 millibarns per steradian at $E_1=1140$ kev; and 2.25 ± 0.16 millibarns per steradian at $E_1=1240$ kev.[10]

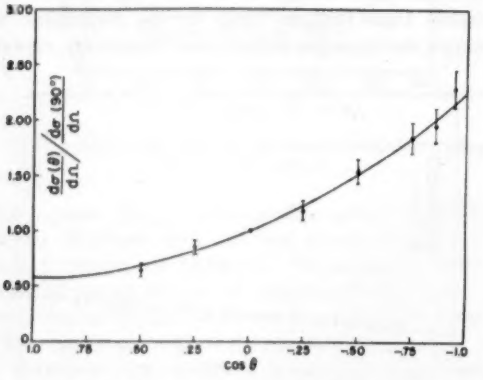

FIG. 3. Differential cross section of the inelastically scattered protons relative to that at 90° at an incident proton energy of 1240 kev.

[10] Differential cross sections were calculated from the inelastic proton yields using equations given in Brown, Snyder, Fowler, and Lauritsen, Phys. Rev. **82**, 159 (1951). The stopping cross section of protons in lithium was taken from reference 5.

The curves of reaction differential cross section relative to that at 90° are shown in Figs. 1, 2, and 3.

These experimental differential cross-section curves indicate the presence of interference effects near the 18.14-Mev resonance level in the compound nucleus, Be^8. This fact is shown by the presence of the $\cos\theta$ term and may possibly be attributed to an interference of the resonance level with a broad background level in the compound nucleus.

In Fig. 4, the coefficients in the equation

$$d\sigma(\theta,E_1)/d\Omega=a(E_1)+b(E_1)\cos\theta+c(E_1)\cos^2\theta$$

have been plotted against E_1, the incident proton energy. Near resonance, the coefficients $b(E_1)$ and $c(E_1)$

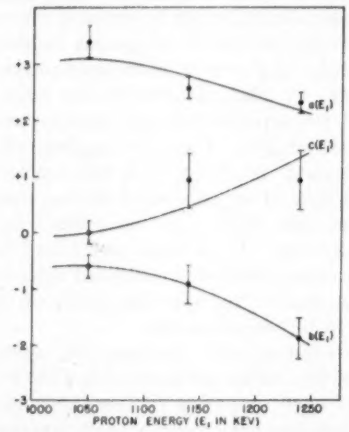

FIG. 4. Coefficients of

$$d\sigma(\theta,E_1)/d\Omega=a(E_1)+b(E_1)\cos\theta+c(E_1)\cos^2\theta,$$

plotted against the incident proton energy in kev. The curves are arbitrarily drawn so as to indicate symmetry about the resonance energy, 1030 kev.

become small, and the angular distribution becomes nearly isotropic. The fact that $b(E_1)$ is small at the resonance is consistent with the assumption of a nonresonant term of one parity interfering with the resonant term of opposite parity. The total cross sections for inelastic scattering $\sigma=4\pi[a(E_1)+\frac{1}{3}c(E_1)]$ are: 41.6 ± 3.0 millibarns at $E_1=1050$ kev; 35.4 ± 2.8 millibarns at $E_1=1140$ kev; and 32.0 ± 2.7 millibarns at $E_1=1240$ kev.

The observed angular distributions do not lead immediately to an assignment of spin and parity for the resonance at 18.14 Mev. The spherical symmetry at resonance and the deviations therefrom above resonance could be consistent with either an s- or a p-wave resonance.

Pulse-Height Measurements of Recoils from $B^{10}(n,\alpha)Li^7$

JAMES A. DE JUREN AND HYMAN ROSENWASSER*
National Bureau of Standards, Washington, D. C.

(Received November 4, 1953)

Thin films of boron deposited over a small area by vacuum evaporation have been exposed to the National Bureau of Standards thermal-neutron flux in pulse ionization chambers. Pulse ionization measurements in the past have yielded He^4-to-Li^{7*} pulse ratios considerably higher than the energy ratio of 1.753 from momentum conservation. Under suitable operating conditions we have obtained ratios as low as 1.778. Columnar recombination appears to cause most of this variation. The probability of the reaction $B^{10}(n,\alpha)Li^7$ going to the ground state was determined to be 6.52±0.05 percent.

I. INTRODUCTION

SEVERAL groups have conducted measurements of the average energy expended to produce an ion pair in argon as a function of energy and type of ionizing particle. The groups may be divided into two categories: one employing total ion collection and the other electron collection in pulse ion chambers or proportional counters. Jesse's[1] group, which has made extensive measurements of the total ionization in argon, found the ionization proportional to energy, independent of the particle type. On the other hand, various experimentalists employing electron collection have found a marked variation in the average energy expended per ion pair created. In general their results indicated that w increases as the ionizing density increases, either by the decreasing velocity of a given type of a particle or by the variation of specific ionization with z. For alpha particles in argon, Cranshaw and Harvey[2] have proposed the following formula:

$$w=27.5+1.9E^{-\frac{1}{2}},$$

where E is the initial alpha energy in Mev, and w is in electron volts.

The $B^{10}(n,\alpha)Li^{7*}$ reaction has permitted measurements of the ionization of particles at initial energies considerably less than alpha-particle energies from radioactive emitters, since the alpha particle and Li^{7*} ion have reaction energies of only 1.473 and 0.841 Mev, respectively. From conservation of momentum, the energy ratio $E_\alpha/E_{Li^{7*}}$ is precisely determined from the atomic masses and is 1.753. Using pulse-ionization techniques, the following ionization ratios have been reported. Stebler, Huber, and Bichsel:[3] 1.89±0.02; Hanna:[4] 1.841±0.025; and Rhodes, Franzen, and Stephens:[5] 1.878±0.014. These values exhibit a considerable departure from the ratio of particle energies, in conflict with Jesse's results. Our laboratory has investigated this reaction under a wide variety of experimental conditions with pulse-ionization chambers.

II. EXPERIMENTAL METHOD

The pulse-height distributions of recoils from thin films of boron exposed to a thermal neutron flux have been obtained in pulse-ionization chambers with argon-carbon dioxide mixtures.

A. Boron Films

Our laboratory has employed boron films (deposited by vacuum evaporation of natural boron from carbon crucibles) in pulse-ionization chambers for measurements in connection with the absolute calibration of the National Bureau of Standards standard neutron source. The films are deposited over an area 2.0×3.4 cm² on thin 15-mil quartz wafers which were initially coated with platinum to render them conductive.

The films are clamped to the inside of the cover plates of small pulse-ionization chambers.

B. Description of Chambers

Two similar pulse-ionization chambers were built, one of brass and one of aluminum, the latter being more suitable for absolute neutron flux measurements because of the low Al absorption cross section. The chambers have a pillbox design, $2\frac{3}{8}$ in. in internal diameter and $1\frac{1}{8}$ in. deep. Myvaseal gaskets were used for the vacuum seal between the cover plate and the chamber flange. A parallel plate mounted on teflon supports at a distance of 1.4 cm from the boron film was used for electron collection within the aluminum chamber. A carbon steel wire 1.14 mm in diameter, mounted with its axis 1.7 cm from the boron film, was the collecting electrode in the brass chamber.

After thorough cleaning with versene, water, and acetone, the chambers were connected to a copper vacuum system and evacuated to a pressure of 10^{-5} mm Hg. Normally the chambers were heated to a temperature of about 50°C for several hours with an infrared lamp until thoroughly degassed. To purify the gas the filling was made through an 850-cm length of copper tubing coiled in a trap containing butyl acetate and dry ice. A mixture of 5 percent carbon dioxide, 95 percent

* Now with Picatinny Arsenal, assigned to Brookhaven National Laboratory, Upton, New York.

[1] Jesse, Forstat, and Sadauskis, Phys. Rev. **77**, 782 (1950).

[2] T. E. Cranshaw and J. A. Harvey, Can. J. Research **26**, 243 (1948).

[3] Stebler, Huber, and Bichsel, Helv. Phys. Acta **22**, 362 (1949).

[4] G. C. Hanna, Phys. Rev. **80**, 530 (1950).

[5] Rhodes, Franzen, and Stephens, Phys. Rev. **87**, 141 (1952).

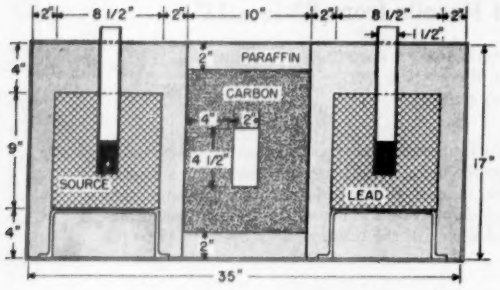

FIG. 1. NBS thermal neutron flux.

argon was used as the filling gas for most of the measurements.

C. Electronic Circuits

The chamber was connected by a cathode follower to a Bell-Jordan[6] preamplifier and amplifier system. When parallel plate collection was used, the first two amplifying tubes of the preamplifier were triode-connected to increase the signal-to-noise ratio. In terms of the particle energies measured, the amplifier rms noise for the collecting wire arrangement was 15 kev for the 20-μsec differentiating-time constant and 18 kev for the 2.0-μsec time constant. Amplifier noise was measured by feeding pulses through 1.35-$\mu\mu$f condenser to the collection electrode. A gain of roughly 200 000 was employed. Spurious counts were almost entirely eliminated by running the filament of the cathode follower attached to the chamber on dc. By heating the high coupling voltage and filter capacitors during the evacuation, counts from high-voltage breakdown were practically eliminated.

Pulses from the amplifier were fed into a three-channel discriminator built at the National Bureau of Standards. Periodic tests of the stability, linearity, and calibration of the system were made with a Model-100 pulser. Both amplifier and analyzer were connected to the line voltage through Sola constant-voltage harmonic transformers. Normally the analyzer was left on continuously, and drifts were small after the amplifier and chamber had warmed up for two hours or longer.

D. Description of Geometry

Exposures were made in the National Bureau of Standards standard slow-neutron flux (Fig. 1) which consists of a $2\frac{1}{8}$ in.$\times 4\frac{3}{8}$ in. slot in a moderating geometry between two equally-spaced one-curie Ra$-$Be(α,n) neutron sources which are imbedded in lead cylinders to reduce the gamma flux in the exposure region. Two inches of paraffin and four inches of carbon are between the cylinders and the slot. An aluminum holder, which slides into the slot, contains the pulse chamber and cathode follower. The holder exterior has been milled for the snug fit of a 0.020-in. Cd cover.

[6] W. H. Jordan and P. R. Bell, Rev. Sci. Instr. **18**, 703 (1947).

III. ANALYSIS OF DATA

Measurements were made with and without Cd, and the Cd difference counting rate was determined as a function of discriminator setting. This procedure almost entirely eliminates spurious counts from the data and the Cd difference counting rate is confined to the pulses resulting from the capture of slow neutrons (less than 0.3 ev) by boron. The Cd counting rate was about 2 percent of the difference counting rate. The pulse-height analyzer can be used as a two-channel differential analyzer or as a triple-integral discriminator unit. For the purpose of locating the leading edges of the He^4 and Li^{7*} pulses from thin films we found it more convenient to use the analyzer in the latter fashion. Assuming the energy of a particle emerging from a plane film is given

$$E=E_0\left(1-\frac{x}{R\cos\theta}\right),$$

where x is the distance from the origin of the particle to the top of the film, θ the angle of the particle direction with respect to the normal to the film, and R the range of the particle in the film material, the energy distribution of N_0 particles emitted per second in the upper hemisphere from a film of thickness L may be calculated to be

$$\frac{dN}{dE}=\frac{N_0R}{2E_0L} \quad \text{for} \quad E_0>E>E_0\left(1-\frac{L}{R}\right).$$

Half of the emerging particles are included in this interval. If discriminator readings are taken in this energy interval, the integral plot of counting rate *versus* discriminator setting permits a linear extrapolation to the leading edge of the pulses. Of course the amplifier noise (and emission of a gamma by the Li^* in flight) causes a deviation of the observed counting rate from the extrapolated value near the maximum energy E_0

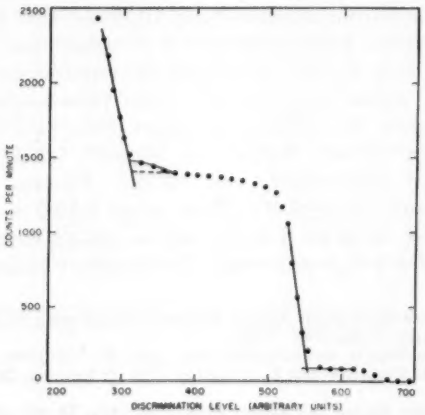

FIG. 2. Pulse-height distribution from B^{10} film, parallel plate collection, 1500 volts, 4 atmos. (99 percent A, 1 percent CO_2).

and points that fall within two rms amplifier noise values are excluded. Typical examples of the measurements for the two geometries are shown in Figs. 2 and 3. No attempt has been made to ascertain the leacing edges of the pulses from the reaction going directly to the ground state. The extrapolation of the Li* leading edge must be terminated at the top of the Li (ground-state) plateau. For relatively thick films this is somewhat difficult since the pulse spread due to noise tends to obscure the level where the extrapolation should be terminated; however, this level may be calculated from the counting rate on the alpha level since

$$\frac{dN}{dE}=\frac{N_0L}{2E_0R[1-(E/E_0)]^2} \quad \text{for} \quad E<E_0\left(1-\frac{L}{R}\right).$$

The path of the ionizing particle in the chamber gas, of course, alters the pulse height perceived at the collecting electrode since the pulse height is proportional to the mean-voltage drop of the ionization electrons divided by the total voltage drop between electrodes. For parallel plate collection the energy distribution of monoergic alphas from a film of infinitesimal thickness is

$$\frac{dN}{dE}=\frac{N_0D}{E_0R_m} \quad \text{for} \quad E>E_0\left(1-\frac{R_m}{D}\right),$$

where D is the plate separation and R_m the mean distance of the ionization electrons from the track origin measured along the track (electric center). Films employed were thin enough so that a linear extrapolation of the leading edges of the integral distribution to determine energy intercepts was valid for both geometries.

Usually a standard alpha emitter such as polonium (5.298-Mev alpha particle) is used to check chamber characteristics and the collecting voltage is varied until a plateau region is found in which the maximum pulse height appears constant. If particles whose average specific ionization is greater than the standard are being investigated, the most heavily ionizing particle should be used to check saturation. In the present case both the 1.473-Mev alpha particle and the 0.841-Mev Li* ion have been investigated for pulse saturation.

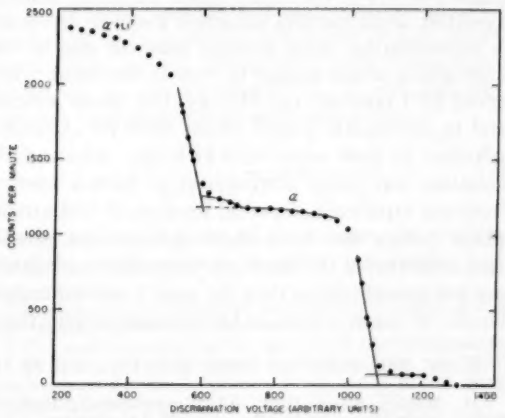

FIG. 3. Pulse-height distribution from B^{10} film, wire collection, 1200 volts, 1½ atmos. (95 percent A, 5 percent CO_2).

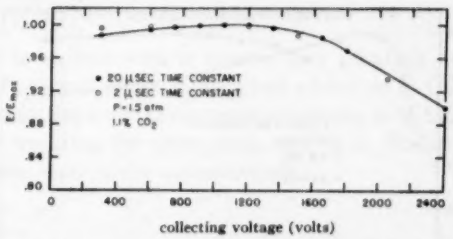

FIG. 4. Variation of pulse height of 1.473-Mev alpha ionization with collecting voltage, parallel plate chamber.

Carbon dioxide or methane (customarily 5 to 10 percent) is usually added to the argon in pulse ion chambers to reduce the random electron velocity by inelastic collisions to the region where electron scattering by argon atoms is minimal because of the Ramsauer effect and a higher drift velocity is thus obtained than with pure argon. When a mixture containing 1 percent of carbon dioxide was used at a pressure of 1½ atmospheres, the alpha-particle pulse heights showed a maximum at 1050 v for parallel plate collection (Fig. 4) and a maximum and 300 v for the collecting wire geometry (Fig. 5). At this partial pressure of carbon dioxide, the mean free path of electrons between collisions with carbon dioxide molecules was great enough so that the electron velocity attained when the field was more than about 800 v/cm was high enough to cause appreciable scattering by the argon atoms and the resulting increased collection time caused loss in pulse height after amplifier differentiation. The steep gradient around the wire causes the optimum voltage to be reached much sooner than with the parallel plate geometry where the field is constant. For a filling with 5 percent carbon dioxide at 1½ atmospheres, the optimum voltage for the collecting wire was discernible at 1200 v. Measurements were always made at voltages below the proportional region. At all other conditions tried (except the last listed), the pulse heights increased or remained constant with increasing high voltage. Some of the results are listed in Table I. The errors listed include an estimated calibration error of 0.5 percent.

IV. BRANCHING RATIO

If neutron capture by B^{10} gave monoergic alpha particles, the number of alphas escaping the film with energies greater than E would be given by

$$N_E=N_0\left[1-\frac{L}{2R(1-E/E_0)}\right] \quad \text{for} \quad E<E_0\left(1-\frac{L}{R}\right).$$

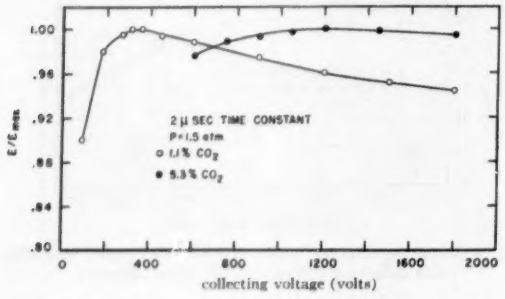

FIG. 5. Variation of pulse height of 1.473-Mev alpha ionization with collecting voltage, 1.14-mm diameter wire.

Since the alphas from the ground state have 20.7 percent more energy than those from the excited state, the range will be increased by 1.207, and to have the same thickness correction for both alpha groups it follows that

$$1-\frac{L}{2R(1-E^*/E_0^*)}=1-\frac{L}{2R(1-E/E_0)\times 1.207},$$

where the asterisks refer to the reaction going to the excited state. This expression reduces to

$$\frac{E^*}{E_0^*}=1.207\frac{E}{E_0}-0.207.$$

When the counting rates are measured on the two alpha plateaus at energy ratios determined by the above equation, the ratio of the counting rates will be independent of film thickness. For the conditions shown in Fig. 3 the ratio was determined at $E/E_0=0.875$ and $E^*/E_0^*=0.849$. (The ground-state alpha counting rate should be calculated at the point where the excited-state counting rate is determined to get the true difference. This refinement is unnecessary for thin films.)

Repeated measurement cycles were taken and the probability of the reaction going to the ground state, for thermal neutrons, was found to be 6.52 ± 0.05 percent (the error quoted is the statistical probable error). This result compares with 5.8 ± 0.1 percent obtained by Hanna,[4] 6.5 ± 0.7 percent by Bichsel *et al.*,[7] and 5.9 ± 0.9 percent by Rhodes *et al.*[5]

TABLE I. Pulse ionization ratios.

Chamber	Pressure (atmos)	Percentage of gas mixed with argon	Collecting voltage (volts)	$E_\alpha/E_{(\mathrm{Li})^*}$ *
Parallel plate	4	1.1 CO_2	1500	1.795±0.015
Parallel plate	4	1.1 CO_2	3000	1.794±0.015
Parallel plate	4	5.3 CO_2	1900	1.82 ±0.02
Parallel plate	1.5	5.3 CO_2	1500	1.779±0.015
Parallel plate	1.5	1.1 CO_2	1050	1.777±0.015
Collecting wire	3	10 CH_4	1500	1.87 ±0.02
Collecting wire	1.5	5.3 CO_2	1200	1.824±0.015
Collecting wire	1.5	1.1 CO_2	310	1.834±0.015
Collecting wire	1.1	10 CH_4	1200	1.84 ±0.02
Collecting wire	1.1	5.3 CO_2	1500	1.80 ±0.02

* The large errors shown in the last column were for natural boron films.

V. DISCUSSION

As the pressure of the 5 percent carbon dioxide, 95 percent argon mixture was decreased from 4 atmospheres, the ratio of the He^4 to Li^{7*} pulse heights decreased from a value above 1.8 to a value approaching the conservation figure of 1.753. Columnar recombination has been reported high in carbon dioxide[8] and the decrease in pulse height with increasing pressure has been noted earlier.[9] When the carbon dioxide proportion was decreased to 1 percent and the pressure to $1\frac{1}{2}$ atmospheres, the optimum voltages for the maximum pulse heights were much lower and in the collecting wire geometry so low that considerable recombination occurred, especially for the Li^{7*} ionization electrons. At $1\frac{1}{2}$ atmospheres pressure, parallel plate measurements with both the 1 percent and 5 percent carbon dioxide mixtures yielded a He^4:Li^{7*} pulse ratio of 1.778 (av), which is 1.4 percent higher than the ratio of particle energies. Assuming the 0.841-Mev Li^{7*} ion has the same value of w as an alpha particle of the same velocity, the Cranshaw-Harvey formula gives a value of 1.823 for the ionization ratio. Our measurements indicate a considerably smaller variation in w and it is quite possible that some recombination was still occuring at our most favorable conditions, but the small size of our chambers precluded measurements at lower pressures. Unfortunately the variation in pulse heights with changing voltage due to the variation in conditions for minimum argon scattering tends to mask the recombination effect.

In conclusion, the lack of proportionality between pulse heights and particle energy observed in argon-filled pulse-ionization chambers seems largely due to columnar recombination. Since the maximum recombination occurs in the region where ionization density is greatest, alpha-particle ionization would be decreased by recombination most severely near the end of the range and w would appear to vary in the manner observed by Cranshaw and Harvey. Our measurements tend to corroborate Jesse's results made with total ion collection in pure argon in which the alpha-particle ionization was found proportional to particle energy. From our experience, a partial pressure of 0.04 atmosphere carbon dioxide is about optimum for parallel plate collection of the electronic component and should give less recombination than the usual 5 percent carbon dioxide, 95 percent argon in high-pressure applications.

[7] Bichsel, Hälg, Huber, and Stebler, Helv. Phys. Acta **25**, 119 (1952).
[8] M. Moulin, thesis, Paris, 1910 (unpublished); Haeberli, Huber, and Baldinger, Helv. Phys. Acta **26**, 145 (1953).
[9] Bridge, Hazen, Rossi, and Williams, Phys. Rev. **74**, 1083 (1948).

For wire collection a greater partial pressure will be required.

It is possible to analyze the boron content of these films by quantitative chemical techniques and films of this type have been used to calibrate the National Bureau of Standards thermal-neutron flux to an error of less than 2 percent.

ACKNOWLEDGMENTS

The authors wish to express their gratitude to Dr. L. F. Curtiss for his interest and advice, to L. Costrell for assisting with the electronics problems, to A. Krinsky for preparing the boron films, and to D. Padgett for taking some of the measurements.

PHYSICAL REVIEW VOLUME 93, NUMBER 4 FEBRUARY 15, 1954

Influence of Chemical State on Stopping of Fast Charged Particles*†

TORBJÖRN WESTERMARK
Division of Physical Chemistry, Royal Institute of Technology, Stockholm, Sweden

(Received October 13, 1953)

The suggestion is made to use the characteristic electron dispersion frequencies or corresponding wavelengths (λ_0) from molar refraction data for the prediction of influences of the chemical state on the stopping power of fast charged particles. Changes in λ_0 for atoms in different chemical states are transformed into changes in mean excitation potentials in the Bethe-Bloch theory and to changes in stopping power. Mass absorption data for Bi^{210} beta rays by Fournier are corrected for the anomalous Z/A-factor for hydrogen and then show the predicted effects for different groups of hydrocarbons. The very accurate data by T. J. Thompson on fast protons are compared with those from the "λ_0 approach" for a number of cases. Qualitative agreement is present for most of them but quantitatively the situation is less satisfactory. Certain favorable cases of large anomalies, not yet investigated, are predicted.

THE influence of the chemical state on the stopping power of fast charged particles was suggested by Bothe[1] to be caused by changes in the dispersion frequencies present in the Bohr stopping theory.[2] A more detailed and modern discussion[3] involves the oscillator strengths at different frequencies and its influence on the mean excitation potential in the Bethe-Bloch theory.

The problem of estimating changes in excitation potentials, without waiting for detailed information on the complete valence electron absorption spectrum of light, might be approached by evaluating the dispersion frequencies from *refractive index data*. This was done by Bohr[2] for H_2 and He, but the procedure should be generalized to polyatomic substances in any state of aggregation (except conductors). The characteristic frequency, ν_0 (or wavelength λ_0), is obtained for a variety of substances from molar refraction

$$R=\frac{n^2-1}{n^2+2}\frac{M}{d}=\text{const}\frac{1}{\nu_0^2-\nu^2}. \quad (1)$$

The value of λ_0 is a sort of mean value, the oscillator strengths of the various transition possibilities being taken into account.[4] As about the same excitation phenomena occur with light and with charged particles,[5] one should be allowed to attribute changes in λ_0 to corresponding changes in stopping power. The use of the ionization potentials may sometimes be of value but would not be general enough for our purpose.

Evaluation of λ_0 for the lightest elements in different chemical states by means of atomic[6] and molar refraction data gives a picture rather analogous to that of chemical refractometry; i.e., those compounds which show increments in refraction (due to absorption in the near ultraviolet[6]) also show increments in stopping power compared with some standard. Aromatic hydrocarbons are, for instance, expected to show higher stopping power than aliphatic ones.

In a study of the mass absorption coefficients of Bi^{210} beta rays for 17 hydrocarbons, Fournier[7] reported large increments (as much as 12 percent) but apparently neglected the anomalous Z/A-factor for hydrogen. After appropriate corrections, by use of a reasonable figure for the hydrogen mass absorption coefficient, the values for the increments are reduced to 3 percent or less. Grouping the data belonging to different hydrocarbon classes together, we find interesting differences as shown in Fig. 1. Actually the same sequence is expected from the λ_0-approach, although the experi-

* Read before the Thirteenth International Congress of Pure and Applied Chemistry, Stockholm, Aug. 1, 1953.

† This work was supported by the Swedish Atomic Committee.

[1] W. Bothe, Jahrb. Radioakt. u. Elektronik **20**, 46 (1923); Handbuch der Physik (J. Springer, Berlin, 1933), Vol. 22, No. 2.

[2] N. Bohr, Phil. Mag. **25**, 10 (1913); **30**, 581 (1915).

[3] R. Platzman, *Symposium on Radiobiology*, Oberlin College, edited by J. Nickson (John Wiley and Sons, Inc., New York, 1952), Chap. 9.

[4] K. L. Wolf and K. F. Herzfeld, *Handbuch der Physik* (J. Springer, Berlin, 1928), Vol. 20.

[5] H. A. Bethe, Ann. Physik **5**, 325 (1930).

[6] N. A. Sörensen, Ann. Chem. Justus Liebigs **546**, 57 (1941).

[7] G. Fournier, Compt. rend. **196**, 412 (1933); Actualités sci. et ind. **57**, (1933).

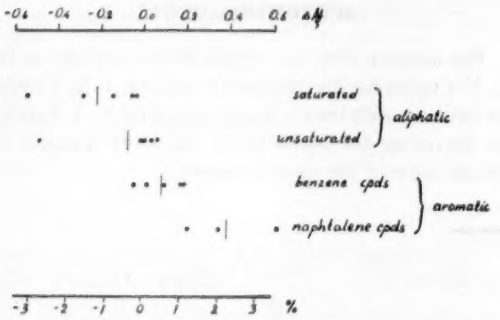

FIG. 1. Deviations in mass absorption coefficient (cm^2/g) for different classes of hydrocarbons according to revised Fournier data (reference 7) for Bi^{210} beta rays. The circles represent values for various hydrocarbons belonging to the groups indicated. The mean of the values in each row is indicated by a vertical line. Note the shifts of these lines for different chemical structures.

mental increments are apparently larger. This might be caused by the uncertainty in the assumed mass absorption coefficient for hydrogen. Range studies of P^{32} beta rays in this laboratory (unpublished) also show aromatic hydrocarbons to have a larger stopping power than aliphatic ones.

It is of interest to compare these results with the stopping data for 340-Mev protons and the corresponding excitation potentials evaluated by Thompson,[8] whose work is probably the most accurate in this field. Table I shows the changes in mean excitation potential expected from the λ_0 approximation and reasonable assumptions on the number of valence electrons, as well as the corresponding experimental changes determined by Thompson. Qualitative agreement is present in all accessible cases of comparison according to Table I. The quantitative picture is bad, the probable reasons being difficulties in accurate evaluation of atomic refractions and the exact number of valence electrons and the fact that (1) may not reflect the changes correctly because of its mathematical form.

[8] T. J. Thompson, University of California Radiation Laboratory Report UCRL-1910, 1952 (unpublished).

Even if the λ_0 approach is an approximation, it should be regarded as a rough guide to chemical effects in stopping power. It shows that the most extreme cases have perhaps not yet been studied experimentally, e.g., compounds absorbing strongly in the near ultraviolet region such as anthracene and other polyaromatic substances as well as substances having strong electronic absorption bands in the visible region, e.g., many colored substances. These interesting possibilities are part of a research program with monoenergetic betatron electrons in this laboratory. Moreover, the theoretical difficulties in this field stress the need for more experimental data.

A more detailed account will be given elsewhere.

The author wishes to thank Professor O. Lamm for the initiation and valuable support of this study and his never-failing interest throughout the work.

TABLE I. Chemical effects in energy loss of fast charged particles. Summary of experimentally established changes in mean excitation potentials[a] (ΔI) and changes estimated by means of optical dispersion data. All values are expressed in ev. C_{el} means elementary carbon (graphite). H_2, O_2, and N_2 refer to the liquid state.

Element	Case compared	Dispersion theory, ΔI	Thompson experiments, ΔI	Qualitative agreement
Hydrogen $Z=1$	$H_2-H_{aliphatic}$	+0.7	+2.7	+
	$H_2-H_{arom(benzene)}$	+4.8	+5.2	+
	$H_2-H_{arom(naphtalene)}$	+5.9	—[b]	+
Carbon $Z=6$	$C_{el}-C_{aliph}$	+4.8	+0.9	+
	$C_{el}-C_{arom}$	+10.1	+3.0	+
	$C_{el}-C_{CCl_4}$	+6.2	+12	+
Nitrogen $Z=7$	$N_2-N_{nitrobenzene,\ aniline}$	?	−13	?
	$N_2-N_{pyridine}$	?	+7.5	?
Oxygen $Z=8$	O_2-O_{ether}	−4.7	−0.2	+?
	$O_2-O_{acetone}$	+6.1	+8.5	+
	O_2-O_{OH}	−4.9	−0.2	+?

[a] See reference 8.
[b] Fast electrons (reference 7); excitation potential change not known.

Elastic Scattering of Protons by Helium at 5.78 Mev*†‡

W. E. KREGER,§ W. JENTSCHKE, AND P. G. KRUGER
Department of Physics, University of Illinois, Urbana, Illinois

(Received November 13, 1953)

The differential cross section for the scattering of 5.78-Mev protons by helium has been measured with an accuracy of ±2 percent. Scattered protons and recoil alpha particles were detected in Ilford C-2 nuclear track plates, allowing the calculation of cross sections for 26 angles from 16.2° to 154° in the center-of-mass system. The differential cross sections per unit solid angle are given as a function of the center-of-mass scattering angle. The results, analyzed in terms of phase shifts, confirm the large splitting of the inverted $P_{\frac{1}{2}}-P_{\frac{3}{2}}$ doublet in Li^5 and indicate the presence of a small negative D wave phase shift.

I. INTRODUCTION

THE experimental determination of the differential cross-section for the scattering of protons by helium provides information on the level scheme of the Li^5 compound nucleus. The levels can be compared with those of the mirror nucleus He^5 formed by a neutron-alpha interaction.[1]

The large width and wide spacing of the levels allow a detailed study and accurate comparison with the theory. Elastic scattering of protons by helium has been studied experimentally in the energy range from 1 to 3.5 Mev,[2] at 5.1 Mev,[3] at 9.48 Mev,[4] and at 32 Mev.[5] The theoretical interpretation for the 1 to 3.5 Mev data has been presented by Critchfield and Dodder[6] in terms of phase shifts. The phase-shifts for our preliminary results and the 9.48-Mev data[4] were calculated by Dodder and Gammel.[7] Moreover, these authors have interpreted the phase shifts in terms of resonances associated with virtual energy levels of Li^5. The most striking results of these analyses are the large splitting between the $P_{\frac{1}{2}}$ and the $P_{\frac{3}{2}}$ energy levels in Li^5 and the broad width of the $P_{\frac{3}{2}}$ level.

We measured the differential cross section for the scattering of 5.78±0.04 Mev protons by a "thin" helium gas target. Scattered protons and recoil alpha particles were detected in nuclear track plates at laboratory angles from 13° to 60°.[8] The results, analyzed in terms of phase shifts, confirm the large splitting of the inverted $P_{\frac{1}{2}}-P_{\frac{3}{2}}$ doublet and the very broad width of the $P_{\frac{3}{2}}$ level in Li^5. The presence of a small negative D wave phase shift is indicated.

II. EXPERIMENTAL APPARATUS AND PROCEDURE

A plan view of the scattering apparatus and the cyclotron is shown in Fig. 1. Protons were obtained by accelerating singly ionized hydrogen molecules to approximately 12 Mev in the cyclotron. The beam was deflected through an angle of 37° by a magnetic field which was accurately controlled by a proton nuclear magnetic resonance probe. The beam entered the scattering chamber through a 0.0005 cm thick Nylon foil which separated the cyclotron vacuum from the helium gas in the chamber. Each singly-ionized hydrogen molecule splits into two protons in passing through the Nylon foil.[9] From here the beam passed through the collimating system, the scattering chamber, a 0.003-cm

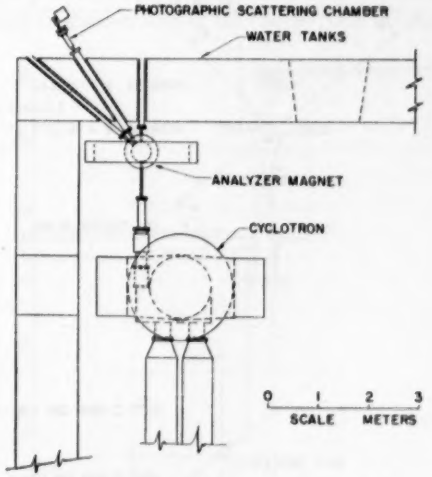

FIG. 1. Plan view of the scattering apparatus and the cyclotron.

* This investigation was supported jointly by the U. S. Atomic Energy Commission and the U. S. Office of Naval Research.

† This report is part of a thesis (W.E.K.) submitted in partial fulfillment of the requirements for the degree of Doctor of Philosophy at the University of Illinois.

‡ A preliminary report of this work was given at the New York meeting of the American Physical Society in January, 1952 [Phys. Rev. **86**, 593 (1952)].

§ Now at U. S. Naval Radiological Defense Laboratory, San Francisco 24, California.

[1] R. K. Adair, Phys. Rev. **86**, 155 (1952); P. Huber and E. Baldinger, Helv. Phys. Acta **25**, 435 (1952).

[2] Frier, Lampi, Sleator, and Williams, Phys. Rev. **75**, 1345 (1949).

[3] C. H. Braden, Phys. Rev. **84**, 762 (1951).

[4] T. M. Putnam, Phys. Rev. **87**, 932 (1952).

[5] Bruce Cork, Phys. Rev. **83**, 893 (1951).

[6] C. L. Critchfield and D. C. Dodder, Phys. Rev. **76**, 602 (1949).

[7] D. C. Dodder and J. L. Gammel, Phys. Rev. **88**, 520 (1952).

[8] In addition to these experiments performed with nuclear plates the reaction had been studied in this laboratory with a scattering chamber using proportional counters as detectors. [A. L. Atkins, thesis, Graduate College of the University of Illinois, 1952 (unpublished).] The results of both experiments agree within the experimental accuracy.

[9] R. E. Meagher, Phys. Rev. **78**, 667 (1950).

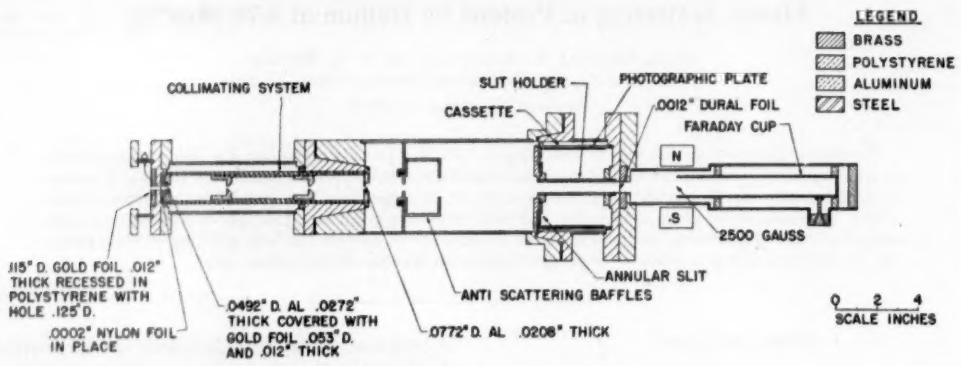

FIG. 2. Cross-sectional view of the photographic scattering apparatus.

Dural foil, and into the Faraday cup where it was collected. Figure 2 shows the scattering chamber, collimating system, and beam collecting cup. The beam in the scattering chamber had an angular divergence of 44 minutes and was accurately aligned with the geometrical axis of the chamber. Baffles prevented protons scattered by more than 2° in the collimator from reaching the scattering volume. A count of tracks in a nuclear plate exposed in the chamber perpendicular to the beam revealed that particles outside the main beam cone constituted less than 0.1 percent of the total number of particles passing through the chamber.

Immediately preceding each scattering run the scattering chamber was filled with pure helium gas to a pressure of 5 cm Hg. Scattered protons and recoil alpha particles passed through an annular slit (Fig. 3) into six 100-micron thick Ilford C-2 nuclear plates mounted around the periphery of a cylindrical photographic plate holder. The position of the track along the length of the plate determined the angle of scattering, thus making it unnecessary to measure the angle of each track separately. The slit geometry and dimensions are shown in Fig. 3 for the high-angle annular slit which passes particles scattered at angles from 20° to 70°. A low-angle annular slit admits particles scattered at angles from 13° to 35°. Two slit systems were used in order to reduce the number of particles which could penetrate the slit edges. Table I contains the dimensions for the low- and high-angle annular slits as explained in Fig. 3. A third annular slit was constructed identical to the high-angle slit except that the two edges of it were brought together. A run was made with this slit in position in order to determine the penetration correction. All distances of importance in calculating the cross section were measured on an optical comparator or an optical bench. The measurements are described by Rodgers *et al.*[10]

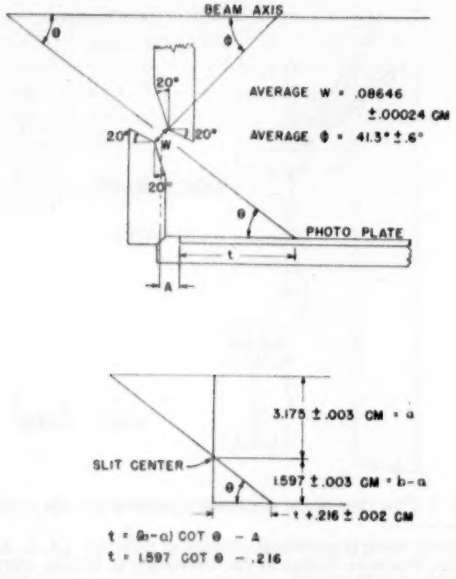

FIG. 3. Detail of the high-angle annular slit and the geometry for the distance t along the plate corresponding to the laboratory scattering angle θ.

The particle tracks in the emulsion were counted in an accurately measured area on the plate at each scattering angle. All alpha tracks and proton tracks having lengths greater than 40 percent of the expected ranges at the given angle were counted. It was thus necessary to measure only those few tracks whose lengths were close to 40 percent of the expected ranges.

The projected lengths of the tracks scattered at an angle of 23° were measured and the number of tracks of each length is plotted against the projected track length in Fig. 4 for the scattered protons and in Fig. 5 for the recoil alpha particles. From these curves the mean projected range of the protons and alpha particles can be derived. After a correction for the angle of the tracks in the plate is applied, the energies of the recoil alpha particles and scattered protons can be determined using the range-energy curves of Rotblat.[11] If, furthermore, allowance is made for the energy loss in the gas

[10] Rodgers, Leiter, and Kruger, Phys. Rev. **78**, 656 (1950).
[11] J. Rotblat, Nature **167**, 550 (1951).

between the scattering center and the plate, the energy of the incident beam can be determined. The accuracy of the scattering angle determination can be checked by comparing the energies of alpha particles and protons at a given laboratory angle with those calculated from the energy- and momentum-conservation laws. Satisfactory agreement was obtained between the calculated and measured results. The variations in track lengths (beyond that expected due to range straggling) caused by slit penetration will be discussed later.

The scattering chamber was evacuated by means of a 20-liter/second oil diffusion pump backed by a mechanical fore pump. No liquid nitrogen was used on any traps exposed to the chamber. After air had been admitted to the scattering chamber and new photographic plates placed in the chamber, about 24 hours were required to reach a vacuum of 5×10^{-6} mm Hg. No scattering run was made until the rate of rise of pressure in the chamber with the pump cut off was 6×10^{-5} mm Hg per minute or less. The purity of the helium gas filling of the chamber was measured mass spectrographically both before and after a run and corrections due to impurities were less than 0.1 percent. The pressure of the gas was measured with an oil manometer and the temperature was measured in the chamber during the runs.

The undeflected protons were collected by the Faraday cup, which is shown in position at the back of the scattering chamber in Fig. 2. The cup was supported on polystyrene insulators in a chamber in which the pressure was maintained at less than 10^{-5} mm Hg by a separate pumping system. The charge was collected at the rate of 2 to 10×10^{-9} ampere over periods from 30 to 50 minutes. This charge was accumulated on four one-microfarad polystyrene condensers connected in parallel with a combined capacitance of 4.102 ± 0.004 microfarads at 24° centigrade. The capacitance of the Faraday cup to ground was negligible compared with that of the condensers. These condensers showed negligible leakage and polarization effects. The voltage across the condensers was measured by a vibrating reed electrometer[12] which has an input resistance of greater than 10^{12} ohms when connected across the condensers and an extremely stable zero reading and calibration. After each scattering experiment readings of the condenser voltage were taken for a period of time equal to the run-time. In all cases, the change in voltage across the condensers was less than 0.1 percent.

A magnetic field of strength 2500 gauss across the open end of the cup was used to keep low-energy secondary electrons from leaving or entering the collector cup. A nuclear plate exposed at a position corresponding to the entrance of the charge collector showed

TABLE I. Dimensions of the low- and high-angle annular slits.

1. Slit width, $W=0.10138\pm0.00044$ cm, low-angle run;
   $W=0.08646\pm0.0002$ cm, high-angle run.
2. Slit angle, $\phi=97.5\pm0.15°$, low-angle run;
   $\phi=41.3\pm0.6°$, high-angle run.
3. Axial distance from slit to the near end of nuclear plate,
   $A=0.309\pm0.001$ cm, low-angle run;
   $A=0.216\pm0.002$ cm, high-angle run.
4. Plate radius, $b=4.7710\pm0.0020$ cm.
5. Slit radius, $a=3.299\pm0.001$ cm, low-angle run;
   $a=3.175\pm0.002$ cm, high-angle run.

[12] Palevsky, Swank, and Grenchik, Rev. Sci. Instr. **18**, 298 (1947).

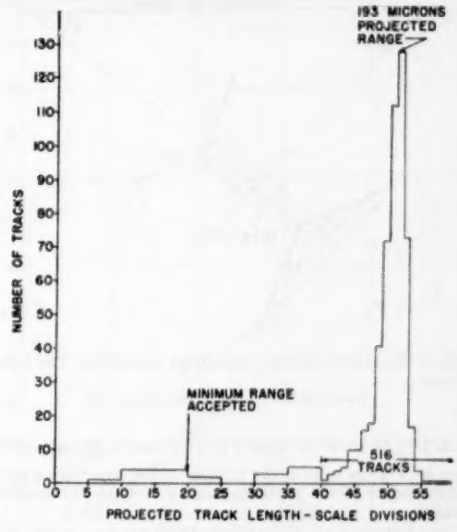

FIG. 4. Range analysis of proton tracks in the photographic plate at a scattering angle of 23°.

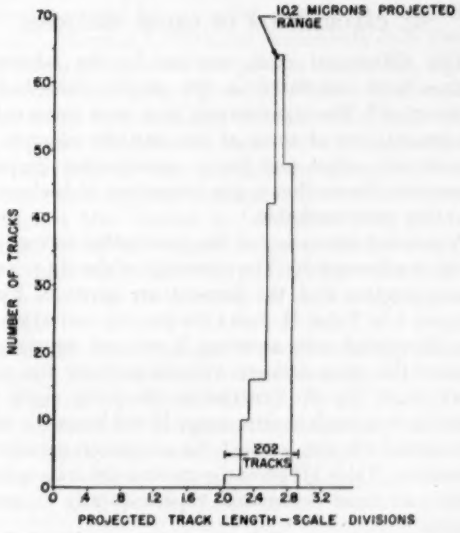

FIG. 5. Range analysis of alpha-particle tracks in the photographic plate at a laboratory angle of 23°.

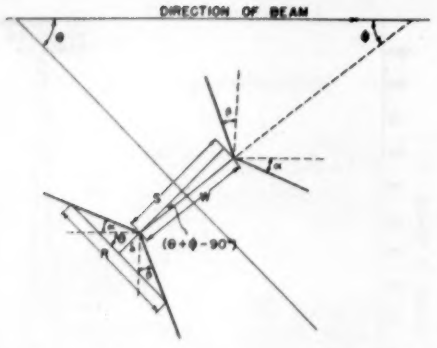

FIG. 6. Geometry for slit penetration correction. The formulas used are:

$$\delta = R \sin(\theta-\alpha) \cos(\theta+\beta)/\cos(\alpha+\beta)$$

and

$$2\delta/S = [2R \sin(\theta-\alpha) \cos(\theta+\beta)]/[W \sin(\theta+\phi) \cos(\alpha+\beta)],$$

where $2\delta/S$ is the ratio of the number of the penetrating particles to the number of the particles passing through the annular slit opening.

that less than 0.1 percent of the particles passing through the Dural foil missed the cup.

Six scattering runs were made. The first was a scattering run with the high-angle range annular slit. The second run used the "closed" slit. The third run was a background run, made with the pumps closed off from the chamber but with no helium gas in the chamber. The fourth run was similar to the first, and the fifth used the low-angle range annular slit. A sixth run was made under similar conditions to the fifth except that the pressure was about one-fifth that of the former run. This last experiment was performed to investigate a possible effect of multiple scattering (see Sec. III).

III. CALCULATION OF CROSS SECTIONS

The differential cross sections in the laboratory system were calculated in the manner described by Leiter *et al.*[13] The experimental data were corrected for the penetration of some of the particles through the annular slit edges and for a second-order geometry correction. Errors due to gas impurities or background counting were negligible.

A detailed discussion of the penetration correction is given in reference 10. The geometry of the slit penetration correction and the formula are given in Fig. 6. Column 4 in Table II shows the percent corrections for the differential cross sections. It was not necessary to correct the cross sections calculated from the alpha track count for slit penetration since the alpha particles have a much shorter range in the brass slit edges. The closed slit run verified the calculated penetration correction. Table III gives the percent corrections calculated and those determined experimentally at several angles.

[13] Leiter, Rodgers, and Kruger, Phys. Rev. **78**, 663 (1950).

A second-order geometry correction was necessary due to the finite size of the beam, its divergence, and the variation of angle and cross section over the swath area. These factors were neglected in the derivation of the simple formula for calculating the cross section. This geometry correction was calculated from a formula derived by R. O. Kerman.[14] The percent corrections for this effect are tabulated in Table II, column 5.

All geometrical factors were measured to at least ±0.1 percent. Charge, gas pressure, and temperature were measured frequently during the run and the uncertainty in the cross section due to these factors is ±0.9 percent.

Because of the finite size of the area (swath) in which the tracks were counted and because of the finite size of the opening in the annular slit, particles from scattering events at several different laboratory angles could be counted on the same swath. Defining the average angular resolution as one-half the total spread in angles represented across the swath at the position along the swath corresponding to the average angle of scattering, the angular resolution varied from ±0.45° at 13° to ±1.83° at 60°.

The effect of multiple scattering on the cross section was investigated by making one low-angle run at one-fifth of the usual pressure. Since no difference in the cross sections was found, presumably no error was incurred due to multiple scattering.

Conversion to center-of-mass cross section was made with the usual formula. At almost all angles at least 10 000 tracks were counted. The final cross-section

TABLE II. Cross section as a function of angle in the center-of-mass system at 5.78-Mev incident particle energy.

1 Particle counted	2 Angle (c.m.)	3 No. of counts	4 Penetrat. correction, %	5 Geom. correct., %	6 Cross section (c.m.) barns/steradian	7 % rms error
Protons, low-angle slit	16.13°	7017	2.01	0.25	1.0120	2.1
	18.60°	7065	2.13	1.22	0.7775	2.1
	21.69°	7493	2.20	0.88	0.6260	2.1
	24.80°	8179	2.15	0.92	0.5425	2.1
	30.96°	9714	1.73	1.43	0.4560	2.1
	37.09°	8950	1.11	1.03	0.3880	2.1
Protons, high-angle slit	28.50°	10 104	0.80	1.23	0.4860	1.9
	30.94°	11 257	1.20	1.42	0.4560	1.8
	34.84°	12 885	1.85	0.73	0.4125	1.7
	43.14°	10 569	2.70	0.89	0.3380	1.8
	49.11°	11 557	2.90	0.68	0.2960	1.8
	55.08°	12 101	2.90	0.19	0.2575	1.8
	60.93°	11 651	2.60	1.33	0.2250	1.7
	66.68°	11 024	2.10	0.66	0.1820	1.6
	72.43°	9930	1.50	0.18	0.1628	1.6
Alphas, high-angle slit	80.33°	9480		0.40	0.1248	1.6
	85.33°	7718		0.86	0.1045	1.8
	95.33°	8185		0.68	0.0732	1.9
	105.32°	10 992		0.87	0.0572	1.8
	115.28°	9520		0.58	0.0514	1.9
	125.26°	9415		0.53	0.0571	1.9
	130.25°	8410		0.96	0.0622	1.9
	134.23°	7872		1.04	0.0670	1.9
Alphas, low-angle slit	140.20°	8195		1.18	0.0760	2.0
	145.18°	7507		0.94	0.0848	2.1
	150.16°	6228		0.96	0.0940	2.1
	154.14°	5302		0.68	0.1024	2.1

[14] Zimmerman, Kerman, Singer, Kruger, and Jentschke (to be published).

values are tabulated in Table II, column 6. Table II also includes the total combined rms errors, in column 7. These errors include those due to statistics of counting tracks, uncertainty of the angle, slit penetration, background, measurements of geometrical dimensions, and measurements of total charge, gas pressure, and temperature.

IV. ANALYSIS OF PROTON-ALPHA DATA

Energy of Incident Protons

The beam energy was measured in the chamber by exposing a nuclear plate to the direct beam, allowing the particles to enter the emulsion at a grazing angle of 3°. The mean range of the particles was 219.4 microns which corresponds to an energy of 5.80 Mev according to the range-energy relation for protons in C-2 emulsion found by Rotblat.[11] This energy was decreased by 0.02 Mev in passing through about 35 cm of the helium gas in the scattering chamber. The probable error in the energy measurement was estimated to be ±0.7 percent based on an uncertainty in determining the mean range and a probable error in the Rotblat curve. The half-width of the observed range distribution at $1/e$ of maximum is about 6.5 microns. On the basis of a simultaneous range-energy measurement in air one can estimate that the actual spread in beam energy corresponded to a Gaussian distribution with a half-width of about ±30 kev or ±0.4 percent. The difference in energy of the beam for the various scattering runs was determined by the frequency change of the proton moment device used to stabilize the analyzer magnet field. Since the difference was not larger than 0.02 Mev no correction was made. The energy value used in the phase shift analysis was 5.78±0.04 Mev. As mentioned on page 838, the beam energy can also be determined directly from the energy of the scattered protons or alpha-recoil particles. The values of the beam energy calculated from these range analyses agree within the claimed accuracy with the direct energy measurement.

Phase-Shift Analysis

With a knowledge of the incident proton energy, all factors needed for an analysis of the differential cross sections in terms of the theory of scattering by partial waves are available. The incident beam, as an infinite plane wave, is expanded in orbital momentum eigenfunctions and the effects of nuclear refraction are introduced as phase shifts in the asymptotic form at large separation. In the presence of spin-orbit coupling the waves will be refracted differently, depending upon the relative orientation of spin and orbital angular momentum.

TABLE III. Comparison of theoretically and experimentally determined penetration corrections. Values are the percentage ratios of the number of penetration particles to the number of particles passing through the annular slit opening.

Laboratory angle	23°	28.2°	40°	50°	60°
Experimental correction (%)	0.88±0.11	1.89±0.15	2.87±0.11	2.36±0.14	1.32±0.11
Theoretical correction (%)	0.80±0.05	1.85±0.10	2.90±0.10	2.60±0.10	1.50±0.08

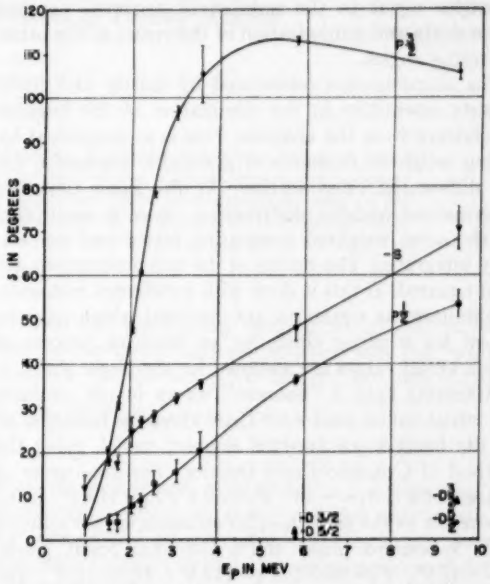

FIG. 7. Phase shifts for p–He^4 scattering as a function of proton bombardment energy. For points below 4 Mev the results of the analysis of reference 6 are used. For 9.48 Mev the values are those of reference 7; for 5.78 Mev the values derived from the experiment described in this paper are used.

The expression for the differential cross section for a proton scattered by a nucleus of spin zero is given in Eq. (1), reference 7. With our preliminary data Dodder and Gammel[7] made an analysis for 3 cases: S, $P_{\frac{1}{2}}$, and $P_{\frac{3}{2}}$ waves only, S, $P_{\frac{1}{2}}$, $P_{\frac{3}{2}}$, and D waves (the $D_{\frac{3}{2}}$ and $D_{\frac{5}{2}}$ phase shifts were assumed to be identical), and S, $P_{\frac{1}{2}}$, $P_{\frac{3}{2}}$, $D_{\frac{3}{2}}$, and $D_{\frac{5}{2}}$ waves. A more accurate evaluation of our experimental data changed the energy and cross-section values by small amounts. The correct energy is 5.78±0.04 Mev instead of 5.81±0.04 Mev, and a recalculation of the second-order geometry correction gave the result that the preliminary values of the differential cross section were on the average ½ percent too high.

Although these changes lie within the experimental accuracy, the phase-shift analysis was repeated assuming three (S, $P_{\frac{1}{2}}$, $P_{\frac{3}{2}}$) and five (S, $P_{\frac{1}{2}}$, $P_{\frac{3}{2}}$, $D_{\frac{3}{2}}$, $D_{\frac{5}{2}}$) nonzero phase shifts. The calculations have been performed by H. Lustig who used a new method developed by Lustig and Blatt.[15] Usually the calculation involves matching of differential cross-section data at a number

[15] H. Lustig, thesis, University of Illinois, 1953 (unpublished); H. Lustig and J. M. Blatt, Phys. Rev. 91, 453 (1953).

of angles equal to the number of assumed nonzero phase shifts and minimization of the errors at the other scattering angles.

The simplification introduced by Lustig and Blatt consists essentially in the elimination of the angular dependence from the analysis. This is accomplished by taking weighted moments of a suitable expression for the differential cross section. At the same time the experimental angular distribution curve is multiplied by the same weighted integrating factor and numerically integrated. The results of the two integrations are then equated. If this is done with n different moments, n simultaneous equations are obtained which may be solved for n phase shifts by an iterative process in which initial values are assumed for the phase shifts.

Assuming only 3 "nonzero" waves in our problem the initial values used were those given by Kreger *et al.* on the basis of an inverted doublet model, using the method of Critchfield and Dodder. The final order of phase shifts is $S_{\frac{1}{2}}=-46°$, $P_{\frac{1}{2}}=39.7°$, $P_{\frac{3}{2}}=113.2°$. Using this result as the zeroeth-order estimate for the solution with 5 nonzero phase shifts the final result reads: $S=-47.9°$, $P_{\frac{1}{2}}=38.7°$, $P_{\frac{3}{2}}=112.9°$; $D_{\frac{3}{2}}=-1.3°$, and $D_{\frac{5}{2}}=-0.49°$. The estimated errors for the S phase shift should be $\pm 3°$ and for the P wave phase shift $\pm 2°$: for the D wave phase shifts it is difficult to estimate the accuracy.

Since these values agree very closely with those derived by Dodder and Gammel,[7] we will not discuss the results on the basis of the resonance theory of nuclear interactions in detail, but refer to their paper.

Considering additional p–He^4 scattering data at different energies, Fig. 7 shows the phase shifts as a function of proton bombardment energy. The results show the large splitting of the $P_{\frac{1}{2}}$ and $P_{\frac{3}{2}}$ level and the very broad width of the $P_{\frac{1}{2}}$ level. Small negative D wave phase shifts also show evidence of an inverted doublet spin-orbit splitting.

ACKNOWLEDGMENTS

The authors would like to express their appreciation to the members of the cyclotron staff for valuable assistance in performing their work. The invaluable advice and help during the performance of the experiment by R. O. Kerman is most gratefully acknowledged. R. Nilson made some of the tedious measurements associated with the experiment.

Production of Positive Mesons in Heavy Nuclei

S. GASIOROWICZ
Radiation Laboratory, Physics Department, University of California, Berkeley, California
(Received October 14, 1953)

The data on the A dependence of low-energy meson production by protons on heavy nuclei are explained by taking into account the following effects: (1) the energy degeneration of the incident proton in nuclear matter, which tends to make meson production possible only in the "front" of the struck nucleus; (2) the subsequent re-absorption of the meson by the nuclear matter it traverses. This last effect is further strengthened by the reflectivity of the Coulomb barrier.

INTRODUCTION

RECENT experiments[1] on the production of positive mesons in collisions of protons with heavy nuclei indicate that for fixed proton and meson energies, $\sigma(A)/A^{\frac{1}{3}}$, and, hence, $\sigma(A)/A$, decrease with A, the number of nucleons in the target nucleus. This suggests that neither a direct "independent-particle" nor a "surface" production mechanism is in itself sufficient to explain the data. It is the purpose of this note to point out that the decrease in the "meson-production efficiency" with A is a consequence of the rapid energy degeneration of the incident proton in nuclear matter, which makes meson production possible only in the "front" of the struck nucleus, together with a meson-attenuation effect which becomes more important with increasing A.

Let us first describe our model of the nucleus. We consider the nucleus as composed of nucleons moving in a self-consistent nuclear potential. This model has been explored by Johnson and Teller[2]; it leads to roughly constant neutron and proton densities, and the consequence of interest to us is that the presence of the Coulomb potential tends to push the protons away from the center as well as from the boundary thus confining them to a region of somewhat smaller radius compared to the nucleus as a whole[3] (see Fig. 1).

PROTON ENERGY DEGENERATION

Let us consider a proton of 240–340 Mev entering a heavy nucleus. The proton has a mean free path for elastic scattering[4] which can be computed by using the free-particle cross sections $\sigma_{pp}\simeq 25$ mb and $\sigma_{np}\simeq 40$ mb in this energy range. The approximate constancy of these values over a fairly wide energy range allows us to ignore the dependence of the scattering mean free path on the momentum distribution of the nucleons forming the target nucleus, provided that the "width" of such a distribution $\lesssim 200$ Mev/c.[5] We thus obtain

$$\lambda_s=(4\pi/3)R^3[Z\sigma_{pp}+N\sigma_{np}]^{-1}$$
$$=RA^{\frac{1}{3}}[0.26Z+0.42N]^{-1}. \quad (1)$$

Now, on the average, after traveling a distance λ_s, the proton will undergo an elastic collision and (again on the average) lose 50 percent of its energy in the process. Hence for a proton of 240 Mev only one zone of depth λ_s is available for meson production, whereas for protons of 340 Mev all particles in the first zone, and roughly half the particles in the second zone (those whose momentum vector have a positive component pointing towards the incoming proton), are available for meson production.

Experiments[6] indicate that the process

$$p+p\rightarrow\pi^{+}+d$$

is a great deal more probable than the process

$$p+n\rightarrow\pi^{+}+2n.$$

The large suppression of the latter process is partly due

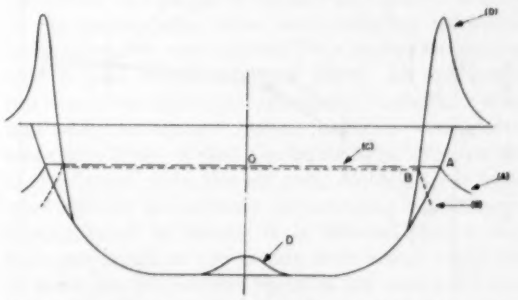

FIG. 1. A schematic representation of potentials acting on the nucleons in a nucleus. $OA=R$, the nuclear radius; $OB=P$, the charge distribution radius; (A) is the neutron tail; (B), the proton tail; (C), the highest proton and neutron levels; and (D), the Coulomb potential.

[1] R. Sagane and W. Dudziak, Phys. Rev. **92**, 212 (1953); D. Clark, Phys. Rev. **87**, 157 (1952).

[2] M. H. Johnson and E. Teller (to be published).

[3] The fact that the radius of the nuclear-charge distribution appears to be smaller than the nuclear radius is indicated by recent measurements of x-rays from mesonic atoms [Proceedings of the Third Annual Conference on High-Energy Physics at Rochester, 1952 (Interscience Publishers, New York, 1953)] and by the scattering of 100-Mev electrons from heavy nuclei.

[4] The concept of a mean free path is meaningful here since, at the energies being considered, the de Broglie wavelength of the proton is much smaller than the inter-nucleonic distance so that diffraction effects are expected to be negligible.

[5] Assuming that the "width" of the momentum distribution is insensitive to changes in A, this condition is met for all A, since it is satisfied for deuterium and carbon. See, Cladis, Hess, and Moyer, Phys. Rev. **87**, 425 (1952).

[6] For example, J. Carothers and C. G. André, Phys. Rev. **88**, 1426 (1952). These experiments have been extended to lower energies by W. Dudziak (private communication).

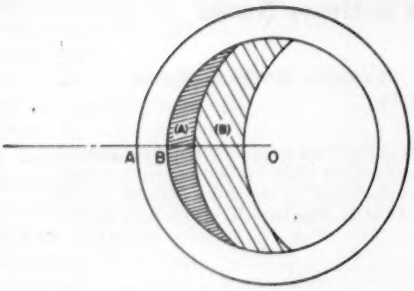

FIG. 2. The meson-production zones in the target nucleus. $OA=R$, the nuclear radius; $OB=P$, the charge distribution radius; (A) first zone; and (B) second zone.

to the exclusion principle: in the latter case there are three particles in the final state and since the two identical neutrons tend to keep away from each other the phase space available to each particle is appreciably reduced. A much larger suppression of the process can be expected if conservation of isotopic spin is assumed together with a strong interaction in the $T=\frac{3}{2}$ state.[7]

We thus assume that only the protons in the target nucleus are effective in producing positive mesons, and so we write

$$\begin{aligned} &\text{for 240-Mev protons:} \quad \sigma=\sigma_0 Z_1, \\ &\text{for 340-Mev protons:} \quad \sigma=\sigma_0'(Z_1+\tfrac{1}{2}Z_2), \end{aligned} \tag{2}$$

where Z_i is the number of protons in the ith zone. We remark here that as pointed out above the protons are confined to a somewhat smaller volume by the Coulomb barrier, and this serves to reduce the number of protons in the first zone (Fig. 2). We find that

$$Z_1(\lambda_s)/Z=(R/P)^3\{\tfrac{1}{2}(P/R)^2[x/R+\lambda_s/R-1] +\tfrac{1}{2}(x/R)[(\lambda_s/R)-1]+\tfrac{1}{2}(P/R)^3-\tfrac{1}{4}(x/R)^2(\lambda_s/R)\}, \tag{3}$$

and

$$(Z_1+Z_2)/Z=Z_1(2\lambda_s)/Z,$$

where

$$(x/R)=[(P/R)^2-(1-\lambda_s/R)^2](R/2\lambda_s),$$

R is the nuclear radius (taken to be $1.5\times10^{-13}A^{\frac{1}{3}}$ cm), and P is the radius of the "charge distribution." We assume that $P=0.90R$.[8]

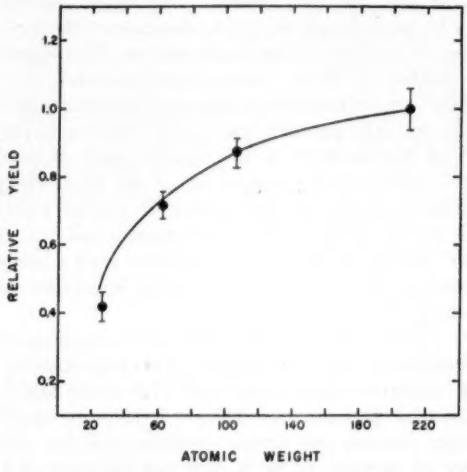

FIG. 4. Comparison with the data of Clark. The solid line is the theoretical curve for $E_\pi=40$ Mev, $f=\frac{1}{3}$. The curve and the experimental points are normalized to unity at Pb.

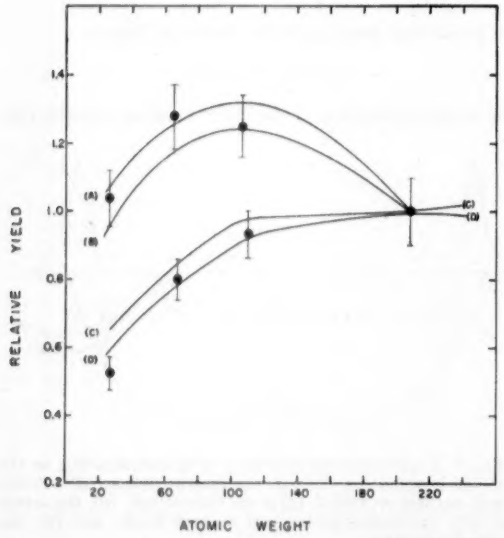

FIG. 3. Comparison with the data of Dudziak and Sagane. The solid lines are the theoretical curves. (A) $E_\pi=13$ Mev, $f=\frac{1}{3}$; (B) $E_\pi=13$ Mev, $f=\frac{1}{9}$; (C) $E_\pi=27$ Mev, $f=\frac{1}{3}$; (D) $E_\pi=27$ Mev, $f=\frac{1}{9}$. All curves and the experimental points are normalized to unity at Pb.

MESON ABSORPTION

Once a meson is produced, it travels through nuclear matter for a distance d. The chance that the meson will undergo absorption may be described by a mean free path for absorption λ_a of the order of $6-7\times10^{-13}$ cm,[9] and the probability of the meson's reaching the boundary is $\exp(-d/\lambda_a)$. The presence of the Coulomb barrier gives rise to a reflection probability $(1-T)$. Consequently the probability that a meson finally gets out of the nucleus without being absorbed is

$$\frac{T\exp(-d/\lambda_a)}{1-(1-T)\exp(-2R/\lambda_a)}\simeq T\exp(-d/\lambda_a). \tag{4}$$

We have calculated T for $l=0$ waves only, since it turns out that the centrifugal barrier contributes less

[7] M. A. Ruderman, Phys. Rev. 88, 1427 (1952). Note that the conclusions regarding the process $p+n\to\pi^-$ must apply identically to the process $p+n\to\pi^+$ by charge symmetry.

[8] A charge distribution radius 10 percent smaller than the nuclear radius is suggested by an interpretation of the experiments of Fitch and Rainwater on x-rays from μ-mesonic atoms. See L. N. Cooper and E. M. Henley, Phys. Rev. 91, 480 (1953).

[9] Brueckner, Serber, and Watson, Phys. Rev. 84, 258 (1951).

than 10 percent to the transmission coefficient. The factor $\exp(-d/\lambda_a)$ was also computed with λ_a chosen equal to 6.5×10^{-13} cm and an average $d=fR$. The calculation was carried out with $f=\frac{1}{2}$ and $f=\frac{1}{3}$,[10] for Al, Cu, Ag, and Pb. A comparison with the data of Dudziak and Sagane and of Clark is made in Figs. 3 and 4, respectively.

CONCLUSION

As Figs. 3 and 4 show, the agreement of theory with experiment is quite satisfactory. In view of uncertainties in the value of λ_a and f, the experiments cannot be said to confirm or deny the conclusions of other experiments which suggest a radius of the charge distribution smaller than the nucleus as a whole. With a choice $P=R$, the theoretical curves would be shifted upwards by 5–10 percent.

In view of difficulties in obtaining Coulomb wave functions for attracting particles, no detailed comparison with the π^- data is here made. The author is grateful to Professor Sagane and Dr. Dudziak for communicating to him the results of their experiments prior to publication. Discussions with Dr. J. Lepore, Dr. W. Heckrotte, Dr. M. H. Johnson, and Dr. T. Kinoshita are gratefully acknowledged.

[10] Small values of f were chosen for the experiments under consideration since the mesons were observed at 90° and ~140°. For mesons at 0° one would have to take $f\simeq1.0-1.5$.

PHYSICAL REVIEW VOLUME 93, NUMBER 4 FEBRUARY 15, 1954

Inelastic Scattering of 220-Mev π^- Mesons in Emulsions*

W. F. Fry
Department of Physics, University of Wisconsin, Madison, Wisconsin
(Received November 9, 1953)

The nuclear interaction of 220-Mev negative π mesons has been studied in photographic emulsions. A particular type of inelastic scattering events has been analyzed. Among 1960 π^- meson interactions, 17 events are observed where the π meson transferred a large fraction of its initial energy to a single proton. The incident π meson, the scattered π meson, and the proton are nearly coplanar in most of these cases. However the three tracks are not exactly coplanar indicating that the meson collision was not with a hydrogen nucleus. The 17 events are interpreted as the interaction of the incident π meson with a single proton of the target nucleus.

I. INTRODUCTION

SEVERAL studies have been made in photographic emulsions[1–3] of the nuclear interaction of π mesons of energy less than 250 Mev. The phenomena most frequently observed are (a) "stars" produced by the absorption of the incident π meson, (b) "stars" produced by inelastic scatterings, (c) elastic scatterings, and (d) "stops" due in part to charge exchange. The nucleus, in part or as a whole, is involved in the collision in events of types (a), (b), and (c). In most cases, the energy lost by the meson is shared among several nucleons. For this reason it is difficult to obtain information on the initial interaction of the π meson in the nucleus.

Several events have been found where nearly all of the energy lost by the π meson was transferred to a single proton. The analysis of these events is described.

* Supported in part by the Research Committee of the Graduate School from funds supplied by the Wisconsin Alumni Research Foundation.

[1] Bernardini, Booth, and Lederman, Phys. Rev. **83**, 1075 (1951); Bernardini, Booth, and Lederman, Phys. Rev. **83**, 1277 (1951); G. Bernardini and F. Levy, Phys. Rev. **84**, 610 (1951).

[2] H. Bradner and B. Rankin, Phys. Rev. **87**, 547 (1952); B. Rankin and H. Bradner, Phys. Rev. **87**, 553 (1952).

[3] A. H. Moorish, Phys. Rev. **90**, 674 (1953).

II. PROCEDURE

Ilford G-5, 600- and 1000-micron thick plates were exposed in the 220-Mev negative π-meson beam of the University of Chicago cyclotron. The general features of the meson beam have been described elsewhere.[4] The plates were area-scanned for π-meson interactions with a total magnification of 250×. An appreciable fraction of the elastic scatterings and inelastic scatterings where no charged nuclear particles were ejected was undoubtedly missed. Undoubtedly, a large fraction of the "stops" were also not seen. Although it is somewhat difficult to estimate the scanning efficiency for various types of events, it is believed that a very high percentage of the events were found where one or more charged nuclear particles are associated with the event. The scanning time that would be required to find the particular events of interest would be excessively long if scanning "along the track" or under a higher magnification were employed. It is estimated, by using the data of Morrish[3] on the number of interactions of various types, that about 70 percent of the total number of interactions were observed.

All events were studied where a lightly ionizing track

[4] R. L. Martin, Phys. Rev. **87**, 1052 (1952).

TABLE I. Characteristics of inelastic scatterings.

Event	Energy of scattered meson	Energy of proton	Angle between incid. π meson and scat. π meson	Angle between proton and incid. π meson	Departure from coplanarity in degrees[c]	Residual momentum in Mev/c[d]
1	35±5	140±30	95	31	12	250
2	15±1	130±20	98	18	11	165
3	50±10	130±20	144	29	23	350
4	120±40	80±15	79	41	14	120
5	~100[a]	120±20	140	33	6	~250
6	80±20	90±20	105	44	28	170
7	110±30	120±30	96	20	32	310
8	80±20	130±20	125	33	26	180
9	>80[a]	100±20	110	50	31	~150
10	70±20	100±20	147	15	13	100
11	18±8	150±30	134	5	2	115
12	6.8±0.5	90±30	60	82	33	460
13	35±10	80±15	176	52	5	340
14	60±15	90±20	120	90	25	310
15[b]	70±40	80±15	120	26	26	200
16[b]	35±10	70±20	112	31	9	280
17[b]	>60[a]	90±15	110	18	18	~450

[a] The track is too short for multiple scattering measurements. However the "blob" density is less than that of a 200-Mev proton. Hence it is assumed that the track was produced by a π meson.
[b] A recoil track is observed at the junction.
[c] The tabulated angle is the angle between the direction of the incident π-meson track and the plane of the scattered meson and proton. In some cases the angle between the plane of the two mesons and the direction of the proton is less, for example in event 9 this angle is 7°.
[d] The vectorial addition of the momentum of the scattered π meson and the fast proton minus the momentum of the incident π meson. The momentum of the recoil, if observed, is not included.

(corresponding to a proton of energy greater than about 70 Mev) was associated with the star.

III. OBSERVATIONS

A total of 1960 π^- meson interactions was observed. Seventeen cases were found where a fast proton was ejected ($E_p > 70$ Mev), along with the scattered π meson. In 3 of the 17 cases a short recoil track is observed at the junction point, while in the remaining 13 events there are no tracks of particles other than low energy electrons. The essential characteristics of the events are given in Table I. Photographs of two typical events, where only a high-energy proton is ejected along with the scattered meson, are shown in Fig. 1 and Fig. 2. The two events are listed in Table I as events 2 and 6, respectively. A photograph of event 16 in Table I is shown in Fig. 3.

The energy of the fast proton in each of the 17 events was estimated from a measurement of the "blob" density along the track. In most cases it was possible to establish, from the multiple scattering, that the particle was much heavier than a meson and therefore assumed to be a proton. The relationship between the "blob" density and velocity was obtained from very long π-meson tracks which stopped in the emulsion. The identity of the scattered meson was determined from the multiple scattering and "blob" density measurements in those cases where the track was sufficiently long. In event 2 the meson stopped in the emulsion. In events 5, 9, and 17 the track which is presumed to be the scattered meson is short. However the "blob" density is less than along a track of a 220-Mev proton. For this reason it is assumed that the track was produced by a π meson.

In addition to the 17 events described above, 4 cases are observed where the ejected proton had an energy

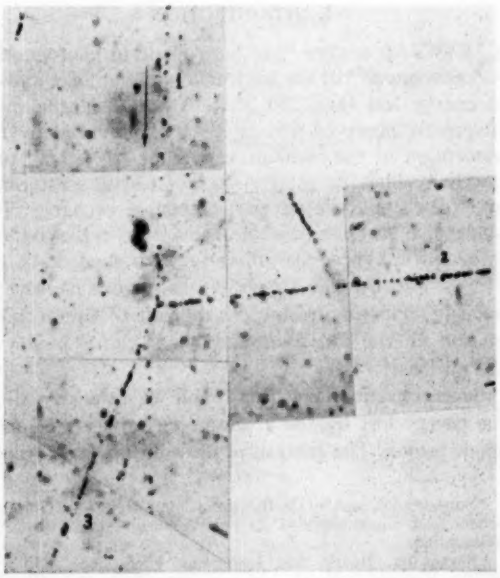

FIG. 1. A photograph of event 2 in Table I is shown above. The scattered π-meson ($E = 15 \pm 1$ Mev) track 2, the proton ($E = 130 \pm 20$ Mev) track 3, and the incident π-meson track 1 are nearly coplanar.

greater than about 70 Mev. However, in each case the incident π-meson track, the scattered π-meson track and the proton track are coplanar (within 2 degrees) and the residual momentum of the three charged particles is less than 70 Mev/c. It is assumed that these 4 events are collisions with hydrogen.

Six interactions were found where a fast proton ($E_p > 70$ Mev) originates from the collision. Five of these events consist of a scattered π meson, slow nucleons and a fast proton. In the remaining event, the π meson is absorbed and only a fast proton is ejected in the forward direction.

IV. DISCUSSION

The difference in the energy of the incident π meson and the scattered π meson is approximately equal to the energy of the fast proton, in the first 11 events in Table I. Also the residual momentum of the three charged particles is not excessively large in these events. These two facts along with the small departure from coplanarity suggest that the π-meson collision occurred with a single proton in the nucleus.

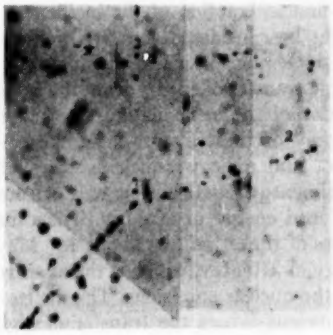

FIG. 2. A photographic mosaic of event 6 is shown above. The scattered π meson (track 2) has an energy of 80 ± 20 Mev. The proton ($E = 90 \pm 20$ Mev) is ejected in the forward direction. The residual momentum of the three charged particles is about 170 Mev/c.

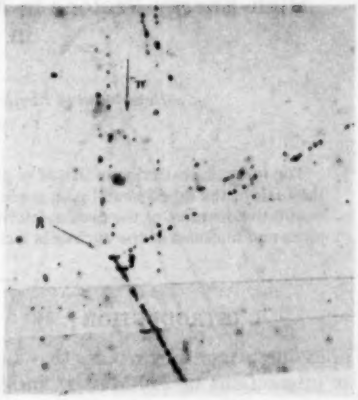

FIG. 3. A recoil track can be observed in the photograph of event 16 in Table I. The recoil track is in such a direction as to conserve momentum.

It may be possible to explain the remaining 6 events by assuming that the initial collision of the π meson was with a single proton and that either the proton or the scattered meson lost a fraction of its energy in a secondary collision. These conclusions are substantiated by the calculations of Dr. Takeda which appear in the following paper.

The author is grateful to Professor H. L. Anderson for the continued use of the facilities of the University of Chicago cyclotron. Many discussions with Professor R. G. Sachs and Dr. G. Takeda were helpful and stimulating.

High-Energy Protons in Nuclear Interaction of 220-Mev π^- Mesons in Nuclear Emulsions*

GYO TAKEDA†
Department of Physics, University of Wisconsin, Madison, Wisconsin
(Received November 9, 1953)

The inelastic scattering of 220-Mev pions by a single collision with a nucleon in a nucleus is treated on the basis of the experimental pion-nucleon cross section. It is found possible to account in this way for the qualitative features of the events described in the preceding paper, if the effect of absorption of scattered pions and nucleons in the nucleus is included.

I. INTRODUCTION

IN the preceding paper[1] Fry reports that among 1960 nuclear interactions of 220-Mev π^- mesons in G5 plates, he observes 17 events in which a high-energy proton is emitted. The energies of the protons are between 70 Mev and 150 Mev. Fourteen of these events seem to be due to a collision between the incident π^- and a heavy nucleus, since they show only the tracks of the scattered π^-, the incident π^-, and the high-energy proton. Three events show an additional short track ascribable to the recoil nucleus, indicating that the collision occurred between the π^- and a light nucleus.

The residual momenta of the incident π^-, the scattered π^-, and the proton are quite small and the three tracks are nearly coplanar. In about half of the 17 events, the sum of the energies of the proton and the scattered π^- are nearly equal to the incident energy, but in no case can the energy and momentum balance be explained by the collision between a π^- and hydrogen. In many of the events the π^- come out in the backward direction and the protons in the forward direction. There are only a few cases in which the scattered π^- of high energy is associated with a single low-energy proton (<70 Mev). Here we shall show the principal features of these events can be understood if they are assumed to be due to a single collision of the incident π^- with a single proton inside the nucleus.

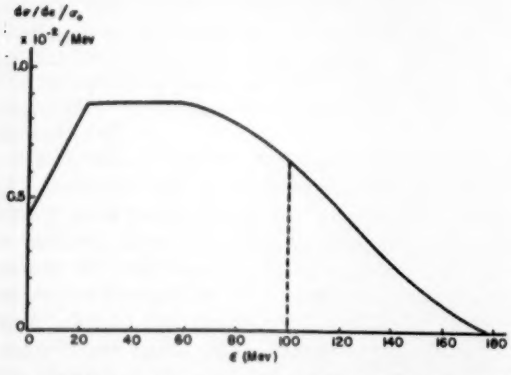

FIG. 1. The average over the proton Fermi distribution of the cross section for energy loss ϵ for a collision between the pion and the proton. σ_0 is the total cross center-of-mass system.

II. CALCULATION

Since the wavelength of the incident π^- ($\lambda \sim 0.6 \times 10^{-13}$ cm) is smaller than the average distance ($2r_0 \sim 3 \times 10^{-13}$ cm) between two neighboring nucleons in the nucleus, the first interaction of the incident π^- with a nucleus might be considered as a collision between the π^- and a single nucleon inside the nucleus.

To explain the large transfer of energy from the π^- to the proton, the motion of the nucleons must be taken into account. As many of these events look like collisions between a π^- and a heavy nucleus, we shall assume a Fermi momentum distribution of nucleons with a maximum Fermi energy of 22 Mev. Then the maximum energy loss of the π^- will be about 180 Mev for an incident energy of 210 Mev, which is the average energy of the π^- in the nuclear emulsions. The nucleon motion inside the nucleus favors the transfer of high energy, and the effect of the Pauli principle after the collision supplements this effect to some extent.

We have calculated the average over the proton Fermi distribution of the cross section for energy loss ϵ for a collision between the pion and the proton. The details of such a calculation have been described by Johnson.[2] The cross section as a function of ϵ is presented in Fig. 1. This curve is calculated on the assumption that the cross section for the scattering of the pions by protons is independent of energy within the energy range involved here.

Furthermore, the scattering was taken to be isotropic in the center-of-mass system of the pion and proton. According to Fig. 1 the average energy loss is about 70 Mev, and the ratio of collisions for $\epsilon > 100$ Mev[3] to those for $\epsilon < 100$ Mev is 2:7.

* Supported by the U. S. Atomic Energy Commission.
† On leave from Kobe University, Kobe, Japan.
[1] W. F. Fry, preceding paper [Phys. Rev. 93, 845 (1954)].
[2] M. H. Johnson, Phys. Rev. 83, 510 (1951). We used a slightly different formula from his Eq. (14), which is more accurate for numerical calculations at 210-Mev incident energy.
[3] The energy of the recoiled proton is nearly equal to the sum of the energy loss ϵ of π^- and the average kinetic energy of the proton before the collision ($\frac{1}{2} \times 22$ Mev). Also, the proton will lose the potential energy (~30 Mev) when it leaves the nucleus. Then an energy loss of 100 Mev will produce a proton of 80 Mev. In all 17 cases except one which has a short track, the proton energies are more than 80 Mev.

The angular distribution of the scattered π^- has also been calculated under the above assumptions. For this purpose the average over the proton momentum has been carried out separately for two cases, that in which the energy loss of the π^- is such that $\epsilon > 100$ Mev and that in which the energy loss is such that $\epsilon < 100$ Mev. The average angular distributions for these cases are shown in Fig. 2 as the solid curves I and I′, respectively.

Since the observed scattering of pions by protons is not isotropic, some correction to curves I and I′ is to be expected. An estimate of the effect has been made by multiplying curves I and I′ by a factor proportional to the observed angular distribution of pion-proton scattering.[4] The results are indicated by curves II and II′ in Fig. 2. These estimates take no account of the difference between the angle of scattering as measured in the center-of-mass system (of pion and proton) and that measured in the experiments under discussion. However, since the differences between curves I and I′ and curves II and II′ are not large, it seems reasonable to assume that the effect is not very important for the following discussion.

In Fry's experiment there is a selection of those events in which the scattered π^- and the proton do not undergo further collisions after the first one. Actually, most of the pions and protons make additional collisions within the nucleus because the pion-nucleon and nucleon-nucleon interactions are so strong. Consequently the angular distribution of the selected events will be quite different from that described by curves I and I′ in Fig. 2. In order to estimate the change, some consideration must be given to the collisions after the first.

TABLE I. The mean free paths for the π^- (l_π) and the proton (l_p) after the first collision. $\bar{\epsilon}$ is the mean energy loss for $\epsilon < 100$ Mev and for $\epsilon > 100$ Mev. r_0 is the radius of a nucleon, $r_0 \sim 1.4 \times 10^{-13}$ cm.

$\bar{\epsilon}$(Mev)	E_{π^-} (Mev)	l_{π^-}	E_p (Mev)	l_p
50	160	$(2/3)r_0$	60	$2r_0$
120	90	$2r_0$	130	$4r_0$

After the first collision the π^- and the proton still have small wavelength and the subsequent collision may again be regarded as occurring between single particles. If we use the experimental value for the cross sections of collisions between a free π^- and a free nucleon and between two free nucleons,[5] the mean free paths for the second collision of the π^- and the proton are given in Table I for a first collision which produces an energy loss of 120 Mev or 50 Mev. These energies are chosen because they are the average energy loss for collisions with $\epsilon > 100$ Mev and with $\epsilon < 100$ Mev,

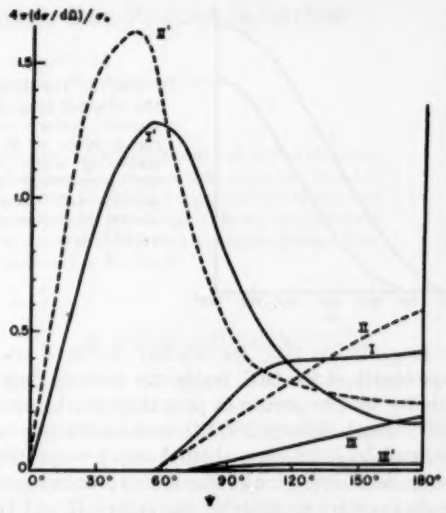

FIG. 2. Differential cross section for the scattering of a π^- by a proton in the nucleus. Curve I: events for which the proton energy loss (ϵ) > 100 Mev. Curve I′: $\epsilon < 100$ Mev. Both curves based on isotropic pion nucleon scattering. Curves II and II′ are corrected to take account of the observed angular distribution of pion-nucleon scattering. Curves III and III′ are obtained from II and II′ by using factors which take account of multiple collisions.

respectively. The difference in mean free paths for the two cases considered is due to the fact that the collision cross section between a π^- and a nucleon increases rapidly with the pion energy, while that between two nucleons decreases roughly as 1/energy. We now wish to show that, because l_π is small compared to the nuclear size, the intensity of pions scattered in the forward direction will be smaller than is indicated by curves I and I′ in Fig. 2. Furthermore, since $l_p(\epsilon < 100$ Mev) is smaller than $l_p(\epsilon > 100$ Mev), the ratio of high-energy to low-energy protons produced by backscattered pions is greater than one would expect on the basis of Fig. 1.

As a result of the strong interaction of the incident π^- with nucleons, the first collision will take place with one of the nucleons at the surface of the nucleus. Because $l_{\pi^-} < l_p$, the probability that the π^- and the proton will have no further collisions is largest when the π^- is scattered away from the surface. To estimate this effect we assume the π^- scattered within some angle θ with the outward normal to the surface suffer no further collisions but that all others are lost. As the value of θ we take the angle for which the intensity of the scattered π^- is reduced by $1/e$ compared with that in the normal direction. Then for the two cases, $l_{\pi^-} = 2r_0$ and $l_{\pi^-} = \frac{2}{3}r_0$, θ is 90° and 63°, respectively. The corresponding relative area $F(\Psi)$ of the surface which can produce π^- at the scattering angle Ψ is given in Fig. 3.

When the π^- is scattered backward it follows from the momentum balance that the proton is emitted into the forward direction, so its path within the nucleus is

[4] Fermi, Glicksman, Martin, and Nagle, Phys. Rev. **92**, 161 (1953).

[5] We used the Chicago data (reference 4) for the cross sections of scattering between a pion and a nucleon.

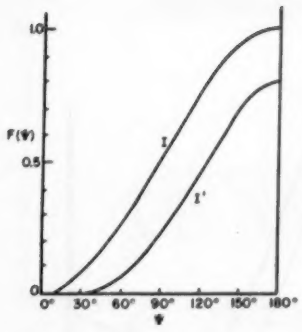

FIG. 3. The ratio of the effective area of the nuclear surface which can produce π^- at the scattering angle Ψ to the geometrical cross sections πR^2. Curve I: $\epsilon > 100$ Mev. Curve I': $\epsilon < 100$ Mev.

fairly long. If we take the nuclear radius R as the average length of the path inside the nucleus, then the probability for the proton to pass through the nucleus without other collisions is e^{-R/l_p}, and for the two cases $l_p = 4r_0$ and $2r_0$ it becomes about $\frac{1}{3}$ and $\frac{1}{9}$, respectively. The angular distribution of the selected tracks is then to be obtained by multiplying the curves II and II' of Fig. 2 by $F(\Psi)$ and e^{-R/λ_p}. We obtain in this way curves III and III' of Fig. 2. These should correspond to the angular distribution of scattered π^- associated with the production of a single high-energy proton. They seem to be in reasonable agreement with Fry's results.

For the scattered π^- of the type $\epsilon > 100$ Mev which undergo further collisions, the sum of the energies of the high-energy proton and the π^- is smaller than the incident energy. About half of the observed 14 events appear to be of this type. This is not inconsistent with the curve I for $F(\Psi)$ in Fig. 3, which shows that about half of the scattered π^- should have other collisions.

The ratio of the cross section of the ordinary scattering ($\pi^- + p \to \pi^- + p$) to the sum of cross sections for all kinds of pion interactions ($\pi^- + p \to \pi^- + p$, $\pi^- + p \to \pi^0 + n$, $\pi^- + n \to \pi^- + n$ and absorption of π^-) is about 1/10,[6] the ratio of the inelastic scattering with a high-energy proton ($\epsilon > 100$ Mev) to the total inelastic scattering is about 2/9 and the intensity decrease of the high-energy protons by multiple collisions inside the nucleus is 1/3. Hence the total cross section for producing a single high-energy proton is about 1/135 of the geometric cross section of the nucleus. Experimentally, the total cross section for nuclear interactions of π^- with the nucleus in G5 plates is near to σ_{geo} for the 210-Mev incident energy[7] and the relative number of those selected events considered here is about 17/1960~1/110,[8] in agreement with the above estimate.

III. CONCLUSION

An attempt has been made to account for observed nuclear events in which an incident negative pion of energy 220 Mev produces a pion and a high-energy proton. The events appear to be due to the scattering of a pion by a single nucleon on the surface of the nucleus. Their principal characteristics can be understood on the basis of the experimental cross section for scattering of pions by protons, if account is taken of the nucleon motion within the nucleus and of the absorption of scattered pions and protons within the nucleus. Simplifications made for the purpose of calculation and uncertainties in the cross sections make the quantitative results somewhat uncertain, but the qualitative features of the phenomenon can be accounted for in this way.

The author is grateful to Professor W. F. Fry for informing him of the experimental results before publication and for many valuable discussions. Also, he is much indebted to Professor R. G. Sachs for his continuous encouragement and valuable discussions.

[6] The cross section for the processes $\pi^- + p \to \pi^- + p$, $\pi^- + p \to \pi^0 + n$, and $\pi^- + n \to \pi^- + n$ is about 25 mb, 35 mb, and 170 mb, respectively (reference 4). The cross section for the absorption of 210-Mev π^- is small compared to other processes.

[7] A. H. Morrish, Phys. Rev. 90, 674 (1953).

[8] In 1960 of Fry's events, simple stops of pions are not counted. Also, as we are concerned with the interaction of pions with the heavy nucleus, corrections resulting from the interaction of pions with the light nucleus must be taken into account. But these corrections may be considered to be small.

The Interaction and Production of Cosmic-Ray Protons in Carbon*

J. BALLAM† AND P. G. LICHTENSTEIN‡
Department of Physics, University of California, Berkeley, California
(Received September 1, 1953)

Protons in the cosmic radiation at sea level were observed under varying thicknesses of carbon absorber. In the energy range 150 to 570 Mev an interaction mean free path for protons was estimated from the ratio of those emerging from the absorber to those incident upon the absorber and is greater than 140 g/cm² in carbon. The spectrum of protons produced in the carbon by neutral cosmic radiation permits the inference of the flux of neutrons in the cosmic radiation, with the result that neutrons with momenta greater than 550 Mev/c are 6 percent as abundant as all ionizing cosmic radiation at sea level.

I. INTRODUCTION

THE presence of protons in the cosmic radiation at sea level has been well established by the work of Mylroi and Wilson,[1] Merkle, Goldwasser, and Brode,[2] Goldwasser and Merkle,[3] and others.[4] Their data indicate that protons in the energy range of approximately 100 to 300 Mev constitute between 10 and 20 percent of the mesons in this interval and that the total vertical intensity of all protons with energies greater than 420 Mev at sea level is about 1 percent of the mesons of energy greater than 300 Mev. Goldwasser and Merkle have further pointed out that a large fraction of protons observed under various thicknesses of lead absorber could be neutron produced.

In the first part of the present experiment an attempt was made to measure the absorption of the protons incident upon carbon by using the momentum spectrum measured by Mylroi and Wilson to evaluate the number of protons entering the absorber per unit energy interval.

The second part of the experiment was undertaken to gather a larger quantity of data on the proton secondaries and thereby to infer the properties of the neutron radiation. During the course of the experiment, work by Barton[5] was published which indicated the occurrence of a component of high-energy neutrons whose manifest behavior was the production of charged secondaries. The possibility of identifying the charged secondaries of Barton's experiment with the neutral produced proton component of Goldwasser and Merkle depends upon the agreement of neutron spectra inferred from the present experiment and from the experiment of Barton.

II. EXPERIMENTAL METHOD

The apparatus employed in these experiments was, with some modifications, essentially the same as that sued by Goldwasser and Merkle[3] and is shown in Fig. 1. In the first experiment, the carbon absorber consisted progressively of thicknesses of 9.8, 19.6, 44.0, and 88.0 g/cm². In the second experiment, the carbon absorber was fixed at 38.0 g/cm². The upper or "momentum" cloud chamber had an illuminated region 22.3 cm in diameter and depths of 2.5 and 5.0 cm, respectively, in the first and second experiments. It was filled with equal pressures of argon and helium to 96-cm Hg and illuminated by two xenon-filled flash tubes placed behind cylindrical lenses. The chamber was temperature controlled to ±0.2°C and was double-walled throughout. It was operated in an average magnetic field of 4700 gauss.

The lower or "range" chamber had an illuminated region of 52×52×21 cm. It was filled with argon to 100-cm Hg and contained, in the first experiment, four $\frac{1}{8}$-inch and twelve $\frac{1}{4}$-inch copper plates with a single $\frac{1}{4}$-inch lead plate on top to help discriminate against electrons. In the second experiment, the range chamber contained plates of thicknesses and materials arranged in the following order from top to bottom: $\frac{1}{4}$-inch Pb, $\frac{1}{2}$-inch Cu, 0.27-inch Pb, three 1-inch Cu, and three

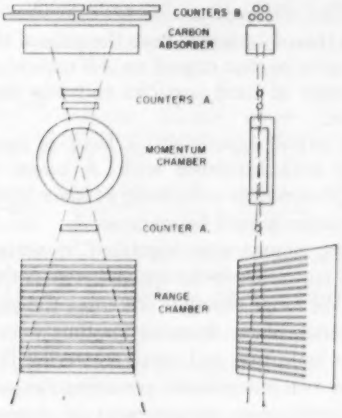

FIG. 1. Diagram of apparatus.

* Assisted by the Joint Program of the U. S. Office of Naval Research and the U. S. Atomic Energy Commission.
† Now at Palmer Physical Laboratory, Princeton University, Princeton, New Jersey.
‡ Now at Department of Physics, University of California, Davis, California.
[1] M. G. Mylroi and J. G. Wilson, Proc. Phys. Soc. (London) **A64**, 404 (1951).
[2] Merkle, Goldwasser, and Brode, Phys. Rev. **79**, 926 (1950).
[3] E. L. Goldwasser and T. C. Merkle, Jr., Phys. Rev. **83**, 43 (1951).
[4] A. L. Rosen (private communication); Henderson, Miller, Potter, and Todd, Phys. Rev. **80**, 133 (1950).
[5] J. C. Barton, Proc. Phys. Soc. (London) **A64**, 1042 (1951).

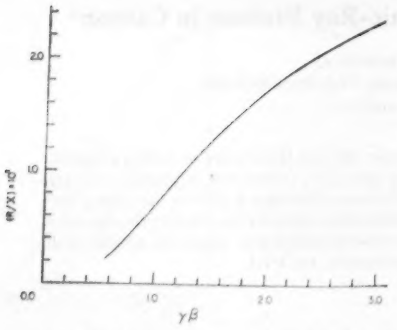

FIG. 2. Mass calculation graph. If $X=(e/m_0c^2)B\rho=5.868\times10^{-4}B\rho$ (with B in gauss and ρ in cm) and R=range of particle in cm Cu equivalent, then ordinate is $R/X\times10^6$ and abscissa is $\gamma\beta$ of the particle. The mass of the particle in electron masses is $X/\gamma\beta$. The curve was calculated from range-energy data for protons.

1.08-inch Pb. Including the ¼-inch Pb plate, which was used solely for discriminating against electrons, the material between the active volume of the momentum chamber and the first absorber plate in the range chamber was equivalent to 1.48-cm Cu in both experiments.

The apparatus was triggered by a triple coincidence of counters A. The solid angle times area of the defining counters A was 0.468 cm²-sterad for the first experiment and averaged 2.30 cm²-sterad in the second experiment. An additional bank of counters B was placed above the carbon absorber and put in coincidence with counters A. An AB coincidence was made to light a neon lamp which was then photographed along with the range chamber. The resolving time of these circuits was 5 microseconds. The purpose of counters B was to determine whether or not the particle observed in the cloud chamber actually had entered the absorber. Since the great majority of events consisted of single fast mu mesons, these appeared as straight tracks in the momentum chamber and went through the range chamber with little or no scattering and were designated as "hard." The efficiency of the AB coincidence arrangement was then determined from the ratio of the number of hard particles that caused an AB coincidence to the total number of hard particles and was found to be 95 percent.

In the second experiment, a bank of counters was placed in anticoincidence with A below the range chamber, covering as completely as space would permit, the solid angle defined by counters A.

Stopping mesons were identified by scattering plus change of ionization in the spaces between the absorber plates in the range chamber preceding the one in which the stop took place. Stopping protons were identified by heavy ionization and small scattering in all plates except the two immediately preceding the stop.

The simultaneous measurement of momentum and residual range for each stopping particle furnished a value for the mass of the particle by calculations made from the graph of Fig. 2. This figure was derived from the numerical integrations of the energy loss formula by Aron,[6] using experimentally obtained values[7] of the excitation potential.

III. FIRST EXPERIMENT

A. Running Time

Since a knowledge of intensities was essential to the interpretation of results, an integral range spectrum of the mu mesons was obtained using the measured solid angle and running time (corrected for the dead time of the cloud chambers) of the equipment. The result is shown in Fig. 3 and is in good agreement with the spectrum given by Rossi.[8] It may be said, therefore, that the operating times quoted in this section of the paper do not have an error greater than 3 percent.

B. Experimental Results

During the course of the experiment 9351 usable pictures were taken in an operating time of 554 hours. Of this total, 6920 were hard particles, 46 were stopping protons, 135 were stopping mesons, and the remainder were mostly single electrons and small electron showers, although penetrating showers, extensive showers, and single stars were observed.

The distribution of stopping particles observed under different thicknesses of carbon is given in Table I.

The absorption of the incident protons in carbon was calculated in the following way. The momentum spectrum of incident protons given by Mylroi and Wilson[1] was converted to an energy spectrum and is shown in Fig. 4. The solid line in this graph is drawn through the points measured by these authors. The dotted line was originally drawn to include the intensity measured by Rochester and Bound[9] and has recently been confirmed by the work of Hodson, Loria, and Ryder at Manchester University.[10] From this spectrum it was possible to calculate the intensity of protons incident on a given

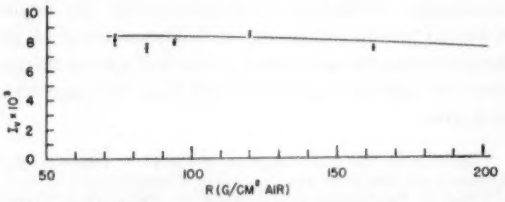

FIG. 3. Integral range spectrum of mesons at sea level. I_v represents flux in particles cm^{-2} sec^{-1} sterad^{-1} and R the range in g cm^{-2} air equivalent. Solid circles represent the data from this experiment; the solid line is the spectrum given by Rossi.

[6] W. A. Aron, Ph.D. dissertation, University of California, 1951 (unpublished).
[7] R. Mather and E. Segrè, Phys. Rev. **84**, 191 (1951).
[8] B. Rossi, Revs. Modern Phys. **20**, 574 (1948).
[9] G. D. Rochester and M. Bound, Nature **146**, 745 (1940).
[10] Hodson, Loria, and Ryder, Phil. Mag. **41**, 286 (1950).

absorber and lying in an energy range such that after ionization loss in the absorber they would stop in the range chamber. The number of protons actually observed to stop under this thickness of absorber will be less than the incident number because some protons will have undergone nuclear scattering or interaction. The geometry was such that all protons scattered by Coulomb forces into a mean half-angle of eight degrees or less from the vertical could be observed, whereas the mean Coulomb scattering angle of protons in this experiment was three degrees. The ratio of observed to incident intensities was used as a measure of the cross section for nuclear scattering and interaction. The data for this calculation are given in Table II. The incident energy band, column (2), was calculated from the range energy curves for protons in carbon[8] and represents the energy limits protons must have on entering a given thickness of absorber if they are to emerge with energies between 90 and 350 Mev. Protons in this latter energy band would stop in the range chamber. Column (3) represents the incident vertical intensity of protons in the corresponding energy band as calculated from the curve of Fig. 4. Column (4) is a correction of column (3) based on the fact that the intensity of protons under no absorber as measured in this experiment is greater by a factor of 1.2 over the intensity measured in the same energy band by Mylroi and Wilson.[1] The points plotted by the above authors were obtained by multiplying the ordinate of the known differential momentum spectrum of mesons at sea level by the ratio of protons to mesons observed in their experiment at some given momentum. The fact that the absolute intensities differ by the amount stated above could be attributed to differences in geometry in the two experiments or to actual differences in intensities, but should not affect the validity of the shape of the spectrum in Fig. 4. The low-energy end of the spectrum has been investigated recently by York,[11] who finds a higher flux of protons of energy less than 150 Mev than did Rochester and Bound[9] and Hodson, Loria, and Ryder.[10] A recent correction to the work of Rochester and Bound by York[12] confirms this higher flux at low energies. If this is the case, one would then expect a higher intensity for the zero point in this experiment. Column (4) represents the observed vertical intensity of stopping protons obtained from the data of Table I, and column (5) is then the ratio of emerging to incident protons.

TABLE I. Proton and meson stops under carbon absorber.

(1) g/cm² carbon	(2) Operating time (hr)	(3) No. of mesons	(4) No. protons with ionizing incident particle	(5) No. protons with neutral incident particle
0	146.0	42	14	0
9.8	49.5	10	5	0
19.6	144.5	38	10	1
44.0	119.0	26	5	4
88.0	95.7	19	4	3

Column (4) is the number stopping and accompanied by an AB coincidence and column (5) is the number stopping and not accompanied by AB coincidence.

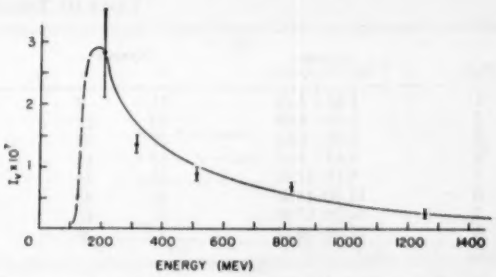

FIG. 4. Differential energy spectrum of protons at sea level. I_e represents flux in particles cm^{-2} sec^{-1} sterad^{-1} (Mev)$^{-1}$ and abscissa, the energy in Mev. The solid circles represent the data of Mylroi and Wilson.

If one assumes an exponential absorption of the form

$$N/N_{0c}=\exp(-X/L), \qquad (1)$$

where X is the absorber thickness in g/cm² and L is the mean free path in the same units, the mean free path can be calculated. The data give a mean value of $L=170$ g/cm² and are not consistent with a value less than 140 g/cm². A reasonable upper limit cannot be given because the thicknesses of carbon used turned out to represent only about one-half a mean free path. In order to obtain an upper limit, one would have to measure intensities under two and three times the maximum thickness used (88 g/cm²). This would have increased the mean Coulomb scattering angle from a maximum of 5 degrees in the present case to about 15 degrees and also necessitated the use of the higher-energy protons, thus drastically reducing the number of incident protons available.

TABLE II. Intensities of incident and emerging protons under carbon absorber.

(1) g/cm² carbon	(2) Incident energy band (Mev)	(3) $N_0\times10^7$	(4) $N_{0c}\times10^7$	(5) $N\times10^7$	(6) N/N_{0c}
0.0	90–350	4.0 ±0.8	5.6	5.6±1.5	1.0 ±0.27
9.8	150–380	4.5 ±0.9	6.1	5.9±2.6	0.97±0.46
19.6	195–410	3.6 ±0.7	4.9	4.1±1.3	0.84±0.32
44.0	290–470	2.35±0.4	3.2	2.5±1.0	0.78±0.35
88.0	410–570	1.7 ±0.5	2.3	2.5±1.3	1.1 ±0.65

(2): energy limits for an entering proton if it is to stop in range chamber and lose energy by ionization alone.
(3): vertical intensity of protons in the corresponding energy band of column (2).
(4): correction to column (3) based on present experiment data with no absorber.
(5): observed vertical intensity of stopping protons.
(6): ratio of emerging to incident protons.

Error in (6) represents combined statistical error in (3) and (5).

[11] C. M. York, Phys. Rev. **85**, 998 (1952).
[12] C. M. York, Proc. Phys. Soc. (London) **A65**, 558 (1952).

TABLE III. Identified stopping particles.

Plate	Range (cm Cu equiv.)	Mesons +	Mesons −	Protons acc.	Protons unacc.	Solid angle area (cm²-sterad)[a] Mesons⁺	Mesons⁻	Protons
1	1.48– 2.75	11	8	1	8	1.17 (*m*)	0.66 (*m*)	1.94 (*m*)
2	2.75– 4.08	20	25	7	6	1.37 (*m*)	1.37 (*m*)	2.28 (*m*)
3	4.08– 6.62	27	38	8	5	1.54 (*m*)	1.54 (*m*)	2.30
4	6.62– 9.16	33	45	3	2	1.60	1.60	2.30
5	9.16–11.70	35	35	6	4	1.64	1.64	2.34 (*m*)
6	11.70–14.36	42	45	2	1	1.68	1.68	2.30
7	14.36–17.02	37	41	3	2	1.72	1.72	2.20
8	17.02–19.68	27	26	1	0	1.76 (*m*)	1.76 (*m*)	2.15 (*m*)

[a] (*m*) indicates solid angle actually measured.

IV. SECOND EXPERIMENT

In the second experiment 6162 usable pictures were taken during a total sensitive time of 123 hours. In Table III are summarized the results for identified stopping particles with the protons classified as "accompanied" or "unaccompanied" according to whether the master coincidence was an AB or an A without B. The former represent cosmic-ray protons and the latter protons locally produced by neutral cosmic radiation. The effective solid angle area available to protons of different ranges were measured for several absorber plates and interpolated for others, their variation becoming small beyond the second absorber plate.

Calculation of the flux of incident cosmic-ray protons proceeds in the following fashion: the momentum limits for protons stopping in various absorber plates, after account is taken of momentum loss in the 38 g/cm² carbon above the apparatus are listed in Table IV, column (2). Allowance for loss of protons from the beam due to nuclear interaction involves the application of the usual correction factor,

$$n_0/n_i = \exp\{-\sum x_i/\lambda_i\}, \qquad (2)$$

where x_i is the element of material traversed and λ_i is a mean free path for nuclear interaction of the type to cause a proton to be lost. Absorption measurements[13] on artificially accelerated neutrons indicate that λ_i is approximately twice the total mean free paths for energies above 120 Mev and continues at this value up to the highest energies obtainable. For C, Cu, and Pb, respectively, these λ_i would be 137, 178, and 234 g/cm². The value of 137 g/cm² for C also would be in agreement with the data of the first experiment. The use of these cross sections to compute the attenuation of the proton beam would assume that the neutron cross sections were equal to the proton cross sections and that these values were preserved up to 500 Mev.

TABLE IV. Protons with accompanied master pulse.

Range design	Momentum limits above 38-g/cm² C (Mev/*c*)	*N*	cm²-sterad	n_0/n_i	Flux[a]
1	757– 800	1	1.94	0.704	1.35±0.43
2	800– 842	7	2.28		
3	842– 915	8	2.30	0.618	1.24±0.26
4	915– 983	3	2.30		
5	983–1044	6	2.34	0.478	1.33±0.32
6	1044–1105	2	2.30		
7	1105–1164	3	2.20	0.368	1.00±0.34
8	1164–1217	1	2.15		

[a] cm⁻² sterad⁻¹ sec⁻¹ (Mev/*c*)⁻¹ ×10⁷.

In Table V are shown the calculations of the attenuation factors,

$$\exp\{-\sum x_i/\lambda_i\},$$

and in Table IV the flux of protons with accompanied master pulse is calculated. In Fig. 5, the results have been plotted on double logarithmic scale, together with results of previous observers where applicable.

The upper limit of penetrating shower contributions to the measured flux of protons can be estimated by the following procedure: Froehlich *et al.*[14] find a geometric mean free path for the production of penetrating showers by ionizing radiation having energies greater than 1 Bev. From estimates of the energy of the penetrating shower producing primary, they arrive at a flux of primaries in good agreement with the results of Mylroi and Wilson for flux of cosmic-ray protons. If we consider protons of energy greater than 1 Bev to be penetrating shower primaries and assume that in every penetrating shower a single low-energy proton is produced which is recorded by the apparatus, we obtain an upper limit for the contribution of penetrating showers to the measured flux of low-energy protons. The mean free path for penetrating shower production is taken as 69 g/cm² in carbon. The result of the calculation of rate of penetrating showers is that, at most, 20 percent of the observed particles were produced in penetrating showers. This fraction should, of course, be somewhat reduced, in that not all penetrating showers will contribute a single low-energy proton.

Since the neutral-produced protons originate in the carbon absorber above the apparatus, the momenta of observed protons must be corrected for energy loss in the absorber. This loss will be a function of the position

[13] Fox, Leith, Wonbers, and MacKenzie, Phys. Rev. **80**, 23 (1950).

[14] Froehlich, Harth, and Sitte, Phys. Rev. **87**, 504 (1952).

of origination of the proton, which in turn can vary over the entire thickness of the absorber. For determination of a probability distribution of momentum loss, it is necessary to derive an expression for the probability distribution of the point of creation. If the neutral primary radiation has an inelastic mean free path λ_{in}, then the number of neutral primaries penetrating to a depth x in the absorber will be

$$N_n(x)=N_n(0)\exp\{-x/\lambda_{in}\}. \quad (3)$$

If this neutral radiation has a mean free path of λ_{np} for the creation of protons, then in a thickness dx at x, the number of protons produced will be

$$N_p(x)dx=N_n(x)dx/\lambda_{np}, \quad (4)$$

and, finally, the number of emergent protons from an absorber of thickness t when produced at depth x will be

$$N_p(t)=N_p(x)\exp\{-(t-x)/\lambda_{ip}\}, \quad (5)$$

where λ_{ip} is the inelastic mean free path for protons in carbon.

Combining Eqs. (3), (4), and (5), we have for the total number of emergent protons produced at depth x

TABLE V. Calculation of attenuation factors.

Range group	x_i(g/cm²)	n_0/n_i
1 and 2	38 C+13.2 Cu	0.704
3 and 4	11.4 Cu+15.5 Pb+above line	0.618
5 and 6	2×22.8 Cu+above line	0.478
7 and 8	22.8 Cu+31.0 Pb+above line	0.368

in a thickness dx

$$N_p(t)dx=N_n(0)\exp\left\{-\frac{x}{\lambda_{in}}-\frac{t-x}{\lambda_{ip}}\right\}\cdot dx/\lambda_{np}. \quad (6)$$

For a primary radiation consisting of neutrons, it would seem reasonable that the inelastic cross sections for protons and neutrons are equal because of the symmetry of the carbon nucleus. Thus $\lambda_{in}=\lambda_{ip}$. It follows that

$$N_p(t)dx=N_n(0)\exp\{-t/\lambda_{ip}\}dx/\lambda_{np}, \quad (7)$$

$$N_p(t)=N_n(0)\exp\{-t/\lambda_{ip}\}t/\lambda_{np}, \quad (8)$$

and protons emerging from the carbon absorber have been produced with equal probability in all depths x of the absorber. Hence, the average point of creation, average momentum, and approximate half-width of momentum band at point of creation for protons stopping in a particular absorber plate in the range chamber are those values associated with production at the center of the carbon.

From Eq. (8) we see that the neutron spectrum is proportional to the spectrum of protons emerging from the carbon absorber $N_p(t)$. This quantity can be obtained from the data on protons with unaccompanied master pulse. Furthermore, the factor $\exp\{t/\lambda_{ip}\}$ in

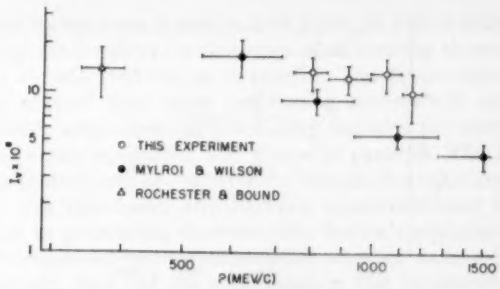

FIG. 5. Differential momentum spectrum of protons at sea level. I_p represents flux in particles cm^{-2} sec^{-1} sterad^{-1} (Mev/c)$^{-1}$ and P, the momentum in Mev/c. Open circles are data of Mylroi and Wilson; solid circles, data of this experiment; and open triangle, data of Rochester and Bound as corrected by York.

Eq. (8) is identical in form to the attenuation correction factor employed with protons with accompanied master pulse. Therefore, calculation of the quantity $N_p(t)\exp\{t/\lambda_{ip}\}$ from the data on protons with unaccompanied master pulse would be identical to the calculation of I_p for protons from the data on protons with accompanied master pulse. In Table VI are shown the calculated $N_p(t)\exp\{t/\lambda_{ip}\}$. This quantity, as a function of momentum, is shown in Fig. 6 and, if assumed to be of the form Cp^{-k}, is best represented with $C=63.4$ and $k=3.0$. The neutron flux is then obtained by inserting this expression into Eq. (8).

V. DISCUSSION OF RESULTS

A. First Experiment

The measurement made in the first experiment of the inelastic cross section for protons in carbon can be considered only as a suggestion of how this cross section behaves as a function of energy because of the very large statistical errors involved. In addition, there is still a correction to be applied for the fact that more protons can be scattered into the solid angle by nuclear scattering than will be scattered out and also for the fact that protons that enter the absorber with energies above 1 Bev can produce secondary protons which could be seen to stop in the range chamber. Either of these effects would make the measured mean free path

TABLE VI. Protons with unaccompanied master pulse.

Range design	N	Momentum interval (Mev/c) (produced at center)	$N_p(t)\exp\{t/\lambda_{ip}\}$ cm^{-2} sec^{-1} sterad^{-1} (Mev/c)$^{-1}$ ×10^7
1	8	635– 698	1.84 ±0.33
2	6	698– 753	
3	5	753– 835	0.732±0.19
4	2	835– 905	
5	4	905– 979	0.734±0.22
6	1	979–1043	
7	2	1043–1104	0.469±0.22
8	0	1104–1162	

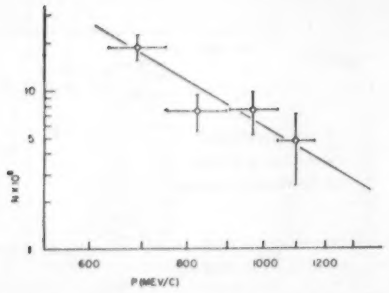

FIG. 6. $N_p(t)\exp\{t/\lambda_{ip}\}$ *vs* momentum. N represents $N_p(t)\times\exp\{t/\lambda_{ip}\}$ in particles cm^{-2} sec^{-1} $sterad^{-1}$ $(Mev/c)^{-1}$ and P, the momentum in Mev/c. Open circles are the calculated points. The solid line is the least-squares fit of the data to a straight line on a logarithmic plot of both scales and has the form $N=63.4P^{-3.0}$.

longer than the interaction mean free path. However, none of the protons which stopped in the lower chamber were observed to suffer a nuclear scatter (>15 degrees) which indicates that nuclear scattering will not have a large effect on the lower-energy incident protons. In addition, since the intensity of protons with energy greater than 1 Bev is only 10 percent of the number with lower energies, the secondary protons will not significantly contribute to the results. However, the measured mean free path using 88 g/cm² of carbon absorber may show a slight increase over the values obtained under the other thicknesses used, indicating that the above two effects are beginning to make their presence felt when the mean free path is measured for incident protons in the energy range 410–570 Mev.

The mean free path for nuclear interaction of the incident protons corresponds to a cross section per nucleus which is 0.38 of geometric. If the total interaction cross section per nucleus is written as

$$\sigma_{\text{interaction}}(\text{geometric})=\pi R^2 A^{\frac{1}{3}},$$

where $R=1.4\times10^{-13}$ cm, this becomes, for carbon,

$$\sigma_{\text{interaction}}(\text{geometric})=0.33 \text{ barn}.$$

The value obtained in this experiment is then

$$\sigma_{\text{interaction}}(\text{measured})=0.13 \text{ barn}.$$

This is partially substantiated by the work of DeJuren and Moyer,[15] who measured the total absorption cross section for neutrons in carbon in an experiment with the Berkeley 184-inch cyclotron. They found that this cross section is essentially flat in the energy range 180–340 Mev. Using carbon as the target nucleus, the absorption of protons and neutrons may be assumed to be the same. This cross section was 0.288 barn. Now if the cross section for interaction is assumed to be on the order of one-half the total absorption cross section, their value becomes $\sigma_{\text{interaction}}=0.144$ barn, a result in good agreement with the present experiment. The closeness of the agreement is however fortuitous in view of the large statistical errors inherent in the present work.

Further evidence of the small loss of energy to nuclei by intermediate-energy protons is given by the recent analysis of stars produced in photographic emulsions by Camerini *et al.*[16] They found that protons of energy between 200 Mev and 1 Bev lose energy for the most part by elastic nuclear scattering and that the interaction cross section for protons does not become geometric until energies above 2 Bev are reached at which point mesons begin to be produced copiously. The present experiment together with the above-mentioned results give a picture of a small interaction nucleon-nucleon cross section at 180 Mev rising very slowly with energy to a geometric value somewhere near 2 Bev since it is known that penetrating shower-producing particles have an interaction cross section very close to geometric. This same conclusion is reached by Puppi and Dallaporta[17] in their review article.

B. Second Experiment

Neutral-Produced Protons

From (8) we have

$$N_n(0)=63.4p^{-3.0}\cdot\lambda_{np}/t. \tag{9}$$

λ_{np} is defined as the mean free path for a neutral primary to produce a proton of approximately the same momentum as the primary and within an angle of approximately 20° to the direction of the primary. Experiments with artificially accelerated neutrons striking carbon indicate that the secondary protons are ejected in a predominantly forward direction with energies approximating the energies of the incident neutrons. The contribution to the proton energy by the internal motion of the carbon nucleus could not be resolved due to lack of homogeneity of the neutron beam and in this experiment is ignored. The cross section for production of protons in carbon by neutrons, which must be smaller than the inelastic cross section for neutrons in carbon, is taken at about half the inelastic neutron cross section, or approximately 280 g/cm². With this value, and $t=38$ g/cm², the neutron spectrum becomes

$$N_n(0)=467p^{-3.0}. \tag{10}$$

Barton quotes an integral value of his neutron flux, i.e., the number of neutrons having momentum greater than the lowest detectable secondary momentum in his experiment constitute 4.5 percent of the ionizing radiation at sea level. In order to compare the flux measured in the present experiment with Barton's result, it is necessary to compute the lowest detectable secondary momentum in Barton's experiment. From

[15] J. DeJuren and B. J. Moyer, Phys. Rev. **81**, 919 (1951).

[16] Camerini, Davies, Fowler, Franzinetti, Lock, Perkins, and Yekuteli, Phil. Mag. **42**, 1241 (1951).

[17] G. Puppi and N. Dallaporta, *Progress in Cosmic Ray Physics* (Interscience Publishers, Inc., New York, 1952), p. 374.

the data given in his work, this value is computed to be 550 Mev/c. Therefore, from his results, the neutron flux at sea level, for all neutrons of momentum greater than 550 Mev/c is 4.5 percent of the ionizing radiation. A comparison figure from the present experiment is obtained by integrating Eq. (10) between the momentum limits 550 Mev/c and infinity. The result is that the flux of neutrons, from the present experiment, constitutes in abundance 6 percent of the flux of ionizing particles in the cosmic radiation at sea level. The discrepancy between 6 percent from this experiment and 4.5 percent from Barton's experiment is probably due to a true difference in triggering events rather than simply to statistical fluctuations. Penetrating showers detected in this experiment but not in Barton's experiment could account for most of the difference in results.

In the estimation of the contribution of penetrating shower secondaries to the observed flux of protons with unaccompanied master pulse, the same procedure is employed as before in determining the contribution of penetrating shower secondaries to the observed flux of protons with accompanied master pulse. Here it is assumed that Eq. (10) describes the neutron flux at all high energies, that neutrons of energy greater than 1 Bev produce penetrating showers, that in these penetrating showers a single proton is detected, and that the mean free path for penetrating shower production by neutrons in carbon is 69 g/cm^2. It is then found that the maximum contribution of penetrating showers to the observed flux is 36 percent. This figure should be reduced since many penetrating showers will contribute single mesons, penetrating particles traversing the entire equipment, and groups of particles. The 25 percent discrepancy between the integral flux calculated in this experiment and Barton's experiment may be due to penetrating showers since Barton's equipment discriminated against penetrating showers more adequately than did the equipment in this experiment. The qualitative effects of the result, Eq. (10), are in agreement with the findings of other studies[18] of the neutral nucleon component. The strong exponent in the momentum power law description of neutrons contrasted with that for protons implies a larger flux of neutrons than protons at momenta below 1 Bev/c. At greater momenta, the neutron and proton fluxes vary in approximately the same fashion.

The writers would like to express their thanks to Professor R. B. Brode and to Professor W. B. Fretter for helpful discussions and advice; to Mr. M. L. MacKnight and Mr. E. Mundt, who designed a part of the equipment and helped to maintain it; and to Mr. J. Lipson, who processed all of the film.

[18] J. G. Wilson, *Progress in Cosmic Ray Physics* (Interscience Publishers, Inc., New York, 1952), p. 362.

Differential Range Spectrum of Cosmic-Ray Mesons at Sea Level*

PHILIP G. LICHTENSTEIN†
Department of Physics, University of California, Berkeley, California
(Received September 1, 1953)

Operation of a cosmic-ray mass-measuring equipment under 8.8 inches of carbon absorber for 123 hours of sensitive time yielded 495 stopping mesons identifiable by their momentum *vs* residual range. After correction for zenith-angle and solid-angle dependence of the stopping particles, it is found that the spectrum of mu mesons for residual ranges 40–105 g/cm² air equivalent is flat and has an intensity of approximately 6.0×10^{-6}/g-sec-sterad.

It is shown that the results of York, when corrected for a very heavy background of electrons at small ranges, yield a μ-meson spectrum in good agreement with the present work.

INTRODUCTION

DURING the course of a recent experiment[1] on the nucleon component in the cosmic radiation, a large amount of data was simultaneously accumulated upon the range distribution of cosmic ray mesons at sea level in the interval 40–150 g/cm² air equivalent range. Since the results of York,[2] who studied the same problem in the same range interval, seemed to indicate a discrepancy of about 20 percent with other[3] investigators' results, it appeared useful to analyze the data available from the previous experiment to consider the nature of the discrepancy.

EXPERIMENTAL

The equipment, as described in reference 1, operating under 8.8 inches of carbon absorber consisted of a magnetic cloud chamber, under which was situated a large multiplate cloud chamber. The upper chamber served to determine the momentum of cosmic-ray particles which stopped in the lower range chamber due to ionization loss. A knowledge of two variables of the particle's motion, momentum *vs* residual range afforded a unique mass determination for the particle. An additional check upon the nature of the particle was afforded by observation of scattering and ionization *vs* residual range in the range chamber.

Momentum measurements were made by means of the sagitta *vs* chord-length method with a traveling stage microscope upon photographs of the particle tracks in the magnetic cloud chamber. Frequent measurements of the tracks of hard particles traversing the chamber while the magnet was turned off were made to afford a check upon the various sources of track distortion.

The range chamber contained absorber plates of the following materials and thicknesses in order from top to bottom: one ¼-inch Pb plate, one ½-inch Cu plate, one ½-inch Pb plate, three 1-inch Cu plates, and three 1-inch Pb plates. Mesons judged to have stopped because of ionization loss were required to scatter strongly in the last two or three plates traversed, the expected scattering being approximately 20° per plate, and were required to be at minimum ionization to within one plate above the stopping plate.

The ¼-inch Pb plate at the top of the range chamber served to distinguish electrons from mesons, and particles stopping in this plate were not analyzed. Any particle producing one or more secondaries in this plate and stopping in the next plate was considered to be an electron and was not analyzed further. The contribution of nonshowering electrons to the meson spectrum will be considered in the Appendix.

DATA

During a total sensitive time of 123 hours, 495 particles satisfying mass, scattering, and ionization criteria for μ mesons were observed to stop in the range chamber. In Table I is shown the distribution of mesons among the various absorber plates.

REDUCTION OF DATA

In calculating absolute values for the fluxes of mesons, it is necessary to know the solid angle area available

TABLE I. Differential meson spectrum. Range in g/cm² air equivalent. N refers to number of observed mesons at particular range interval. $\sigma\Omega$ is the area-solid angle factor for particular range interval in cm²-steradians. I_v is the computed vertical differential meson intensity in sec^{-1} $sterad^{-1}$ $g^{-1}\times10^6$

Plate	Range interval	N	$\sigma\Omega$	I_v
1	47.13– 55.76	11+	1.17	
		8–	0.664	7.17±0.72
2	55.76– 64.83	45	1.37	
3	64.83– 82.09	65	1.54	5.37±0.45
4	82.09– 99.35	78	1.60	6.40±0.49
5	99.35–116.61	70	1.64	5.60±0.46
6	116.61–134.71	87	1.68	6.48±0.47
7	134.71–152.81	78	1.72	5.68±0.43
8	152.81–170.91	53	1.76	3.77±0.35

Mass stopping powers relative to air used:
Cu: 0.761; Pb: 0.574; C: 0.979.

* Assisted by the Joint Program of the U. S. Office of Naval Research and the U. S. Atomic Energy Commission.
† Now at the Department of Physics, University of California, Davis, California.
[1] J. Ballam and P. G. Lichtenstein, preceding paper [Phys. Rev. 93, 851 (1954)].
[2] C. M. York, Phys. Rev. 85, 998 (1952).
[3] For a compilation of recent results, see L. Del Rosario and J. Davila-Aponte, Phys. Rev. 88, 998 (1952).

to particles stopping in the equipment. In the absence of a magnetic field, this quantity,

$$\int_{s_1}\int_{s_2}\frac{(\mathbf{ds}_1\cdot\mathbf{r})(\mathbf{ds}_2\cdot\mathbf{r})}{r^4},$$

is readily calculated analytically. For the case of a magnetic field present, it proved advantageous to use a method combining analytical and graphical techniques to calculate the solid angle-area factors. A half scale diagram of the apparatus was drawn, including the geometrically interesting quantities such as solid angle defining counters, visible region of the magnetic cloud chamber, and visible region of the range chamber. Each plate in the lower chamber was divided into 1-inch segments laterally, and the allowable regions on the top counter of the solid angle defining counters from which mesons could originate in order to strike a given segment of absorber plate was determined. Simultaneously, the upper and lower zenith angles and distance along the trajectory from top counter to absorber plate were measured. For the purpose of taking into account the fact that zenith-angle dependence of particles will make certain elements of solid angle less effective than others in calculating a vertical intensity, the measured element of solid angle was multiplied by a factor $\cos^n\theta$, where θ is the entering zenith angle. Zar and Shamos[4] and Kraushaar[5] have measured the zenith angle dependence of μ mesons, and n is found to vary from 3.2 to 2.0 for mesons of average energy 235 and 890 Mev, respectively. Since the incident zenith angles were appreciable only for low-energy mesons in this experiment, which have energies at the lower limit of Zar and Shamos' work, n was taken as 3.0. Solid angle-area measurements were for absorbers 1, 2, 3, and 8, and the other values interpolated.

Because of the situation of an ammeter on the range chamber, positive and negative mesons had different available solid angle area for stopping in the first plate. For this reason, positive and negative mesons stopping in plate one are listed separately in columns three and four of Table I.

Calculation of the range intervals in terms of g/cm² air equivalent, a commonly quoted unit of measure, utilized the mass stopping power of various materials for 340-Mev protons as measured by Bakker and Segrè.[6] Although the velocities of mesons traversing the material in the range chamber were those corresponding to protons of energies between 300 and 2500 Mev, the variation in stopping power ratios of the several materials is small as can be seen from tables for dE/dx *vs* E.

Range intervals 1 and 2 have been combined to yield a range interval approximately the same size as the others in Table I.

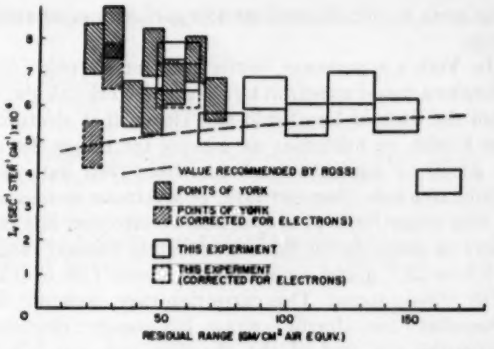

FIG. 1. Differential range spectrum of μ mesons. The ordinate represents vertical intensity in sec^{-1} sterad^{-1} $\text{g}^{-1}\times10^9$. The abscissa is range in g/cm² air equivalent.

In Fig. 1 is shown I_r, the differential meson intensity, as a function of range in g/cm² air equivalent. The probable errors of data represent the errors based on counting statistics, $0.675/\sqrt{n}$, where n is the number of counts. The horizontal spread of points is the spread of the particular absorber plates. The figure also includes the results of York and the value recommended by Rossi.[7]

DISCUSSION OF RESULTS

The resulting differential range spectrum of μ mesons would seem to indicate a fairly uniform value for the flux between ranges of 60 and 150 g/cm² air equivalent. The value, however, appears to lie approximately 10 percent higher than that recommended by Rossi although appearing to give a better fit to the data of York, where applicable. No great importance should be given to the high value for the flux at small range since azimuthal corrections were very large in this experiment for mesons of short range; on the other hand, the agreement at this point with the value of York would appear to be more than fortuitous. In the Appendix it is shown that electrons of correct momentum could be mistaken for mesons stopping in the first Cu plate with approximately 7 percent probability and in the first Pb plate with 4 percent probability. If the number of electrons in equal momentum intervals were a small fraction of the number of mesons, this effect would be negligible, but according to the data of Lombardo and Hazen[8] there are 1.6 times as many electrons as mesons in the momentum interval 100–200 Mev/c, the momenta appropriate to the ranges considered. Hence, it follows that roughly 8 percent of the measured particles at the smallest ranges are electrons. With this correction, also shown in Fig. 1, a fairly uniform value of 6.0×10^{-6}/g-sec-sterad would

[4] J. L. Zar and M. H. Shamos, Phys. Rev. **79**, 207 (1950).
[5] W. L. Kraushaar, Phys. Rev. **76**, 1045 (1949).
[6] C. J. Bakker and E. Segrè, Phys. Rev. **81**, 74 (1945).
[7] B. Rossi, Revs. Modern Phys. **20**, 574 (1948).
[8] B. Lombardo, Jr., and W. E. Hazen, Phys. Rev. **68**, 74 (1945).

thus seem to obtain from 40–150 g/cm² air-equivalent range.

In York's experiment, corrections for electron contributions would appear to be too small. York calculates from the data of Lombardo and Hazen that electrons are 1/20th as numerous as mesons for ranges 18 to 34 g/cm² air equivalent, whereas from their data one would conclude that the ratio of electrons to mesons in this range interval is 4.6. This recorrection has the effect of changing the flux value for his smallest range (17.9 to 25.7 g/cm² air equivalent) from 7.69 to 5.26 $\times 10^{-6}$/g-sec-sterad. This correction may, however, be somewhat too drastic, since low-energy electrons traversing the roof of the chamber and two ½-inch Pb plates used in York's experiment will scatter considerably more than mesons and might thereby be subjectively distinguished and rejected.

The results of York and of this experiment, after correction for electrons, give a consistent value approximately 10 percent higher than Rossi. That this remainder can be accounted for solely by electrons is doubtful; a small percentage of locally-produced π mesons could possibly account for the remainder. Delayed coincidence techniques utilizing scintillation counters would appear to be the only adequate method of resolving this difficulty since the characteristic lifetime of the μ meson would then distinguish these particles unequivocally.

The writer wishes to express his thanks to Professor Robert B. Brode for his help in directing the research and preparing this paper and to Dr. C. M. York for a very helpful discussion of the results.

APPENDIX

The contribution of electrons to the μ-meson spectrum may be calculated in the following manner: in order to be mistaken for a meson, an electron must have a momentum between 100 and 200 Mev/c and to stop in one of the absorber plates in the range chamber, unaccompanied through any plate by secondary shower particles. For an electron of approximately 100 Mev, the probability of traversing the ½-inch Pb plate and of emerging unaccompanied by secondaries is by Monte Carlo method equal to[9] 0.7. The electron's probability of stopping in the plate immediately below, the ½-inch Cu plate, is 0.1. Hence, the probability for an electron to be mistaken for a meson stopping in the first absorber plate is the product of the above probabilities, 0.07.

On the other hand, the electron may emerge from the ½-inch Cu plate and produce no secondary shower particle with probability 0.55. Its probability of stopping in the next plate, ½-inch Pb, is 0.1. The probability for an electron to be mistaken for a meson stopping in the second absorber plate is then the product of three probabilities: the probability for penetrating the ½-inch Pb plate without showering, the probability for penetrating the ½-inch Cu plate without showering, and the probability for stopping in the 0.54-inch Pb plate without secondaries. The product yields 0.04.

To determine the contribution of electrons to the μ-meson flux, one has merely to combine these probabilities with the electron flux. This is done in the section on Discussion of Results.

[9] R. R. Wilson, Phys. Rev. 86, 261 (1952). Use has been made of the curves of Fig. 1 of this paper to calculate results for electron initiated showers.

Production of Heavy Unstable Particles by Negative Pions*

W. B. FOWLER, R. P. SHUTT, A. M. THORNDIKE, AND W. L. WHITTEMORE
Brookhaven National Laboratory, Upton, New York

(Received November 10, 1953)

In addition to two previously discussed cloud-chamber examples of V-particle production by 1.5-Bev π^- mesons from the Cosmotron, four further examples are discussed here. In two of the new examples a $\Lambda^0(V_1^0)$ and a $\vartheta^0(V_4^0)$ are seen to decay in a geometry indicating that they were produced together in a $\pi^- - p$ collision. A third example is best interpreted as production of a $\Lambda^-(V_1^-)$ together with a $K^+(V_2^+)$ by a π^- colliding with a proton. A fourth example shows a probable Λ^- decaying into a π^- and a neutron with a Q value of about 130 Mev. A cross section of $\sim$1 millibarn for V-particle production is inferred from the number of $\pi^- - p$ collisions observed.

IN a previous letter[1] we have reported two examples of Λ^0 particles[2] produced in hydrogen by negative pions (π^-) of 1.5-Bev kinetic energy. For both examples it was shown that if there were only two resulting particles the second was a K^0 particle of a mass of about 650 Mev. Since, however, the K^0 was not seen to decay it was also possible to balance energies and momenta by assuming two lighter neutral particles (including π^0) instead of one K^0 in addition to the Λ^0.

Observations on heavy unstable particles in cosmic radiation indicate lifetimes as long as 10^{-10} to 10^{-9} second with production cross sections at least 10^{-2} times those for π mesons. These facts can be reconciled theoretically[3] if it is assumed that the particles must be produced doubly (two at a time). Different particles may be produced simultaneously, in addition to pairs of identical ones. It appears that no evidence for double production of such particles, exceeding purely statistical coincidence, has been reported in cosmic radiation although a few examples might perhaps be interpreted in this manner.[4] The two examples of production in hydrogen reported by this group indicate multiple production. This interpretation is uncertain, however, since the K^0 particles are not observed to decay and the computed masses are higher than the value of about 500 Mev most commonly found for K particles.

We now wish to describe three additional cases where double production of heavy unstable particles by 1.5-Bev π^- is indicated with more certainty then in the previous two examples. We shall refer to the previous examples as cases A and B. Case C shows a Λ^0 together with a ϑ^0 probably produced in a heavy nucleus. Case D shows the same combination produced in hydrogen. Case E shows what may well be a Λ^- together with a K^+ with mass of about 500 Mev produced in hydrogen. A few cases of Λ^+ have been observed in cosmic radiation[5,6] but evidence for Λ^- is less certain. In a fourth case, called F, we shall describe an additional example best interpreted as a Λ^-.

Details of the experimental method will be described in a later article. A diffusion cloud chamber filled with 20 atmospheres of hydrogen was exposed to a 1.5-Bev π^- beam produced in a carbon target by the 2.2-Bev circulating proton beam in the Cosmotron. The pions were selected and collimated by the field of the Cosmotron magnet and a channel in the concrete shielding around the machine. The beam thus obtained is quite monoenergetic with a spread probably less than ± 0.1 Bev. The beam was finally deflected by a magnet into a concrete house containing the cloud chamber mounted between the pole faces of a magnet providing an average field of 10 500 gauss. This magnetic field has been calibrated to 1 percent accuracy and its vertical and horizontal components have been mapped throughout the chamber.

The examples to be described were obtained out of a total of 26 000 photographs obtained at a rate of one every 7 to 8 seconds. In addition many examples of V events were found for which no associated V event or nuclear interaction in the gas was observed. Finally, we have observed about 170 pion interactions in hydrogen, most of which lead to single and multiple production of pions. These will be described in a later article.

CASE C: Λ^0 WITH ϑ^0

Figure 1 (case C) shows a photograph of two V events, of which (a) is considered to be a Λ^0, and (b) a ϑ^0. Data which lead to this identification are given in Table I. Row 2 gives the momenta as measured on the 35-mm film by means of a Cooke microscope. The measure-

* Work performed under the auspices of the U. S. Atomic Energy Commission.

[1] Fowler, Shutt, Thorndike, and Whittemore, Phys. Rev. **91**, 1287 (1953).

[2] We are using here the nomenclature suggested for V events at the International Congress on Cosmic Radiation, Bagnères-de-Bigorre, France. Accordingly $\Lambda^{0,+,-} \rightarrow$ nucleon + pion + Q_Λ; $K^{0,+,-}$ is any particle whose mass falls between those of pion and proton; for example, $\vartheta^0(\rightarrow \pi^+ + \pi^- + Q\vartheta)$ is a K^0.

[3] A. Pais, Phys. Rev. **86**, 663 (1952). References to previous work are cited in this article. A. Pais, Proceedings of the Lorentz-Kamerlingh Onnes Conference, Physica (to be published); M. Goldhaber, Phys. Rev. **92**, 1279 (1953); M. Gell-Mann, Phys. Rev. **92**, 833 (1953).

[4] Leighton, Wanlass, and Anderson, Phys. Rev. **89**, 148 (1953); Fretter, May, and Nakada, Phys. Rev. **89**, 168 (1953); G. D. Rochester and C. C. Butler, Repts. Progr. in Phys. **16**, 364 (1953), give a comprehensive review of cosmic-ray results.

[5] York, Leighton, and Bjornerud, Phys. Rev. **90**, 167 (1953).

[6] International Congress on Cosmic Radiation, Bagnères-de-Bigorre, France (unpublished).

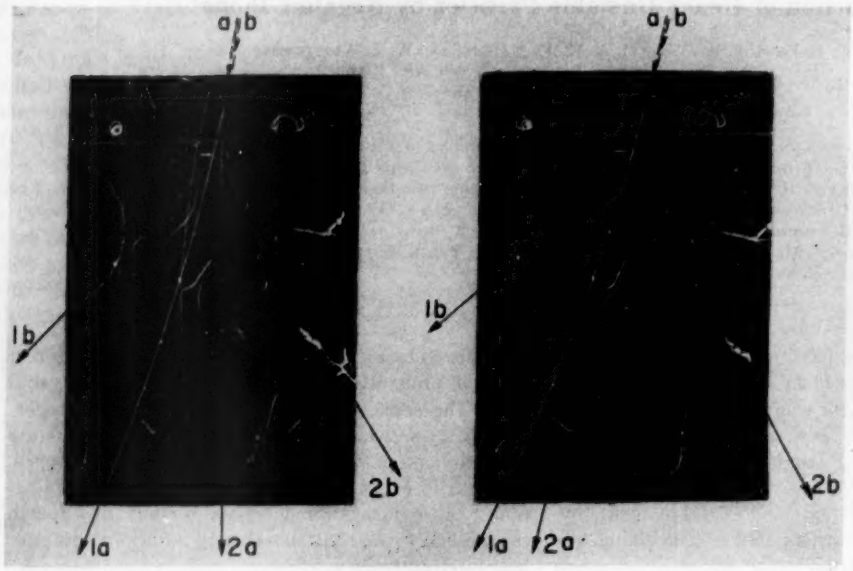

FIG. 1. Case C. Diffusion cloud-chamber photograph of two neutral V particles (a) and (b), whose lines of flight are almost colinear. (a) is believed to be a Λ^0 decaying into a proton (1a) and a negative π meson (2a). Tracks 1a and 2a practically coincide in the right view. (b) is probably a ϑ^0 decaying into π^+ (1b) and π^- (2b).

ments have been corrected for dip angle and space variations of magnetic field and magnification. The mass limits given in row 4 were deduced from measured momenta and estimated ionization densities. Row 5 shows what particle was assumed for further calculation. The angles between tracks in row 6 were obtained from a 3-dimensional reprojecting system as well as by geometrical reconstruction and calculation. The Q value for (a) is, within the given error, consistent with the usually accepted value of 37 Mev for a Λ^0. The Q value for (b) is rather large compared to the best value of 214 Mev given in the literature[7] for a ϑ^0.

From the measured momenta and angles in space for each track one can infer that the lines of flight of the Λ^0 and ϑ^0 practically coincide. From the total number of Λ^0 and ϑ^0 (originating in the walls) found in the 26 000 pictures one concludes that the probability for random association of the two particles in such a geometry is $\sim 10^{-9}$. We therefore should be justified in assuming that the Λ^0 and ϑ^0 were produced in one act. Since no incident particle is visible in the chamber and since the Λ^0 and ϑ^0 travel at an angle of about 24° upwards from the bottom of the chamber, we assume that they were produced in or below the bottom glass plate, though probably not much further down since the pion beam was fairly well collimated. The origin must, of course, lie on the line of intersection of the decay planes of the Λ^0 and ϑ^0. Both particles travel in directions between 0.5° and 1.5° to this line for a range of reasonable choices for the position of the origin.

The following procedure can now be used to determine the Q values more accurately than before. Since we know the directions of the lines of flight of Λ^0 and ϑ^0 with fair certainty we can deduce the momentum of one decay product in each V event from the momentum of the other. As row 2, Table I, shows, the momenta of 1a and 2b are known much better than those of 1b and 2a. We therefore have deduced the momenta of 1b and 2a. For the momenta of 1a and 2b we have chosen their lowest values within the given experimental errors. This choice will result in somewhat lower Q values than calculated above. The new momenta are given in row 8 and the recalculated Q values in row 9. The indicated remaining errors are now mainly due to the mentioned uncertainty in the directions of flight of Λ^0 and ϑ^0. The Q value for the ϑ^0 is still not in good agreement with the usual value of 214 Mev.

From the momenta in row 8 and the given angles one finds the momenta of Λ^0 and ϑ^0 given in row 10. Assuming that the particles were produced in a collision between a π^- and a nucleon and that no additional particle was involved ($\pi^- + p \rightarrow \Lambda^0 + \vartheta^0$) one calculates from the resultant of the momenta of Λ^0 and ϑ^0 that the total energy of incident pion and nucleon must have been 2050±25 Mev before the collision. On the other hand, with the mases of 1119±10 and 546±20 Mev for Λ^0 and ϑ^0, respectively, one finds for the sum of their energies a value of 2068±30 Mev. This value must be equal to the initial energy just calculated, if no other particles are involved in the collision, and one indeed finds agreement. Therefore the Λ^0 and ϑ^0 could have been produced in a $\pi^- - p$ collision, the π^- previously having been scattered upward by 24°, with the required energy. Such repeated interactions could take place in a heavy nucleus. For this interpretation the almost colinear flight of the Λ^0 and ϑ^0 would mean that in the

[7] Thompson, Buskirk, Etter, Karzmark, and Rediker, Phys. Rev. 90, 1122 (1953).

TABLE I. Measurements and results for case *C*.

	Track	Event a 1a	Event a 2a	Event b 1b	Event b 2b
1	Sign of charge	+	−	+	−
2	Measured momenta (Mev/c)	272±8	205±40	451±70	391±15
3	Estimated ionization density	>5×min	<1.5×min	<1.5×min	<1.5×min
4	Mass limit (Mev)	>780	<170	<380	<330
5	Assumed particle	proton	pion	pion	pion
6	Angle between tracks (degrees)	31.1±1		70±1	
7	Q values calculated from above data (Mev)	54±20		271±30	
8	Momenta for (2a) and (1b) calculated from direction of line of flight, assuming lowest momenta for (1a) and (2b) (Mev/c)	264	189±20	441±15	376
9	Q values recalculated (Mev)	49±10		266±20	
10	Momentum of unstable particle (Mev/c)	437		673	

center-of-mass system (c.m.s.) of π^- and nucleon the Λ^0 went almost straight backward. The same will be found for the next example to be discussed. From the observed momenta and angles a π^- of the beam colliding with a nucleon could *not* have produced the Λ^0 and ϑ^0 traveling in the observed direction, with simultaneous production of some other particle going downward to balance transverse momenta.

CASE *D*: Λ^0 AND ϑ^0 PRODUCED IN $\pi^- - p$ COLLISION

Figure 2 (case *D*) shows a photograph of a π^- track (marked π^-) disappearing abruptly in the hydrogen, and two nearby *V* events of which (a) is considered to be a Λ^0 and (b) a ϑ^0. Data which lead to this identification are given in Table II. The measured momentum of the incident particle (row 2) agrees well with the momentum of 1630 Mev/c for a 1.5-Bev π^-. The other momenta are not well determined, mostly because the tracks are of short length. The longest track (2b), furthermore, seems to show a slight deflection, perhaps due to scattering or to $\pi-\mu$ decay, which makes its momentum also unreliable. The given mass limits (row 4), however, seem to justify the assumed choices for the individual particles (row 5). In particular, since in a collision in hydrogen only one proton was present and since this proton is probably found in 1a, 2b could hardly be another proton in spite of the rather high upper mass limit.

The decay planes of both particles contain the end point of the incident track. The directions of flight of Λ^0 and ϑ^0 and incident π^- appear coplanar, though this is not accurately determined because of the small angle between π^- and ϑ^0 (b). Therefore no additional neutral particle has to be assumed, although calculation shows that kinematically this would be possible. One is therefore justified in assuming the same reaction as in case *C* ($\pi^- + p \rightarrow \Lambda^0 + \vartheta^0$). All pertinent angles are given in rows 6 and 7. From these angles and the momentum of the incident π^- one can calculate the momenta of the decay products directly. The results (row 9) agree with the measured values (row 2) within the errors. With the momenta from row 9, Q values have been calculated (row 10). Two experimental errors are given separately with each Q value. The first was determined from the probable variation of Q with the possible variations of all of the angles (rows 6 and 7) used for the computation. The second error was found from the variation of Q with a possible uncertainty of ±100 Mev/c for the momentum of the incident π^-. One sees that within the errors both Q's may agree with the usual values of 37 and 214 Mev, respectively, although the Q for the ϑ^0 is again rather high and agrees with the value found for case *C*. It should be pointed out that the error for the Q for the Λ^0 depends most strongly on the measurement

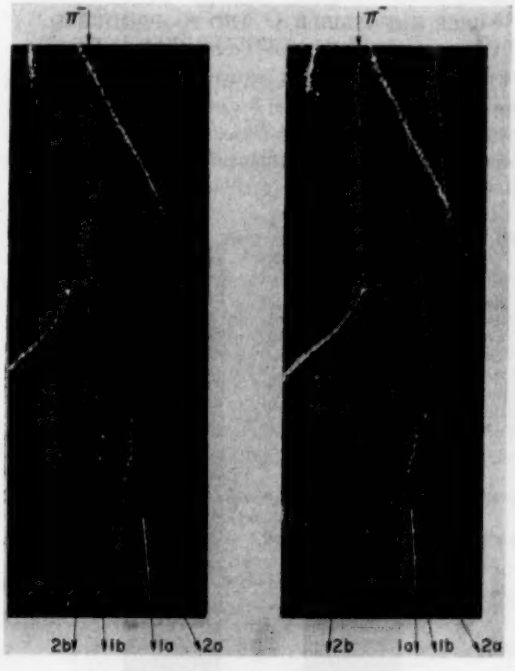

FIG. 2. Case D. Photograph of a 1.5-Bev π^- producing two neutral *V* particles in a collision with a proton. Tracks 1a and 2a, believed to be proton and π^-, respectively, are the decay products of a Λ^0. A ϑ^0 is probably seen to decay into π^+ (1b) and π^- (2b). Because of the rather "foggy" quality of this picture tracks 1b, 2a, and 2b have been retouched for better reproduction.

TABLE II. Data for case *D*.

		Incident track	Event a 1a	Event a 2a	Event b 1b	Event b 2b
1	Sign of charge	−	+	−	+	−
2	Measured momenta (Mev/c)	1620±160	210^{+210}_{-70}	140^{+300}_{-60}	210^{+210}_{-70}	840±300
3	Estimated ionization density	<1.5×min	>5×min	<1.5×min	<1.5×min	<1.5×min
4	Mass limit (Mev)		>400	<370	<350	<870
5	Assumed particle	pion	proton	pion	pion	pion
6	Angle between incident π^- and direction of flight (degrees)		11.1±1		2.3±0.5	
7	Angle between direction of flight and decay products (degrees)		8.8±1	11.3±1.5	29.3±2	11.0±2
8	Momentum of (a) and (b) calculated from incident momentum and angles (Mev/c)	1630	282		1357	
9	Momenta of decay products from momenta of (a) and (b) and angles (Mev/c)		160	125	400	1027
10	Q values calculated from rows 7 and 9		27±11±3		258±35±21	

of the small angle (2.3°) between incident π^- and ϑ^0 (b). Modifying this angle to make Q_{Λ^0} equal to 37 Mev would reduce Q_{ϑ^0}, which depends on this angle less strongly, to a value of 244 Mev.

From the momenta (row 8) of the Λ^0 and ϑ^0 and their masses of 1097±12 and 538±40 Mev, respectively, one calculates that the kinetic energy of the incident π^- must have been 1.52±0.04 Bev which is quite consistent with the 1.5-Bev beam energy.

CASE *E*: POSSIBLE Λ^- AND K^+ PRODUCED IN $\pi^- - p$ COLLISION

Figure 3 (case *E*) shows a photograph of what on first sight appears to be a π^- scattered forward by a proton with a subsequent decay of the π^-. Closer inspection shows that the momentum of the decay product

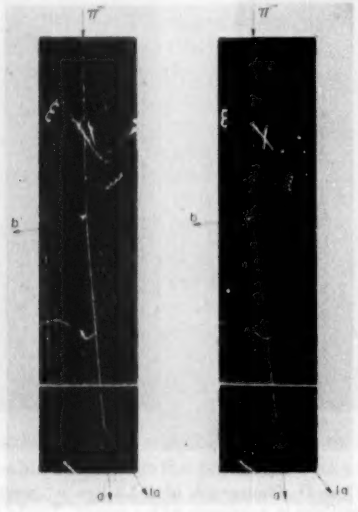

FIG. 3. Case E. Photograph of a $\pi^- - p$ collision event possibly resulting in a Λ^- (a) with a π^- (1a) as a decay product and a K^+ whose decay is not seen.

(1a) and its angle with respect to the track of the decaying particle (a) are much too large for a $\pi-\mu$ or $\mu-\beta$ decay. Therefore (a) must have been a heavy unstable particle.

As far as can be ascertained from the "scattering" event, particle (a) might have been produced at the Cosmotron target or at the cloud chamber wall, and scattered by a proton in the cloud chamber. Certainly the rate of production of heavy mesons would have to be large (~10 percent of that for pions) and their decay lifetime long (~10^{-8} sec) for the beam to contain an appreciable contamination of heavy mesons. No beam particles have shown a decay resembling that of (a). If (a) were produced in the target, it would be quite remarkable that it lives until it reaches the cloud chamber, is scattered, and then decays within the chamber. Such an origin is possible but seems unlikely. If (a) were a particle produced in the wall and scattered in the chamber, it would be remarkable that the incident track has both direction and momentum characteristic of beam tracks. For these reasons we assume that the incident particle is a beam π^- producing a charged unstable particle in a collision with a proton.

Data are given in Table III. Since the tracks are short and the momenta are high, the latter are not well determined. We therefore assume that the incident particle had the beam energy of 1.5 Bev, and compute the momenta of (a) and (b) by assuming that no additional neutral particle was produced. This assumption is very probably justified because (a), (b), and incident track are coplanar. One finds the momentum values given in row 8. If the mass of (a) is given, that of (b) is determined so that their total energies equal that of the incident π^-. In Table IV a number of such consistent values are given. The errors on the mass values of (b) include the uncertainties given for the angle measurements as well as an improbably large uncertainty of ±300 Mev for the energy of the incident π^-. To obtain a mass of 930 Mev (proton) for (b) does not seem to be possible unless (a) is a pion, without making

TABLE III. Data for case *E*.

		Incident track	Track a	Track 1a	Track b
1	Sign of charge	−	−	−	+
2	Measured momenta (Mev/c)	1800±600	1400±400	>120[a]	−
3	Estimated ionization density	<1.5×min	<1.5×min	<1.5×min	3 to 6×min
4	Mass limit (Mev)		<1500		
5	Assumed particle	pion		pion	
6	Angle between incident track and collision products (degrees)		8±1		79±3
7	Angle between (a) and its decay product (degrees)			36±1	
8	Momenta from incident momentum and angles (Mev/c)	1630	1604		227

[a] Track 1a is slightly distorted. Therefore only a lower limit can be given.

quite unreasonable assumptions for the uncertainties of the measured angles and of the incident momentum.[8] In the cosmic radiation Λ^+ particles have been found[6] with Q values of about 130 Mev, leading to a mass of 1200 Mev. Row 5 of Table IV shows that such a mass for (a) would lead to a mass for (b) which is quite consistent with that usually found for K particles. Case E can therefore be interpreted as the charged counterpart of case C and case D in which Λ^0 and K^0 were produced. For this interpretation the present photograph is an example of the reaction $\pi^-+p\rightarrow\Lambda^-+K^+$.

A calculation has been performed to investigate whether a neutrino (ν) or π^0 could have been produced in addition, which might then change the above conclusions. One finds that only the combinations $[\Lambda^-, K^+, \pi^0]$ or $[\Lambda^-, K^+, \nu]$ are possible (though unlikely because of the observed coplanarity) while the combinations $[\Lambda^+, K^-, \pi^0]$, $[\Lambda^+, K^-, \nu]$, $[p, K^-, \pi^0]$, or $[p, K^-, \nu]$ are kinematically not possible.

From the mass of (b) of 520 Mev and its momentum of 227 Mev/c one finds that (b) should show an ionization density of $\sim$4×min which agrees with the estimated ionization density given in row 3.

Assuming a decay of $\Lambda^-\rightarrow n+\pi^-$, the calculated momentum for 1a of 1604 Mev/c and measured momentum for (b) of $\geqslant$120 Mev/c lead to a Q value $\geqslant$50 Mev. Track 1a may be somewhat distorted so that these figures probably represent lower limits only. If much of the apparent curvature of 1a is due to distortion, the Q value may be as high as 130 Mev, corresponding to a momentum of 440 Mev/c for 1a, as has been assumed in the previous discussion.

[8] For the present discussion it is of particular importance to exclude the possibility that the mass of (b), M_b, could be that of a proton (930 Mev) for the assumption that (a) is a K^- of mass 500 Mev. One finds that $\partial M_b/\partial p_0=8.1$ Mev/(100 Mev/c), where p_0 is the momentum of the incident π^- (so far assumed to be the beam momentum of 1630 Mev/c). Furthermore $\partial M_b/\partial\alpha_a=-11.3$ Mev/degree and $\partial M_b/\partial\alpha_b=-3.7$ Mev/degree, where α_a and α_b are the angles recorded in Table III, row 6, for (a) and (b), respectively. It is very hard to conceive how π^- of momenta >1700 Bev/c could be contained in the beam. With this upper limit and the uncertainties for α_a and α_b given in Table IV one sees that $M_b\leqq$890 Mev if all uncertainties are assumed to act together in a direction to increase M_b. Only by decreasing α_a by 3° and α_b by 9°, for example, could one obtain a value for M_b of 930 Mev. The values for M_a and M_b noted in rows 2 and 3 of Table IV are then not possible without destroying a nucleon.

CASE *F*: EXAMPLE OF A Λ^-

The photograph shown in Fig. 4 (case F) shows another V event which may be interpreted as a Λ^-. The picture shows a negative particle (a) of momentum 1190±170 Mev/c and of estimated ionization density $\leqslant$1.5×min, apparently produced in the wall of the chamber. The angle between (a) and the beam direction is 8°. Particle (a) decays into a negative particle (1a) of momentum 83±3 Mev/c and estimated ionization density 2 to 3×minimum.[9] The mass of the decay product thus lies between 110 and 150 Mev, identifying it as a π^-. The angle between (a) and 1a is 76°. If one additional neutral decay product is assumed one calculates Q values and mass values for (a) as given in Table V. One sees that only the assumption of a neutron (row 1) leads to Q and mass values compatible with those found in cosmic radiation. Particle (a) can also not be identified as a $\tau^-\rightarrow2\pi^0+\pi^-+70$ Mev because 1a alone would have an energy of 230 Mev in the rest system of the τ^-. The assumption in row 4 ($K^-\rightarrow\mu^-+2\nu$) is unlikely because the decay product is most probably

TABLE IV. Consistent masses for particle (a) and particle (b) of case *E*.

	Particle (a)	Mass of (a) (Mev)	Particle (b)	Mass of (b) (Mev)
1	π^-	140	proton	934±6
2	K^-	500	?	860±20
3	?	760	?	760±30
4	$\Lambda^-(Q=37$ Mev)	1107	K^+	570±50
5	$\Lambda^-(Q=130$ Mev)	1200	K^+	520±50

TABLE V. Q values and masses for case F, assuming different masses for the neutral decay product.

	Charged decay product	Neutral decay product	Mass of neutral decay prod. (Mev)	Q for (a) (Mev)	Mass of (a) (Mev)
1	π^-	n	930	130^{+25}_{-15}	1200
2	π^-	π^0	140	430 ±70	710
3	π^-	K^0	500	230±35	870
4	μ^-	2ν	0	>520±80	>620

[9] For the assumption of a Λ^0 traveling backwards the momentum of (a) is much too high.

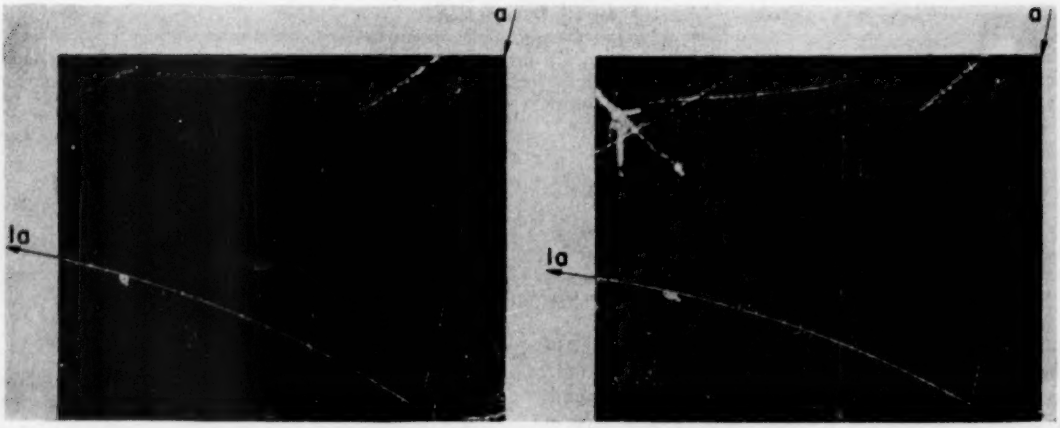

FIG. 4. Case F. Photograph of a negative unstable particle (a) best interpreted as a Λ^-. The decay product (1a) is identified as a π^- from momentum and ionization density.

identified as a π^-. We therefore are left with the conclusion that the present photograph shows the decay of a $\Lambda^- \rightarrow n + \pi^- + Q$, where $Q = 130_{-15}^{+25}$ Mev. The errors on the latter are due to the uncertainty of the measured momentum of (a).

It has been pointed out[10] that if the hypothesis of charge independence applies to $\Lambda^{+,-,0}$, then the Λ^- must have isotopic spin z component $(-3/2)$ with isotopic spin $3/2$, in which case a doubly-charged Λ^{++} should also exist. No Λ^{++} decays have been reported to date, but the number of observed Λ^- and Λ^+ is so small that no significant discrepancy exists. A track which might be interpreted as a Λ^{++} has been reported by Ascoli.[11]

LIFETIMES, CROSS SECTION, AND ANGULAR RELATIONSHIPS

The role played by chance in apparent lifetimes, cross sections, and angular relationships deduced from a small number of cases is very large. Nevertheless the few available observations will be compiled in the following paragraphs.

Table VI shows the lifetimes. All values are consistent with mean lifetimes of 10^{-10} to 3×10^{-10} sec cited in the literature.[4-6]

TABLE VI. Observed lifetimes of all particles in units of 10^{-10} sec.

Particle	*A*	*B*	*C*	*D*	*E*	*F*
Λ^0	0.4	0.3	6	9		
Λ^-					2	3
ϑ^0			2	0.1		
K^0	>4[a]	>3[a]				
K^+					>0.7	

[a] Not taking into account that decay may result in two neutral particles and thus be invisible.

[10] D. C. Peaslee, Phys. Rev. **86**, 127 (1952).
[11] G. Ascoli, Phys. Rev. **90**, 1079 (1953).

For a mean lifetime of 3×10^{-10} sec for the Λ^0 and 1.5×10^{-10} for the ϑ^0, the given cloud-chamber geometry, a π^--beam energy of 1.5 Bev, and isotropic angular distributions (in the c.m.s.) of Λ and K particles one can estimate that 60 percent of the Λ and 50 percent of of the K should be seen to decay inside the chamber. One can conclude that for 80 percent of all occurring cases one should see at least one of the two particles decay and for 20 percent of all cases one should see both decaying. (For shorter lifetimes or angular distributions peaked forwards or backwards the probabilities are even larger.) Therefore the 4 cases of unstable particle production in hydrogen (A, B, D, E) observed here may correspond to 5 ± 3 cases that actually happened.[12] This number can be compared with the other 170 $\pi^- - p$ interactions observed, including events with two and four outgoing prongs. Making use of Fermi's statistical theory of meson production[13] and of the isotopic spin formalism, Fermi[14] has calculated the probabilities for the different combinations. One finds that combinations resulting in no outgoing prongs are expected to occur in only 12 percent of all interactions. Therefore our 170 observed cases may correspond to 190 actual interactions. The total interaction cross section has been found to be 34 ± 3 millibarns.[15] Therefore the cross section for heavy unstable particle production by 1.5-Bev π^- in hydrogen is $\sim$1 millibarn.

Table VII gives the angles between the decay planes of the particles and their production planes (the plane formed by the incident track and the line of flight of the unstable particle.) The absence of large angles for the Λ particles is surprising and might be taken as an indication for a large spin for these particles. In fact the

[12] Decays of Λ^0 and ϑ^0 into neutral particles cannot be observed in this experiment and are not taken into account here.
[13] E. Fermi, Progr. Theoret. Phys. (Japan) **5**, 570 (1950).
[14] E. Fermi (private communication).
[15] Cool, Madansky, and Piccioni, Phys. Rev. **93**, 637 (1954).

separation between the decay and production planes seems smaller than would be expected unless the spin is taken to be unreasonably large.

Table VIII shows the angles between incident π^- and direction of emission of Λ^0 in the c.m.s. Again the result is surprising because of the absence of angles near 90° for which the solid angle is largest. The solid angle between 170° and 180° amounts to only 1.5 percent of the hemisphere, yet both *C* and *D* fall into this region. This may indicate that large angular momentum states are involved in the production of these particles, which might be consistent with the possibility

TABLE VII. Angles between decay plane and production plane.

Particle	*A*	*B*	*C*	*D*	*E*
Λ^0	5°±5°	30°±20°	18°±7°	27°±10°	7°±5°
Λ^-					
ϑ^0			60°±6°	70°±5°	

of a large spin of the Λ^0. Since $\lambda_0 \approx 2\times10^{-14}$ cm in the c.m.s. for a π^- of 1.5-Bev laboratory energy, angular momentum states up to $L=6$ may be possible.

SUMMARY

These examples of the production of heavy unstable particles in $\pi^- - p$ collisions have been shown to be consistent with a double production process,

$$\pi^- + p \rightarrow \Lambda + K,$$

occurring with a cross section of about 1 millibarn for 1.5-Bev π^-. Further work is required to determine whether production is *always* double in these and nucleon-nucleon collisions.

In four cases the Λ is a Λ^0, and in two of these the K^0 is observed to decay and can be considered to be a ϑ^0, although the *Q* values of about 260 Mev are not quite consistent with the cosmic-ray value of 214 Mev. One case is interpreted as a Λ^-, and an additional charged decay originating outside the chamber is thought to be a Λ^- with *Q* value of 130 Mev.

The data suggest an angular correlation between Λ-decay planes and production planes, which may mean that Λ particles have large spin, and a preferred backward (or forward) emission in the c.m.s., which may mean that Λ particles are produced in states of high angular momentum. Many more data are needed to determine such angular relationships.

We wish to express our thanks to the many members of the Cosmotron Department whose efforts have created the opportunity for this work and whose cooperation is enabling us to pursue it. Our thanks are also due to the other members of the cloud-chamber group without whose support this work could not be continued.

TABLE VIII. Angle between incident π^- and direction of emission of $\Lambda^{0,-}$ in c.m.s.

Particle	*A*	*B*	*C*	*D*	*E*
Λ^0	141°	125°	177°	174°	
Λ^-					30°

Interaction of Pions with Complex Nuclei

DONALD HARVEY STORK
Radiation Laboratory, Department of Physics, University of California, Berkeley, California
(Received November 12, 1953)

Attenuation cross sections and cross sections for scattering into a fixed angular interval have been measured in a well-defined geometry for pions of energies 33, 46, and 68 Mev. The targets were beryllium, carbon, aluminum, and copper. The results were analyzed by means of the optical model, and a strong energy dependence was found for the pion interaction mean free path in nuclear matter. A satisfactory representation of this energy dependence is the equation

$$\lambda_a/r_0=[2b(kr_0)^4/\gamma^2]^{-1},$$

where λ_a is the mean free path, r_0 is the pion Compton wavelength, b is a constant, k is the pion number, and γ is the total pion energy divided by its rest energy. The results of an optical model calculation with the above energy dependence were compared with other published pion-nucleus data and agreement was found. A partial wave analysis gave essentially the same results but required mean free paths about twice as long.

Published values of the pion-nucleon phase shifts at several energies were used to calculate the mean free path by means of multiple-scattering theory. The results agree with the above energy dependence and are intermediate between the mean free paths of the optical model and those of the partial wave analysis.

INTRODUCTION

THE total cross section for pions in complex nuclei may be considered to consist of two parts: an elastic (coherent) scattering cross section, σ_s, and an interaction cross section, σ_a. The latter includes all processes—such as star formation, inelastic scattering, and charge-exchange scattering—that remove pions from the coherent wave. If a model is adopted in which the pion-nucleus interaction is represented by a complex square well, of depth V_r+iV_i and of radius R, an experimental measurement of σ_s and σ_a permits determination of the depth of this complex well. It is expected that the variation of the well depth with pion energy should reflect the characteristics of the pion-nucleon interaction.

The first experiments employing artificially produced pions for the study of pion cross sections in complex nuclei were performed by observation of the interactions occurring along both positive and negative pion tracks in nuclear emulsions.[1-3] A number of pion energies between 30 and 100 Mev were used. The study was extended to pure carbon targets in cloud-chamber experiments for 48-Mev[4] and 62-Mev[5] positive and negative pions. In addition to the total cross-section measurements, the above experiments gave further information, such as the star-prong distributions and the inelastic and elastic scattering distributions. Tracy[6] has recently made a cloud-chamber study of the pion interaction in aluminum at several energies. Measurements of the attenuation of negative pions as a function of A have been made by Chedester *et al.*[7] at 85 Mev and by Martin[8] at 113 and 137 Mev. In the latter case the results were analyzed to give the interaction cross section, σ_a.

The attenuation and scattering experiment described in this paper is intended to provide further pion-nucleus cross-section data at relatively low energies and thus to make possible a better understanding of the behavior of the pion-nucleus interaction.

EXPERIMENTAL PROCEDURE

Three pion energies were chosen for this study: 33, 46, and 68 Mev. The target nuclei were beryllium, carbon, aluminum, and copper. For the purpose of distinguishing the pions from the background, a momentum selection and a pulse-height analysis were made. The attenuation cross sections for the various targets at the three pion energies were measured in a well-defined geometry. The cross sections for pion scattering into a fixed angular interval were obtained simultaneously.

The general physical arrangement for the experiment is shown in Fig. 1. The pion beams were produced by bombarding either a polyethylene or a carbon production target by the 340-Mev external scattered proton beam at the 184-inch synchrocyclotron. The target was placed in the 5-inch gap of a large pair spectrometer magnet. Pions produced in the forward direction were bent through an arc of 90° in an 18.5-inch radius, leaving the magnet gap through a brass slit in a direction 35° to the normal of the magnetic field boundary. The pions continued through a hole in the 5-foot-thick concrete shielding, passed through a collimating counter inside the shielding, and entered the main counting

[1] Bernardini, Booth, and Lederman, Phys. Rev. **83**, 1075 and 1277 (1951).
[2] G. Bernardini and F. Levy, Phys. Rev. **84**, 610 (1951).
[3] H. Bradner and B. Rankin, Phys. Rev. **87**, 547 and 553 (1952).
[4] A. M. Shapiro, Phys. Rev. **84**, 1063 (1951).
[5] Byfield, Kessler, and Lederman, Phys. Rev. **86**, 17 (1952).
[6] J. Tracy, Phys. Rev. **91**, 960 (1953).
[7] Chedester, Isaacs, Sachs, and Steinberger, Phys. Rev. **82**, 958 (1951).
[8] R. Martin, Phys. Rev. **87**, 1052 (1952).

system just outside the shielding. The geometry was such that because of the properties of the fringing field at the exit of the magnet gap, a first-order focus of the pion beam in the vertical plane was obtained. Thus, in the vertical plane, a pion image of the proton beam at the production target was formed at the counter system. This focusing effect was verified experimentally by observation of the counting rate as the magnet was raised and lowered.

For the 33- and 46-Mev cross-section measurements, a polyethylene $[(CH_2)_n]$ target was used to produce the beam pions. Advantage was taken of the large cross section for the reaction $p+p\rightarrow\pi^++d$,[9] from which monoenergetic pions are obtained in the forward direction for a given incident proton energy. The energy of these pions upon emerging from the target depends upon the thickness of the target but is essentially independent of the target depth at which they are produced.[10] Thus the polyethylene target provided monoenergetic positive pion beams whose energy could be varied by changing the target thickness (the magnetic field being adjusted to maximize the pion flux). For the 68-Mev cross-section measurements, the required pion beam energy was too high to be obtained from the reaction $p+p\rightarrow\pi^++d$. In this case a 2-inch carbon production target was used. For protons incident upon carbon, positive pions are produced over a broad energy spectrum.[11] Consequently, the value of the magnetic field was set to bend pions of the appropriate energy through the field exit and in the direction of the counting system.

The pion energy distributions for the three beams were determined by range in copper with a pulse-height selection that is described below. The energy was measured before and after each experimental run, and in no case was a significant change in energy found. As the pions entered the attenuation target, after passing through the collimating, pulse-height, and passing counters (Fig. 1), the three pion beams had mean energies and half-widths at half-maximum of 37.5 ± 4, 51 ± 3, and 73 ± 8 Mev. For the two lower energies, most of the beam pions were from the reaction $p+p\rightarrow\pi^++d$, and the energy distributions were somewhat narrower than that defined solely by the momentum selection. For the pion beam of higher energy, from the carbon production target, the energy distribution was determined almost entirely by the momentum selection. The momentum selection in turn was determined by the positions and widths of the production target, field exit slit, and counters.

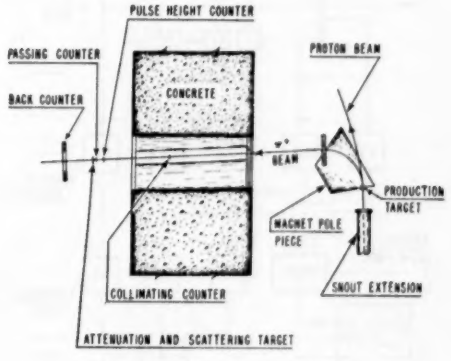

FIG. 1. Physical arrangement.

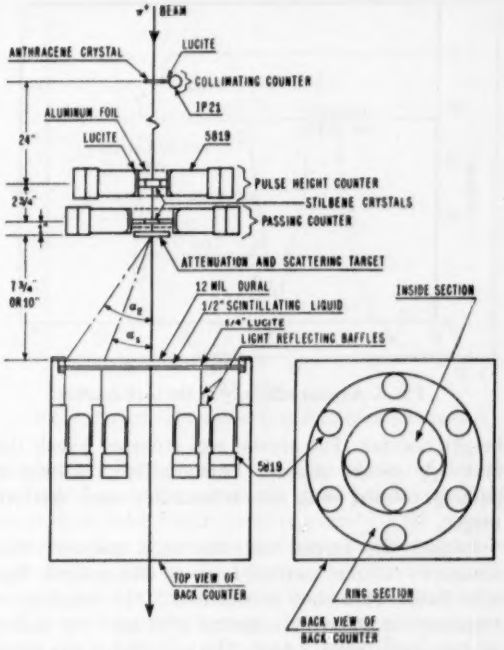

FIG. 2. Counter system and geometry.

The pion beam flux at the counter system varied between one and two pions per square inch per second. This low flux required an efficient method of taking data. Such a method was found in the photographic-recording method described below.

The geometry of the counter system is shown in Fig. 2. The first ("collimating") counter consisted of a $\frac{1}{8}$-inch thick, $1\frac{1}{2}$-inch square anthracene crystal viewed through a short Lucite light pipe by a 1P21 photomultiplier. The second ("pulse-height") counter consisted of a $\frac{1}{2}$-inch thick, $1\frac{1}{4}$-inch square stilbene crystal viewed on two sides through short Lucite light pipes by 5819 photomultipliers. Short signal leads from the two 5819's were connected together at a coaxial tee, and the tubes were matched in gain by suitably adjusting their voltages. The third counter was a "passing" counter, similar in construction to the pulse-

[9] Cartwright, Richman, Whitehead, and Wilcox, Phys. Rev. **91**, 677 (1953).
[10] Richman, Skinner, Merritt, and Youtz, Phys. Rev. **80**, 900 (1950).
[11] W. Dudziak (private communication).

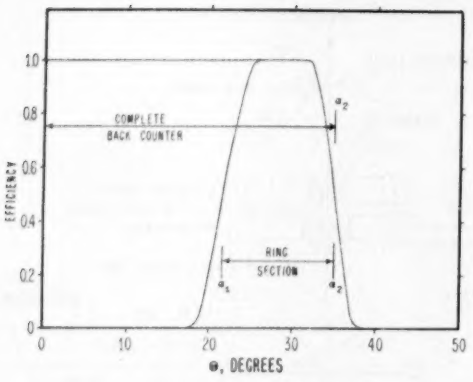

FIG. 3. Angular efficiency of the back counter.

height counter. The crystal was stilbene, $\frac{1}{4}$ inch thick and $1\frac{3}{16}$ inches square. Immediately following the passing counter was the attenuation and scattering target.

Behind the target was the back counter, whose sensitive volume consisted of a disk-shaped liquid scintillator 14 inches in diameter. The solution was terphenyl in phenylcyclohexane with the "red shifter," diphenylhexatriene, added. The scintillator was divided into two sections by means of aluminum-foil light reflectors placed behind the Lucite back face. By means of this division an inner 8-inch diameter circle was viewed by four 5819 photomultipliers, and an outer 3-inch ring was viewed by six 5819 photomultipliers. Signal leads from the inner four 5819's were connected together to a single coaxial connecter, and leads from the outer six 5819's were connected together to a second coaxial connecter. In this way separate signals from the two sections of the back counter could be obtained. The gains of the tubes were matched by suitably adjusting their individual voltages. The response across the face of the back counter was found to be uniform to about 10 percent. The fraction of statistically zero pulses caused by fluctuations in the number of photoelectrons collected for each pulse was determined to be negligibly small.

Because of the overlap in light collection, the full 14-inch diameter could be used, with no blind spots, for attenuation measurements. Particles passing through the scintillator near the division between the inner and outer sections gave rise to a pulse from both sections. However, by the establishment of a pulse-height criterion for distinguishing through which side of the division a particle passed, the separation became satisfactorily distinct. In this way the back counter was made suitable for the simultaneous measurement of the attenuation cross section and of the cross section for scattering into a fixed angular interval.

An attenuation event was defined as an event in which a particle that passed through the front three counters failed to reach either section of the back counter. A ring-counter (scattering) event was defined as one in which a particle traversed the front three counters and appeared to pass through the ring section of the back counter, the pulse-height criterion's being used if pulses from both the inside and outside sections of the back counter were present. Since the pion beam was of finite extent, it was required that the back counter be large enough for the geometry to be well defined. The angular efficiency of the back counter as a whole and of the ring-counter section is shown in Fig. 3 for a 10-inch separation from the target to the back counter. For this separation, the two sections of the back counter subtended half-angles with respect to the target of 21.7° (α_1) and 35° (α_2) (see Fig. 2). For Al and Cu targets at low energy, multiple Coulomb scattering necessitated thinner targets and greater angles. The back counter was then placed $7\frac{3}{4}$ inches from the target, giving $\alpha_1 = 26.6°$ and $\alpha_2 = 42°$.

A block diagram of the electronics is shown in Fig. 4. If a particle passed through the front three counters, a coincidence was formed and the coincidence output triggered the oscilloscope sweep. Pulses from the pulse-height counter, the passing counter, and from either section of the back counter, if present, appeared on the oscilloscope trace. A separation of the pulses on the trace was accomplished by means of the different lengths of *RG65/U* delay line.

The oscilloscope traces were photographed on continuously moving Kodak Linagraph Pan 35-mm film by means of a General Radio camera. Upon completion of a run, the film was processed and the images of the oscilloscope traces were examined in a Recordak microfilm viewer. The position and height of each pulse

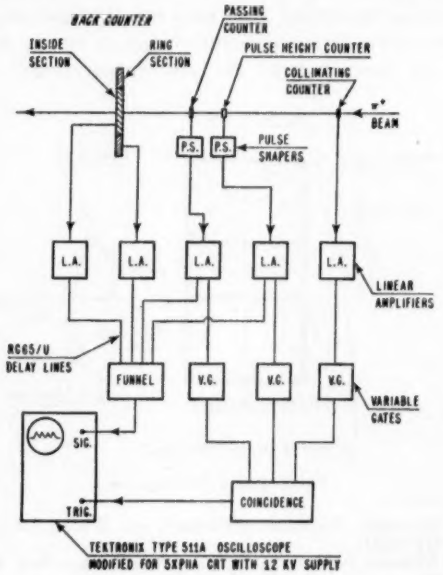

FIG. 4. Block diagram of the electronics.

appearing on the traces could be conveniently measured by projecting the image on ordinary graph paper. A sample strip of the film is reproduced in Fig. 5. The time separation of the pulses, obtained by the different lengths of delay line used for each signal, was about 0.8 microsecond. Measurement of the separation of the pulses could be converted to a time measurement, and separation of the starting points of the pulses could be readily determined to within 0.04 microsecond. This was considered the effective resolving time for determining coincidences. The pulse heights were measured on a scale of one hundred divisions on which a reading resolution of one division could be obtained.

The principal use of pulse-height measurements was to aid in the separation of the pions from the background. For this purpose the relative heights of the pulses from the pulse-height counter were measured. The pulse-height distribution for the total beam flux was determined in a random sampling of the traces on the film. (The solid curve in Fig. 6 represents the pulse-height distribution of the beam flux at 46 Mev. The distributions at 33 and 68 Mev are similar.) A peak in the pulse-height distribution (of about 20 percent full-width at half-maximum) was caused by the pions in the beam. The pulse-height resolution was sufficiently narrow to distinguish the pions from electrons. The largest background was found in the large-pulse region and was well separated from the pion pulse height. The number of pions passing through the target was thus determined by multiplication of the total

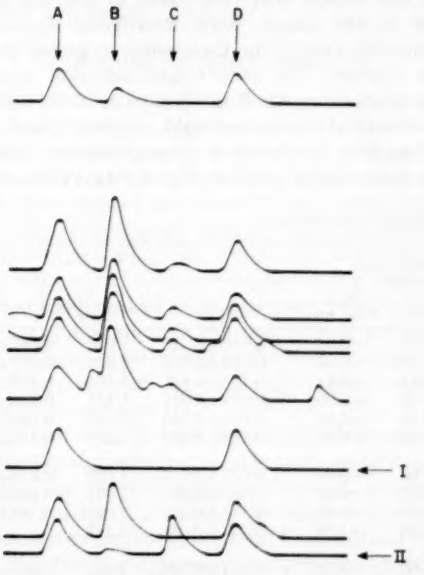

FIG. 5. Reproduction of the traces on a sample strip of film. Pulse *A* is from the pulse-height counter, pulse *B* is from the inside section of the back counter, pulse *C*—when present—is from the ring section of the back counter, and pulse *D* is from the passing counter. Traces I and II correspond to an attenuation event and a ring-counter event, respectively.

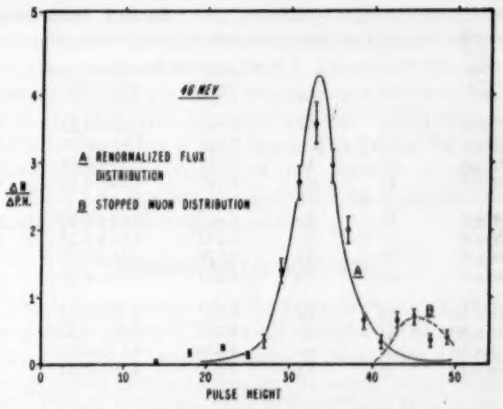

FIG. 6. Pulse-height distribution of attenuation events.

number of photographed oscilloscope traces by the fraction of traces for which the pulse height was inside the narrow pulse-height band representing the pions.

The number of events was determined by examining each image of the oscilloscope traces. In an attenuation event (trace I in Fig. 5), there was no pulse from either section of the back counter. In a ring-counter event (trace II in Fig. 5), there was a pulse from the ring section but not from the inside section of the back counter, or—if the particle passed near the division between the two sections of the back counter—the pulse from the ring section was larger and that from the inside section smaller than a predetermined pulse height. For every event the pulse height was measured, and the same pulse-height selection that was used for the total number of pions was applied to the events. (The pulse-height distribution of the attenuation events is shown in Fig. 6 for the 46-Mev measurements.) All events in which the pulse height fell outside the narrow pion pulse-height band were discarded.

From the total number of pions and of events, both selected on the basis of pulse height, the fraction of the pions causing events was calculated. Runs were made with the target in and with the target removed. A subtraction gave the fraction of pions causing events in the target. After the corrections described below were made, the attenuation and ring-counter cross sections per target nucleus were computed using the equation $f=\exp(-N\sigma x)$, where f is the fraction of pions causing events, N the number of target nuclei per gram, σ the cross section in cm², and x the thickness of the target in grams/cm².

CORRECTIONS

A. Accidentals

The number of accidental coincidences triggering the oscilloscope sweep was negligible. Accidental single pulses, however, appeared fairly frequently on the oscilloscope traces. (Several of these accidental pulses

TABLE I. The measured attenuation cross sections.

Pion energy, Mev	α_1	Target	Target thickness g/cm²	Fraction of pions attenuated[a] (times 100)	Correction fraction (times 100) Accidentals	Decay muons	$\sigma_m/\pi R^2$	$1+V_c/T_\pi$	$\sigma_m\left(1+\frac{V_c}{T_\pi}\right)\Big/\pi R^2$
33±6	35°	Be	2.587	1.88±0.20	+0.07	−0.27	0.366±0.044	1.058	0.387±0.047
33±6	35	C	2.555	1.84±0.21	+0.07	−0.30	0.389±0.050	1.079	0.420±0.054
33±5	42	Al	2.012	1.25±0.19	+0.07	−0.21	0.456±0.088	1.131	0.515±0.099
33±5	42	Cu	2.342	1.20±0.19	+0.07	−0.21	0.486±0.090	1.220	0.593±0.105
46±6	35	Be	3.452	2.93±0.27	+0.07	−0.14	0.473±0.044	1.042	0.492±0.046
46±6	35	C	3.232	3.05±0.27	+0.08	−0.17	0.570±0.052	1.057	0.603±0.055
46±6	35	Al	3.826	3.21±0.28	+0.07	−0.17	0.666±0.058	1.094	0.730±0.064
46±6	35	Cu	4.224	2.45±0.25	+0.08	−0.17	0.606±0.064	1.158	0.702±0.074
68±10	35	Be	4.601	5.28±0.32	+0.19	−0.01	0.684±0.041	1.028	0.703±0.042
68±10	35	C	4.190	4.46±0.30	+0.17	−0.01	0.695±0.046	1.038	0.722±0.048
68±10	35	Al	4.748	4.75±0.32	+0.16	−0.02	0.840±0.055	1.064	0.903±0.059
68±10	35	Cu	5.620	4.20±0.31	+0.15	−0.02	0.847±0.061	1.107	0.938±0.068

[a] Corrected for 4 percent muon-flux contamination.

may be seen in Fig. 5.) If an accidental pulse had appeared at the position of the pulse from either section of the back counter in the case of an event, the event would have been misinterpreted or missed. Consequently, it was necessary to determine the accidental-pulse frequency and pulse-height distribution for each section of the film in order to correct for the effect of these spurious pulses. The corrections are shown in Tables I and II.

B. Pion-Muon Decay

The presence in the beam of muons originating from the decay of pions in flight required a correction to both the flux and the number of events. The muons from decay in flight were carried forward from the point of decay, by the center-of-mass motion, within a narrow cone with the maximum laboratory decay angle depending upon the pion energy. The laboratory energy of the muons varied widely. Where the decay occurred before the pulse-height counter and passed through the counter system, some of the low-energy muons could be distinguished from the beam pions by the pulse-height selection.

The correction for the muon flux through the target was determined by range measurements. Most of the decay muons had ranges greater than that of the pions. From the number of long-range particles present in the beam it was estimated that about 4 percent of the pulse-height selected particles in the beam were muons. It was assumed that the muons did not interact in the target, and a 4 percent correction was made to the beam flux.

A correction to the number of attenuation events was required because of the presence of decay muons having such low energy that they came to the end of their range in the target. Such occurrences appeared as attenuation events, for there were no pulses from the back counter. The pulse-height selection eliminated these spurious events if the decays occurred before the pions reached the pulse-height counter. (Such events are found in the excess of large pulses just above the pion pulse-height peak in Fig. 6.) However, for low-

TABLE II. The measured ring-counter cross sections.

Pion energy, Mev	α_1	α_2	Target	Target thickness g/cm²	Fraction of pions causing ring counter events[a] (times 100)	Correction fraction (times 100) Accidentals	Decay muons	Mult. Coul. scat.	$\Delta\sigma_m/\pi R^2$	$1+\frac{V_c}{T_\pi}$	$\Delta\sigma_m\left(1+\frac{V_c}{T_\pi}\right)\Big/\pi R^2$
33±6	21.7°	35°	Be	2.587	0.32±0.14	−0.03	−0.14	−0.00	0.031±0.030	1.058	0.032±0.031
33±6	21.7	35	C	2.555	0.55±0.15	−0.03	−0.18	−0.02	0.074±0.034	1.079	0.081±0.037
33±6	21.7	35	Al	2.704	1.13±0.25	−0.01	−0.23	−0.41	0.137±0.071	1.131	0.155±0.080[b]
33±5	26.6	42	Al	2.012	0.40±0.13	−0.03	−0.14	−0.00	0.085±0.045	1.131	0.096±0.051
33±6	21.7	35	Cu	3.242	4.90±0.60	−0.01	−0.29	−4.42	0.038±0.165	1.220	0.046±0.201[b]
33±5	26.6	42	Cu	2.342	0.91±0.16	−0.06	−0.22	−0.40	0.090±0.060	1.220	0.110±0.073
46±6	21.7	35	Be	3.452	0.27±0.13	−0.03	−0.06	−0.00	0.027±0.021	1.042	0.028±0.022
46±6	21.7	35	C	3.232	0.45±0.15	−0.03	−0.09	−0.00	0.061±0.026	1.057	0.065±0.028
46±6	21.7	35	Al	3.826	1.02±0.18	−0.03	−0.20	−0.08	0.148±0.034	1.094	0.161±0.037
46±6	21.7	35	Cu	4.224	1.24±0.17	−0.03	−0.30	−1.66	(−0.23 ±0.05)	1.158	...[b]
68±10	21.7	35	Be	4.601	0.65±0.17	−0.07	−0.00	−0.00	0.071±0.020	1.028	0.073±0.021
68±10	21.7	35	C	4.190	0.64±0.18	−0.06	−0.00	−0.00	0.084±0.026	1.038	0.087±0.026
68±10	21.7	35	Al	4.748	0.92±0.18	−0.06	−0.00	−0.00	0.146±0.029	1.064	0.155±0.031
68±10	21.7	35	Cu	5.620	1.04±0.18	−0.06	−0.00	−0.36	0.105±0.020	1.107	0.116±0.035[b]

[a] Corrected for 4 percent muon-flux contamination.
[b] Omitted from analysis because of uncertainty in multiple-Coulomb-scattering correction.

energy muons arising from pion decays between the pulse-height counter and the target and stopping in the latter, it was necessary to derive a correction analytically (basing the derivation on the geometry, the stopping power of the counters and targets, and the pion-muon decay lifetime and kinematics). The correction is shown in Table I for each measurement.

Similarly, a correction to the number of ring-counter events was required because of decay muons that passed through the ring counter. The angular distribution of the decay muons was peaked near the maximum laboratory decay angle. Since the maximum decay angle was generally close to α_1 (see Fig. 2), it was necessary to take into account the multiple Coulomb scattering of the pions and muons in the crystals and target. The correction was derived by means of a graphical analysis and was based upon the pion-muon decay lifetime and kinematics, geometry and stopping power, and multiple Coulomb scattering. This correction can be traced to three effects: first, the increased multiple Coulomb scattering with the target in position; second, the stopping in the target of some muons that would have reached the ring counter in the absence of the target; and third, the decreased energy of pions after passing through the target and the subsequent increase in maximum pion-muon decay angle. The correction for each measurement is shown in Table II. In several cases the correction was comparable to the statistical uncertainty of the measurement. The correction, however, is considered to be of sufficient accuracy for its uncertainty to be small compared with the statistical uncertainty.

C. Multiple Coulomb Scattering

The distribution in angle of multiple Coulomb scattering was taken to be Gaussian. The Rossi and Greisen[12] expression for the mean-square angular deviation was used with the nuclear radius substituted for the minimum impact parameter. It was found that the contribution of large-angle multiple Coulomb scattering to the measured attenuation cross section was negligible. For the ring-counter cross section, however, a significent correction was required in several cases to account for pions that passed through the ring counter because of multiple Coulomb scattering in the front counters and target. The correction for each ring-counter measurement is given in Table II.

For Cu and Al at 33 Mev, two target thicknesses and back-counter angles were chosen in order empirically to determine the effect of multiple Coulomb scattering. With the thicker Cu target, the ring-counter effect was almost entirely due to multiple Coulomb scattering (see Table II); the agreement between the corrected cross sections for the two Cu thicknesses was thus interpreted as a satisfactory test of the validity of the multiple Coulomb scattering correction at this energy. At 46 Mev, however, the multiple-Coulomb-scattering correction for Cu was vastly overestimated, and led to a negative cross section (Table II). Because of this large discrepancy, the Cu ring-counter cross sections at both 46 and 68 Mev were discarded and were not considered in the analysis that follows below. Except for the cases noted above, the correction for multiple Coulomb scattering was significantly smaller than the statistical uncertainty of the measurement.

[12] B. Rossi and K. Greisen, Revs. Modern Phys. 13, 263 (1941).

EXPERIMENTAL RESULTS

The data and results for the attenuation cross sections are given in Table I. The pion energies listed are the mean energies of the pion beams in the targets, and the energy spread is that caused by the energy width of the beam and by the energy loss in the targets. The uncertainties shown for the fraction of pions attenuated and for the resulting cross sections are statistical standard deviations. The measured attenuation cross section divided by nuclear area is denoted by $\sigma_m/\pi R^2$. The nuclear area was taken to be πR^2, where $R=r_0A^{\frac{1}{3}}$. A is the atomic mass number, and $r_0=\hbar/m_\pi c=1.4\times10^{-13}$ cm.

For the analysis that follows, it was desired to remove the effects due to Coulomb suppression of the positively charged pion wave function at the nucleus. A correction factor,[5] $1+V_c/T_\pi$, may be derived by use of the classical-particle picture for Coulomb scattering, for the purpose of determining the impact parameter for a pion passing at a distance R from the center of the nucleus. This impact parameter is then considered to be the effective nuclear radius. V_c is the Coulomb potential at R and T_π is the pion kinetic energy. Values for the correction factor and for the corrected cross section divided by nuclear area are given in the last two columns of Table I.

Similar information is listed for the ring-counter cross section in Table II, wherein α_1 and α_2 refer to the half-angles subtended by the two boundaries of the back counter (see Fig. 2). The measured ring-counter cross section is designated $\Delta\sigma_m$. Except for the cases that were discarded because of the uncertainty in the multiple-Coulomb-scattering correction, the systematic errors were estimated to be small compared to the statistical standard deviations for both the ring counter and the attenuation cross sections.

ANALYSIS OF THE DATA

Because of the unique geometry used in the experiment, the measured cross sections could not readily be interpreted in themselves, and a model was required for the analysis of their various components. A model was chosen in which the nuclear interaction potential is represented by a complex square well, V_r+iV_i, of radius R. This complex square well is the basis of the optical model of Fernbach, Serber, and Taylor.[13] It

[13] Fernbach, Serber, and Taylor, Phys. Rev. 75, 1352 (1949).

has been used in connection with the optical model by Bethe and Wilson[14] in a discussion of the 48-Mev pion-carbon interaction results of Shapiro.[4] It has also been used in connection with a partial wave analysis by Byfield *et al.*[5] in an analysis of their results for the pion-carbon interaction at 62 Mev.

A plane wave amplitude outside the square well may be written with the spatial dependence e^{ikz}, where $k=p_\pi/\hbar$ is the outside wave number and p_π is the initial pion momentum. Inside the square well the plane wave amplitude may be written as $e^{ik'z}$, where

$$k'=k+k_1+ik_2=p_\pi'/\hbar \tag{1}$$

is the wave number inside. Here p_π' is the complex momentum of the pion inside the square well; although the analysis was implicitly based on the Schrödinger wave equation, relativistic momenta were used throughout in deriving the wave numbers. Here k_1 is the difference between the real part of the inside wave number and the outside wave number; k_2 is the imaginary part of the inside wave number.

Two cross sections result from this model: an elastic-scattering (coherent) cross section, σ_s, and an interaction cross section, σ_a. The latter includes all incoherent processes such as absorption or star formation, inelastic scattering, and charge exchange scattering. The amplitude of a plane wave inside the square well contains the term e^{-k_2z}. This decrease in amplitude is interpreted as the removal of pions from the coherent wave, and k_2 may be expected to be directly related to the interaction cross section. The coherent scattering cross section is strictly a wave phenomenon and will depend upon both k_1 and k_2. Hereafter, k_1 and k_2, rather than the complex square well, will be considered as the parameters of the analysis and will be written and evaluated as k_1r_0 and k_2r_0.

The cross sections measured in this experiment may be written in terms of σ_s and σ_a. The measured attenuation cross section includes all of σ_a except for a small fraction of cases in which an ionizing particle from the interaction passed through the back counter. It also includes all elastic scattering for angles greater than α_2 (see Fig. 2). The measured attenuation cross section may therefore be written as

$$\sigma_m=F_a\sigma_a+F_a\sigma_s, \tag{2}$$

where F_a is the fraction of the interaction cross section included in the measurement and F_s is the fraction of the total elastic scattering cross section for angles greater than α_2. The ring-counter cross section included primarily the elastic scattering for angles between α_1 and α_2 and a small contribution due to ionizing particles from interaction events. Single Coulomb scattering also contributed to the ring-counter cross section, as did the interference between the nuclear and the Coulomb scattering. The measured ring-counter cross section may therefore be written as

$$\Delta\sigma_m=\Delta F_a\sigma_a+\Delta F_s\sigma_s+\Delta\sigma_{\text{Coul.}}+\Delta\sigma_{\text{interf.}}, \tag{3}$$

where ΔF_a and ΔF_s are the fractions of interaction and scattering events reaching the ring counter.

The purpose of the analysis was to find a unique pair of parameters k_1r_0 and k_2r_0, at each energy, that would provide a best fit to both the measured attenuation and ring-counter cross sections. The various contributions to Eqs. (2) and (3) were determined by the following methods: (1) σ_a, σ_s, F_a, and ΔF_s were calculated by means of the optical model; (2) $\Delta\sigma_{\text{Coul.}}$ and $\Delta\sigma_{\text{interf.}}$ were determined by means of the Born approximation; (3) F_a and ΔF_s were estimated from the results of other experiments.

(1) Although an exact solution for σ_a and σ_s may be obtained for the complex square well by means of a partial wave analysis, calculation of the required phase shifts as a function of the two arbitrary parameters k_1r_0 and k_2r_0 for each nucleus and pion energy was found to be excessively time-consuming and was beyond the scope of this paper. Consequently, the approximate derivation of σ_a and σ_s by the optical model of Fernbach, Serber, and Taylor[13] was used. The approximation in the optical model is the neglecting of reflection and refraction of the incident wave at the boundary of the nucleus. The scattering angular distribution is also given in reference 13. From this, there could be derived the fraction scattered through angles greater than α_2, F_a, and the fraction scattered into the ring counter, ΔF_s. This was done for several different pairs of parameters, k_1r_0 and k_2r_0, with the result that these fractions were found to be independent of k_1r_0 and k_2r_0 and were a function only of kR.

(2) The Coulomb scattering and Coulomb interference were calculated by means of the Born approximation. The potential was taken to be the screened Coulomb potential of a uniformly charged sphere of radius R and with charge Ze, in addition to the complex well V_r+iV_i, also of radius R. It was found that the contribution from the square well alone gave the same scattering angular distribution as the optical model. The magnitude of the scattering, however, was larger for the Born approximation than for the optical model. For small k_1r_0 and k_2r_0, the two models gave equal scattering, but if either parameter became large, that is, if there was appreciable disturbance of the incident wave, the discrepancy between the Born approximation

TABLE III. Parameters for the best fit to the measured cross sections.

T_π, Mev	k_1r_0	k_2r_0
33	$0.18^{+0.03}_{-0.04}$	$0.04^{+0.03}_{-0.02}$
46	$0.26^{+0.03}_{-0.05}$	$0.03^{+0.04}_{-0.03}$
68	$0.17^{+0.05}_{-0.13}$	$0.17^{+0.05}_{-0.04}$

[14] H. A. Bethe and P. R. Wilson, Phys. Rev. 83, 690 (1951).

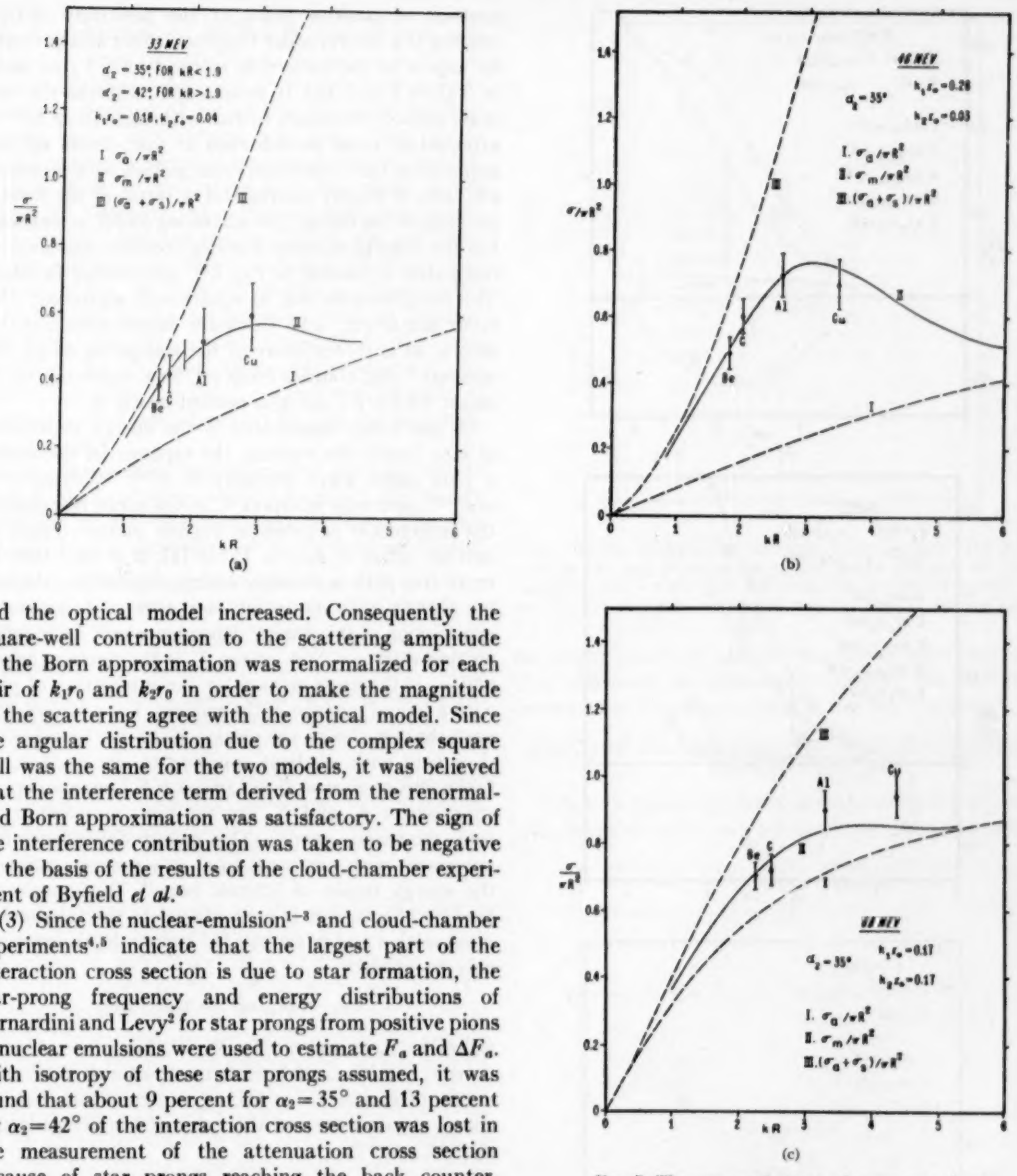

FIG. 7. The measured attenuation cross sections. The solid curve represents Eq. (2).

and the optical model increased. Consequently the square-well contribution to the scattering amplitude in the Born approximation was renormalized for each pair of k_1r_0 and k_2r_0 in order to make the magnitude of the scattering agree with the optical model. Since the angular distribution due to the complex square well was the same for the two models, it was believed that the interference term derived from the renormalized Born approximation was satisfactory. The sign of the interference contribution was taken to be negative on the basis of the results of the cloud-chamber experiment of Byfield *et al.*[5]

(3) Since the nuclear-emulsion[1–3] and cloud-chamber experiments[4,5] indicate that the largest part of the interaction cross section is due to star formation, the star-prong frequency and energy distributions of Bernardini and Levy[2] for star prongs from positive pions in nuclear emulsions were used to estimate F_a and ΔF_a. With isotropy of these star prongs assumed, it was found that about 9 percent for $\alpha_2=35°$ and 13 percent for $\alpha_2=42°$ of the interaction cross section was lost in the measurement of the attenuation cross section because of star prongs reaching the back counter. Consequently, F_a was taken to be 0.91 and 0.87 for the two geometries. Similarly, for the ring-counter cross sections, ΔF_a was found to be 0.05 for the smaller angle geometry and 0.07 for the larger angle geometry. Although these calculations are subject to serious question, the relative contribution of the star prongs was small.

By means of the above methods, σ_m and $\Delta\sigma_m$ were computed according to Eqs. (2) and (3) as a function of the two arbitrary parameters k_1r_0 and k_2r_0 for each target nucleus and pion energy. For each of the three pion energies a graphical analysis was performed to determine the values of k_1r_0 and k_2r_0 giving a best fit of Eqs. (2) and (3) to the several measured cross sections. The results are listed in Table III.

For the best-fit values of the parameters, attenuation cross sections, calculated according to Eq. (2), are plotted *versus* the dimensionless quantity kR in Fig. 7 for the three pion energies. Also shown are the measured cross sections corrected by the factor $1+V_c/T_\pi$. (The Born approximation treatment of the Coulomb scattering in the analysis is a first-order effect. The sup-

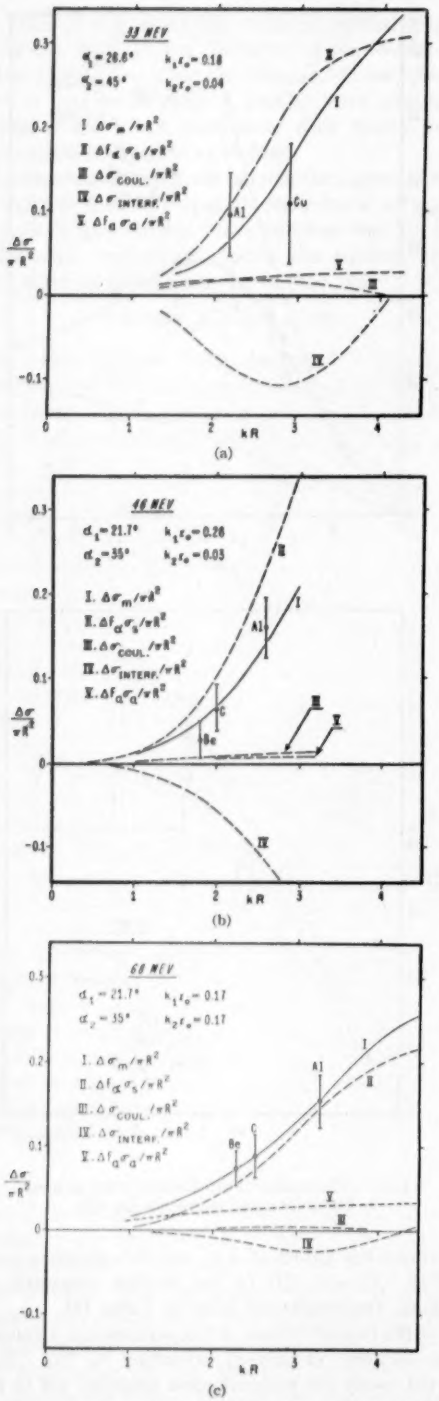

FIG. 8. The measured ring-counter cross sections. The solid curve represents Eq. (3). The Be and C cross sections at 33 Mev were determined in a different geometry and are not shown. They are, however, consistent with the choice of parameters k_1r_0 and k_2r_0.

pression of positive pions at the positively charged nucleus is a second-order Coulomb effect and is treated by means of the correction factor $1+V_c/T_\pi$ as shown in Tables I and II.) It is seen that whereas the total cross section continues to rise with increasing kR, the attenuation cross section rises at first, levels off, and approaches the interaction cross section with increasing kR. This is readily understood in terms of the forward peaking of the diffraction scattering as kR is increased. For the same parameters the ring-counter cross sections, calculated according to Eq. (3), are plotted in Fig. 8. The contributions due to square-well scattering, Coulomb scattering, and Coulomb interference are also shown, as is the estimate of the star-prong effect. The measured ring-counter cross sections, corrected by the factor $1+V_c/T_\pi$, are also plotted in Fig. 8.

Of particular significance is the energy dependence of k_2r_0. Inside the nucleus, the exponential decrease of a pion plane wave intensity is e^{-2k_2z}. Writing $e^{-2k_2z}=e^{-z/\lambda_a}$, one may interpret λ_a as the mean free path for the interaction of pions in nuclear matter. From the best-fit values of k_2r_0 in Table III, it is seen that the mean free path is strongly energy dependent—decreasing sharply with increasing pion energy. A qualitative explanation of this energy dependence may be found by writing $e^{-2k_2z}=e^{-N\sigma_n z}$, where N is the nucleon density and σ_n is the cross section for the interaction of pions with a bound nucleon in the nucleus. For a lowest-order perturbation theory calculation using the pseudoscalar pion field with gradient coupling to the nucleon, the free nucleon cross section has a p_π^4/E_π^2 energy dependence, where p_π and E_π are the pion momentum and total relativistic energy. This energy dependence is in agreement with measured total $\pi^+ + p$ cross sections in the energy region of interest here.[15] Thus, neglecting binding effects, k_2r_0 is proportional to the free-nucleon cross section and has a p_π^4/E_π^2 energy dependence that may be written

$$k_2r_0=(2\lambda_a/r_0)^{-1}=b(kr_0)^4/\gamma^2, \tag{4}$$

where $k=p_\pi/\hbar$ and $\gamma=E_\pi/R_\pi$, R_π being the pion rest energy; and b is considered to be a constant. The best-fit values of k_2r_0 in Table III are in agreement with this energy dependence and the value of b is determined to be $0.21_{-0.03}{}^{+0.04}$.

COMPARISON WITH OTHER DATA

Although Eq. (4) is a satisfactory representation of the energy dependence for k_2r_0 found in this experiment, the fairly large statistical uncertainties do not allow a detailed comparison. The results of this experiment, however, may be combined with the results of other experiments in order to make a more quantitative determination of the energy dependence. There have been several experiments in which the carbon nucleus has been used as a target.[4,5,8] The results for the inter-

[15] S. Leonard and D. Stork, Phys. Rev. **93**, 568 (1954).

action cross section, σ_a, divided by nuclear area and corrected for the Coulomb effect, are shown in Fig. 9. From the cloud-chamber data,[4,5] the interaction cross section was determined by adding the cross sections for stars, stops, and inelastic scattering. The results from the present experiment are also shown, determined by means of the optical model from the values of k_2r_0 in Table III. Similarly, the nuclear emulsion interaction cross sections[1-3] (determined by adding the published cross sections for stars, stops, and inelastic scattering) are shown in Fig. 10. They are divided by the weighted average for πR^2 for nuclear emulsion given by Bradner and Rankin,[3] and they are multiplied by $1\pm V_c/T_\pi$ to correct for the Coulomb effect—suppression of the positive pion wave function (+) and enhancement of the negative pion wave function (−) at the positively charged nucleus.

These cross sections were compared with the results of two methods of wave analysis in which the energy dependence of Eq. (4) was used for k_2r_0. The two methods of wave analysis were the optical model and

TABLE IV. Values of b from least-squares fit.

Method of analysis	Source of data	b in Eq. (4)
Optical model	This experiment	$0.21^{+0.04}_{-0.03}$
Optical model	All carbon data (see Fig. 9)	0.26±0.03
Optical model	Nuclear emulsion data for π^+ (see Fig. 10)	0.24±0.04
Optical model	Nuclear emulsion data for π^- (see Fig. 10)	0.36±0.07
Optical model	All of the above data	0.26±0.02
Partial wave analysis	Carbon data only (see Fig. 9)	0.14±0.02

the partial wave analysis. In the optical model the interaction cross section is independent of k_1r_0. The solid curves in Figs. 9 and 10 are the best fits to the data as determined by the optical model and Eq. (4). The least-squares values of b in Eq. (4) are given in Table IV. In contrast to the optical model, the partial wave analysis requires the specification of k_1r_0 as well as k_2r_0 for determination of σ_a. Two values of k_1r_0 were arbitrarily chosen: $k_1r_0=0$ and $k_1r_0=0.25kr_0$. The latter is in rough agreement with the values of k_1r_0 listed in Table III. The partial wave analysis was carried out for carbon only. The dashed curves in Fig. 9 are the best fits to the carbon data as determined by the partial wave analysis and Eq. (4). The least-squares value of b is given in Table IV, the result being the same for both choices of k_1r_0. At the lower values of kR the curves derived by means of the partial wave analysis coincide with the curve from the optical model. Consequently, equally good agreement with the carbon data may be obtained by either method of wave analysis through the use of Eq. (4) for the energy dependence of k_2r_0. The striking difference is the requirement of mean free paths differing by a factor of almost two—the shorter mean free path for the optical model and

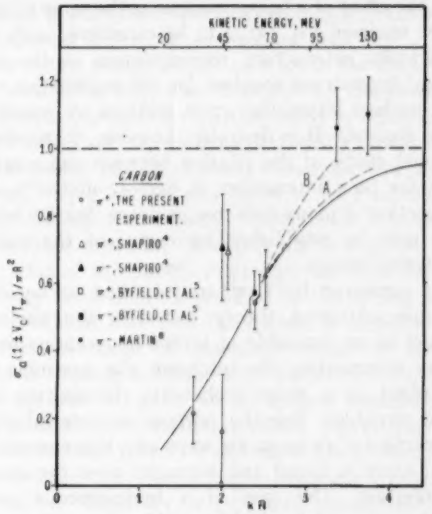

FIG. 9. The pion-carbon interaction cross section. The solid curve is the best fit using the optical model and Eq. (4). The dashed curves are the best fits using the partial wave analysis and Eq. (4). For curve A, $k_1r_0=0$, and for curve B, $k_1r_0=0.25kr_0$.

the longer mean free path for the partial wave analysis. This difference is presumably due to the different treatment of boundary effects in the two methods.

RELATION TO THE PION-NUCLEON SCATTERING AMPLITUDES

Although the energy dependence given in Eq. (4) was introduced in an *a priori* manner by the assumption

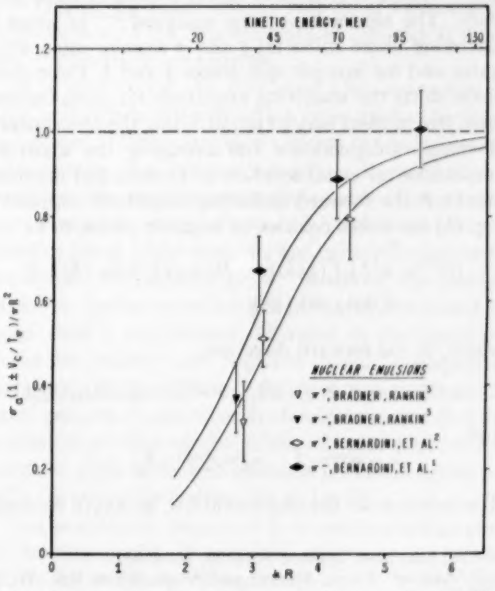

FIG. 10. The pion interaction cross section in nuclear emulsion. The solid curves are the best fits to the negative and to the positive pion data using the optical model and Eq. (4).

that the effect of a bound nucleon is the same as that of a free nucleon, Eq. (4) is to be considered only as an empirically satisfactory representation of the strong energy dependence required for the explanation of the pion-nucleus interaction cross sections by means of a wave analysis. It is desirable, however, to return to a detailed study of the relation between the mean free path for pion interaction in nuclear matter and the interaction of pions with free nucleons. Such a relationship may be established by means of the multiple-scattering theory.

As presented by Lax[16] and applied to nuclei, the multiple-scattering theory considers the nucleus to consist of an ensemble of interaction centers or scatterers representing the nucleons, the ensemble being described by a given probability distribution in the state variables. For the purpose of determining the interaction of an incoming wave with this ensemble, the total wave is found and averaged over the ensemble distribution. The case of a homogeneous medium (uniform spatial density) is considered and the equation

$$k'^2-k^2=4\pi nc f(0^\circ) \tag{5}$$

is found to determine the magnitude of the propagation vector in the medium of the scatterers. The symbols k' and k are the inside and outside wave numbers, n is the density of scatterers given by $n=(4\pi r_0^3/3)^{-1}$, and c is a constant depending upon the correlation between pairs of scatterers. For the present application, c was taken to be unity. $f(0^\circ)$ is the forward scattering amplitude in the case of a free nucleon.

A number of measurements of the angular distribution of pions scattered in liquid hydrogen have been made. The results have been analyzed[17–19] in terms of scattering phase shifts for s and p angular momentum states and for isotopic spin states $\frac{1}{2}$ and $\frac{3}{2}$. From these phase shifts the scattering amplitude for pions incident upon free protons may be found. Using the consequences of charge independence and averaging the scattering amplitudes for equal numbers of protons and neutrons, one finds the forward scattering amplitude required in Eq. (5) for either positive or negative pions, to be

$$\begin{aligned} f(0^\circ)&=a/2+[(1/3)(a+2b)+(\sqrt{2}/3)(a-b)]/2 \\ &=0.901a+0.118b, \end{aligned} \tag{6}$$

where, in the forward direction,

$$a=(\epsilon_3+\epsilon_{31}+2\epsilon_{33})/2ik, \quad b=(\epsilon_1+\epsilon_{11}+2\epsilon_{13})/2ik,$$

and

$$\epsilon_3=e^{2i\alpha_3}-1, \quad \epsilon_{31}=e^{2i\alpha_{31}}-1, \quad \cdots.$$

The notation for the phase shifts, α, is that of Anderson *et al.*[17] The scattering amplitudes a and b are for the isotopic spin states $\frac{3}{2}$ and $\frac{1}{2}$, respectively.

From the sets of phase shifts given for each pion energy, the forward scattering amplitudes were calculated by means of Eq. (6). From Eqs. (1) and (5) the parameters k_1r_0 and k_2r_0 were determined. The interaction mean free path, λ_a/r_0, was calculated from k_2r_0. The results are given in Table V. The forward scattering amplitude is listed in units of r_0 and has been transformed to the laboratory system as is appropriate for the use of Eq. (5). Except at 120 and 135 Mev, the given scattering amplitudes were derived from $\pi^+ + p$ scattering and consequently did not include scattering in the isotopic spin $\frac{1}{2}$ state. However, the contribution of b ($\frac{1}{2}$ isotopic spin state) in Eq. (6) is small. Furthermore, where $\pi^- + p$ ordinary and charge exchange scattering were also measured and the phase shifts for isotopic spin $\frac{1}{2}$ were given (135, 120 Mev),[17] it was found that the magnitude of b was considerably smaller than a. Consequently, the neglect of b for the lower energies should not be serious.

Where the signs of the phase shifts were arbitrary, the signs corresponding to a positive value of k_1r_0 were used. In the case of Bodansky *et al.*,[18] Coulomb interference was a significant factor in their measurements and two different sets of phase shifts were determined by them corresponding to positive and negative interference. The results for both cases are given in Table V. Perry and Angell[19] give two sets of phase shifts (A,B) giving an equally good fit to their data. The results from both sets are shown in Table V. At 120 and 135 Mev, Anderson *et al.*[17] find two equally good sets of phase shifts ("first solution" and "Yang solution"). Both sets give identical results for the forward scattering amplitude.

In Fig. 11 the interaction mean free paths resulting from the above calculation are plotted *versus* pion energy. The uncertainties in the phase shifts are difficult to ascertain and are not given in the references. Consequently, no attempt was made here to determine the uncertainties in the derived mean free paths. The results from the complex-nucleus data are also shown in Fig. 11. The solid curve is from the optical model analysis and corresponds to a value of $b=0.26$ in Eq. (4). The dashed curve is the result of the partial wave analysis with $b=0.14$.

TABLE V. Mean free path from scattering amplitudes.

Source of phase shifts	T_π Mev	$f(0^\circ)/r_0$ (lab.)	k_1r_0	k_2r_0	λ_a/r_0
Anderson *et al.*[a]	135	$4.08+3.94i$	0.600	0.463	1.08
Anderson *et al.*[a]	120	$3.58+2.94i$	0.556	0.370	1.35
Anderson *et al.*[a]	78	$1.94+0.80i$	0.329	0.128	3.9
Anderson *et al.*[a]	53	$3.02+0.43i$	0.072	0.100	5.0
Bodansky *et al.*[b] (−)	58	$-0.33+0.36i$	−0.076	0.080	6.2
Bodansky *et al.*[b] (+)	58	$1.20+0.36i$	0.246	0.068	7.3
Perry, Angell[c] (A)	40	$0.47+0.20i$	0.125	0.051	9.8
Perry, Angell[c] (B)	40	$1.88+0.24i$	0.430	0.047	10.6

[a] See reference 17.
[b] See reference 18.
[c] See reference 19.

[16] M. Lax, Revs. Modern Phys. **23**, 287 (1951).
[17] Anderson, Fermi, Martin, and Nagle, Phys. Rev. **91**, 155 (1953).
[18] Bodansky, Sachs, and Steinberger, Phys. Rev. **90**, 997 (1953).
[19] J. P. Perry and C. E. Angell, Phys. Rev. **91**, 1289 (1953).

DISCUSSION

That the two inside wave numbers could be adjusted to give internal consistency between the four attenuation cross section measurements and the three or four scattering-cross-section measurements at each energy (Figs. 7, 8) indicates the usefulness of the optical model in interpreting the data of this experiment. It has been pointed out[5] that a wave analysis fails to explain the large amount of backscattering found in the nuclear emulsion, and cloud-chamber experiments.[1–6] The experiment of Heckman and Bailey[20] is also pertinent. Le Levier has suggested[21] that a strong repulsive core of the nuclear potential would give rise to backscattering in the wave analysis. Peaslee[22] has attempted to explain these results by adopting an extreme single nucleon scattering model. While these backscatterings are elastic within the rather broad uncertainty of the energy measurements, they may, however, be incoherent scatters in which the pion interacts with a single nucleon rather than with the nucleus as a whole. If so, the large backscattering is expected from the results of measurements of the angular distribution of pion-nucleon scattering.[17–19] In terms of the analysis considered in the present experiment, such events would be included in the interaction cross section, σ_a, rather than the coherent scattering cross section, σ_s.

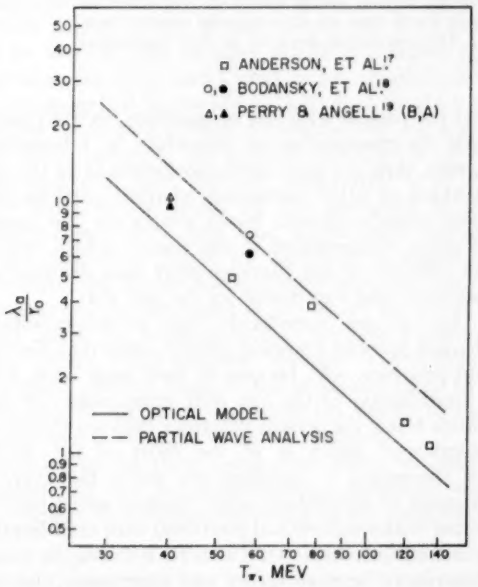

FIG. 11. The mean free path for the interaction of pions in nuclear matter. The points are determined from pion-nucleon scattering phase shifts by means of multiple-scattering theory. The dashed and solid curves are best-fits of Eq. (4) to the pion-nucleus interaction data using the partial-wave analysis and the optical model, respectively.

The strong energy dependence found for the interaction parameter, k_2r_0, was confirmed by comparison of the interaction cross sections reported in other experiments with the cross sections derived by means of the optical model and partial-wave analysis (see Figs. 9 and 10). Equation (4) was found to be a satisfactory representation of the energy dependence required for k_2r_0 in both methods. However, the interaction mean free paths of the partial-wave analysis were found to be nearly twice those determined by the optical model. It is presumed that this discrepancy is caused by the different treatment of boundary effects in the two methods of wave analysis. The optical model neglects reflection and refraction at the nuclear boundary and thus underestimates boundary effects. The partial-wave analysis includes reflection and refraction at the nuclear boundary and thus overestimates boundary effects since the nuclear boundary is probably considerably less abrupt than that in the square-well representation. It is to be expected that a more suitable wave analysis may be found between the two extremes.

A different approach to the interaction mean free path was found in the multiple-scattering theory treatment of the interaction of pions with free nucleons. The results, shown in Fig. 11, are seen to lie generally between the two curves representing Eq. (4) for the two methods of wave analysis. Although this agreement may be to a certain extent fortuitous in view of the approximations in the multiple-scattering theory, the results confirm the strong energy dependence of Eq. (4) and suggest the preference of a method of wave analysis intermediate to the two extremes of the optical model and the partial wave analysis.

It is seen in Fig. 10 that even after correction for Coulomb effects the interaction cross section for negative pions in nuclear emulsion appears to be significantly greater than that for positive pions. It was found in applying the multiple-scattering theory that protons are somewhat more effective in the interaction of positive pions while neutrons are more effective in the interaction of negative pions. However, the neutron excess in nuclear emulsion is insufficient to account for more than a two percent difference in the mean free paths for positive and negative pions. Consequently, the source of the difference in cross sections, if significant, remains in question. It should be noted that the statistical average of the values of b for positive and negative pions in nuclear emulsion is in good agreement with the value for carbon (see Table IV).

Reabsorption is important in the production of pions in complex nuclei. If boundary effects are to be neglected in estimates of reabsorption, it would seem appropriate to use the mean free paths derived on the basis of the optical model. In Fig. 11 it is seen that at

[20] H. H. Heckman and L. Evan Bailey, Phys. Rev. **91**, 1237 (1953).
[21] R. LeLevier, Phys. Rev. **87**, 217 (1952).
[22] D. C. Peaslee, Phys. Rev. **87**, 862 (1952).

low energies the mean free path becomes longer than the average nuclear radius, and thus below about 40 Mev even the largest nucleus should be fairly transparent. Consequently, for low pion energies, the dependence of production cross sections upon atomic mass number, A, may be expected to deviate from the usual $A^{\frac{2}{3}}$ law and, except for Coulomb effects, approach a linear dependence. It should also be noted that Heckman and Bailey[20] find an A dependence for the backscattering of 30-Mev pions.

ACKNOWLEDGMENTS

The encouragement and guidance of Professor Chaim Richman are gratefully acknowledged. The author is indebted to Dr. Stanley Leonard for his assistance throughout a major portion of the experiment. Mr. George Hahn performed the calculations required in the partial wave analysis. Mr. James Vale and the cyclotron crew are to be thanked for their aid in setting up the apparatus and for their efficient operation of the cyclotron.

PHYSICAL REVIEW VOLUME 93, NUMBER 4 FEBRUARY 15, 1954

Elementary Particles and the Lamb-Retherford Line Shift*

LESLIE L. FOLDY† ‡
Case Institute of Technology, Cleveland, Ohio, and Institute for Theoretical Physics, Copenhagen, Denmark
(Received October 26, 1953)

According to the principles of contemporary quantum electrodynamics, the existence of a charged particle field of any kind results in a vacuum polarization contribution to the Lamb-Retherford line shift of an amount proportional to the square of the charge and inversely proportional to the square of the mass of the field particle. On the basis of the present agreement between theory and experiment with respect to the line shift in hydrogen, one may conclude that no singly charged particles of spin-$\frac{1}{2}$ with mass less than four electron masses, other than the electron and positron, can exist without spoiling this agreement. Similar reasoning argues against the existence of singly charged particles of spin-0 with mass less than twice the electron mass. For doubly charged particles these limits are quadrupled. The assumptions involved in these conclusions as well as some experimental evidence are briefly discussed.

THE polarization of the vacuum[1] as a consequence of the existence of the electron-positron field seems now to be a well established phenomenon since it appears to be essential to obtain agreement between experiment[2] and theory[3] for the Lamb-Retherford line shift in the hydrogen atom. To this line shift the vacuum polarization term contributes -27.13 Mc/sec which is some fifty times the discrepancy at present between theory (including fourth order corrections) and experiment.[4] It is characteristic of the theory of the line shift that the existence of any charged particle field which is invariant under charge conjugation will also make a corresponding contribution to the line shift from its vacuum polarization. The contribution of such a particle field is always of the same sign[5] (negative) and, for given spin of the particle, is proportional to the square of the charge and inversely proportional to the square of the mass of the particle. It follows that if one assumes that the present structure of quantum electrodynamics with its renormalization procedure is substantially correct, then one may draw conclusions as to the very existence of other elementary charged particles than those already known, based simply on the present accuracy of agreement of the theory (which neglects the existence of any particles other than electrons and positrons) and experiment for the line shift.

One can see immediately that all well-established charged particles known at present, other than electrons and positrons, will, because of their large mass, make a contribution to the line shift many orders of magnitude below the present difference between theory and experiment[4] which is of the order of 0.5 Mc/sec (= theoretical − observed line shift). However, the existence of elementary singly-charged spin-$\frac{1}{2}$ particles (other than electrons and positrons) with mass less than four electron masses would more th n double the present discordance between theory and experiment. One may thus conclude that the present agreement between theory and experiment argues against the existence of such particles. For doubly-charged particles of spin-$\frac{1}{2}$ this limit of four electron masses would be quadrupled to sixteen electron masses.

For a spin-0 charged particle field[6] theory predicts a vacuum polarization effect which is only one-eighth that

* Publication assisted by National Science Foundation.
† Fulbright and John Simon Guggenheim Memorial Fellow.
‡ On leave for academic year 1953–1954.
[1] E. A. Uehling, Phys. Rev. **48**, 55 (1935).
[2] W. E. Lamb and R. C. Retherford, Phys. Rev. **79**, 549 (1950); **81**, 222 (1951); **86**, 1014 (1952); Triebwasser, Dayhoff, and Lamb, Phys. Rev. **89**, 98 (1953).
[3] R. P. Feynman, Phys. Rev. **74**, 1430 (1948); N. M. Kroll and W. E. Lamb, Phys. Rev. **75**, 388 (1949); J. B. French and V. F. Weisskopf, Phys. Rev. **75**, 1240 (1949).
[4] E. E. Salpeter, Phys. Rev. **89**, 92 (1953).
[5] H. Umezawa and S. Kamefuchi, Progr. Theoret. Phys. Japan **6**, 543 (1951).
[6] R. G. Moorhouse, Phys. Rev. **76**, 1691 (1949); D. Feldman, Phys. Rev. **76**, 1369 (1949).

for a spin-½ particle of the same charge and mass. Thus we also have an argument against the existence of singly charged spin-0 particles of mass less than about two electron masses and doubly-charged particles of mass less than about eight electron masses. For spin-1 particles one encounters a divergence in the vacuum polarization calculation[6] which precludes any trustworthy conclusion from being drawn.

It is appropriate to examine briefly the assumptions underlying the above conclusions. These are (1) the validity of the principle of charge conjugation invariance, (2) the assumption that all spin-½ particles are properly described by the Dirac equation and that all spin-0 particles are properly described by the Klein-Gordon equation (or its equivalent), and (3) the assumption that the current scheme of quantum electrodynamics is valid down to distances of the order of the Compton wavelength of the particles whose contribution to the vacuum polarization is under consideration. Unfortunately very little may be positively asserted with respect to these assumptions. Our principal evidence for charge-conjugation invariance stems from the existence of positive-negative partners for the electron, mu meson, and pi meson. However, the antiparticle to the proton is still unknown, but there is also no evidence against its existence. For the various recently discovered particles the evidence is still unclear.

With respect to the second assumption little more can be said but that no other satisfactory representations than the Dirac and Klein-Gordon equations have been proposed. It is also not unlikely that should it be possible to construct other representations for spin-½ and spin-0 particles, the vacuum polarization effects associated with such particles would still be of the same order of magnitude as that predicted in the familiar cases; hence only small quantitative changes in our conclusions might be expected. It should be mentioned that the calculations of vacuum polarization which have been employed in the above are actually made under the assumption that the spin-½ particle has a normal Dirac magnetic moment. The inclusion of a Pauli moment term in the equations leads to a divergence in the vacuum polarization similar to that encountered in the case of spin-1 particles.

Relative to the third assumption above we should mention that the charge distribution associated with the vacuum polarization resulting from particles of mass M extends over a region of dimensions $\hbar/Mc$ about an external point charge. Now we have every reason to believe that with the present renormalization procedure, the quantum electrodynamics of the electron is valid at least to the point where the electron explores regions of the order of 10^{-13} cm in extent. Thus we should expect the theory to be valid in its applications to the cases in which we obtained our conclusions. Some question might however be raised concerning the applicability of the theory to the case of vacuum polarization associated with particles of mesonic mass for which the polarization charge would be distributed over regions of the order of 10^{-13} cm in linear dimensions.

It should finally be remarked that there exists some meagre and controversial experimental evidence relative to the conclusions we have drawn above. There have repeatedly been reported observations of positive particles, with masses of several times the electron mass, in the neighborhood of certain negative beta-emitting nuclei (particularly P^{32}) which are energetically incapable of emitting positrons.[7] On the other hand, some observers have not been able to confirm their existence. Without taking any position in this controversy we can only suggest that our conclusions would favor these particles, *if* they do indeed exist, being bosons unless their masses have been underestimated. It is probably only a fortuitous circumstance that the real existence of charged spin-0 particles of mass 2.5 times the electron mass would make up the present difference between theory and experiment on the hydrogen line shift—a difference which has been suggested to be a little large to be accounted for by (at present, unknown) sixth order terms in the theoretical calculation.[4] If only because of its interest relative to the theory of the line shift, it would seem to be of importance to clarify the experimental situation relative to the existence of these particles.

It is a pleasure to acknowledge the assistance granted the author under a Fulbright Research Grant and a John Simon Guggenheim Memorial Fellowship. The author would also like to express his thanks for the gracious hospitality extended to him by the Institute for Theoretical Physics and its director, Professor Niels Bohr.

[7] G. Groetzinger and F. L. Ribe, Phys. Rev. 87, 1003 (1952), and references contained therein.

On the Classical Theory of Particles Interacting with Electromagnetic and Mesonic Fields. I*

PETER HAVAS
Department of Physics, Lehigh University, Bethlehem, Pennsylvania
(Received August 10, 1953)

The classical equations of motion of particles which are simple poles of both the electromagnetic and the neutral (scalar or vector) mesonic field are formulated both for field theory and for the theory of action at a distance. These equations are used to discuss the field contributions to the mass of the particles, the scattering of electromagnetic radiation, photomeson production, mesonic production of electromagnetic radiation, and the electromagnetic corrections for meson scattering.

I. INTRODUCTION

A QUANTITATIVE description of phenomena on the elementary particle level can only be expected on the basis of a quantum theory. The calculation of such effects on the basis of classical theory is undertaken here for two reasons. First, as has been noted by Bhabha,[1] classical theory may allow us to calculate some radiation phenomena to a very good approximation in a region of energy in which typical quantum effects are not yet of great importance, while the usual first-order approximation of quantum theory is already entirely insufficient. Although higher-order approximations can be obtained by the recently developed methods of quantum field theory, this procedure is very tedious and not very suitable for a field in which the main need is to obtain a survey of the characteristic features of the phenomena to be expected rather than extremely accurate calculation of a particular effect. Second, at present we are limited to a classical discussion of the possible experimental distinction between the points of view of field theory and the theory of action at a distance. The present form of quantum theory is based on the concepts of field theory, which gained acceptance by the successful description of radiation phenomena; although the possibility of such a description in a theory of action at a distance had been indicated by Wheeler and Feynman,[2] no consistent quantum theory has yet been developed from this point of view.

On the basis of pure electrodynamics no experimental distinction appears to be possible between the two points of view.[3-4] For interaction through meson fields, however, the two theories lead to different equations of motion, and an experimental decision is possible at least in principle.[5] With this in view, the scattering of neutral mesons by nucleons was calculated according to the theory of action at a distance[6] and compared with earlier field-theoretical results.[7,8] Characteristic, though small, differences between the predictions of the two theories were found. Similar effects, much easier to investigate experimentally, were to be expected if the force acting on the nucleon was taken as electromagnetic rather than mesonic. Thus the present study is concerned with phenomena involving particles capable of interaction both with an electromagnetic and a mesonic field. These phenomena are investigated both from the point of view of field theory and from that of the theory of action at a distance. It is found that both these theories predict the same general features, but show the same type of small differences as were found previously in the case of scattering of neutral mesons.

All of the calculations reported here, as those of MH, are carried out for simple poles of the meson field, i.e., for scalar theory with scalar coupling and for vector theory with vector coupling. A second part of this paper, to be published shortly, will deal with dipoles, i.e., pseudoscalar theory with pseudovector coupling and vector theory with tensor coupling. All of the explicit calculations are carried out for neutral meson fields. However, as discussed in Sec. II, all the results obtained also hold for charge-symmetric meson fields if no external charged field is present, as long as any direct interaction between the mesonic and the electromagnetic field is neglected. Only the beginnings of a field theory and no action-at-a-distance theory exist which take this interaction into account.

II. THE EQUATIONS OF MOTION

The field-theoretical equations of motion of point particles interacting with both electromagnetic and mesonic field can be found easily by the method of Dirac,[9] which was extended by Harish-Chandra[10] to particles interacting with any generalized wave field.

* Assisted by the National Science Foundation.
[1] H. J. Bhabha, Proc. Roy. Soc. (London), **A178**, 314 (1941).
[2] J. A. Wheeler and R. P. Feynman, Revs. Modern Phys. **17**, 157 (1945).
[3] P. Havas, Phys. Rev. **74**, 456 (1948); hereafter referred to as H.
[4] P. Havas, Phys. Rev. **86**, 974 (1952).
[5] P. Havas, Phys. Rev. **87**, 309 (1952); hereafter referred to as H I.
[6] C. R. Mehl and P. Havas, Phys. Rev. **91**, 393 (1953); hereafter referred to as MH. An extension of this work to charged mesons is expected to be published shortly.
[7] H. J. Bhabha, Proc. Roy. Soc. (London) **A172**, 384 (1939).
[8] Harish-Chandra, Proc. Indian Acad. Sci. **21**, 135 (1945).
[9] P. A. M. Dirac, Proc. Roy. Soc. (London) **A167**, 148 (1938).
[10] Harish-Chandra, Proc. Roy. Soc. (London) **A185**, 269 (1946).

In this method the finite force and self-force terms in the equations of motion are obtained from the energy-momentum tensor of the field; if several noninteracting fields are involved, we obtain, because of the additivity of the energy-momentum tensors of the different fields, the sum of the corresponding force and self-force terms.[11]

Throughout this paper we use the same notation as in H I, except for dropping the subscript a designating the particle under consideration, as we are only concerned with a single particle. By the procedure outlined above, we obtain for the equations of motion of a particle in an electromagnetic field $F_{\mu\nu}$ and a neutral vector meson field $G_{\mu\nu}$ (compare H, 4[12] and H I, 21a)

$$M\dot{v}_\mu-\tfrac{2}{3}(e^2+g^2)(\ddot{v}_\mu+v_\mu\dot{v}^2)-g^2\chi^2v^\nu\int_{-\infty}^{\tau}\frac{s_\mu v_\nu(\tau')-s_\nu v_\mu(\tau')}{s^2}J_2(\chi s)d\tau'=(eF_{\mu\nu}+gG_{\mu\nu})v^\nu, \tag{1}$$

if the field of the particle is assumed to be purely retarded. If it is taken as half-retarded, half-advanced, we obtain instead (compare H, 3 and H I, 22a)

$$M\dot{v}_\mu-\tfrac{1}{2}g^2\chi^2v^\nu\int_{-\infty}^{\infty}\frac{s_\mu v_\nu(\tau')-s_\nu v_\mu(\tau')}{s^2}J_2(\chi s)d\tau'=(eF_{\mu\nu}+gG_{\mu\nu})v^\nu. \tag{2}$$

Here M, e, and g are the mass, charge, and mesonic charge of the particle with position z_μ, velocity v_μ, and proper time τ; J is the Bessel function; χ is a constant (equal to $1/\hbar$ times the meson mass in the quantized theory); $s_\mu(\tau')=z_\mu(\tau)-z_\mu(\tau')$, and $s=(s_\mu s^\mu)^{\frac{1}{2}}$.

If the particle is a singularity of a neutral scalar meson field F_μ (with potential U) instead of a vector meson field, we get (compare H I, 21b and H I, 22b)

$$M\dot{v}_\mu-\tfrac{1}{3}(2e^2+g^2)(\ddot{v}_\mu+v_\mu\dot{v}^2)-\tfrac{1}{2}g^2\chi^2v_\mu+g^2\chi^2\int_{-\infty}^{\tau}\frac{s_\mu}{s^2}J_2(\chi s)d\tau'+g^2\chi\frac{d}{d\tau}\left[v_\mu\int_{-\infty}^{\tau}\frac{1}{s}J_1(\chi s)d\tau'\right]=eF_{\mu\nu}v^\nu+gF_\mu+g\frac{d}{d\tau}(Uv_\mu) \tag{3}$$

for the retarded case, and

$$M\dot{v}_\mu+\tfrac{1}{2}g^2\chi^2\int_{-\infty}^{\infty}\frac{s_\mu}{s^2}J_2(\chi s)d\tau'+\tfrac{1}{2}g^2\chi\frac{d}{d\tau}\left[v_\mu\int_{-\infty}^{\infty}\frac{1}{s}J_1(\chi s)d\tau'\right]=eF_{\mu\nu}v^\nu+gF_\mu+g\frac{d}{d\tau}(Uv_\mu) \tag{4}$$

for the symmetric case.

As discussed in H I for the case of particles interacting with meson fields only, equations of this type are not suitable for a theory of action at a distance. As in H I, we propose to take as the fundamental equations of this theory the expressions obtained by omitting the integrals over the entire motion of the particle from the equations of the symmetric case of field theory, and taking the external fields and potentials to be the symmetric fields and potentials of all other particles. The theory of these new equations can then be developed in complete analogy to the one presented in H I. They can be derived from a variational principle, which is simply the principle (H I, 27) with the addition of the interaction integral appearing in Fokker's principle (H I, 26). Detailed conservation laws of the form (H I, 37) can be formulated, using the particle momenta (H I, 39) and energy-momentum tensors which are the sum of the tensors (H I, 40) or (H I, 41) and the corresponding tensors of the electrodynamic action-at-a-distance theory of Frenkel, Synge, and Wheeler and Feynman.[13] An application of the Wheeler-Feynman method to the new equations leads to the equations (corresponding to H I, 50) containing radiation terms

$$M\dot{v}_\mu-\tfrac{2}{3}(e^2+g^2)(\ddot{v}_\mu+v_\mu\dot{v}^2)-\tfrac{1}{2}g^2\chi^2v^\nu\left\{\int_{-\infty}^{\tau}\frac{s_\mu v_\nu(\tau')-s_\nu v_\mu(\tau')}{s^2}J_2(\chi s)d\tau'-\int_{\tau}^{\infty}\frac{s_\mu v_\nu(\tau')-s_\nu v_\mu(\tau')}{s^2}J_2(\chi s)d\tau'\right\}$$
$$=(eF_{\mu\nu}+gG_{\mu\nu})v^\nu, \tag{5}$$

[11] Another way of obtaining the equations of motion for particles in noninteracting fields is discussed by F. R. Crownfield, Jr., and P. Havas, Phys. Rev. (to be published shortly).

[12] The notation used in H differs slightly from that of H I. Also $F_{\mu\nu}$ as used here is defined in terms of the potentials in analogy to $G_{\mu\nu}$ (defined by H I, 2a), and thus equals $F_{\nu\mu}$ as used in H.

[13] For references see H I.

and

$$M\dot{v}_\mu-\tfrac{1}{3}(2e^2+g^2)(\ddot{v}_\mu+v_\mu\dot{v}^2)-\tfrac{1}{2}g^2\chi^2v_\mu+\tfrac{1}{2}g^2\chi^2\left\{\int_{-\infty}^{\tau}\frac{s_\mu}{s^2}J_2(\chi s)d\tau'-\int_{\tau}^{\infty}\frac{s_\mu}{s^2}J_2(\chi s)d\tau'\right\}$$
$$+\tfrac{1}{2}g^2\chi\frac{d}{d\tau}\left\{v_\mu\left[\int_{-\infty}^{\tau}\frac{1}{s}J_1(\chi s)d\tau'-\int_{\tau}^{\infty}\frac{1}{s}J_1(\chi s)d\tau'\right]\right\}=eF_{\mu\nu}v^\nu+gF_\mu+g\frac{d}{d\tau}(Uv_\mu), \quad (6)$$

for the vector and scalar meson case, respectively. Now the external fields and potentials are to be taken as the retarded fields and potentials of all other particles.

Similar considerations can be applied in the case of particles interacting with electromagnetic and charge-symmetrical mesonic fields, as long as the interaction between these two fields is neglected. For the purposes of the present investigation we do not need the explicit form of the equations of motion of this case, as they reduce to the equations of the neutral case (1)–(6) for the problems considered, which do not involve an external charged meson field. This can be seen from a consideration of the case of the charge-symmetrical meson field alone, for which the field-theoretical equations of motion were found by Le Couteur;[14] an action-at-a-distance formulation was given in a recent paper.[15] In the charge-symmetrical theory the mesonic charge-current density of the particle is taken to be proportional to a unit vector of "isotopic spin" τ. The variation of τ is determined by Eqs. (16) of reference 15, which remains valid in the presence of an electromagnetic field. It can easily be seen that for the problems considered in this paper a possible solution of these equations is given by $\tau=-\gamma$, which by Eqs. (17) of reference 15 corresponds to a constant charge e for the particle; but then the equations of motion reduce to those of the neutral case. Therefore all the results obtained here for neutral mesons remain valid in the charge-symmetrical meson theory; the processes considered are not changed by any effects of charged self-fields.

III. THE MASS OF THE PARTICLE

The field-theoretical investigations of Bhabha[7] showed that for very slow oscillations ($\omega\ll\chi$) of a particle interacting with a vector meson field [our Eq. (1) with $e=0$] the effective mass M_e is given by

$$M_e=M-\tfrac{1}{2}g^2\chi; \quad (7)$$

in the case of such oscillations of a particle in a scalar meson field [our Eq. (3) with $e=0$], Harish-Chandra[8] found that

$$M_e=M+\tfrac{1}{2}g^2\chi. \quad (8)$$

It was also found by Bhabha that if the particle is permanently at rest, the vector meson field contributes an amount $-\frac{1}{2}g^2\chi$ to its energy (apart from an infinite self-energy, which is eliminated by Dirac's method), in accord with (7); a similar calculation for the case of a scalar meson field yields a field contribution $+\frac{1}{2}g^2\chi$, in accord with (8).

On the other hand, it was shown in MH that in the theory of action at a distance we have, for a particle oscillating with any frequency

$$M_e=M \quad (9)$$

in both the vector and scalar meson case [Eqs. (5) and (6) with $e=0$]; in such a theory no physical meaning is attributed to the concept of "field contribution to the energy."

From these results it may be expected that the same effective mass will be obtained for other motions with small acceleration, and thus M_e rather than M should be identified with the mass as determined experimentally. In this section this is shown to be the case for motion in a constant electric or magnetic field. We are forced to limit our discussion to such special cases, in which a solution for the entire motion of the particle can be obtained, because of the appearance of the integrals over the motion in Eqs. (1)–(6); thus the behavior of the particle is not determined by the initial conditions and the instantaneous value of the external field, in contrast to the usual situation in mechanics.

We first consider a charge e in a constant electric field in the x direction, i.e., we take $F_{01}=E$ as the only nonvanishing component of the field. In the case of a charge which has no mesonic interaction ($g=0$) our Eqs. (1), (3), (5), and (6) reduce to the Lorentz-Dirac equations, which are known to possess a solution[16] identical with the solution of Eqs. (2) and (4) (with $g=0$) which do not contain any radiation reaction terms.[17] With a suitable choice of the origin of the coordinate system this solution is given by

$$z_0=\alpha\sinh(\tau/\alpha), \quad z_1=-\alpha\cosh(\tau/\alpha), \quad z_2=z_3=0, \quad (10)$$

and, therefore,

$$v_0=\cosh(\tau/\alpha), \quad v_1=-\sinh(\tau/\alpha), \quad (11)$$

with

$$\alpha=M/eE. \quad (12)$$

We shall now show that our equations with $g\neq0$ allow the same solution (10), with the same value for α in the case of the equations of the theory of action at a

[14] K. J. Le Couteur, Proc. Cambridge Phil. Soc. **45**, 429 (1949).
[15] P. Havas, Phys. Rev. **91**, 997 (1953).
[16] G. A. Schott, Phil. Mag. **29**, 49 (1915).
[17] M. Born, Ann. Physik **30**, 1 (1909).

distance (5) and (6), but with different ones in the case of the field-theoretical equations (1) and (3).

For this we first consider the $\mu=1$ component of Eq. (1) of the vector case. From Eq. (11) we get $\bar{v}_\mu+v_\mu\dot{v}^2=0$ regardless of the value of α. The only nonvanishing integral can be transformed using Eqs. (10) and (11). We obtain

$$\int_{-\infty}^{\tau}\frac{s_1v_0(\tau')-s_0v_1(\tau')}{(s)^2}J_2(\chi s)d\tau'=-\int_0^\infty\frac{J_2(\chi s)ds}{(4\alpha^2+s^2)^{\frac{1}{2}}}.$$

This integral is evaluated on p. 435 of Watson.[18] Inserting the result in Eq. (1), we obtain an equation in which each term is proportional to $\cosh(\tau/\alpha)$ and which is thus satisfied if the coefficient of this function vanishes. The same coefficient, but multiplying $\sinh(\tau/\alpha)$, is obtained from a consideration of the $\mu=0$ component of Eq. (1). Therefore Eq. (10) is indeed a solution of Eq. (1), provided that α satisfies the equation

$$-M/\alpha+g^2\chi^2I_1(\alpha\chi)K_1(\alpha\chi)=-eE. \tag{13}$$

Here I and K are the modified Bessel and Hankel functions defined on pp. 77–78 of Watson. If $\alpha\chi\gg1$, we can use their asymptotic expressions and obtain

$$\alpha=(M-\tfrac{1}{2}g^2\chi)/eE, \tag{14}$$

in agreement with Eq. (7). If the mass and charge of the proton are taken for M and e, α is of the order of 10^3 cm for $E=10^6$ v/cm, and thus $\alpha\chi$ is of the order of 10^{16}. Therefore the use of the asymptotic expressions is justified for all available field strengths.

If Eq. (5) of the theory of action at a distance is used, we have to evaluate $\frac{1}{2}(f_{-\infty}^{\tau}-f_{\tau}^{\infty})$ instead of $f_{-\infty}^{\tau}$, with the same integrand as before; as this integrand is an even function of $\tau-\tau'$ for a solution of the form (10), this expression equals zero. Therefore all the radiation terms vanish, and we obtain the same Eq. (12) as in the case $g=0$, in agreement with Eq. (9).

In the scalar case a consideration of the field-theoretical Eq. (3) shows that Eq. (10) is a solution of this equation provided that α satisfies

$$-M/\alpha+g^2\chi^2I_0(\alpha\chi)K_0(\alpha\chi)=-eE; \tag{15}$$

using the asymptotic expressions we obtain

$$\alpha=(M+\tfrac{1}{2}g^2\chi)/eE, \tag{16}$$

in agreement with Eq. (8). From Eq. (6) of the theory of action at a distance we obtain Eq. (12) as in the vector case.

As a second example, we now consider a charge in a constant magnetic field in the z direction, i.e., we take $F_{21}=H$ and all other field components equal to zero. Only the nonrelativistic approximation will be considered. We also neglect the electromagnetic radiation reaction, but not the mesonic one; for the frequencies considered these are of different character, as there is no emission of mesonic radiation if $\omega<\chi$.[7,8] We assume a solution of the form

$$z_0=t,\quad z_1=R\sin\omega t,\quad z_2=R\cos\omega t. \tag{17}$$

Therefore we have

$$v_1=R\omega\cos\omega t,\quad v_2=-R\omega\sin\omega t, \tag{18}$$

where $R\omega\ll1$, so that we can neglect higher powers of this quantity. In this approximation, the 1-component of Eq. (1) equals

$$-MR\omega^2\sin\omega t+\tfrac{2}{3}g^2R\omega^3\cos\omega t$$
$$-g^2\chi^2R\int_{-\infty}^{t}\frac{(\sin\omega t-\sin\omega t')-s\omega\cos\omega t'}{(s)^2}J_2(\chi s)dt'$$
$$=-eHR\sin\omega t,$$

where $s=s_0=t-t'$. Evaluating the integral we find that the coefficient of $\cos\omega t$ vanishes; to assure the vanishing of the coefficient of $\sin\omega t$, we must have

$$M+\tfrac{1}{8}g^2\chi\omega^{-2}[1-(1-\nu^2)^{\frac{1}{2}}(1+2\nu^2)]=eH/\omega^3, \tag{19}$$

where

$$\nu=\omega/\chi. \tag{20}$$

For $\nu\ll1$ this reduces to

$$M-\tfrac{1}{2}g^2\chi=eH/\omega^2, \tag{21}$$

in agreement with Eq. (7). A consideration of the 2-component of Eq. (1) leads to the same result.

Using the same approximations we find that Eq. (17) is a solution of Eq. (3) provided that

$$M-\tfrac{1}{8}g^2\chi^3\omega^{-2}[1-(1-\nu^2)^{\frac{1}{2}}-3\nu^2]=eH/\omega^2. \tag{22}$$

For $\nu\ll1$ this becomes

$$M+\tfrac{1}{2}g^2\chi=eH/\omega^2, \tag{23}$$

in agreement with Eq. (8). In the case of Eqs. (5) and (6) of the theory of action at a distance we obtain

$$M=eH/\omega^2, \tag{24}$$

in agreement with Eq. (9).

Thus, regardless of the form of meson theory used, we can conclude that observations in a constant electric or magnetic field determine e/M_e rather than e/M. On the other hand, it might be thought that experiments in a gravitational field would determine M instead of M_e. A calculation of the motion of a particle interacting with both a gravitational and a mesonic field is beyond the scope of the theory presented here; however, an application of the principle of equivalence to the case of motion in a uniform electric field shows that the gravitational mass of the particle must also be identified with the effective mass M_e.

Thus in all the results of Secs. IV and V we shall have to express M in terms of M_e by Eqs. (7)–(9) before we can compare them with experiment.

[18] G. N. Watson, *A Treatise on the Theory of Bessel Functions* (Cambridge University Press, Cambridge, 1922).

IV. SCATTERING OF ELECTROMAGNETIC RADIATION AND PHOTOMESON PRODUCTION

We now consider the phenomena associated with the motion of a charge in the field of an electromagnetic wave. Assuming that the amplitude of oscillation of the charge is small compared to the wavelength, we take the electric field of the incident wave at the position of the charge as

$$F_{01}=-\gamma\cos\omega t. \tag{25}$$

In this and the following section we use the same nonrelativistic approximation as for the motion of a charge in a magnetic field treated in Sec. III, without neglecting the influence of the electromagnetic radiation terms, however. The coordinates of the particle are assumed to be

$$z_0=t,\quad z_1=(\beta/\omega)\sin(\omega t+\delta),\quad z_2=z_3=0. \tag{26}$$

This form of the field and of the coordinates is chosen in analogy to that used in references 6–8;[10] β and δ can then be calculated as in these papers. The only modifications necessary are those due to the presence of the electromagnetic radiation reaction in Eqs. (1), (3), (5), and (6) and of an applied force proportional to e instead of g.

In the vector meson case we obtain thus

$$\beta=\frac{e\gamma}{\omega[(M+g^2\chi P^2)^2+(4/9)\omega^3(e^2+g^2Q)^2]^{\frac{1}{2}}} \tag{27}$$

and

$$\cos\delta=\tfrac{2}{3}(e^2+g^2Q)\omega^2\beta/\gamma, \tag{28}$$

with

$$Q=\begin{cases}0, & \nu<1\\ \frac{1}{2}(\nu^2-1)^{\frac{1}{2}}/\nu^3+(\nu^2-1)/\nu, & \nu>1\end{cases} \tag{29}$$

for both Eqs. (1) and (5); for the field-theoretical equation (1) P is given by

$$P=\begin{cases}\frac{1}{3}[1/\nu^3-(1-\nu^2)^{\frac{1}{2}}/\nu^3-2(1-\nu^2)^{\frac{1}{2}}], & \nu<1\\ 1/3\nu^3, & \nu>1\end{cases}, \tag{30}$$

while for Eq. (5) of action-at-a-distance theory we have

$$P=0. \tag{31}$$

For $\nu\ll1$, Eq. (30) reduces to

$$P=-\tfrac{1}{3}. \tag{32}$$

Equations (31) and (32) are in agreement with Eqs. (9) and (7).

The energy flow associated with the incoming plane wave is

$$\gamma^2/8\pi \tag{33}$$

and the flow of electromagnetic energy into the solid angle $d\Omega$ emitted by a charge oscillating according to Eq. (26) equals

$$e^2\beta^2\omega^2\sin^2\theta\,d\Omega/8\pi, \tag{34}$$

where θ is the angle between the direction of oscillation of the particle and the direction of propagation of the scattered wave. The differential cross section for scattering is obtained by taking the ratio of expressions (34) and (33) and using Eq. (27). On integration we obtain the total cross section

$$\sigma=\frac{(8\pi/3)e^4}{(M+g^2\chi P)^2+(4/9)\omega^2(e^2+g^2Q)^2}. \tag{35}$$

Therefore for $\nu<1$ in the theory of action at a distance the scattering cross section is the same as that obtained in the usual theory neglecting mesonic effects. In field theory it is also experimentally indistinguishable from that obtained in the usual theory for $\nu\ll1$, as the only difference is in the different effective mass.

The cross section for scattering by bound charges (dispersion) can be obtained in the same manner. Because of the smallness of the binding energy only the case $\nu\ll1$ is of importance; here again the different theories lead to identical predictions.

In addition to electromagnetic radiation, the oscillating charge also emits neutral mesonic radiation provided that $\nu>1$, just as in the case of motion due to a mesonic field. No charged mesonic radiation can be emitted on the basis of the theory considered here, which does not consider either a direct interaction of the electromagnetic and the mesonic field, or a magnetic moment of the particle. The flow of energy into the solid angle $d\Omega$ is given (see MH 18 and 19) by

$$g^2\beta^2\omega(\omega^2-\chi^2)^{\frac{1}{2}}\sin^2\theta\,d\Omega/8\pi, \tag{36}$$

and

$$g^2\beta^2\chi^2(\omega^2-\chi^2)^{\frac{1}{2}}\cos^2\theta\,d\Omega/8\pi\omega, \tag{37}$$

for transverse and longitudinal vector mesons, respectively. The differential cross sections for photomeson production are obtained by dividing these expressions by the electromagnetic energy flow (33) and using Eq. (27). On integration we obtain for the total cross sections

$$\sigma_{et}=\frac{(8\pi/3)[(\omega^2-\chi^2)^{\frac{1}{2}}/\omega]e^2g^2}{(M+g^2\chi P)^2+(4/9)[e^2\omega+g^2(\omega^2-\chi^2)^{\frac{1}{2}}(1+\frac{1}{2}\chi^2/\omega^2)]^2} \tag{38}$$

and

$$\sigma_{el}=\tfrac{1}{2}(\chi^2/\omega^2)\sigma_{et} \tag{39}$$

for the production of transverse and longitudinal mesons, respectively.

In the scalar meson case we again obtain Eqs. (27) and (28), but with different meanings for P and Q. We get

$$Q=\begin{cases}0, & \nu<1\\ \frac{1}{2}(\nu^2-1)^{\frac{1}{2}}/\nu^3, & \nu>1\end{cases} \tag{40}$$

for both Eqs. (3) and (6). For the field-theoretical

[10] In Eq. (4) of MH, corresponding to our Eq. (26), the parentheses were omitted in $\sin(\omega t+\delta)$ through a printer's error.

equation (3) we get

$$P=\begin{cases}1+\frac{1}{3}(1-\nu^2)^{\frac{1}{2}}/\nu^2-1/3\nu^2, & \nu<1\\ 1-1/3\nu^2, & \nu>1\end{cases} \tag{41}$$

while for Eq. (6) of the theory of action at a distance we have again

$$P=0. \tag{42}$$

For $\nu\ll 1$, Eq. (41) reduces to

$$P=\tfrac{1}{2}. \tag{43}$$

Equations (42) and (43) are in agreement with Eqs. (19) and (18).

The cross section for the scattering of electromagnetic radiation is thus again of the form (35), with P and Q now given by Eqs. (40)–(43); the remarks made concerning this expression and also the scattering by bound charges in the vector case are also valid for the scalar case.

The flow of energy emitted in the form of scalar mesonic radiation into the solid angle $d\Omega$ is given by [see Eq. (22) of reference 8]

$$g^2\beta^2(\omega^2-\chi^2)^{\frac{1}{2}}\cos^2\theta d\Omega/8\pi\omega, \tag{44}$$

and thus we obtain for the total cross section for the photoproduction of scalar mesons

$$\sigma_{es}=\frac{(4\pi/3)[(\omega^2-\chi^2)^{\frac{1}{2}}/\omega^3]e^2g^2}{(M+g^2\chi P)^2+(4/9)[e^2\omega+\frac{1}{2}g^2(\omega^2-\chi^2)^{\frac{1}{2}}/\omega^2]^2}. \tag{45}$$

V. MESONIC PRODUCTION OF ELECTROMAGNETIC RADIATION AND ELECTROMAGNETIC CORRECTIONS FOR MESON SCATTERING

We now consider the phenomena arising if the motion of the particle is due to a neutral meson wave instead of an electromagnetic one. In analogy to Eq. (25) we take the field of the incoming wave at the position of the charge as

$$G_{10}=\gamma\cos\omega t \tag{46}$$

in the vector meson case, and as

$$F_1=\gamma\cos\omega t \tag{47}$$

in the scalar meson case. To have a real traveling wave we must have $\omega>\chi$. The coordinates of the particle are again assumed to be given by Eqs. (21). Then β is given by g/e times expression (27), and $\cos\delta$ is again related to it by Eq. (28); P and Q are given by Eqs. (29)–(32) and (40)–(43) as before. The energy flow associated with the incoming wave is given (see MH 20 and 21) by

$$\gamma^2(\omega^2-\chi^2)^{\frac{1}{2}}/8\pi\omega \tag{48}$$

for transverse vector mesons, and by

$$\gamma^2\omega(\omega^2-\chi^2)^{\frac{1}{2}}/8\pi\chi^2 \tag{49}$$

for longitudinal vector mesons. For scalar mesons it is given [see Eq. (21) of reference 8] by

$$\gamma^2\omega(\omega^2-\chi^2)^{-\frac{1}{2}}/8\pi. \tag{50}$$

The energy flow of the emitted electromagnetic radiation is given by (34), with the new value for β; dividing it by the expressions (48)–(50) and integrating we obtain the total cross sections for the production of electromagnetic radiation by a mesonic wave. In terms of the cross sections (38), (39), and (45) for photomeson production these are

$$\sigma_{te}=\omega^2(\omega^2-\chi^2)^{-1}\sigma_{el}, \tag{51}$$

$$\sigma_{le}=2\omega^2(\omega^2-\chi^2)^{-1}\sigma_{el}, \tag{52}$$

and

$$\sigma_{se}=2\omega^2(\omega^2-\chi^2)^{-1}\sigma_{es} \tag{53}$$

for an incoming transverse vector, longitudinal vector and scalar meson wave, respectively.

Similarly we can obtain the cross sections for the scattering of mesons, using the expressions (36), (37), or (44) for the energy flow of the emitted mesonic radiation. We get

$$\sigma_{tt}=\frac{(8\pi/3)g^4}{(M+g^2\chi P)^2+(4/9)[e^2\omega+g^2(\omega^2-\chi^2)^{\frac{1}{2}}(1+\frac{1}{2}\chi^2/\omega^2)]^2} \tag{54}$$

if the incoming and the scattered waves are both transverse. With an analogous notation we obtain for the other possible cases for the scattering of vector mesons:

$$\sigma_{tl}=\tfrac{1}{2}\sigma_{lt}=\tfrac{1}{2}(\chi^2/\omega^2)\sigma_{tt},\quad \sigma_{ll}=\tfrac{1}{2}(\chi^4/\omega^4)\sigma_{tt}. \tag{55}$$

The cross section for the scattering of scalar mesons is given by

$$\sigma_{ss}=\frac{(4\pi/3)[(\omega^2-\chi^2)^2/\omega^4]g^4}{(M+g^2\chi P)^2+(4/9)[e^2\omega+\frac{1}{2}g^2(\omega^2-\chi^2)^{\frac{1}{2}}/\omega^2]^2}. \tag{56}$$

VI. DISCUSSION

As noted in the introduction, the calculations reported here were undertaken to obtain information about the effects of radiation damping and about the relation between the classical points of view of field and of action-at-a-distance theory. Previous calculations had indicated that there is no possibility of distinguishing between the predictions of these points of view on the basis of electrodynamics alone. The calculations of this paper of course go beyond pure electrodynamics by including an interaction between particle and meson field; nevertheless, some of them refer to effects in which the over-all processes considered are purely electrodynamic ones. These are the motion of a charge in a constant electric or magnetic field and the scattering of electromagnetic radiation (for $\omega<\chi$). In the language of the perturbation theory of quantum mechanics, these are processes in which only virtual, but no real, mesons participate.

For these processes it was found that for small accelerations the only effect produced by the meson fields is a change in the effective mass of the particle. It appears that it is this changed mass which has to be identified with the mass as determined experimentally, and thus for any processes involving only small accelerations there is no distinction between the predictions of the two classical points of view. In particular, this will always be the case for the motion of a charge in the macroscopic electromagnetic fields available in practice. However, there is such a distinction in the case of scattering of electromagnetic radiation for frequencies comparable to or higher than χ, although for such high frequencies the approximations used in deriving Eq. (35) are not very good. Here, as well as in all other cross sections calculated in Secs. IV and V, the two points of view differ only in the terms $M+g^2\chi P$. The values for Q and the angular distribution of any mesonic radiation emitted, although different for the vector and the scalar case, do not introduce any difference between field and action-at-a-distance theory.

If the electromagnetic radiation damping terms are neglected, our results for meson scattering [Eqs. (54)–(56)] agree with those obtained earlier by several authors from both points of view.[20] The radiation damping due to mesonic (and also to electromagnetic) radiation has the effect of producing a maximum in these as well as in all other cross sections calculated in this paper. This maximum occurs at energies too high to agree with that observed for photomeson production; however, much better agreement appears to be possible if other forms of meson theory are used. This will be discussed in the second part of this paper.

[20] These are summarized in Table I of MH; however, a factor 2 was omitted there erroneously in all cross sections for incoming longitudinal mesons.

PHYSICAL REVIEW VOLUME 93, NUMBER 4 FEBRUARY 15, 1954

Ingoing Waves in Final State of Scattering Problems

G. Breit, *Sloane Physics Laboratory, Yale University,* New Haven, Connecticut*

AND

H. A. Bethe, *Institute for Nuclear Studies, Cornell University, Ithaca, New York*

(Received November 9, 1953)

The employment of the ingoing wave modification of plane waves in final states is justified by a general argument.

THE fact that the calculation of transition probabilities by means of matrix elements with modified plane waves should be made employing the ingoing rather than outgoing wave modification of the final state has been known for some time and proofs are available in special cases.[1] This fact has assumed more pronounced importance in connection with recent work on bremsstrahlung.[2] In the last-mentioned publication there is an indication of a way of understanding the reason for employing the ingoing wave modification in terms of a temporal sequence of events. The present note is a presentation of relations which give a general reason for the choice of the final state function.

The related and simpler case of scattering by a central field has a sufficient bearing on the problem to justify a preliminary brief discussion. In this case it is customary to employ the boundary condition that at large distances from the center r the time-independent wave function $\psi_{\mathbf{k}}$ have the asymptotic form

$$\psi_{\mathbf{k}}\sim e^{i\mathbf{k}\cdot\mathbf{r}}+f(\theta)e^{ikr}/r, \tag{1}$$

with θ and $\mathbf{k}$ standing, respectively, for colatitude and propagation vector. Among the various ways of justifying the outgoing wave modification represented by the last term in Eq. (1), the one closest to that used below for the main problem consists in the consideration of a wave packet for a time-dependent ψ. At the time $t=0$ this wave packet will be supposed to be moving along the z axis toward the scattering center. The time-dependent function can be represented as

$$\Psi=\int C_{\mathbf{k}}\psi_{\mathbf{k}}e^{-iEt/\hbar}d\mathbf{k}, \tag{2}$$

* Assisted by the joint program of the U. S. Office of Naval Research and U. S. Atomic Energy Commission and the Air Research and Development Command of the U. S. Air Force.

[1] A. Sommerfeld, *Atombau und Spektrallinien* (F. Vieweg and Son, Braunschweig, 1939), Vol. 2, pp. 457 and 502; N. F. Mott and H. S. W. Massey, *Atomic Collisions* (Oxford University Press, London, 1949), second edition, pp. 111–113; also first edition (1933) pp. 82–84; Rose, Biedenharn, and Arfken, Phys. Rev. **85**, 5 (1952), see Sec. III, p. 9. One of the authors (GB) would like to thank Dr. L. C. Biedenharn for a helpful and stimulating discussion of the last reference. General arguments resulting in employment of ingoing waves along lines differing from those of the present note have been given by K. M. Watson, Phys. Rev. **88**, 1163 (1952) as well as by M. Gell-Mann and M. L. Goldberger, Phys. Rev. **91**, 398 (1953). Watson works out the probability of a spin direction by means of Wigner's time reversal transformation.

[2] L. Maximon and H. A. Bethe, Phys. Rev. **87**, 156 (1952); Bethe, Maximon and Low, Phys. Rev. **91**, 417 (1953).

where E is the energy corresponding to k so that nonrelativistically $E=\hbar^2k^2/2m$, where m=mass. Since for $t<0$ the wave packet has not yet hit the field, it behaves like a free space packet and can be made to look as in "Condition I" of Fig. 1. On the other hand, after the collision with the scattering field there is also a scattered wave as in "Condition F" of Fig. 1.

The wave packet is taken to be so far from $r=0$ at $t=0$ that the difference between plane and spherical wave fronts in the packet is negligible. Similarly, for condition F the time t is taken so large that the same condition obtains. For $t=0$ the coefficients C_k can be found by Fourier-analyzing the preassigned $\Psi_{t=0}$ and first constructing the packet out of plane waves e^{ikr} rather than out of the ψ_k. The coefficients so found may be identified with the C_k as may be seen by explicit construction in special cases or from the following argument. Before the packet hits the field there can be no scattered wave. Therefore the presence of the second term in Eq. (1) cannot matter in this epoch. Hence

$$\int C_k e^{i[kr-Et/\hbar]}d\mathbf{k}=0, \quad (t<0). \tag{2'}$$

Since for $t<0$, $z<0$ one has

$$kr=-kz, \quad (t<0), \tag{2''}$$

which shows that as one goes along z through the packet the phases change in opposite ways for the two terms of Eq. (1). This circumstance accounts for the difference in the behavior of the two terms, one of which reproduces the plane-wave packet while the other gives zero by destructive interference. On the other hand for $t>t_{coll}$ the signs of r and z are the same so that constructive interference occurs in the same locations for both terms of Eq. (1). If one used e^{-ikr} in the second term the relative phase relations would reverse themselves and the process described would not be the intended one.

It is now possible to visualize the actual problem. It is supposed that one deals with solutions of

$$\left(\frac{\hbar}{i}\frac{\partial}{\partial t}+H_0\right)\Psi_0=0, \tag{3}$$

where H_0 is the Hamiltonian of a scattering problem. In Eq. (3) there may be variables additional to the space variables such as the spin coordinate. The function Ψ_0 is taken to be a wave packet such as that of Eq. (2). The problem is now modified through the introduction of a perturbing Hamiltonian H'. The latter may be caused by the incidence of a plane light wave, coupling to radiation oscillators, emission of a nuclear γ ray, etc. The wave equation is

$$\left(\frac{\hbar}{i}\frac{\partial}{\partial t}+H_0+H'\right)\Psi=0. \tag{4}$$

It is convenient to introduce time-independent solutions of Eq. (3) by means of

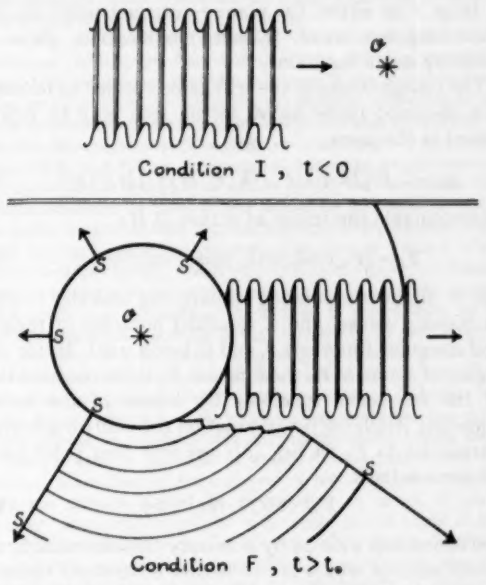

FIG. 1. Illustration of scattering conditions. In condition I the incident train of waves (wave packet) has not yet reached scattering center 0. In condition II the train has passed over 0 and has produced scattered waves S.

$$(H_0-E_j)u_{j,s}=0, \tag{5}$$

where the subscript s enumerates the continuum of possibilities for solutions at a fixed energy E_j. It covers the possibilities of waves having different propagation vectors and spin specifications, and in more complicated problems it could be made to enumerate additional variables such as internal excitation quantum numbers. The normalization of the functions $u_{j,s}$ may be chosen so that

$$\int\int u_{j,s}^*(\mathbf{r},\mu)u_{j,s}(\mathbf{r}',\mu')djds=\delta_{\mu\mu'}\delta(\mathbf{r}-\mathbf{r}'), \tag{6}$$

where μ is the spin coordinate. In the region of discrete levels the integrals in the above formula are understood to be replaced by summations. By means of Eq. (6) one can solve Eq. (4) to first order in H' obtaining

$$\Psi(\mathbf{r},\mu,t)=\Psi_0(\mathbf{r},\mu,t) -\frac{i}{\hbar}\int_0^t dt\int\int djds(u_{j,s}(\mathbf{r}',\mu'), H'\Psi_0(\mathbf{r}',\mu',t))\exp[iE_j(t'-t)/\hbar]u_{j,s}(\mathbf{r},\mu), \tag{7}$$

where the ( ) indicate the scalar product involving integration over $\mathbf{r}'$ and summation over μ'. In the specification of the $u_{j,s}$ the boundary conditions at large r were left unrestricted, the only essential requirement being that of completeness as expressed by Eq. (6). One can satisfy this relation by having the $u_{j,s}$ be asymptotic

at large r to either (a) plane+outgoing wave or (b) plane+ingoing wave. Either modification gives a complete set of functions.

The completeness of the set can be verified as follows. The distorted plane waves for no spin may be represented in the form

$$\varphi_{\mathbf{k}}=\Sigma_L i^L(2L+1)P_L((\mathbf{k}\cdot\mathbf{r})/kr)\mathfrak{F}_L(kr)/(kr), \qquad (8)$$

where outside the region of action of H_0

$$\mathfrak{F}_L=(F_L\cos\delta_L+G_L\sin\delta_L)\exp(\pm i\delta_L), \qquad (9)$$

the + sign corresponding to outgoing and the − sign to ingoing waves, and a standard notation of regular and irregular functions F and G being used. Inside the region of action of H_0 the function $\mathfrak{F}_L$ is the continuation of the free-space functions by means of the radial equation. Applying the summation theorem for spherical harmonics to P_L in Eq. (8), one sees that polar coordinate solutions

$$Y_L^m(\mathbf{r}/r)\mathfrak{F}_L(kr)/(kr) \qquad (10)$$

are connected with $\varphi_{\mathbf{k}}$ by a unitary transformation, the coefficients of which are to within a constant factor

$$Y_L^{m*}(\mathbf{k}/k)d\Omega_{\mathbf{k}}.$$

Here the Y_L^m are normalized spherical harmonics of order L and magnetic quantum number m and $d\Omega_{\mathbf{k}}$ is the element of solid angle in the direction of $\mathbf{k}$. The two arguments of the spherical harmonics are indicated by specification of the unit vector defined by the polar angles. If the functions of Eq. (10) form a complete set, then the $\varphi_{\mathbf{k}}$ do also as a consequence of the unitary character of the transformation. It is immediately obvious that in field-free space the functions of Eq. (10) form a complete set. Establishing H_0 adiabatically the set remains complete as long as for every L the radial equations have no discrete spectrum. In order to keep it complete when there is a discrete spectrum, all the discrete-level functions must be included among the $u_{j,s}$ and the integration must be supplemented by a summation. The extension of the above proof of completeness to the Dirac equation is readily made by observing, in analogy to a similar contact transformation used by Dirac[3] in his introduction of the two Dirac-Darwin radial functions, that the transformation to the two radial functions from the four-component spinor is a contact transformation. The Y_L^m are now replaced by column matrices containing the Y_L^m and the single radial function $\mathfrak{F}_L$ is replaced by a column matrix having for elements two radial functions. In order to keep the set complete negative-energy states have to be included but, on account of the fact that the physical problem with Dirac's equation is concerned with an infinite number of electrons, the negative-energy solutions are removed from the first-order answer by the exclusion principle.

In the above sense one may use Eq. (7) with the $u_{j,s}$ being either ingoing or outgoing wave modifications of plane waves, the choice of sign in Eq. (9) being immaterial for the unitary nature of the transformation.

If the outgoing wave modification is employed, then in the region of large positive $\mathbf{k}\cdot\mathbf{r}$ for $\mathbf{r}$ along $\mathbf{k}$ the $u_{j,s}$ contain terms in e^{ikr} coming from $e^{i\mathbf{k}\cdot\mathbf{r}}$ and also terms in e^{ikr} coming from the outgoing wave as in the second term of Eq. (1). In (7) the second term represents the first-order effect of H' in the form of a superposition of the $u_{j,s}$. For large t standard considerations show that there is a selection by interference arising in $\int dt$ of narrow-energy regions corresponding to conservation of energy for inelastic processes such as photon absorption in inverse bremsstrahlung. The inelastically-scattered electron wave in each energy region is represented as a superposition of the $u_{j,s}$. Since in the direction of $\mathbf{k}_s$ each $u_{j,s}$ contains two terms with the same phase, they both contribute to the wave packet of inelastically-scattered particles. It might be thought at first sight that $e^{i\mathbf{k}\cdot\mathbf{r}}$ and e^{ikr}/kr contribute amounts of different order at large r. This is not the case, however, as may be seen from the fact that $e^{i\mathbf{k}\mathbf{r}}$ when analyzed in Legendre functions of angle consists mainly of terms in e^{ikr}/kr and e^{-ikr}/kr. In fact it is interference of the outgoing wave parts of Eq. (1) with the unscattered wave packet that accounts for the reduction of intensity of the primary beam due to the existence of particles scattered out of the beam in connection with Eq. (2). One cannot neglect, therefore, the outgoing wave part of $u_{j,s}$ in the calculation of the inelastically-scattered wave packet. The calculation by means of Eq. (7) in terms of distorted plane waves with outgoing wave modifications is thus possible but not directly interpretable in terms of a differential cross section.

On the other hand, if the $u_{j,s}$ are taken to be distorted plane waves with *ingoing* wave modifications, then in the direction of each $\mathbf{k}_s$ the phases of the ingoing waves are just opposite to those of the plane wave parts. For the ingoing wave part one has, accordingly, destructive interference as in Eq. (2′). The second part of Eq. (7) gives, therefore, a representation of the inelastically-scattered wave packet in terms of *undistorted* plane waves and is consequently immediately interpretable in terms of the number of particles. The coefficients, given by the scalar products in Eq. (7) must of course be calculated by means of distorted wave functions since in the matrix element the wave function is needed at small values of r', within the interaction zone, so that the mere knowledge of the asymptotic behavior does not suffice. The transition to undistorted plane waves occurs on account of the vanishing of contributions from the ingoing part of the $u_{j,s}$ *outside* the matrix element. It is clear that Eq. (7) gives the standard formula for the transition probability in terms of squares of matrix elements and it follows, therefore, that for the usually desired application to the calculation of the flux of particles in a given direction, one should use the ingoing wave modification.

[3] P. A. M. Dirac, Proc. Roy. Soc. (London) **A118**, 351 (1928).

Letters to the Editor

PUBLICATION of brief reports of important discoveries in physics may be secured by addressing them to this department. The closing date for this department is five weeks prior to the date of issue. No proof will be sent to the authors. The Board of Editors does not hold itself responsible for the opinions expressed by the correspondents. Communications should not exceed 600 words in length and should be submitted in duplicate.

Structural Defects in Copper and the Electrical Resistivity Minimum

T. H. BLEWITT, R. R. COLTMAN, JR., AND J. K. REDMAN
Oak Ridge National Laboratory, Oak Ridge, Tennessee
(Received December 21, 1953)

THE observation of de Haas, de Boer, and van den Berg[1] that a minimum in the electrical resistivity of polycrystalline gold wires occurred in the vicinity of liquid helium temperatures resulted in considerable interest as this raised some doubt as to the validity of Matthiessen's rule. Since that experiment, many others have been performed with the result that not only has the effect been verified in gold, but a similar minimum has been found in many other metals. Several explanations and suggestions to account for this anomalous behavior have been advanced. While many of these comments have attributed the anomalous behavior to the presence of chemical defects, particularly ferromagnetic impurities, Lane[2] on the basis of Meissner's[3] data suggested that grain boundaries might play a predominate role in the phenomena. It is the purpose of this note to discuss the role of structural defects, especially grain boundaries, in the electrical minimum found in copper.

In the course of investigating the effect of plastic deformation[4] on the residual resistivity of high-purity copper single crystals,[5] several factors arose which seemed to suggest that a substantial fraction of the residual resistivity observed during the investigation of the resistance minimum arose from the interaction of conduction electrons with structural defects (especially grain boundaries). It has generally been assumed that the residual resistivity was determined by the scattering of conduction electrons by chemical defects. The suggestion of the importance of structural defects arose from the observation that the annealed single crystals had a resistivity many times lower than the usual values reported for polycrystalline materials; that severe tensile deformation could increase the resistivity to the order of that usually observed in polycrystalline materials; and that recrystallization of the worked crystals by annealing in high vacuums (10^{-6} mm or better) at 1000°C only slightly reduced the resistivity.

TABLE I. The resistivity of copper (in ohm-cm) at various temperatures. The values are multiplied by 10^8.

Temperature °K	4.2	3.4	2.7	1.67	1.60
	Sample 305*D*				
Annealed single crystal	0.080				
Worked single crystal	1.308	1.310	1.308		1.306
After recrystallization	0.908				0.933
	Sample 305*C*				
Annealed single crystal	0.036	0.035	0.035		0.035
Worked single crystal	1.099				1.101
	Sample 304*C*				
Annealed single crystal	0.080				
Worked single crystal	1.140				
After recrystallization	0.830			0.846	0.847
	Sample 305*F*				
Annealed single crystal	0.090				
Worked single crystal	0.720				
After recrystallization	0.636			0.648	0.650

This situation, which was observed in many crystals, is typified by the data of crystal 304*C* in Table I.

If then a substantial fraction of the residual resistivity is associated with grain boundaries, as the above observations suggest, it would seem that the minimum in the resistivity may arise as a result of the scattering or trapping properties of the grain boundaries. A survey-type experiment was then made to examine this hypothesis. The effect of temperature in the region from 1.6°K to 4.2°K on the electrical resistivity was determined on single crystals of copper as well as polycrystalline copper. The results are shown in Table I. The results for crystal 305*D* are of particular interest in that the resistance minimum was not found until recrystallization had occurred. The data of Table I, while only of a survey nature, would seem to indicate that grain boundaries are one type of defect which can result in a negative temperature coefficient of resistance in metals. It would seem to be especially significant that the defects introduced by the deformation, presumably dislocations (apparently the vacant lattice sites have been annealed out), scatter in a normal fashion until they have been polygonized to form grain boundaries. Whether impurity atoms, especially those which are ferromagnetic, can cause similar effects as measurements on polycrystalline metals seem to show, is open to question. It would, however, seem that the apparent indications of the influence of impurity atoms on the resistance minima should be re-examined in terms of grain boundary scattering, especially with regard to the effect of the impurities on the grain size. In the case of the results described here it would, however, seem to be difficult to ascribe the negative temperature gradient in any way to the presence of chemical defects as the magnitude of the effect is in excess of the residual resistivity of the annealed single crystals.

It may be pertinent to point out that the magnitude of the residual resistivity of single copper crystals is in good accord with the data of Meissner's values for gold and zinc single crystals. Meissner, however, found polycrystalline wires of these metals to have a residual resistivity of the same magnitude. In neither of these samples was a resistance minimum found. It may be that the grain size of Meissner's samples were large compared with the wire diameter so that the contribution of grain boundary scattering to the total residual resistivity was small.

In conclusion, it may be stated that the manner in which the conduction electrons and the grain boundaries interact is not clear. It would appear that suitable experiments, possibly Hall constant measurements, should be made to distinguish between the scattering and trapping properties of the grain boundary.

[1] De Haas, De Boer, and Van den Berg, Physica **1**, 1115 (1934).
[2] C. T. Lane, Phys. Rev. **76**, 304 (1949).
[3] W. Meissner, Z. Physik **38**, 647 (1926).
[4] To be published.
[5] The sample preparation and experimental technique used is similar to that described previously. See T. H. Blewitt, Phys. Rev. **91**, 1115 (1953).

Interaction of Beta Particles with Matter

RALPH H. MÜLLER
Los Alamos Scientific Laboratory, University of California, Los Alamos, New Mexico
(Received September 9, 1953)

THE back-scattering of beta particles[1] and positrons[2] from various elements has shown a marked dependence upon atomic number or atomic weight. When the results are confined to a few elements, widely distributed over the whole range of Z, it is possible to represent them fairly simply by a Z^1 relationship. It is only when more detailed information is obtained that significant discontinuities become apparent.

A systematic study has been made of the back-scattering of 2.0-Mev betas from Y^{90} by samples of infinite thickness for 32 elements ($Z=4$ to $Z=83$) and 22 compounds. It is definitely established that the relative back-scattering is a discontinuous

function of Z, but strictly linear in Z within each period of the periodic system. The linear equations, relating back-scattering to Z within each period, when solved simultaneously, indicate discontinuities at $Z=10$, 18, 36, and 54, corresponding to the rare gases which terminate the periods.

The back-scattering from compounds is accurately predicted from the scattering of their constituent atoms. In this connection an equivalent atomic number $\bar{Z}$ is computed for the compound. For the compound B_nC_m,

$$\bar{Z}=\frac{n(A_BZ_B)+m(A_CZ_C)}{\text{molec. wt. of } B_nC_m}, \quad (1)$$

where A_B and A_C are the atomic weights of B and C. So defined, $\bar{Z}$ is simply the sum of each atomic number multiplied by the weight percent of that atom which is present in the compound. The value of $\bar{Z}$ for calcite ($CaCO_3$) is 12.565. This indicates that back-scattering from calcite should be intermediate between Mg ($Z=12$) and Al ($Z=13$). Linear interpolation between the back-scattering for calcite and these two metals yields a value of $\bar{Z}$ within 0.08 percent of the calculated value. Equally accurate results have been obtained for quartz (SiO_2), halite (NaCl), fluorite (CaF_2), kernite ($Na_2B_4O_7\cdot 4H_2O$), and celestite ($SrSO_4$). Other minerals yield the predicted value with lesser precision, unless careful corrections are made for impurities.

There are small but definite differences in the back-scattering from various planes of a crystal. This has been verified in quartz and aragonite ($CaCO_3$). In general, the scattering is greater the smaller the interplanar distance, though not simply in the ratio of the respective interplanar distances. The nature of this possible dependence upon lattice constants is being examined in greater detail. As might be expected, Eq. (1) predicts an average value.

Back-scattering from organic compounds is equally well predicted, but with results which are low in increasing proportion to their hydrogen content. Fortunately, the decrease in back-scattering is directly proportional to the hydrogen content and precise corrections can be made.

The scattering of beta particles by matter is an extremely complex phenomenon. Theoretical considerations have indicated that one can hope to understand the process *only* when the experimental procedure approximates the condition of single scattering.

These results, however, indicate that, even for multiple scattering, there are generalizations and regularities enabling one to predict the relative scattering for any element or compound.

Details of these and related investigations will be submitted to this journal shortly.

* Work performed under the auspices of the U. S. Atomic Energy Commission.

[1] George Hevesy and F. A. Paneth, *A Manual of Radioactivity* (Oxford University Press, London, 1938), p. 46.

[2] H. H. Seliger, Phys. Rev. **78**, 491 (1950).

Self-Diffusion in Germanium*

HARRY LETAW, JR., LAWRENCE M. SLIFKIN, AND WILLIAM M. PORTNOY
Electrical Engineering Research Laboratory, University of Illinois, Urbana, Illinois

(Received December 31, 1953)

ALTHOUGH the mechanism of substitutional diffusion in close-packed metal lattices is generally believed to be one of vacancy motion, no such acceptance prevails in the case of germanium. To provide information concerning this question we have undertaken a study of self-diffusion in germanium, preliminary results of which are reported in this letter.

Diffusion specimens in the form of thin slabs of about 1-cm² area were cut from a zone-melted single crystal. Both faces of each specimen were polished to 4/0 paper on a precision grinding machine[1] which is capable of polishing the faces parallel to within a tolerance of about 0.5μ. About 1 μC of Ge^{71} was plated onto each face from a hot alkaline oxalate solution of GeO_2.[2] The specimen, supported by a quartz flat, was sealed off in a small, evacuated Vycor tube and placed in a constant temperature furnace (± 1°C). After diffusion, the specimen was sectioned on the grinder. The mass and thickness of each cut were determined from the weight loss of the specimen. The concentration of Ge^{71} in each cut was determined by assaying the polishing paper with a Tracerlab TGC-3 tube. Typical penetration data are shown in Fig. 1.

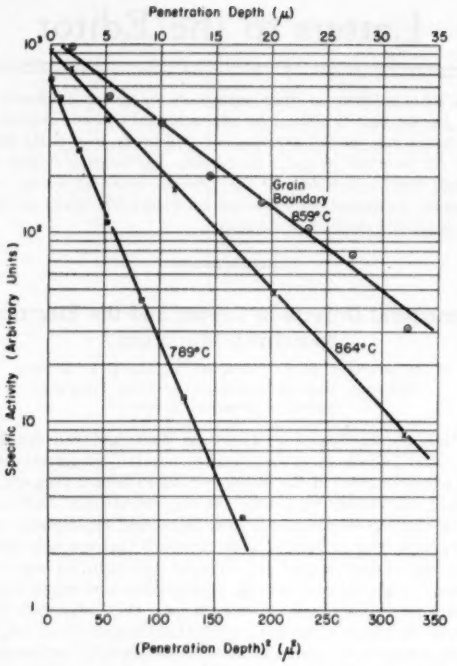

FIG. 1. Typical penetration data. The upper scale of the abscissa refers to the upper curve which represents grain boundary diffusion. The lower curves illustrate volume diffusion.

Because of the small values of the diffusion constant D, the penetration depths, measured by $(Dt)^{\frac{1}{2}}$, were often only a few microns. If the alignment error in sample mounting were as much as a few tenths of a micron, it would produce an apparently high D; therefore, at each temperature, several measurements were made and only the lower values of D accepted. These data are shown in Fig. 2 and are described by the equation $D=87\exp(-73500/RT)$ cm²/sec. Significantly, the penetration data for the lowest D at a given temperature generally showed the least scatter. The validity of the experimental method was checked by measuring D for indium in Ag at 613°C. Here, with $(Dt)^{\frac{1}{2}}=32\mu$, the value of D obtained agreed to 1 percent with the data of Tomizuka[3] taken by conventional techniques.

The value (87) of D_0, good to order of magnitude, is higher than usually found for self-diffusion in metals and much greater than the 0.3 cm²/sec predicted by the theory of Zener.[4] It is comparable to the value of 10 reported by Dunlap and Brown[5] for Sb in Ge.

If one assumes a vacancy mechanism and takes 50 kcal/mole as the energy of formation of a vacancy,[6] then our activation energy indicates the activation energy of mobility to be about 23.5 kcal/mole. From the expression for the vacancy fraction as a function of temperature given by Mayburg and Rotondi,[6] one estimates a diffusion coefficient for vacancies:

$$D_v=D_{\text{self}}\times 1/(\text{vacancy fraction})=3.9\exp(-23{,}500/RT)\ \text{cm}^2/\text{sec}.$$

For two runs, the specific activity varied exponentially with the first power of the depth, as is found in grain boundary diffusion.[7]

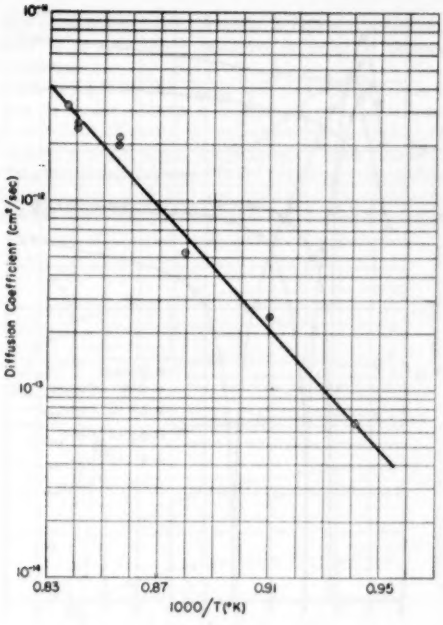

FIG. 2. Diffusion coefficient as a function of $1/T$.

Clarke and Hopkins[8] have shown that polishing Ge can produce a distorted surface layer of the order of 10^{-4} cm deep. Presumably, such a layer could be induced to recrystallize. If some grain growth followed, grain boundary diffusion would result. The grain boundary D's calculated by means of Fisher's theory[7] were of order 10^{-8} cm²/sec, about 10^4 larger than the respective volume D's.

These experiments are being extended, using longer diffusion times, etched surfaces to preclude recrystallization, and finer alignment techniques.

We wish to thank Dr. J. Burton and Dr. W. Pfann for supplying the germanium crystal. We are grateful to Professor John Bardeen for his interest and contributions throughout the course of this research.

* Supported in part by the U. S. Office of Naval Research and by a grant from the Motorola Corporation.

[1] Letaw, Slifkin, and Portnoy (to be published).
[2] Schwarz, Heinrich, and Hollstein, Z. anorg. u. allgem. Chem. **229**, 146 (1936).
[3] C. T. Tomizuka (to be published).
[4] C. Zener, J. Appl. Phys. **22**, 372 (1951).
[5] W. C. Dunlap, Jr., and D. E. Brown, Phys. Rev. **86**, 417 (1952).
[6] S. Mayburg and L. Rotondi, Phys. Rev. **91**, 1015 (1953); R. Logan, Phys. Rev. **91**, 759 (1953).
[7] J. C. Fisher, J. Appl. Phys. **22**, 74 (1951).
[8] E. Clarke and R. Hopkins, Phys. Rev. **91**, 1566 (1953).

Neutron Diffraction Study of the Anisotropy Transition in α-Fe_2O_3†

L. M. CORLISS, J. M. HASTINGS, AND J. E. GOLDMAN*
Brookhaven National Laboratory, Upton, New York
(Received December 1, 1953)

MORIN,[1] Néel,[2] and others have noted an anomaly in the magnetic behavior of α-Fe_2O_3 at approximately -25°C. Shull[3] has examined this material by means of neutron diffraction at room temperature and -190°C and finds evidence for an antiferromagnetic structure in which the threefold axis of the crystal, which is of rhombohedral symmetry, is the stable direction of the spin system at the lower temperature. At the higher temperature, the spins lie in the (111) plane and may be oriented toward one of the nearest neighbors in or close to that plane. The anomaly below room temperature is thus interpreted as a transition point at which the antiferromagnetic crystalline anisotropy changes. However, the temperature of the transition appears to vary markedly in the various investigations. Urquhart and Goldman[4] have reported unusual field-dependent strain effects in the neighborhood of the transition. It appeared desirable, therefore, to investigate this transition and its possible dependence on field, choice of crystal, etc., by means of neutron diffraction. One natural single crystal, the same one used in the investigation of Urquhart and Goldman, and a synthetic crystal on which Anderson *et al.*[5] have made resonance measurements were studied.

The intensity of the (111) diffraction peak depends completely on the magnetic state of the system.[3] When the magnetic vectors are in the (111) plane and the usual antiferromagnetic symmetry is observed, there is an appreciable intensity to this peak. However, if the spins are oriented perpendicular to this plane, the magnetic scattering for this reflection vanishes and the line virtually disappears. The experiment was done using the spectrometer previously described.[6] The crystal was mounted on a goniometer and oriented in the neutron beam so as to obtain the maximum intensity. A vacuum-jacketed quartz vessel was then lowered over the crystal, and air that had been passed through a mixture of solid CO_2 and alcohol was passed over the crystal. The temperature was controlled by regulating the flow of air and was measured by means of two copper-constantan thermocouples in contact with different parts of the crystal. The temperature could be controlled to within 0.2°C during the scanning of a peak.

The data thus obtained are shown in Figs. 1 and 2. In Fig. 1

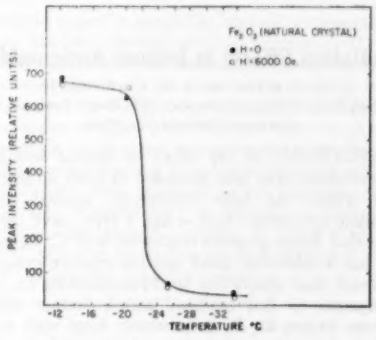

FIG. 1. Temperature dependence of the integrated intensity of the (111) reflection from a natural single crystal of Fe_2O_3.

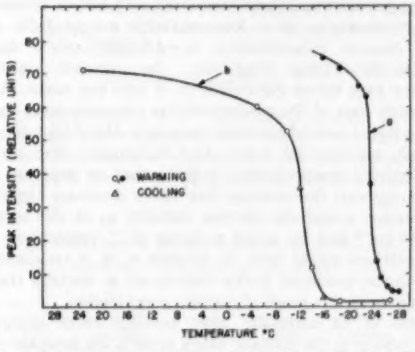

FIG. 2. Variation with temperature of the (111) peak height for single crystals of Fe_2O_3. Curve *a* represents a natural crystal (same as in Fig. 1) and curve *b* a synthetic crystal.

we have plotted the integrated intensity of the (111) reflection as a function of temperature for the natural crystal. It is to be noted that, to within the accuracy of our experiment, there is no noticeable effect of a magnetic field on the transition or on the line intensity above and below the transition. Figure 2, curve *a* shows the results of another experiment with the same crystal in which only the peak intensity was measured as the sample was allowed to warm up. The agreement between these two method of observing the transition is satisfactory, and it can be concluded that the type of anisotropy transition predicted to occur does in fact occur at this temperature, and that the transition is quite sharp, i.e., of the order of 4° wide for the natural crystal. Curve *b* in Fig. 2 represents the peak height as a function of temperature for the synthetic crystal provided by Anderson. It is seen that the transition occurs at a temperature approximately 10° higher than in the natural crystal and appears to be somewhat wider. The higher transition temperature confirms the results of Anderson from resonance measurements.

We are indebted to Helen M. A. Urquhart for helpful assistance in orienting the crystal and in making some of the preliminary measurements and to Dr. P. W. Anderson for making available to us his synthetic crystal and discussing the results of his work with us in advance of publication.

† Work carried out under the auspices of the U. S. Atomic Energy Commission.
* Visiting Scientist. Permanent address: Carnegie Institute of Technology, Pittsburgh, Pennsylvania.

[1] F. J. Morin, Phys. Rev. **78**, 819 (1950).
[2] L. Néel, Ann. phys. **3**, 137 (1948); **4**, 249 (1949).
[3] Shull, Strauser, and Wollan, Phys. Rev. **83**, 333 (1951).
[4] H. M. A. Urquhart and J. E. Goldman, Phys. Rev. **91**, 435 (1953).
[5] Anderson, Meritt, Remeika, and Yager, Phys. Rev. **93**, 717 (1954).
[6] J. M. Hastings and L. M. Corliss, Revs. Modern Phys. **25**, 114 (1953).

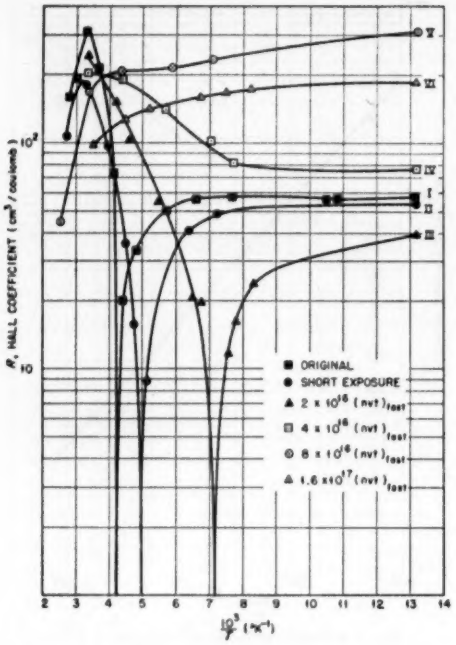

FIG. 1. Hall coefficient of InSb as a function of temperature after various exposures in the reactor.

Radiation Effects in Indium Antimonide

J. W. CLELAND AND J. H. CRAWFORD, JR.
Oak Ridge National Laboratory, Oak Ridge, Tennessee
(Received December 30, 1953)

INVESTIGATIONS of the effect of reactor irradiation on semiconductors have been extended to InSb, an intermetallic compound which has been extensively studied recently.[1-3] Polycrystalline specimens,[4] both *n* and *p* type, have been irradiated in the Oak Ridge graphite reactor at ~30°C. In contrast to Ge which has a relatively small neutron capture cross section,[5] with the result that effects due to transmutations are relatively minor compared to fast neutron lattice damage effects, the capture cross section for In is extremely large with the decay-product Sn, a donor impurity when substituted for an In atom. Thus, for the neutron energy spectrum encountered in the reactor, effects caused by transmutations are expected to be comparable to, if not greater than, those associated with lattice disordering.

The conductivity of a low-resistivity *n*-type InSb sample (initial electron concentration $n_0 = 4.8\times10^{18}$ cm^{-3}) decreases monotonically during irradiation, the decrease approaching saturation long before conversion to *p* type can occur. Analysis of the early part of the conductivity *vs* exposure curve indicates that the initial rate of electron removal is about four times that previously reported for *n*-type Ge.[6] Subsequent Hall coefficient and resistivity measurements indicate that an exposure of ~2 $\times10^{17}$ integrated fast-neutron flux $(n\nu t)_f$ decreases the electron concentration *n* and the electron mobility μ_n of this sample by 1.6×10^{18} cm^{-3} and by about a factor of 2, respectively. Since transmutations would tend to increase *n*, it is concluded that bombardment-produced lattice defects act as electron traps and predominate in this range of carrier concentration.

Because of its unusually large mobility ratio[3] ($\mu_n/\mu_p \cong 85$), *p*-type InSb is in the intrinsic range at 30°C for acceptor concentrations $<2\times10^{17}$ cm^{-3}. Consequently, for *p*-type specimens with moderate acceptor concentrations, conductivity *vs* exposure curves are not a sensitive index of the carrier concentration during irradiation. Instead it is necessary to use Hall coefficient and resistivity data as a function of temperature. Such data for an originally *p*-type sample after successive exposures are shown in Figs. 1 and 2. Except for a certain anomalous behavior in the low-temperature portion in the Hall coefficient curves during the early part of bombardment (Curves II, III, and IV, Fig. 1),[7]

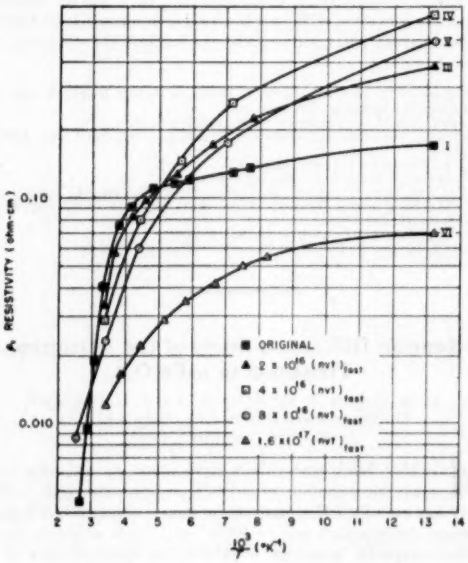

FIG. 2. Resistivity of InSb as a function of temperature after various exposures.

these data show a progressive decrease in hole concentration and conversion to n type. Such behavior is expected because of transmutations.

In order to separate the effects due to transmutations from those due to lattice defects, a second p-type sample was (1) exposed to $\sim 2.5\times10^{17}(nvt)_f$, (2) subsequently annealed at 350°C for 16 hours, and (3) then, while shielded from thermal and resonance neutrons with Cd and In foil, exposed to an additional $2.5\times10^{17}(nvt)_f$. Hall coefficient and resistivity curves taken after each of these operations are shown in Fig. 3. The first exposure

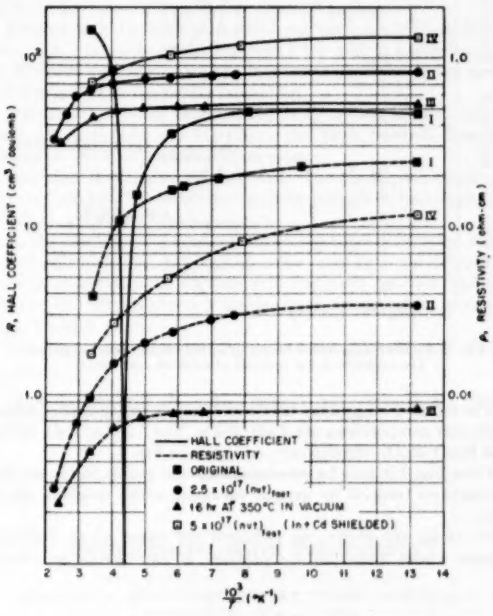

FIG. 3. Hall coefficient and resistivity of irradiated InSb. The Hall coefficient curves are denoted by R and the resistivity curves by ρ.

converts the sample to n type (Curves II) in the expected manner. The heat treatment presumably anneals the lattice defects, thereby causing an increase in both n and μ_n (Curves III). On further irradiation, the specimen being shielded from thermal neutrons, both the Hall coefficient and resistivity are increased (Curves IV). The results of the last two operations, in agreement with the findings for n-type material, indicate strongly that fast neutron induced lattice defects act as electron traps in InSb.

These preliminary studies indicate that (1) donor impurities are introduced into InSb by transmutations in the expected manner, and (2) lattice defects introduced by fast neutron bombardment act as electron traps in n-type material. Data are insufficient at the present time to show whether these defects behave predominantly as acceptors or hole traps in p-type material.

The authors wish to acknowledge the aid of E. S. Schwartz who assisted in the bombardment work.

[1] H. Welker, Z. Naturforsch. **7a**, 744 (1952).
[2] Breckenridge, Holzer, and Oshinsky, Phys. Rev. **91**, 243 (1953).
[3] M. Tanenbaum and J. P. Maita, Phys. Rev. **91**, 1009 (1953).
[4] We are indebted to Miss Louise Roth of Purdue University for the samples used in these experiments.
[5] Cleland, Lark-Horovitz, and Pigg, Phys. Rev. **78**, 814 (1950).
[6] J. H. Crawford, Jr., and K. Lark-Horovitz, Phys. Rev. **78**, 815 (1950).
[7] Because of the large capture cross section of In, there is an appreciable attenuation of the thermal neutron flux toward the center of the specimen. Hence the concentration of Sn impurity is expected to be significantly higher at the surface than at the interior of the specimen. Such an effect may possibly explain these anomalies, since one might expect the Hall voltage of a p-type interior and that of an n-type exterior to neutralize each other to some extent.

Incoherent Neutron Scattering by Polycrystals

G. PLACZEK
Institute for Advanced Study, Princeton, New Jersey
(Received December 21, 1953)

IN evaluating the total incoherent cross section σ of a polycrystal, it is customary to decompose σ into partial cross sections σ_l for the production or destruction of l phonons:

$$\sigma=\sum_{l=0}^{\infty}\sigma_l. \tag{1}$$

The convergence of (1) becomes progressively poorer with increasing neutron energy and the structure of the higher terms is exceedingly complicated.[1] Furthermore, it results from the extensive numerical calculations of Squires[2] for magnesium that in this case, at a temperature about twice the Debye temperature θ, the terms with $l>1$ give a sizable contribution to the cross section even at zero-incident neutron energy.

The separate consideration of one-phonon processes has some merit in the study of the energy distribution of the scattered neutrons and of coherent effects.[3] Because of the existence of strong compensation effects, however, (1) is not a reasonable expansion for the total incoherent cross section. This may be illustrated by the example of the static approximation, which neglects the energy changes in the scattering process. Here σ is independent of neutron energy and temperature, while the partial cross sections σ_l depend on these quantities by

$$\sigma_l/\sigma=\frac{1}{l!}\frac{1}{x}\int_0^x t^l e^{-t}dt=x^{-1}-e^{-x}\sum_{m=0}\frac{x^{m-1}}{m!}, \tag{2}$$

with $x=4k^2\alpha(T)$. (k is the wave number of the incident neutron, $\alpha(T)$ the mean-square nuclear displacement, and T the temperature.)

In a previous paper[4] a simple asymptotic expression for the cross section has been derived without recourse to (1) and has been explicitly evaluated in the Debye approximation. For heavy nuclei this expression holds as soon as the neutron energy is slightly larger than the Debye temperature, and for lighter nuclei at somewhat higher energies. There remains, however, the problem of finding a simple and accurate representation of the cross section valid for all energies. This may be achieved by using a procedure, which has previously been discussed for the particular case of an oscillator at zero temperature.[4] It consists in expressing the neutron variables (wavelength, velocity) in terms of the neutron energy E and thereupon expanding the cross section in powers of the ratio M^{-1} of neutron to nuclear mass:

$$\sigma=s+\sum_{n=1}\sigma^{(n)}M^{-n}, \tag{3}$$

where s is the bound incoherent nuclear cross section. In contrast to (1), the expansion (3) converges rapidly for all energies provided that M is moderately large compared to both one and T/θ. Under these conditions, which are well satisfied in most practical cases for temperatures right up to the melting point, σ is well represented at all energies by

$$\sigma=s+\sigma^{(1)}/M+\sigma^{(2)}/M^2, \tag{4}$$

and often the contribution of $\sigma^{(2)}$ amounts to a small correction only. Furthermore, the structure of $\sigma^{(1)}$ and $\sigma^{(2)}$ is considerably simpler than even that of σ_1 and σ_2, and thus the evaluation of the cross section in the Debye approximation becomes a relatively easy matter.

TABLE I. The coefficients in the expression (5) for the cross section.

n	a_n	b_n	c_n	d_n	e_n	f_n	g_n
0	1.2	0.4286	0.0556	1.3221	2.1141	0.7410	−0.1044
2	5	1.5	0.1786	−8.0590	3.8562	1.6600	0.1877
3	−12	0	−0.3333	0	0	0	0
4	5.25	0.825	0.0825	−41.042	−5.439	−1.262	0.2666
5	0	0	0	96	0	5.333	0

The following results for the particular case of low energy and high temperature ($E \ll \theta$, $T \gg \theta/2\pi$), which is of frequent experimental interest,[3,5] may serve to illustrate the advantages of the method, which of course come even more fully into play at higher energies.

$$\sigma^{(1)} = s \sum_{n=0,2,3,4} \lambda^{1-n}(a_n T - b_n + c_n T^{-1}) + O(\lambda^{-5}),$$
$$\sigma^{(2)} = s \sum_{n=0,2,4,5} \lambda^{1-n}(d_n T^2 - e_n T + f_n + g_n T^{-1}) + O(\lambda^{-5}). \quad (5)$$

Here T is measured in units of θ, and $\lambda = (\theta/E)^{\frac{1}{2}}$ is the neutron wavelength in dimensionless units. The coefficients are given in Table I.

For Mg, taking $\lambda = 5.94$, $T = 2.05$, Squires[3] calculates σ by using six terms in (1). The terms with $l > 1$ amount to 46 percent of σ_1. His result is in agreement with that obtained from (4) and (5), with the $\sigma^{(3)}$ term amounting to only half a percent of the $\sigma^{(1)}$ term.

The results for general energy and temperature, which will be given in a forthcoming paper, provide a detailed answer to questions previously raised[6] about the energy dependence of the cross section.

The author is indebted to L. Van Hove and G. C. Wick for valuable discussions.

[1] In the Debye approximation, expressions for σ_l for $l=0$ and 1 have been given by J. M. Cassels [Progr. Nuclear Phys. **1**, 185 (1950)] and for general l by Squires (reference 2).
[2] G. L. Squires, Proc. Roy. Soc. (London) **A212**, 192 (1952).
[3] G. Placzek and L. Van Hove, Phys. Rev. (to be published).
[4] G. Placzek, Phys. Rev. **86**, 377 (1952).
[5] H. Palevsky and D. J. Hughes, Phys. Rev. **92**, 202 (1953).
[6] A. Akhiezer and I. Pomeranchuk, J. Phys. (U.S.S.R.) **11**, 167 (1947).

Color Centers in Alkali Silicate Glasses

RYOSUKE YOKOTA
Matsuda Research Laboratory, Tokyo-Shibaura Electric Company, Kawasaki, Kanagawa-ken, Japan
(Received December 15, 1953)

THE study of color centers in quartz and fused quartz was reported elsewhere.[1] We have extended our study to the color centers in silicate glasses which contain alkali ions.

We melted the glass from the purest chemicals (Merck for analysis except in the case of rubidium carbonate which is cp grade) in a platinum crucible in an electric furnace whose heater is platinum ribbon. The glass was annealed and polished. The increase of absorption resulting from irradiation with x-rays (45 kv, 10 ma, tungsten target) at room temperature was measured with a Beckman DU spectrophotometer at room temperature.

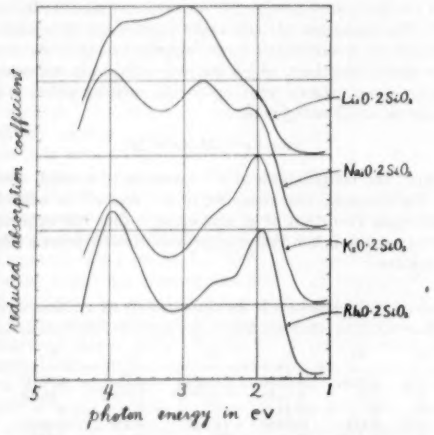

FIG. 1. Induced absorption bands in alkali disilicate glasses. The ordinate is the reduced absorption coefficient.

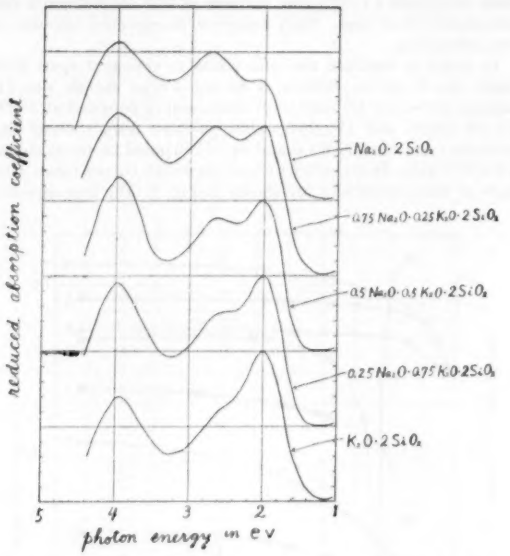

FIG. 2. Induced absorption bands in mixed alkali disilicate glasses. The ordinate is the reduced absorption coefficient.

The induced absorption bands in alkali disilicate glasses whose molecular compositions are $Li_2O \cdot 2SiO_2$, $Na_2O \cdot 2SiO_2$, $K_2O \cdot 2SiO_2$, and $Rb_2O \cdot 2SiO_2$, respectively, are given in Fig. 1.

From Fig. 1 it may be concluded that the visible bands are due to electrons trapped by oxygen vacancies which neighbor alkali ions.

To verify the above, we prepared the mixed alkali disilicate glasses whose molecular composition is represented as $x Na_2O$

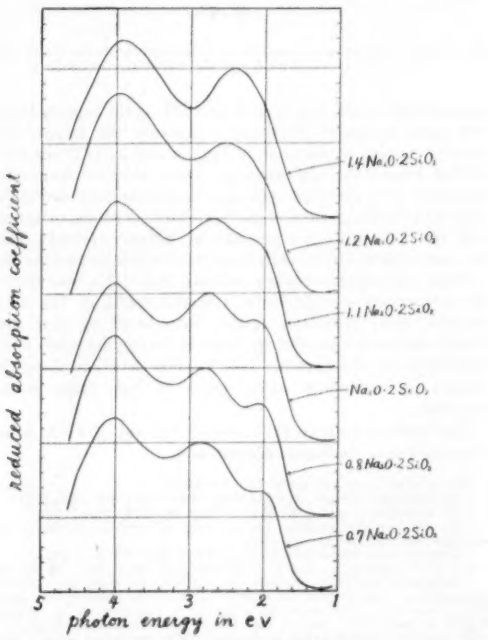

FIG. 3. Induced absorption bands of Na_2O-SiO_2 glasses. The ordinate is the reduced absorption coefficient.

$\cdot(1-x)K_2O\cdot 2SiO_2$ ($x=0-1$). The induced absorption bands are given in Fig. 2.

Figure 2 shows clearly that the relative intensity of the two visible bands is nearly proportional to the molecular ratio of Na_2O to K_2O.

Moreover the induced absorption bands of Na_2O-SiO_2 series glasses are given in Fig. 3. Therefore it is concluded that the visible bands in alkali silicate glasses are due to electrons trapped by oxygen vacancies which neighbor alkali ions.

The ultraviolet band is bleached with the visible bands by irradiation with visible light and the visible bands are bleached with the uv band by irradiation with 313 $m\mu$ light.

Further, in $K_2O\cdot 2SiO_2$ glass which was prepared in the reducing condition, the uv band decreases and the visible bands increase in intensity compared with the intensities observed in the specimens prepared in the neutral condition.

On the other hand, the uv band in all glasses studied has its peak at about 3.98 ev. Moreover, this peak position does not change in the mixed alkali silicate glasses.

Therefore it is concluded that the uv band is the one characteristic of "oxygen," that is, it arises from positive holes trapped by alkali vacancies neighboring oxygen.

In the alkali silicate glasses studied, the three absorption bands are always observed, although in some cases they are difficult to resolve. A remarkable regularity in the peak position and the relative intensity of the two visible bands was found, as shown in Figs. 1 and 3.

A full account will appear in the *Journal of the Physical Society of Japan*.

[1] Ryosuke Yokota, J. Phys. Soc. Japan **7**, 316 (1952); **7**, 222 (1952); Phys. Rev. **91**, 1013 (1953).

Submillimeter Wave Spectroscopy*

CHARLES A. BURRUS† AND WALTER GORDY
Department of Physics, Duke University, Durham, North Carolina
(Received December 21, 1953)

AN extension of microwave spectroscopy into the submillimeter wave region has been achieved. A spectrum line at 0.77-mm wavelength (389 kMc/sec) has been precisely measured with harmonics from a 5-Mc/sec marker monitored by the standard 5-Mc/sec signal broadcast by the National Bureau of Standards. This and other submillimeter wave lines of OCS which have been measured are listed in Table I.

Figure 1 shows a recording of several rotational lines in the sub-millimeter range obtained with different harmonics of a *K*-band klystron (Raytheon 2K33). Because of centrifugal stretching the rotational lines are not exactly integral multiples as are the harmonics from the oscillator. For this reason, the different rotational lines are separated on the tracing. The tuning was such as to optimize the lines of highest frequency. Therefore, this recording does not indicate the optimum performance which was obtained on the lower-frequency lines. With tuning to maximize it, the line at 0.88 mm could be recorded with a signal-to-noise ratio of 30 to 1; that at 0.95 mm, with 60 to 1; that at 1.03 mm, with 100 to 1.

The highest frequency previously recorded by electronic methods is the 1.03-mm line of OCS for which a signal-to-noise ratio of 7 to 1 was obtained.[1] The signal-to-noise ratio obtainable at one millimeter has now been increased by a factor of at least 10. Figure 2 shows a scope tracing of the 1.03-mm line obtained with a 60-cps video sweep spectrometer. A recording of it is included in Fig. 1.

TABLE I. Observed lines of $O^{16}C^{12}S^{32}$.

Oscillator harmonic	Transition	Frequency in Mc/sec Calculated[a]	Observed[b]	Wavelength in mm
12	23–24	291 839.27	291 839.23 ±0.60	1.03
13	25–26	316 145.59	316 144.7 ±1.0	0.949
14	27–28	340 448.64	340 449.2 ±1.0	0.881
15	29–30	364 748.16	364 747.5 ±1.5	0.823
16	31–32	389 043.12	389 041 ±2.0	0.771

[a] Calculated with $B_0=6081.494$ Mc/sec and $D_J=1.310$ kc/sec.
[b] The two lower-frequency lines were measured on the scope, and the others on the recorder.

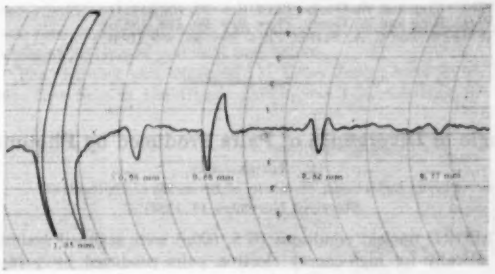

FIG. 1. Recording of the 24th, 26th, 28th, 30th, and 32nd rotational lines of OCS with the 12–16th harmonics of a *K*-band klystron. A phase sensitive lock-in amplifier tuned to 4000 cps was used with 2000-cps propeller modulation of the klystron. Cell length 15 cm, cell volume 0.2 cc. Wavelength of lines are indicated on the chart; frequencies range from 291 to 389 kMc/sec.

The present results have been made possible by a further reduction in size and by refinements of the crystal multiplier and detector units already described by King and Gordy.[1,2] More experimental details will be given in a full length report to be written later. It is evident that the coherent electronic methods of the radio region now overlap effectively the noncoherent optical or heat methods customarily employed in the far infrared region. Rotational lines of such light diatomic hydrides as DCl and HI now fall within the microwave region. Already lines of DBr have been measured in the one-millimeter region.[3]

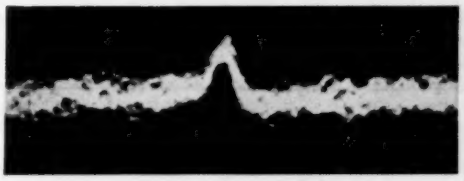

FIG. 2. Cathode-ray oscilloscope trace of the 24th rotational line of OCS at 1.03-mm wavelength (291 kMc/sec). An ordinary crystal video receiver was employed with a 60-cps sweep and an amplifier band width of 6 kc/sec.

Although there are many obvious uses of high-resolution spectroscopy in the 1-mm region, one advantage which probably is not generally realized is the small quantity of material required for spectral examination in this region. The total volume of the wave-guide cell used in the present work is 0.2 cc. In this cell with a pressure of only 5×10^{-3} mm of Hg, the signal-to-noise ratio of 100 to 1 could be obtained at 1-mm wavelength. This represents a total of 5×10^{13} molecules, or one hundredth of a microgram of OCS, neglecting that adsorbed on the cell walls. Actually the lines could easily be detected with only 5×10^{12} molecules or one-thousandth microgram of OCS in the absorbing path. We have in progress a cooperative program with Dr. Ralph Livingston's group at the Oak Ridge National Laboratory for utilizing

this advantage of the shorter millimeter wave region for measurement of the moments of radioactive nuclei.

We wish to thank Mr. M. Whitfield, shop supervisor, for his cooperation and advice, and Mr. W. B. Francis, instrument maker, for his excellent work on the microwave components.

* This research was supported by the United States Air Force under a contract monitored by the Office of Scientific Research, Air Research and Development Command.
† Shell Oil Company Fellow.
[1] W. C. King and W. Gordy, Phys. Rev. **93**, 407 (1954).
[2] W. C. King and W. Gordy, Phys. Rev. **90**, 319 (1953).
[3] W. Gordy and C. A. Burrus, Phys. Rev. **93**, 419 (1954).

Angle of Divergence of Pairs Produced by Photons

K. HINTERMANN*
Physics Department, University of Berne, Berne, Switzerland
(Received November 19, 1953)

ILFORD nuclear emulsions ($G\,5$, 600μ) were scanned systematically for high-energy electron pairs produced by γ rays from cosmic radiation. The plates were exposed for three weeks on the Monte Rosa (Capanna Margherita 4550 m) and processed at our laboratory in Berne according to the Brussels method.[1] The plateau blob density obtained was 30.6 blobs per 100μ.

The angle of divergence and the photon energy of 126 pairs have been measured for 212 pairs found in a certain area. The photon energy $k=E_+ + E_-$ was determined by multiple scattering measurements on both tracks of the pairs. E_+ and E_- are the total energies, the pairs being supposed to be electron-positron pairs. The measured values of the angle ω were reduced to values

$$\omega_{\text{red}}=\omega[\phi(a=0.5)/\phi(a)], \quad a=E_1/k,$$

corrected for symmetrical energy partition, E_1 being the lower one of the particle energies. $\phi(a)$ is a function given by Borsellino,[2] which represents the influence of the energy partition according to his Eq. (15) for the most probable values of the angle:

$$\omega_p=(4mc^2/k)\phi(a).$$

Figure 1 shows the values of k *vs* ω_{red}. Curve 1 is Borsellino's theoretical most probable value ω_p for $a=0.5$. Curve 2 is the root-mean-square value $\langle\omega^2\rangle$ of Stearns.[3] Both curves represent the values for symmetrical energy partition. The limits of error of the experimental values were calculated with the relative mean deviation $0.75/\sqrt{N}$ of the second differences (sagitta method of multiple scattering measurement), N being the number of the independent second differences on the track. The points indicated by triangles are measurements given by Occhialini.[4]

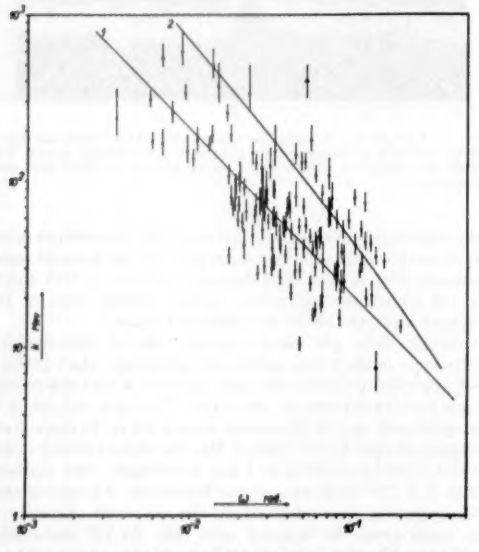

FIG. 1. The correlation between angle of divergence and photon energy k. The experimental points represent the reduced values ω_{red} belonging to the symmetrical energy distribution. Curve 1 is Borsellino's most probable value ω_p and curve 2 the root-mean-square value $\langle\omega^2\rangle$ of Stearns.

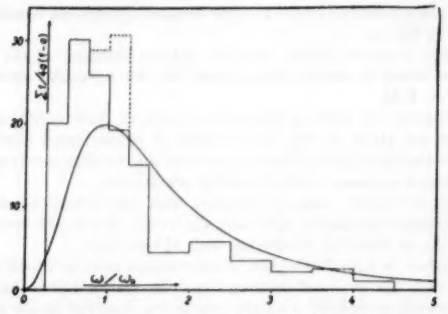

FIG. 2. The distribution of pairs in ω/ω_0. The full-line histogram includes the pairs with $a>0.1$; the dotted line shows the histogram including all pairs where both ω and k have been measured. Theoretical curve: Borsellino's probability.

Figure 2 represents the frequency distribution of the pairs in ω/ω_0, with

$$\omega_0=(mc^2k)/(E_+E_-).$$

The histogram represents the correct number of pairs in a interval 0.25 of ω/ω_0. Each pair has been multiplied by a weight factor

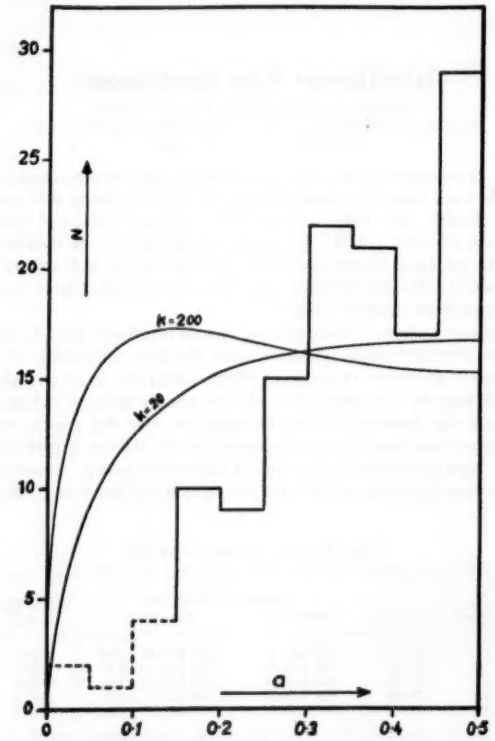

FIG. 3. The distribution of pairs in a. Theoretical curves: Bethe and Heitler for $k=20$ Mev and $k=200$ Mev, normalized to the same area with the histogram in the interval $0.15<a<0.5$.

$1/4a(1-a)$ in order to correct for symmetrical energy partition. The fully drawn line includes the pairs with $a>0.1$, the dotted line includes all pairs for which ω and k have been determined. The theoretical curve is derived from the probability curve of Borsellino (Fig. 3 in his paper) for $k=51$ Mev by normalizing it to the same area as the experimental histogram in the interval $0<\omega/\omega_0<5$. The probability curves for different values of k do not vary considerably, the maximum probability being displaced to $\omega/\omega_0=1.02$ for $k=100$ Mev and to 1.06 for $k=\infty$.

In Fig. 3 are plotted the experimental and theoretical frequency distributions of the pairs *vs* a. The theoretical probability curves are those of Heitler[5] and of Bethe and Ashkin[6] for $k=20$ Mev and $k=200$ Mev, both normalized to the same area as the experimental histogram in the interval $0.15<a<0.5$ (the energy distribution of the pairs can be seen in Fig. 1). The histogram for $a<0.15$ is plotted in dotted lines, because pairs with strong asymmetrical partition are more easily overlooked in scanning than others.

The results indicate that Borsellino's most probable value ω_p is more useful for estimating energies from pair angles than the root-mean-square value of Stearns. The histogram in ω/ω_0 also seems not to be in contradiction with Borsellino's probability (cross section) curve. However, the experimental distribution in a is different from the Bethe-Heitler theoretical curves. It seems that for low a values, the probability is less than that predicted by theory.

The writer is indebted to Professor F. G. Houtermans and Dr. M. Teucher for suggesting this work and for many useful discussions. I am also grateful to the "Bernische Hochschulstiftung" and the "Schweizerischer Nationalfonds" for making possible the exposure of Monte Rosa plates. I also want to thank Mr. A. Graven and Mrs. Busca and Mrs. Catella who organized the exposure at Capanna Margherita on the top of Monte Rosa.

The detailed account of this work will be published in *Helvetica Physica Acta*.

* Present address: Eidg. Amt für Mass und Gewicht, Berne, Switzerland.

[1] Dilworth, Occhialini, and Vermaesen, Bull. centre phys. nucléaire l'univ. libre Bruxelles, No. 13a (1950).
[2] A. Borsellino, Phys. Rev. **89**, 1023 (1953).
[3] M. Stearns, Phys. Rev. **76**, 836 (1949).
[4] G. P. S. Occhialini, Nuovo cimento, Suppl. **6**, 413 (1949).
[5] W. Heitler, *The Quantum Theory of Radiation* (Oxford University Press, London, 1944).
[6] H. A. Bethe and J. Ashkin in *Experimental Nuclear Physics I*, edited by E. Segrè (John Wiley and Sons, Inc., New York, 1952).

A Čerenkov Counter-Cloud Chamber Measurement of Multiply-Charged Primary Cosmic Rays*

JOHN LINSLEY
University of Minnesota, Minneapolis, Minnesota
(Received December 31, 1953)

THE flux of fast particles with $Z\geq 2$ has been measured at balloon altitude by means of a cloud chamber triggered by a Čerenkov counter.

The geometry of the apparatus is shown in Fig. 1. An incoming beam was defined by a Geiger counter telescope whose area-solid angle product was measured to be 0.72 ± 0.03 cm² steradian. The average angle to the vertical of incoming particles was about six degrees. The Čerenkov counter was calibrated by measuring the pulse-height distribution for cosmic-ray muons with a multichannel analyzer. The measured distribution had a width at half-maximum 0.75 times the mean pulse height and fitted $P(10,n)$, the Poisson distribution for a mean of 10, except for a "tail" from knock-on electrons. Most of the width is the result of fluctuations in the number of photoelectrons from the multiplier cathode. The cloud chamber was triggered by a coincidence between the upper GM counter tray, the lower GM counter, and a pulse from the Čerenkov counter $\geq 2.1\pm0.2$ times the mean from a fast muon. The cloud chamber sensitive region was 4 in. ×8 in. in plan and 8 in. in height and contained five transverse ¼-in. thick copper plates (28 g/cm² total). A track within the telescope solid angle traversed all the plates within the illuminated region. Stereoscopic photographs were taken of the events.

The balloon flight[1] was extremely level at mean atmospheric depth 16.4 millibars for 345 minutes. During that time the pressure, which was recorded by photographing the dial of a calibrated Wallace and Tiernan aneroid gauge, varied no more than 0.3 millibar from its mean value. There was no evidence of any significant malfunction of the equipment. After the flight it was recovered undamaged and as soon as spent batteries were replaced performed just as it had before.

The chamber was triggered 157 times during level flight. The sensitive time of the trigger circuit was $1.015\pm0.012\times10^4$ sec.

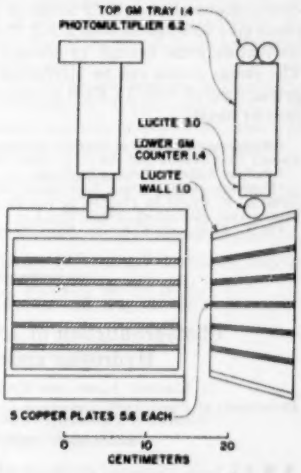

FIG. 1. Diagram of telescope and cloud chamber. Thicknesses are given in g/cm².

Sixty-two photographs showed counter-age tracks identified to be those of He nuclei by their ionization and the fact that the photographs showed no evidence of related incoming particles. In but two cases there was reasonable uncertainty about the identification of an alpha track. Each of them satisfied the necessary condition that its projection on the focal plane of each stereo camera pass through the projection of the telescope apertures. Thirteen photographs showed unaccompanied counter-age tracks of particles with $Z>2$ that satisfied the same projection criterion. One heavily ionizing particle stopped in the fourth copper plate and therefore had $Z\geq 7$, since its energy had to be above 350 Mev/nucleon when it entered the Čerenkov counter. By comparison with that track and among all the tracks, it is estimated that at least three of the particles had $Z<6$.

At the latitude of the flight (55°N geomagnetic) the energy spectra of the particles detected were cut off by the Čerenkov detector rather than geomagnetic effects. The mean threshold energy for He nuclei entering the counter was 650 ± 100 Mev/nucleon entering the counter. For particles with $3\leq Z\leq 5$ the threshold would be 410-Mev/nucleon and for $6\leq Z\leq 8$, 375-Mev/nucleon—only slightly above the energy, 342-Mev/nucleon, corresponding to the critical velocity in Lucite. The uncertainty in threshold caused by that in the pulse-height bias was insignificant except for alphas.

To consider flux above the atmosphere one must correct the energy thresholds for ionization loss in the material above the Čerenkov counter and must take into account nuclear interactions in all material above the cloud chamber sensitive volume (17-g/cm² air, 13-g/cm² local matter). The corrected thresholds are 710 ± 100-, 540-, 600-Mev/nucleon for He, (Li Be B), (C N O) in that order. The mean free paths 44 g/cm² in air, 60 g/cm² (average) in local matter[2] were used to correct the He flux for attenuation. The number of fast alphas expected to be secondary

is small. The extrapolated He flux comes out $160\pm27/m^2$ sec steradian. Both systematic and statistical errors in the flux that entered the cloud chamber are included in the estimate.

The absorption mean free path in local matter for $Z>2$ nuclei should not be greater than about 50 g/cm², since heavy secondary from local interactions should nearly always enter the chamber accompanied by other secondaries. (Two such events were photographed, and they are not included in the 13.) The $Z>2$ flux that entered the cloud chamber, corrected about 30 percent for local absorption, implies a vertical flux $23\pm6/m^2$ sec steradian of nuclei with $Z>2$ and energy >500-Mev nucleon at atmospheric depth 17 g/cm².

If one accepts the flux measurements of Bradt and Peters[3] for primaries with $Z\geq 6$, such primaries can account for only half the events observed, even if six tenths of their collisions in the atmosphere give secondaries with $Z>2$. The probability of a statistical fluctuation great enough to account for the other half is 0.01. The excess events can be attributed to such a fluctuation or to primary nuclei with $3\leq Z\leq 5$ in abundance comparable to that of heavier nuclei.

* Research supported in part by the joint program of the U. S. Atomic Energy Commission and the U. S. Office of Naval Research.

[1] Balloon flight by Project Skyhook.

[2] Collision cross sections have been calculated from Peters' empirical formula. B. Peters in *Progress in Cosmic Ray Physics* (Interscience Publishers, Inc., New York, 1952), Vol. 1.

[3] H. L. Bradt and B. Peters, Phys. Rev. **77**, 54 (1950).

Photoproduction of π^+ Mesons from Hydrogen and Carbon*

G. Sargent Janes and William L. Kraushaar
Department of Physics and Laboratory for Nuclear Science, Massachusetts Institute of Technology, Cambridge, Massachusetts

(Received November 19, 1953)

We have measured π^+-meson photoproduction cross sections for hydrogen and carbon at a laboratory angle of 90°. Mesons having energies down to 10 Mev were detected.

Our experimental arrangement is shown schematically in Fig. 1. γ rays from the M.I.T. Synchrotron strike the polyethylene or carbon target. The π^+ mesons are detected and identified upon coming to rest in a single scintillation counter. The meson detection solid angle was determined by the counter itself and not by a meson collimator. A collimator would scatter some mesons into the counter, and this effect would distort the meson energy spectrum because the scattered mesons would have undergone energy losses. Pulses from the photomultiplier are amplified and fed into a delayed coincidence arrangement. The characteristic π-μ decay serves to trigger an oscilloscope upon which the triggering pulses are displayed.

A pulse corresponding to a π^+ meson had a height directly indicative of the energy of the incident π^+ meson. The largest π^+ pulse heights observed corresponded to π^+ mesons with a range just equal to the thickness of the scintillation counter. The energy corresponding to this range was 21.2 Mev. This provided an energy pulse-height calibration.

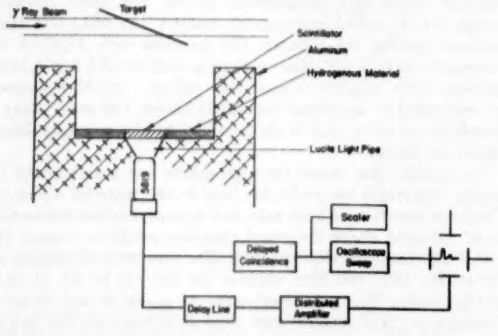

Fig. 1. Schematic experimental arrangement.

All the pulses corresponding to μ mesons had very nearly the same height. Since the energy of a μ^+ meson from the decay of a π^+ meson at rest is known to be 4.15 Mev, the average μ pulse height was used to establish a second independent energy pulse-height calibration.

The detection of π^+ mesons by π-μ decay has three important advantages over detection by μ-e decay: (1) the mean life of the π meson is about 1/80 of that of the μ meson so that accidental delayed coincidences can be kept smaller; (2) because of the uniform μ pulse heights, it is not necessary to extrapolate a decay-particle pulse-height distribution to zero pulse height for evaluation of the detection efficiency; and (3) the sensitive volume of the detector is well defined because the range of the decay μ meson (0.153 g cm^{-2}) is small compared to practical counter dimensions. The principal source of uncertainty (±3 percent) entering the evaluation of our detection efficiency was the standard error in the measurements of the π^+-meson mean life.

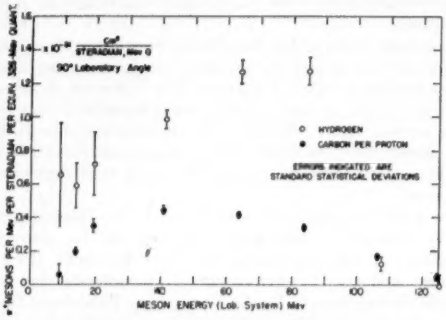

Fig. 2. Meson-energy distribution from hydrogen and carbon, observed at 90° in the laboratory system.

Uncertainties in the absolute beam calibration (in our case ~40 percent) do not enter the comparison of our results with other measurements made in this laboratory. Recent intercalibrations with Cornell and Illinois indicate that our cross sections should be decreased by a factor of approximately 1.7.

In one series of measurements, very thin carbon and polyethylene targets were used (0.153 g cm^{-2} and 0.121 g cm^{-2}, respectively), and no absorber was placed in front of the counter. The measured π^+ pulse-height distributions were thus direct measures of the produced meson-energy distributions subject only to small corrections for target absorption. For the higher meson energies, absorbers were placed in front of the counter, and the initial meson-energy intervals were determined by the thickness of the counter.

The energy distribution of the mesons observed at 90° in the laboratory system is plotted in Fig. 2. All errors shown are standard statistical deviations. The hydrogen π^+ cross sections in the center-of-mass system are plotted against laboratory photon energy and against center-of-mass meson momentum in Fig. 3. For photon energies above 200 Mev, our results are in agreement with those obtained by Steinberger and Bishop.[1] The π^+ cross section appears to be linear with meson momentum (see Fig. 3) from threshold up to about 185 Mev/c (285-Mev γ-ray energy). This is consistent with a pure S-state hypothesis for photon energies up to about 200 Mev. The continued linearity above 200 Mev cannot be taken as evidence of continued pure S-wave predominance in view of the angular distributions.

The meson-energy distribution for carbon is seen to be in agreement with earlier measurements[1,2] made at meson energies

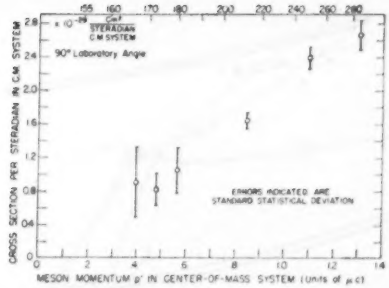
CROSS SECTION PER STERADIAN IN C.M. SYSTEM
STERADIAN C.M. SYSTEM
90° Laboratory Angle
ERRORS INDICATED ARE STANDARD STATISTICAL DEVIATION
MESON MOMENTUM p' IN CENTER-OF-MASS SYSTEM (units of μc)

FIG. 3. π^+ photoproduction cross sections in the center-of-mass system of coordinates *versus* initial photon energy in the laboratory system and meson momentum in the center-of-mass system.

above 25 Mev, but our results seem to indicate a sharp drop near 15 Mev.

Dr. Guiseppe Fidecaro participated in the early phases of this experiment. The assistance of the M.I.T. Synchrotron crew is greatly appreciated.

* This work was supported in part by the joint program of the U. S. Office of Naval Research and the U. S. Atomic Energy Commission.

[1] J. Steinberger and A. S. Bishop, Phys. Rev. **86**, 171 (1952).
[2] Peterson, Gilbert, and White, Phys. Rev. **81**, 1003 (1951).

A Double Star Connected by a Heavy Meson

S. ROSENDORFF, R. STAHL, AND G. YEKUTIELI
*Israel Atomic Energy Commission, Cosmic Ray Section, Tel Aviv, Israel**
(Received December 28, 1953)

IN the course of measurements of the mass distribution of fast particles produced in high-energy nuclear explosions, a case of a double star connected by a heavy meson of mass $1310m_e$ was found.

The double star was observed in a G5 Ilford plate, exposed to cosmic radiation at 30 km. The first star is a $4+4\alpha$ star induced by an alpha particle of 5 Bev (the energy of the primary was estimated by multiple scattering). The heavy meson travels 34 mm before it produces a $5+0K$ secondary star. Multiple scattering and grain density measurements were made along the connecting track. Using the method described by Gottstein *et al.*,[1] we found a value of $p\beta=427\pm41$ Mev/c for the first 16 mm of the track, and a value of $p\beta=417\pm42$ Mev/c for its last 18 mm. The grain density of the track along the first 5 mm is 16.55 ± 0.41 grains per 50μ.

Together with the heavy meson a proton is produced in the same nuclear collision. The proton travels in the emulsion in the direction of the heavy meson and leaves the emulsion after 6.4 mm. Measurements of multiple scattering and grain density (G.D.), for the proton, yield $p\beta=550\pm90$ Mev/c and G.D. $=17.45\pm0.42$ grains/50μ.

The plateau value of the grain density on this plate is 11.5; and the normalized value of ionization, for the heavy meson and proton are 1.44 ± 0.036 and 1.52 ± 0.037, respectively. With the help of the $p\beta$ *vs* grain density curves of Gottstein *et al.*[1] and Daniel *et al.*[2] we have found that the masses of the proton and the heavy meson are 1830 ± 295 and $1300\pm125m_e$, respectively. If we take the correct mass of the proton $m_p=1838m_e$, the corresponding mass of the heavy meson is $m_K=1310\pm245m_e$.

In deriving the last mass value we have used the formula:

$$\frac{m_K}{m_p}=\frac{K_K}{K_p}\frac{\bar{\alpha}_p}{\bar{\alpha}_K}\frac{(\gamma\beta^2)_p}{(\gamma\beta^2)_K},$$

where K_K and K_p are the scattering constants of the heavy meson and the proton, respectively. The value of $\gamma\beta^2$ has been found according to the curve: grain density *vs* γ of Shapiro and Stiller.[3] The mass of the heavy meson derived in this way is almost independent of the plateau value of the grain density.

In the same set of measurements we have found six other heavy mesons with mass between 1000 and $1300m_e$. The total length in the emulsion of the tracks of all the seven heavy mesons is 7.62 cm. According to Daniel and Perkins,[4] 10 cm of track of identified K particles with mass $1200\pm40m_e$ were examined, without finding any nuclear interaction. Assuming that all the observed heavy mesons are K particles and combining the results obtained in Bristol and in this laboratory, we have found one nuclear interaction produced by a K particle along 17.6 cm of emulsion. The interaction mean free path of pions, in the same range of energy, is 25.6 ± 7.56 cm,[5] and it seems likely that both K particles and pions have the same interaction mean free path. This is in agreement with the observation of Daniel *et al.*[2] on the interaction mean free path of shower particles ejected from jets and supports the suggestion[6] that pions and K particles interact with nuclear matter in a similar way.

We are greatly indebted to Dr. M. M. Shapiro of Nucleonics Division, Naval Research Laboratory, Washington, D. C., for the plates in which the double star was observed. We also wish to thank Mrs. M. Weinberg for careful scanning of the plates.

* Post address: P.O.B. 7056, Tel Aviv, Israel.
[1] Gottstein, Menon, Mulvey, O'Ceallaigh, and Rochat, Phil. Mag. **42**, 708 (1951).
[2] Daniel, Davies, Mulvey, and Perkins, Phil. Mag. **43**, 753 (1952).
[3] M. Shapiro and B. Stiller, Bagnères de Bigorre Conference, July, 1953 (unpublished).
[4] R. R. Daniel and D. H. Perkins, Royal Society Conference, London, January, 1953 (unpublished).
[5] W. O. Lock and G. Yekutieli, Phil. Mag. **43**, 231 (1952).
[6] U. Haber-Schaim and G. Yekutieli, Phil. Mag. **43**, (997) (1952).

Nonconservation of Rest Mass and the Dirac Equation

LLOYD MOTZ
Rutherfurd Observatory, Columbia University, New York, New York
(Received November 18, 1953)

IN recent years a number of attempts have been made to introduce a fundamental length into the quantum theory of a particle without destroying the covariance of the equations. The most notable of these attempts are the nonlocalizable field theory of Yukawa[1] and the reciprocity theories of Born and Green.[2] These theories are closely related to the notion that the coordinates and time describing the motion of a particle are not parameters but observables that must be represented by operators.

It is possible to arrive at a somewhat similar point of view by considering a system in which the rest mass m_0 is not conserved. This would be true in systems in which nonmechanical energy of some sort is produced. Let us suppose that Q is the amount of nonmechanical energy developed per unit time in the rest system of a particle. Then the rest mass will no longer be conserved, and we have[3]

$$dm_0/d\tau=Q/c^2, \tag{1}$$

where τ is the proper time and is related to the velocity u of the particle and the time t by the equation

$$d\tau=(1-u^2/c^2)^{\frac{1}{2}}dt. \tag{2}$$

We must therefore have

$$dm_0/dt=[1-(u^2/c^2)]^{\frac{1}{2}}(Q/c^2). \tag{3}$$

From this equation it is obvious that m_0 cannot be a constant of the motion and therefore cannot commute with the Dirac Hamiltonian of the particle. Since in a relativistic quantum theory of a particle $[1-(u^2/c^2)]^{\frac{1}{2}}$ is represented by the Dirac matrix β, we shall write

$$[m_0,H]=i\hbar(Q/c)\beta \tag{4}$$

as the quantum-mechanical equivalent of (3). This means that

the Dirac Hamiltonian must be enlarged by the addition of a term which does not commute with m_0.

We introduce an operator O such that

$$[m_0,O]=ih/c^2. \tag{5}$$

With the aid of this operator we can now generalize Dirac's Hamiltonian to give (4). We write

$$H=c\boldsymbol{\alpha}\cdot\mathbf{p}+\beta(m_0+QO/c^2)c^2. \tag{6}$$

We must now investigate the operator O. We see first of all from (5) that it has the dimensions of a time. Secondly, we note that it plays the same conjugate role to m_0c^2 that $\mathbf{p}$ does to $\mathbf{r}$ and H to the time. It appears reasonable, therefore, to identify O with the proper time τ of the moving particle. This means that the rest mass and proper time of a particle are canonically conjugate variables and therefore do not commute.

Since the proper time of a moving particle is a measure of the line element, the introduction of an uncertainty relationship of the form (5) is equivalent to saying that it is impossible to introduce an exact metric geometry for a system whose rest mass is accurately known. This does not seem unreasonable since an exact geometry presupposes the possibility of localizing a physical particle (e.g., an electron) at any desired point of our frame of reference, and any attempt to do this would bring with it the creation of pairs. This would result in an indeterminancy in the rest mass of our original particle.

Let us now consider a particle which is under observation between the two space-time points (x_k') and (x_k''). The proper time associated with this observation is given by

$$\tau^2=-\frac{1}{c^2}\sum_{k=1}^{4}(x_k'-x_k'')^2. \tag{7}$$

From this we obtain

$$\tau=\pm\frac{i}{c}\sum_{k=1}^{4}\gamma_k(x_k'-x_k''), \tag{8}$$

where the γ_k are the 4×4 Dirac matrices. We thus obtain from (6):

$$H=c\boldsymbol{\alpha}\cdot\mathbf{p}+\beta\left[m_0\pm i\frac{Q}{c^2}\sum_k\gamma_k(x_k'-x_k'')\right]c^2. \tag{9}$$

It is interesting to note that this form of the Hamiltonian has a formal similarity to that suggested by Pais.[4]

Since under ordinary conditions the rest mass of a particle such as an electron is constant, it is clear that the time-average value of Q must vanish and (1) then represents the instantaneous fluctuations of rest mass of the particle. This is obviously connected with the virtual creation and destruction of pairs in the neighborhood of the particle produced by the virtual emission of photons.

[1] H. Yukawa, Phys. Rev. 76, 300 (1949).
[2] M. Born, Revs. Modern Phys. 21, 463 (1949). H. S. Green, Proc. Roy. Soc. (London) A197, 73 (1949).
[3] For a complete discussion of this point see C. Møller, *Theory of Relativity* (Oxford University Press, London, 1951), p. 106.
[4] A. Pais, Physica 19, 869 (1953).

Artificially Produced Negative Heavy Meson*

J. Hornbostel and E. O. Salant
Brookhaven National Laboratory, Upton, New York
(Received December 29, 1953)

NEGATIVE heavy mesons, of mass about $1000m_e$, are known in cosmic rays,[1,2] but the energies of the causative particles are unknown. An experiment for finding out if such mesons are produced in bombardment of a beryllium target by the Cosmotron's 2.2-Bev protons was undertaken, and one such particle has now been found.

The experimental arrangement is sketched in Fig. 1. Negative particles ejected from the target A are analyzed by the magnetic field of the accelerator, leave the vacuum chamber E through the

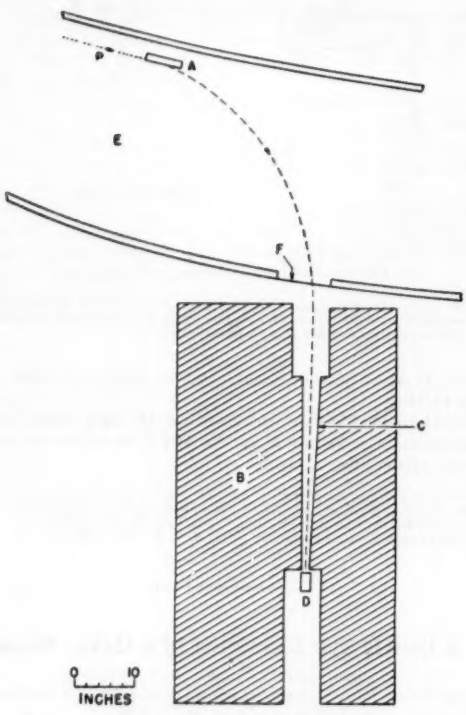

FIG. 1. Schematic diagram of experimental arrangement. Top view.

$\frac{1}{16}$-in. aluminum window F, pass through a collimator C in a lead housing B, and enter a stack D containing 2-inch×3-inch 400μ G5 Ilford emulsions with their planes horizontal. The particles arriving at the stack were ejected between 2° and 17° to the direction of the proton beam P, traverse a distance A to D of 235 cm, enter the stack nearly parallel to the emulsion plane with a horizontal angular spread of 6°, and cover the momentum interval of 310–380 Mev/c. Particles heavier than $700m_e$ come to rest in the stack; endings were looked for in a region in which particles of about half the proton mass should stop. Loss of heavy particles from an emulsion layer by multiple scattering was compensated by embedding pairs of plates in material with the same range-energy relationship as emulsion.

In a scanned area of 28.2 cm² there were observed (besides neutron and conventional σ stars) 2000 stars with 2 or more prongs caused by the fast pions of the incoming beam and also the star shown in Fig. 2. The particle making track 1 (3.6 mm long in the emulsion) moves in the direction of the incoming beam and must have traversed a total of 43 mm in the stack to the end of its range. Track 2 has a grain count less than 1.5 minimum ($E_{\text{kin}}>0.3$ mc²); it is too short (110μ), steep, and distorted to identify the particle. Track 3 is 840μ long, stops in the emulsion, and, according to multiple scattering, is probably due either to a triton or an alpha particle. The spatial angle between tracks 2 and 3 is 112°.

Measurements of gap length *vs* range[3] and of multiple scattering *vs* range both verify that the particle of track 1 is incoming to the star. The gap measurements give the mass of the particle as $1050\pm150m_e$ and the scattering measurements as $1200\pm300m_e$; both values were obtained by comparison with proton and pion tracks, and the quoted errors include the errors of the proton and pion measurements. From the range within the stack and the momentum, the mass of the particle is $1080\pm220m_e$. These results are consistent with the masses reported by Peters[2] for negative

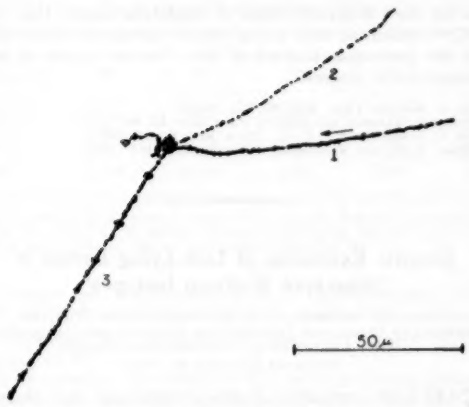

FIG. 2. Trace of projection of heavy meson star. Short curly track is typical of an Auger electron.

heavy mesons and overlap the values given for τ and K mesons[2-4] and also the larger masses found by Daniel *et al.*[5]

The target-to-star path corresponds to 1.2×10^{-8} sec for the heavy meson in its rest system. If the mean life of such mesons were as low as 1 millimicrosecond, it can easily be shown (using cosmic ray evidence that the ratio R of heavy mesons to pions created is less than 0.1) that the probability of observing 1 heavy meson in our experimental arrangement would be less than 0.01. If, on the other hand, the mean life of 8 millimicroseconds indicated for cosmic ray heavy mesons[6] is adopted, the observed proportion of 1 heavy meson star to 2000 pion stars (a proportion that may, of course, change markedly with more observations) would correspond to a value of about 10^{-4} for R.

The creation process of this meson cannot be analyzed unambiguously because of the thickness of the target; the heavy meson could have lost as much as 100 Mev in the beryllium and, besides, could have been made by a fast secondary (pion or proton).

We are particularly indebted to Dr. William H. Moore for his essential share in setting up the experiment, and to Dr. Morton F. Kaplon for initiating us in the gap-length determinations. We take great pleasure in acknowledging the invaluable aid given by our scanning and processing staff, R. Mildred Bracker, Margaret D. Carter, Barbara M. Cozine, Jeanne C. Dennison, Mary C. Hall, Alice C. Lea, and Jacqueline D. Leek.

* Work performed under the auspices of the U. S. Atomic Energy Commission.

[1] L. LePrince-Ringuet, Revs. Modern Phys. **21**, 42 (1949); W. F. Fry and J. J. Lord, Phys. Rev. **87**, 533 (1952).
[2] Lal, Pal, and Peters, Phys. Rev. **92**, 438 (1953).
[3] D. M. Ritson, Phys. Rev. **91**, 1572 (1953).
[4] Crussard, LePrince-Ringuet, Morellet, Orkin-Lecourtois, and Trembley, Phys. Rev. **90**, 1127 (1953).
[5] Daniel, Davies, Mulvey, and Perkins, Phil. Mag. **43**, 753 (1952).
[6] J. W. Keuffel and L. Mezzetti, Bull. Am. Phys. Soc. **29**, No. 1, 60 (1954); Astbury, Buchanan, Chippindale, Millar, Newth, Page, Rytz, and Sahlar, Phil. Mag. **44**, 242 (1953).

Radiative Corrections in Positronium

THOMAS FULTON* AND PAUL C. MARTIN†
Harvard University, Cambridge, Massachusetts
(Received December 7, 1953)

ALL corrections of order α^4 to the $n=2$ energy levels of positronium have been evaluated using the relativistic two-body equation[1,2] with techniques recently proposed by several authors.[3,4] The corrections arise from three sources:

(1) The self-energy and vacuum polarization effects analogous to those which yield the main part of the Lamb shift in hydrogen.

(2) Recoil and retardation corrections to the Breit interaction. Similar contributions have been calculated by Salpeter[5] for hydrogen. In hydrogen such terms account for less than 0.05 percent of the Lamb shift. The effect is much larger in positronium since the mass dependence is of the form $m_1^3m_2^3/(m_1+m_2)^3$.

(3) Corrections to the α^4 virtual annihilation interaction[6-8] and α^5 annihilation processes.[9] These are of course peculiar to a particle-antiparticle system.

Items (1) and (2) above have been calculated with arbitrary masses m_1 and m_2 so as to determine the mass dependence in general. In the limit m_1 small and m_2 large, we confirm Salpeter's numerical result[5] and Arnowitt's hyperfine structure calculation.[10] In the limit $m_1=m_2$ we confirm the results of Karplus and Klein.[9] We also agree with them on item (3). The energy shift due to items (1) and (2) is given by the expression below:

For the $2S$ state:

$$\Delta E_1=\frac{\alpha^5\mu^3}{m_1+m_2}\frac{1}{8\pi}\Big\{-\frac{4}{3}+\frac{8}{3}\Big[\frac{25}{12}+\ln\frac{2Ry_\infty}{\alpha k_0(2,0)}\Big]+2\Big[\ln\alpha+\frac{7}{4}+\frac{4}{3}(1-\ln 2)-(m_1^3-m_2^3)^{-1}(m_2^3\ln\eta_2-m_1^3\ln\eta_1)\Big]-2(2S^2-3)m_1m_2(m_1^3-m_2^3)^{-1}\ln\frac{m_1}{m_2}\Big\},\quad(1)$$

$$\Delta E_2=\frac{\alpha^5\mu^2}{m_1+m_2}\frac{1}{6\pi}\Big\{\frac{m_1^3+m_2^3}{m_1m_2}\Big(\frac{5}{6}-\frac{1}{5}^{\dagger}-\ln\frac{\alpha^2k_0(2,0)}{Ry_\infty}\Big)-\frac{m_2}{m_1}\ln\eta_2-\frac{m_1}{m_2}\ln\eta_1+\frac{1}{2}\langle 2S^2-3\rangle\Big\}.\quad(2)$$

For the $2P$ state:

$$\Delta E_1=-\frac{\alpha^5\mu^2}{m_1+m_2}\frac{1}{8\pi}\Big(\frac{7}{18}-\frac{8}{3}\ln\frac{Ry_\infty}{k_0(2,1)}\Big),\quad(3)$$

$$\Delta E_2=\frac{\alpha^5\mu^2}{m_1+m_2}\Big\{\frac{-1}{6\pi}\Big(\frac{m_1^3+m_2^3}{m_1m_2}\Big)\ln\frac{k_0(2,1)}{Ry_\infty}\Big\}+\frac{\alpha^2}{m_1m_2}\Big\{\frac{1}{4\pi}\Big\langle\Big(\frac{m_2}{m_1}\boldsymbol{\sigma}_1+\frac{m_1}{m_2}\boldsymbol{\sigma}_2\Big)\cdot\frac{\mathbf{L}}{r^3}\Big\rangle+\frac{1}{2\pi}\Big\langle\frac{\mathbf{S}\cdot\mathbf{L}}{r^3}-\frac{1}{2}\Big[\frac{\boldsymbol{\sigma}_1\cdot\boldsymbol{\sigma}_2}{r^3}-\frac{3\boldsymbol{\sigma}_1\cdot\mathbf{r}\boldsymbol{\sigma}_2\cdot\mathbf{r}}{r^5}\Big]\Big\rangle\Big\},\quad(4)$$

where

$$\mu=\frac{m_1m_2}{m_1+m_2},\quad \eta_1=\frac{m_1}{m_1+m_2},\quad \eta_2=\frac{m_2}{m_1+m_2},\quad \mathbf{S}=\tfrac{1}{2}(\boldsymbol{\sigma}_1+\boldsymbol{\sigma}_2),$$

and $k_0(2,0)$ and $k_0(2,1)$ are given by Bethe, Brown, and Stehn.[11] $\langle A\rangle$ denotes the expectation value of A. The dagger in Eq. (2) signifies that in positronium, this vacuum polarization term is 1/10.

In positronium, there is no accidental α^4 degeneracy. Hence, the α^5 shifts must be added to the much larger α^4 fs and hfs in order to obtain the corrected level spacing. Table I gives the α^4 corrections determined by Ferrell[8] and the α^5 contributions we have found.

TABLE I. Additions to the nonrelativistic $n=2$ level of positronium, Mc/sec.

Order	$^1S_0$	$^3S_1$	$^1P_1$	$^3P_2$	$^3P_1$	$^3P_0$
α^4	−18135	7413	−3536	−981	−5360	−10835
α^5	357	232	−3	1	−5	−16
Total	−17778	7645	−3539	−980	−5365	−10851

The α^6 correction to the 2^1S_0 (2^3S_1) level may be broken down as follows: 112 (61) Mc/sec arise from recoil effects; 261 (295) Mc/sec come from vertex parts; −16 (−124) Mc/sec are due to the annihilation interaction. All these effects are much smaller in P states.

It is hoped that work now in progress elsewhere will provide experimental level shifts sufficiently accurate to compare with those predicted theoretically. The details of this calculation will be published later. We wish to thank Professor R. Karplus, Professor J. Schwinger, and Dr. A. Klein for helpful discussions.

* Harvard Veterans National Scholar.
† National Science Foundation Predoctoral Fellow.
[1] J. Schwinger, Proc. Natl. Acad. Sci. U. S. **37**, 452, 455 (1951).
[2] E. E. Salpeter and H. A. Bethe, Phys. Rev. **84**, 1232 (1951).
[3] R. J. Eden, Proc. Roy. Soc. (London) **219**, 519 (1953).
[4] T. Fulton and R. Karplus, Phys. Rev. **93**, 257 (1954).
[5] E. E. Salpeter, Phys. Rev. **87**, 328 (1952).
[6] V. B. Berestetskii and L. D. Landau, J. Exptl. Theoret. Phys. (U. S. S. R.) **19**, 673 (1949).
[7] J. Pirenne, Arch. sci. phys. et nat. **29**, 207 (1947).
[8] R. A. Ferrell, Phys. Rev. **84**, 858 (1951) and PhD thesis, Princeton, 1951 (unpublished).
[9] R. Karplus and A. Klein, Phys. Rev. **87**, 848 (1952).
[10] R. Arnowitt, PhD thesis, Harvard, 1952 (unpublished).
[11] Bethe, Brown, and Stehn, Phys. Rev. **77**, 370 (1950).

The Nuclear Magnetic Moments of Xe^{129} and Xe^{131}

E. Bloch, J. Oeser, H. H. Staub, and C. G. Telschow
Physikalisches Institut der Universität, Zürich, Switzerland
(Received November 27, 1953)

THE nuclear magnetic resonances of Xe^{129} and Xe^{131} in pure Xe gas at a pressure of approximately 50 atmos have been detected with a nuclear induction spectrometer similar to the one described by Weaver.[1] A sample of ordinary Xe gas at 50 atmos without any catalyst was used. The signal of Xe^{131}, abundance 21.17 percent which from hfs is known to have a spin $I=\frac{3}{2}$, and a quadrupole moment $Q\approx-0.15$, appeared as a slow-passage signal with a signal-to-noise ratio of about 40:1. The nature of the signal caused by Xe^{129} ($I=\frac{1}{2}$; abundance $f=26.23$ percent) in the same sample, indicated that the experimental conditions for this isotope were not these of slow passage, the relaxation time T_1 being at least several minutes. Comparison of the proton resonance frequency in water containing 0.1-molar $MnSO_4$ with the resonance frequencies of Xe^{129} and Xe^{131} in the same magnetic field yielded the following results:

$$\nu_{129}/\nu_p=0.276633\pm0.000005, \quad \nu_{131}/\nu_p=0.081976\pm0.000001.$$

Using the value of the proton moment of Sommer, Thomas, and Hipple[2] ($\mu_p=2.79268\pm0.00006$ nm) the above frequency ratios lead to the following magnetic moments for Xe^{129} and Xe^{131}:

$$\mu_{129}=-0.77255\pm0.00002 \text{ nm}, \quad \mu_{131}=+0.68680\pm0.00002 \text{ nm}.$$

Both values are given without diamagnetic corrections. From these values the ratio of the magnetic moments is obtained as

$$\mu_{129}/\mu_{131}=-1.12485\pm0.00002.$$

The value of μ_{129} agrees within the experimental error with that obtained by Proctor and Yu[3] ($\mu_{129}=-0.7726\pm0.0001$ nm) in a sample of Xe gas at 12 atmos and containing Fe_2O_3 powder as paramagnetic catalyst. The ratio of the magnetic moments is also in fair agreement with the value of Bohr, Koch, and Rasmussen[4] ($\mu_{129}/\mu_{131}=-1.131\pm0.005$) obtained by hfs measurements.

The mechanism of relaxation is apparently caused by strong van der Waals forces since pure nuclear dipole-dipole interaction would lead to enormous relaxation times ($\sim10^6$ sec). This explanation is corroborated by the work of Proctor and Yu, who were unable to detect signals of either odd isotope in pure Xe at a pressure of 12 atmos without catalyst. In our experiment, the van der Waals forces are appreciable since at a pressure of 50 atmos the density of the gas is roughly 1.6 times that to be expected for an ideal gas. It is also worth noting that the relaxation time for Xe^{131} is several orders of magnitude smaller than that of Xe^{129}, indicating that strong electric interaction takes place with the quadrupole moment of Xe^{131}. Further studies of these processes are in progress.

[1] H. E. Weaver, Phys. Rev. **89**, 923 (1953).
[2] Sommer, Thomas, and Hipple, Phys. Rev. **82**, 697 (1951).
[3] W. G. Proctor and F. C. Yu, Phys. Rev. **81**, 20 (1951).
[4] Bohr, Koch, and Rasmussen, Arkiv Fysik **4**, 455 (1952).

Electric Excitation of Low-Lying Levels in Separated Wolfram Isotopes*

C. L. McClelland, Hans Mark, and Clark Goodman
Department of Physics and Laboratory for Nuclear Science, Massachusetts Institute of Technology, Cambridge, Massachusetts
(Received December 30, 1953)

ELECTRIC excitation of heavy nuclei was first observed simultaneously by two groups.[1,2] Subsequently, this has been confirmed by a number of others[3] and a major improvement in the technique for determination of the energy of the excited state has been achieved by Huus and Bjerregaard[4] using magnetic analysis of the internal conversion electrons. These investigators established that the broad peak observed[1] at 105–125 kev (see Fig. 1)[5] is composed of three separate peaks at 102, 113, and 124 kev. The Bohr-Mottelson theory[6] predicts that each even-even isotope of wolfram has a 2+ low-lying rotational level above the 0+ ground state, that these levels should have nearly the same energy, and that in this element the energy of the level in a given isotope should increase with atomic weight. It is known that W^{186} has a 2+ level at about 123 kev.[7] Accordingly Huus and Bjerregaard tentatively assigned the above three levels to the

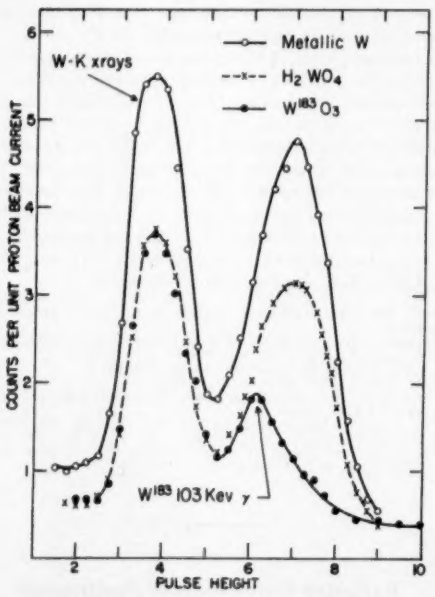

FIG. 1. NaI(Tl) scintillation spectrometer pulse spectra from three wolfram targets during bombardment with 2.5-Mev protons. The broad gamma photopeak shown for metallic wolfram and H_2WO_4 is produced by unresolved gammas from all wolfram isotopes. The pulse spectrum from W^{183} is shown for comparison. Spectra from even-even wolfram isotopes are displayed in Fig. 2. The energy of the W^{183} gamma is given to an accuracy of ±8 kev. The breadth of this peak on the high-energy side results from the appreciable concentrations of the heavier isotopes as impurities (see Table I). In each case a 0.1-inch copper absorber was used to reduce the intensity of the K x-ray background. The intensity of the W^{183} gamma has not been corrected for absorption in copper.

TABLE I. Isotopic composition of WO_3.

Target designation	Mass analysis in atom percent 180	182	183	184	186
W^{182} [a]	0.017	92.33	3.62	2.71	1.31
W^{183} [a]	0.098	4.19	86.21	7.14	2.36
W^{184} [a]	0.056	0.902	1.25	95.72	2.07
W^{186} [a]	0.013	0.501	0.379	1.57	97.54
W [b]	0.143	26.09	14.24	30.68	28.85

[a] As reported by Isotopes Division, U. S. Atomic Energy Commission.
[b] R. F. Hibbs, U. S. Atomic Energy Commission Report AECU-556 (1949), from National Bureau of Standards Circular 499.

three major even-even isotopes of nearly equal abundance: W^{182}, W^{184}, and W^{186}, respectively. We have confirmed this assignment by measurements on isotopically enriched wolfram (see Table I) obtained as WO_3.

Thick targets of the powdered WO_3 as received were prepared by compression into lead disks. Targets of natural W in the form of powdered H_2WO_4(cp) were also prepared in the same way. The data for W^{183} appear in Fig. 1, and that for the even-even isotopes of wolfram in Fig. 2.

The theory[6] predicts that the cross sections for electric excitation of the three even-even isotopes of wolfram should decrease in the order of W^{182}, W^{184}, W^{186}. After correction for absorption in copper, and rough estimates of the effects of internal conversion from the data of Huus and Bjerregaard[4] and Steffen,[8] our measured intensities support this theory. We hope to be able to give quantitative values for the relative cross sections in the near future.

Absolute reaction cross-section measurements have not yet been completed, but the experimental gamma intensity from the even-even W isotopes appears to be of the same order as that for Ta, reported previously.[1,2] After correction for absorption in copper, the yield of the W^{186} gamma is substantially smaller than that of the even-even isotopes.

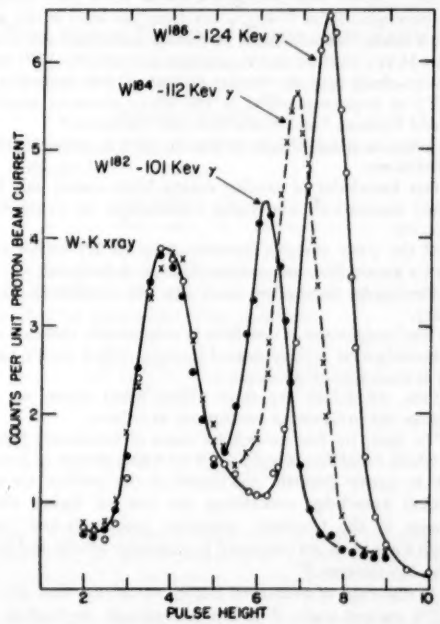

FIG. 2. Superposition of the pulse-height spectra obtained during bombardment of the three even-even isotopes of wolfram with 2.5-Mev protons. The gamma rays observed result from de-excitation of the first level in the isotope after electric excitation. Gamma energies are considered reliable to ±4 kev. In each case an absorber of 0.1-inch copper was used to reduce K x-ray background. The figure does not include correction for gamma absorption in the copper or internal conversion which have been estimated in the text. Counting statistics at the photopeaks are about twice the size of the symbols used.

The scintillation spectrometer was calibrated with the gamma from electric excitation of the first level in tantalum taken as 136.5 kev[9] and with the K x-ray series peak from W taken as 60 kev. The energy assigned this peak results from graphical analysis of our experimental data combined with measurements of the relative intensities of the K series from wolfram.[10]

* This work was supported by the joint program of the U. S. Office of Naval Research and the U. S. Atomic Energy Commission.
[1] T. Huus and Č. Zupančič, Kgl. Danske Videnskab. Selskab, Mat.-fys. Medd. **28**, No. 1 (1953).
[2] C. L. McClelland and C. Goodman, Phys. Rev. **91**, 760 (1953).
[3] Gove (Chalk River), Williamson (Duke), and Temmer, and Heydenburg (Carnegie Institution of Washington).
[4] T. Huus and J. H. Bjerregaard, Phys. Rev. **92**, 1579 (1953). We appreciate these authors' sending us their data prior to publication.
[5] Some of these data were reported at the Albuquerque Meetings of the American Physical Society, September 4, 1953; C. L. McClelland, Phys. Rev. **92**, 1092 (1953).
[6] A. Bohr and B. R. Mottelson, Kgl. Danske Videnskab. Selskab, Mat.-fys. Medd. **27**, No. 16 (1953).
[7] M. Goldhaber and R. D. Hill, Revs. Modern Phys. **24**, 226 (1952).
[8] R. M. Steffen, Phys. Rev. **82**, 830 (1951).
[9] Cork, Nester, LeBlanc, and Brice, Phys. Rev. **92**, 119 (1953).
[10] A. H. Compton and S. K. Allison, *X-Rays in Theory and Experiment* (D. Van Nostrand Company, Inc., New York, 1935), p. 638.

On H. Alfvén's Theory of the Effect of Magnetic Storms on Cosmic-Ray Intensity*

W. F. G. SWANN
Bartol Research Foundation of the Franklin Institute, Swarthmore, Pennsylvania
(Received December 31, 1953)

THE theory of Alfvén[1] envisages a stream of gas shot out from a place on the sun where there is a large magnetic field. The gas, supposed highly conducting, carries the magnetic field H with it, and the field is supposed to be perpendicular to the velocity v. A stationary observer observes an electric polarization perpendicular to H and v, and the potential change across the beam of width h is calculated as Hvh/c. A cosmic ray crossing the beam is supposed to change its energy by $Hvhe/c$, and by making H or h large this change of energy can be made as great as is desired. Alfvén calculates a 10 percent change for the energy of a 3×10^{10} ev ray on crossing a beam of width 5×10^{13} cm carrying a magnetic field of 3×10^{-4} gauss and travelling with a velocity of 2×10^{8} cm/sec.

The present paper recognizes that an observer moving with the beam observes no change of energy, and by a relativity transformation, it is shown that a fixed observer cannot observe a change of energy greater than $2vW/c$, where W is the energy of the cosmic ray. This change amounts to only about 1.4 percent.

The essence of this matter is the following: If v is along the axis of x, if u is the velocity of the particle, W the total energy of the particle, and $\beta=(1-v^2/c^2)^{-\frac{1}{2}}$, then Wu_x, Wu_y, Wu_z, Wic constitute a 4 vector. If S and S' refer, respectively, to the fixed axes and the axes moving with the system, it results that if W' is the energy in S', which energy does not change with time, the change W_2-W_1 in crossing the beam as measured in S is:

$$W_2-W_1=\beta W'(u_{x2}'-u_{x1}')v/c^2,$$

so that

$$(W_2-W_1)<2\beta W'v/c,$$

from which it can readily be shown that

$$(W_2-W_1)<(2v/c)W_1.$$

The discrepancy between the conclusions from relativity and those drawn by Alfvén are shown to arise from the fact that the cosmic-ray path in the example considered by Alfvén would have, in the beam, a radius of curvature 15 times smaller than the beam width and so could never cross it. Thus relativity gives for the change of energy of the beam an upper limit of the order

$2v/c$ times the energy of the beam, and this limit can never be exceeded, however large H or h may be chosen.

An analysis of the considerations resulting from the assumption of a finite conductivity for the space external to the beam shows that the existence of such a conductivity does not change the conclusions.

* The full mathematical details pertaining to this paper, together with a discussion of their ramifications, will appear in the Journal of the Franklin Institute, for March, 1954.

[1] H. Alfvén, Phys. Rev. 75, 1732 (1949).

Coulomb Excitation of Heavy and Medium Heavy Nuclei by Alpha Particles. II

N. P. Heydenburg and G. M. Temmer
Department of Terrestrial Magnetism, Carnegie Institution of Washington, Washington, D. C.

(Received December 28, 1953)

We wish to report the results of the completion of our preliminary survey[1,2] of low-lying excited states of nuclei by 3-Mev alpha-particle Coulomb excitation, as well as some conclusions we can draw from the large amount of data now at hand.

Our experimental setup has been briefly described previously.[2] Of the 66 elements we have investigated, 45 show one or more excitation levels. Because of the inherent danger of being misled by impurities and surface contaminations of target materials, we felt it desirable to investigate as many elements as possible; as an example, we found a strong line in spectroscopically pure bismuth metal which later turned out to be due to a very small (0.01 percent) fluorine impurity. Certain generalizations concerning the nature of the levels reached will be given below.

In Table I we present a supplement to the list of elements previously given in I, Table I. Some very low-intensity lines we observe are not reported in this table pending further study by photographic means. It should be remembered that the rough relative intensities indicated in the fourth column (relative to 1.00 for the 137-kev line of Ta^{181}) are preliminary and even if accurate must still be subject to several transformations before they become meaningful for the determination of transition probabilities between energy levels. The principal obscuring factor is the strong dependence of the excitation cross section on the quantity $\xi = Z_1 Z_2 e^2/\hbar v$ (Z_1 and Z_2 are the charges of projectile and target, v is their relative velocity, ΔE is the excitation energy of the nucleus, and E is the center-of-mass energy of the projectile).[3] This factor is connected with the details of the excitation mechanism and is not related to the problem of interest, i.e., the determination of nuclear transition matrix elements between states. Furthermore, since we have used thick targets so far, a stopping-power correction must be made.

TABLE I. Continuation of survey of levels below 500 kev observed by Coulomb excitation with 3-Mev alphas. Approximate intensities relative to 137-kev line in Ta^{181} (*uncorrected* for relative abundance and internal conversion). For meaning of intensity, see text.

Element[a]	Abundance (%)	E_γ (observed) kev	Approx int.[b]	E_γ (known)[c] kev
$_{35}Br^{79}$	50.6	44, 213, 266	0.03, 0.23, 0.11	44, 263
$_{44}Ru^{?}$	?	91, 128, 360	0.31, 0.24, 0.05	?
$_{53}I^{127}$	100	57, 205	0.28, 0.90	57, 145, 200
$_{56}Ba^{?}$	?	60, 118	0.013, 0.013	?
$_{57}La^{139}$	99.9	56	0.005	166
$_{58}Ce^{140,142}$	88.5, 11	77, 129[d]	0.005, 0.005	?
$_{60}Nd^{?}$	?	70, 130	0.03, 0.36	135, 170, 329
$_{62}Sm^{?,152}$	?, 26.6	82,[e] 122	1.2	122
$_{64}Gd^{156,158}$	2.2, 14.7	82, 124	3.5, 0.21	85, 106, 124, 132
$_{71}Lu^{175}$	97.4	77, 113, 184?	0.15, 1.5, 0.036	89, 113, 138, 228
$_{73}Hf^{177,180}$ [f]	18.4, 35.4	112, 93	0.13, 1.14	89, 93, 112
$_{75}Re^{187}$	62.9	130	0.81	73, 133
$_{76}Os^{188,?}$	13.3, ?	157, 180, 188, 202	all ~0.2[g]	152
$_{77}Ir^{191}$	38.5	129	>0.06	42, 65, 129
$_{78}Pt^{194}$ [h]	32.8	213, 328[i]	0.06, 0.02	290, 328
$_{78}Pt^{195}$ [h]	33.7	29, 98, 128	?, 0.03, 0.03	29, 97, 126
$_{79}Au^{197}$ [h]	100	77, 190, 277[i]	?, 0.0013, 0.001	77, 191, 279
$_{80}Hg^{200}$	16.9	163	0.03	50, 159, 209
$_{92}U^{238}$	99.3	44, 424(?)[i]	0.05, 0.06	?

[a] No lines were observed in V, Sn, and Pb. For other elements, see I.
[b] Relative to the 137-kev line of Ta^{181} (=1.00).
[c] Only low-energy lines listed; see references 7 and 8.
[d] According to the regularity of first excited states of even-even nuclei [G. Scharff-Goldhaber, Phys. Rev. 90, 587 (1953)], these energies seem too low for cerium, which has only even-even isotopes and $N \cong 82$.
[e] This line was accidentally omitted in I.
[f] Previously seen as impurity (3 percent) in Zr target; see I.
[g] Incompletely resolved because of 4 isotopes of comparable abundance.
[h] Listed as showing no lines in I; see text.
[i] With protons and alphas.

It is interesting to note that an electric quadrupole transition lifetime of about 4×10^{-9} second (taking the specific example of Ta^{181}) corresponds to a Coulomb excitation cross section for alpha particles of about one millibarn for the inverse transition. Whereas it becomes easier to excite and detect states of *shorter* lifetime, measurement of the latter by delayed-coincidence techniques becomes more difficult, especially since our estimate *does not* include the speeding-up effect of internal conversion. Thus the two methods are seen to be complementary, with a comfortable overlap region. Our limit of detection is of the order of 10^{-30} cm^2, depending somewhat on the particular nucleus. In the case of mixed multipole transitions (e.g., $M1+E2$) we clearly measure only the *partial* lifetime for the quadrupole component.

A few special remarks are in order concerning some of the nuclei in Table I. Our careful reexamination of platinum revealed the three known gamma rays (29, 97, and 126 kev) belonging to the two first excited states of Pt^{195} at 97 kev and 126 kev, plus a line at 328 kev (probably the first excited state of Pt^{194}) and an unknown one at 213 kev.[4] A more thorough look at gold yielded lines at 190 and 277 kev coming from known levels; a comparison of x-ray line shapes as obtained with proton- and alpha-particle excitation, coupled with critical absorption tests, gave evidence for the presence of the 77-kev γ ray from the level of the same energy. A similar reexamination of lead did not reveal any γ rays. The new 44-kev level we find in uranium (presumably U^{238}) seems to fit very nicely into the regular pattern of first excited states (spin 2^+) of even-even nuclei in the heavy elements noted by Asaro and Perlman,[5] and Rosenblum and Valadares.[6]

The following points should be kept in mind in connection with our conclusions:

(1) Our knowledge of existing energy levels comes only from published summaries[7,8] and varies considerably as to reliability of spins, etc.

(2) If the γ-ray energies determined by us fall within about 3 kev of a known line, we consider them to be identical.

(3) Previously unreported lines are not considered in the summary.

The final assignment of new lines in polyisotopic elements must await investigation with separated isotopes, which we are undertaking in some important cases.

If, then, we accept the three points listed above, we may summarize our preliminary conclusions as follows:

(1) To date, we find no definite cases of transitions between levels which could not be connected by a spin change of 2 and no change in parity (electric quadrupole);[9] the present status of theoretical knowledge concerning the role of higher electric multipoles in the Coulomb excitation process is not clear,[10] although some ideas are contained in papers by Mullin and Guth[11] and Ter-Martirosyan.[12]

(2) In the case of even-even nuclei, we *always* find that the first (2^+) excited state, if it lies low enough, is reached with appreciable probability; this occurs mainly in the regions between $A=145$ and $A=200$ (rare earths), and $A>220$ (in practice, thorium and uranium). There are 12 such cases.

(3) In the case of even-odd and odd-even nuclei, we find about 9 cases where the excited state (according to present level assignments) has a spin *smaller* than the ground state. This seems to

rule out the possibility of a simple rotational interpretation.[12] In addition, we find 5 cases where the excited state spin *exceeds* that of the ground state (the latter being $\frac{3}{2}$ or greater), Ta^{181} being a well-known example, plus 8 cases having ground state spin $\frac{1}{2}$.

We are planning to study the excitation functions of some additional nuclei in this survey in the hope that higher multipole-order contributions might show up as deviations from the theoretical shape predicted for quadrupole excitation.[3]

We are greatly indebted to a long list of people from the National Bureau of Standards who so generously supplied us with samples of most of the rare substances appearing in the tables of this paper and reference 2.

[1] G. M. Temmer and N. P. Heydenburg, Bull. Am. Phys. Soc. **29**, 10 (1954).
[2] G. M. Temmer and N. P. Heydenburg, Phys. Rev. **93**, 351 (1954), hereafter referred to as I.
[3] K. Alder and A. Winther, Phys. Rev. **91**, 1578 (1953).
[4] This nucleus was reported in I as showing no lines below 500 kev. We are indebted to Professor Clark Goodman for private communication concerning work of his group on proton excitation of platinum, tantalum, tungsten, and lead. They find lines in platinum at 150, 215, and 330 kev.
[5] F. Asaro and I. Perlman, Phys. Rev. **87**, 393 (1952); **91**, 763 (1953). We are indebted to Professor Perlman for informing us that his group has some tentative evidence [F. Asaro, University of California Radiation Laboratory Report UCRL-2180 (unpublished)] for a level in U^{238} at around 45 kev from alpha-ray spectrography of plutonium.
[6] S. Rosenblum and M. Valadares, Compt. rend. **235**, 711 (1952).
[7] K. Way *et al.*, "Nuclear Data," Natl. Bur. Standards Circ. **499** (1950), and supplements.
[8] Hollander, Perlman, and Seaborg, Revs. Modern Phys. **25**, 469 (1953).
[9] One strange exception is the case of Ge^{73}(?) which will be studied with an enriched sample (see reference 2).
[10] K. Alder and A. Winther (private communication).
[11] C. J. Mullin and E. Guth, Phys. Rev. **82**, 141 (1951).
[12] K. A. Ter-Martirosyan, J. Exptl. Theoret. Phys. (U.S.S.R.) **22**, 284 (1952).
[13] A. Bohr and B. R. Mottelson, Kgl. Danske Videnskab. Selskab, Mat.-fys. Medd. **27**, No. 16 (1953).

A New Spinor Theory of Elementary Particles

FERDINAND CAP
Department of Theoretical Physics, University of Innsbruck, Innsbruck, Austria
(Received December 4, 1953)

THE usual spinor theory of elementary particles[1] uses spinors of the kind

$$a^{\dot\mu_1\cdots\dot\mu_M}_{\nu_1\cdots\nu_N},\qquad b^{\dot\mu_0\dot\mu_1\dot\mu_2\cdots\dot\mu_M}_{\nu_2\cdots\nu_N}$$

which possess dotted and undotted indices. The rank of these spinors is $r=M+N=2s$, where s is the spin of the particle. The spinors obey the generalized Dirac equations:

$$\partial^{\dot\mu_0\nu_1}a^{\dot\mu_1\dot\mu_2\cdots\dot\mu_M}_{\nu_1\nu_2\cdots\nu_N}=i\frac{mc}{\hbar}b^{\dot\mu_0\dot\mu_1\dot\mu_2\cdots\dot\mu_M}_{\nu_2\cdots\nu_N},$$

$$\partial_{\dot\mu_0\nu_1}b^{\dot\mu_0\dot\mu_1\dot\mu_2\cdots\dot\mu_M}_{\nu_2\cdots\nu_N}=i\frac{mc}{\hbar}a^{\dot\mu_1\dot\mu_2\cdots\dot\mu_M}_{\nu_1\nu_2\cdots\nu_N}.$$

These are 2×2^{2s} equations to which must be added the conditions of symmetry for all spinor indices as all spinors used have to be totally symmetric.[1] So the number of independent components is $(M+1)(N+1)$ for the a spinor and $N(M+2)$ for the b-spinor. One can see that the number of all spinor components used, namely $2MN+3N+M+1$, is greater than the number of states of the elementary particle. An elementary particle possesses two degrees of freedom: charge and spin. The charge contains two possibilities, $+e$ and $-e$, and the spin has $2s+1$ possibilities. Measurements made on an elementary particle distinguish, therefore, $2(2s+1)$ different states of a quantized spinor wave field of spin s. It must therefore be possible to describe an elementary particle sufficiently by only $2(2s+1)$ spinor components. As will be seen, this new method[2] has several advantages—for instance any problem can be solved regardless of the value of the spin. Furthermore, bosons and fermions differ only after quantization. So general electromagnetic (or other) interactions[3] or the scattering of particles with spin s by a Coulomb field have to be calculated only once for the spin s and not separately for $s=0$,[4] $s=\frac{1}{2}$,[5] and $s=1$.[6] Furthermore, it might be that the slightly different transformation properties of spinors (*vis à vis* tensors, used now for the description of bosons) give other results[7] for interacting particles.

By multiple application of formulas of the kind

$$\partial_{\dot\mu_M\nu_{N+1}}a^{\dot\mu_1\cdots\dot\mu_{M-1}\dot\mu_M}_{\nu_1\cdots\nu_{N-1}\nu_N}=i\frac{mc}{\hbar}a^{\dot\mu_1\cdots\dot\mu_{M-1}}_{\nu_1\cdots\nu_{N-1}\nu_N\nu_{N+1}},$$

one arrives finally at the spinors $a^{\dot\mu_1\cdots\dot\mu_{2s}}$ and $a_{\nu_1\cdots\nu_{2s}}$ which contain only indices of one kind and exactly $2(2s+1)$ components. These new spinors obey second-order differential equations:

$$(\Box-m^2c^2/\hbar^2)a^{\dot\mu_1\cdots\dot\mu_{2s}}=0,\quad(\Box-m^2c^2/\hbar^2)a_{\nu_1\cdots\nu_{2s}}=0,$$

which describe the propagation of the unquantized spinor wave field. There are no longer any first-order differential equations which, according to Pauli,[8] are not at all necessary.

It is possible to build up a relativistically- and gauge-invariant theory which is also invariant against inversions $x_k\to-x_k$ $(k=1,2,3)$, $x_4\to x_4$. After quantization,[9] the new theory reproduces for the free particle the well-known results of the usual theory[10] in a generalized manner, so that, for instance, the whole charge Q or the whole energy H is given by:

$$Q_{B,F}=e\sum_{r,k}^{\infty}(\mathfrak{N}^{(+)}{}_{r,k}{}^{B,F}-\mathfrak{N}^{(-)}{}_{r,k}{}^{B,F}),$$

$$H_B=\sum_{k,r}^{\infty}E_k(\mathfrak{N}^{(-)}{}_{k,r}{}^{B}+\mathfrak{N}^{(+)}{}_{k,r}{}^{B})+\sum_{k}^{\infty}E_k,$$

$$H_F=\sum_{k,r}^{\infty}|E_k|\,\mathfrak{N}^{(-)}{}_{k,r}{}^{F}+\sum_{k,r}^{\infty}|E_k|\,\mathfrak{N}^{(+)}{}_{k,r}{}^{F},$$

where B, F means boson *or* fermion, where $\hbar k$ is the momentum and r the spin number $r=0\cdots2s+1$. The matrices $\mathfrak{N}^{(+)}{}_{r,k}{}^{B,F}$, $\mathfrak{N}^{(-)}{}_{k,r}{}^{B,F}$ are the well-known diagonalized matrices with infinite rows for bosons and with two rows for particles subject to the Pauli principle (fermions), depending on k and r and giving the number of particles present. Besides the possibility of giving other results for interacting particles, the new theory has the advantage of being a consistent general theory without superfluous components or accessory conditions, able to give the basis for a proposed unified nonlinear spinor theory of all elementary particles.[11]

[1] P. A. M. Dirac, Proc. Roy. Soc. (London) **A155**, 447 (1936); M. Fierz, Helv. Phys. Acta **12**, 3 (1939).
[2] F. Cap, Z. Naturforsch. **8a**, No. 11 (1953).
[3] F. Cap, "Electromagnetic interactions in the new spinor theory of elementary particles" (to be published).
[4] G. Wentzel, *Quantum Theory of Fields* (Deuticke, Vienna, 1943).
[5] N. F. Mott, Proc. Roy. Soc. (London) **A124**, 425 (1929); **135**, 429 (1932); F. Sauter, Ann. Physik **18**, 61 (1933).
[6] O. Laporte, Phys. Rev. **54**, 905 (1938); J. Gunn, Proc. Roy. Soc. (London) **A193**, 559 (1938); Massey, and Corben, Proc. Cambridge Phil. Soc. **35**, 463 (1939); N. F. Mott and H. S. W. Massey, *The Theory of Atomic Collisions* (Clarendon Press, Oxford, 1949), second edition.
[7] H. Donnert, "Über geladene Elementarteilchen mit Spin 1," Z. Physik (to be published).
[8] W. Pauli, Phys. Rev. **58**, 716 (1940).
[9] F. Cap, Z. Naturforsch. **8a**, No. 12 (1953).
[10] A. March, *Quantum Theory of Particles and Wave Fields* (John Wiley and Sons, Inc., New York, 1951); see also reference 4.
[11] W. Heisenberg, Z. Naturforsch. **5a**, 251 (1950).

Transcurium Isotopes Produced in the Neutron Irradiation of Plutonium

S. G. Thompson, A. Ghiorso, B. G. Harvey, and G. R. Choppin
Radiation Laboratory and Department of Chemistry, University of California, Berkeley, California
(Received December 21, 1953)

We have succeeded in producing isotopes of three transcurium elements by the irradiation of the starting material Pu^{239} in the Materials Testing Reactor. The heaviest elements were separated completely from plutonium, fission products, americium, and curium by methods involving combinations of precipitation and ion exchange.[1-4] In the element 97 (berkelium) fraction, soft beta particles were observed. In the californium fraction, alpha particles of three different energies were observed, namely, about 6.15 Mev, 6.05 Mev, and 5.8 Mev. In the fraction just preceding the californium in elution from the hot Dowex-50 resin column, specifically the element 99 fraction,[5] alpha particles of 6.6-Mev energy were observed. The amount of activity observed in this fraction was extremely small; nevertheless, its assignment to element 99 is regarded as certain. All of these isotopes have half-lives longer than one week.

The berkelium isotope which decays by the emission of soft beta particles is probably Bk^{249}. Other work[6] has indicated that Bk^{247} is probably a relatively short-lived isotope which decays by electron capture to Cm^{247} which is beta stable. Therefore the lightest curium isotope which decays to berkelium would be Cm^{249}. The assignment to Bk^{249} is also reasonable since its radiations should be very soft whereas Bk^{248} or Bk^{250} (both odd-odd isotopes) would be expected to emit energetic radiation. On the basis of this assignment, it is interesting to note that there are no beta-stable berkelium isotopes.

The californium isotope or isotopes emitting the above-mentioned alpha particles must be heavier than 248. From alpha systematics, the alpha half-lives corresponding to the measured energies should range from a few years to several hundred years.[7]

The isotope of element 99 emitting 6.6-Mev alpha particles is logically assigned as 99^{253}. A reasonable half-life estimated from systematics, assuming a hindrance factor of ten, would be very roughly a month.

The isotopes mentioned here were all produced as a result of combinations of successive neutron captures and beta decays. A possible sequence leading to the production of 99^{253} might be the following:[8]

$$\begin{array}{l}
Pu^{239}(n,\gamma)Pu^{240}(n,\gamma)\,Pu^{241}\,(n,\gamma)\,Pu^{242}\,(n,\gamma)\,Pu^{243} \\
\qquad\qquad\qquad\qquad\quad \downarrow \qquad\quad \uparrow \qquad\quad \downarrow \\
\qquad\qquad\qquad\qquad Am^{241}(n,\gamma)Am^{242}(n,\gamma)Am^{243}(n,\gamma)Am^{244} \\
\qquad\qquad\qquad\qquad\qquad\quad \downarrow \qquad\qquad\quad \downarrow \\
\qquad\qquad\qquad\qquad\qquad Cm^{242}(n,\gamma)Cm^{243}(n,\gamma)Cm^{244},
\end{array}$$

$$\begin{array}{l}
Cm^{244}(n,\gamma)Cm^{245}(n,\gamma)Cm^{246}(n,\gamma)Cm^{247}(n,\gamma)Cm^{248}(n,\gamma)Cm^{249} \\
\qquad\qquad\qquad\qquad\qquad\qquad\qquad\qquad\qquad\qquad\qquad\quad \downarrow \\
\qquad\qquad\qquad\qquad\qquad\qquad\qquad\qquad\qquad\qquad\qquad\quad Bk^{249},
\end{array}$$

$$\begin{array}{l}
Bk^{249}(n,\gamma)Bk^{250} \\
\quad \downarrow \qquad\quad \downarrow \\
Cf^{249}(n,\gamma)\,Cf^{250}(n,\gamma)Cf^{251}(n,\gamma)Cf^{252}(n,\gamma)Cf^{253} \\
\qquad\qquad\qquad\qquad\qquad\qquad\qquad\qquad\quad \downarrow \\
\qquad\qquad\qquad\qquad\qquad\qquad\qquad\qquad\quad 99^{253}.
\end{array}$$

There is unpublished information relevant to element 99 at the University of California, Argonne National Laboratory, and Los Alamos Scientific Laboratory. Until this information is published, the question of the first preparation should not be prejudged on the basis of this paper or the preceding one.[5]

We wish especially to thank Professor Glenn T. Seaborg for continued advice and encouragement in the experimental work. We wish to acknowledge the help of Dr. W. B. Lewis and the entire Phillips MTR staff for aid in the irradiation of the sample, of Dr. F. W. Albaugh, Dr. E. M. Kinderman, H. H. Van Tuyle, and Lee Miller of the General Electric Company at Richland, Washington, for aid in the initial chemical separations and of the Health Chemistry Group of the University of California, particularly N. B. Garden and W. B. Ruehle for providing special equipment for handling the highly radioactive materials. We also wish to thank Dr. E. K. Hulet, Alfred Chetham-Strode, Docia B. McKennon, Margaret Nervik, and Therese Pionteki for extensive help in the experimental work. Finally, we wish to thank A. S. Coffinberry, V. O. Streubling, R. E. Tate, and B. W. Marshall of Los Alamos, and M. H. Studier, F. G. Foote, and A. B. Shuck of the Argonne National Laboratory for preparation of the plutonium in a form suitable for irradiation.

[1] Thompson, Ghiorso, and Seaborg, Phys. Rev. **80**, 781 (1950).
[2] Thompson, Street, Ghiorso, and Seaborg, Phys. Rev. **80**, 790 (1950).
[3] Thompson, Cunningham, and Seaborg, J. Am. Chem. Soc. **72**, 2798 (1950).
[4] Street, Thompson, and Seaborg, J. Am. Chem. Soc. **72**, 4832 (1950).
[5] Ghiorso, Rossi, Harvey, and Thompson, Phys. Rev. **93**, 257 (1954).
[6] E. K. Hulet, Ph.D. thesis, University of California Radiation Laboratory Report UCRL-2283, August, 1953 (unpublished).
[7] Perlman, Ghiorso, and Seaborg, Phys. Rev. **77**, 26 (1950).
[8] G. T. Seaborg, University of California Radiation Laboratory Report UCRL-1942, March, 1952 (unpublished); Ohio State University Third Annual Phi Lambda Upsilon Lecture Series.

"V Dinucleons"*

H. Primakoff and W. Cheston
Washington University, St. Louis, Missouri and University of Minnesota, Minneapolis, Minnesota
(Received December 21, 1953)

In a previous paper[1] (hereafter referred to as A) we have suggested the possibility of the existence of "V deuterons": particles involving a nuclearly stable structure of a proton bound to a neutral V.[2] These V deuterons are subject to nonmesonic and mesonic decay according to the schemes:

$$V\text{ deuteron} \equiv [V^0+p] \rightarrow \begin{cases} p+n+\approx 175\text{-Mev K.E.} & (1) \\ p+p+\pi^- +\approx 35\text{-Mev K.E.} & (2) \\ p+n+\pi^0+\approx 35\text{-Mev K.E.} & (3) \\ d+\pi^0+\approx 35\text{-Mev K.E.} & (3') \\ n+n+\pi^+ +\approx 35\text{-Mev K.E.} & (4) \end{cases}$$

Schemes (3′) and (4) were not mentioned in A; on the basis of charge symmetry, scheme (4) should obviously occur if scheme (2) occurs, while scheme (3′) is an alternative to (3) since the n and p may on occasion be produced in a bound (deuteron) state. The relative probabilities of the nonmesonic decay scheme (1) and of the mesonic decay schemes (2), (3), (3′), (4) have been shown in A to be of the same order of magnitude; the mean life of the V deuteron has been shown in A to be of the same order as the mean life (for the mesonic decay) of a free V^0 ($\approx 3\times 10^{-10}$ sec).

We now wish to point out that an alternative structure of the V deuteron is also possible, namely $[V^+ + n]$, i.e., a nuclearly stable structure of a neutron bound to positively charged V; this alternative V deuteron will also be capable of decay according to schemes (1) through (4) but with a considerably larger kinetic energy release, since the rest energy of the $V^\pm$ is some 85 ± 40 Mev larger than the rest energy of the $V^0[M(V^0)\approx(2185\pm 10)m_e$; $M(V^\pm)\approx(2350\pm 80)m_e]$.[3]

In addition, particles which might be called "negative V deuterons," "V diprotons," and "V dineutrons" can be nuclearly stable even if the "specifically nuclear" attractive forces between nucleons and V's in various angular momentum states are no stronger than the corresponding forces between nucleons and other nucleons. For unlike ordinary dinucleons, all of these "V dinucleons" can exist in ${}^3S_1$ states (Pauli exclusion inoperative between a V and a nucleon); moreover the relatively greater mass of the V will tend to increase the binding energy of a V dinucleon relative to that of a deuteron. Having postulated the

existence of these particles, one must envisage the following possible mesonic and nonmesonic decay schemes:

$$\text{negative } V \text{ deuteron} \equiv [V^- + n] \rightarrow n + n + \pi^- \quad (5)$$

$$V \text{ diproton} \equiv [V^+ + p] \rightarrow \begin{cases} p + p & (6) \\ p + n + \pi^+ & (7) \\ d + \pi^+ & (7') \\ p + p + \pi^0 & (8) \end{cases}$$

$$V \text{ dineutron} \rightarrow \begin{cases} \equiv [V^0 + n] \rightarrow \begin{cases} n + n & (9) \\ n + p + \pi^- & (10) \\ d + \pi^- & (10') \\ n + n + \pi^0 & (11) \end{cases} \\ \equiv [V^- + p] \rightarrow \begin{cases} n + n & (12) \\ n + p + \pi^- & (13) \\ d + \pi^- & (13') \\ n + n + \pi^0 & (14) \end{cases} \end{cases}$$

The mean lives of these particles will again be $\approx 10^{-10}$ sec [assuming comparable mean lives (for the mesonic decay) of the free V^0, the free V^+ and the free V^-] while the branching ratios for the mesonic and nonmesonic decays will, as before, be of the order of unity.[1]

It is very interesting to note that the mesonic decay of a V dineutron according to scheme (13′) will appear in an emulsion or a cloud chamber as the two-body decay into a deuteron and a π^- meson of a neutral particle with mass: $[\{2350 \pm 80\} + \{1836\} - [V^- + p]$ binding energy$]m_e \approx \{4180 \pm 80\} m_e$.[4] A decay of just this type has recently been reported by Lal, Pal, and Peters[5] who estimate the mass of the neutral particle as $\{4120 \pm 20\} m_e$.

It should also be mentioned, as pointed out to us by Bolsterli, that neutral particle→visible $\{p + \pi^-\}$ decays, with a Q (calculated on a two-body basis) considerably different from (e.g., very much larger than), 35–40 Mev,[6] might actually be V-dineutron decays according to schemes (13) or (10). On such an assumption, these anomalous Q values would form a distribution with an upper limit given by the Q of the V^- decay (≈ 125 Mev).

We wish to thank Professor R. D. Sard for a helpful discussion.

* Assisted by the joint program of the U. S. Office of Naval Research and the U. S. Atomic Energy Commission.

[1] W. Cheston and H. Primakoff, Phys. Rev. **92**, 1537 (1953).

[2] According to a notation now coming into use: V^0, V^+, $V^- = \Lambda^0$, Λ^+, Λ^- = neutral, positive, negative hyperon.

[3] We take 38 Mev for the Q value of $V^0 \rightarrow p + \pi^-$, and suppose that $M(V^+) \cong M(V^-)$, Q values for the decay: $V^\pm \rightarrow$ neutron $+ \pi^\pm$ may be obtained from Lal, Pal, and Peters, Phys. Rev. **92**, 438 (1953). ($Q = 135 \pm 35$ Mev); King, Seeman, and Shapiro, Phys. Rev. **92**, 838 (1953). ($Q = 103 \pm 20$ Mev); M. Ceccarelli and M. Merlin, Nuovo cimento **10**, 1207 (1953) ($Q = 131 \pm 24$ Mev). We also suppose that the V^+ possesses the alternative decay scheme: $V^+ \rightarrow$ proton $+ \pi^0$ [with a Q, according to Bonetti, Setti, Panetti, and Tomasini, Nuovo cimento **10**, 1736 (1953), of 115.3 Mev].

[4] We take the $[V^- + p]$ binding energy as ≈ 3 Mev; assumption of the scheme (10′) would predict a mass of $\{4015 \pm 10\} m_e$ for the neutral particle, provided that the $[V^0 + n]$ binding energy is also taken as ≈ 3 Mev. We also suppose that the rates of the energetically possible processes: $[V^- + p] \rightarrow V^0 + n$ and $[V^+ + n] \rightarrow V^0 + p$ are not appreciably greater than $\approx 10^{16}$ sec^{-1}.

[5] Lal, Pal, and Peters (reference 3).

[6] Leighton, Wanlass, and Anderson [Phys. Rev. **89**, 148 (1953)] find, in decays of neutral particles into $p + \pi^-$, Q values ranging from 10 ± 3 Mev to 87 ± 15 Mev; it is likely that at least several of these anomalous Q's are not consequences of experimental error.

PHYSICAL REVIEW VOLUME 93, NUMBER 4 FEBRUARY 15, 1954

Proceedings of The American Physical Society

Minutes of the 1953 Thanksgiving Meeting Held at Chicago, November 27–28, 1953

IN 1953 the Thanksgiving meeting of the American Physical Society returned to its traditional home at the University of Chicago after two years of wandering: the dates were Friday and Saturday, November 27 and 28. The programme was of excellent quality; it is all the more surprising to have to record that both the number of contributed papers (142) and the number of registrants (516) dropped below the peaks of past years. This may have been because some of our members overlooked the announcement printed in the Rochester Bulletin in lieu of being made by summons-card, or it may have been because the deadline (September 25) came so soon after the academic year began: the Secretary has no facts to support either theory. Perhaps the November meeting has definitely yielded to the March meeting its former rank of the third largest of the year. The meeting was very efficiently administered by Mrs. Dorothy C. Johnson.

The banquet of the Society was held on the Friday evening in Hutchinson Commons, with a regrettably small attendance (170). The after-dinner speakers were S. K. Allison, D. H. Loughridge, and R. S. Mulliken.

The Council met on the Friday afternoon. It elected to Fellowship four candidates, and to Membership 285 whose names are appended.

Elected to Fellowship: W. R. Fredrickson, A. W. Friend, J. A. Sanderson, and L. Seren.

Elected to Membership: Walter Abramowitz, Rutherford H. Adkins, Victor S. Aiello, Richard Ballantine Allen, Saul Altshuler, Sa'adia Amiel, Brita Aminoff, Cecil Earl Angell, George Ludwig Appleton, Tetsuo Arase, Bernell Edwin Argyle, George Edward Austin, Milton Ash, Bjorn Astrom, Leon S. August, Glen Gordon Bach, Winslow Furber Baker, Nandor L. Balazs, William Chalmers Barr, Asim O. Barut, Robert H. Bassel, Philip Baumel, Allan Frank Beck, Leon Edward Beghian, Edgar D. Berners, Edward Joseph Bernier, William Bertozzi, Bruce Joseph Biavati, Rudolf Hermann Bieri, Charles Huffman Blakewood, Herbert Howard Bolotin, Howard Colson Borough, Gene Braught, Francis Christopher Brosnan, Arthur Austin Brown, Edward Byerly Brucker, Paul James Bryant, Joseph Ignatius Budnick, Charles Andrew Burrus, Jr., Anthony John Calio, Chieh Chien Chang, Lloyd Fremont Chase, Jr., Ivan Gabriel Chasalow, Morris Samuel Chester, Donald Ray Childs, William Gilbert Clark, Darwin Wayne Clutter, Carolus Melville Cobb, Malcolm Young Colby, Robert Vincent Coleman, Joseph Lawrence Collins, Charles Philippe Courtoy, Walter Leslie Crider, William Edwin Cummins, Robert Hanson Cunningham, John Spillers Dahler, Bascom S. Deaver, Jr., John Hans Dessauer, Peter Joseph Drevinsky, Richard Henry Duncan, Lucille Anne DuSault, Alexander J. Elwyn, Frank Durrell Enck, Karl Lembit Erdman, Robert Arthur Farrall, Fabio Maria Ferrari,

George Filipovich, Arnold R. Flammersfeld, Thomas Patrick Flood, Charles Putnam Foster, Jr., Theodore Dean Foster, Allan Ray Fowler, Richard Morris Friedman, Tadao A. Fujii, Ruth Carter Gallman, Augusto Gamba, Brother Gerard Gardner, Raffaele Raul Gatto, George Leonard Gerstein, George Gioumousis, Paul A. Goldhammer, Hideo Goto, Harold Grad, Thomas James Gray, John Morgan Greene, James Joseph Griffin, Joseph J. Gruber, Stanley Alan Hagstrom, Howard S. Halpern, Marion Joan Hamann, Frank Bower Harris, Jr., Frank Ephraim Harris, Edward Gerhardt Hatlem, Carl Hugo Hayn, Mark Aiken Heald, Arthur Herschman, Albert Joachim Herz, Shigeru Higashi, Ichiro Higashino, Richard Warren Hillendahl, Kensaku Hinotani, Heinrich Hintenberger, Stuart Alfred Hoenig, Joseph Marion Holt, Jr., Herbert Leslie Hoover, Alvin M. Hudson, Akira Imamura, Hideo Inuzuka, Peter Jack Price, Ira Jacobs, Howard Arthur Johnson, William Bruce Johnson, Emerson Jones, Malcolm Stephen Jones, Jr., Jess J. Josephs, Masaharu Kabata, William Henry Kasner, Sidney Oscar Kastner, Henry Sour Katzenstein, David Thomas Keating, Rolland O. Keeling, Jr., Thomas E. Kilpatrick, John Swinton King, Leonard Sol Kisslinger, Takashi Kitamura, James Francis Kenney, Melvin Phillip Klein, Robert H. Klein, Alfred Klemm, Richard Hubert Knipe, Shiro Koizumi, Robert Daniel Korytoski, Julius Stephen Kovacs, Willis Frederick Kraemer, Robert William Kreplin, Herald W. Kruse, Tadayoshi Kubozoe, Robert John Kurland, Kenneth Lande, George Walter Landwehr, Christoph Herbert Lang, Robert Eugene Lanou, Jr., John Edward Lauer, Thomas Harolde Leary, Jr., William Lewis Lichten, Donald Henry Liebenberg, William A. Livingston, Jr., Walter Bernard Loewenstein, Harry Lustig, David Keith Chalmers MacDonald, Kaichi Maeda, Morton Mandel, Phillip Warren Mange, Irwin Manning, Robert Samuel Marty, John William Marx, George Edward Masek, Josef H. E. Mattauch, Jack Anthony Mauro, Leonard C. Maximon, Paul Mazur, Banks Holt Mebane, Paul H. E. Meijer, George Pearson Mellor, George Merkel, Franklin Joseph Meyers, Richard Edwin Michel; William B. Mims, Mitsuo Miwa, Hironari Miyazawa, Michael Julius Moravcsik, Ira L. Morgan, Thomas Wendell Morris, David Moskowitz, Peter Hill Moulthrop, Charles Muckenfuss, Arthur H. Muir, Jr., Daniel Richard Muller, Boris Musulin, Ira Thomas Myers, Teruo Nakamura, Charles Presley Nash, Donald John Nelson, Carol Marilyn Newton, James A. Noland, Kanichi Nunogaki, Allen Nussbaum, Shoroku Ohnuma, Irwin Oppenheim, Seinosuke Ozaki, Shih I. Pai, Howard Hunt Pattee, Jr., Wilbur B. Payne, Leighton Hartwell Peebles, Jr., Frank Murray Pelton, Howard Earle Petch, Thomas Edgar Petriken, Gordon Hemenway Pettengill, Richard James Plano, Hans Siegfried Plendl, William Stephen Quigley, John Michael Radcliffe, Rolf Ragnhult, George H. Rawitscher, Jonathan F. Reichert, Robert James Reithel, Robert Henry Richard, James Alexander Rickard, John A. Rider, Rufus H. Ritchie, Ronald Marshall Rockmore, Edward Albert Rollor, Jr., Lawrence Rosenson, Arthur I. Rubin, Herbert Bruno Sachse, Kiyosi Sakuma, Nicholas Peter Samios, Sol Sandhaus, Robert Irvin Scace, Francis James Schell, Herbert Schlosser, Fred William Schmidlin, Robert James Schneeberger, Martin Schneider, Robert Louis Schoenfeld, William W. Schriever, Melvin Schwartz, Anthony Gray Scott, Luke Madeira Shuler, James Henry Simpson, Jr., Rolf M. Sinclair, Julian Michael Siomkajlo, Robert Franklin Sippel, Orville Ray Skinner, Glen A. Slack, John Casimir Slonczewski, Alexander Smakula, Carroll Eugene Smith, James Murat Smith, Max Solow, Carl Philip Spaulding, Joseph Spontak, David Stauff, Hans Andor Steinherz, James Constantine Sternberg, Mirek Jaromir Stevenson, Albert James Stone, 3rd, Wolf Deter Straub, Walter Strauss, William Chas. Herbert Stroh, III, Tokuo Suita, Chih Ree Sun, Seymour Sutkin, Donald LeRoy Swanson, Gyo Takeda, Eileen Tannenbaum, John Waldon Taylor, Sidney Teitler, Aaron Temkin, Robert Clarence Thompson, Donald H. Thurnau, James Howard Tillotson, William M. Trenholme, Emilio Joseph Troinello, Eugene Bonner Turner, Herbert Ueberall, Georges Valladas, Robert Dale Vanselow, Claudio Alberto Villi, William Baker Voss, Ludwig Waldmann, Thomas Gerald Walsh, Kenji Watanabe, Shigueo Watanabe, John F. Waymouth, Gustav Weber, Robert A. Weeks, Irving Weiman, Eugene Victor Weinstock, William Alfred Wenzel, Bette Zaye Wertz, Donald Robertson White, David Ballinger Williams, Harry Bernard Wolfe, and Frederick Lynn Yarger.

KARL K. DARROW, *Secretary*
American Physical Society
Columbia University
New York 27, New York

Errata Pertaining to Papers C6, G7, K2, K5, L3, N7, N10, Q5, R7, and SP1

B7, by R. H. Dalitz. A footnote should be added, reading "Supported in part by the joint program of the U. S. Office of Naval Research and the U. S. Atomic Energy Commission."

C6, by A. W. Schardy and Joan P. Welker. In reference 1, (1943) should read (1953). The face brackets in the "$\gamma-\gamma$ coincidences" column should be deleted. In the "Rel. intensities" column 1.00 and 0.84 ± 0.10 should read }1.00 and }0.84 ± 0.10.

K2, by H. McManus, W. T. Sharp, and H. Gellman. In Table I, 50 should read 60.

K5, by N. M. Hintz, J. M. Blair, and D. M. Van Patter. In line 20, 2×10^{-38} cm^2 should read 0.5×10^{-38} cm^2.

L3, by F. J. Lynch. In line 14, μg should read g.

N7, by P. W. Kruse and E. A. Coomes. In line 10, 10^8 volts cm^{-1}, should read 4×10^7 volts cm^{-1}.

N10, by William E. Woolf and Richard B. Belser. Mr. Woolf's name was misspelled.

Q5, by W. Y. Kato, D. J. Hughes, and J. S. Levin. In line 15, 7.75 should read 7.78. In line 16, 55×10^{-3} should read 64×10^{-3}.

R7, by S. Stein, E. Gerjuoy, and T. Holstein. In the title, momonuclear should read homonuclear.

SP1, by Lester Winsberg. In line 7, isotopes of mass 117 and 118 should read Te isotopes of mass 117 and 118. In reference 1, B8 should read B11.

PROGRAMME

FRIDAY MORNING AT 10:00

Mandel Hall

(A. W. LAWSON presiding)

Semiconductors

A1. On the Electrical Conductivity of Graphite. G. K. HORTON* AND G. E. TAUBER,† *National Research Council, Canada.*—The electrical conductivity of graphite has been calculated in the layer approximation using the Lukesh-Pauling stacking of graphite. This stacking is distinguished from the older Bernal stacking, in the layer approximation,[1] by the fact that the individual carbon atoms are no longer situated at the corners of *perfect* hexagons. The band structure is given using the Bloch (tight binding) approximation. The existence of an energy gap at the corners of the Brillouin zone is established and its magnitude calculated. Graphite has one conduction electron per atom in the $2p$ state. This is described by a wave function of the form $z(ae^{-\alpha r}+be^{-\beta r})$, where the constants a, b, α, β, have been matched against the known numerical values of the $2p$ wave functions calculated by Jucys for the $^5S_0$ (quadrivalent) state of the carbon atom. By assuming a *heuristic* lattice potential with adjustable parameters, it has been possible to make reasonable estimates of the various parameters (overlap integrals) occurring in the theory. Finally, the electrical conductivity has been calculated and compared with the experimental and the theoretical (Wallace) results based on the usual Bernal stacking. The conductivity is found to be an order of magnitude too small.

* On leave of absence from the University of Alberta.
† National Research Laboratories Postdoctorate Fellow.
[1] The three-dimensional case is also considered and it is shown that the main features of the layer approximation are preserved.

A2. Conduction Properties of *P*-Type Germanium between 25 C and 925 C. W. C. DUNLAP, JR., D. E. MCMILLAN, AND R. A. BROOKS, *General Electric Research Laboratory.*—A study has been made of three p-type single crystals of germanium between 25 C and 925 C. The samples had resistivities of 1.5, 0.2, and 0.005 ohm cm. Hall coefficient, resistivity, and mobility were determined. The theory of intrinsic conduction was applied to obtain the values of hole and electron mobilities and their variations with impurity content and temperature. The best fit was obtained with a variable parameter C (between 0.5×10^{32} and 5.0×10^{32}) in the equation $n_i^3 = CT^3\exp(-\Delta E/kT)$, where n_i is the density of intrinsic electrons and ΔE is the band gap. The room temperature hole mobilities were 2300, 1700, and 400 cm²/volt sec. and varied as T^{-n}, where n was 1.9, 1.7, and 1.5, respectively. The electron mobility was the same for all samples, and varied as T^{-2}. All the data were described satisfactorily using a band gap 0.72 ev. Between 900 and 925 C there was a sudden drop in Hall coefficient and resistivity, suggestive of incipient melting. It was concluded that a number of properties supposedly characteristic of the lattice itself are strongly affected by extremely dilute concentrations of impurities.

A3. Infrared Absorption Photoconductivity and Impurity States in Germanium.* W. KAISER AND H. Y. FAN, *Purdue University.*—Measurements of infrared absorption and photoconductivity were made on germanium containing gold and copper as impurities. Electrical data gave an acceptor activation energy of 0.21 ev for the gold-doped sample. Photoconductivity at liquid nitrogen and liquid helium temperatures showed a threshold at 6 microns in good agreement with the impurity activation energy. At 300°K the absorption coefficient beyond 7 microns agreed with values for other p-type germanium of the same hole concentration.[1] At 77°K, where the hole concentration became very small, only lattice absorption remained beyond 3 microns. Coppered-doped germanium was prepared by heating the sample with copper deposit on the surfaces at elevated temperatures, followed by quenching. The p-type sample had a hole concentration of 2×10^{16} cm⁻³ and an acceptor activation energy of 0.052 ev. Both the photoresponse and the absorption at helium temperature showed a maximum around 22 microns, corresponding to this activation energy. At 300°K the absorption beyond 7 microns was again the same as for other p-type samples of comparable hole-concentration. At low temperatures, the absorption decreased smoothly from the maximum toward shorter wavelengths without pronounced minima as observed in other p-type samples. This behavior is consistent with photoionization of acceptors.

* Work supported by the U. S. Signal Corps.
[1] Kaiser, Collins, and Fan, Phys. Rev. 91, 1380 (1953).

A4. Photoelectric Hall Effect in Germanium Single Crystals. JOHN J. OBERLY, *Sprague Electric Company.*—The potential differences produced in an illuminated semiconductor by a magnetic field were first observed by Kikoin and Noskov[1] and Groetzinger[2] in cuprous oxide, and were interpreted theoretically by Frenkel.[3] The same effect has now been investigated with germanium single crystals. The experimental arrangement is that of the ordinary Hall effect except that the current is produced photoelectrically by illumination of one surface of the sample. The illumination generates electrons and holes which diffuse into the bulk of the sample and are deviated in opposite directions by the magnetic field, causing a photoelectric Hall current or voltage. Since the electrons and holes recombine on their way through the sample, the photoelectric Hall effect decreases with increasing distance from the illuminated surface at a rate given by the bulk life time of minority carriers. The variation of the photoelectric Hall effect across the surface of the sample will be discussed as function of magnetic field (up to 26 kilogauss), light intensity (up to 12 lumens/cm²) from a tungsten filament lamp), and resistivity of the germanium sample.

[1] I. K. Kikoin and M. M. Noskov, Physik. Z. Sowjetunion 5, 586 (1934).
[2] G. Groetzinger, Physik. Z. 36, 168 (1935).
[3] J. Frenkel, Physik. Z. Sowjetunion 5, 597 (1934).

A5. Low-Temperature Recombination and Trapping in Germanium.* D. NAVON AND H. Y. FAN, *Purdue University.*—The lifetime of injected carriers was determined for P-type germanium from 300°K to 100°K. It decreases with decreasing temperature, rapidly at first, then more slowly. In some N-type samples the determination of the hole-electron recombination rate at low temperatures is complicated by the presence of traps,[1] which are found to be distributed through the sample volume. The recombination rate may be determined by an experiment in which a steady state with respect to the traps is established so that recombination will proceed as in the absence of traps. Using dc emitter current and long-pulse sweep-

ing field, the product of the minority carrier lifetime and mobility was obtained from the dependence of the steady-state collector current on the sweep voltage. The mobility was obtained by an independent measurement, in which the sample is flooded with light to saturate the traps. The variation of recombination rate with temperature for this N-type sample was similar to that of the P-type sample, whereas the excess conductivity caused by trapped carriers disappeared with *increasing* time constant as the temperature decreased.

* Work supported by a U. S. Signal Corps contract.
[1] D. Navon and H. Y. Fan, Phys. Rev. **91**, 491 (1953).

A6. Magnetic Field Dependence of Hall Coefficient in InSb.* R. K. Willardson, A. C. Beer, and A. E. Middleton, *Battelle Memorial Institute.*—The dependence of the Hall coefficient on magnetic field can be described in terms of a dimensionless parameter involving the product of the applied magnetic field and the carrier mobility in the semiconductor.[1] Since in InSb the electron mobility is approximately 20 times that in germanium, it is expected that variations in the Hall coefficient could occur even at weak magnetic fields. Changes in Hall coefficient with magnetic field were determined over the temperature range from 80° to 700°K for both N- and P-type specimens. Of especial interest are the results for the P-type specimens in which the Hall coefficients determined at fixed temperatures may vary by several orders of magnitude and even change sign. This occurs because of variations in the temperatures at which the crossover points and the maxima occur for different magnetic fields. However, significant variations in the magnitudes of the maxima are also observed. These results, as well as the magnitudes of the effects observed in the intrinsic regions, appear consistent with theoretical predictions.

* Supported by Wright-Patterson Air Force Base, Ohio.
[1] V. A. Johnson and W. J. Whitesell, Phys. Rev **89**, 941 (1953).

A7. Degeneracy in High-Purity InSb.* A. C. Beer, R. K Willardson, and A. E. Middleton, *Battelle Memorial Institute.*—The forbidden zone in pure InSb is quite narrow, approximately 0.28 ev at 77°K and decreases significantly with increasing temperature, being approximately 0.18 ev at 300°K.[1] Consequently, a Fermi level in intrinsic InSb midway between the bands would be within 4 kT of the conduction band at 300°K. Furthermore, in intrinsic InSb, resulting from the large ratio of hole-to-electron effective masses indicated by unusual electron-hole mobility ratios and substantiated by thermoelectric power measurements, the Fermi level is actually raised significantly above the mid-point. Consequently, for calculations at high temperatures, the classical expressions should be replaced by Fermi-Dirac functions. It also follows that the relatively low effective electronic mass causes even fairly high-purity N-type specimens to be degenerate at all temperatures. For P-type specimens, however, the classical approximations appear adequate at intermediate temperatures. The use of the singular points of the Hall and thermoelectric power curves to evaluate parameters of such specimens is discussed.

* Supported by Wright-Patterson Air Force Base, Ohio.
[1] M. Tanenbaum and H. B. Briggs, Phys. Rev. **91**, 1561 (1953).

A8. Temperature Dependence of Transverse Magnetoresistance Effect in InSb.* T. C. Harman, R. K. Willardson, and A. C. Beer, *Battelle Memorial Institute.*—Transverse magnetoresistance effects were determined from 80°K to 700°K for both N- and P-type specimens of InSb. The magnitude of the effect for the N-type material was quite low. The P-type specimens, on the other hand, exhibited as a function of temperature magnetoresistance maxima at which unusually large values were observed. These maxima occurred at temperatures near those at which the Hall coefficients also exhibited maxima. With increasing magnetic field, these maxima shifted to higher temperatures, as was also true for the Hall coefficients. For a P-type specimen containing 1.5×10^{16} ionized acceptors per cc, a value of 1.3 for $\Delta\rho/\rho_o$ was observed at 270°K for a magnetic field of 8000 gauss. The variation of $\Delta\rho/\rho_o$ with field was linear between 3500 and 8000 gauss, with no indications of saturation. As the temperature was increased to a point where the conduction was essentially intrinsic, the magnetoresistance values for specimens of various impurity concentrations, including the N-types, approached a common value, as would be expected. For example, a value of 0.08 for $\Delta\rho/\rho_o$ was observed at 650°K and 8000 gauss.

* Supported by Wright-Patterson Air Force Base, Ohio.

A9. Optical Properties of Some Group III-Group V Compounds. H. B. Briggs, R. F. Cummings, H. J. Hrostowski, and M. Tanenbaum, *Bell Telephone Laboratories.*—Infrared spectra of the semiconducting compounds InSb, GaSb, AlSb, InAs, and GaAs have been observed. The antimonides were prepared by melting together stoichiometric amounts of the components. The arsenides were prepared by heating stoichiometric amounts of the elements above the melting point of the compound in sealed quartz tubes with continual shaking of the mixture. Grain sizes of the compounds were sufficiently large to give good transmission in the infrared. Except for the anomalous behavior reported for InSb,[1] optical activation energies have been directly determined. Refractive indexes of these compounds have been measured with a Gaertner spectrometer by the prism method as described by H. B. Briggs.[2] A modification of this technique was used for InSb. It has been suggested[3] that the relation $E\epsilon^3$=constant holds for the semiconducting elements of Group IV where ϵ is the dielectric constant and E the activation energy. This equation is obeyed reasonably well by these intermetallic compounds with the exception of InSb.

[1] M. Tanenbaum and H. B. Briggs **91**, 1561 (1953).
[2] H. B. Briggs, Phys. Rev. **77**, 287 (1950).
[3] T. S. Moss, *Photoconductivity in the Elements* (Butterworths Scientific Publications, London, 1952).

A10. Magnetoresistance in InSb and GaSb Single Crystals. M. Tanenbaum, G. L. Pearson, and W. L. Feldmann, *Bell Telephone Laboratories.*—The magnetoresistance of polycrystalline InSb has been studied by Pearson and Tanenbaum[1] and by Weiss.[2] Similar measurements have now been performed on oriented single crystals of both InSb and the analogous compound GaSb. The preparation of single crystals by zone-refining and crystal pulling will be described. Crystals of n- and p-type InSb and p-type GaSb were studied. With current flowing along either the 100- or 110-crystal direction, the magnetoresistance was measured as a function of magnetic field strength, field orientation, and as a function of temperature from 78°K to 300°K. The variation of magnetoresistance with magnetic field orientation shows the same simple behavior in the single crystals of InSb and GaSb as was previously reported for polycrystalline InSb. These results are in agreement with the theory of the magnetoresistance effect based on the assumption of spherical energy surfaces. In GaSb the hole mobility at 300°K is 1000 cm^2/volt sec for magnetoresistance and 700 cm^2/volt sec from Hall effect, and both mobilities show the same temperature dependence. In InSb the relationship is more complex because of the reversal in sign of the Hall constant at about 200°K.

[1] G. L. Pearson M. Tanenbaum, Phys. Rev. **90**, 153 (1953).
[2] H. Weiss, Z. Naturforsch. **8a**, 463 (1953).

A11. Some Analogies between Lattice Defects and Current Carriers in Semiconductors. J. Rothstein, *Signal Corps Engineering Laboratories.*—Except for differences in statistics, Frenkel defects are analogous to hole-electron pairs, Schottky

defects to extrinsic carriers. Defect analogies exist for impurity carriers, trapping, injection, impurity cancellation, and perhaps breakdown. Near any insterstitial atoms or near large substitutional impurities, lattice strain reduces Frenkel activation energy and tends to trap vacancies, thus donating interstitials or accepting vacancies. Small impurities are vacancy donors or interstitial acceptors. Impurities should thus enhance diffusion as they do conductivity, large and small impurity effects should cancel (like $n-p$ cancellation), intense local stress should generate defects like carrier injection in high fields (compressive: interstitial free, vacancy trapped; tensile: vacancy free, interstitial trapped), photoinjection of pairs is analogous to bombardment defects, decay of injected conductivity to relaxation processes, stress induced migration to electrical conductivity, orientation of adjacent impurities of different size in stress fields to dipole orientation, and perhaps dielectric breakdown to fracture and Zener current to slip. The analogies are of particular interest for semiconductors, where vacancies are acceptors and interstitials donors, and defects and carriers are linked through deformation potentials and the phonon field.

A12. Capacity Measurements on Point Contact Germanium Diodes. MAYNARD DAWSON AND GEORGE FINN, *Sylvania Electric Products, Inc.*—Measurements of capacity as a function of reverse applied voltage have been carried out on high-peak inverse voltage germanium point contact rectifiers. Description of the measuring apparatus and techniques is given. The capacity measured was about 0.4$\mu\mu$f at 5 volts applied reverse bias, decreased to a value of the order of 0.01 $\mu\mu$f at values of between 20 volts and 30 volts reverse bias, and remained constant within experimental error over the remaining range of measurements. A model of the reverse barrier of point contact diodes is proposed, and the dependence of the capacity of the barrier upon applied reverse voltage which is calculated from this model is compared with the experimental results.

A13. A New Galvanomagnetic Effect. I. Theory. COLMAN GOLDBERG, *Westinghouse Research Laboratories.*—Using the following equation[1] for the electrical field in a cubic crystal carrying an electric current i in the presence of a magnetic field H,

$$E=\rho_0[i+ai\times H+biH^2+cH(i\cdot H)+dMi],$$

we can deduce that for the experimental conditions $i_y=i_z=H_x=0$ the electric field in the y direction is $\rho_0 c i_z H_x H_y$. Thus the coefficient c can be evaluated experimentally and can be used to check values for this coefficient obtained from magnetoresistance experiments.[1] Theoretical evaluation of c using certain simplifying assumptions[2] shows that c and, hence, measurements of this new effect can be used to calculate the carrier mobility which should be equal to the mobility calculated from Hall measurements.

[1] G. L. Pearson and H. Suhl, Phys. Rev. **83**, 768 (1951).
[2] F. Seitz, Phys. Rev. **79**, 372 (1950).

A14. A New Galvanomagnetic Effect. II. Experiments with Germanium. R. E. DAVIS AND COLMAN GOLDBERG, *Westinghouse Research Laboratories.*—Working with single crystals of germanium we have found that for $i_y=i_z=H_z=0$ the voltage in the y direction can be represented by

$$V_y=Gi_zH^2\sin 2\psi,$$

where ψ is the angle between H and the x axis. This is in agreement with the theory presented in the preceding paper. Care must be taken to eliminate a voltage caused by the Hall effect. This Hall voltage appears if the magnetic field does not lie precisely in the xy plane and, hence, $H_z\neq 0$. The coefficient c and the mobility μ are calculated from the coefficient G of the above equation.

FRIDAY MORNING AT 10:00

Kent 106

(J. A. SIMPSON presiding)

Cosmic Rays; Particles Other Than Pi-Mesons

B1. Cosmic-Ray Ionization Bursts in an Eight-Inch Sphere at Sea Level. H. CARMICHAEL AND J. F. STELJES, *A.E.C.L. Chalk River Laboratory.*—The complete size-frequency distribution curve of ionization bursts in an 8-inch diameter spherical steel ion-chamber, with a 1/16-in. thick wall containing argon at 50 atmos pressure, has been carefully measured in 4500 hours of observation at sea level. The sizes of the bursts range from 4×10^4 to nearly 10^8 ion-pairs and the corresponding frequencies from 2×10^4 to 2×10^{-4} per hour. Plotted in the conventional double logarithmic manner the size-frequency distribution appears to involve three clearly separable components. One component corresponds closely to the bursts expected from the known number of single μ mesons and single electrons that intersect the ion-chamber, including the Landau-Symon fluctuation of size: another corresponds to the bursts expected from the extensive air showers as measured by counters. The third component, comprising bursts of intermediate size, evidently results mainly from the nucleon component of the cosmic radiation and an attempt is being made to measure separately the contributions from the known nucleon events; stars, single protons and heavier particles, penetrating showers, etc.

B2. The Influence of Lead Shielding on Ionization Bursts at Sea Level. J. F. STELJES AND H. CARMICHAEL, *A.E.C.L. Chalk River Laboratory.*—Bursts in the ion-chamber described in the preceding paper have been measured with close fitting lead hemispheres of various thicknesses between 0.3 cm and 17 cm above the ion-chamber. Bursts of size between 4×10^4 and 10^5 ion-pairs diminish in number in the first centimeter of lead by slightly more than 20 percent and thereafter with increasing thickness diminish in number only a further 20 percent. This behavior is consistent with the rapid replacement of the single electrons by cascade showers which cause bursts of larger size, the single mesons being much more slowly absorbed by the lead. In the region of intermediate burst sizes the transition curve has a sharp maximum, the size and shape of which changes progressively with burst size. The largest bursts, in the 5×10^5 to 10^8 ion-pair range of size, increase in number slowly at first and then rapidly to 100 times their number in the unshielded ion-chamber and thereafter this rate appears to be maintained with increasing thickness of lead. Lead placed underneath the unshielded ion-chamber has practically no effect on the bursts.

B3. Cross Section for Trident Production by Electrons of the Cosmic Radiation. W. W. WADA AND D. T. KING, *Naval Research Laboratory.*—Among ~200 tridents—direct production of electron pairs by charged particles of great energy—we have been able to determine in 67 cases the energy of the incident particle. Fourteen of these have primary energy between 10^3–10^4 Mev and originate on one arm of an electron pair starting in the emulsion. In the same volume the total length of electron track arising from pair creation is found to be 1340±350 cm. The cross section for trident production by electrons of mean energy 1 Bev is thus $(1.3\pm0.5)\times10^{-25}$ cm^2. This result is in agreement with the theoretical prediction of Racah[1] but is smaller than that of Bhabha,[2] in contrast to a recently reported[3] determination at higher energies.

[1] G. Racah, Nuovo cimento 14, 93 (1937).
[2] H. J. Bhabha, Proc. Roy. Soc. (London) **A152**, 559 (1935).
[3] J. E. Naugle and P. S. Freier, Bull. Am. Phys. Soc. **28**, No. 5 (1953).

B4. Charged Particles Intermediate in Mass Between Protons and Deuterons. M. M. SHAPIRO, D. T. KING, AND N. SEEMAN, *Naval Research Laboratory.*—Two examples of singly charged particles with masses 2560±500 m_e and 2980±850 m_e, respectively, are described. The phenomenological aspects and methods of measurement are different for the two "hyperons." The first is a track 18.6 mm long, with grain density 2.57 times minimum, which originates in a "fundamental" collision in a G.5 emulsion. The second example presents a track 3.7 mm long, characteristic of a particle arrested by ionization. From its end arises the thin track of an apparent decay particle, of mass 330±90 m_e. The decay scheme $H^{\pm}\rightarrow V_1^0+\pi^{\pm}+(101_{-11}^{+99})$ Mev is consistent with our observations and yields a computed mass of 2650 m_e. The V_1^0, rather than a secondary neutron, is postulated since a V_1^0 is known to be emitted as a secondary of a charged hyperon.[1] If our observation is correctly identified with the "V-particle cascade," then it follows that the light charged secondary in the latter process is probably a pion.

[1] Anderson, Cowan, Leighton, and Van Lint, Bull. Am. Phys. Soc. **28**, No. 5, (1953).

B5. $K^{\pm}$ Mesons from "Fundamental" Nuclear Collisions. D. T. KING, N. SEEMAN, AND M. M. SHAPIRO, *Naval Research Laboratory.*—A series of measurements on 67 tracks associated with nuclear interactions in photographic emulsions has enabled us to distinguish a group of three particles of mass 1115±90 m_e, and another particle of 895±240 m_e. Mass discrimination was enhanced in this study by selecting tracks of adequate length for multiple scattering determination, and having grain densities between 1.3 and 3.0 times the minimum. These grain densities lie well above the insensitive region close to the minimum and below that where serious clumping occurs. The same criteria were applied to the calibration tracks of protons and pions. Of the 67 tracks, 23 were due to the products of "fundamental" collisions as inferred from the absence of evaporation phenomena. Altogether, 4 mesons heavier than the pion, and one hyperon,[1] were observed among these 23, the rest being protons and pions. The remaining 44 tracks, found in the more usual types of stars, were all due to protons and pions.

[1] See preceding abstract by Shapiro, King, and Seeman.

B6. V_0^1 Particle as a High Angular State of Meson-Nucleon System. B. P. NIGAM, *University of Rochester.*—Following Levy, the Salpeter-Bethe equation for the π-nucleon system ($I=3/2$) is reduced to a three-dimensional equation in the adiabatic approximation. This agrees with the equation obtained by Arnowitt and Deser[1] from the relativistic π-nucleon equation[2] derived from Schwinger's Green function method. Their investigation shows the existence of a virtual state of π nucleon at $Q=40$ Mev and angular momentum $L=5$, with a lifetime $\tau=2\times10^{-10}$ sec. In the Tamm-Dancoff formalism, which corresponds to dropping the negative frequency part of the wave function in S-B equation, under similar approximation, a lifetime $\tau=2\times10^{-11}$ sec is obtained for $Q=35$ Mev and $\tau=2\times10^{-10}$ sec for $Q=25$ Mev. The discrepancy in the results arising from the neglect of the negative component seems rather large and the analysis of the problem in the new Tamm-Dancoff formalism proposed by Dyson[3] is in progress.

[1] R. Arnowitt and S. Deser, Phys. Rev. **91**, 459, JA4 (1953).
[2] S. Deser and P. Martin, Phys. Rev. **90**, 1075 (1953).
[3] F. J. Dyson, Phys. Rev. **90**, 994 (1953).

B7. Angular Correlations in τ-Meson Decay. R. H. DALITZ,* *Cornell University* (introduced by H. A. Bethe).—A study of the distribution of 3π-decay configurations in τ-meson decay may lead to some information on the τ-meson spin (j) and parity (w), since the angular correlation between the outgoing π mesons will depend on (j, w). A convenient triangular representation will be described for the specification of τ-meson decay events both (a) when the signs of the π-meson charges are known and (b) when they are not, and the available data on τ-meson decay will be displayed in this representation. The distribution of decay configurations may be estimated for given (j, w) by considering only those outgoing π-meson waves of lowest allowable angular momenta and some typical cases will be compared with the data. The distributions following from some more specific τ-meson models will also be presented. Data of type (a) will clearly have a far more sensitive dependence on (j, w) and other τ-meson properties than the more common data of type (b). The possible effects of strong interactions between π-mesons on the distribution of decay configurations will be mentioned and their possible identification considered.

* On leave of absence from Department of Mathematical Physics, University of Birmingham, England.

B8. The Light Elements of the Cosmic Radiation—Experimental.* G. W. RACETTE, M. F. KAPLON, AND D. M. RITSON,† *University of Rochester.*—A stack of 27–250μ Ilford emulsions on glass was flown with vertical orientation for 8 hours at White Sands, N. M. ($\lambda=41°$) at a mean depth of 20 g; the 27 plates consisted of 9 triads of G-5, C-2, and D-1 emulsions. The G-5 emulsions were scanned for all tracks with $I>6I$ min and with projected length $>725\mu$. All tracks obtained were traced as far as possible through the stack, the variation of I with range being used to differentiate tracks with $Z\geq3$ from nonrelativistic α particles, slow protons, and deuterons. Charge determination was made by gap density and grain count in the insensitive emulsions. In a survey of 15 cm^2 of emulsion we have found 21 particles with $3\leq Z\leq5$ (L nuclei), 26 with $6\leq Z\leq10$ (M nuclei), and 8 with $Z>10$ (H nuclei). The primary flux values obtained for M and H nuclei are in accord with values previously reported.[1]

* This research was supported in part by the U. S. Air Force.
† Now at Massachusetts Institute of Technology, Cambridge, Massachusetts.
[1] Kaplon, Peters, Reynolds, and Ritson, Phys. Rev. **85**, 295 (1952).

B9. The Light Elements of the Primary Cosmic Radiation—Interpretation.* M. F. KAPLON, G. W. RACETTE, AND D. M. RITSON, *University of Rochester.*—To analyze the preceding data we have considered the diffusion equations for the three charge groups (L, M, H). Besides the depth of observation, the solutions depend upon λ_I (interaction mean free path) and P_{I-J} (probability of J-type production when an I type interacts) which are not well known for atmosphere (particularly P_{I-J}). It is necessary in our experiment to sum over all zenith angles consistent with our scanning criteria. Letting α be the calculated ratio of observable L nuclei emerging from collisions in the residual atmosphere to observable M nuclei with our scanning criteria, we find $\alpha=0.35$; 0.61 for $P_{ML}=0.23$; 0.40[1], respectively; if, for $P_{ML}=0.40$, λ_L is increased by 10

percent, $\alpha=0.69$. Thus, the interpretation of the observed ratio $L/M=21/26=0.81$ depends on the λ_I and P_I. Though our observations differ markedly with those of Bradt and Peters[3] and tend to confirm those of the Bristol Group,[4] we believe that a primary flux value of L nuclei derived by extrapolation cannot yet be unequivocally given, though at present the evidence favors the existence of some primary flux of the light elements. $(0.10 \lesssim L_0/M_0 \lesssim 0.5)$.

* The research was supported in part by the U. S. Air Force.
[1] J. H. Noon (private communication); the value 0.40 is derived from an analysis of heavy nuclei interactions in emulsion. $P_{\alpha l}=0.23$ is used in references 2 and 3.
[3] H. Bradt and B. Peters, Phys. Rev. **80**, 943 (1950). They find $L_0/M_0 < 0.1$.
[4] Dainton *et al.*, Phil. Mag. **43**, 729 (1952). They find $L_0/M_0 \sim 1$.

B10. Search for the Production of μ-Meson Pairs by 340-Mev Bremsstrahlung.* A. WATTENBERG, B. T. FELD, A. JULIAN, A. ODIAN, AND L. S. OSBORNE, *M.I.T.*—A search is in progress for the production of $\mu^+\mu^-$ meson pairs by the 340-Mev bremsstrahlung from the M.I.T. synchrotron. Special detectors and electronics were constructed for this experiment and will be described. At the time of the submission of this abstract, it has been established that the cross section for the production of μ-meson pairs is less than 2×10^{-31} cm² per equivalent quanta. This value is based on runs with beryllium as a target with two detectors at 90° to the x-ray beam.

* This work was supported in part by the joint program of the U. S. Office of Naval Research and the U. S. Atomic Energy Commission.

B11. A Pure Negative Muon Beam. LESTER WINSBERG, *University of Chicago.*—The 102 Mev π^- beam from the Chicago synchrocyclotron contains approximately 20 percent negative muons as shown by a range curve in copper. The beam is cleansed of neutral and positive particles by means of a 45° deflecting magnet. The pions are removed by placing a graphite filter, 36.0 g/cm² thick, against the end of the magnet pole-piece facing the synchrocyclotron. The purity of the beam was tested by irradiating one kilogram of iodine against the other end of the pole-piece. A copper plate one-half inch thick was placed in front of the sample for the maximum number of muon endings to occur in the sample. The absence of 6*d* Te^{118}, which is produced in relatively high yield by pions,[1] demonstrated the purity of the beam. The presence of 9.3*h* Te^{127} from the reaction $I^{127}(\mu^-, \nu)$ and examination of track endings in photographic plates demonstrated that the beam indeed consisted of negative muons.

[1] L. Winsberg, Phys. Rev. **90**, 343(A) (1953).

FRIDAY MORNING AT 10:00

Eckhart 133

(L. M. LANGER presiding)

Beta Emitters

C1. End-Point Energy Determination of Beta Emitters.* M. FORRO, *Evanston, Illinois.*—It was found that the absorption of beta spectra in materials of high atomic number is exponential and the absorption coefficients in gold are inversely proportional to the 3/2 power of the end-point energy of the spectrum. This experimental law holds with 2 percent accuracy in the energy-interval from 0.3 Mev to 2.2 Mev; and in the intensity domain from ½ to 1/100 of the original intensity, if a detector with small opening is used. The end-point energy of beta emitters can be, therefore, determined by measuring only two points on a gold absorption curve and is expressed by the equation, $E=9\mu^{-1}+0.017$, with 2 percent accuracy from 0.17 Mev to 2.2 Mev, where E is the end-point energy in Mev, and μ the absorption coefficient in gold in cm²/g. The results obtained on 12 isotopes, and the influence of certain factors and a semi-automatic equipment for the determination of the end-point energies will be discussed.

* Research supported by Frederick Gardner Cottrell grant of Research Corporation.

C2. Positron-Capture Branching Ratios.* PAUL F. ZWEIFEL, *Knolls Atomic Power Laboratory.*—First-forbidden correction factors for K and L capture have been calculated for the five invariant interactions and linear combinations. Also, the effect of screening on first-forbidden positron spectra has been calculated, the screening corrections being essentially identical with those given by Reitz[1] for allowed spectra. Branching ratio analyses of Zn^{65}, Na^{22}, and V^{48} were made. Assuming, as predicted by the shell model, an L forbidden $\Delta J=1$, $\Delta L=2$ transition for Zn^{65}, agreement with experiment was obtained. If screening is neglected, the theoretical branching ratio is outside experimental limits. The Na^{22} spectrum has an allowed shape but can also be fitted by a first-forbidden tensor interaction[2] with $\int\beta\alpha=-2.25\int\beta\sigma\times r$. The latter yields a branching ratio close to the theoretical allowed ratio, so in view of the lack of experimental data, no choice can be made between the two possible degrees of forbiddenness. For V^{48}, the linear combinations discussed by Pursey[3] were investigated. The following interactions give both linear Kurie plots and reasonable branching ratios: Allowed; first forbidden, $\Delta J=1$, $T+Y_sS$ or $T+Y_vV$, where $1/16 \lesssim Y_s \lesssim 1/4$ or $1/6 \lesssim Y_v \lesssim 1/2$. Pursey's method for estimating nuclear matrix elements was used.

* Based on author's Ph.D. thesis to be submitted to Duke University Graduate School.
[1] J. R. Reitz, Phys. Rev. **77**, 10 (1950).
[3] D. L. Pursey, Phil. Mag. **42**, 1193 (1951).

C3. Methane Proportional Counter Method for C^{14} Age Determinations. W. H. BURKE, JR., AND W. G. MEINSCHEIN, *Magnolia Petroleum Company.*—A method has been developed for making C^{14} age determinations on samples containing 0.8 gram of carbon by conversion to methane and counting the C^{14} beta radiation in a proportional counter filled with the sample methane. The sample is burned to get the carbon in the form of CO_2. The CO_2 is purified and then converted to methane by circulating it with an excess of hydrogen over a hot ruthenium catalyst. After excess hydrogen is removed, the methane is entered into the counter at 2 atmospheres absolute pressure. The counter is operated at 3500 volts in the center of the proportional plateau which is 600 volts in length and has a slope of less than 1 percent per hundred volts. The counter is surrounded by anticoincidence cosmic counters and eight inches of iron in the manner described by Anderson, Arnold, and Libby.[1] The counting rate with a modern organic sample in the counter is eight counts per minute over background. Thus about two thirds of the beta particles from the C^{14} in the counter are being counted. There is good reason to believe that this counting efficiency can be considerably improved.

[1] Anderson, Arnold, and Libby, Rev. Sci. Instr. **22**, 225 (1951).

C4. Inner Bremsstrahlung from P^{32}. MAX GOODRICH AND WILBUR B. PAYNE, *Louisiana State University.*—The inner bremsstrahlung from P^{32} has been measured[1-3] from 3 to 240 kev and found to agree satisfactorily with theory[4] for an allowed beta spectrum. The authors have extended the measurements to 900 kev, using a NaI scintillation spectrometer. By using different beta-ray absorbers, the contribution of external bremsstrahlung to the data was found to be of the order of a few percent. Applying the crystal's known response curve to the theoretical spectrum, and normalizing at one energy, the data and calculations have been found to agree within 10 percent from 75 to 900 kev.

[1] T. B. Novey, Phys. Rev. **89**, 672 (1953).
[2] Bolgiano, Madansky and Rasetti, Phys. Rev. **89**, 679 (1953).
[3] G. A. Renard, J. Phys. et radium **14**, 361 (1953).
[4] C. S. Wang Chang and D. L. Falkoff, Phys. Rev. **76**, 365 (1949).

C5. The Disintegration of Co^{56}. R. S. CAIRD AND ALLAN C. G. MITCHELL, *Indiana University.**—The spectrum of Co^{56} (18 hr) has been investigated with the help of a magnetic lens spectrometer, coincidence lens, a 180° magnetic spectometer, and scintillation counters. The decay scheme of Deutsch and Hedgran[1] has been found to describe the main features of the decay but certain new positron groups and gamma-ray lines have been found, which make the scheme more complicated than originally supposed. Positron groups are found at 1.508 Mev (53 percent), 1.00 Mev (40 percent), 0.53 Mev (5 percent), and 0.26 Mev (2 percent). Gamma rays of 0.477, 0.935, 1.41, 0.251, 1.78, and 2.24 Mev have been found. The last three are very weak. A disintegration scheme will be presented.

* Supported by the joint program of the U. S. Office of Naval Research and the U. S. Atomic Energy Commission.
[1] M. Deutsch and A. Hedgran, Phys. Rev. **75**, 1443 (1949).

C6. Decay Scheme of Se^{75} and Ge^{75}.* A. W. SCHARDT AND JOAN P. WELKER, *Brookhaven National Laboratory.*—The energy levels of As^{75} have been investigated using Se^{75} and Ge^{75} sources, a scintillation spectrometer, and gray wedge coincidence analyzer.[1] The results are summarized in Table I.

TABLE I.

Transition energy (kev)[a]	Se^{75} data $\gamma-\gamma$ coincidences	Se^{75} data Rel. intensities	Ge^{75} data $\gamma-\gamma$ coincidences	Ge^{75} data Rel. intensities
405	None	0.17±0.02		<0.02
281	124	1.00		
269	138		None	1.00
203	67, 138(?)	~0.021	67	~0.11
138	67, 269	0.84±0.10		
124	281			
98		~0.036		
76		<0.002		
67	138, 203	~0.012	203	observed

[a] Taken from Jensen, Laslett, Martin, Hughes, and Pratt, Phys. Rev. **90**, 557 (1953).

In addition, the 269-kev line from Ge^{75} is in coincidence with an 11.2±1.0 percent beta branch, the end-point of which is ~250 kev below that of the main beta group. It may be concluded that the 405-, 269-, and 203-kev lines are transitions to the ground state of As^{75}.

* Work performed under the auspices of the U. S. Atomic Energy Commission.
[1] Chase, Bernstein, and Schardt, Phys. Rev. **90**, 353 (1943).

C7. The Gamma Spectra of Cd^{117} and In^{117}. J. M. LEBLANC, J. M. CORK,* AND S. B. BURSON, *Argonne National Laboratory.*—The gamma spectra of Cd^{117} and In^{117} have been studied with 180° photographic spectrometers and with a 10-channel coincidence scintillation spectrometer. Sources were obtained by irradiating enriched Cd^{116} in the Argonne heavy water reactor. Internal conversion electrons associated with 0.160-, 0.267-, 0.281-, and 0.312-Mev gamma rays were observed. In addition to these, transitions of energy 0.43, 0.55, 0.72, 0.84, 1.27, 1.55, and 2.00 Mev were detected with the scintillation spectrometer. The decay of each peak has been followed. Chemical separations of the In from the Cd were made and the spectra of each fraction studied with the scintillation spectrometer. Then 0.160-, 0.312-, 0.55-, and 0.72-Mev gamma rays are associated with the In fraction, and all decay with a 2.3-hour half-life. The remaining gamma rays are in the Cd fraction. The 0.312-Mev gamma ray is the most strongly converted, and, furthermore, is not in coincidence with beta-rays. It is interpreted as an isomeric transition in In^{117}. Results of beta-gamma and gamma-gamma coincidence measurements will be discussed.

* University of Michigan.

C8. Disintegration of the 10-Year Ba^{133}. R. W. HAYWARD, D. D. HOPPES, AND H. ERNST, *National Bureau of Standards.*—The radiations from the 10-year K-capturing Ba^{133} activity have been investigated using scintillation pulse height and coincidence counting techniques. A low specific activity source of $Ba(NO_3)_2$ was used, the material having been irradiated in the Oak Ridge pile and subsequently aged for eighteen months. Four gamma rays were observed with the following energies and intensities per disintegration: 57 kev (0.01), 82 kev (0.22), 300 kev (0.31), and 357 kev (0.69), where the probable errors in the energy are approximately one percent. Coincidences were observed between the 357- and 82-, 300- and 82-, 300- and 57-, and 82- and 57-kev gamma rays, but none were observed between the 300- and 357- or the 357- and 57-kev gamma rays. From the observed intensities and the assumed disintegration scheme, the conversion coefficient of the 82-kev transition was found to be $\alpha=3.5$ which is consistent with a magnetic dipole. A level scheme in Cs^{133} consistent with the experimental evidence is as follows: ground level, *g* 7/2; 82-kev level, *d* 5/2; 382-kev level, *d* 3/2; and 439-kev level, *s* 1/2. The *K*-capture branching is such that 75 percent of the transitions go to the 439-kev level and 25 percent to the 382-kev level.

C9. Transmission of 0–50 Kilovolt Electrons by Thin Films With Applications to Beta Spectra.* R. O. LANE AND D. J. ZAFFARANO, *Iowa State College.*—Electron transmission curves have been obtained for aluminum-coated plastic films of 24–630$\mu g/cm^2$ surface density by the use of an electron accelerating tube and a Faraday collector. Good agreement was found with the range-energy data of Schonland[1] whose thinnest film was ~250$\mu g/cm^2$ aluminum. The comparison between the measured ranges and those predicted by energy-loss theory and by the extrapolation of empirical relations will be discussed. A vacuum-distilled $Pm^{147}Cl_3$ source of ~0.2 $\mu g/cm^2$ on a 6$\mu g/cm^2$ collodion backing was examined in a thin lens beta-ray spectrometer employing a G-M counter having one of the above films (320$\mu g/cm^2$) as a side window. Assuming that the true Fermi plot for Pm^{147} is linear, application of the measured window transmission curve to these data gave an apparent overcorrection by a maximum of 4 percent at 14 kev. This is probably caused by the unavoidable slight difference in the solid angle subtended by the Faraday collector and the G-M tube.

* This work was performed in the Ames Laboratory of the U. S. Atomic Energy Commission.
[1] B. F. J. Schonland, Proc. Roy. Soc. (London) **A108**, 187 (1925).

Invited Papers

C10. The Influence of Extra-Nuclear Fields on the Angular Correlation of Nuclear Radiation. R. M. STEFFEN, *Purdue University.* (30 min.)

C11. The Influence of the Electric Quadrupole Interaction on Angular Correlation. T. B. NOVEY, *Argonne National Laboratory.* (15 min.)

FRIDAY MORNING AT 10:00

Oriental Institute

(R. ROLLEFSON presiding)

Invited Papers

D1. Interactions of Fast Neutrons with Heavy Nuclei. H. H. BARSCHALL, *University of Wisconsin.* (30 min.)

D2 and D3. Capture of Polarized Neutrons by Polarized Mn-55 and Sm-149 Nuclei: (a) Production of the Nuclear Polarization, (b) Observation of Effects Due to Nuclear Polarization. L. D. ROBERTS AND SEYMOUR BERNSTEIN, *Oak Ridge National Laboratory.* (40 min, to be divided between the two.)

FRIDAY AFTERNOON AT 2:00

Mandel Hall

(R. W. THOMPSON presiding)

Invited Paper

F1. Pion-Hydrogen Scattering. ENRICO FERMI, *University of Chicago.* (45 min.)

Pi-Mesons

F2. Internal Conversion of Mesic γ Rays.* C. P. SARGENT, M. C. RINEHART, R. C. CORNELIUS, L. M. LEDERMAN, AND K. ROGERS, *Columbia University.*—The Nevis 17-in. diffusion cloud chamber has been employed to observe negative pions stopping in hydrogen gas. Thirty events were recorded in which electron pairs were associated with stopped pions. 3800 stopped pions were counted. Momentum analysis in the 7800-gauss magnetic field showed that 19 of the events correspond to the reaction $\pi^-+P\rightarrow\pi^0+N$, $\pi^0\rightarrow e^++e^-+\gamma$, and 11 of the events correspond to $\pi^-+P\rightarrow N+e^++e^-$. These lead to conversion coefficients of 0.0055 for the π^0 decay and 0.0057 for the radiative reaction. This assumes a branching ratio of 0.90 for the mesic to radiative absorption rates. The angular correlation and energy distribution of the π^0 pairs agree well with theory.[1] The same pictures are being used to measure the momentum distribution of electrons arising from the decay of negative μ mesons.

* This work was performed under the joint program of the U. S. Office of Naval Research and the U. S. Atomic Energy Commission.
[1] Dalitz, Proc. Phys. Soc. (London), **A64**, 667 (1950).

F3. Mass Difference of Neutral and Negative π Mesons.* W. CHINOWSKY, A. SACHS, AND J. STEINBERGER, *Columbia University.*—A measurement has been performed on the angular correlation of the γ-ray pair from the decay of π^0 mesons produced by the interaction of π^- mesons stopped in liquid hydrogen. The deviation of the correlation from 180° is a measure of the π^0 velocity and therefore can be used to determine the $\pi^--\pi^0$ mass difference. Analysis of our results yields for the π^0 velocity $v/c=0.200\pm0.009$ and $m_{\pi^-}-m_{\pi^0}=8.8\pm0.6\ m_e$, in agreement with the earlier result of Panofsky,[1] $10.6\pm2\ m_e$.

* This work was performed under the joint program of the U. S. Office of Naval Research and U. S. Atomic Energy Commission.
[1] Panofsky, Aamodt, and Hadley, Phys. Rev. **81**, 565 (1951).

F4. The Energy Spectrum of Negative Pions Produced in Be by 2.3-Bev Protons.* S. J. LINDENBAUM AND LUKE C. L. YUAN, *Brookhaven National Laboratory.*—Preliminary results for the energy spectrum of negative pions emitted at 32° (laboratory angle) from a 2×2×6-inch beryllium target bombarded by 2.3-Bev protons have been obtained. The experimental arrangement was similar to that previously described.[1] A 3-inch collimator looked directly at the beryllium target (in a straight section outside the magnet quadrant) at an angle of 32° from the incident beam direction. A double coincidence counter telescope defined and minotored the incident beam. An analyzing magnet followed by a third counter, displaced by 30°, in triple coincidence measured the relative fraction of negative particles of a particular momentum range. By varying the magnet current, the relative momentum spectrum of the negative particles issuing from the target was determined. The percentage of pions at each momentum was determined by range curve analysis of the beam as previously described.[1] The relative momentum spectrum deduced for negative pions in the laboratory system at 32° will be shown and discussed. The momentum resolution was approximately constant and about 10 percent total width for all points.

* This research was performed under the auspices of the U. S. Atomic Energy Commission.
[1] Luke C. L. Yuan and S. J. Lindenbaum, Phys. Rev. (to be published).

F5. Total Interaction Cross Section of Hydrogen for Positive and Negative 200–700 Mev Pions.* LUKE C. L. YUAN AND S. J. LINDENBAUM, *Brookhaven National Laboratory.*—Measurements of the total interaction cross section of hydrogen for positive and negative pions of several energies have been made. A direct meson beam from the Brookhaven Cosmotron was incident upon a fast triple coincident scintillation counter telescope containing an analyzing magnet arranged to select either negative or positive particles of the required momentum. A large liquid scintillation counter was placed behind the third counter in quadruple coincidence with the monitor telescope. Good geometry attenuation measurements were made for both polyethylene and carbon absorbers placed between the third and fourth counters. Some of the total interaction cross sections of hydrogen deduced from the difference are sum-

TABLE I.

Mean energy	$\sigma\pi^+$ in mb	$\sigma\pi^-$ in mb
265 Mev		56±16
340 Mev	48±9	21±11
450 Mev	28±6	25± 3

marized in Table I. These results demonstrate that both the positive and negative pion cross sections drop rapidly from the values obtained by Anderson, Fermi *et al.* and others in the region of 135 to 200 Mev, thus enhancing the possibility of a resonance or near resonance interaction.

* This research was performed under the auspices of the U. S. Atomic Energy Commission.

F6. Total Interaction Cross Section of Negative Pions at Kinetic Energies of 1.0 and 1.45 Bev.* R. L. COOL, L. MADANSKY, AND O. PICCIONI, *Brookhaven National Laboratory.*—The mesons were produced by the 2.3-Bev proton beam of the Cosmotron and emerged after being deflected by the Cosmotron magnet. Attenuation differences CH_2-C and D_2O-H_2O have been measured in "good geometry" with counter telescope and external analyzing magnet. The results are: $\sigma(\pi^-, P) = 49\pm4$ mb at 1.0 Bev; $=34\pm3.5$ at 1.45 Bev and $\sigma(\pi^-, D_2O) - \sigma(\pi^-, H_2O) = 21\pm3$ at 1.0 Bev; $=29\pm3$ at 1.45 Bev. It appears reasonable to assume that at these energies ($\lambda\sim2\times10^{-14}$ cm) the total cross section of deuterium is close to the sum of $\sigma(\pi^-, P)$ and $\sigma(\pi^-, N)$, at least when these two are not larger than $1/2\pi(\hbar/\mu c)^2$. Thus the difference $\sigma(\pi^-, D_2O) - \sigma(\pi^-, H_2O)$ gives $\sigma(\pi^-, N)$. Then, by the currently accepted principle of charge symmetry, $\sigma(\pi^-, N) = \sigma(\pi^+, P)$. Results thus indicate $\sigma(\pi^-, P)$ twice as large as $\sigma(\pi^+, P)$ at 1 Bev which fact has to be contrasted with the low-energy situation where $\sigma(\pi^-, P)$ is as little as about 1/3 of $\sigma(\pi^+, P)$. Comparing our data with those of Lindenbaum and Yuan $\sigma(\pi^-, P) = 25\pm3$ at 0.45 Bev, $\sigma(\pi^+, P) = 48\pm9$ at 0.34 Bev, it appears that $\sigma(\pi^-, P)$ has a second maximum in the 1-Bev region, while $\sigma(\pi^+, P)$ has a minimum in the same region. The data of Shapiro, Leavitt, Chen $\sigma(\pi^-, P) = 47\pm5$ at 0.84 Bev, $\sigma(\pi^-, P) = 27\pm5$ at 0.47 Bev add strength to the conclusion about the high-energy maximum of $\sigma(\pi^-, P)$.

* Under contract with the U. S. Atomic Energy Commission.

F7. Signs of the Phase Shifts in Pion-Proton Scattering.* JAY OREAR, *University of Chicago.*—Ilford G.5 plates were exposed to the 122-Mev external π^+ beam of the Chicago cyclotron. Scatterings with hydrogen in the emulsion were located by area scanning for the recoil protons.[1] Care was taken to observe all single protons down to 10μ in length. This corresponds to a scattering of 12° in the baricentric system. A scanning efficiency greater than 80 percent for these small angle scatterings was established by duplicate scanning. Depending on the signs of the phase shifts, Coulomb interference should give either a large decrease or increase in $d\sigma/d\omega$ in the region of 12° to 19°. Assuming the phase shifts recently determined,[2] positive sign for α_{33} predicts one event while negative sign predicts four events in this region. Of 93 scatterings obtained so far, only one was in this region. These results give 5 to 1 odds on a destructive interference or attractive $P_{\frac{3}{2}}$ force. Scanning will continue until the odds become convincing. Fortunately this is a case where doubling the data more than doubles the odds.

* Supported by the U. S. Office of Naval Research and the U. S. Atomic Energy Commission.
[1] Jay Orear, Phys. Rev. 91, 156 (1953).
[2] Anderson, Fermi, Martin, and Nagle, Phys. Rev. 91, 155 (1953).

F8. Scattering of 65-Mev Pions in Hydrogen. D. BODANSKY, A. M. SACHS, AND J. STEINBERGER, *Columbia University.*—A measurement has been made of the angular distribution of $\pi^-+P\rightarrow\pi^-+P$ and $\pi^-+P\rightarrow\pi^0+N$, using a liquid hydrogen target and scintillation detectors. In the charge exchange scattering one γ ray was detected.

θ_{CM}	$d\sigma/d\Omega(\pi^-\rightarrow\pi^-)$, mb	θ_{CM}	$d\sigma/d\Omega(\pi^-\rightarrow\gamma)$, mb
42	0.91±0.13	50	1.09±0.14
53	0.51±0.08	97	2.13±0.23
70	0.29±0.06	150	3.24±0.37
101	0.23±0.06		
151	−0.01±0.11		

The π^0 angular distribution $d\sigma/d\Omega(\pi^-\rightarrow\pi^0) = [0.96\pm0.03 - (1.38\pm0.09)\cos\theta + (0.14\pm0.23)[(3\cos^2\theta-1)/2]](1.0\pm0.1)$. The experiment, together with previous results on π^+ scattering, offers the possibility of determining the signs of the phase shifts on the basis of the Coulomb interference. The best fit is obtained with $\delta_0^3 = -6.3^0$, $\delta_1^3 = -2.0^0$, $\delta_2^3 = +9.1^0$, $\delta_0^1 = +10.4^0$, $\delta_1^1 = +0.3^0$, $\delta_2^1 = -2.1^0$, corresponding to attractive $P_{\frac{3}{2}}$ interaction. A possible, but poorer, fit with different signs is $\delta_0^3 = +14.5^0$, $\delta_1^3 = -1.4^0$, $\delta_2^3 = -2.8^0$, $\delta_0^1 = -3.7^0$, $\delta_1^1 = -1.6^0$, and $\delta_2^1 = +6.8^0$. The latter, however, is inconsistent with a reasonable extrapolation of the phase shifts reported by the Chicago group at higher energies.

F9. A Measurement of the Fraction of $n+p\rightarrow\pi^0$ Events in which a Deuteron is Formed.* ROGER H. HILDEBRAND, *University of Chicago.*—The branching ratio between the processes $n+p\rightarrow\pi^0+d$ and $n+p\rightarrow\pi^0+n+p$ is of interest since it involves the competition between states of isotopic spin 0 and 1. A measurement of this ratio for 400-Mev neutrons has been performed by measuring the range of the charged particles in coincidence with the two π^0 decay gamma rays. The experimental arrangement was similar to that used for determining the π^0 angular distribution.[1] The conditions were such that the deuteron range was twice the proton range. The results of this measurement indicate that a deuteron is formed in 100 percent of all the π^0 production events. The standard deviation of this figure based on counting statistics is 15 percent.

* Research supported by the joint program of the U. S. Office of Naval Research and the U. S. Atomic Energy Commission.
[1] Roger H. Hildebrand, Phys. Rev. 89, 1090 (1953).

F10. Scattering of Negative Pions by Deuterium.* D. E. NAGLE, *University of Chicago.*—The scattering of 123-Mev negative pions by liquid deuterium has been studied, using scintillation counter telescopes, and 123-Mev pions from the Chicago synchrocyclotron. The differential cross sections for the scattering without charge exchange of negative pions are, in the laboratory system, $6.63\pm0.60\times10^{-27}$ cm²/sterad, $5.05\pm0.40\times10^{-27}$ cm²/sterad, and $(7.33\pm0.50)10^{-27}$ cm²/sterad at angles of 45°, 90°, and 135°. The differential cross sections for the production of photons by 123-Mev negative pions incident on deuterium are 2.39±0.3, 2.30±0.2, and 3.14±0.4 in the same units and at the same angles. A comparison with the cross sections to be expected from a model which assumes incoherent scattering from the neutron and proton in deuterium, using the data from hydrogen scattering[1] and the assumption of charge independence, shows only qualitative agreement.

* Research supported by a joint program of the U. S. Office of Naval Research and the U. S. Atomic Energy Commission.
[1] Anderson, Fermi, Martin, and Nagle, Phys. Rev. 91, 155 (1953).

F11. Photo Production of Low-Energy Charged π Mesons.* J. R. VOSS, T. R. PALFREY, AND R. O. HAXBY, *Purdue University.*—Following the method of White,[1] the Purdue 300-Mev synchrotron has been used to expose some Ilford 600-micron G-5 plates. A thin Carbon target was placed in the γ-ray beam and reaction products at 90° from the beam were captured in the emulsion. At this time 31 mesons have been identified in the energy range 0–10 Mev, $15\pi^+$, and $15\pi^-$,

and one uncertain. The corrected π^-/π^+ ratio is then 1.4 ± 0.5. A calculation of the cross section for photomeson production in this energy range is 0.4 of the value found here at 30 Mev in similar geometry with nuclear emulsions. However, the tentative absolute cross sections obtained are somewhat smaller than values found by other observers. Preliminary exposures with Cu, Sn, and Pb targets have been made with the aim of extending the low-energy measurements to the higher Z materials.

* Work supported in part by contract with U. S. Atomic Energy Commission.

[1] R. H. White, University of California Radiation Laboratory Report, 1319, (1951).

F12. Interactions of 500-Mev Negative Pions with Emulsion Nuclei.* M. CAULTON, M. BLAU, AND J. E. SMITH, *Brookhaven National Laboratory.*—Four-hundred micron Ilford G-5 emulsions have been exposed to the 500-Mev negative meson beam of the Brookhaven Cosmotron. In 600 identified meson induced stars, the nature and energy of the particles causing the outgoing tracks have been determined (grain density, scattering, range), whenever the track length and ionization made this meaningful. For about 30 percent of the light tracks this procedure was possible. On the basis of these measurements in 38 ± 3 percent of the interactions at least one meson has been observed to leave the nucleus. Most of the mesons have suffered great energy losses; however there is no observed relation between angle of emission and meson energy. The angular distribution of the emitted mesons in the laboratory system yields approximately equal backward and forward integrated scattering cross sections. An estimate of charge exchange is obtained by comparing star energies and prong distributions in events with and without emitted charged mesons. Accordingly charge exchange may have occurred in 15 to 20 percent of all interactions. Seven cases of meson production have been identified. The characteristics of the stars and the emitted mesons will be discussed.

* Research carried out under the auspices of the U. S. Atomic Energy Commission.

FRIDAY AFTERNOON AT 2:00

Kent 106

(G. E. PAKE presiding)

Magnetic Resonance, Electronic and Nuclear; Quadrupole Resonance

G1. Hyperfine Structure in the Paramagnetic Resonance of X-Rayed LiF. E. E. SCHNEIDER, *Duke University.**—Single crystals of LiF, irradiated by 180-kv x-rays, have been investigated at 9450 Mc in the sensitive microwave resonance apparatus in Newcastle. Spectrophotometric measurements showed the crystals to have a normal F band at 2480A with color center concentrations ranging from 5 to 15×10^{16} cm^{-3}. The paramagnetic resonance spectrum has a complex structure: There is an intense central peak of about 90 gauss width with a g factor larger than the free-electron value ($g/g_0=1.009$). Superimposed on this is a pattern of 19 weaker and narrower lines which are of equal intensity and are equally spaced at about 60-gauss interval. It is suggested that the broad peak is due to V centers while the 19-line pattern is ascribed to F centers and is interpreted as a resolved hyperfine structure due to interaction with Li nuclei in contrast with the unresolved hfs effect which accounts for the width of F-center resonances in other alkali halides.[1,2]

* On leave from King's College, University of Durham, Newcastle upon Tyne, England.

[1] A. H. Kahn and C. Kittel, Phys. Rev. 89, 315 (1953).
[2] Kip, Kittel, Levy, and Portis, Phys. Rev. 91, 1066 (1953).

G2. Paramagnetic Resonance Absorption of Mn^{++} in Single Crystals of $CaCO_3$.* F. KENNETH HURD, MENDEL SACHS, AND W. D. HERSHBERGER, *University of California at Los Angeles.*—A study has been made of the magnetic behavior of single crystals of $CaCO_3$ diluted with 0.06 wt percent of Mn^{++} by means of the paramagnetic resonance absorption spectrum at 9300 mc. The Mn^{++} spectrum consists of 30 well-resolved lines, approximately 3.5 gauss wide, and extending over a range of 1100 gauss. The fine structure splitting is explained in terms of an axial crystalline field, wherein the spectroscopic splitting factors $g_\parallel$ and $g_\perp$ are introduced, and the crystalline field coefficients D' and d' are introduced. The hyperfine structure is explained in terms of the interaction between electronic and nuclear magnetic moments, wherein the factors A' and B' are introduced. The values obtained for the parameters are:

$g_\parallel=2.0022$	$D'=37.5\times10^{-4}$ cm^{-1}	$A'=87.82\times10^{-4}$ cm^{-1}
$g_\perp=2.0014$	$d'=0.04\times10^{-4}$ cm^{-1}	$B'=87.74\times10^{-4}$ cm^{-1}.

* Work supported in part by the U. S. Office of Naval Research.

G3. Magnetic Resonance in Some Cr^{+3} Complexes. L. S. SINGER, *Naval Research Laboratory.*—The magnetic resonance spectra of several trichelate complexes of Cr^{+3} (the oxalate, acetylacetonate, and ethylene diamine) have been measured at a wavelength of 1.2 cm. In these compounds, the zero-field splitting of the ground-state spin quartet, which is much larger than that observed in the chrome alums, gives rise to a rather complicated fine structure. Detailed measurements of the fine structure of the tri-acetylacetonate complex have been carried out on single crystals of both the pure substance and solid solutions containing the isomorphous Al compound. A comparison of the experimental results with a crystalline field theory will be presented. The information concerning molecular structure and chemical bond type which can be inferred from this comparison will also be discussed.

G4. Effects of Imperfections and of Electron Interactions on Magnetic Resonance in Alkali Metals. D. F. HOLCOMB AND R. E. NORBERG, *University of Illinois.*—Nuclear spin lattice relaxation times (T_1) and spin phase memory times (T_2) have been measured between -65°C and 270°C for metallic Na^{23} and Li^7. Spin echo measurements in both metals yield T_2 data which extend to higher temperatures, the diffusion-induced line narrowings previously reported. Coefficients and activation energies for self-diffusion are determined. Above room temperature the T_2 data show lifetime broadening arising from an electron-induced T_1. In the vicinity of the melting points and above an additional broadening becomes observable. Upon melting the lines *broaden* by a factor of about two. We attribute this to a quadrupolar interaction with lattice imperfections. Over much of the temperature

range investigated, T_1 for both metals is nearly inversely proportional to temperature. In addition, Li^7 shows a dipolar T_1 minimum whose shape and position agree well with the self-diffusion hypothesis and the coefficients deduced from the T_2 data. In both metals there are discrepancies between $(T_1)_e$, the component of the observed T_1 which appears to be determined by the conduction electrons, and the predictions of theory. Observed effects which may arise from interactions among the electrons include: a dependence of $(T_1)_e$ on the applied magnetic field, values of $(T_1)_e$ greater than those predicted by Korringa's theory, and a small deviation of the temperature dependence of $(T_1)_e$ from $1/T$.

G5. Nuclear Quadrupole Resonance of Hg^{201}.* H. G. DEHMELT, H. G. ROBINSON, AND WALTER GORDY, *Duke University.*—Five nuclear quadrupole resonance lines have been observed in polycrystalline $HgCl_2$, one due to the mercury isotope Hg^{201} at 354 207±60 kc/sec and four due to the chloring isotopes $Cl^{35,37}$ at 22 230.3±0.8, 22 050.5±0.7, 17 519.7±0.9, and 17 378.9±1 kc/sec. From these frequencies the quadrupole coupling constants $eQq_zh^{-1}(Hg^{201}) = 720$ Mc/sec and $eQq_zh^{-1}(Cl^{35}) = 44.3$ Mc/sec are evaluated. A quadrupole coupling constant per p electron in the $6s6p$ configuration of free Hg, $eQq_zh^{-1}(Hg^{201}, p_z) = 950$ Mc/sec, is deduced from the Hg^{201} coupling in $HgCl_2$. This value can be directly compared with the coupling of the $6s6p\ ^3P_2$ HgI term, $eQq_zh^{-1} \times (Hg^{201}, p_z) = 780$ Mc/sec, which is equivalent to the value of the quadrupole parameter $B = 0.27\times10^{-3}$ cm^{-1} known from optical hfs investigations.[1] However, while a standard analysis of the hfs of the $^3P_2$ term gives $Q(Hg^{201}) = 0.5\times10^{-24}$ cm^2,[1] a discrepant value $Q(Hg^{201}) = 0.2\times10^{-24}$ cm^2 [2] is obtained from the $^1P_1$ term. Our result favors the larger value found for the $^3P_2$ term. An investigation of the Zeeman-Effect of the Hg^{201} nuclear quadrupole resonance line is in progress.

* Supported by the U. S. Office of Ordnance Research.
[1] Schuler and Schmidt, Z. Physik **89**, 239 (1936).
[2] Murakawa and Suwa, J. Phys. Soc. Japan **5**, 429 (1950).

G6. The Effect of Molecular Motion on the Intensity of Pure Quadrupole Resonances.* MYER BLOOM, H. S. GUTOWSKY, D. W. MCCALL, AND J. G. POWLES, *University of Illinois.*—The Cl^{35} pure quadrupole resonance has been observed as a function of temperature in a number of molecular solids. In some cases the absorption changes more rapidly with temperature than predicted by the Boltzmann factor and the resonance disappears at temperatures considerably below the melting point. The anomalous attenuation extends over temperature ranges of 10° to 40° in the compounds studied thus far and is accompanied by relatively small increases in line width. A theoretical analysis, which accounts for the available data, is based on a model in which there are low-frequency, thermally activated, "sudden" reorientations of molecular groups, such as CCl_3. The following explicit equation has been derived for f, the fractional decrease in the surplus population of the lower state compared to the Boltzmann value:

$$f = 1 - \frac{T_1}{\tau}\ln\left(\frac{\tau+T_1}{T_1}\right)\frac{1-(1-\frac{3}{2}\sin^2\theta)}{1-(1-\frac{3}{2}\sin^2\theta)[T_1/(\tau+T_1)]}$$

τ is the average time between jumps, which are assumed to be random; the field gradient is taken to have axial symmetry around the Cl-M bond, and θ is its reorientation angle.

* Assisted in part by the U. S. Office of Naval Research and a Grant-in-Aid from E. I. Du Pont de Nemours Company, Inc.

Invited Paper

G7. Polarization of Nuclear Spins in Metals by the Overhauser Method. C. P. SLICHTER, *University of Illinois.* (30 min.)

FRIDAY AFTERNOON AT 2:00

Eckhart 133

(N. S. GINGRICH presiding)

Apparatus of Nuclear Physics

H1. Loading of Nuclear Emulsions with Lithium Gloss Specks.* J. H. ROBERTS, J. HAUGSNES, AND D. E. WOOD, *Northwestern University.*—In order not to rely primarily upon triton-alpha discrimination to identify the point of disintegration in tracks resulting from $Li^6(n, \alpha)H^3$ in nuclear emulsions, the lithium has been incorporated into the emulsion in the form of a single layer of specks of lithium glass at the center of the emulsion. The lithium glass, containing 30 percent Li_2O, prepared by H. P. Hood of the Corning Glass Works, is ground in a ball mill into specks having diameters of the order of three microns. The specks, suspended in absolute alcohol, are sprayed on a 50-micron layer of Eastman NTA, Ilford C2 or E1 emulsion to a density of about 50 micrograms of glass/cm^2. As soon as the alcohol has dried another 50-micron layer of emulsion is added. The glass can be made in sufficiently small quantities to use lithium highly enriched in Li^6. Measurements of a few hundred tracks in plates exposed to 260-kev neutrons indicate that a resolution of ±75 kev is possible at this energy under conditions of isotropic neutron incidence. The specks are clearly visible with a microscope suitable for measuring the tracks.

* Work supported by U. S. Atomic Energy Commission contract.

H2. Kinetics of the Circulating-Fuel Nuclear Reactor. WILLIAM KRASNY ERGEN, *Oak Ridge National Laboratory.*—In nuclear reactors power oscillations are usually damped because of the influence of delayed neutrons. In a circulating fuel reactor, such as the Oak Ridge Homogeneous Reactor, a part of the delayed neutrons are given off outside the reactor and their damping influence is thus lost. However, if the reactor has a negative temperature coefficient of reactivity, the circulation of the fuel introduces some damping of power oscillations, independently of delayed neutrons. At least this is true if there is no interaction between the power oscillations on one hand and mechanical oscillations of the reactor or the flow pattern of the fuel on the other. The damping by fuel circulation can be maximized by proper choice of design parameters, but it vanishes in limiting cases. A simple discussion of the foregoing for the nonlinearized case will be presented.

H3. Scintillation Detector for the Brookhaven Fast Chopper. H. PALEVSKY, H. R. MUETHER, AND A. STOLOVY, *Brookhaven National Laboratory.**—We have been investigating the properties of a fused mixture of ZnS-Ag and B_2O_3 for a neutron

detector to be used with the Brookhaven fast chopper for energies from 10 ev to 10 kev. The detector is required to have fast response ($\sim 0.2\mu$sec) and low γ sensitivity. ZnS-Ag seems to be the best suited to these requirements. The decay of the phosphor under α bombardment has been investigated from 0.02 to 25μsec. The decay can be fitted to a power law of the form $ct^{-\alpha}$, where $\alpha = 1.36$, so that in 0.2μsec the integrated voltage signal rises to 25 percent of the signal level at 10μsec. The low gamma sensitivity is attributed to the high density of traps relative to the density of secondary electrons formed from the Compton processes.† The problem of getting maximum neutron efficiency is twofold. First, the penetration of the α particles from the $B^{10}(n, \alpha)$ reaction into the ZnS, and second, the generation and transmission of the light through the ZnS. An investigation has been made of these factors as a function of ZnS grain size, and varying proportions of ZnS and B_2O_3. The results will be presented at the meeting.

* Work carried out under contract with the U. S. Atomic Energy Commission.
† H. Kallman (private communication).

H4. A Method of Eliminating Cathode Activation Effects in the G-M Counter.* H. R. CRANE, *University of Michigan.*—Activation of the cathode by positive ions, resulting in immediate or delayed emission of thermal-energy electrons,[1,2] accounts for much of the capricious behavior in Geiger counters, especially when gases other than the "standard" ones are used. A counter and circuit have been devised in which this effect is eliminated. A grid is interposed between anode wire and cathode cylinder. While waiting for a discharge, the grid is negative with respect to the cylinder, so that electrons originating at the cylinder due to activation are prevented from reaching the anode. When a discharge occurs, the grid is made positive with respect to the cylinder, and held so until ion collection is complete. This (a) lowers the field around the anode, quenching the discharge, and (b) causes the positive ions to be collected on the cylinder and not on the grid. Thus, the grid, which is the only electrode which can emit electrons which will cause counts, is not subject to activation by positive ions. Behavior of this counter with a number of gases will be reported.

* Supported by the Michigan Memorial-Phoenix Project.
[1] H. R. Crane, Phys. Rev. **75**, 985 (1949).
[2] M. L. Wiedenbeck and H. R. Crane, Phys. Rev. **75**, 1268 (1949).

H5. An Ion Source for Doubly Charged Helium. C. E. BRADFORD, T. KIKUCHI, AND W. E. BENNETT, *Illinois Institute of Technology.*—A Zinn type ion source used on an an electrostatic generator has been modified in several ways. The probe canal was replaced by an exit aperture and focusing lenses, increasing the usable output of singly charged helium ions by a factor of seven, to thirty microamperes. The "nose" was eliminated to make the arc self-starting, and a circular filament of smaller diameter was used. It was then possible to operate the ion source at smaller gas pressures than had previously been used. With the gas flow one-fourth of that required to start an "arc," the ion source still gave ten microamperes of helium. The beam of doubly charged helium was then one-half percent of the total. This is near the theoretical maximum for 300-volt electrons. Magnetic analysis was used to separate the doubly charged helium and molecular hydrogen beams. The latter beam would affect the usability of the helium beam if it struck the target since it varied during the day as the ion source was outgassed.

Post-Deadline Papers, If Any

FRIDAY AFTERNOON AT 2:00

Oriental Institute

(CYRIL S. SMITH presiding)

Whiskers and Solid-State Physics

I1. Mercury Whiskers. G. W. SEARS, *General Electric Research Laboratory* (introduced by D. Turnbull).—It has been found that whiskers of solid mercury about 1 mm long and 0.01μ in radius can be grown on a cold glass surface by vapor condensation. The whiskers grow 5000 times faster than can be accounted for by an impingement rate of mercury atoms on the advancing end from the vapor. The new whiskers are in Brownian motion. When a whisker grows to about 1 mm long it ceases preferential growth and grows isotropically. The whisker first ceases Brownian motion and later shows cyclic appearance of interference colors. The supersaturation ratio necessary to nucleate an atomic layer of mercury on a low-index plane is 4×10^6. The whiskers appear at supersaturation ratios 10 000-fold less than this figure. The whiskers are deduced to form on crystallites of devitrified glass which present the end of a screw dislocation. The whisker can only grow along the screw axis which is transposed into the mercury structure. The faces parallel to the axis are low index and present no growth sites. The rapid growth occurs by impingement on the faces parallel to the axis followed by surface diffusion to the end.

I2. Accelerated Growth of Tin Whiskers. R. M. FISHER, L. S. DARKEN, AND K. G. CARROLL, *United States Steel Corporation.*—It is found possible to accelerate markedly the growth of the tin whiskers, first observed[1] as a spontaneous growth on tin plate. Acceleration, by a factor on one hundred or more, is achieved by application of static pressure (of the order of a ton per square inch) applied by mounting tin plate in a ring-type metallographic clamp. Edgewise cross sections are polished, and the growth of the tin whiskers from the tin layer is observed under a microscope. A sequence of photomicrographs showing the growth of the whiskers will be shown. The whiskers grow at constant rates, as high as 100A/sec, until they nearly reach their maximum length (about 2 mm).

[1] Compton, Mendizza, and Arnold, Corrosion **7**, 327 (1951).

I3. Strain Sensitivity of AuCu and $AuCu_3$ Alloys.* G. C. KUCZYNSKI, *University of Notre Dame.*—Wires of ordered and disordered AuCu and $AuCu_3$ alloys were stretched elastically, their electrical resistance measured and the strain coefficient of electrical resistance $(dR/Rd\epsilon)_{\epsilon=0}$ determined, where R is electrical resistance and ϵ strain. It has been found that: (1) The AuCu wires ordered at 390°C increased steadily their resistance with strain. $(dR/Rd\epsilon)_{\epsilon=0}$ ranged from +1.0 to +2.0. (2) The AuCu wires ordered at 350°C decreased markedly their electrical resistance. $(dR/Rd\epsilon)_{\epsilon=0}$ ranged from −20 to −100. After a certain strain was exceeded the increment of resistance was observed. (3) Similar behavior was observed in the case of $AuCu_3$ wires ordered at 370°C $(dR/Rd\epsilon)_{\epsilon=0}$ ranged from −4 to −10. (4) The fully disordered alloys exhibited small positive coefficients of strain sensitivity of the order of +1.2 for AuCu and +1.5 for $AuCu_3$ alloy.

* Supported by Baldwin-Lima-Hamilton Corporation.

I4. Internal Friction of Alloys of Gold and Nickel. C. ANG AND C. WERT, *University of Illinois.*—The internal friction behavior of some Au-Ni alloys has been determined in the temperature range 20°C to 700°C. Two peaks are seen for all alloys; one of these is the grain boundary peak at about 400°C and the other the "pair-relaxation" peak of Zener at somewhat lower temperatures. The presence or absence of the second peak depends markedly on the heat treatment prior to measurement. To observe it, one must quench the alloy from the solid solution region above the phase separation line. The height and position in temperature of the peak depends somewhat on the quench temperature in this solid solution region. The peak disappears upon isothermal annealing at temperatures areound 300°C. This disappearance is thought to be associated with the occurrence of phase separation in the quenched alloys. The data obtained by this method show that some processes are taking place upon annealing much earlier than would be deduced from measurements of changes of electrical resistance or mechanical properties. The activation energy for the relaxation process is about the same as that for diffusion in the alloys. The data obtained can thus far be given only tentative explanations.

I5. Internal Friction of Dilute Alloys of Lead. J. WEERTMAN AND E. I. SALKOVITZ, *Naval Research Laboratory.*—The internal friction of single crystals of binary alloys of lead containing 0.01 to 1 (nominal) atomic percent of Bi, Cd, and Sn was measured as a function of temperature and strain amplitude. Measurements were made from room temperature to 300°C using the Marx technique[1] and operating at 30 kc. The decrement increased with increasing temperature. At low strains the decrement was independent of the amplitude of vibration. As the strain amplitude was increased the decrement started to rise when a "critical" amplitude was reached. This critical amplitude was increased by increasing the alloying content of the material and was decreased by as much as a factor of ten by raising the temperature from room to 300°C. The critical strain amplitude at room temperature decreased from 10^{-6} to 10^{-7} as the alloying content was lowered.

[1] J. Marx, Rev. Sci. Instr. **22**, 503 (1951).

I6. Diffusion of Cadmium, Indium, and Tin in Single Crystals of Silver.* C. T. TOMIZUKA, *University of Illinois.*—In the periodic table, silver is followed by cadmium, indium, tin, and antimony in this order. Since the measurements of self-diffusion in silver[1] and of diffusion of antimony in silver,[2] a study has been continued to determine the activation energy and frequency factor for the diffusion of other neighboring elements in silver single crystals of 99.99 percent purity. Using Cd^{115}, In^{114}, and Sn^{113} as tracers, satisfactory results were obtained with a thin-wall immersion beta-counter for counting a cylindrical layer of solution. Diffusion of cadmium in silver yields $D=0.2\exp(-40\,500/RT)$ and of indium in silver gives $D=0.2(-39\,700/RT)$. These as well as the expression for tin are compared with the data of Seith and Peretti[3] and with the expression for self-diffusion and diffusion of antimony in silver.

* Supported in part by the U. S. Atomic Energy Commission.
[1] Slifkin, Lazarus, and Tomizuka, J. Appl. Phys. **23**, 1032 (1952).
[2] Sonder, Slifkin, and Lazarus, Phys. Rev. **91**, 245 (1953).
[3] W. Seith and E. Peretti, Z. Elektrochem. **42**, 570 (1936).

I7. Reflectivity of Silver in the Near Infrared.* L. G. SCHULZ, *University of Chicago.*—The reflectivity of a glass silver interface was measured in the wavelength range of 1 to 3 microns. Each of the samples used was prepared by depositing silver from the vapor on part of the hypotenuse face of a right-angled glass prism. The intensity of the light reflected internally at the glass-metal interface was compared with that which was totally reflected at the glass-air interface. The ratio of values for the s and p planes agreed with that predicted by electromagnetic theory. Using reflectivities obtained by this method together with previously determined values of the absorption coefficient, the index of refraction n was calculated. With this value of n the calculated reflectivity at an air-silver interface was found to be 0.993 as compared with 0.996 given by the free-electron theory of metals. The difference of 0.003 between experimental and calculated values, which was found also for silver-gold alloys, could be an experimental error or it might indicate an anomalous optical surface behavior. It will be shown that the well-known work of Hagen and Rubens is incorrect both experimentally and theoretically.

* Supported in part by the U. S. Air Force.

I8. The Electrical Resistivity of Pure Tellurium at the Melting Point and in the Liquid State.* A. EPSTEIN AND H. FRITZSCHE, *Purdue University.*—The electrical resistivity of doubly distilled, spectroscopically pure tellurium undergoes a discontinuous change at the melting point. Near the melting point its value in the liquid is 0.00055 ohm-cm and in the solid between 0.006 ohm-cm and 0.012 ohm-cm depending on the crystal orientations of the solidified material. In the liquid the resistivity continues to decrease with increasing temperature to a value of about 0.0004 ohm-cm at 550°C. At higher temperatures the resistivity curve flattens out, and resistivity finally increases above 625°C. The resistivity-temperature curve can be followed reproducibly by heating and cooling in the liquid state as well as in the solid, if one ascertains that the solidified material has the same orientation.

* Work supported by U. S. Army Signal Corps.

I9. The Variation of Magnetoresistivity and Resistivity of AuCu during Annealing from the Cold-Worked and Thermally-Disordered States. B. WIENER AND G. GROETZINGER, *Lewis Flight Propulsion Laboratory.*—In order to study the changes occurring in the states of AuCu during the processes of thermal disordering, of cold working, and of annealing from the disordered condition, measurements were made of the resistivity and magnetoresistivity of samples of AuCu which had been thermally disordered and were then annealed at 150°C and 265°C; of samples completely disordered by cold work and then annealed at 265°C; and of initially ordered samples when subjected to varying amounts of cold work. It was found that AuCu has a coefficient of magnetoresistivity of 1.8×10^{-13} $gauss^{-2}$ in the ordered state and of 6×10^{-14} $gauss^{-2}$ in the disordered state regardless of the method of disordering. Furthermore, the curves of magnetoresistivity against resistivity obtained for the thermally disordered samples annealed at the two different temperatures are different from each other; and both differ from the curve obtained for the samples completely disordered by cold work and then annealed. The last curve, however, cannot be distinguished from that found

for the samples subjected to varying amounts of cold work. It follows that thermally disordered samples pass through different sequences of states when annealed at different temperatures; and that, in general, samples initially disordered by cold work do not go through the same set of states when ordered by annealing as do samples disordered by quenching.

I10. Diffuse Magnetic Scattering of Neutrons: Zinc Ferrite.* B. N. BROCKHOUSE,† L. M. CORLISS, AND J. M. HASTINGS, *Brookhaven National Laboratory.*—Diffuse scattering of neutrons of wavelength 1.06A has been studied with apparatus which permits work close to the forward direction under conditions of low and flat background. Corrections for multiple scattering (in flat specimens) were made by using calculations of Chandrasekhar and of Vineyard. This procedure was tested by extensive measurements on beryllium, lead, bismuth, and thorium, in which multiple scattering is the only important diffuse scattering. For zinc ferrite, the scattering at room temperature can be extrapolated to the theoretical value in the forward direction, At larger angles, separation of magnetic and thermal diffuse scattering involves difficulties. The Debye-Waller factor and measurements of diffuse scattering as a function of the temperature, have been used in attempts to separate the two. A form factor will be presented and discussed. The diffuse scattering at liquid nitrogen temperatures shows anomalies, including some excess small angle scattering. This behavior, still under investigation, suggests short-range magnetic coupling between ions. Long-range magnetic order, as indicated by the presence of diffraction peaks, becomes noticeable only in the neighborhood of helium temperatures.

* Research carried out under the auspices of the U. S. Atomic Energy Commission.
† Guest scientist, on leave from Atomic Energy of Canada, Ltd., Chalk River, Canada.

I11. Neutron Diffraction in Vitreous Silica.* R. J. BREEN† AND A. H. WEBER, *Saint Louis University and Argonne National Laboratory.*—The theory of liquid structure determinations by x-rays[1] has been extended to neutron scattering in vitreous silica. A method of analysis[2] using total neutron scattering cross sections from transmission experiments is developed and the results are compared to those from differential scattering. The radial density distribution of atoms is obtained and results are compared with Warren's values from x-ray diffraction.[3]

* This work was supported in part by the Owens-Illinois Glass Company and the U. S. Army Office of Ordnance Research.
† Now at Mound Laboratory, Miamisburg, Ohio.
[1] N. S. Gingrich, Revs. Modern Phys. **15**, 90 (1943).
[2] Suggested by M. Hamermesh.
[3] B. E. Warren, J. Am. Ceram. Soc. **17**, 249 (1934); B. E. Warren and A. D. Loring, J. Am. Ceram. Soc. **18**, 269 (1935).

I12. The Thermal Conductivity of Sodium Chloride.* WILLIAM H. BESSEY AND HAROLD WEISBROD, *Missouri School of Mines and Metallurgy.*—An apparatus has been essentially completed for measuring the thermal conductivity of ionic crystals as a function of temperature from a little above room temperature nearly up to the melting point. It is a modification of the steady-state guard-ring type of apparatus, and consists of a heater sandwiched between two identical cylindrical samples and placed between independent large copper receivers which are kept at the same temperature. The whole arrangement is placed in a vacuum to cut down convection losses and sample corrosion. Synthetic optical windows of sodium chloride were used for the initial testing of the equipment. Preliminary results for the conductivity at 100°C are in reasonable agreement with the values given by Ballard *et al.*[1]

* Supported by a grant from the Research Corporation.
[1] Ballard, McCarthy, and Davis, Rev. Sci. Instr. **21**, 905 (1950).

FRIDAY EVENING AT 7:00

Hutchinson Commons

(ENRICO FERMI presiding)

Banquet of the American Physical Society

After-dinner speakers: S. K. ALLISON, D. H. LOUGHRIDGE, AND R. S. MULLIKEN.

SATURDAY MORNING AT 9:30

Eckhart 133

(W. H. ZINN presiding)

Reactions of Transmutation; Nuclear Energy Levels

K1. Nuclear Coulomb Excitation by Heavy Particles. DAVID L. HILL, *Los Alamos Scientific Laboratory and Vanderbilt University.*—Recent observations[1] on proton bombardment of tantalum and other materials have confirmed theoretical expectations[2] on the Coulomb excitation of low-lying rotational states of aspherical nuclei. However, the excitation of x-rays complicates the measurement of the relevant gamma rays. The advantages of using heavier particles are simply illustrated by comparing the results expected with beams of, say, 1-Mev protons, 4-Mev alpha particles, and 14-Mev nitrogen ions. The K x-ray production by projectiles of charge z, velocity v, and reduced mass m is roughly proportional to z^2v^3, while the Coulomb excitation of rotational nuclear states goes[2] as m^2v^2g, g being a function which decreases as the collision becomes more nearly adiabatic. That the z/m ratio for protons is twice its value for other projectiles more than doubles the g value pertinent to heavier projectiles. Hence, the cross section for Coulomb excitation increases by factors

of about 37 and 400 in passing, respectively, to bombardment by alpha particles and by nitrogen ions, while the relative x-ray excitation diminishes by a factor of about eight.

[1] T. Huus and Č. Zupančič, Danske Math.-fys. Medd. **28**, No. 1 (1953); C. L. McClelland and C. Goodman, Phys. Rev. **91**, 760 (1953).
[2] K. A. Ter-Martirosyan, J. Exptl. and Theoret. Phys. (U.S.S.R.) **22**, 284 (1952); A. Bohr, and B. R. Mottelson, Danske Math.-fys. Medd. **28**, No. 16 (1953).

K2. Nuclear Interactions of High-Energy Nucleons. H. McMANUS, W. T. SHARP, AND H. GELLMAN, *Chalk River Laboratories.*—Cascade nucleon yields and residual excitation energies have been calculated by a Monte Carlo method[1] with the Toronto Ferranti computer for aluminum, silver-bromine, and uranium, bombarded by 90- to 700-Mev nucleons. The observed differential free nucleon-nucleon cross sections (extrapolated to 700 Mev) are used, and neutrons and protons are distinguished throughout. Averages per inelastic event for silver-bromine are summarized in Table I.

TABLE I.

E Mev	Nucleon in	Excitation energy Mev	No. of prompt neutrons	No. of prompt protons
90	n	42	1.1	0.4
90	p		1.0	0.6
400	n	52	2.0	0.8
400	p		1.4	1.9
700	n	50	2.8	1.5
700	p		1.3	2.2

The residual excitation energy at 400 Mev is 35 Mev for aluminum and 94 Mev for uranium. For 400-Mev incoming neutrons, the neutron-proton ratio is 1.7 for aluminum and 2.4 for uranium.

[1] Bernardini, Booth, and Lindenbaum, Phys. Rev. **88**, 1017 (1952).

K3. Yields near Threshold for (p, n) Reactions in Intermediate Nuclei. C. H. JOHNSON AND C. C. TRAIL, *Oak Ridge National Laboratory.*—Relative neutron yields have been observed for neutron energies up to 100 kev above the threshold for the (p, n) reaction in ten intermediate nuclei. Thick targets were bombarded with protons from the Oak Ridge 2.5-Mev Van de Graaff, and neutrons were detected with three BF_3 counters in paraffin surrounding the target. The (p, n) reaction cross sections were thereby determined relative to each other to thirty percent accuracy. The ten cross section curves show an extreme variation of 10^6. The entire set is in good agreement with the cross sections predicted on the basis of the continuum theory of the compound nucleus.[1] Ground-state spins and parities were assigned according to the nuclear shell model. This description requires a single arbitrary constant, namely, the absolute neutron counting efficiency. A preliminary measurement of this efficiency is in rough agreement with the required arbitrary constant. For one of the yield curves, $A^{78}(p, n)Se^{78}$, the nuclear shell model gives two possible Se^{78} ground-state assignments, $p_{\frac{1}{2}}$ or $g_{9/2}$. Of these, $p_{\frac{1}{2}}$ gives better agreement between theory and experiment.

[1] W. Hauser and H. Feshbach, Phys. Rev. **87**, 366 (1952).

K4. Low-Energy Yield of (α, n) Reactions. W. E. BENNETT, P. A. ROYS, AND B. J. TOPPEL, *Illinois Institute of Technology.*—The yield of neutrons from a thin beryllium target bombarded by helium from an electrostatic generator was measured as a function of bombarding energy up to 1.5 Mev. The curve was continued to higher energies using doubly charged helium. The known strong resonance at 1.9 Mev was observed and also resonances at 0.53 and 0.61 Mev, the latter being unusually narrow. Both resonances were observed also in the yield curve of gamma radiation. The angular distribution of neutrons showed marked assymmetry, the yields at zero and at about ninety degrees being large. The high-energy group of neutrons from the reaction is responsible for the maximum at zero degrees and the large energy group for the second maximum. In bombarding boron, five resonances in the yield of neutrons were observed below 1.5 Mev.

K5. Gamma-Radiation from an Excited State of Li^5.* N. M. HINTZ, J. M. BLAIR, AND D. M. VAN PATTER, *University of Minnesota.*—$He^3(d, \gamma)Li^5$ capture gamma radiation has been observed from a chamber containing helium enriched to 95 percent He^3 purified over a charcoal trap, using a NaI scintillation counter and single-channel discriminator. Measured relative to the $Li^7(p, \gamma)$ gamma rays, the extrapolated end point of the pulse distribution corresponded to 16.6 ± 0.2 Mev at $E_d = 0.46$ Mev. The observed shift of gamma-ray energy with deuteron energy was consistent with assignment to the $He^3(d, \gamma)Li^5$ reaction. This gamma radiation was not observed when the chamber was filled with He^4 or air. The excitation curve was measured at 90° from $E_d = 0.2$ to 2.6 Mev. This curve rises rapidly to a broad maximum at approximately 0.46 Mev, in a manner similar to the $He^3(d, p)He^4$ excitation curve.[1] Above this energy, the yield drops slightly, then rises slowly to the highest energy measured, suggesting the presence of nonresonant capture. The angular distribution was found to be roughly isotropic from 0 to 90°. A preliminary cross section of 2×10^{-28} cm² has been estimated at $E_d = 0.46$ Mev, assuming a thick-target yield of 1.9×10^{-8} γ rays/proton for the 441-kev $Li^7(p, \gamma)$ resonance.[2]

* This work has been supported by the joint program of the U. S. Office of Naval Research and the U. S. Atomic Energy Commission.
[1] Yarnell, Lovberg, and Stratton, Phys. Rev. **90**, 292 (1953).
[2] W. A. Fowler and C. C. Lauritsen, Phys. Rev. **76**, 314 (1949).

K6. Angular Distribution of $Li^6(n, \alpha)H^3$ for Fast Neutrons.* JAMES B. WEDDELL,† AND JAMES H. ROBERTS, *Northwestern University.*—We have previously reported investigation[1] of the angular distribution and cross section of $Li^6(n, \alpha)H^3$ occurring in photographic emulsions containing enriched Li^6. We have determined the yield of tritons per steradian, in the center-of-mass system, for neutron energies 1.1, 1.5, 2.0, and 2.5 Mev. Using spherical harmonics, these yields were fitted to series $Y = A + B\cos\phi_0 + C\cos^2\phi_0$, where ϕ_0 = neutron-triton angle. Values of A, B, C will be given. The statistical accuracy of the data is not adequate to rule out terms of higher order. We have also measured the capture cross section of Li^6 for 1.5- and 2.0-Mev neutrons, obtaining 0.32 ± 0.06 and 0.27 ± 0.04 barn, respectively. These values agree, within the limits stated, with those reported by Ribe.[2]

* This work was performed under U. S. Atomic Energy Commission contract.
† Now at Westinghouse Research Laboratories, East Pittsburgh, Pennsylvania.
[1] J. B. Weddell and J. H. Roberts, Phys. Rev. **89**, 891 (1953); Darlington, Hangsnes, Mann, and Roberts, Phys. Rev. **90**, 1049 (1953).
[2] F. L. Ribe, Phys. Rev. **87**, 205 (1952); private communication.

K7. $Li^7(d, t)Li^6$ Reaction. R. L. MACKLIN AND H. E. BANTA, *Oak Ridge National Laboratory.*—The cross section for the reaction $Li^7(d, t)Li^6$ has been measured by collecting and measuring the tritium produced by the reaction. The targets are evaporated enriched Li^7F on aluminum disks. About 200 $\mu g/cm^2$ of aluminum was evaporated on top of each target to stop the tritons emerging in the backward hemisphere. The tritium produced was driven out by heating in a hydrogen-argon atmosphere and collected in a proportional counter where the beta disintegrations of the tritium were then counted. Using this method, approximately 11^9 atoms of tritium equals the counter background counting rate. The procedure has been calibrated by two methods: tritium produced by the $Li^6(n, \alpha)t$ reaction is a known neutron flux has been used and also tritium from a Cockcroft-Walton accelerator. Although further work is necessary, on the second method in particular, a final accuracy of ± 10 percent for the cross sections does not seem unreasonable. The cross section in-

creases from threshold (1.3 Mev) to the maximum energy obtainable with the 2-Mev Van de Graaff (2.5 Mev) and is approximately 100 millibarns at this maximum energy.

K8. Neutrons from the Proton Bombardment of N^{14}.† F. AJZENBERG. *M.I.T. and Boston University*, W. FRANZEN* AND J. G. LIKELY, *Princeton University*.—A foil of melamine[1] ($N_6C_3H_6$), 200 kev thick, has been bombarded with 17.3-Mev protons from the Princeton cyclotron. The resultant neutrons have been studied by means of Ilford C-2 emulsions, 200 and 400 microns thick, mounted approximately 4.5 inches from the target and at five angles to the incident beam. Preliminary measurements at 30, 60, and 150 degrees (1700 tracks) indicate a ground-state Q value of -6.0 ± 0.2 Mev, giving a mass defect for O^{14} of 12.2 Mev, in good agreement with beta-decay results.[2] The data also indicate levels at excitation energies greater than 5 Mev.

† This work has been supported in part by the joint program of the U. S. Office of Naval Research and the U. S. Atomic Energy Commission.
* Now at the University of Rochester.
[1] We are indebted to K. G. Standing for this foil.
[2] R. Sherr and G. B. Gerhart, Phys. Rev. **91**, 909 (1953).

K9. Gamma Rays from the Inelastic Scattering of Protons by Neon.* MASON C. COX, JAN J. VAN LOEF, AND D. A. LIND, *University of Wisconsin*.—Observations have been made on the protons resulting from elastic and inelastic scattering of neon.[1,2] We have observed the gamma rays arising from inelastic scattering on Ne^{20} and Ne^{22}, using a 2- ×2-inch cylindrical NaI(Tl) crystal spectrometer with pulse-height analysis. Measurements of the yield of the 1.64-Mev gamma from Ne^{20} and the 1.28-Mev gamma from Ne^{22} were made for bombarding energies between 1.35 and 4.4 Mev. Levels in Na^{21} are found at 1.97-, 2.09-, 2.15-, 2.73-, 3.19-, 3.45-, 3.56-, 3.57-, 3.84-, and 4.00-Mev proton bombarding energy as measured in the laboratory system. No evidence for a level at 2.2 Mev in Ne^{20}, nor for the level at 0.4 Mev in Ne^{22}, was observed, and no other prominent gamma rays were observed.[3] Angular distributions of the 1.64-Mev radiation and the capture cross sections for protons by Ne^{20} as measured by the Na^{21} positron activity were taken at several resonances.

* Work supported by Wisconsin Alumni Research Foundation and the U. S. Atomic Energy Commission.
[1] Haeberli, Galonsky, Goldberg, and Douglas, Phys. Rev. **91**, 438 (1953).
[2] Galonsky, Haeberli, Goldberg, and Douglas, Phys. Rev. **91**, 439 (1953).
[3] F. Ajzenberg and T. Lauritsen, Revs. Modern Phys. **24**, 321 (1952).

K10. Angular Distribution of α Particles from the $Na^{23}(p, \alpha)Ne^{20}$ Reaction. P. H. STELSON, *Oak Ridge National Laboratory*.—The angular distribution of α particles produced by the $Na^{23}(p, \alpha)Ne^{20}$ reaction and leading to the ground state of the residual Ne^{20} nucleus has been measured at six resonances occurring in the region $Ep=1$ to 2 Mev. The particles were detected with a gas-filled counter fitted with a thin (0.5 air-cm thickness) nickel foil window. By means of pulse-height selection those α particles leaving Ne^{20} in the ground state could be clearly distinguished from those leading to the first excited state. The targets were prepared by evaporation in vacuum of NaI onto thin (25 micrograms/cm²) Formvar backings. The ground state of Ne^{20} is a 0^+ state and this has the consequence that certain types of resonant states are strictly forbidden to decay by this channel. If the ground state of sodium is assigned on even parity, as is indicated by the shell model, the states which can decay by this channel are restricted to the sequence 0^+, 1^-, 2^+, 3^-, etc. The calculated angular distribution for a given type of state is not unique in many cases in that an unknown mixture of the channel spins enters as well as possible admixtures of higher l values. The most plausible assignments for the character of the resonances will be given.

K11. Slow Neutron Capture Gamma Rays from Titanium.* HENRY T. MOTZ, *Brookhaven National Laboratory*.—Six gamma rays have been measured from the $Ti(n, \gamma)Ti$ reaction in the energy range of 300 kev to 2000 kev by means of the photoelectric effect in uranium converters. In order to reduce the background, coincidences between the K photoelectrons focused in a thin-lens spectrometer and the K x-rays of the uranium converter are recorded. This technique also eliminates the L photopeaks. $Ti^{48}(n, \gamma)Ti^{49}$ is known to account for 0.95 of the thermal neutron absorption in natural titanium,[1] and, since the intensities of all six lines are >0.05, they originate from this isotope. Preliminary energy values are 0.34, 0.51, 1.385, 1.51, 1.59, and 1.78 Mev. These values agree with the level scheme of Ti^{49} as given by Pieper[2] and Kinsey[3] except for the 510-kev line.

* Research performed at Brookhaven National Laboratory under the auspices of the U. S. Atomic Energy Commission.
[1] H. Pomerance, Phys. Rev. **88**, 412 (1952).
[2] G. Pieper, Phys. Rev. **88**, 1299 (1952).
[3] B. B. Kinsey and G. A. Bartholomew, Phys. Rev. **89**, 375 (1953).

K12. Angular Distribution of Protons from the Reaction $Zn^{68}(d, p)Zn^{69}$. F. S. EBY, R. D. HILL, AND W. K. JENTSCHKE, *University of Illinois*.*—The (d, p) stripping theory of Butler has been employed in the interpretation of the angular distributions of protons from the reaction $Zn^{68}(d, p)Zn^{69}$. Deuterons of 12 Mev were used to bombard a target of isotopically enriched Zn^{68} deposited on a thin gold backing, and a sodium iodide scintillation counter was used to detect protons emitted between angles of 7 and 90 degrees. The theoretical curves which most nearly fit the observed proton distributions are those with $l_n=1$ and $l_n=4$ for the groups associated with the ground state and the 439-kev 13.6-hr isomeric level, respectively. These values of l_n are consistent with the shell theory assignments[1] of $p_{\frac{1}{2}}$ for the ground state and $g_{9/2}$ for the metastable state of Zn^{69}. The magnitude of the peak associated with the isomeric level is 0.4 times that of the ground level and is significantly greater than is predicted by stripping theory and a one-particle nuclear model. The Q value for the reaction leaving Zn^{69} in the ground state has been determined as 4.16 ± 0.15 Mev.

* Assisted by the joint program of the U. S. Office of Naval Research and the U. S. Atomic Energy Commission.
[1] M. Goldhaber and R. D. Hill, Revs. Modern Phys. **24**, 179 (1952).

K13. Proton Induced Reactions in Bismuth. C. G. ANDRE, W. J. RAMLER, E. G. RAUH, R. J. THORN, AND J. R. HUIZENGA, *Argonne National Laboratory*.—The (p, γ), (p, n), and $(p, 2n)$ cross sections of bismuth for 6-11 Mev protons were determined by measuring the alpha activities of the polonium isotopes produced. The thin bismuth targets were prepared by evaporation. The excitation curves were obtained using the stacked foil technique. The protons were accelerated as H_3^+ ions in the Argonne National Laboratory 60-inch cyclotron using the deuteron frequency. The deuterium contamination of natural hydrogen was removed magnetically after the H_2^+ ions were ionized to protons. The $\sigma_{(p,n)}/\sigma_{(p,\gamma)}$ ratio was approximately 10^2. The $(p, 2n)$ threshold was found to be 9.78 ± 0.10 Mev.

SATURDAY MORNING AT 10:00

Rosenwald 2

(R. A. FISHER presiding)

Invited Papers

L1. The Effect of Pressure on Self-Diffusion of Sodium. N. H. NACHTRIEB, *University of Chicago.* (30 min.)

L2. The Chemisorption of Oxygen on Tungsten. ROBERT GOMER, *University of Chicago.* (30 min.)

General Physics

L3. A New Fluorescence Photometer. F. J. LYNCH, *Argonne National Laboratory.*—An instrument for measuring fluorescence is described which is sensitive, linear, and stable. Both an unknown and a standard fluorescent sample are irradiated with ultraviolet light from a mercury arc lamp operated on the 60-cps power line. Fluorescent light from each sample is incident on a separate vacuum phototube. The system automatically compares the 120-cps component of the photoelectric currents flowing in the two phototubes. In this way, the measurement is independent of intensity of the exciting ultraviolet source. Either solid or liquid samples may be rapidly measured. For uranium analysis the instrument may be calibrated to read 1000 divisions for 10^{-9}, 10^{-8}, 10^{-7}, or 10^{-6} μg of uranium. Although the fluorescence photometer is designed primarily for uranium analysis, the filters may be readily changed to permit measurements of other elements.

L4. Charge States of Ion Beams in Various Gases. P. M. STIER, C. F. BARNETT, AND G. E. EVANS, *Oak Ridge National Laboratory.*—Measurements have been made of the fraction of a heavy particle beam in the various possible charge states (neutral, singly, and doubly ionized), after passing through various gases. Ion beams, with energies from 10 to 250 kev, are passed through a windowless (differentially pumped) gas cell, and are electrostatically analyzed according to charge. The pressure in the stopping cell is sufficiently high to establish equilibrium between competing capture and loss reactions (i.e., the gas cell length is several mean free paths for charge exchange). This condition is compatible with the requirement that the fraction of the energy lost by the high-energy particle within the cell may be neglected. The incident ions H^+, He^+, N^+, Ne^+, and A^+ have been studied in the stopping gases, hydrogen, helium, nitrogen, oxygen, air, neon, and argon. The average charge of H^+ and He^+ ion beams after passing through a gas appears to be somewhat less than reported in the literature. No comparison data are available for the other ions at these energies.

L5. Some Characteristics of Gridded Parallel-plate Ionization Chambers. L. O. HERWIG, G. H. MILLER, AND N. G. UTTERBACK, *Iowa State College.*—Characteristics of a gridded parallel-plate ionization chamber employing electron collection were investigated by observing pulse height of alpha particles in various gases as a function of electrode voltages. The theoretical minimum ratio of collector to source fields for complete electron collection was 1.32 for the present geometry. Experimental values of the minimum ratio ranged from 2.2 for argon to 1.5 for argon plus 3 percent carbon dioxide. Correlation was found between calculated electron diffusion and observed minimum ratio of fields. Gas multiplication, presumably near the grid, was observed in argon and neon for X/P values of about 1.3 and 0.4, respectively, where X was calculated as a uniform field between the grid and collector electrodes. Saturation curves, pulse height *versus* source field, were obtained for argon, helium, nitrogen, neon, krypton, argon plus carbon dioxide, and argon plus nitrogen. Saturation properties of argon plus carbon dioxide, which gave faster drift velocities than argon, were found to be a function of mixture pressure and percentage of carbon dioxide. The use of argon-nitrogen mixtures, which also gave faster drift velocities, gave consistent saturation properties at pressures and percentages investigated.

L6. Use of a Pinhole for Producing Glow to Arc Transitions. B. PEARSON DELANY AND PAUL L. COPELAND, *Illinois Institute of Technology.*—In studies of electrical discharges in mercury vapor at low pressure, the surface of a large mercury cathode has been separated into two areas.[1] A small area is divided from the rest of the pool by a glass tube of small diameter dipping into the mercury. This tube is flared and connected to the wall of the main tube by means of a ring seal. In such a tube, there is no discharge path between the large area of the cathode pool and the anode, because the glass wall of the constriction completely separates this portion of the cathode from the anode. If, however, a pinhole is left either in the ring seal or in the constriction above the mercury surface, at pressures of a few millimeters, when the potential of the anode is raised to set up a glow, it is always observed that a glow to arc transition occurs rapidly with an arc path passing through the pinhole to the area external to the constriction. Dependence of this phenomenon on pressure and circuit conditions has been studied.

[1] P. L. Copeland, Rev. Sci. Instr. 16, 154 (1945).

L7. Stability of Low-Pressure Mercury Arcs with Positive Conducting Rod. J. T. KOUBA AND P. L. COPELAND, *Illinois Institute of Technology.*—Previous work with low-pressure mercury arcs has indicated that under fixed operating conditions the number of arcs surviving for time t plotted against t fell along curves of the form $\exp(-kt)$. The present study incorporated a high-resistance (approx. 20 000 ohms) carbon rod partially submerged in the cathode pool and electrically insulated from the plasma. The rod was subjected to a positive dc voltage and the average life determined as a function of rod voltage and cathode current. The experimental apparatus was set up so as to obtain a large amount of data in a reasonable amount of time. A switching circuit was devised so that after an arc extinguished an adjustable time delay allowed for data recording and then automatically ignited the arc by momentarily energizing a spark coil. It was found: (1) A positive conducting rod increases the stability somewhat, diameter rods being more effective. (2) The average life as a function of rod voltage can be expressed as $T_a = G\exp(hE_p)$; where T_a is the average life, G is a constant, h is a constant of the order 10^{-2} to 10^{-3}, and E_p is the rod voltage. (3) Spontaneous ignition took place erratically at $E_p = 200$ volts.

L8. Evapor-ion Pump.* AJAY S. DIVATIA, ROBERT H. DAVIS, AND R. G. HERB, *University of Wisconsin.*—The Evapor-ion Pump[1] which utilizes both the gettering action of titanium and ion pumping has undergone considerable

development and improvement. High pumping speeds and reasonable lifetime are obtainable with moderate power consumption. The pump chamber, free of organic materials, is baked out with a mechanical pump connected to it. It is then cooled and disconnected from the mechanical pump. Titanium, fed in a wire form onto a graphite post heated by electron bombardment, evaporates and condenses on the cylindrical chamber wall which is water-cooled to about 20°C. Gettering by continuously condensed titanium produces a pumping action. Components not pumped by this gettering are ionized and are driven into the chamber wall, where they are buried by the condensing titanium. Pumping speeds achieved are: 7000–8000 liters/sec at 3×10^{-6} mm of Hg for hydrogen, 6500–7500 liters/sec at 1.5×10^{-6} mm for nitrogen and oxygen, approximately 9 liters/sec at 4×10^{-6} mm for argon, and approximately 4 liters/sec at 3×10^{-5} mm for helium. The lowest pressure obtained is about 2×10^{-7} mm of Hg. Pumping speeds for some gases have been investigated as a function of the temperature of the gettering surface, the pressure and the rate of evaporation of titanium.

* Work supported by the Wisconsin Alumni Research Foundation and the U. S. Atomic Energy Commission.

[1] Herb, Davis, Divatia, and Saxon, Phys. Rev. **89**, 897 (1953).

L9. The Application of Solutions of Boltzmann Equation to Turbulence. M. Z. v. KRZYWOBLOCKI, *University of Illinois* (introduced by G. J. Plain).—The author discusses thoroughly the fundamentals underlying the derivation of Boltzmann equation, particularly the condition of the slowly varying distribution function and of the molecular chaos. Next he presents the available solutions of this equation: Hilbert, Enskog, Chapman, Burnett, and Grad. He points out the advantages and disadvantages of these solutions as well as the regions of their applicability in fluid dynamics. Next he discusses the application of these equations as the fundamental equations of the turbulent motion in the compressible fluid flow regime. The following items are treated more thoroughly: steady state of turbulence, transient one, and decay of turbulence.

L10. Velocity Attenuation of Explosive Produced Air Shocks. JACOB SAVITT, *U. S. Naval Ordnance Laboratory*.—The results of measurements of the velocities of explosive produced air shocks very close to the explosive-air interface will be presented. In tubes it was found that the data is consistant within certain limits with the semi-empirical relation, $1/U=1/U_0+Kd^2f_0X$, where U is the air shock velocity at the distance X in the air tube from the explosive-air interface, d is the cylindrical air tube internal diameter, f_0 is the undisturbed air density, and K is a constant. The origin of this equation, its limitations, and some of its application will be discussed.

SATURDAY MORNING AT 9:30

Kent 106

(H. L. ANDERSON presiding)

Mostly Elastic Scattering

M1. $P-P$ Differential Elastic Scattering Cross Sections at 144, 271, and 429 Mev. V. A. NEDZEL, J. MARSHALL, AND L. MARSHALL, *University of Chicago*.—The $P-P$ differential elastic scattering cross section at 90° baricentral angle has been measured for three proton energies and has been found to be independent of energy in this range. Sizable intensities of proton beams of a wide range in energy were obtained by the proper azimuthal positioning of a beryllium scattering target at 76 in. radius in the Chicago synchrocyclotron. The protons collimated by a channel in the heavy shield were of definite energy for a given target position. They were further analyzed by an additional magnet. The analyzed collimated beam was defined and measured before the scatterer by a telescope of 2 scintillation counters (1 and 2). The scatterer was a 4-in. vertical cylinder of liquid hydrogen contained in styrofoam walls. Two scintillation counters (3 and 4) were placed on opposite sides of the beam, connected in coincidence with counters 1 and 2 in such a way that they counted the two elastically scattered protons in coincidence with the incident proton. In order to avoid counting loss corrections, a fifth counter which counted protons scattered out of the main beam was used to normalize the incident flux at low-beam intensities and to normalize the quadruple coincidence rate at high beam intensity. The cross section at 90° was measured in millibarns per steradian as follows: 3.21 ± 0.11 at 144 Mev, 3.67 ± 0.34 at 271 Mev, and 3.42 ± 0.13 at 429 Mev.

M2. $P-P$ Elastic Scattering and Pion Production at 419 Mev. J. MARSHALL, L. MARSHALL, AND V. A. NEDZEL, *University of Chicago*.—The differential $P-P$ elastic scattering cross section at 419 Mev was measured from 90° to 54° baricentral angle by the method in which the two elastically scattered protons were detected in coincidence with the incident proton. From 54° to 28° a second method was used which counted all charged particles scattered at the angle in question in coincidence with an incident proton provided that no charged particle was simultaneously scattered near the forward direction. This method depended on several facts. First, the only reaction which seriously interferes with detection of scattered protons is (*a*) $P+P\rightarrow\pi^++D$. The related reaction (*b*) $P+P\rightarrow\pi^++P+N$ probably occurs less than 1/5th as frequently. In the case of (a) all deuterons and in the case of (b) many protons are scattered forward close to the beam. In a reversal of this method the π^+ production cross section at 45° laboratory angle was measured by counting charged particles scattered in coincidence with an incident proton and with a charged particle scattered simultaneously near the forward direction. By the first method were obtained the following cross sections in millibarns per steradian: 3.42 ± 0.13 at 90°, 3.51 ± 0.23 at 80°, 3.11 ± 0.19 at 65°, and 2.84 ± 0.12 at 54°. By the second method were obtained 2.80 ± 0.21 at 54°, 3.18 ± 0.21 at 43°, and 2.86 ± 0.20 at 28°. Correspondingly the differential π^+ production cross section at 80° was found to be 0.163 ± 0.024.

M3. A Search for Polarization of Protons from the 450-Mev Synchrocyclotron. L. MARSHALL, V. A. NEDZEL, AND J. MARSHALL, *University of Chicago*.—Maximum polarization of a scattered proton beam from the internal beryllium target was sought. By proper selection of the azimuthal target position, the first scattering angle θ_1 and the energy of protons emerging into the experimental area through the heavy shield collimator were chosen approximately equal to the angle and energy of a proton scattered from a free nucleon-nucleon collision. The

collimated beam was further analyzed by magnetic deflection. Beam polarization should have shown itself as an asymmetry of a second scattering from beryllium in the plane of the first scattering. Protons scattered at 30° up, down, left, and right were measured with detection equipment swung around the beam. The counter support was oriented to beam coordinates previously determined by counter exploration. Two different methods were used to search for asymmetry. In the first method (a) only protons scattered as though from a free $p-p$ or $p-n$ collision in the beryllium nucleus were detected. The second method (b) examined only protons scattered from $p-p$ collisions. The background was about 5 percent. No asymmetry was evident. The results are for (a) $\theta_1=36°$ left, $\theta_2=30°$, up-down asymmetry $=-(3\pm6)$ percent, right-left asymmetry $=-(0.005\pm6)$ percent, and for (b) $\theta_1=36°$ left, $\theta_2=30°$, right-left asymmetry $=-(5\pm6)$ percent; $\theta_1=26°$ right, $\theta_2=30°$, right-left asymmetry $=+(2.7\pm3.0)$ percent.

M4. The Elastic Scattering of Protons by Nitrogen. H. E. GOVE, A. J. FERGUSON, AND J. T. SAMPLE, *Chalk River Laboratory.*—The elastic scattering of protons by nitrogen has been studied in the range 1.3 Mev to 1.9 Mev using the Chalk River electrostatic accelerator. A gas target was used in a large scattering chamber similar to that described by Blair *et al.*[1] There are three resonances in this region at energies 1.53, 1.72, and 1.78 Mev. Angular distributions were determined by measuring the scattered intensity at eleven different angles in the range 50° to 153°, at about ten different energies near the resonances. From these it is concluded that the spin and parity assignment for the 1.53 Mev resonance is $\frac{1}{2}(+)$ with only the channel spin $\frac{1}{2}$ contributing. The 1.72-Mev resonance is not adequately resolved in energy, but a probable assignment of $\frac{3}{2}(-)$ with only channel spin $\frac{1}{2}$ contributing has been made. Throughout the energy range there is a "background" scattering markedly different from pure Coulomb scattering, and showing larger S-wave and smaller P-wave phase shifts than predicted from hard sphere scattering.

[1] Blair, Freier, Lampi, Sleator, and Williams, Phys. Rev. **74**, 553 (1948).

M5. Differential Cross Sections for the Elastic Scattering of Protons by He^3.† K. F. FAMULARO, R. J. S. BROWN, H. D. HOLMGREN, AND T. F. STRATTON, *University of Minnesota.*—Differential cross sections for protons elastically scattered from He^3 have been measured at laboratory energies of 1.01, 1.60, 2.25, and 3.52 Mev for nine center-of-mass angles extending from 36° to 169°. Also, the differential cross sections at center-of-mass angles of 44° and 169° have been measured in 30-kev steps for proton energies from 0.7 Mev to 3.5 Mev. The small volume scattering chamber and associated equipment used for these measurements have been described earlier.[1,2] The cross section at 1.01 Mev has a constant value of 0.12 barns/sterad for center-of-mass angles greater than 90°, and approaches the values expected from Coulomb scattering at lower angles. At 1.60, 2.25, and 3.52 Mev, the angular distributions have broad minima whose values are 0.11, 0.09, and 0.08 barns/sterad, respectively, in the neighborhood of 90° (center of mass). The cross section at 169° increases from 0.11 barns/sterad at 0.9 Mev to 0.27 barns/sterad at 3.5 Mev.

† Assisted by the joint program of the U. S. Office of Naval Research and U. S. Atomic Energy Commission.

[1] Brown, Freier, Holmgren, Stratton, and Yarnell, Phys. Rev. **88**, 253 (1952).

[2] Stratton, Freier, Keepin, Rankin, and Stratton, Phys. Rev. **88**, 257 (1952).

M6. Elastic Scattering of Deuterons by Helium.* A. GALONSKY, R. DOUGLAS, W. HAEBERLI, M. MCELLISTREM, AND H. T. RICHARDS, *University of Wisconsin.*—$He^4(d,d)$ differential cross sections were measured from 0.3 to 4.6 Mev with a differentially pumped gas scattering chamber. A resonance with peak cross section at $E_d=1.076$ Mev (for 173.6° c.m.) and $\Gamma\sim35$ kev was observed at 9 angles from 90° to 173.6° c.m. The cross section at 90° c.m. drops from 0.20 to 0.07 rising again to 0.14 barns/sterad; this dip indicates even parity for the 2.187-Mev state of Li^6. Data at 3-kev intervals were taken in the region of the 3.58-Mev state. No anomaly being observed agrees with the assignment $J=0^+$, $T=1$. Conservation laws do not permit the formation of such a state with a deuteron and an α particle. The cross section curves are flat above the 1.076-Mev resonance up to 3 Mev. Above 3 Mev the 173.6° c.m. cross section rises from 0.1 to 0.5 barns/sterad at 4.6 Mev while the 90° c.m. cross section drops by about a factor of two. Further analysis is in progress.

* Work supported by the U. S. Atomic Energy Commission and the Wisconsin Alumni Research Foundation.

M7. Neutron-Proton Scattering at 395 Mev.—I.* A. J. HARTZLER AND R. T. SIEGEL, *Carnegie Institute of Technology.*—The equipment used in a study of differential $n-p$ scattering (see following abstract) will be described. Recoil protons ejected from hydrogen (CH_2-C difference) were detected by a three-crystal scintillation telescope. To make the apparatus insensitive to recoils from incident neutrons of less than 365 Mev, a variable copper absorber was placed between the last two counters. Calibration of the telescope to determine the loss of protons in the absorber was done in an auxiliary experiment, in which the external proton beam from the synchrocyclotron was scattered in proton-proton collisions with the same geometry and scatterers used in the measurement of the neutron-proton cross section. In the calibration experiment the recoil protons were counted both by the double coincidences between the first two counters and also by triple coincidences. The ratio of the two counting rates gives the telescope efficiency, while the variation of double coincidences with angle yields some information about the differential $p-p$ cross section. The method is also used in determining the neutron spectrum from a range curve of the neutron-proton recoils.

* Supported in part by the U. S. Atomic Energy Commission.

M8. Neutron-Proton Scattering at 395 Mev.—II.* R. T. SIEGEL AND A. J. HARTZLER, *Carnegie Institute of Technology.*—The equipment described in the preceding abstract has been used to study the neutron-proton angular distribution, using the neutron beam of the Carnegie cyclotron. The effective neutron spectrum had a mean energy of 395 Mev with a full width at half-maximum of 40 Mev, and intensity of $\sim10^5$ cm^{-2} sec^{-1}. Recoil protons from polyethylene-carbon differences were detected at eighteen laboratory angles between 0° and 68°, corresponding to neutron scattering angles between 40° and 180° in the center-of-mass system. Angular resolution for c.m. angles between 40° and 160° was ~7°, and was improved to 3.5° for angles between 160° and 180°. Statistical errors of <5 percent were obtained at all angles except 180°, where further measurements are in progress. Our results indicate a deviation from symmetry about 90°, with a minimum in the cross section at ~100°. The ratio of the cross sections at 175° and 90° is ~7, indicating a strong peak at 180°. Detailed results will be presented.

* Supported in part by the U. S. Atomic Energy Commission.

Invited Paper

M9. Elastic Scattering of Positive and Negative Electrons from Nuclei. P. S. JASTRAM, *Washington University.* (30 min.)

M10. Double Scattering of Protons at High Energies. C. L. OXLEY, *University of Chicago.* (30 min.)

SATURDAY MORNING AT 9:30

Oriental Institute

(A. S. EISENSTEIN presiding)

Electron Physics; Thin Films

N1. Luminescent Centers in X-Ray Excited Fluorescence of Ice. L. I. GROSSWEINER AND M. S. MATHESON, *Argonne National Laboratory.*—The emission spectrum of x-ray excited ice at low temperatures is shifted in wavelength and intensified by the presence of ionic additives. The intensification increases with additive concentration and saturates at about 0.01 molar for sodium chloride. The spectral shifts are specific to the cation of the additive. A luminescent model is proposed in which the primary process is the radiative capture of electrons by additive cations. Approximate emission energies calculated from a thermodynamic cycle agree with those obtained experimentally. For the monovalent cations the emission energies are substantially given by the difference of the corresponding atomic ionization potentials and the heats of solvation of the ions in ice. This suggests that the reciprocals of the average emission energies should vary with the cationic radii of the additives. The correlation is valid for the additives tested.

N2. Electroluminescence with Nonsinusoidal Electric Fields. SOL NUDELMAN AND FRANK MATOSSI, *U. S. Naval Ordnance Laboratory.*—A variety of luminescent wave shapes were obtained when electric fields in the form of rectangular pulses, saw-tooth waves, exponential waves, and various nonsymmetrical waves were applied to an electroluminescent phosphor. The luminescent patterns observed were examined separately in the blue and green bands by means of filters. In general, the character of the light output from the phosphor was independent of whether the applied field was reversed every half cycle or pulsed unidirectionally. The phosphor light output can be interpreted qualitatively by considering (1) the growth and decay of the effective field caused by space charges near the particle surface, (2) the natural decay of the blue and the green luminescence, and (3) the different efficiency of excitation of the two colors. Luminescence excitation is assumed to be caused by some collision process with field-accelerated electrons; the efficiency depending on field strength, number of conduction electrons, and number of excitable centers. The green luminescence is supposed to involve transitions from the conduction band and traps, while the blue band is assumed to be due to transitions within the centers only.

N3. Electroluminescence in ZnS:Mn Films. R. E. HALSTED AND L. R. KOLLER, *General Electric Research Laboratory.*—Ten micron films of ZnS phosphors which will withstand voltage gradients approaching 5×10^5 v/cm have been prepared by vapor reaction techniques. Qualitative experiments with ZnS:Mn films reveal excitation, emission, and photoconductivity characteristics of conventionally prepared ZnS:Mn phosphors. Variations from previously reported results for other phosphors in the electroluminescent emission and its dependence on voltage, frequency, and temperature will be presented.

N4. Photoinduced Conductivity in Solutions of Anthracene in *n*-Hexane.* L. W. AUKERMAN, *Purdue University.*—Dilute solutions (approx. 5×10^{-4} to 5×10^{-3} M) of purest anthracene in carefully purified *n*-hexane show a conductivity in the dark of less than 10^{-17} mho/sec (measured with a vibrating reed electrometer). Illumination near 1950 A produces an increase in conductivity up to several hundred times the dark conductivity, thus verifying the results of Volmer.[1] The behavior of this "photocurrent" indicates that the additional carriers are produced in the bulk of the liquid by light which is absorbed by the anthracene molecules. By measuring the photocurrent as a function of light intensity, as a function of concentration of the anthracene, and as a function of time, one must conclude that ions are formed with mobilities of the order of 5×10^{-4} cm²/volt-sec. The current i as a function of light intensity I is given by $i=a+b\sqrt{I}$.

* This work supported in part by the Office of Naval Research.
[1] M. Volmer, Ann. Physik **40**, 775 (1913).

N5. Photoconductivity of Single Crystals of Anthracene.* G. J. GOLDSMITH, *Purdue University.*—Photoconductivity in single crystals of anthracene has been observed with crystals illuminated in the near ultraviolet (threshold near 4000A) and the spectral dependence of photocurrent corresponds to the optical absorption. The photocurrent i depends on intensity I as $i=aI^{0.7}$. The field dependence of photocurrent does not show saturation with fields up to 10 000 volts/cm in vacuum. From the experiments we conclude that both electrons and holes participate in the conduction process. An oxygen atmosphere causes an increase in the conductance both in the dark and in the light. The dark conductance (σ_d) can be described as $\sigma_d=\sigma_0 e^{-\epsilon/2kT}$ with ϵ about 1.60 ev.[1]

* This work supported in part by the U. S. Office of Naval Research.
[1] H. Mette and H. Pick, Z. Physik **134**, 566 (1953). These authors give $\epsilon=1.65$ ev.

N6. Energy Distribution of Secondary Electrons from Solids. ERNEST J. STERNGLASS,* *Cornell University.*—Measurements of the energy distribution of the secondary electrons from Au, Pt, Ta, Cu, and C under bombardment by 0.2–2.5-kv electrons have been made using a spherically symmetric retarding field. When corrected for the high energy (>50 ev) backscattered fraction, the form of the energy distribution and the values of the most probable and median energies were found to be the same for all materials to ±1 ev, independent of primary energy. The shape of the curves and the location of the most probable and mean values agree closely with data on air and H_2,[1] except for a small excess between 10 and 15 ev and a more rapid decrease beyond 25–30 ev found for all solids relative to the gases. Similar features, explainable by discrete energy losses, have been observed by previous investigators for Mo and Ta. The similarity of the curves for all substances independent of their state of aggregation is in agreement with the dominant role of bound electrons as demanded by the author's theory of secondary emission.[2]

* Now at Westinghouse Research Laboratories.
[1] M. Ishino, Phil. Mag. **32**, 202 (1916).
[2] Thesis, Cornell University, February, 1951; also summary in Report on 13th Annual Electronics Conference, Massachusetts Institute of Technology, 1953.

N7. A Study of SrO on Mo by Use of the Field Emission Microscope.* P. W. KRUSE AND E. A. COOMES, *University of Notre Dame.*—Observations of the migration of SrO over a Mo point have been made by means of the field emission microscope technique. An etched Mo point mounted in a Mueller tube[1] was flashed until a reproducible pattern, similar to that obtained by Becker[1] for clean W, was observed. SrO evaporated from a Pt ribbon source[2] was deposited in varying amounts on one side of the point. On heating the point to approximately

1200°K in the presence of a field of about 10^8 volts cm^{-1}, migration was complete within 17 minutes, with a tendency to build up in the 221 region. On heating in the absence of a field migration rates were similar, but there were differences in the migration patterns.

* Sponsored by the U. S. Navy Bureau of Ships.
[1] J. A. Becker, Bell System Tech. J. **30**, 907 (1951).
[2] G. E. Moore and H. W. Allison, Phys. Rev. **77**, 246 (1950).

N8. Effect on the Periodic Schottky Deviations Resulting from a SrO Layer Deposited on Clean Molybdenum.* G. A. HAAS† AND E. A. COOMES, *University of Notre Dame.*—Periodic deviations in the Schottky effect for a polished polycrystalline Mo filament have been compared for the clean state and states corresponding to monomolecular coverage with SrO. Deviations for the clean state were of the usual form;[1] agreement was found for the mirror image λ coefficient, but not for the box-model μ coefficient. The Schottky plot for this filament had a long patch free region, which allowed an accurate study of deviation amplitude as a function of temperature. The inverse temperature dependence in accordance with theory[2] was found for the 1500–1700°K range. When SrO was deposited the periodic deviations disappeared; as little as 1/100 monolayer coverage made the deviations unobservable, and at approximately $\frac{1}{4}$ monolayer coverage deviation from the Schottky line was less than 0.01 percent.

* Sponsored by the U. S. Navy Bureau of Ships.
† Now at the Naval Research Laboratory, Washington, D. C.
[1] Brock, Houde, and Coomes, Phys. Rev. **89**, 851 (1953).
[2] E. Guth and C. Mullin, Phys. Rev. **59**, 575 (1941).

N9. The Electrical Resistances of Dual Layer and Simultaneously Evaporated Bimetal Films before and after Artificial Aging.* RICHARD B. BELSER AND MARGARET C. CHESTER, *Georgia Institute of Technology.*—Bi-metal films of a number of metal pairs have been deposited on glass substrates in two successive layers, with the layer order reversed, and by simultaneous evaporation. The resistances of the latter were several times those of dual layer films of equivalent metals and thickness. After aging by heating in an infrared vacuum oven, the resistances of the simultaneously evaporated films were usually reduced by factors of 2–10 whereas those of the dual layer films appeared to behave in accordance with the alloying characteristics of the metal pair. Where intermetallic compounds or solid solutions were readily formed rapid resistance rises after aging at temperatures of 100–150°C were noted. Where the alloying action was of a less degree, a reduction in resistance was frequently noted on aging followed by a rise in resistance of more moderate slope on further heating. Where no appreciable alloying occurred, resistances were decreased by aging until aging temperatures of 500°C were exceeded. X-ray diffraction and micrographic studies of the same samples were made. The techniques described may allow observation of the diffusion and alloying characteristics of minute amounts of metals.

* Supported by U. S. Army Signal Corps.

N10. X-Ray Diffraction Studies of Dual Layer and Simultaneously Evaporated Bimetal Films After Artificial Aging by Heating.* WILLIAM E. WOLF AND RICHARD B. BELSER, *Georgia Institute of Technology.*—The bimetal films described in the previous paper have been examined by x-ray methods similar to those employed by Burr, Coleman, and Davey.[1] Results using a recording Geiger counter spectrometer were generally unsatisfactory because of the high background due to scattering by the glass substrate. More satisfactory results were obtained when the metal was scraped from the glass substrate and used as the sample in a Hull-Debye-Scherrer camera. Using this technique the various phases present could be identified. In addition, it was possible to determine that for certain specimens the time of heating had been insufficient to allow complete diffusion of the metals. In some cases, in which the phase diagram is unknown, the presence of lines not attributable to the two elements indicated the presence of new phases. The x-ray data, in general, confirm the observations regarding the alloying characteristics and diffusion of metals made during the resistance studies. The method appears to offer promise as a means of obtaining partial x-ray information on the binary systems of rare or precious metals.

* Supported in part by the U. S. Army Signal Corps.
[1] Burr, Coleman, and Davey, Trans. Am. Soc. Metals **33**, 73 (1944).

N11. Metallographic Studies of Dual Layer and Simultaneously Evaporated Bimetal Films After Artificial Aging by Heating.* ROBERT J. RAUDEBAUGH AND RICHARD B. BELSER, *Georgia Institute of Technology.*—In conjunction with resistivity and x-ray diffraction studies of dual layer and simultaneously evaporated metal films a number of metallographic observations have been made. Micrographs taken of gold-indium and iron-indium films after various stages of artificial aging are discussed. Some interesting effects have been observed. For gold and indium, simultaneously evaporated and heated to 350°C, a spectacular dendritic structure appeared. For iron, overcoated with indium, the indium film aggregated into globules upon the surface of the iron at a temperature of 190°C. These two cases respectively represent examples of vigorous alloying and apparent mutual insolubility of the component metals. Utilization of the techniques herein described appears to offer a means of making metallographic studies of alloys with minute quantities of metals and a minimum preparation of the surfaces. Further work on etch techniques and interpretation of observations are necessary before this procedure may be considered a method of real value for the study of unknown binary systems.

* Supported in part by the U. S. Army Signal Corps.

SATURDAY MORNING AT 9:30

Mandel Hall

(ENRICO FERMI presiding)

Invited Papers

P1. Photomesons Near the Production Threshold. GILBERTO BERNARDINI, *University of Illinois.* (30 min.)

P2. Reports on the Cosmic-Ray Conferences Held in July, 1953, at Bagnères-de-Bigorre. (a) Conference on Intensity-Time Variations. J. A. SIMPSON, *University of Chicago.* (b) Conference on Fundamental Particles. MARCEL SCHEIN, *University of Chicago.* (60 min. to be divided between the two speakers).

P3. Evidence for the Existence of the V_4 Particle. R. W. THOMPSON, *Indiana University.* (30 min.)

P4. Theoretical Speculations about New Unstable Particles. MURRAY GELL-MANN, *University of Chicago.* (30 min.)

SATURDAY AFTERNOON AT 1:30

Kent 106

(JOHN MARSHALL presiding)

Neutrons, and Other Topics in Nuclear Physics

Q1. Scattering of Polarized Neutrons from Heavy Nuclei.* S. E. DARDEN, R. E. FIELDS, AND R. K. ADAIR, *University of Wisconsin.*—The polarization P_1 of $Li^7(p, n)$ neutrons emitted at 50° in the laboratory system was measured at a neutron energy around 400 kev, using liquid oxygen as an analyzer. The level parameters of the 435-kev oxygen resonance are sufficiently well known to allow calculation of P_1 from the measured 90° left-right scattering asymmetry. The scattering asymmetry was then observed using thirteen heavy elements as analyzers. From these measurements the polarization P_2 produced by the heavy elements was inferred. Values of P_2 around 20 ± 5 percent were found for nuclei with A around 100, while lighter and heavier elements gave no measurable polarization. These results can be accounted for by adding a term of the form -2 Mev $(\mathbf{l}\cdot\mathbf{s})$ to the complex potential proposed by Feshbach, Porter, and Weisskopf.[1]

* Work supported by the U. S. Atomic Energy Commission and the Wisconsin Alumni Research Foundation.
[1] Feshbach, Porter, and Weisskopf, Phys. Rev. **90**, 166 (1953).

Q2. Polarization of Neutrons. C. P. STANFORD, T. E. STEPHENSON, L. W. COCHRAN, AND S. BERNSTEIN, *Oak Ridge National Laboratory.*—The neutron polarization cross section of iron has been measured as a function of energy from 0.7 to 3.3A by two methods: using the single transmission effect in a block of polycrystalline iron at energies selected by a quartz crystal monochromator; using a single crystal of magnetized magnetite to analyze the beam emerging from the iron polarizer, the magnetite crystal itself serving as monochromator. The measured values are compared with those of other observers and the theoretically expected values. These are found to agree fairly well within the limits of accuracy of the measurements and existing knowledge of the wave function of the iron 3*d* shell. The two techniques were used also to determine the average polarization (32 percent) as seen by a $1/v$ detector in a beam of reactor neutrons emerging from a 4 cm thick polarizing block of iron.[1] Problems and techniques associated with the measurement of the average polarization of a continuous spectrum are discussed. A simplified experimental treatment of the problem of beam "hardening" is described. A description is given of the use of the magnetic resonance method in conjunction with a single crystal magnetite analyzer for the measurement of neutron polarization.

[1] This information is pertinent to an associated project on the capture of polarized neutrons by polarized nuclei.

Q3. Recent Measurements on the Lowest Neutron Scattering Resonance in Cobalt. F. G. P. SEIDL, *Brookhaven National Laboratory.**—Using the Brookhaven fast chopper, the variation of neutron transmission $T(E)$ with energy E has been measured for two thicknesses of cobalt. The energy range included the lowest cobalt resonance, and the resonance peak was observed at 134 ± 2 ev which is somewhat higher than has been published previously.[1] The effect of experimental resolution was largely eliminated by considering the integral over energy of $1-T(E)$; this can be expressed in terms of a single-level Breit-Wigner formula. Previous experiments[2] have shown this resonance to be predominantly scattering; accordingly, by assuming the resonance to be entirely scattering, a peak cross section may be computed for each of the two possible spin states. One of these is consistent with the measurements on each thickness; i.e., $j=3$ for the compound nucleus. The corresponding level width comes out $\Gamma=5.5\pm0.5$ ev. No corrections were made for Doppler broadening which is $\Delta=0.48$ ev, Δ being the half-width at $1/e$ of maximum.

* Work carried out under contract with the U. S. Atomic Energy Commission.
[1] W. W. Havens, Jr., and L. J. Rainwater, Phys. Rev. **83**, 1123 (1951); A. W. Merrison and E. R. Wiblin, Proc. Roy. Soc. (London) **A215**, 278 (1952).
[2] F. G. P. Seidl, Phys. Rev. **75**, 1508 (1949); Harris, Muehlhause, and Thomas, Phys. Rev. **79**, 11 (1950).

Q4. Doppler Effect in the Slow Neutron Resonance of Rhodium.* H. H. LANDON, *Brookhaven National Laboratory.*—The variation in transmission of a rhodium foil to 1.26-ev neutrons has been measured as a function of foil temperature using the BNL crystal spectrometer. A change in transmission of approximately two percent per 100 degree temperature change has been observed over a temperature range from 120°K to 860°K. After correction for instrument resolution and Doppler, a peak cross section of 4850 ± 200 barns results as compared to the predicted $\sigma_0=5000\pm200$ barns of Sailor.[1] Comparison with the theory of Bethe and Placzek[2] as extended by Lamb[3] will be made.

* Research supported by the United States Atomic Energy Commission.
[1] V. L. Sailor, Phys. Rev. **91**, 53 (1953).
[2] H. A. Bethe and G. Placzek, Phys. Rev. **51**, 450 (1937).
[3] W. E. Lamb, Jr., Phys. Rev. **55**, 190 (1939).

Q5. Determinstion of Scattering Resonance Parameters from the Total Cross Section. W. Y. KATO,* D. J. HUGHES, AND J. S. LEVIN, *Brookhaven National Laboratory.*†—An analysis has been devised to obtain $g\Gamma_n$ from the total cross section of a resonance even when capture predominates. It is found possible to determine $g\Gamma_n$ by measuring the variation of the total cross section with energy away from resonance where the interference effect from resonance and potential scattering predominates. The interference or cross-term effect decreases as $1/\Delta E$ whereas the resonance effect decreases as $1/\Delta E^2$, therefore, this analysis may be used even though the resonance is mostly capture. The value $g\Gamma_n$ for the 4.90-ev level in Au has been determined to be 8.6×10^{-3} ev in reasonable agreement with the value of 10×10^{-3} ev obtained by Landon and Sailor.[1] For the 7.75-ev level in Hf^{178} Γ_n has been found to be 55×10^{-3} ev which is in good agreement with the value obtained by using a thick and thin sample analysis. The present method is applicable for relatively isolated resonances and can be used at energies where insufficient resolution renders the usual methods inapplicable.

* Now at Argonne National Laboratory, Lemont, Illinois.
† Work carried out under contract with the U. S. Atomic Energy Commission.
[1] H. Landon and V. Sailor (private communication).

Q6. Neutron Binding Energy in Bi^{210}. C. G. ANDRE AND J. R. HUIZENGA, *Argonne National Laboratory.*—Several authors[1] have suggested that the 0.5-Mev energy discrepancy in the closed energy cycle, $Po^{210}-Pb^{206}-Pb^{207}-Pb^{208}-Pb^{209}-Bi^{209}-Bi^{210}-Po^{210}$, results from the measured neutron binding energy in Bi^{210} [from (d, p) and (n, γ) reactions in Bi^{209}] being underestimated. Therefore, an independent value of the binding energy of a neutron in Bi^{210} is calculated from the experimental $Bi^{209}(p, 2n)Po^{208}$ threshold[2] and existing decay data. It can be shown readily that, $E_n(Bi^{210})=E_{n-H}1(0.78)+E_n(Tl^{205})+E_n(Tl^{206})+E_\beta(Tl^{206})+E_\alpha Po^{206}-E_\alpha Po^{210}$

$-E_\beta(\mathrm{Tl}^{204})-E_\beta(\mathrm{Bi}^{210})-E_{Th}[\mathrm{Bi}^{209}(p,\ 2n)\mathrm{Po}^{208}]$. Substitution of the best available data in this equation gives a value of 4.19 ± 0.16 Mev for the Bi^{210} neutron binding energy.

[1] Huizenga, Magnusson, Simpson, and Winslow, Phys. Rev. **79**, 908 (1950); Kinsey, Bartholomew, and Walker, Phys. Rev. **82**, 380 (1951); J. A. Harvey, Can. J. Phys. **31**, 278 (1953).
[2] Andre, Ramler, Rauh, Thorn, and Huizenga (previous abstract).

Q7. Direct Integration of the Neutron Transport Equation.* J. HELLER AND H. KELLER, *New York University.*—The distribution of neutrons in a moderator or shield is governed by the Boltzmann equation which, under assumptions which are frequently valid, reduces to the transport equation. It is proposed to solve this equation directly, for some simple one-dimensional geometries, with the aid of a high-speed digital computer. In particular we are first considering a plane shield of finite thickness symmetrically placed about a plane fission spectrum source of zero thickness. The shield may consist of several regions each of which is composed of different compounds. It seems probable that the method is applicable to spherical regions and could be adapted to reactor problems.

* This work is being carried on at the U. S. Atomic Energy Commission Computing Facility at New York University.

Q8. Nuclear Energy Surface and Isotopic Mass Values. J. R. STEHN, *Knolls Atomic Power Laboratory.**—Based on isotopic masses and radioactive decay schemes, a plot has been made of nuclear mass M *vs* charge Z for each total nucleon number A and the position of the minimum estimated to be at Z_0. Z_0 is a smooth function of A, the values lying on the same curve whether from even-even, odd-odd, or odd A nuclides. The over-all plot of $Z_0(A)$ shows bends at the expected closed shells where Z or N is 20, 28, 50, 82, or 126 and shows irregularities near $Z=41$, $N=54$, $Z=64$, and $N=85$ which may be merely the result of incorrect nuclear data or assignments. This plot is the basis of the line of maximum beta stability on the General Electric Chart of the Nuclides. Since actual stable nuclides are seldom at the exact minima of M *vs* Z curves, and since there are well-known effects differentiating even-even, odd-odd, and odd A nuclides, experimentally measured packing fractions are bound to vary somewhat irregularly with mass number. A smoothed-out packing fraction curve, adjusting the foregoing effects to fit the minima of the even-even nuclides, will be shown.

* Operated by the General Electric Company for the U. S. Atomic Energy Commission.

Q9. Harmonic Mean Energy of the Nuclear Photoeffect. J. S. LEVINGER, *Louisiana State University.*—Levinger and Bethe[1] used sum rules to determine the harmonic mean energy for electric dipole photon absorption as

$$W_H = 5\hbar^2/2MR^2 = 50A^{-1}\ \text{Mev},$$

assuming ordinary forces between the nucleons and no correlations among the nucleons. This value is considerably smaller than that calculated from Burkhardt's results[2] based on the independent particle model (IPM) for neutrons in Cu^{63}. The discrepancy is the result of correlations, present even in the IPM, caused by the Pauli exclusion principle. Calculations with a Fermi gas model show that Pauli principle correlations increase the sum-rule value of W_H by about a factor of two. Calculations of W_H for several nuclei are in progress using IPM wave functions for a square well. A similar discrepancy between the sum-rule results and the direct calculation of $\bar{W}$ is also resolved by including the Pauli principle correlations in the sum-rule calculation.

[1] J. S. Levinger and H. A. Bethe, Phys. Rev. **78**, 115 (1950).
[2] J. L. Burkhardt, Phys. Rev. **91**, 420 (1953).

Q10. Ionization Yields for Fission Fragments. GLENN H. MILLER AND LLOYD O. HERWIG, *Iowa State College.*—Fission fragment mass and velocity distributions previously derived from data obtained from double ionization chambers using argon plus CO_2 disagree with other measurements of these distributions.[1] These differences were explained in terms of an ionization defect for argon. The ionization defect is thought to result from energy transfer through elastic collisions and hence should be a function of the atomic mass of the gas. In this experiment, an investigation was made of the relative defects in He, Ne, A, Kr, A plus CO_2, and A plus N_2. Ionization distributions were obtained for fission and alpha particles using a parallel-plate gridded chamber employing electron collection. A natural uranium film was irradiated with $d-d$ reaction neutrons. Comparison of the most probable pulse voltages for fission fragments with those of alpha particles, combined with known alpha energies, gave the so-called fission energies. These energies and associated defects are presented for the gases mentioned. It appears that part of the defect previously attributed to pure argon may be the result of molecular effects of small percentages of CO_2 customarily added to argon.

[1] R. B. Leachman, Phys. Rev. **87**, 444 (1952).

Q11. Origin of Anomalous Abundances of the Elements in Giant Stars. A. G. W. CAMERON, *Iowa State College.*—Following the exhaustion of hydrogen in a giant star, the core is expected to contract and the central temperature to rise until thermonuclear reactions with the helium set in. At approximately 1×10^8 °K the reaction $C^{12}(\alpha, n)O^{16}$ will proceed rapidly. It is assumed that C^{13} has an equilibrium abundance of about 20 percent of the carbon plus nitrogen nuclei in the Bethe cycle in order to explain the large carbon abundance in stars with R and N spectra. The resulting neutrons will be captured by the surrounding material in proportion to the products of cosmic abundances times capture cross sections (at $E_n\sim10$ kev). The latter quantities are poorly known in the most abundant light elements, but a crude calculation gives the formal result that a typical heavy nucleus ($A\sim100$) will capture about 20 neutrons. The "magic number" nuclei Sr^{88}, Y^{89}, Zr^{90}, Ba^{138}, La^{139}, Ce^{140}, Pr^{141}, Nd^{142}, and Pb^{208} will act as sinks for the collection of heavy nuclei. Most of these elements have been observed to have anomalously large abundances in stars with S spectra and in "BaII" stars. The formation of a large amount of technicium (observed in some S spectra) in equilibrium with neighboring elements also follows from this theory.

Q12. Annihilation of Positrons in Flight.* H. W. KENDALL AND MARTIN DEUTSCH, *M.I.T.*—The cross section for annihilation of positrons in flight has been measured for positron energies of 0.765, 1.02, 2.2, and 3.33 Mev. The method used was basically that of Shearer and Deutsch.[1] Positron energies were selected by means of a magnetic lens monochromator and a differential energy interval of about 0.1 Mev defined by the pulse height from an anthracene crystal in which the positrons were annihilated. The annihilation radiation was detected in a scintillation counter biased to record only quanta above 0.51 Mev. The angular distribution of the annihilation radiation is in good agreement with that given by Heitler,[2] modified by the scattering of the positrons in anthracene. The total differential cross section at all energies agrees with the theoretical value[2] within the accuracy of the experiment, estimated to be about ±5 percent.

* This work was assisted in part by the joint progrm of the U. S. Office of Naval Research and the U. S. Atomic Energy Commission.
[1] J. W. Shearer and M. Deutsch, Phys. Rev. **82**, 336 (1951).
[2] W. Heitler, *The Quantum Theory of Radiation* (Oxford University Press, Oxford, 1944), pp. 204–208.

Q13. The Čerenkov Effect and the Dielectric Constant. S. M. NEAMTAN, *University of Manitoba.*—A quantum mechanical theory of the Čerenkov radiation is developed wherein the refractive medium is treated not as a continuum, but as an

aggregation of atoms. The atoms and the electromagnetic field are considered as forming a single system which interacts with an incident charged particle. The Čerenkov radiation arises in first-order transitions induced by this interaction. The nature of this process suggests a quantum mechanical definition of the dielectric constant with the aid of which the theory yields the well-known properties of the Čerenkov radiation. The definition of the dielectric constant is shown to lead to the same expression for this quantity as is given by the Kramers-Heisenberg dispersion formula.

SATURDAY AFTERNOON AT 1:30

Eckhart 133

(R. S. MULLIKEN presiding)

Invited Paper

R1. Isotope Shift in the Spectra of Some Elements of Intermediate Atomic Number. HACK ARROE, *University of Wisconsin.* (30 min.)

Optical and Chemical Physics

R2. The Continuous Emission Spectra of Kr and Xe in the Vacuum Ultraviolet Region. YOSHIO TANAKA AND MURRAY ZELIKOFF, *Air Force Cambridge Research Center.*—Using the Ratheon Manufacturing Company's "Microtherm" as a power supply, we studied the emission spectra of Kr and Xe in the vacuum ultraviolet region. When the pressure was increased to about 10 mm Hg, the first resonance lines of these elements (Kr, 1236A; Xe, 1470A) were considerably broadened towards the longer wavelength side, that is, to about 1330A and 2200A, respectively. For the emission mechanisms of the continua, the same explanation can be applied as in the case of absorption of the resonance lines of Xe which was observed by McLennan and Turnbull.[1]

[1] J. C. McLennan and R. Turnbull, Proc. Roy. Soc. (London) **A129**, 266 (1930); **133**, 683 (1933).

R3. Forbidden Line in the Spectrum of PI. S. MROZOWSKI, *University of Buffalo.*—The spectrum of PI was excited by high-frequency oscillations in presence of several millimeters of helium gas. The pressure of the vapor was varied by heating an appendix containing highly purified red phosphorus. The experiments were undertaken to check the feasibility and limitations of this method for excitation of spectra in light elements. Difficulties were experienced due to an exceedingly strong emission of the molecular spectrum of PO (bands around λ6390, 5960, 5580, and 5250, observed previously in a flame spectrum by Rump and others) at slightest contaminations. When the impurities were eliminated the line λ5333 [$^3P_1^0 \rightarrow {}^4S_1^0$ both levels belonging to the configuration $(3p)^3$] was identified in the spectrum and found to be emitted with a reasonably high intensity (½-hr exposures on a Bausch & Lomb spectrograph) at vapor pressures for which the PI spectrum begins to weaken giving way to the molecular (P_2) emission. The line $^3P_1^0 \rightarrow {}^4S_1^0$ does not appear on these spectrograms, this being in agreement with the general trend as observed in the corresponding spectra of SbI and AsI[1] and with the theoretical expectations.[2]

[1] M. Hults and S. Mrozowski, Phys. Rev. **86**, 587 (1952).
[2] Shortley, Aller, Baker and Menzel, Astrophys. J. **93**, 178 (1941).

R4. Forbidden Lines in the Spectrum of Bi II. C. D. COLE AND S. MROZOWSKI, *University of Buffalo.*—The spectrum of bismuth was excited by high-frequency oscillations under well controlled conditions (temperature and pressure), the apparatus being an improved version of the one used in the study of the Bi I spectrum.[1] Several forbidden lines corresponding to transitions between levels all belonging to the configuration $(6p)^2$ in Bi II were identified and found to be the strongest at vapor pressures of bismuth somewhat lower than those for which the forbidden lines of Bi I appear with greatest intensity. The lines found are: λ3241 ($^1S_0 \rightarrow {}^3P_1$) a pure magnetic dipole line similar to the well-known line λ4618 of PbI, λ4850 ($^1D_2 \rightarrow {}^3P_1$) and λ5914 ($^1D_2 \rightarrow {}^3P_2$) both mixed character (electric quadrupole and magnetic dipole), and finally a line λ7504 ($^3P_1 \rightarrow {}^3P_0$) of a pure magnetic dipole type for the first time observed as a nonintercombination transition. A line is observed at λ3683, the expected position for the pure electric quadrupole transition $^1S_0 \rightarrow {}^3P_2$, but its excitation conditions and too high intensity make it certain that it is not the forbidden line sought. A study of the hyperfine structure of the lines found is in progress.

[1] S. Mrozowski, Phys. Rev. **69**, 169 (1946).

R5. Raman and Infrared Spectra of $C^{13}H_3I$. FORREST F. CLEVELAND, RICHARD B. BERNSTEIN, AND FRED L. VOELZ, *Illinois Institute of Technology.*—Raman (liquid) and infrared (liquid and gas, with KBr and NaCl prisms) spectra have been obtained for two mixtures of $C^{13}H_3I$ (9.3 and 61 atom percent) and $C^{12}H_3I$, and from these the vibrational spectrum of $C^{13}H_3I$ has been deduced. In the Raman spectrum, only $\nu_2(a_1)$—the C−I stretching frequency—could be resolved from the $C^{12}H_3I$ lines; the isotopic shift was 17.7±0.5 K (K = kaysers = cm^{-1}). In the infrared spectrum (gas), five isotopic shifts were obtained; they were: $\nu_1(a_1)$10±3, $\nu_3(a_1)$5.5 ±1.0, $\nu_3(a_1)$16.1±1.0, $\nu_5(e)$4.6±0.6, and $\nu_6(e)$3.7±0.3 K. For the remaining fundamental, $\nu_4(e)$, the shift was obtained by use of the Redlich-Teller product rule; the value was 9.4±2.3 K. Analysis of the perpendicular bands yielded, with the aid of microwave data, values of the rotational constants, Coriolis interaction constants, and band origins for the $\nu_6(e)$, $\nu_5(e)$, and $\nu_4(e)$ bands of $C^{12}H_3I$ and $C^{13}H_3I$, though the values for the $\nu_4(e)$ band of $C^{13}H_3I$ are only estimated values since the sub-bands were not resolved in this case.

R6. Raman and Infrared Spectra of Dimethyltriacetylene. ALFONS WEBER, FORREST F. CLEVELAND, AND SALVADOR M. FERIGLE, *Illinois Institute of Technology.*—The infrared spectrum of $H_3C-C\equiv C-C\equiv C-C\equiv C-CH_3$ (2,4,6-octatriyne) has been obtained in the region 400–4000 K, for both CCl_4 and CS_2 solutions, with a Perkin-Elmer double beam spectrometer with NaCl optics and a Beckman IR-2 spectrometer with KBr optics. The agreement with results privately communicated by E. R. H. Jones is good. Except for the $-C\equiv C-$ stretching frequency in the series of molecules $H_3C-(C\equiv C)_n$

$-CH_3$ ($n=2$ to 6),[1] no infrared spectral data could be found in the literature. The Raman spectrum has been obtained with a Hilger E-612 spectrograph with exchangeable cameras, utilizing previously described methods.[2] The Raman shifts obtained in CCl_4 solution are: 337, 342, 483, 1074, 1129, 1377, 1522, 2148, 2179, 2227, 2775, and 2917 K.[3] Work on the Raman spectrum in CS_2 solution and the determination of reliable depolarization factors is in progress.

[1] Cook, Jones, and Whiting, J. Chem. Soc. **1952**, 2883.
[2] F. F. Cleveland, J. Chem. Phys. **11**, 1, 227 (1943); **13**, 101 (1945).
[3] K = kaysers = cm^{-1} [see J. Opt. Soc. Am. **43**, 410 (1953)].

R7. Rotational Excitation of Momonuclear Molecules.* S. STEIN, E. GERJUOY, AND T. HOLSTEIN, *University of Pittsburgh and Westinghouse Research Laboratories.*—Cross sections are calculated for excitation of rotation of diatomic homonuclear molecules by very slow electrons (energy ~0.1 ev) with neglect of exchange. It is assumed that the excitation results from interaction of the electron with the quadrupole field of the molecule; for this type of potential, use of the Born approximation is defensible at these low energies. For kinetic energies large compared to the separation of rotational levels, the cross section approaches a constant value $\sim 10^{-17}$ cm^2, using measured quadrupole moments.[1] The average fractional energy losses per collision in N_2 and H_2 are evaluated and are in moderately good agreement with recent measurements.[2]

* This research was supported in part by the U. S. Air Force.
[1] W. V. Smith and R. Howard, Phys. Rev. **79**, 132 (1950).
[2] R. W. Crompton and D. J. Sutton, Proc. Roy. Soc. (London) **A215**, 467 (1952).

R8. Threshold Field *vs* Temperature Slope for Paraelectric-Ferroelectric Change in $BaTiO_3$. A. DEBRETTEVILLE, JR., AND E. D. HARRIS, *Signal Corps Engineering Laboratories.*—Recent work of Merz[1] and others has shown that the paraelectric-ferroelectric phase change in $BaTiO_3$ is a first-order transition. A relation[2] developed by one of us for the slope of the threshold field E_t *vs* the temperature for the antiferroelectric to ferroelectric phase transition in lead zirconate can be applied to calculate the paraelectric-ferroelectric phase transition in $BaTiO_3$. The equation of the initial slope is $(\partial E_t/\partial T)_{E=0} = \Delta H/T_c N v \Delta P$, where ΔH is the heat of transition, T_c the Curie temperature, Nv the atomic volume, and ΔP the jump in spontaneous polarization. Using our single crystal oscilloscope data for $\Delta H/T_c$ obtained from the slope of the free energy *vs* temperature, we obtain 1.06 kv/cm°C compared to an observed 1.26 kv/cm°C. Calculation of the slope from the above formula using the data of Merz' crystal[1] and taking 46.6 cal/mole for ΔH gives 0.74 kv/cm°C compared to his experimental value of 0.70 kv/cm°C, while the Devonshire theory, using Merz' data[1] gives 0.53 kv/cm°C.

[1] W. J. Merz, Phys. Rev. 513–517 **91**, (1953).
[2] A. deBretteville, Jr., Phys. Rev. 213(A) **91**, (1953).

R9. Dielectric Absorption of Liquid Crystalline Biaxial Molecules. C. KIKUCHI, *Electricity Division, Naval Research Laboratory.*—To account for the anisotropic absorption of liquid crystals in a steady magnetic field,[1] Debye's theory of dielectric absorption was generalized.[2] The molecules of liquid crystals that have been investigated are characterized by two axes, the electric and the magnetic. Consequently the steady magnetic field tends to freeze the motion of the magnetic axis, whereas the electric axis will attempt to follow the electric field. In addition, the molecular axes will undergo rotational Brownian motion. The diffusion equation, to which the above processes lead, is similar to the one given by Gans and Perrin.[3] The solution of the equation for various cases will be discussed.

[1] E. F. Carr and R. D. Spence, Phys. Rev. **90**, 339 (1953).
[2] P. Debye, *Polar Molecules*, p. 77.
[3] R. Gans, Ann. Physik **86**, 628 (1928); F. Perrin, J. phys. **5**, 497 (1934).

R10. A New Method of Calculation of Effective Ionic Radii of Lanthanides. N. EFREMOV, *1061 Intervale Avenue, New York, N. Y.*—The effective ionic radii of lanthanides may be obtained from the ionic radius of lanthanum. According to our method of calculation of effective ionic radii[1] the radius of lanthanum may be determined by means of the general formula: $R(\mathrm{La}) = (n \times K)P$, where n is the principal quantum number, K is the matrix number corresponding to the given ions, and P(portion) is a constant ($P = 0.01462369$A) which can be derived from the Rydberg constant. Thus $R(\mathrm{La}) = (6 \times 14)P = 84P$; $R(\mathrm{La}) = 1.22$A. The formula for calculation of the ionic radii of lanthanides[2] is the following: $R = 84P - (Z-57)P$, where Z is the atomic number of any lanthanide and 57 is the atomic number of lanthanum, e.g., $R(\mathrm{Gd}) = 84P - (64-57)P = 77P = 1.11AE$. The number of portions directly decreases by one with the direct increase of the atomic number of the rare earth element by one. Values calculated by means of this formula are in substantial agreement with the values determined by V. M. Goldschmidt (who found $R(\mathrm{La}) = 1.22$A, $R(\mathrm{Gd}) = 1.11$A) and by K. Stockar.

[1] Paper given at the September 1953 meeting of the American Physical Society in Albuquerque, New Mexico.
[2] For the crystalline lattices of the NaCl type.

SATURDAY AFTERNOON AT 1:30

Oriental Institute

(E. M. LONG presiding)

Cryogenics; Theoretical Physics

T1. Hall Effect in Bismuth at Low Temperatures.* LAIRD C. BRODIE, *Northwestern University.*—The Hall effect and magnetoresistance of bismuth monocrystals have been measured at 14°K as a function of magnetic field strength to 18 kilogauss. The trigonal axis was parallel to the specimen axis, and the magnetic field was perpendicular to a binary axis. Using residual resistance and magnetoresistance as a criterion of perfection and purity, the best crystals proved superior to those of Gerritsen and de Hass,[1] and compared favorably with those grown by Schubnikow and de Haas, and Alers and Webber. For the orientation measured, the Hall coefficient is negative and increases in magnitude monotonically to 6500 emu at 18 kilogauss. The slope of the curve is less between 10 and 12 kilogauss, and also between 16 and 18 kilogauss, corresponding to the anomalies at these same field strengths in the magnetoresistance curve at 14°K. These results indicate that, while there is a parallelism between the field dependence of the Hall coefficient and the de Haas-van Alphen effect, this parallelism is of the same character as that between magnetoresistance and de Haas-van Alphen effect, rather than that found by Gerritsen and de Haas.[1]

* Supported by the National Science Foundation.
[1] Gerritsen and de Haas, Physica **7**, 802 (1940).

T2. A Strong-Field Induced Paramagnetic Anomaly in $NiSiF_6 \cdot 6H_2O$. WARREN E. HENRY, *Naval Research Laboratory.*—The Brillouin mathematical simplification of the space quantized dipole model has been previously tested up to practical (99.5 percent) saturation[1] for substances chosen so as to minimize interionic interaction. It was pointed out that this Brillouin dependence requires linearity of the pertinent energy levels with field. There has been considerable speculation on the causes and consequences of nonlinear field dependence of these energy levels.[2] We have chosen a case (nickel fluosilicate) in which the higher power terms may be significant at attainable high fields. The magnetization of nickel fluosilicate has been carried out in the liquid helium range (1.3–4.2°K) and in magnetic fields up to 60 000 gauss. For H/T about 5000 gauss/deg, the magnetic isotherms practically superimpose to within about 1 percent. However, for high values of H/T, this apparent superposition is lost and for a given value of H/T, the lower the temperature, the lower the moment. The total moment separation is greater than 6 percent for 14 000 gauss/deg. The introduction of a suitable quadratic dependence of the energy levels gives qualitatively the moment branching which is observed experimentally.

[1] W. E. Henry, Phys. Rev. **88**, 559 (1952).
[2] J. H. Van Vleck (private communication); E. F. Carr and C. Kikuchi, Phys. Rev. **80**, 1107 (1950); O. M. Jordahl, Phys. Rev. **45**, 87 (1934).

T3. Some Thermodynamic Properties of $Mn(ND_4)_2(SO_4)_2 \cdot 6D_2O$ Below 1°K. J. W. T. DABBS AND L. D. ROBERTS, *Oak Ridge National Laboratory.*—In connection with the Mn^{55} nuclear polarization experiments using $Mn(ND_4)_2(SO_4)_2 \cdot 6D_2O$, reported elsewhere at this meeting, we have made measurements of the magnetic moment and absolute temperature of this salt as a function of final field in adiabatic demagnetizations from fields of 10–17 kilogauss and temperatures of ~1.2°K. These measurements have been carried out over a final field range $0 < H_f \leq 4560$ gauss, and a temperature range 0.119°K–0.35°K. γ-ray heating was used to establish one point at 0.201°K of the $T-H$ relation with M as the "thermometric parameter," and the region was covered using the equation

$$T_1 - T_2 = \int_{H_1}^{H_2} (\partial M/\partial S)_H dH.$$

Calibration of the γ-ray heat input was obtained by direct comparison with a measured electrical heat input in the region 0.4–0.5°K. This approach has several advantages. A curve of measured specific heat *versus* magnetic temperature in the region 0.3–0.8°K is presented.

T4. The Interaction between Two Nucleons at Low Energies.* DAVID FELDMAN, *The University of Rochester.*—We have investigated the problem of the derivation of a two-nucleon Schrödinger equation from quantum field theory, taking into account only those mesons which are exchanged between the nucleons. One expects that the two-particle Schrödinger picture will be useful if the energy (less rest energy) is small ($\sim\mu^2/M$), and if the important matrix elements are those which couple states of small momenta ($\sim\mu$). Our procedure has been to go over to Fock space in the manner of Tamm and Dancoff, and then to decouple the two-particle T.D. amplitude from all the others by a series of canonical transformations (the over-all coupling is assumed weak). Unlike the methods developed by Lévy-Klein and Bethe-Salpeter, the characteristic difficulties such as energy-dependent and non-Hermitian potentials are avoided. We have thus far used the formalism to analyze the second- and fourth-order adiabatic nuclear forces for the neutral scalar and charge-symmetric *ps-ps* theories. In this approximation, there is agreement with the results of Lévy-Klein, as is expected. It should be emphasized that the "non-adiabatic velocity-dependent" corrections of Lévy-Klein appear explicity, in our treatment, as the adiabatic higher-order ladder corrections to the second-order potential, and cannot be dropped, as has been suggested.

* This research was supported by the U. S. Atomic Energy Commission.

T5. Positon Theory without "Holes." F. J. BELINFANTE, *Purdue University.*—By modification of Fock's formalism of second quantization one can formulate positon theory avoiding Dirac's "hole" concept altogether, and one can ascribe wave functions in configuration space to states with finite numbers of positons and negatons. The wave functions are no arbitrary functions, but are superpositions of positive free-electron energy states only. Explicit formulas can be given for the superposition of many-free-electron states describing the "bound" electron vacuum or the bound electron of a hydrogen ion or atom, and for the operation of the quantized ψ-function on many-electron wave functions. Operators for observables are defined by the Furry-Oppenheimer prescription. If one wants to treat the bound vacuum as a no-electron state and use the total electron energy for judging energy signs, then the Dirac-Heisenberg-Kramers definition of operators for observables must be used, and a trivial infinity thus introduced for certain observables must be subtracted. Problems of vacuum polarization etc. can be treated by this formalism, which differs from the conventional hole theory not by its essential contents but by its less controversial formulation allowing an easier interpretation in a language similar to that used in Schrödinger's wave mechanics.

T6. A New Modification of Classical Electromagnetic Theory. A. SCHILD, *Carnegie Institute of Technology.*—Modifications of classical electrodynamics have been suggested by Bopp,[1] Peierls and McManus,[2] Feynman,[3] and others.[4] A new modification has been studied in which the rest mass of a charged particle is treated as a variable of the motion. A new action principle for classical electrodynamics been obtained which is simpler than the usual one. In this new action principle, the rest mass of a particle is varied as well as its coordinates. The constancy of the rest mass then follows as a consequence of the equations of motion. Modifications of the old action principle can yield finite electromagnetic rest masses which are, however, determined uniquely by the particular "structure function" used in the modification; thus, for example, this unique rest mass can be fitted to that of electrons or of protons, but not to both. Similar modifications of the new action principle give purely electromagnetic rest masses to all charged fundamental particles. In this new modification of electrodynamics, particles interacting at small distances no longer have constant rest masses.

[1] F. Bopp, Ann. phys. **42**, 573 (1943).
[2] R. E. Peierls and H. McManus, Proc. Roy. Soc. (London) **A195**, 323 (1948).
[3] R. P. Feynman, Phys. Rev. **74**, 939 (1948).
[4] See review article by H. Hönl, Erge. exakt. Naturw. **26**, 291 (1952).

T7. On a Class of Solutions of Maxwell's Equations.* G. E. HUDSON, *New York University*, AND D. H. POTTS, *Navy Electronics Laboratory.*—The usual plane wave solutions of Maxwell's electromagnetic equations in a homogeneous isotropic medium are exceedingly special in that the phases of the electric and magnetic vectors differ by a constant and their amplitudes are in a constant ratio. This suggests that one should investigate plane wave solutions in which this specialization is not made at the outset. Maxwell's equations then furnish the necessary condition that the phases of the two vectors are not only functionally related but their phase difference satisfies a certain nonlinear ordinary differential equation of second order. Since the usual plane wave solutions correspond to singular solutions of this equation, the question of the stability of the usual solutions in an important one and will be discussed. The amplitude ratio, too, is seen to depend on this phase difference, indicating that the concept of a characteristic impedance of the medium would need to be generalized for use with such waves. If, in addition, one considers certain generalized solutions of this kind which do not necessarily represent plane waves, a further consequence is that the spatial part φ of the phase function of the waves exactly satisfies an eikonal equation, and the electric and magnetic vectors are orthogonal to each other and to the direction of propagation of the wave.

* Work performed while Professor Hudson was in residence at the Navy Electronics Laboratory, summer of 1953.

T8. A Kinetic Approach to Collision Processes in Gases. I.* M. KROOK AND P. L. BHATNAGAR, *Harvard University*, AND E. P. GROSS, *M.I.T.*—A kinetic theory approach to collision processes in gases is presented. This approach is adequate for the unified treatment of many of the dynamic properties of gases over a continuous range of pressures from the Knudsen limit at low pressures to the high-pressure limit where the aerodynamic equations are valid. It is also possible to satisfy correct microscopic boundary conditions. The method consists in altering the collision terms in the Boltzmann equation so that a mathematically more tractable equation results. The modified collision terms are constructed so that each collision conserves particle number, momentum, and energy; other characteristics such as persistence of velocities and angular dependence may be included. An extreme case of the general model involves the establishment of equilibrium in a time equal to the mean time between collisions; another extreme case involves an infinite relaxation time.

* Sponsored by the U. S. Office of Naval Research, the U. S. Army Signal Corps, and the U. S. Air Force.

T9. A Kinetic Approach to Collision Processes in Gases. II.* E. P. GROSS, *M.I.T.*, AND M. KROOK, *Harvard University.*—The method described in the previous abstract is applied to the study of the small amplitude oscillations of one-component ionized and neutral gases. The initial-value problem in unbounded space is solved in detail for a simple collision model involving the assumption of a collision time independent of velocity. For uncharged gases, there results the corrected adiabatic limiting law for sound-wave propagation at high pressures. In addition, one obtains a theory of the absorption and dispersion of sound for arbitrary pressures. For ionized gases the difference in the nature of the organization in the low-pressure plasma oscillations and in high-pressure sound-type oscillations can be studied. At high pressures it is not permissible to treat an ionized gas as a one-component system; the electron ion coupling must be studied more carefully. The approach of the previous abstract is therefore generalized to treat many-component systems and is applied to the treatment of the oscillations of ionized gases and to the propagation of sound in mixtures of neutral gases.

* Sponsored by the U. S. Office of Naval Research, the U. S. Army Signal Corps, and the U. S. Air Force.

T10. On the Universal Fermi Interaction. E. J. KONOPINSKI, *Indiana University.* (30 min.)

SUPPLEMENTARY PROGRAMME

SP1. Interaction of μ^- Mesons with I^{127}. LESTER WINSBERG, *University of Chicago.**—One-kilogram samples of iodine were exposed to the negative muon beam from the Chicago synchrocyclotron.[1] Radiochemical purification revealed the presence of Te isotopes of mass 125 and 127 in relatively high yield, Sb isotopes of mass 122 and 124 in low yield, and the absence of isotopes of mass 117 and 118 and Sb isotopes of mass <121. The intensity of the muon beam was not large enough to permit the detection of any Sn isotopes. These results indicate that the average number of nucleons emitted per muon captured is much smaller than is the case for pion capture[2] and that the probability of charged particle emission is low in agreement with the counter studies of Conforto and Sard[3] and the photographic plate work of Fry.[4] Thus further proof is given for the weak nature of the interaction of negative muons with nuclear matter.

* To be given at the end of Session B if the Chairman rules that time permits.
[1] L. Winsberg, paper B8 in this *Bulletin*.
[2] L. Winsberg, Phys. Rev. **90**, 343(A) (1953).
[3] A. M. Conforto and R. D. Sard, Phys. Rev. **86**, 465 (1952).
[4] W. F. Fry, Phys. Rev. **85**, 676 (1952).

SP2. Observation of Diffusion Effects Occurring During the Artificial Aging of Dual Layer Bi-Metal Films.* RICHARD B. BELSER AND MARGARET C. CHESTER, *Georgia Institute of Technology.*†—During the artificial aging by heating of dual-layer metal films in the infrared vacuum oven films of the colored metals, copper and gold were observed to disappear at certain temperatures by intermingling with their partner films. Gold evaporated onto an indium film disappeared at the temperature of the substrate during the evaporation process. Paired with silver, the gold disappeared at 120°C and 175°C when it, respectively, overcoated and undercoated the silver. For gold and copper paired with aluminum, there was a distinct difference between the temperatures of disappearance according to whether they undercoated or overcoated the aluminum. In the undercoating position, these temperatures were 190°C and 260° for gold and copper, respectively, whereas in the overcoating position the temperatures of 480°C and 495°C, respectively, were recorded. The differences in temperatures of intermingling, in accordance with position in regard to the aluminum film, imply the presence of a barrier on the surface of the aluminum film. Resistance and x-ray data confirm its presence. The barrier remained effective up to temperatures of approximately 450°C and is believed to consist of aluminum oxide formed within the vacuum chamber, at pressures under 8×10^{-6} mm of mercury, during the short interval between successive film depositions.

* Supported in part by the U. S. Signal Corps.
† To be given at the end of Session N if the Chairman rules that time permits.

SP3. Effects of the Alloying Actions of Dual-Layer Bi-Metal Electrodes on the Frequencies of Piezoelectric Quartz Resonators.* RICHARD B. BELSER AND WALTER H. HICKLIN, *Georgia Institute of Technology.*†—Aluminum overcoated separately with silver and gold, and nickel undercoated separately with silver, gold, and copper, have been deposited as electrodes on 6-mc AT-cut quartz resonator blanks. The crystal blanks, after plating by evaporation, sputtering, or electroplating, were mounted and oscillated continuously in Pierce-type oscillators at a constant temperature (48°C). Daily frequency measurements were made. Of the metal pairs examined, only silver plus nickel gave resonators of exceptional stability. These changed only 30 cycles in 180 days. Sputtered gold plus electroplated nickel, on limited tests, showed good stability. The crystals coated with other metal pairs changed hundreds of cycles within 30 days. The behavior of these metal pairs as electrodes, from the standpoint of stable frequency performance of the coated resonators, appeared to correlate with the alloying properties of the metals employed as defined by the known binary alloy phase diagrams. The techniques employed, in conjunction with the studies performed concurrently by resistance and x-ray diffraction measurements, appear to provide an additional means of measuring alloying rates and affinities of suitable metal pairs.

* Supported by the U. S. Army Signal Corps.
† To be given at the end of Session N if the Chairman rules that time permits.

Author Index to Papers Presented at the Chicago Meeting

Ajzenberg, F., W. Franzen, and J. G. Likely—K8
Andre, C. G. and J. R. Huizenga—Q6
——, W. J. Ramler, E. G. Rauh, R. J. Thorn, and J. R. Huizenga—K13
Ang, C. and C. Wert—I4
Arroe, Hack—R1
Aukerman, L. W.—N4
Barschall, H. H.—D1
Beer, A. C., R. K. Willardson, and A. E. Middleton—A7
Belinfante, F. J.—T5
Belser, Richard B. and Margaret C. Chester—N9, SP2
—— and Walter H. Hicklin—SP3
Bennett, W. E., P. A. Roys, and B. J. Toppel—K4
Bernardini, Gilberto—P1
Bessey, William H. and Harold Weisbrod—I12
Bloom, Myer, H. S. Gutowsky, D. W. McCall, and J. G. Powles—G6
Bodansky, D., A. M. Sachs, and J. Steinberger—F8
Bradford, C. E., T. Kikuchi, and W. E. Bennett—H5
Breen, R. J. and A. H. Weber—I11
Briggs, H. B., R. F. Cummings, H. J. Hrostowski, and M. Tannenbaum—A9
Brockhouse, B. M., L. M. Corliss, and J. M. Hastings—I10
Brodie, Laird C.—T1
Burke, W. H., Jr., and W. G. Meinschein—C3
Caird, R. S. and Allan C. G. Mitchell—C5
Cameron, A. G. W.—Q11
Carmichael, H. and J. F. Steljes—B1
Caulton, M., M. Blau, and J. E. Smith—F12
Chinowsky W., A. Sachs, and J. Steinberger—F3
Cleveland, Forrest F., Richard B. Bernstein, and Fred L. Voelz—R5
Cole, C. D. and S. Mrozowski—R4
Cool, R. L., L. Madansky, and O. Piccioni—F6
Cox, Mason C., Jan J. van Loef, and D. A. Lind—K9
Crane, H. R.—H4
Dabbs, J. W. T. and L. D. Roberts—T3
Dalitz, R. H.—B7
Darden, S. E., R. E. Fields, and R. K. Adair—Q1
Davis, R. E. and Colman Goldberg—A14
Dawson, Maynard and George Finn—A12

deBretteville, A., Jr. and E. D. Harris—R8
Dehmelt, H. G., H. G. Robinson, and Walter Gordy—G5
DeLany, B. Pearson, and Paul L. Copeland—L6
Divatia, Ajay S., Robert H. Davis, and R. G. Herb—L8
Dunlap, W. C., Jr., D. E. McMillan, and R. A. Brooks—A2
Eby, F. S., R. D. Hill, and W. K. Jentschke—K12
Efremov, N.—R10
Epstein, A. and H. Fritzsche—I8
Ergen, William Krasny—H2
Famularo, K. F., R. J. S. Brown, H. D. Holmgren, and T. F. Stratton—M5
Feldman, David—T4
Fermi, Enrico—F1
Fisher, R. M., L. S. Darken, and K. G. Carroll—I2
Forro, M.—C1
Galonsky, A., R. Douglas, W. Haeberli, M. McEllistrem, and H. T. Richards—M6
Gell-Mann, Murray—P4
Goldberg, Colman—A13
Goldsmith, G. J.—N5
Gomer, Robert—L2
Goodrich, Max and Wilbur B. Payne—C4
Gove, H. E., A. J. Ferguson, and J. T. Sample—M4
Gross, E. P. and M. Krook—T9
Grossweiner, L. I. and M. S. Matheson—N1
Haas, G. A. and E. A. Coomes—N8
Halsted, R. E. and L. R. Koller—N3
Harman, T. C., R. K. Willardson, and A. C. Beer—A8
Hartzler, A. J. and R. T. Siegel—M7
Hayward, R. W., D. D. Hoppes, and H. Ernst—C8
Heller, J. and H. Keller—Q7
Henry, Warren E—T2
Herwig, L. O., G. H. Miller, and N. G. Utterback—L5
Hildebrand, Roger H.—F9
Hill, David L.—K1
Hintz, N. M., J. M. Blair, and D. M. Van Patter—K5
Holcomb, D. F. and R. E. Norberg—G4
Horton, G. K. and G. E. Tauber—A1
Hudson, G. E. and D. H. Potts—T7
Hurd, F. Kenneth, Mendel Sachs, and W. D. Hershberger—G2
Jastram, P. S.—M9
Johnson, C. H. and C. C. Trail—K3
Kaiser, W. and H. Y. Fan—A3
Kaplon, M. F., G. W. Racette, and D. M. Ritson—B9
Kato, W. Y., D. J. Hughes, and J. S. Levin—Q5
Kendall, H. W. and Martin Deutsch—Q12
Kikuchi, C.—R9
King, D. T., N. Seeman, and M. M. Shapiro—B5
Konopinski, E. J.—T10
Kouba, J. T. and P. L. Copeland—L7
Krook, M., P. L. Bhatnagar, and E. P. Gross—T8
Kruse, P. W. and E. A. Coomes—N7
Kuczynski, G. C.—I3
Landon, H. H.—Q4
Lane, R. O. and D. J. Zaffarano—C9
LeBlanc, J. M., J. M. Cork, and S. B. Burson—C7
Levinger, J. S.—Q9
Lindenbaum, S. J. and Luke C. L. Yuan—F4
Lynch, F. J.—L3
McManus, H., W. T. Sharp, and H. Gellman—K2
Macklin, R. L. and H. E. Banta—K7
Marshall, J., L. Marshall, and V. A. Nedzel—M2
Marshall, L., V. A. Nedzel, and J. Marshall—M3
Miller, Glenn H. and Lloyd O. Herwig—Q10
Motz, Henry T.—K11
Mrozowski, S.—R3
Nachtrieb, N. H.—L1
Nagle, D. E.—F10
Navon, D. and H. Y. Fan—A5
Neamtan, S. M.—Q13
Nedzel, V. A., J. Marshall, and L. Marshall—M1
Nigam, B. P.—B6
Novey, T. B.—C11
Nudelman, Sol and Frank Matossi—N2
Oberly, John J.—A4
Orear, Jay—F7
Oxley, C. L.—M10
Palevsky, H., H. R. Muether, and A. Stolovy—H3
Racette, G. W., M. F. Kaplon, and D. M. Ritson—B8
Raudebaugh, Robert J. and Richard B. Belser—N11
Roberts, J. H., J. Haugsnes, and D. E. Wood—H1
Roberts, L. D. and Seymour Bernstein—D2, D3
Rothstein, J.—A11
Sargent, C. P., M. C. Rinehart, R. C. Cornelius, L. M. Lederman, and K. Rogers—F2
Savitt, Jacob—L10
Schardt, A. W. and Joan P. Welker—C6
Schild, A.—T6
Schneider, E. E.—G1
Schulz, L. G.—I7
Sears, G. W.—I1
Seidl, F. G. P.—Q3
Shapiro, M. M., D. T. King, and N. Seeman—B4
Siegel, R. T. and A. J. Hartzler—M8
Simpson, J. A. and Marcel Schein—P2
Singer, L. S.—G3
Slichter, C. P.—G7
Stanford, C. P., T. E. Stephenson, L. W. Cochran, and S. Bernstein—Q2
Steffen, R. M.—C10
Stehn, J. R.—Q8
Stein, S., E. Gerjuoy, and T. Holstein—R7
Steljes, J. F. and H. Carmichael—B2
Stelson, P. H.—K10
Sternglass, Ernest J.—N6
Stier, P. M., C. F. Barnett, and G. E. Evans—L4
Tanaka, Yoshio and Murray Zelikoff—R2
Tannenbaum, M., G. L. Pearson, and W. L. Feldmann—A10
Thompson, R. W.—P3
Tomizuka, C. T.—I6
v. Krzywoblocki, M. Z.—L9
Voss, J. R., T. R. Palfrey, and R. O. Haxby—F11
Wada, W. W. and D. T. King—B3
Wattenberg, A., B. T. Feld, A. Julian, A. Odian, and L. S. Osborne—B10
Weber, Alfons, Forrest F. Cleveland, and Salvador M. Ferigle—R6
Weddell, James B. and James H. Roberts—K6
Weertman, J. and E. I. Salkovitz—I5
Wiener, B. and G. Groetzinger—I9
Willardson, R. K., A. C. Beer, and A. E. Middleton—A6
Winsberg, Lester—B11, SP1
Woolf, William E. and Richard B. Belser—N10
Yuan, Luke C. L. and S. J. Lindenbaum—F5
Zweifel, Paul F.—C2

Minutes of the Stanford Meeting December 28, 29, and 30, 1953

THE 1953 Winter meeting of the American Physical Society was held at Stanford University on Monday, Tuesday, and Wednesday, December 28, 29, and 30, 1953. This meeting turned out to be an unexpectedly large one, in spite of the fact that the Summer meeting in the West had been held in September instead of in June. There were about 300 registrations at this meeting, as compared with 436 at the Albuquerque meeting.

There were two outstanding sessions of invited papers, and accounts of these will appear in *Physics Today*. The experiment of devoting one day to a symposium, with no overlapping sessions, proved to be unusually successful. The Secretary is grateful to Professor Schiff and Professor Bloch for suggesting and arranging the Symposium on Nuclear Magnetism, and to Professor W. P. Dyke for his work in arranging the session of invited papers sponsored by our Division of Electron Physics. Both of these sessions were outstanding and were well attended.

There were no post-deadline papers, but an unusually large number of papers were read by title. These were papers B7, F2, F3, F4, F12, and I10. The Secretary appreciates receiving early notice when papers are to be given by title, but he also feels that those who submit papers should try to give them or to arrange for the papers to be read. It is not fair to those who attend to remove papers after the program has been printed. Paper E4 on the nuclear magnetism symposium was briefly reviewed by Dr. G. E. Pake, because the author was unable to attend.

At the opening of the Monday afternoon session of the Division of Electron Physics, the Chairman, Professor L. B. Loeb, called for a moment of silence as an indication of the respect and admiration that all of us felt for the late Professor R. A. Millikan. Although Professor Millikan was an important member of the world community of scientists, and an important force in the life of this Nation, those of us in the West had particularly personal reasons for regretting his passing. Professor Millikan would have enjoyed the leisurely and stimulating atmosphere of the Stanford meeting, and he will be missed by all of us as we carry on the development of physics in the West, a development to which he gave such a fine impetus.

The Secretary wishes to thank the staff of the Department of Physics at Stanford, and in particular those who made possible the excellent accommodations in the campus living facilities and the excellent meals at the Stanford Union.

J. Kaplan, *Local Secretary for the Pacific Coast*

Errata Pertaining to Papers A3, G6, and SP1

A3, by B. Smaller, E. Yasaitis, and M. Brachman. Mr. Brachman's name was misspelled.

G6, by Ervin C. Woodward, Jr. Cd II ($4d^{10}5p^2P_{3/2}-4d^95S^{22}D_{5/2}$) should read Cd II ($4d^{10}5p^2P_{3/2}-4d^95s^{22}D_{5/2}$).

SP1, by Ervin C. Woodward, Jr. In line 7, prison should read prism.

PROGRAMME

MONDAY MORNING AT 10:00

Physics 370

(W. E. MEYERHOF, presiding)

Contributed Papers

A1. Nuclear Resonance of Nb^{93} in $KNbO_3$.* R. M. COTTS AND W. D. KNIGHT, *Department of Physics, University of California, Berkeley.*—$KNbO_3$ is known to exist in rhombohedral, orthorhombic, tetragonal, and cubic modifications of the perovskite structure. X-ray, optical, and dielectric data[1] show phase transitions at about -50, $+220$, and $+435$°C. $KNbO_3$ is ferroelectric[2] below the Curie temperature, 435°C. We have examined the nuclear magnetic resonance spectrum of Nb in a single crystal† and have observed the effects of the transitions on the quadrupole splitting of the spectrum. Our data confirm the three transition temperatures and verify the hysteresis effect seen in the dielectric constant (ϵ) around 220°C. The expected change as the crystal passes from the tetragonal to the cubic phase at 435°C is striking: in the cubic nonferroelectric phase the quadrupole splitting vanishes completely. The splitting ($\Delta\nu$) of the ($\frac{3}{2}$, $\frac{1}{2}$) line from the Larmor frequency is a smoothly varying function between 220° and 435°C. At 435° $\Delta\nu$ falls abruptly from about 100 kcps to zero within a range of 2°C. The data for both $\Delta\nu$ and ϵ indicate that this is a transition of the first order. It is hoped that independent measurements of the Nb quadrupole moment will make it possible to evaluate the crystalline ∇E from the $\Delta\nu$ measured in this experiment.

* Supported in part by the U. S. Office of Naval Research.
[1] E. A. Wood, Acta Cryst. **4**, 353 (1951); Pepinsky, Thakur, and McCarty, Phys. Rev. **86**, 650 (1952); B. T. Matthias and J. P. Remeika, Phys. Rev. **82**, 727 (1951).
[2] B. T. Matthias, Phys. Rev. **75**, 1771 (1949).
† Kindly furnished by the Bell Telephone Laboratories.

A2. Saturation Behavior of a Gaussian Magnetic Resonance Line.* D. F. ABELL† AND W. D. KNIGHT, *Department of Physics, University of California, Berkeley.*—We have extended previously reported work[1] to cover the Gaussian saturation behavior of the derivatives of absorption and dispersion modes, for modulation frequencies both long and short compared to $1/T_1$, where T_1 is nuclear spin-lattice relaxation time. The experimental data for metallic copper have been improved, and more accurate values for T_1 are 7.8 ± 1 and 6.8 ± 1 milliseconds, for Cu^{63} and Cu^{65}, respectively, at 300°K. T_1 shows no dependence on applied dc magnetic field in the region corresponding to resonance frequencies of 2 and 4 mcps. The measured relaxation times are in the expected ratio to each other, but both are about three times longer than free-electron theory[2] predicts. Exchange and correlation effects have been shown to reduce the density of states at the Fermi surface, and the deviations in measured T_1 from predictions of free-electron theory are interpreted as a measure of this reduction. The measured copper line width decreases markedly with increasing saturation, which is contrary to expectation. We are indebted to Dr. C. D. Jeffries and to Varian Associates for the use of apparatus.

* Supported in part by the U. S. Office of Naval Research.
† Now at the University of Nevada, Reno, Nevada.
[1] W. D. Knight, Phys. Rev. **91**, 206 (1953.
[2] J. Korringa, Physica **16**, 601 (1950).

A3. Paramagnetic Resonance of Mn^{++} at Radiofrequencies. B. SMALLER, E. YASAITIS, AND M. BROCHMAN,* *Chemistry and Physics Divisions, Argonne National Laboratory.*—Studies on the paramagnetic resonance of the Mn^{++} ion in the radiofrequency range 10 to 500 Mc reveal a single line with a g value near unity, in agreement with $I=J=5/2$. The line shape is best fitted by a Gaussian distribution throughout the range while the line width reaches a minimal value of about 6 gauss rms at low frequency, high temperature, and low concentration. The effect of neighboring dipole ions can be evaluated as can the "motion narrowing" contribution. The residual line width must then be assumed to be due to transitions between magnetic substrates of low total quantum number, F. Since the dependence of g on frequency corresponds to an $F=5$ or 4 state, the transitions in the low F states apparently become rapidly forbidden with increasing frequency. An interesting effect occurs where the resonant field strength is less than the line width. The resonance shows an anamolous broadening which can be explained in terms of contributions existing at negative values of the external field.

* Present address: Texas Instruments, Inc., Dallas, Texas.

A4. Temperature Dependence of the Nuclear Resonance Shift in Metals.* B. R. MCGARVEY AND H. S. GUTOWSKY, *University of Illinois.*—The temperature dependence of the nuclear resonance shift in metals has been investigated in lithium, sodium, rubidium, cesium, and gallium. The resonance shifts were found to change by no more than 5 to 6 percent over temperature ranges of 200°, including the melting point. For sodium, the observed temperature dependence of the resonance shift is correlated directly with the volume dependence predicted theoretically for the mass magnetic susceptibility due to the conduction electrons. In the other metals, effects appear which are related apparently to the volume dependence of the wave functions for electrons at the top of the conduction band. The room temperature resonance shifts of Sn^{117} and Sn^{119} and the temperature dependence of the Rb^{87} line width will also be reported upon.

* Supported in part by the U. S. Office of Naval Research.

A5. Nuclear Resonance of P^{31} in CS_2 Solutions.* BROTHER SIMON PETER, F. S. C.,† *University of California, Berkeley.*—A concentration-dependent shift of the P^{31} nuclear magnetic resonance frequency has been observed in solutions of white phosphorus in CS_2. For a given fixed external field the resonance frequency is lower for a more dilute solution. The frequency shift relative to pure white phosphorus varies approximately linearly with the mole fraction of phosphorus in the solution for the mole fraction range of from 0.02 to 1.0. Extrapolated to infinite dilution, the measured relative shift is $(5.3\pm0.7)\times10^{-6}$. The solutions were made and used under water. The measuring apparatus included a Pound recording spectrometer and a permanent magnet which provided a field of 7300 oersteds. Samples were interchanged in the same position in the field. The observed effect is ascribed to an interaction of the dissolved phosphorus with the solvent. Other experiments, to be reported elsewhere, on a large number of phosphorus compounds, have been analyzed in terms of additive partial shifts for each atom bonding to phosphorus. Each of these partial shifts turns out to be diamagnetic, and it is

then to be expected that, since solvation effects increase with increasing dilution, the local magnetic field at the phosphorus nucleus would also decrease. Possible effects of chemical association among the P molecules will be discussed, as well as possible effects of the bulk susceptibility of the solutions.

* Supported in part by the U. S. Office of Naval Research.
† Now at Saint Mary's College, California.

A6. Experiment for Measurement of the Magnetic Moment of the Neutron.* VICTOR W. COHEN AND NOEL R. CORNGOLD, *Brookhaven National Laboratory*, AND NORMAN F. RAMSEY, *Harvard University*.—An experiment is being performed to make a determination of the ratio of magnetic moments of the neutron to proton, to a greater precision than has heretofore been attained. The method is somewhat similar to that used by Bloch and co-workers[1] and the atomic beam resonance method with separated oscillatory fields.[2] The slow neutrons are highly polarized by reflection at small glancing angles from a magnetized colbalt mirror. These will be reflected from a second analyzing mirror. Between the mirrors, the neutrons pass a region of uniform permanent magnetic field where they may become depolarized by a resonant rf magnetic field. This will result in a decrease in neutron beam intensity reflected from the second mirror. The ratio of the neutron resonance frequency to that of a proton field probe gives the ratio of the magnetic moments. In order to achieve high precision, the path in the magnetic field is about 150 cm. The separated oscillatory field method[2] is used to average the magnetic field along the path of the neutron and thereby to obviate the need for great uniformity. The path length between loops is long enough to give a natural line width for the neutron resonance of about 1 part in 25 000. The magnetic field is explored point-by-point with a small proton resonance probe. Rough preliminary results are in agreement with previous investigators.[1]

* Work carried out under contract with the U. S. Atomic Energy Commission.
[1] Bloch, Nicodemus, and Staub, Phys. Rev. **74**, 1025 (1948).
[2] N. F. Ramsey, Phys. Rev. **78**, 695 (1950).

A7. Free Nuclear Induction in the Earth's Magnetic Field. MARTIN PACKARD AND RUSSELL VARIAN, *Varian Associates*.—Free nuclear induction signals have been observed in the earth's magnetic field. The very simple experimental apparatus does not use a rotating magnetic field but relies on a polarizing field to preorient the magnetic moments at right angles to the earth's field. The polarizing field of about 100 gauss is left on for a time longer than T_1 after which it is reduced to zero rapidly enough to satisfy the nonadiabatic conditions, leaving the moments perpendicular to the earth's field. The precession of the magnetic moments about the homogeneous earth's field at a frequency of 2185 cycles is observed as a voltage induced in a receiver coil oriented perpendicularly to both the earth's field and the polarizing field. The free induction signal from 500 cc of water is observed to persist for a time greater than one second. This free decay time is probably determined by an instrumental T_2 rather than by the real T_2 of the water. A sample of HF shows a beat pattern which occurs at a frequency of about 120 cycles which is compatible with the difference in γ for hydrogen and fluorine. The absolute value of the earth's field can be easily measured by measuring the precessional frequency. The present signal-to-noise of 20 is adequate to permit a measurement of the earth's field to about one part in 15 000.

A8. Measurement of Nuclear Induction Relaxation Times in Weak Magnetic Fields. ARNOLD BLOOM AND DOLAN MANSIR, *Varian Associates*.—The spin-lattice and spin-spin relaxation times of nuclear magnetic moments in weak magnetic fields (of the order of the earth's magnetic field) have been measured through the use of the free precession apparatus described in the previous abstract. To measure T_1 in very weak fields the polarizing field is reduced at $t=0$ from its initial value of about 100 gauss to a residual value of about 2 gauss. The residual field is then removed at $t=\tau$ and the resulting free precession signal has an initial amplitude proportional to $\exp(-\tau/T_1)$. By varying τ, T_1 can be measured. T_2 can be determined directly from the time decay of the signal if the earth's field is homogeneous. If the earth's field is not homogeneous, a form of spin-echo technique can be employed for measuring T_2. In this technique a short pulse of inhomogeneous polarizing field is applied at $t=\tau$, following the initial removal at $t=0$. At $t=2\tau$ a spin echo occurs whose amplitude, under certain conditions, is proportional to $\exp(-2\tau/T_2)$ and is independent of the amplitude and duration of the polarizing field pulse. Experimental results will be discussed.

A9. Isotopic Spin and Odd-Odd $N=Z$ Nuclei.* S. A. MOSZKOWSKI† AND D. C. PEASLEE, *Columbia University*.—The recent discovery of a $T=1$, $J=0$ ground state[1] in Cl^{34} provides the first known exception to the usual expectation that a nuclear ground state has the minimum isotopic spin possible; e.g., $T=0$ for an odd-odd $N=Z$ nucleus. The position of the lowest $T=1$ state of an odd-odd $N=Z$ nucleus relative to the $T=1$ ground state of the neighboring even-even $N=Z+2$ isobar can be estimated theoretically and is in fair agreement with experimental data. For the lightest odd-odd $N=Z$ nuclei, H^2 to Na^{22}, the ground state has $T=0$. However, the energy difference between the lowest $T=0$ and lowest $T=1$ state decreases with increasing A. The known positron emitting states of Al^{26}, P^{30}, and K^{38} appear to have $T=1$, 0, and 0, respectively. Tentative predictions regarding the decay of the lowest $T=1$ state in Na^{22} and K^{38} and the decay of the lowest $T=0$ state in Al^{26} will be presented.

* Work supported by the U. S. Atomic Energy Commission.
† Now at University of California, Los Angeles, California.
[1] W. Arber and P. Stähelin, Helv. Phys. Acta **26**, 433 (1953).

MONDAY MORNING AT 10:00

Physics 372

(PAUL KIRKPATRICK, presiding)

Contributed Papers

B1. Uniformity of Pulse Heights from a Large-Area Photomultiplier.* A. M. HUDSON AND F. X. ROSER,† *Department of Physics and W. W. Hansen Laboratories of Physics, Stanford University*.—Following a suggestion of R. Hofstadter, a specially designed light baffle has been constructed for use with a large-area photomultiplier (RCA type C7157). This baffle improves the uniformity of pulse heights for scintillation events originating at various regions near the photocathode.

One end of a 2-in.×4-in.×4-in. liquid scintillator cell was viewed by the 2-in.×4-in. photocathode surface. When Co^{60} γ rays were collimated through different parts of the cell, the pulse heights for events near the ends of the photocathode were 14 percent lower than those near the center of the photocathode. With the baffle, this variation is less than 3 percent. Similar measurements using a 5819, (a) in contact with the cell, and (b) 4 inches away with a hollow, smoked MgO cone as a "light pipe," result in an improvement from 20 percent to 4 percent. These improvements in uniformity are at the expense of a loss of between one-half and one-third of the light collected with corresponding decrease in resolution.

* The research reported in this document was supported jointly by the U. S. Office of Naval Research and the U. S. Atomic Energy Commission.
† Sponsored by the National Research Council of Brazil.

B2. Proton-Deuteron Scattering at 20 Mev.* DAVID O. CALDWELL,† J. REGINALD RICHARDSON, AND HERBERT N. ROYDEN, *Department of Physics, University of California.*—The absolute differential cross-section for the elastic scattering of 20.6-Mev protons from deuterons has been measured using the external proton beam of the University of California, Los Angeles synchrocyclotron. A triple-coincidence proportional counter telescope with variable absorbers between the second and third counters and differential pulse-height discriminators on all three counters was used to select the desired particle by range and specific ionization. Measurements have been made at 22 angles from 12° to 164° (all angles are center-of-mass). A few values of the center-of-mass differential cross-section (in millibarns/steradian), subject to considerable revision by corrections yet to be made, are: 15.0°, 72.8; 18.7°, 69.8; 22.5°, 73.9; 29.9°, 77.8; 51.7°, 52.2; 91.9°, 15.5; 130.0°, 2.7; 150.0°, 16.5; 160.0°, 32.9. This shows the familiar deep minimum, but in addition a shallower minimum near 20°, due to Coulomb-nuclear interference. Presumably, this latter minimum should allow the fitting of the data with a unique set of phase shifts. Heretofore such three-body scattering experiments have by themselves yielded two ambiguous sets of phase shifts, and consequently doublet and quartet scattering lengths.

* Assisted by the joint program of the U. S. Office of Naval Research and U. S. Atomic Energy Commission.
† This work was performed while under U. S. Atomic Energy Commission and National Science Foundation Fellowships. Now at Physikalisches Institut, E. T. H., Zurich, Switzerland.

B3. Radiations from Scandium-40, Chlorine-32, Phosphorus-28, and Aluminum-24.* NEEL W. GLASS AND J. REGINALD RICHARDSON, *Physics Department, University of California, Los Angeles.*—Scandium-40, a new positron emitter of the series $Z=2n+1, A=4n$ has been produced by the $Ca^{40}(p,n)Sc^{40}$ reaction using 20-Mev protons in the University of California, Los Angeles cyclotron. The half life is 0.22±0.03 sec and the threshold 15.9±1.0 Mev. A single γ ray of energy 3.75±0.04 Mev and positrons of maximum energy 9.0±0.4 Mev are present. Measurements on previously reported[1,2] members of the series, Cl^{32}, P^{28}, and Al^{24} yielded the following results: Four γ rays up to an energy of 4.77±0.04 Mev and maximum positron energy of 9.4±0.3 Mev for Cl^{32}; seven or possibly eight γ rays up to an energy of 7.59±0.15 Mev and maximum positron energy of 10.6±0.4 Mev for P^{28}; five γ rays up to an energy of 7.12±0.10 Mev for Al^{24}. The reported[1] delayed heavy particles from Al^{24} have been determined to be alpha particles. Delayed alpha particles in the Cl^{32} decay have also been detected. Although energetically possible, no delayed heavy particles were detected in the P^{28} and Sc^{40} decays.

* Supported in part by joint program of U. S. Atomic Energy Commission and U. S. Office of Naval Research.
[1] A. C. Birge, Phys. Rev. **85**, 753 (1952).
[2] Glass, Jensen, and Richardson, Phys. Rev. **90**, 320 (1953).

B4. Specific Ionization of High-Energy Electrons in Hydrogen and Nitrogen.* W. C. BARBER, *Hansen Laboratories of Physics, Stanford University.*—The specific ionization of electrons has been measured for hydrogen and nitrogen over the energy range 13 to 31 Mev. The electrons were accelerated in the Stanford 35-Mev accelerator, magnetically analyzed to approximately one percent energy spread, and collimated into a beam of ¼-in.×½-in. cross section. This beam was passed through an ion chamber, whose sensitive length was 2½ inches, then collected in a Faraday cup. Ion and electron currents were integrated simultaneously, the ratio of the collected charges being proportional to the specific ionization. The specific ionization of both gases showed a steady rise of 5 percent over the energy range 13 to 31 Mev. At 31 Mev the data corrected to N.T.P. gave 8.3 ion pairs per cm for hydrogen and 60 ion pairs per cm for nitrogen. Although individually measured points show a reproducibility of better than one percent, uncertainties in the response of the Faraday cup integrator make the absolute values and the rise with energy uncertain to 2 or 3 percent. Experiments to improve the integrator performance and to extend the measurements to higher and lower energies are in progress.

* The research reported in this document was supported jointly by the U. S. Office of Naval Research and the U. S. Atomic Energy Commission.

B5. Measurements of Reflection of 8-Angstrom X-Rays by Mirror Surfaces.* ROY W. HENDRICK, JR., *Stanford University.*—X-radiation for these measurements originated in a 2.5-kv x-ray tube whose target was an aluminum wire 0.01 inch in diameter, bombarded laterally at about 1 watt of power. After filtration by 0.001 inch of aluminum foil to emphasize the aluminum K lines, the radiation underwent reflection at a plane mirror surface and was absorbed in a detector consisting of a CeBr (Th activated) scintillator and an RCA 6199 photomultiplier tube. The photomultiplier was cooled to liquid-nitrogen temperature to reduce background noise. Reflection coefficients were measured as functions of the small, grazing angle of incidence for mirrors of glass, magnesium, aluminum, copper, silver, and gold. The metal mirrors were formed by condensation upon glass flats, the coating process taking place within the vacuum chamber which housed the whole ray path from source to detector. Graphs will be presented showing the decline of reflecting power to zero with increase of the grazing angle.

* Supported in part by a Grant-in-Aid from the American Cancer Society upon recommendation of the Committee on Growth of the National Research Council.

B6. X-Ray Microscope Mirror Systems.* A. V. BAEZ AND M. WEISSBLUTH, *Stanford University.*—Rays were traced through several x-ray microscope mirror systems with the aid of an IBM electronic computer. Simple mirror systems of circular and of elliptical profile were investigated as were also two compound systems each consisting of a combination of hyperbolic and elliptical mirrors. The circular mirror was combined with a stop placed so as to have maximum effect in rectifying the image. With angles of incidence limited to about 10 mr, an object distance of 2 cm, a magnification of 75 and an aperture angle of 1 mr, the results indicated a resolving distance at the object of about 4000A over a field of 30μ. Over this field the resolution and magnification vary by about 20 percent. An elliptical mirror, computed with comparable numerical assumptions, provides similar resolution but only over a field of about 5μ. The Gaussian image surface is very oblique and the use of an auxiliary aperture stop is less effective than for the sphere. The principal aberration of compound systems is field curvature, comatic effects being unimportant. With a magnification of 40, and aperture angle of 1 mr, it is possible in a four-mirror system to achieve a resolving distance of 1500A over a field of 20μ.

* Supported in part by a Grant-in-Aid from the American Cancer Society upon recommendation of the Committee on Growth of the National Research Council.

B7. Photosensitive Cell Response to Sinusoidally Varying Light Flux. R. L. CONGER AND L. E. SCHILBERG, *Michelson Laboratory, U. S. Naval Ordnance Test Station.*—The effect of sinusoidally modulated light produced by a light chopper on PbS cells has been measured. It was found that a curve of PbS cell signal attenuation as a function of chopping frequency based on the assumption of an exponential response for the PbS cell fit the experimental data quite well.

B8. Sodium Iodide Counting Response for Gamma Rays. W. E. KREGER AND L. MCISAAC, *U. S. Naval Radiological Defense Laboratory.*—The response of a sodium iodide crystal spectrometer to gamma rays of 0.279, 0.411, 0.662, 0.745, and 1.11 Mev has been measured using an automatic recording pulse-height analyzer. Five cylindrical NaI crystals were used having the following sizes: 1 cm×1 cm, 1 in.×1 in., 2 in.×2 in., 4 in.×4 in., 1½ in.×1 in., and 2 in.×1 in. The effect of different sources distances and preparation on the response has been determined for the 0.662-Mev gamma ray. Spectrometer resolution has been determined as a function of crystal size and gamma-ray energy. The photoelectric yield has been compared to total counting response in order to determine relative efficiency of the crystals for different gamma-ray energies by photoelectric peak yield.

B9. Quantitative Measurement of Magnetic Absorption Utilizing a Null-Balance System. R. H. ELSKEN AND T. M. SHAW, *Western Regional Research Laboratory.**—Nuclear magnetic absorption spectroscopy is being used to investigate the sorption of water by hygroscopic solids.[1] To obtain improved precision for quantitative measurements, the r-f spectrometer employed has been designed to operate as a null-balance instrument. A calibrated modulated electronic resistance[2] serves as an artificial absorption. The artificial absorption signal is adjusted to oppose the nuclear resonance signal obtained under conditions of slow sweep operation, with modulation less than line width. Lack of balance between the nuclear absorption and the artificial absorption results in an error signal at the output of the phase detector of the conventional r-f spectrometer. The error signal is used to control a motor which varies the artificial absorption. Provision for recording is made by mechanically coupling the motor to the pen of a conventional strip-chart recorder. Tests show this type of spectrometer has several advantages over other systems primarily because of the reduction in the number of components of the spectrometer that require stabilization to achieve high precision.

* Bureau of Agricultural and Industrial Chemistry, Agricultural Research Administration, U. S. Department of Agriculture.

[1] T. M. Shaw and R. H. Elsken, J. Chem. Phys. **21**, 565 (1953).

[2] G. D. Watkins and R. V. Pound, Phys. Rev. **82**, 343 (1951).

MONDAY AFTERNOON AT 2:00

Physics 370

(L. B. LOEB, presiding)

Division of Electron Physics

Invited Papers

C1. Correlation of Electronic Band Structure with Properties of Silicon and Germanium. CONYERS HERRING, *Bell Telephone Laboratories.* (40 min.)

C2. Recent Developments in Field Emission. JOSEPH E. HENDERSON, *University of Washington.* (40 min.)

C3. Microwave Studies of Electron Diffusion in Gases. SANBORN C. BROWN, *Massachusetts Institute of Technology.* (40 min.)

Contributed Papers

C4. Absorption Cross Sections for Photoionizing Radiations in Low-Pressure Gases.* C. D. MAUNSELL, *Department of Physics, University of California, Berkeley, California.*—Experiments have been carried out to obtain absorption coefficients of pure gases for photoionizing radiations produced in the same gas. The photon source region was a field free box into which an electron beam of 0–50-volt energy was sent. Photons could leave a hole in this box and after traversing the gas enter a Kingdon cage space-charge detector used to measure the number of positive ions produced. The distance between the photon source and Kingdon cage was varied to obtain absorption coefficients. Since the radiations of interest were in the vacuum ultraviolet, no windows could be used to separate the various regions of the apparatus so all parts were operated at the same low pressure (1–10 microns). The variation in Kingdon cage current caused by the photoionization was measured either in a dc bucking circuit or by using pulsed excitation and a synchronous amplifier. The dependence of photoionization on source voltage, source current and pressure has been studied for various gases.

* This work was supported by the U. S. Office of Naval Research.

C5. The Effect of Temperature on Field Emission.* W. W. DOLAN, W. P. DYKE, J. K. TROLAN, AND J. P. BARBOUR, *Physics Department, Linfield College.*—Both the current density and the distribution in energy of electrons emitted from metals are calculated for various combinations of temperature, applied surface electric field and work function. A wider range of those variables than previously achieved is made possible by use of numerical integration. The integrand is the usual function based on the free-electron theory of metals and the wave-mechanical barrier transmission coefficient of Sommerfeld and Bethe which assumes a classical image force and a plane surface. Results, which are presented in graphical form, are consistent with the Fowler-Nordheim field emission equation for low temperatures, and with the Richardson thermionic emission formula at low fields. Predicted emission at temperatures up to 3000°K is compared with cold emission at fields between 10^7 and 10^8 v/cm. The calculated current densities are confirmed experimentally for a work function of 4.5 ev, at fields from 2.6 to 6.8×10^7 v/cm, and temperatures up to 1400°K at the lower fields and up to 2000°K at the higher fields.

* This work was supported by the U. S. Office of Naval Research.

C6. Refined Electron Beam Probe Studies in Glow Discharges.* ROGER W. WARREN, *Department of Physics, University of California, Berkeley.*—The electric field in a glow discharge has been measured by probing high-energy electron beam. The probing beam crossing the discharge is acted on by two parallel but opposing forces; that due to the electric field,

and that due to an externally applied magnetic field. The total deflection is detected by a fluorescent screen and two photomultipliers. The signal from the photomultipliers is used to automatically adjust the magnetic field so that net beam deflection is zero. The electric field is thus directly proportional to the compensating magnetic field, which is readily measured. Fields from less than one to greater than one thousand volts per centimeter have been measured. The electrodes of the discharge are moved with respect to the electron beam at a constant speed and a recorder is used to make a direct plot of field *versus* position over the whole discharge in minutes. The magnetic compensating field is so small relative to the electric fields that the discharge is little affected. Data to date covers air.

* This work was initially supported by the U. S. Office of Naval Research. The results reported were obtained under a National Science Foundation Grant.

C7. Current Growth in the Formative Time Lag of Sparks.* H. W. BANDEL, *Department of Physics, University of California, Berkeley.*—Following the work of Fisher and associates,[1,2] an oscilloscopic study has been made of the growth of current preceding streamer spark breakdown during long formative time lags at low over-voltages. Time lags from 10–100 microseconds are being observed in dried air. Currents have been observed from microamperes in the early part of the formative time rising to 10^{-3} ampere just before breakdown. Data will be presented showing the variations in the current buildup caused by changes in the photoelectric i_0, gap length, and gas pressure.

* The project during development of the intricate instrumentation was supported by the U. S. Office of Naval Research and the Research Corporation of America. The collection of the present data was done with a National Science Foundation Grant.

[1] L. H. Fisher and B. Bederson, Phys. Rev. **81**, 109 (1951).
[2] G. A. Kachickas, Doctor's Thesis, New York University.

TUESDAY MORNING AT 9:00

Cubberley Auditorium

(L. I. SCHIFF, presiding)

Symposium on Nuclear Magnetism

Invited Papers

D1. Recent Developments in Nuclear Induction. FELIX BLOCH, *Stanford University.* (40 min.)

D2. Nuclear Interactions in Molecules. N. F. RAMSEY, *Harvard University.* (30 min.)

D3. Some Recent Results in Nuclear Magnetism. R. V. POUND, *Harvard University.* (30 min.)

D4. Free Nuclear Induction Experiments Involving Pure Nuclear Electric Quadrupole Interactions. ERWIN HAHN, *Watson Scientific Computing Laboratory (IBM), Columbia University.* (30 min.)

D5. Quadrupole Splitting of Nuclear Magnetic Resonance Lines in Single Crystals. G. M. VOLKOFF, *University of British Columbia.* (30 min.)

TUESDAY AT 12:15

Stanford Union

(J. KAPLAN, presiding)

Luncheon of the American Physical Society

TUESDAY AFTERNOON AT 2:00

Cubberley Auditorium

(FELIX BLOCH, presiding)

Symposium on Nuclear Magnetism

Invited Papers

E1. Paramagnetic Relaxation in Free Radical Solutions Exhibiting Hyperfine Structure. G. E. PAKE, *Washington University.* (30 min.)

E2. Some Recent Measurements of Nuclear Moments. CARSON JEFFRIES, *University of California, Berkeley.* (30 min.)

E3. Nuclear Magnetic Resonance Phenomena in Metals and Alloys. W. D. KNIGHT, *University of California, Berkeley.* (30 min.)

E4. Nuclear Magnetism Study of Polymers. EUGENE GUTH, *University of Notre Dame.* (30 min.)

WEDNESDAY MORNING AT 9:00

Physics 372

(R. T. BIRGE, presiding)

Contributed Papers

F1. Measurements of Cyclotron Neutron and Gamma Fields for Animal Irradiation Studies. S. W. ROSS, E. TOCHILIN, AND B. W. SHUMWAY, *U. S. Naval Radiological Defense Laboratory.*—Physical Dosimetry measurements were made at the U. C. 60-in. cyclotron. Neutrons were produced by bombarding a thick Be target with 20-Mev deuterons. Fast neutron flux intensity and angular field distribution were measured with sulfur threshold detectors. In the forward direction, 30 in. from the cyclotron target, the flux was found to be 5×10^{8} neutrons/cm²/μamp-min. The half-width of the angle for half-maximum intensity was found to be 16°, which agrees with Schecter's observations.[1] An estimate of the relative neutron flux above the sulfur threshold was made using the neutron spectrum given by Cohen and Falk for 15-Mev deuterons on Be.[2] For 20-Mev deuterons this ratio will not change appreciably. On this basis 2×10^{8} neutrons/cm² equal 1 rep. The associated thermal neutron flux, measured with gold foils, was sufficiently low to produce no appreciable ionization. Gamma radiation, measured by standard film techniques, constituted no more than 10 percent of the total rep dose. Investigations at NBS have indicated that 20 rep of 2-Mev neutrons produce film blackening equivalent to 1 *r* of Ra gamma rays.

[1] L. Schecter, Phys. Rev. **83**, 695 (1951).
[2] B. L. Cohen and C. E. Falk, Phys. Rev. **84**, 173 (1951).

F2. Limiting Range of Reynolds' Number in Determining Flow Permeability. H. L. MORRISON AND G. J. PLAIN, *Michelson Laboratory, U. S. Naval Ordnance Test Station.*—In determining flow permeability of porous media by some application of Darcy's law,[1] it is usually assumed essential that the flow velocity be kept low enough to keep the flow laminar. The flow permeability of 14 media composed of nearly spherical glass beads, randomly packed, has been ascertained after the method of Terzaghi.[1,2] Using three fluids (water and two Dow-Corning silicons) having viscosities of 0.00874, 0.0940, and 0.968 poise, respectively, it was found that for a Reynolds' number of 75 or less, there was excellent agreement in the measured permeabilities. The range of permeabilities in the 14 media was from 6×10^{-8} cm² to $39\,000\times10^{-8}$ cm².

[1] M. Muskat, *The Flow of Homogeneous Fluids through Porous Media* (J. W. Edwards, Inc., Ann Arbor, Michigan, 1946).
[2] D. P. Krynine, *Soil Mechanics* (McGraw-Hill Book Company, Inc., New York, 1941).

F3. On Some Numerical Regularities in the Periodic System of Ions. N. EFREMOV, *1061 Intervale Avenue, New York, New York.*—According to the proposed method of calculation of ionic radii* the magnitudes of ionic radii may be characterized by means of simple small numbers obtained from the new form of the periodic system of ions based on special matrix. These numbers may be considered as "compensators of valence." These compensators are directly proportional to the magnitude of the ionic radii. Quadruple groups of ions show a simple numerical regularity. The sum which is obtained from adding the compensator of valence and the valence of an ion is a constant number for the given quadruple group of ions arranged in the order of increasing atomic numbers, e.g.,

Ions	Na	Mg	Al	Si
Numbers of electrons:	10	10	10	10
Ionic radii in AE:	0.95(=5×0.19)	0.76(=4×0.19)	0.57(=3×0.19)	0.38(=2×0.19)
Compensator:	5	4	3	2
Valence:	1	2	3	4
Constant number:	6	6	6	6

In this way "compensator of valence" may be linked with valence in a straight line equation: $y=b-x$, where y = valence, x = compensator of valence, and b = simple constant number (4, 5, 6, etc). The "compensator of valence" notion is useful, as pairs of ions with equal or nearly equal compensators of valence (such as Li−Mg, Mg−Sc, Be−Al, B−Si, Na−Ca, etc.) are characterized by joint migration and mutual isomorphous substitution in crystalline lattices.

* Paper given at the September, 1953, meeting of the American Physica Society in Albuquerque, New Mexico.

F4. An Improved High-Intensity Short-Duration Light Source. FRANK N. MILLER, *Michelson Laboratory, U. S. Naval Ordnance Test Station.*—A high-intensity, short-duration, compact point light source is described. The gap was developed for use in photography and shadowgraphy of projectiles that travel several mm/μsec. The source is characterized by ample intensity over an effective time interval of 11×10^{-8} μsec.

F5. The Shock-Wave Valve. RICHARD I. CONDIT, *Broadview Research and Development.*—A convenient and versatile source of shock waves has been realized in the shock-wave valve. It allows the production of shock waves from the sudden release of compressed gas. The sudden release is accomplished by a series of quick-opening mechanical valves cascaded from the size appropriate to the output down to the size that is readily controlled by a solenoid. The assembly is self-contained and automatically recycling, so that shock waves can be repeatedly produced by merely activating the solenoid. (Operation requires no disassembly or replacement of frangible diaphragms.) Operating characteristics of a small model will presented. The device appears promising as a means for exciting shock tubes in the laboratory or in the field. In this application single units have been useful in producing simple plane shock fronts, while multiple units would seem to be useful in producing shock fronts of considerable complexity exhibiting multiple peaks and valleys and other pressure-time relations of practical interest. A new degree of control of experimental sources of shock waves may thus be allowed by shock-wave valves.

F6. Thermal Microstructure in the Ocean. W. N. ENGLISH, *Pacific Naval Laboratory, Esquimalt, British Columbia, Canada.*—The thermistor equipment previously described[1] has been used in conjunction with a tape recorder and a Kay Electric Company "Vibralyser" to obtain a one-dimensional Fourier analysis of some temperature structures in the Esquimalt approaches. A tape speed of eleven inches per hour is used for recording, and a speed of 7½ or 15 inches per second for playback to the Vibralyser. The "spectra" obtained show good agreement with paper records and are also being checked by a photographic process. Representative spectra will be presented and discussed.

[1] W. N. English, Phys. Rev. **92**, 1087(A) (1953).

F7. Response Currents in Coupled Circuits by the Laplace Transformation and a Mechanical Harmonic Synthesizer. CHU JUI LEE AND S. LEROY BROWN, *University of Texas.*—For a linear system of networks having constant lumped elements, the determination of the response current in any mesh of network involves the solution of a set of simultaneous linear

constant-coefficient integrodifferential equations in one independent variable with driving functions having bounded variations in every finite interval and with general initial or boundary conditions. Cases of special interest are electrical circuits to which electromotive forces of periodic nature are applied. Since linear equations possess additive properties, the law of superposition can be applied, and from a system of linear equations it is possible to add the separate solutions found by using each driving function alone and get the composite solution for all driving functions present. The complete solution of a system of these integrodifferential equations can be obtained through one of four methods—the classical method, the Heaviside operational method, the Fourier transformation method, or the Laplace transformation method. If Laplace transformation is used, a mechanical harmonic synthesizer may be used to determine the roots of polynomial equations to facilitate the Heaviside partial fraction expansion in the process of solving the inverse transforms. Solutions of specific problems illustrate the use that may be made of a harmonic synthesizer.

F8. Asymptotic Spherical Shock Decay. L. M. TANNENWALD, *U. S. Naval Ordnance Test Station.*—Quasi-stationary approximations are used to solve the equations of motion of a weak, expanding spherical shock wave propagating through a viscous and heat-conductive medium far from the origin of the initial disturbance. An ordinary first-order differential equation is obtained which describes the shock strength attenuation as a function of distance from the center of the spherical wave. An approximate solution of the above-mentioned differential equation is also given.

F9. A Jet-Tone Orifice Number for Orifices of Small Thickness-Diameter Ratio. A. B. C. ANDERSON, *Michelson Laboratory, U. S. Naval Ordnance Test Station.*—The dependence of a jet-tone orifice number $tf/(\Delta p/\rho)^{\frac{1}{2}}$ on Reynolds number $[\rho t(\Delta p/\rho/\mu)^{\frac{1}{2}}]$ is shown for thin sharp-edged circular orifices whose thickness and diameter both vary from approximately $\frac{1}{4}$ to $\frac{3}{4}$ in., where t is thickness of orifice plate, f frequency, Δp pressure difference across orifice, ρ density, and μ viscosity of gas. Each jet-tone, in general, is composed of harmonics (fundamental and overtones) as well as subharmonics (tones whose frequencies are less than the fundamental). The subharmonics are relatively unsteady in amplitude compared to the harmonics, and may, at times, have a greater amplitude. The jet tones at low Reynolds numbers appear relatively free of noise background. In general, as Reynolds number is increased to high values, the noise background at first engulfs the subharmonics, then the harmonics. The fundamental is the last to remain, finally disappearing in the noise background.

F10. Fast Jet Actuated Shock Tubes.* F. J. WILLIG, *University of California, Los Alamos Scientific Laboratory.*—A small glass shock tube partitioned at its center by means of a thin diaphragm is actuated by directing a fast jet[1] into one end. In traversing the distance to the partition, a high pressure is generated which in turn imparts a high shock velocity to the region beyond. The entire process is highly self-luminous, hence may be recorded by means of a moving image slit camera operating at high speed. Hydrogen gas at a pressure of about one-third of an atmosphere is used in the first part of the tube while the pressure in the other part is maintained at a much lower value. If the latter region is highly evacuated, velocities in the neighborhood of 10^7 cm/sec may be obtained.

* Work performed under the auspices of the U. S. Atomic Energy Commission.
[1] Koski, Lucy, Shreffler, and Willig, J. Appl. Phys. **23**, 1300 (1952).

F11. New Observations of Hydrocarbon Flame Growth.* R. K. SHERBURNE AND J. S. ARNOLD,† *Physical Science Laboratory, New Mexico College of Agriculture and Mechanic Arts.*—Minimum ignition energies of hydrocarbon air mixtures in terms of a measured "critical radius" have been discussed previously.[1] Using the same experimental method the studies have been extended from the original mixtures, methane, ethane, butane, and propane with air, to include isobutane (altered molecular form), ethylene (double bond), acetylene (triple bond) and ratios of oxygen to nitrogen other than the 21/79 value for air. Earlier work[1] showed that ignition occurs most readily for mixtures in which the number of hydrogen atoms is equal to the number of oxygen. This criterion is found to hold for isobutane and variations in the oxygen to nitrogen ratio but fails for ethylene and acetylene mixtures.

* Supported by U. S. Office of Ordnance Research.
† Now at Stanford Research Institute, Menle Park, California.
[1] J. S. Arnold, and R. K. Sherburne, *Fourth Symposium (International) on Combustion* (Williams and Wilkins, Baltimore, Maryland, 1953), p. 139.

F12. Atmospheric Disturbances and Stellar Scintillations. F. ZWICKY, *California Institute of Technology.*—Perturbations in the clear atmosphere can be analyzed through observations of stellar scintillations. Size, location, and velocity of vortices are obtained from drifted spectra and extrafocal images of stars. Density changes within vortices are determined from extrafocal images using various color filters. The instantaneous mass per cm² column in direction of a star follows from the instantaneous location of lines in the drifted spectrum. Shock waves, oscillations, as well as vortices subtending large angles, cause related changes in the drifted spectra of many stars as they appear in the field of a wide angle telescope. Through the use of two telescopes the element of triangulation is introduced with corresponding gain in accuracy of lengths measured. Among the many applications which can be made of the above-mentioned methods, observations on the internal seeing in the solar and planetary atmospheres appear most suggestive. The author intends to make such observations during the total eclipse of the sun in 1954 for the purpose of exploring perturbations in the sun's atmosphere and for further clarification of the nature of the gravitational deflection of light rays.

F13. Shift and Broadening of the Blue Cs Doublet Produced by Argon and Helium.* SHANG-YI CH'EN AND WILLIAM J. PARKER, *Department of Physics, University of Oregon.*—The shift and broadening of the 2nd member of the principal series of caesium produced by argon and helium were observed for pressures up to 170 and 90 atmospheres, respectively. The shift produced by argon was linear throughout the entire range of relative densities and was nearly the same for both doublet components. The average slope was 2.7 cm^{-1}/r.d. with the short wavelength component ($^2P_{\frac{1}{2}}$) having a slightly higher value. For helium the shift obeyed a linear relationship for relative densities above 8 and 16 with slopes of 3.5 and 4.4 cm^{-1}/r.d. for the $^2P_{\frac{1}{2}}$ and the $^2P_{\frac{3}{2}}$ components, respectively. The broadening for both lines in the case of argon appeared to be linear up to a relative density of 45 beyond which there was a marked increase in slope, changing from 2.0 to 5.1 cm^{-1}/r.d. The broadening of the $^2P_{\frac{1}{2}}$ component was consistently higher than that of the $^2P_{\frac{3}{2}}$ component. For helium the $^2P_{\frac{1}{2}}$ component was broadened more than the $^2P_{\frac{3}{2}}$ component at relative densities less than 12.5. Beyond this value the broadening of the $^2P_{\frac{1}{2}}$ component was considerably higher. With helium for densities greater than 32.4, the lines overlapped too much to allow a reliable determination of the half-widths, although the shifts were measured up to a relative density of 44. These results are in general agreement with previous observations for rubidium.[1]

* Supported by the National Science Foundation.
[1] S. Y. Ch'en and D. A. Kohler, Phys. Rev. **90**, 1019 (1953).

F14. The OPW Method for Calculating Energy Eigenvalues Extended to Crystals of Compounds.* TRUMAN O. WOODRUFF, *California Institute of Technology and Hughes Research and Development Laboratories.*—Recent theoretical work by Herman[1] on the energy band structure of diamond-type valence crystals and experimental studies in various laboratories of the properties of crystals of semiconducting materials with the zincblende-type structure[2] have led the author to undertake calculations of important details of the energy band structure of some semiconducting zincblende-type crystals. In connection with this work, Herring's orthogonalized plane wave (OPW) method[3] for calculating energy eigenvalues in a crystal has been extended to cases in which the unit cell of the crystal contains s atoms all of different kinds. Expressions for the matrix elements entering into such calculations will be presented.

* This work was carried out while the author was a Member of the Technical Staff of the Hughes Research and Development Laboratories and while a holder of a Howard Hughes Fellowship.

[1] F. Herman, Phys. Rev. **88**, 1210 (1952); Ph.D. Thesis, Columbia University, January, 1953.

[2] H. Welker, Z. Naturforsch. **7a**, 744 (1952); Breckenridge, Hosler, and Oshinsky, Phys. Rev. **91**, 243 (1953); Willardson, Beer, and Middleton, Phys. Rev.**91**, 243 (1953); M. Tanenbaum and G. L. Pearson, Phys. Rev. **91**, 244 (1953).

[3] C. Herring, Phys. Rev. **57**, 1169 (1940).

WEDNESDAY MORNING AT 9:00

Physics 370

(W. K. H. PANOFSKY, presiding)

Contributed Papers

G1. Photospallation Yields of N^{17}.* DARYL KEAGAN, *W. W. Hansen Laboratories of Physics and Department of Physics, Stanford University.*†—The yields of N^{17} [1] arising from the 180-Mev x-ray bombardment of several low Z elements have been measured. Preliminary results for the integrated cross sections for the following reactions are: $O^{18}(\gamma,p)N^{17}$, 0.5-Mev barn; $F^{19}(\gamma,2p)N^{17}$, 0.02-Mev barn; $Na^{23}(\gamma,\alpha,2p)N^{17}$, 2×10^{-3} Mev barn; $Mg^{24}(\gamma,\alpha,3p)N^{17}$, 5×10^{-4} Mev barn; $Al^{27}(\gamma,2\alpha,2p)N^{17}$, 3×10^{-4} Mev barn; $Si^{28}(\gamma,2\alpha,3p)N^{17}$, 3×10^{-5} Mev barn; $P^{31}(\gamma,3\alpha,2p)N^{17}$, 3×10^{-4} Mev barn; $S^{32}(\gamma,3\alpha,3p)N^{17}$, $<10^{-4}$ Mev barn; $Cl^{35}(\gamma,4\alpha,2p)N^{17}$, and $Cl^{37}(\gamma,5\alpha)N^{17}$, $<10^{-4}$ Mev barn.

* The research reported in this document was supported jointly by the U. S. Navy (Office of Naval Research) and the U. S. Atomic Energy Commission.

† Introduced by W. K. H. Panofsky, Stanford University.

[1] Knable, Lawrence, Leith, Moyer, and Thornton, Phys. Rev. **74**, 1217 (1948).

G2. Classical Theory of Heavy Nuclei I.* E. TELLER AND M. H. JOHNSON, *University of California, Berkeley.*—The nuclear shell model indicates the existence of a smooth average potential within nuclei. This potential might be generated by a smooth and nearly spherical pion wave function. In heavy nuclei the positive, negative, and neutral wave functions will be occupied by several π mesons so that the field will be classical. As a consequence of isotopic spin invariance, a potential proportional to the meson wave function does not give effective nuclear binding. Therefore more complicated interactions must be explored. The pseudoscalar nature of the meson suggests that the main interaction with the meson field occurs by emission and absorption of meson pairs, thereby making the potential depend on the square of the meson wave function. Spin-orbit coupling would be due to an additional pseudovector term which depends linearly on the meson wave function. In the classical description it is necessary to distinguish between six fields representing positive, negative, and neutral mesons present in even and odd numbers.

* Work supported by the U. S. Atomic Energy Commission.

G3. Classical Theory of Heavy Nuclei II.* M. H. JOHNSON AND E. TELLER, *University of California, Berkeley.*—Definite eigenvalue equations governing the meson (ϕ) and nucleon (ψ) wave functions follow from minimizing the energy in which nucleons are treated as a degenerate gas. A constant density approximation indicates that equilibrium for the correct nuclear radii, with correct nuclear binding and proper meson scattering properties, can be achieved by the interaction $\psi^2 a\phi^2(1+b\phi^2)^{-1}$ for $b\phi^2\sim3$ and $a\phi^2\sim-160$ Mev. Numerical integration of the equations for different radii gives the appropriate surface energy. However, if separate neutron and proton fields are introduced, the energy minimum occurs for too small proton densities. An additional term in the interaction proportional to the nucleon kinetic energy raises the proton densities. It is equivalent to decreasing the nucleon's effective mass. As the meson field is intimately related to the nucleon's self-energy, an external meson field may well change the nucleon's effective mass. Moreover, the change necessary to obtain a correct neutron-proton ratio reduces the potential scattering of heavy nuclei to zero at 150 Mev in agreement with experiment.[1]

* Work supported by the U. S. Atomic Energy Commission.

[1] S. Fernbach, UCRL Report 1382, July 1951.

G4. Cosmic-Ray Transition Phenomena Due to Electrons, Photons, and Mesons.* ROBERT B. BRODE, *University of California, Berkeley.*—With a suitable arrangement of over a hundred Geiger counters, it has been possible to study in some detail the characteristics of the transition as the cosmic radiation passes from air to denser matter. Narrow pairs of electrons initiated by electrons and by photons showed a maximum in their transition at about one radiation length of matter. Showers showed a maximum of the Rossi type at about three radiation lengths of matter. No evidence was found for a second maximum in the transition curves produced by incident photons, electrons, and mesons. The dependence on atomic number and radiation length of material of the transition curves for the knock-on electrons due to mesons is qualitatively in agreement with theoretical predictions.

* Assisted by the joint program of the U. S. Office of Naval Research and the U. S. Atomic Energy Commission.

G5. Comments on Fermi's Theory of the Origin of Cosmic Rays. LEVERETT DAVIS, JR., *California Institute of Technology.*—Fermi's[1] collisions between cosmic-ray particles and moving pieces of the galactic magnetic field **B** reverse the component along **B** of the particles momentum and, on the average, slightly increase its magnitude. The normal component is unchanged. With chaotic **B** very high-energy particles result; but with the roughly uniform **B** that now seems more probable, energy increases by a large factor are not easily built up. Therefore, introduce type C or betatron collisions in which a particle spiraling around a field line passes through a region

where **B** is changing in time. Space variations do not matter. This produces random changes in energy of the same magnitude as did Fermi's collisions, if the observed interstellar gas velocity is ascribed to vibrations in **B**. Even without positive second-order terms, random walk analysis gives the observed energy spectrum. The increased momentum normal to **B** enables Fermi's collisions to increase the parallel component. Random walk analysis applied to Fermi's collisions shows that statistical fluctuations are about as important as the positive second-order term.

[1] E. Fermi, Phys. Rev. **75**, 1169 (1949).

G6. Isotope Displacement in λ4415A Cd II. ERVIN C. WOODWARD, JR.,* *Department of Physics, University of California, Berkeley.*—Using mixtures of separated isotopes of cadmium in a modified Schüler hollow cathode discharge tube with a Fabry-Perot etalon in conjunction with a large prism spectrograph, the transition

$$\text{Cd II}\,(4d^{10}5p\ ^2P_{\frac{1}{2}}-4d^{9}5S^2\ ^2D_{\frac{3}{2}})$$

at λ4415A was investigated for the isotope displacement of the isotopes Cd^{111} and Cd^{113} since earlier work of Schüler and Westmeyer,[1] and Brix and Steudel[2] gave meager and inconclusive data for these two isotopes. The centers of gravity of both the Cd^{111} and Cd^{113} hyperfine structure patterns were found to lie between the Cd^{110} and the Cd^{112} levels. The shift between Cd^{111} and Cd^{113} is 39.7×10^{-3} cm^{-1}. This is some 26 percent less than the displacement between either Cd^{110} and Cd^{112} and Cd^{112} and Cd^{114}. Though only a relative shift was measured, the difference is in such a sense as to possibly indicate an abnormally large nuclear radius for Cd^{111}.

* Now at Radiation Laboratory, University of California, Livermore, California.
[1] H. Schüler and H. Westmeyer, Z. Physik **82**, 685 (1933).
[2] P. Brix and A. Steudel, Z. Physik **128**, 260 (1950).

G7. Triplet Production in Hydrogen at 300 Mev by a Total Absorption Method. J. D. ANDERSON, C. A. MCDONALD, JR., AND R. F. POST, *Radiation Laboratory, Department of Physics, University of California, Berkeley.*—The attenuation of 300-Mev photons in liquid hydrocarbons has been measured and used to infer the cross section for triplet production (pairs produced in the field of an electron). Targets of benzene (C_6H_6) and cyclohexane (C_6H_{12}) were used in good geometry; attenuation was measured by substitution of a dummy target. A pair spectrometer with fast counter channels was used. The beam was monitored by a 300-Mev monitor.[1] The total attenuation cross sections in hydrogen and carbon found are: $\sigma_H=(1.95\pm0.2)\times10^{-26}$ cm^2 and $\sigma_C=(31.8\pm0.3)\times10^{-26}$ cm^2 (statistical errors—about 10^6 total counts). At 300 Mev three processes dominate: (1) Compton effect,[2] (2) ordinary pair-production, and (3) triplet production, σ_T(theoretical) $=7.96\times10^{-27}$ cm^2.[3] Subtraction of (1) and (2) from σ_H yields $\sigma_T(H)=(8.4\pm2.0)\times10^{-27}$ cm^2, in agreement with theory. In σ_H photonuclear processes are negligible by comparison. σ_T can also be calculated from σ_C, giving σ_T(carbon) $=(8.0\pm0.5)\times10^{-27}$ cm^2, in agreement with σ_T(H). Although the statistical error in σ_T(carbon) is smaller than that in σ_T(H), it is believed that σ_T(H) is more reliable because of uncertainties in shielding and other corrections necessary in calculating σ_T(carbon).

[1] McDonald, Kenney, and Post, Paper No. H14, this meeting.
[2] Kenney, Dudley, and McDonald, Paper No. H13, this meeting, gives an experimental verification of the theoretical value.
[3] J. Wheeler and W. Lamb, Phys. Rev. **55**, 858 (1939).

G8. Compton Effect at 250 Mev. F. H. COENSGEN, *Radiation Laboratory, Department of Physics, University of California, Berkeley, California.*—The electron Compton effect has been investigated using photons of the bremsstrahlung beam from the Berkeley synchrotron. Photons in a 27-Mev energy band about a mean energy of 250 Mev were selected by selecting recoil electrons in a given momentum interval and measuring the angle through which the photons were scattered. It is estimated that the primary energy band is known within three percent. Cesium fluoride crystals were used to detect photons and phenylcyclohexane activated with 4 g/liter of terphenyl was used in all other detectors. A Compton event is identified as a coincidence between a pulse from a photon detector and a pulse from an electron detector. The amplitude and length of the pulses from the photomultipliers are limited but not amplified before reaching a germanium diode coincidence circuit. A resolving time of 2×10^{-8} second was used. Precautions against contamination by pair production were taken. Counting rates have been measured to approximately 10 percent for photon scatter angles of 4, 8, 16, 20, and 25 degrees. Cross sections computed from these measurements agree within the limits of the experiment with those computed from the differential Klein-Nishina formula.

G9. Relative Low-Energy Pion Production Cross Sections by Photons on Hydrogen. RYOKICHI SAGANE AND WALTER F. DUDZIAK. *Radiation Laboratory, Department of Physics, University of California, Berkeley.*—A successful method of shielding a synchrotron from an external strong horizontal magnetic field has been found. As a result it is now possible to use a magnet as a spiral orbit spectrometer near a synchrotron for the study of numerous problems where the counting rate is very small. In particular the study of relative pion production cross sections at 90 degrees to the gamma-ray beam in the low-energy region ($T_\pi>4$ Mev) where the spectrometer is most efficient, becomes greatly simplified. A test experiment was made using a maximum gamma-ray energy of 300 Mev for the problem of pion production from hydrogen. A carbon-polyethylene subtraction technique was used. The created pions were detected by C-2 200μ nuclear emulsions positioned in the stable orbit. The preliminary results from this test experiment at pion energies of ($T_\pi=10$, 20, 35, 45, 55) will be presented.

G10. Dependence of Relative Low-Energy $\pi^\pm$ Production Cross Section on Atomic and Neutron Numbers. WALTER F. DUDZIAK AND RYOKICHI SAGANE. *Radiation Laboratory, Department of Physics, University of California, Berkeley, California.*—Preliminary data[1-3] at three pion energies ($T_\pi=12.5$, 27, and 35 Mev) have been obtained on the relative yield of charged pions from the interaction of 340-Mev protons with complex nuclei. For the experiment a 22-in. spiral orbit spectrometer was used. As a result production cross sections at 90 degrees to the proton beam from Be, C, Al, Cu, Ag, Ta, Pb, and U were obtained. The charged mesons were detected by means of C-2 200μ nuclear emulsions located at the stable orbit A comparison of the plots for the positive pions clearly reveals that the variation with atomic number is not the same at the three energies. A deviation occurs from the $T_\pi=35$-Mev data as the pion energy is lowered. The direction of this deviation is the same as would be expected from the effect of the nuclear Coulomb field. However, there is reason to believe that the nuclear Coulomb field may not suffice to explain this deviation. A comparison of negative pion production when plotted against neutron number does not reveal an appreciable opposite effect.

[1] R. Sagane and W. Dudziak, Phys. Rev. **92**, 212 (1953).
[2] W. Dudziak and R. Sagane, UCRL-2304.
[3] R. Sagane and W. Dudziak, UCRL-2317.

G11. Phase Shift Calculation of High-Energy Electron Scattering by Nuclei. I.* D. R. YENNIE, R. N. WILSON, AND D. G. RAVENHALL, *Stanford University.*—In this paper we shall describe the computational program for calculating the elastic scattering of electrons from spherically symmetrical charge distributions, and in the following paper the results will be presented and compared with experiment. The calculation follows in general the methods given by Parzen[1] and Acheson,[2] with some modifications in the details. To calculate the phase shifts, the radial wave functions inside the nucleus

are integrated numerically and fitted to Coulomb functions (obtained by series expansion about the origin) outside the nucleus. In order to obtain relatively accurate differential cross sections for large angles ($>90°$), it is necessary that the phase shift errors be kept small (less than 10^{-4} radian) In this angular region it is also necessary to know the Coulomb scattering amplitude very accurately. A new method of summing the series for this amplitude will be given.

* Supported by the U. S. Office of Scientific Research, Air Research and Development Command.
[1] G. Parzen, Phys. Rev. **80**, 355 (1953).
[2] L. K. Acheson, Jr., Phys. Rev. **82**, 488 (1951).

G12. Phase Shift Calculation of High-Energy Electron Scattering by Nuclei. II.*[1] D. G. RAVENHALL, D. R. YENNIE, AND R. N. WILSON, *Stanford University.*—For gold, $Z=79$, we have calculated differential cross sections for uniform, exponential and intermediate charge distributions. Compared with the first Born approximation, the maxima and minima given by the uniform charge distributions are smoothed out, the first minimum appearing only as a point of inflection. The slope of the cross section for the exponential distribution is greater than that given by the first Born approximation; this effect can be understood qualitatively as being due to the increase of the electron's wave number inside the attractive potential of the nucleus. For comparison, some distributions for copper ($Z=29$) have also been obtained. The maxima and minima are more pronounced and are shifted to smaller angles relative to the Born approximation, an effect explainable qualitatively in terms of the effective wave number. Further calculations now in progress will be reported and compared with the experimental results of Hofstadter, Fechter, and McIntyre.[2]

* Supported by the U. S. Office of Scientific Research, Air Research and Development Command.
[1] Some of these results have been reported in a Letter to the Editor of *The Physical Review.*
[2] Hofstadter, Fechter, and McIntyre, Phys. Rev. **91**, 422 (1953); **92**, 978 (1953).

G13. Second Born Approximation to the Scattering of Fast Electrons and Positrons by Nuclei.* R. N. WILSON, *Stanford University.*—The scattering of a Dirac particle in an electrostatic potential is calculated in second Born approximation. A charge distribution of the form

$$\rho(r) = (Ze/8\pi a^3)\exp(-r/a)$$

is chosen because the integrations can be performed exactly and because it is of interest to compare the result with an exact calculation by phase shift analysis, as reported in the preceding two papers. In the imaginary part of the second-order contribution to the scattering amplitude there appear divergent terms which are to be interpreted as phase corrections to the first-order contribution.[1] A comparison is made of the results of this calculation with the first Born approximation and with the exact phase shift calculation.

* Supported by the U. S. Office of Scientific Research, Air Research and Development Command.
[1] R. H. Dalitz, Proc. Roy. Soc. (London) **206**, 514 (1951).

G14. Achromatic Translation System for High-Energy Beams.* WOLFGANG K. H. PANOFSKY, *W. W. Hansen Laboratories of Physics and Department of Physics, Stanford University.*—The beam of electronuclear machines frequently requires magnetic analysis in order to provide a beam of known energy and energy width, free from secondary particles. A system has been designed which achieves this aim without destroying the geometrical character of the beam. The system achieves a parallel translation of the beam, the amount of the translation being independent of energy to the first order. The system consists of a deflecting magnet followed by three quadrupole lenses, followed by a second deflecting magnet which bends the beam into a path parallel to the initial beam. Construction details will be given.

* The research reported in this document was supported jointly by the U. S. Navy (Office of Naval Research) and the U. S. Atomic Energy Commission.

WEDNESDAY AFTERNOON AT 2:00

Physics 370

(R. HOFSTADTER, presiding)

Contributed Papers

H1. On the Decay of Cl^{33}. W. E. MEYERHOF, *Stanford University,* AND G. LINDSTROM, *Nobel Institute of Physics, Stockholm.**—In the decay of Cl^{33} (half-life $\sim$2.5 sec) a gamma ray of energy 2.9 Mev has been found with a branching ratio of $\sim\frac{1}{4}$ percent. The log-ft for the positron branch leading to the 2.9-Mev state of S^{33} is 4.0 ± 0.3, indicating even parity for this state (assuming that the ground state of Cl^{33} has even parity). This result is in agreement with $S^{32}(n,\gamma)$ data,[1] but does not agree with interpretation of $S^{32}(d,p)^2$ and $S^{32}(d,n)^3$ scattering experiments leading to the 2.9-Mev state of S^{33} and the corresponding state in Cl^{33}.

* Work performed at Stanford University.
[1] Kinsey, Bartholomew, and Walker, Phys. Rev. **85**, 1012 (1952).
[2] J. R. Holt and T. N. Marsham, Proc. Phys. Soc. (London) **A66**, 467 (1953).
[3] Middleton, El-Bedewi, and Tai, Proc. Phys. Soc. (London) **66**, 95 (1953).

H2. Photoproduction of Neutral Pions at High Energies.* D. C. OAKLEY, R. L. WALKER, J. G. TEASDALE, AND J. I. VETTE, *California Institute of Technology.*—Measurements of the excitation function for photoproduction of neutral pions in hydrogen at photon energies between 250 and 470 Mev have been continued with the Cal-Tech synchrotron by a different method than previously reported.[1] The magnetic spectrometer used for the π^+ photoproduction cross section[2] has been used to count the recoil protons from the photoproduction of π^0's in a high-pressure, liquid nitrogen cooled hydrogen target, assuming these protons are due only to the π^0 photoproduction. Measurements have been made at $12\frac{1}{2}°$ and 32° for the proton in the lab system at energies corresponding to incident photons from 250 to 470 Mev. These results are in approximate agreement with those obtained previously by counting both a proton and one of the π^0 decay γ rays.[1]

* This work was supported by the U. S. Atomic Energy Commission.
[1] Walker, Oakley, and Tollestrup, Phys. Rev. **89**, 1301 (1953).
[2] Walker, Teasdale, and Peterson, Phys. Rev. **92**, 1090(A), (1953).

H3. Photofission Produced by 335-Mev Bremsstrahlung. J. JUNGERMAN, *University of California at Davis,* AND H. STEINER, *University of California, Berkeley.*—We have determined the photofission cross section for several substances

at the maximum energy of the Berkeley synchrotron. A cancellation technique was employed in a hydrogen-filled ionization chamber that gives a 2π geometry for the fission fragments and a background from the beam ionization of less than one percent. The number of equivalent quanta were determined by using replicas of the thermally calibrated Cornell and Illinois ionization chambers, and the maximum energy of the spread-out beam was found to be 335 Mev using a pair spectrometer. The fission cross section per equivalent quantum is found to be 225 mb, 160 mb, 43.5 mb, and 2.52 mb for U^{235}, U^{238}, Th^{232}, and Bi^{209}, respectively. The counting statistical error is two percent or better in all cases.

H4. Interpretation of Experiments on Nuclear Temperatures.* DAVID BREED BEARD, *University of California at Davis and the University of Connecticut Inelastic Neutron Scattering Project.*—The expression for particle emission spectra common to many theories of heavy nuclei, $E\exp 2\{a(E_m-E)\}^{\frac{1}{2}}$, has been approximated by Weisskopf to const $E\exp\{-E/T\}$, where $T=(E_m/a)^{\frac{1}{2}}$, E is the emitted particle energy, E_m is the excitation energy of the compound nucleus above its ground state, and a is constant. Hurwitz and Bethe have remarked that capture cross section data indicate the energy of the excited nucleus should be measured, not from the ground state, but from a characteristic level which is a smooth function of atomic mass. Additional and rather strong evidence comes from: (1) plots of experimentally observed nuclear temperatures, T, *vs* atomic mass for equal excitation energies in which temperature is observed to remain constant or even increase with atomic mass. (This indicates E_m increases with atomic mass at least as fast as a, as would follow from a decrease in binding energy per nucleon with increasing mass number.) And (2) observations of how nuclear temperature depends on excitation energy, in which nuclear temperature is found to increase faster with excitation energy that $(E_m)^{\frac{1}{2}}$ if E_m is measured from the ground state. Characteristic levels have been estimated.

* This work was supported in part by the U. S. Atomic Energy Commission.

H5. Velocity of Spread of Burst Pulses in Air with Coaxial Cylindrical Geometry.* ELSA L. HUBER, *Department of Physics, University of California, Berkeley.*—Bursts pulses in room air at a pressure of 300 mm in a coaxial cylindrical system have been investigated with a high-speed synchroscope. The velocity of spread along the central positive wire has been determined using two collimated α-particle beams for triggering the pulses, one directed parallel to the wire, and the other perpendicular to it. In the former case, the primary ionization occurs essentially instantaneously along the entire length of the wire, while in the latter it is initially confined to a single point on the wire, with the subsequent spread depending on photoionization of the gas. The observed difference in rise time of the two types of pulses yields the time and hence velocity of the spreading process. By diluting the air with nitrogen, but maintaining a constant pressure, this velocity has been found to vary with the partial pressure of oxygen.

* This work was initially supported by the U. S. Office of Naval Research; but the data here reported were obtained under a grant from the National Science Foundation.

H6. A Monitor for High-Energy Electron or γ-Ray Beams.* A. V. TOLLESTRUP AND W. A. WENTZEL, *California Institute of Technology.*—A monitor for use with high-energy γ-ray beam of the Cal-Tech synchrotron has been developed which has some advantages not possessed by the conventional ionization chamber. First, it may be gated easily, and secondly, its response is very fast and is not limited as is an ionization chamber by ion-collection time. Unfortunately, it is not an absolute device and hence it must be calibrated. The monitor consists of a one-meter long gas-filled metal tube with a thin aluminum window at the front and rear for the beam to pass through. Electrons made in a thin converter in front of the apparatus emit Čerenkov radiation in the gas which is reflected onto the cathode of a 5819 photomultiplier by a thin aluminized Lucite mirror set at 45° to the beam direction. The 5819 which is located one meter away from the beam axis and is shielded with 2 in. of lead is gated by a pulse applied to its last two dynodes and its output goes to a standard current integrator. βn must be greater than 1 for Čerenkov radiation to be emitted and this corresponds to a low-energy cutoff of 20 Mev for air at STP and to 60 Mev for helium at STP and is inversely proportional to the square root of the pressure. Turning the monitor end-for-end shows the light produced by ionization is negligible. Leakage and dark current constitute a small background.

* This work was supported in part by the U. S. Atomic Energy Commission.

H7. A 500-Mev Pair Spectrometer.* DUANE H. COOPER, DAVID C. OAKLEY, AND ROBERT L. WALKER, *California Institute of Technology.*—A pair spectrometer has been built for measuring the photon spectrum and some absorption coefficients in the Bremsstrahlung beam from the Cal-Tech synchrotron. The 50-kw 35-ton magnet can produce 15 000 gauss in a 4-inch gap over a 40-inch equilateral triangular area. This places 550-Mev photons in the central energy channel. The detectors are 10 plastic scintillators on each side of a 60° V inside the gap, each coupled through a Lucite light pipe to its photomultiplier on top of the magnet. Instead of having a separate coincidence circuit for every possible pairing of detectors across the V, we use a time-delay multiplexing scheme, suggested by Matthew Sands. This reduces the number of amplifiers from 20 to only 4, which need feed only as many coincidence channels as there are energy channels. The use of distributed amplifiers readily permits a coincidence resolving time of 10 millimicroseconds.

* This work was supported in part by the U. S. Atomic Energy Commission.

H8. Lifetime Measurements for the First Excited States of O^{17} and B^{10} from Recoil Studies.* JACQUES THIRION AND VALENTINE L. TELEGDI,† *Kellogg Radiation Laboratory, California Institute of Technology.*—The measurement of the distance traversed by an excited recoil nucleus before deexcitation can be used for determining lifetimes of the order of 10^{-11} sec or longer.[1] We have applied this method to the γ rays emitted by the first excited states of O^{17} (870 kev) and B^{10} (720 kev).[2] These states were excited by deuteron-induced reactions on O^{18} and Be^{9}. A collimated deuteron beam ($\frac{1}{4}$ in. diameter) strikes a thin target mounted on Ni backing (0.6 mg/cm^2) and the recoils are ejected into vacuum. The γ rays are detected by means of a NaI spectrometer (10 channels) of 8 percent resolution for the 870-kev photopeak. The crystal sees the region accessible to the recoils through a tungsten collimator. Mechanical displacement of the target with respect to the collimator enables one to vary the distance of flight of the recoils seen by the detector. The following lifetimes have been obtained: O^{17} 870-kev level $(2.5\pm1)10^{-10}$ sec; B^{10} 720-kev level $(7\pm2)10^{-10}$ sec.

* Assisted by the joint program of the U. S. Office of Naval Research and U. S. Atomic Energy Commission.
† Visiting Research Fellow from the Institute for Nuclear Studies, University of Chicago.
[1] J. C. Jacobsen, Phil. Mag. **47**, 23 (1924); Devons, Hereward, and Lindsay, Nature **164**, 586 (1949).
[2] R. G. Thomas and T. Lauritsen, Phys. Rev. **88**, 969 (1952).

H9. Gamma-Radiation from $C^{13}+D^2$.† R. J. MACKIN, JR., W. B. MIMS,* AND W. R. MILLS, *Kellogg Radiation Laboratory, California Institute of Technology.*—A magnetic lens spectrometer was used to investigate the gamma radiation above 3.5 Mev produced by the deuteron bombardment of C^{13}-enriched

soot. A study of the Compton electron spectra from a thin converter (20 mg/cm² C plus 21 mg/cm² Al) at $E_d = 1.42$ Mev revealed the following gamma lines (energies in kev, not corrected for possible Doppler shift): 4930±40, 5130±30, 5730±30, 6119±25. A weak line at 3910±50 kev was established with the spectrum from a 125 mg/cm² Al converter. At $E_d = 1.9$ Mev, additional lines appeared at 6450±50 and 6730±40 kev. No new lines were discovered at $E_d = 2.6$ Mev. The well-known 6.12-Mev line is from C^{14},† as is probably the 6.73-Mev line. All other lines correspond to known levels of N^{14}. A predicted line at 5.82 Mev[1] was not observed; its intensity at $E_d = 1.42$ Mev is less than 0.15 that of the 5.73-Mev line.

† Assisted by the joint program of the U. S. Office of Naval Research and U. S. Atomic Energy Commission.
* Commonwealth Fund Fellow, now at the Clarendon Laboratory, Oxford, England.
[1] Woodbury, Day, and Tollestrup, Phys. Rev. **92**, 1199 (1953).

H10. Inelastic Scattering of Protons by F^{19}.† R. W. Peterson, C. A. Barnes, W. A. Fowler, and C. C. Lauritsen, *Kellogg Radiation Laboratory, California Institute of Technology.*—Two previously unreported groups of inelastically scattered protons have been found, corresponding to the two low-lying levels of F^{19} reported by Mileikowsky and Wahling.[1] Measurements of the energies of these two groups at 100° and 159° in the lab system at several bombarding energies yields values of 108±2 kev and 200±3 kev for the excitation energies of these two levels. The excitation curve for the protons to the first-excited state shows the well-known 1.355- and 1.381-Mev resonances, and in addition a much stronger resonance at 1.419 Mev. The elastic scattering of protons from this level in Ne^{20} indicates that it is 1^+. The γ rays from these two levels to the ground state and from the 200-kev level to the 108-kev level have been observed. Further work on the proton groups and the associated γ rays is in progress.

† Assisted by the joint program of the U. S. Office of Naval Research and the U. S. Atomic Energy Commission.
[1] C. Mileikowsky and W. Whaling, Phys. Rev. **88**, 1254 (1952).

H11. Neutron Total Cross Section for Bismuth and Uranium Between 45 and 130 Mev. W. I. Linlor and B. Ragent, *Radiation Laboratory, Department of Physics, University of California, Berkeley.*—Neutron total cross sections for bismuth and uranium have been measured in a good geometry transmission experiment, using a time-of-flight instrumentation.[1,2] Uncertainties shown are standard deviations based on counting statistics only and on energy channel width.

Neutron		Bismuth		Uranium	
Energy (Mev)	Error (Mev)	σ (Barns)	$d\sigma$ (Barns)	σ (Barns)	$d\sigma$ (Barns)
45	4	4.74	0.18	4.96	0.21
53	3	4.50	0.18	4.44	0.21
62	4	4.14	0.14	4.53	0.17
70	3	4.92	0.12	5.30	0.15
78	4	4.74	0.10	5.13	0.12
89	5	4.71	0.09	5.10	0.11
100	6	4.54	0.09	5.00	0.11
113	7	4.22	0.11	4.67	0.13
131	8	3.63	0.17	4.29	0.21

[1] University of California Radiation Laboratory Report.
[2] W. I. Linlor and B. Ragent, Phys. Rev. **91**, 440 (1953).

H12. Total Neutron Cross Sections for Carbon, Iron, Antimony, and Tantalum from 35 to 180 Mev. B. Ragent and W. I. Linlor, *Radiation Laboratory, Department of Physics, University of California, Berkeley.*—The total neutron cross sections for carbon, iron, antimony, and tantalum have been measured in the region of 35 to 180 Mev in a good geometry absorption experiment using time-of-flight instrumentation developed for the 184-inch cyclotron. Tantalum exhibits a shallow dip in the cross section curve in the region of 50 to 70 Mev. It is apparent within the statistics that antimony has a dip at about the same energies, and that iron and carbon have a relatively flat region at these energies.

H13. Absolute Photon Attenuation Cross Section for Non-Pair Processes in Beryllium at 300 Mev. Robert W. Kenney, John M. Dudley, and Charles A. McDonald, Jr., *Radiation Laboratory, Department of Physics, University of California, Berkeley.*—The total cross section for the attenuation of 300-Mev photons by nonpair forming processes in beryllium has been found to be $0.0148 \pm 0.0011 \cdot 10^{-24}$ cm²/Be atom. This result is 18 percent higher than the theoretical total Compton cross section in beryllium at 300 Mev. A discussion of photon interactions with nuclei will be given, their cross sections in beryllium at 300 Mev will be estimated, and their theoretical dependences on Z and energy included. The nonpair, non-Compton processes contribute at least 10 percent of the measured cross section. From the tentative data, one can conclude that the Klein-Nishina formula is correct to within 6 percent at 300 Mev. Final results will be presented. The total absorption cross sections at 300 Mev in beryllium and lead have been found to be $0.1599 \pm 0.0007 \cdot 10^{-24}$ cm²/Be atom and $37.57 \pm 0.07 \cdot 10^{-24}$ cm²/Pb atom, respectively. The ratio of the pair forming cross section at 300 Mev in beryllium to that in lead has been found to be $3.90 \pm 0.01 \cdot 10^{-4}$.

H14. A Monitor for High-Energy Photons. C. A. McDonald, Jr., R. W. Kenney, and R. F. Post, *Radiation Laboratory, Department of Physics, University of California, Berkeley.*—It has been common practice to use ionization chambers for monitoring the bremsstrahlung beams of high-energy electron accelerators. An ionization chamber was found to be inadequate for monitoring the 330-Mev spectrum of the Berkeley synchrotron when a single channel pair spectrometer was used at energies above 300 Mev. The contribution of a small-energy interval, in a bremsstrahlung spectrum, to the over-all response of an ionization chamber becomes small as the mean energy of that interval approaches the quantum limit of the spectrum. An ionization chamber is therefore a poor monitor for bremsstrahlung flux in an energy interval near the quantum limit, particularly if the quantum limit fluctuates. An adequate magnetic-type monitor will be described, in which electrons from a thin lead converter are analyzed by a magnetic field. Only 300±15-Mev electrons are accepted by a narrow momentum channel and detected by a 2-in. diameter sodium iodide crystal. The crystal is viewed by a 5819 photomultiplier, the output of which is integrated on a condenser and recorded by an electrometer circuit. The instantaneous photomultiplier current is 3 orders of magnitude smaller than rated maximum current. It will be shown that the magnetic-type monitor tracks the pair spectrometer better than an ionization chamber. The monitor discriminates very sharply against low-energy background.

WEDNESDAY AFTERNOON AT 2:00

Physics 372

(J. KAPLAN, presiding)

Contributed Papers

I1. Ionization by Ultra-Speed Pellets.* C. D. HENDRICKS, JR., M. E. VAN VALKENBURG, W. G. CLAY, AND R. A. DAVIDSON, *University of Utah.*—Ultra-speed pellets have been produced having velocities from 2 to 10 km/sec using techniques developed by Rinehart, White, and Allan at Inyokern. The ionization produced as the pellets pass through the air has been studied by means of microwave reflections and by measuring charge with high potential plates. Preliminary measurements show that at least 10^{13} electrons per cm of path are created by pellets in the velocity range studied. Visual flares have been observed in all ultra-speed pellets fired thus far.

* This research was supported by the U. S. Office of Ordnance Research.

I2. A Slotted Resonant Cavity for Dielectric Measurements. J. J. WINDLE AND T. M. SHAW, *Western Regional Research Laboratory.**—Cavities operating in the TM_{010} mode at 3030 and 9300 Mc have been constructed with a narrow slot cut parallel to the direction of current flow in the walls. The slot, which can be considered as a perturbation[1] of the cavity boundaries, has only a small effect on the resonant frequency and Q. The applications of such cavities to the determination of the dielectric properties of wool fibers is being investigated[2]. In one application two slotted cavities are used. One cavity contains the test specimen, the other (reference cavity) contains a composite dielectric and an H-field tuner which are calibrated and provide independent controls of the resonant frequency and Q, so that the response curve of the reference cavity can be matched to that of the cavity containing the test specimen. In a study of the effect of radiation on the dielectric properties of materials, the slot can serve as a window through which the specimen can be irradiated over its entire length, yet the high Q necessary for sensitivity can be maintained.

* Bureau of Agricultural and Industrial Chemistry, Agricultural Research Administration, U. S. Department of Agriculture.
[1] J. C. Slater, Revs. Modern Phys. **18**, 441 (1946).
[2] T. M. Shaw and J. J. Windle, J. Appl. Phys. **21**, 956 (1950).

I3. Kinetics of Ordering in AuCu Alloys.* G. C. KUCZYNSKI AND R. HOCHMAN, *University of Notre Dame.*—Gold copper alloys corresponding to almost the exact composition AuCu were disordered at 415°, 440°, and 650°C for twenty hours. Subsequently, the samples were water quenched and ordered isothermally at various temperatures below 400°C. Electrical resistivity measurements and x-ray and metallographic examination revealed the following: (1) The faster the ordering process, the higher was the disordering temperature. The samples disordered at lower temperatures (415°, 440°C) exhibited long induction periods when ordered at temperatures close to 400°C. (2) It has been found that there are two temperature zones defined by two sharply different mechanisms of transformation. *Zone A* extends from 360° to 405°C. The ordering in this zone is a function of nucleation only and its rate increases with decreasing temperature. The resulting structure contains plates of an ordered phase readily observable under a microscope. These plates form and propogate in an extremely short time (a fraction of a second). *Zone B* contains all temperatures below 375°C. The rate of ordering in this zone decreases with decreasing ordering temperatures. An analysis of the electrical resistivity *versus* time curves reveals that this phase also is nucleated but its growth is slow.

* Work supported by the U. S. Army Office of Ordnance Research and the Union Carbon and Carbide Company.

I4. Thermal Conductivity of Graphite. ALAN W. SMITH, *North American Aviation, Inc., Atomic Energy Research Department.*—The thermal conductivity of a number of types of graphite has been measured over the range 10°K to 300°K. The measurements were made by passing current through a sample and measuring the resulting parabolic temperature profile. The results substantiate those of Berman,[1] and Tyler and Wilson.[2] The thermal conductivity varies as $T^{2.7}$ in some samples at low temperatures while the specific heat varies as T^3. An increase in conductivity with increased crystallite size is observed. However, it is to be emphasized that, due to uncertain orientation and density corrections as well as the anomalous temperature dependence of the conductivity, determinations of crystallite size from thermal conductivity are apt to be entirely erroneous. The effect of anisotropy of the graphite lattice is shown to alter the relationship between the thermal conductivity and the specific heat only by a geometric factor. The anomalous thermal conductivity can possibly be explained by an isotropic intergranular region if 5 to 10 percent of the total carbon is in this region. The effect of scattering by electrons is discussed and the use of brom-graphite compounds to study this effect proposed.

[1] R. Berman, Proc. Phys. Soc. (London) **A65**, 1029 (1952).
[2] W. W. Tyler and A. C. Wilson, Jr., Phys. Rev. **89**, 870 (1953).

I5. Cyclotron Resonance in Germanium Crystals. A. F. KIP, G. DRESSELHAUS, AND C. KITTEL, *Department of Physics, University of California, Berkeley.*—Cyclotron resonance has been observed[1] in n- and p-type germanium crystals near 4°K near 9000 Mc and 24 000 Mc. The conduction electrons or holes are curved in spiral orbits by the application of a static magnetic field. The angular frequency of the orbits is given by $\omega = eH/m^*c$, where m^* is the effective mass of the carrier. Resonance absorption of energy occurs when the applied frequency is equal to the frequency of the orbits. In n-Ge the effective mass is $m^*/m = 0.1$; in p-Ge two resonances are observed, corresponding to $m^*/m = 0.04$ and 0.3. The effective mass found for n-Ge accounts approximately for the anomalous infrared absorption reported by Fan and Becker.[2] The cyclotron resonances have been observed under conditions of both thermal ionization and rf induced carrier multiplication.

[1] Dresselhaus, Kip, and Kittel, Phys. Rev. **92**, 827 (1953).
[2] *Semiconducting Materials* (Butterworths Scientific Publications, London, 1951).

I6. Electron-Spin Resonance Absorption in Bulk and Dispersed Lithium and Sodium. G. FEHER AND T. W. GRISWOLD,* *Department of Physics, University of California, Berkeley.*—Electron spin resonance has been observed in plates of lithium and sodium thick in comparison with a skin depth. According to unpublished calculations by Dyson, the absorption line shape is expected to depend on the ratio T_D/T_2, where T_D is the time associated with diffusion of conduction electrons out of the skin depth, and T_2 is the spin relaxation time. The line shape was observed to vary as expected with the ratio T_D/T_2, which varies with temperature and frequency. This effect demonstrates unequivocably that the resonance is caused by conduction electrons. The g values, as determined by direct comparison with a free radical, are: Li, 2.002 ± 0.001; Na, 2.001 ± 0.001. When the particle size is less than the skin

depth, the line width is a direct measure of the intrinsic relaxation time. The intrinsic width between absorption inflection points is, at room temperature and 300 Mc, approximately 5 oersteds in lithium and 10 oersteds in sodium. With decreasing temperature the width increases in lithium and decreases in sodium.

* Now at Hughes Aircraft Company.

I7. Pure Rotational Spectra of the Alkali Halides. A. HONIG,* M. MANDEL, M. L. STITCH,† AND C. H. TOWNES, *Columbia University.*—The pure rotational spectra of most of the alkali halides have been observed using a high-temperature microwave spectrometer[1] operating at temperatures up to 900°C. Internuclear distances, vibration-rotation interactions, and mass ratios of the stable isotopes of the alkali and halogen nuclei have been determined with great accuracy. In several of the lighter molecules, electric quadrupole coupling constants and electric dipole moments have been measured. In the cases of LiBr and LiI, it has been found possible to estimate the amount of ionic character of the bond by comparing the mass ratio of the Li^6 and Li^7 isotopes determined by nuclear reaction methods with the mass ratio determined from the rotational constants in this present work. The discrepancy indicates the proportion of time the Li valence electron spends at the halogen. Figures of $77\pm3\%$ percent, and $75\pm3\%$ percent ionic character have been obtained for LiBr and LiI, respectively. It has also been possible to determine the first four coefficients in the Dunham[2] expansion of the potential, $V[(r-r_e)/r_e]$, for many of the molecules investigated, provided information concerning the vibrational spectra is available.

* Now with the Department of Physics, University of California, Berkeley, California.
† Now with Varian Associates, Palo Alto, California.
[1] Stitch, Honig, and Townes, Phys. Rev. **86**, 813 (1952).
[2] J. L. Dunham, Phys. Rev. **41**, 721 (1932).

I8. Formation Energy of Vacancies in Copper. C. J. MEECHAN AND R. R. EGGLESTON, *Atomic Energy Research Department, North American Aviation, Inc.*—The electrical resistance of a pure copper wire has been measured as a function of temperature from 0°C to 950°C. The experimental data between 160°C and 500°C were fitted by the empirical expression $R=R_0(1+\alpha T+\beta T^2)$, which gave an adequate fit within the experimental error up to 600°C. Above 600°C, the resistance values exceed the extrapolated curve by an amount ΔR which has the following temperature dependence: $\Delta R=A\exp(-E/kT)$. Because of the Boltzman temperature dependence, this excess resistance is attributed to the presence of vacant lattice sites existing in thermal equilibrium at the high temperatures. By plotting $\ln\Delta R$ *vs* $(1/T)$, a formation energy for vacancies in copper of 0.90 ± 0.05 ev was obtained. This paper is based on studies made for the U. S. Atomic Energy Commission.

I9. The Specific Heat of the Alloy $FeNi_3$ and of a Sigma Phase FeCr. DAVID S. BLOOM, *Michelson Laboratory, U. S. Naval Ordnance Test Station.*—The specific heat of a sigma-phase alloy FeCr and of the alloy $FeNi_3$, which is considered to undergo an order-disorder reaction, has been measured in the range from 0 to 1000°C. Some unexpected complications were observed.

I10. Measurements of the Rittenger's Number for Glass and Decomposed Granite. M. E. BACKMAN AND H. L. MORRISON, *Michelson Laboratory, U. S. Naval Ordnance Test Station.*—An important parameter in the study of the breaking of brittle materials is Rittenger's number,[1] the ratio of the increase in area to the energy put into the crushed sample. Measurements have been made of Rittenger's number for glass and decomposed granite. A Gross and Zimmerley[2] type impact crusher was used for the measurement of the breaking energy. Measurements of the new surface were by permeabilities after the method of Terzaghi.[3] Three-mm glass beads were crushed to give a value of 10.5 sq cm/kg cm$\pm$4 percent. Sifted decomposed granite of two sizes was used. The first size passed a No. 5 sieve and was retained on No. 8 and the other passed through the No. 8 and was retained on a No. 14 sieve. Both of these sizes gave the same Rittenger's number, 33.6 sq cm/kg cm$\pm$3 percent.

[1] P. R. von Rittenger, *Lehrbuch der Aufbereitungskunde* (Berlin, 1867).
[2] J. Gross and S. R. Zimmerley, Am. Inst. Mining Met. Engrs. Tech. Pub. No. 126 (1928).
[3] M. Muskat, *The Flow of Fluids through Porous Media* (J. W. Edwards, Inc., Ann Arbor, Michigan, 1946).

I11. Aging of Evaporated Silver Films. W. F. KOEHLER, *Michelson Laboratory, U. S. Naval Ordnance Test Station.*—Precise measurements of the reflectance and the change in phase upon reflection as a function of wavelength and age will be presented to reveal some interesting aging effects of evaporated silver films.

I12. Coloring and Bleaching of Alkali Halide Crystals Containing *U* Centers. R. S. ALGER, *U. S. Naval Radiological Defense Laboratory.*—Additional evidence regarding the role of traps in gamma-ray coloring and optical bleaching has been obtained by comparing crystals with and without *U* centers. Measurements of energy storage efficiency and *F*-center equilibrium concentration support the hypothesis that colorability is largely controlled by the type and availability of electron traps. Storage efficiency varies with temperature, increases with vacancy or *U*-center concentration and trap depth while equilibrium concentration increases with exposure rate. Under *F*-band illumination the *F* centers in both plane and *U*-centered crystals exhibit an initial period of rapid bleaching followed by a long slow bleaching period indicating that all *F* centers do not bleach with equal ease. Interrupting the bleaching of *U*-centered crystals by storage in the dark reinstates the higher bleaching rate. The slow rate is strongly temperature dependent, and varies slightly with light intensity or *U*-center concentration. If an *F*-center electron combines with a hydrogen atom and a vacancy in the *F*- to *U*-center reaction, the reaction rate appears to depend on the availability of hydrogen in the vicinity of vacancies. Favorably located hydrogens would be depleted during the initial rapid bleaching period while the slow bleaching depends on the speed with which hydrogens and vacancies reach favorable locations.

I13. Influence of Deuteron Bombardment and Strain Hardening on Mild Steel. ROBERT A. MEYER, *U. S. Naval Radiological Defense Laboratory.*—Schnadt-type impact specimens of mild steel were irradiated with 18.6-Mev deuterons from the purpose of studying the influence of radiation on the brittle property as measured by the change in transition temperature. The effect was compared with that of two, five, and ten percent strain hardening. Micro-hardness studies were made to determine the extent and location of the radiation effect. An integrated flux of 29.5 microampere-hr per cm^2 shifted the transition temperature from -1°C to 18°C. The embrittling action was not a linear function of dose. Hardness was increased from 180 to 264 Knoop numbers. It was found to depend on the depth of penetration as well as the integrated flux. While radiation caused an effect similar to strain hardening, the nature of this effect was different. Annealing studies showed recovery of the irradiated material occurred between 260°C and 480°C. An interstitial vacancy diffusion process was indicated. Activation energies increased as recovery progressed. Recovery of the five percent strain hardened material occurred between 316°C and 372°C and would appear to be grain boundary relaxation.

SUPPLEMENTARY PROGRAMME

SP1. Nuclear Spins of Mo^{95} and Mo^{97}.* ERVIN C. WOODWARD, JR.,† *Department of Physics, University of California, Berkeley.*—Because of the inconclusiveness of previous data[1,2] on the nuclear spins of Mo^{95} and Mo^{97}, especially separated isotopes of these two mass numbers‡ were employed in a modified Schüler hollow-cathode discharge tube with a Fabry-Perot etalon in conjunction with a large prison spectrograph, to obtain hyperfine structure patterns of spectral lines representing the transitions MoI ($4d^55s\ {}^6S_3 - 4d^55p\ {}^6P_{12\frac{1}{2}}$) and MoI ($4d^45s^2\ {}^5Do - 4d^45p\ {}^5P_1$). The appearance of the respective patterns of the two isotopes was very similar. The hyperfine structure of the $4d^55s\ {}^6S_2$ state is normal, indicating in this case that both isotopes possess negative nuclear magnetic moments. Comparison of the observed hyperfine structure patterns with calculated patterns shows that the nuclear spin of both isotopes are 5/2. The nuclear spin value of 5/2 together with a negative magnetic moment for these two isotopes is in agreement with predicted values based on the shell model of the nucleus. The ratio of the nuclear magnetic moments of Mo^{97} to that of Mo^{95} is 1.022, in good agreement with the ratio obtained using nuclear induction techniques.[3]

* To be called for at the end of Session H if the Chairman rules that time permits.

† Now at Radiation Laboratory, University of California, Livermore, California.

[1] N. S. Grace and K. R. More, Phys. Rev. **45**, 166 (1935).

[2] O. H. Arroe, Phys. Rev. **79**, 212 (1950).

‡ Especially separated isotopes kindly supplied by Isotope Research and Production Division, Y-12 Research Laboratories of the Union Carbide and Carbon Corporation, Oak Ridge, Tennessee.

[3] W. G. Proctor and F. C. Yu, Phys. Rev. **81**, 20 (1951).

Author Index to Papers Presented at the Stanford Meeting

Abell, D. F. and W. D. Knight—A2
Alger, R. S.—I12
Anderson, A. B. C.—F9
Anderson, J. D., C. A. McDonald, Jr., and R. F. Post—G7
Backman, M. E. and H. L. Morrison—I10
Baez, A. V. and M. Weissbluth—B6
Bandel, H. W.—C7
Barber, W. C.—B4
Beard, David Breed—H4
Bloch, Felix—D1
Bloom, Arnold and Dolan Mansir—A8
Bloom, David S.—I9
Brode, Robert B.—G4
Brown, Sanborn C.—C3
Caldwell, David O., J. Reginald Richardson, and Herbert N. Royden—B2
Ch'en, Shang-Yi and William J. Parker—F13
Coensgen, F. H.—G8
Cohen, Victor W., Noel R. Corngold, and Norman F. Ramsey—A6
Condit, Richard I.—F5
Conger, R. L. and L. E. Schilberg—B7
Cooper, Duane H., David C. Oakley, and Robert L. Walker—H7
Cotts, R. M. and W. D. Knight—A1
Davis, Leverett, Jr.—G5
Dolan, W. W., W. P. Dyke, J. K. Trolan, and J. P. Barbour—C5
Dudziak, Walter F. and Ryokichi Sagane—G10
Efremov, N.—F3
Elsken, R. H. and T. M. Shaw—B9
English, W. N.—F6
Feher, G. and T. W. Griswold—I6
Glass, Neel W. and J. Reginald Richardson—B3
Guth, Eugene—E4
Hahn, Erwin—D4
Henderson, Joseph E.—C2
Hendrick, Roy W., Jr.—B5
Hendricks, C. D., Jr., M. E. Van Valkenburg, W. G. Clay, and R. A. Davidson—I1
Herring, Conyers—C1
Honig, A., M. Mandel, M. L. Stitch, and C. H. Townes—I7
Huber, Elsa L.—H5
Hudson, A. M. and F. X. Roser—B1
Jeffries, Carson—E2
Johnson, M. H. and E. Teller—G3
Jungerman, J. and H. Steiner—H3
Kenney, Robert W., John M. Dudley, and Charles A. McDonald, Jr.—H13
Kip, A. F., G. Dresselhaus, and C. Kittel—I5
Knight, W. D.—E3
Koehler, W. F.—I11
Kreger, W. E. and L. McIsaac—B8
Kuczynski, G. C. and R. Hochman—I3
Lee, Chu Jui and S. Leroy Brown—F7
Linlor, W. I. and B. Ragent—H11
Mackin, R. J., Jr., W. B. Mims, and W. R. Mills—H9
Maunsell, C. D.—C4
McDonald, C. A., Jr., R. W. Kenney, and R. F. Post—H14
McGarvey, B. R. and H. S. Gutowsky—A4
Meechan, C. J. and R. R. Eggleston—I8
Meyer, Robert A.—I13
Meyerhof, W. E. and G. Lindstrom—H1
Miller, Frank N.—F4
Morrison, H. L. and G. J. Plain—F2
Moszkowski, S. A. and D. C. Peaslee—A9
Oakley, D. C., R. L. Walker, J. G. Teasdale and J. I. Vette—H2
Packard, Martin, and Russell Varian—A7
Pake, G. E.—E1
Panofsky, Wolfgang K. H.—G14
Peter, Simon—A5
Peterson, R. W., C. A. Barnes, W. A. Fowler, and C. C. Lauritsen—H10
Pound, R. V.—D3
Ragent, B. and W. I. Linlor—H12
Ramsey, N. F.—D2
Ravenhall, D. G., D. R. Yennie, and R. N. Wilson—G12
Reagan, Daryl—G1
Ross, S. W., E. Tochilin, and B. W. Shumway—F1
Sagane, Ryokichi and Walter F. Dudziak—G9
Sherburne, R. K. and J. S. Arnold—F11
Smaller, B., E. Yasaitis, and M. Brochman—A3
Smith, Alan W.—I4
Tannenwald, L. M.—F8
Teller, E. and M. H. Johnson—G2
Thirion, Jacques, and Valentine L. Telegdi—H8
Tollestrup, A. V. and W. A. Wentzel—H6
Volkoff, G. M.—D5
Warren, Roger W.—C6
Willig, F. J.—F10
Wilson, R. N.—G13
Windle, J. J. and T. M. Shaw—I2
Wodruff, Truman O.—F14
Woodward, Ervin C., Jr.—G6, SP1
Yennie, D. R., R. N. Wilson, and D. G. Ravenhall—G11
Zwicky, F.—F12